Transactions of the ASME®

Transactions of the ASME, Journal of Heat Transfer (ISSN 0222-1481) is published quarterly (Feb., May, Aug., Nov.) by The American Society of Mechanical Engineers, Three Park Avenue, New York, NY 10016. Periodicals postage paid at New York, NY and additional mailing offices. POSTMASTER: Send address changes to Transactions of the ASME, Journal of Heat Transfer, c/o THE AMERICAN SOCIETY OF MECHANICAL ENGINEERS, 22 Law Drive, Box 2300, Fairfield, NJ 07007-2300.
CHANGES OF ADDRESS must be received at Society headquarters seven weeks before they are to be effective. Please send old label and new address.
 INDEXED by Applied Mechanics Reviews and Engineering Information, Inc. Canadian Goods & Services Tax Registration #126148048.

Journal of Heat Transfer

Published Quarterly by The American Society of Mechanical Engineers

VOLUME 122 • NUMBER 2 • MAY 2000

TECHNICAL PAPERS

(Contents continued on inside back cover)

This journal is printed on acid-free paper, which exceeds the ANSI Z39.48-1992 specification for permanence of paper and library materials. ♾™
♻ 85% recycled content, including 10% post-consumer fibers.

TECHNICAL NOTES

DISCUSSION

LETTER TO THE EDITOR

ERRATUM

ANNOUNCEMENTS AND SPECIAL NOTES

M. A. Al-Nimr
e-mail: malnimr@just.edu.jo

M. Naji

Mechanical Engineering Department,
Jordan University of Science and Technology,
Irbid 22110, Jordan

V. S. Arbaci
Department of Mechanical Engineering
and Applied Mechanics,
The University of Michigan,
Ann Arbor, MI 48109

Nonequilibrium Entropy Production Under the Effect of the Dual-Phase-Lag Heat Conduction Model

In the present work, the nonequilibrium entropy production under the effect of the dual-phase-lag heat conduction model is investigated. It is shown that the entropy production cannot be described using the classical form of the equilibrium entropy production where using this form leads to a violation for the thermodynamics second law. The effect of the phase-lags in temperature and in heat flux on the nonequilibrium entropy production is investigated. Also, the difference between the equilibrium and the nonequilibrium temperatures under the effect of the dual-phase-lag heat conduction model is studied.
[S0022-1481(00)01502-4]

Keywords: Conduction, Heat Transfer, Heat Waves, Microscale, Nonequilibrium, Thermodynamics

Introduction

For situations involving very low temperatures near absolute zero, a heat source, such as a laser or microwave with extremely short duration or very high frequency, a very high temperature gradient, and extremely short times, heat is found to propagate at a finite speed. To account for the phenomena involving the finite propagation velocity of the thermal wave, the classical Fourier heat flux model should be modified. Cattaneo [1] and Vernotte [2] suggested independently a modified heat flux model in the form of

$$\mathbf{q}(t+\overline{\tau},\mathbf{r})=-k\nabla T(t,\mathbf{r}). \tag{1}$$

The constitution law of Eq. (1) assumes that the heat flux vector (the effect) and the temperature gradient (the cause) across a material volume occur at different instants of time and the time delay between the heat flux and the temperature gradient is the relaxation time $\overline{\tau}$. The first-order expansion of $\mathbf{q}$ in Eq. (1) with respect to t bridges all the physical quantities at the same time. It results in the expansion

$$\mathbf{q}(t,\mathbf{r})+\overline{\tau}\frac{\partial \mathbf{q}}{\partial t}(t,\mathbf{r})=-k\nabla T(t,\mathbf{r}). \tag{2}$$

In Eq. (2) it is assumed that $\overline{\tau}$ is small enough so that the first-order Taylor expansion of $\mathbf{q}(t+\overline{\tau},\mathbf{r})$ is an accurate representation for the conduction heat flux vector. The equation of energy conservation for such problems is given as

$$\rho c\frac{\partial T}{\partial t}=-\nabla\cdot\mathbf{q}+g. \tag{3}$$

Elimination of $\mathbf{q}$ between Eqs. (2) and (3) leads to the classical hyperbolic heat conduction equation

$$\frac{1}{\alpha}\frac{\partial T}{\partial t}+\frac{\overline{\tau}}{\alpha}\frac{\partial^2 T}{\partial t^2}=\nabla^2 T+\frac{g}{k}+\frac{\overline{\tau}}{k}\frac{\partial g}{\partial t}. \tag{4}$$

To remove the precedence assumption made in the thermal wave model, as proposed in Eq. (1), the dual-phase-lag model is proposed ([3–5]). The dual-phase-lag model allows either the temperature gradient (cause) to precede the heat flux vector (effect) or the heat flux vector (cause) to precede the temperature gradient (effect) in the transient process. Mathematically, this can be represented by ([3–5])

$$\mathbf{q}(t+\overline{\tau}_q,\mathbf{r})=-k\nabla T(t+\overline{\tau}_T,\mathbf{r}). \tag{5}$$

For the case of $\overline{\tau}_T>\overline{\tau}_q$, the temperature gradient established across a material volume is a result of the heat flow, implying that the heat flux vector is the cause and the temperature gradient is the effect. For $\overline{\tau}_T<\overline{\tau}_q$, on the other hand, heat flow is induced by the temperature gradient established at an earlier time, implying that the temperature gradient is the cause, while the heat flux vector is the effect. The first-order approximation of Eq. (5) yields

$$\mathbf{q}(t,\mathbf{r})+\overline{\tau}_q\frac{\partial \mathbf{q}}{\partial t}(t,\mathbf{r})=-k\left\{\nabla T(t,\mathbf{r})+\overline{\tau}_T\frac{\partial}{\partial t}[\nabla T(t,\mathbf{r})]\right\}. \tag{6}$$

Elimination of $\mathbf{q}$ between Eqs. (3) and (6) leads to the heat conduction equation under the dual-phase-lag effect

$$\frac{1}{\alpha}\frac{\partial T}{\partial t}(t,\mathbf{r})+\frac{\overline{\tau}_q}{\alpha}\frac{\partial^2 T}{\partial t^2}(t,\mathbf{r})=\nabla^2 T(t,\mathbf{r})+\overline{\tau}_T\frac{\partial}{\partial t}[\nabla^2 T(t,\mathbf{r})]+\frac{1}{k}\left[g+\overline{\tau}_q\frac{\partial g}{\partial t}(t,\mathbf{r})\right]. \tag{7}$$

In the absence of the temperature gradient phase-lag ($\overline{\tau}_T=0$), Eq. (7) reduces to the classical hyperbolic heat conduction equation as described by Eq. (4). Also, in the absence of the two phase-lags ($\overline{\tau}_T=\overline{\tau}_q=0$), Eq. (7) reduces to the classical diffusion equation employing Fourier's law.

Investigation of the entropy production under the effect of the classical hyperbolic heat conduction model has motivated different researchers ([6–15]). Due to the phase-lag between the heat flux and the temperature gradient in the Cattaneo and Vernotte and in the dual-phase-lag constitution laws, the entropy production cannot be derived from the concept of local-equilibrium entropy as presented by the fundamentals of classical thermodynamics. When the assumption of local equilibrium is relaxed, the concepts of entropy and temperature in nonequilibrium will be changed. The concepts of nonequilibrium entropy and temperature have been investigated by different workers ([7–8,10–12,15]) and discussed in different references ([9,14]). The behavior of entropy in the classical hyperbolic heat conduction model has been investigated in ([8–10,14–15]).

Contributed by the Heat Transfer Division for publication in the JOURNAL OF HEAT TRANSFER. Manuscript received by the Heat Transfer Division, June 29, 1999; revision received, Jan. 10, 2000. Associate Technical Editor: D. Zumbrunnen.

Up to the authors' knowledge, the nonequilibrium entropy production under the effect of the dual-phase-lag heat conduction model is not yet investigated. In the present work, we will investigate the entropy production, based on the equilibrium and the nonequilibrium thermodynamics concepts, under the effect of the dual-phase-lag heat conduction model. Also, we will investigate the effect of the phase-lag concept on the equilibrium and the nonequilibrium entropy production and on the difference between the equilibrium and the nonequilibrium temperatures. A case study will be presented to demonstrate these effects.

Analysis

According to the extended irreversible thermodynamics, the generalized nonequilibrium entropy s^* is given as ([15])

$$s^*(u,v,\mathbf{q}) = s(u,v) - \frac{\overline{\alpha}}{2}\mathbf{q}\cdot\mathbf{q} \tag{8}$$

where $\overline{\alpha}$ is given as ([15])

$$\overline{\alpha} = \frac{\overline{\tau}_q}{\rho k T^{*2}}. \tag{9}$$

Equation (8) is an expansion of second-order approximation in $\mathbf{q}$ for the deviation of the nonequilibrium entropy from the equilibrium entropy. This expansion is obtained from the extended irreversible thermodynamics which assumes that the thermodynamic fluxes are independent variables of the system in addition to the classical variables such as the specific internal energy and specific volume.

As a result, the nonequilibrium entropy does not depend only on u and v but also on $\mathbf{q}$. It is clear that Eq. (8) is no more valid in applications involving very high heat fluxes. To account for these applications, one has to use higher order expansion around $\mathbf{s}$. It is worth noting here that applications that involve very fast and high heating rates must be modeled using the microscopic two-step heat conduction model ([13]). Also, note that the coefficient $\overline{\alpha}$ in Eq. (8) may be evaluated under local equilibrium conditions.

In Eq. (9), T^* is the nonequilibrium temperature which differs from the equilibrium one by the following relation ([15]):

$$\frac{1}{T^*} = \frac{1}{T} - \frac{1}{2}\frac{\partial\overline{\alpha}}{\partial u}\mathbf{q}\cdot\mathbf{q}. \tag{10}$$

Now, Eq. (8) is differentiated to yield

$$ds^* = ds - \overline{\alpha}\mathbf{q}\cdot d\mathbf{q}. \tag{11}$$

For incompressible materials,

$$ds = \frac{du}{T^*}. \tag{12}$$

Also, consider the energy equation

$$\rho\frac{du}{dt} = -\nabla\cdot\mathbf{q} + g. \tag{13}$$

Substitute for du/dt from (13) into (12) to yield

$$\frac{ds}{dt} = \frac{1}{\rho T^*}(-\nabla\cdot\mathbf{q} + g) \tag{14}$$

and substitute for ds/dt from (14) into (11), after dividing (11) by dt, to yield

$$\frac{ds^*}{dt} = \frac{1}{\rho T^*}(-\nabla\cdot\mathbf{q} + g) - \overline{\alpha}\mathbf{q}\cdot\frac{d\mathbf{q}}{dt}. \tag{15}$$

The nonequilibrium entropy production is given as

$$\sigma^* = \rho\frac{ds^*}{dt} + \nabla\cdot\left(\frac{\mathbf{q}}{T^*}\right). \tag{16}$$

Substitute for ds^*/dt from (15) into (16), yields

$$\sigma^* = \frac{g}{T^*} - \frac{\mathbf{q}}{T^{*2}}\cdot\left(\nabla T^* + \frac{\overline{\tau}_q}{k}\dot{q}\right). \tag{17}$$

Now, rewrite the dual-phase-lag constitution law (6) in terms of the nonequilibrium temperature T^* and substitute for $\nabla T^* + (\overline{\tau}_q/k)\dot{q}$ from Eq. (6) into Eq. (17) to yield

$$\sigma^*(t,\mathbf{r}) = \frac{g(t,\mathbf{r})}{T^*(t,\mathbf{r})} + \frac{\mathbf{q}(t,\mathbf{r})}{T^{*2}(t,\mathbf{r})}\cdot\left[\frac{\mathbf{q}(t,\mathbf{r})}{k} + \overline{\tau}_T\frac{\partial}{\partial t}(\nabla T^*(t,\mathbf{r}))\right]. \tag{18}$$

For most practical operating conditions, the difference between the equilibrium and the nonequilibrium temperatures may be neglected, and as a result, $T(t,\mathbf{r}) = T^*(t,\mathbf{r})$.

To show that the difference between T and T^* is not significant, rewrite Eq. (10) in the form

$$\frac{T - T^*}{T^*} = -\frac{T}{2}\frac{\partial\overline{\alpha}}{\partial u}q^2 \tag{19}$$

and for constant thermal properties,

$$\frac{\partial\overline{\alpha}}{\partial u} = \frac{1}{c}\frac{\partial\overline{\alpha}}{\partial T} = -\frac{2\overline{\tau}_q}{c\rho k T^3}. \tag{20}$$

Substitute for $\partial\overline{\alpha}/\partial u$ from (20) into (19) to yield

$$\frac{T - T^*}{T^*} = \frac{\overline{\tau}_q}{c\rho k}\left(\frac{q}{T}\right)^2. \tag{21}$$

For most practical materials, $\overline{\tau}_q$ is of order of picoseconds, q and T have the same order of magnitude, and $c\rho k \gg 1$. As a result

$$\frac{T - T^*}{T^*} \ll 1. \tag{22}$$

Hence, Eq. (18) is rewritten as

$$\sigma^*(t,\mathbf{r}) = \frac{g(t,\mathbf{r})}{T(t,\mathbf{r})} + \frac{\mathbf{q}(t,\mathbf{r})}{T^2(t,\mathbf{r})}\cdot\left[\frac{\mathbf{q}(t,\mathbf{r})}{k} + \overline{\tau}_T\frac{\partial}{\partial t}(\nabla T(t,\mathbf{r}))\right]. \tag{23}$$

In the absence of the temperature gradient phase-lag ($\overline{\tau}_T = 0$), Eq. (23) reduces to

$$\sigma^*(t,\mathbf{r}) = \frac{g(t,\mathbf{r})}{T(t,\mathbf{r})} + \frac{q^2(t,\mathbf{r})}{kT^2(t,\mathbf{r})} \tag{24}$$

which predicts the nonequilibrium entropy production under the effect of the classical hyperbolic heat conduction model. Also, in the absence of the two phase-lags ($\overline{\tau}_T = \overline{\tau}_q = 0$), Eq. (23) combined with Eq. (6) yields

$$\sigma^*(t,\mathbf{r}) = \frac{g(t,\mathbf{r})}{T(t,\mathbf{r})} + k\frac{\nabla T(t,\mathbf{r})\cdot\nabla T(t,\mathbf{r})}{T^2(t,\mathbf{r})} \tag{25}$$

which is the nonequilibrium entropy production under the effect of the classical parabolic heat conduction model. For this special case, Eq. (25) can also predict the equilibrium entropy production under the effect of the classical parabolic heat conduction model.

In contrast to the nonequilibrium entropy production form (23), the classical equilibrium entropy production has the form

$$\sigma(t,\mathbf{r}) = \frac{g(t,\mathbf{r})}{T(t,\mathbf{r})} - \frac{1}{T^2}\mathbf{q}(t,\mathbf{r})\cdot\nabla T(t,\mathbf{r}). \tag{26}$$

In both expressions for σ^* and σ, we need an expression for $\mathbf{q}(t,\mathbf{r})$ in terms of $T(t,\mathbf{r})$. This expression is obtained directly after integrating Eq. (6) to yield

$$\mathbf{q}(t,\mathbf{r}) = \mathbf{q}(0,\mathbf{r})e^{-t/\overline{\tau}_q} + k\frac{\overline{\tau}_T}{\overline{\tau}_q}e^{-t/\overline{\tau}_q}\nabla T(0,\mathbf{r}) - k\frac{\overline{\tau}_T}{\overline{\tau}_q}\nabla T(t,\mathbf{r}) - \frac{k}{\overline{\tau}_q}\left(1 - \frac{\overline{\tau}_T}{\overline{\tau}_q}\right)\cdot\int_0^t e^{-(t-v)/\overline{\tau}_q}\nabla T(v,\mathbf{r})dv. \tag{27}$$

As a result of Eq. (27), it is clear that the equilibrium and the nonequilibrium entropy production, under the effect of the dual-phase-lag heat conduction model, depends on the accumulation in the gradient of temperature with respect to time. This implies that the history of T (and ∇T) has a significant effect on the equilibrium and the nonequilibrium entropy. As an example, if the instantaneous value of ∇T is zero, the nonequilibrium entropy production will not vanish due to the previous accumulation in ∇T. The history of ∇T plays a significant effect on σ^* but this effect decreases as time proceeds. Also, it is clear from Eqs. (23) and (26) that the dual-phase-lag concept has more significant effect on σ^*, due to the presence of $\mathbf{q}\cdot\mathbf{q}$, as compared to its effect on σ, due to the presence of $\mathbf{q}$ alone. Also, it is clear from Eq. (25) that the entropy production under the effect of the parabolic energy equation is directly proportional to ∇T. For this case, history of ∇T has nothing to do with σ^*. At the instant when ∇T diminishes, σ^* will instantaneously diminish in the absence of $g(t,\mathbf{r})$.

There is another important conclusion we may draw from Eqs. (23) and (25). It is clear from Eq. (25) that the entropy production under the effect of Fourier law is always positive. This is due to the fact that $\mathbf{q}(t,\mathbf{r})$ and $\nabla T(t,\mathbf{r})$ have always opposite signs and, as a result, their product is always positive. However, if the equilibrium expression for entropy is used to describe σ under the effect of the dual-phase-lag concept, as described by Eq. (26), there is no guarantee that $\mathbf{q}(t,\mathbf{r})$ and $\nabla T(t,\mathbf{r})$ have opposite signs. Due to the presence of the dual-phase-lags τ_q and τ_T between the heat flux and the temperature gradient, the heat flux may transfer in the direction of increasing temperature at a given instant of time and at a given location of space. As a result, the expression for equilibrium entropy production, as described by Eq. (26), may yield negative values for σ and this violates the second law of thermodynamics. This suggests that the entropy production under the effect of the dual-phase-lag model cannot be described by expressions based on local-equilibrium concepts. On the other hand, the nonequilibrium expression for entropy production (23) gives always a positive value for the entropy production.

In the following section we demonstrate different ideas developed and discussed previously by a simple case study.

Case Study

Consider a semi-infinite medium which is initially at a uniform temperature T_i. For times $t>0$ the boundary surface is kept at constant temperature T_w. Using the dimensionless parameters defined in the Nomenclature, the governing equations are given as

$$\frac{\partial\theta}{\partial\eta}+\tau_q\frac{\partial^2\theta}{\partial\eta^2}=\frac{\partial^2\theta}{\partial\xi^2}+\tau_T\frac{\partial^3\theta}{\partial\eta\partial\xi^2} \tag{28}$$

$$\theta(0,\xi)=\frac{\partial\theta}{\partial\eta}(0,\xi)=0$$

$$\theta(\eta,0)=\theta_w,\quad \theta(\eta,\infty)\to 0. \tag{29}$$

Also, the dual-phase-lag constitutive law in dimensionless form is written as

$$Q(\eta,\xi)+\tau_q\frac{\partial Q}{\partial\eta}(\eta,\xi)=-\frac{\partial\theta}{\partial\xi}(\sigma,\xi)-\tau_T\frac{\partial^2\theta}{\partial\eta\partial\xi}(\eta,\xi) \tag{30}$$

with

$$Q(0,\xi)=\frac{\partial\theta}{\partial\xi}(0,\xi)=0 \tag{31}$$

and the equilibrium and the nonequilibrium entropy production in dimensionless forms are given as

$$S(\eta,\xi)=-\frac{Q}{(\theta+1)^2}\frac{\partial\theta}{\partial\eta} \tag{32}$$

$$S^*(\eta,\xi)=\frac{Q^2}{(\theta+1)^2}+\tau_T\frac{Q}{(\theta+1)^2}\frac{\partial^2\theta}{\partial\eta\partial\xi} \tag{33}$$

and the dimensionless temperature difference between the equilibrium and the nonequilibrium temperatures is given as

$$\frac{T-T^*}{T^*}=\frac{Q^2}{(\theta+1)^2}. \tag{34}$$

Now, using Laplace transformation technique, Eqs. (28)–(31) are solved for $\theta(\eta,\xi)$, $Q(\eta,\xi)$, $\partial\theta/\partial\xi(\eta,\xi)$, and $\partial^2\theta/\partial\eta\partial\xi(\eta,\xi)$ to yield

$$\theta(\eta,\xi)=\mathcal{L}^{-1}\{w(p,\xi)\} \tag{35}$$

$$Q(\eta,\xi)=\mathcal{L}^{-1}\left\{-\left[\frac{\tau_T}{\tau_q}+\frac{\left(1-\frac{\tau_T}{\tau_q}\right)}{1+\tau_q p}\right]\frac{\partial W}{\partial\xi}\right\} \tag{36}$$

$$\frac{\partial\theta}{\partial\xi}=\mathcal{L}^{-1}\left\{\frac{\partial W}{\partial\xi}\right\} \tag{37}$$

$$\frac{\partial^2\theta}{\partial\eta\partial\xi}=\mathcal{L}^{-1}\left\{p\frac{\partial W}{\partial\xi}\right\} \tag{38}$$

where

$$W(p,\xi)=\frac{1}{p}e^{-\sqrt{\frac{p(1+\tau_q p)}{1+\tau_T p}}\xi} \tag{39}$$

$$\frac{\partial W}{\partial\xi}(p,\xi)=-\sqrt{\frac{(1+\tau_q p)}{p(1+\tau_T p)}}e^{-\sqrt{\frac{p(1+\tau_q p)}{1+\tau_T p}}\xi} \tag{40}$$

Equations (35) to (38) are inverted in terms of Riemann sum approximation as ([13])

$$F(\eta,\xi)=\frac{e^{\gamma\eta}}{\eta}\left[\frac{1}{2}\overline{F}(\gamma,\xi)+\mathrm{Re}\sum_{n=1}^{N}\overline{F}\left(\gamma+\frac{in\pi}{\eta},\xi\right)(-1)^n\right] \tag{41}$$

where $\overline{F}(p,\xi)$ is the Laplace transformation of $F(\eta,\xi)$, and for faster convergence of Eq. (41), it has been shown that γ may be obtained from ([13])

$$\gamma\eta=4.7. \tag{42}$$

In Eq. (41), $F(\eta,\xi)$ stands for $\theta(\eta,\xi)$, $Q(\eta,\xi)$, $\partial\theta/\partial\xi(\eta,\xi)$, and $\partial^2\theta/\partial\eta\partial\xi(\eta,\xi)$, and $\overline{F}(p,\xi)$ stands for Laplace transformation of $\theta(\eta,\xi)$, $Q(\eta,\xi)$, $\partial\theta/\partial\xi(\eta,\xi)$, and $\partial^2\theta/\partial\eta\partial\xi(\eta,\xi)$. Expressions for $S(\eta,\xi)$ and $S^*(\eta,\xi)$ are obtained directly from Eqs. (32) and Eq. (33).

Results and Discussion

Figure 1 shows the spatial distribution of the dimensionless temperature at different dimensionless times, and Fig. 2 shows the same spatial distribution for the dimensionless heat flux Q. Figures 3 and 4 show the effect of the dimensionless heat flux phase-lag τ_q on the spatial distribution of the temperature and the heat flux for a fixed τ_q/τ_T ratio. Due to the fact that $(\tau_q/\tau_T)<1$, increasing τ_q makes the difference $\tau_T-\tau_q$ increases. This implies that the temperature gradient (the effect) occurs at an advanced time η. This means that increasing the difference $\tau_T-\tau_q$ has the same effect as increasing η or the same effect as the advancement in the time domain. Comparing Fig. 3 with Fig. 1 and Fig. 4 with Fig. 2 verifies this conclusion.

The spatial distribution of the nonequilibrium entropy production at different times is shown in Fig. 5. As time proceeds, both the total and the maximum values of entropy decreases due to the decrease in heat flux from the boundary to the domain. Also, as time proceeds, the maximum entropy production occurs at deeper location within the semi-infinite domain.

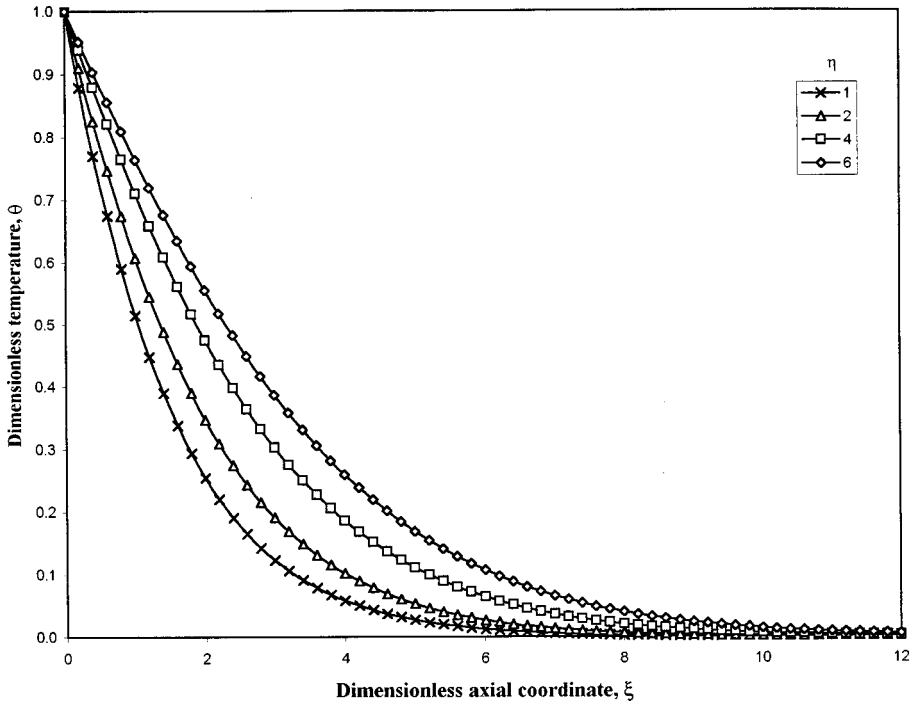

Fig. 1 Spatial distribution of the dimensionless temperature at different dimensionless times for $\tau_q=0.01$, $\tau_T=1.0$, and $\theta_w=1.0$

The effect of the dimensionless heat flux phase-lag τ_q on the spatial distribution of the nonequilibrium entropy production S^* is shown in Fig. 6. As we have mentioned previously, increasing τ_q under a fixed ratio of τ_q/τ_T has the same effect as of increasing η, and this is clear by comparing Fig. 6 with Fig. 5.

In Fig. 7, the spatial distribution of the entropy production is evaluated based on the classical equilibrium formula as described by Eq. (32). Due to the phase shift between θ and Q, we may face situations in which $\partial\theta/\partial\xi$ and Q have the same sign, i.e., we may have heat flux in the direction of increasing temperature. Such situations yield negative values for S as is clear in Fig. 7. This phenomena violates the second law of thermodynamics and implies that using the equilibrium entropy production formula to describe the thermal behavior of systems, under the effect of the dual-phase-lag model, is inadequate.

Figure 8 shows the spatial variation in the dimensionless difference between equilibrium and nonequilibrium temperatures. It is clear from this figure that in its worst conditions, this difference does not exceed 3.5 percent. As a result, neglecting the difference between equilibrium and nonequilibrium temperatures is a valid

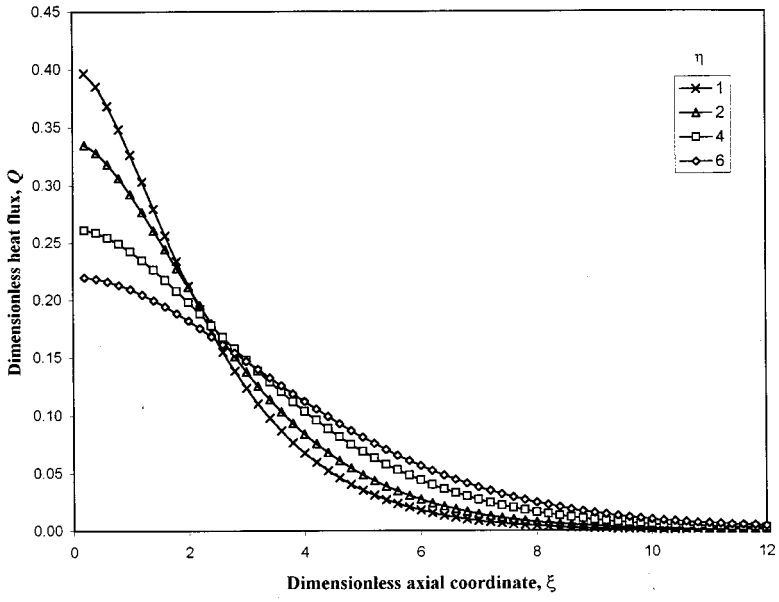

Fig. 2 Spatial distribution of the dimensionless heat flux at different dimensionless times for $\tau_q=0.01$, $\tau_T=1.0$, and $\theta_w=1.0$

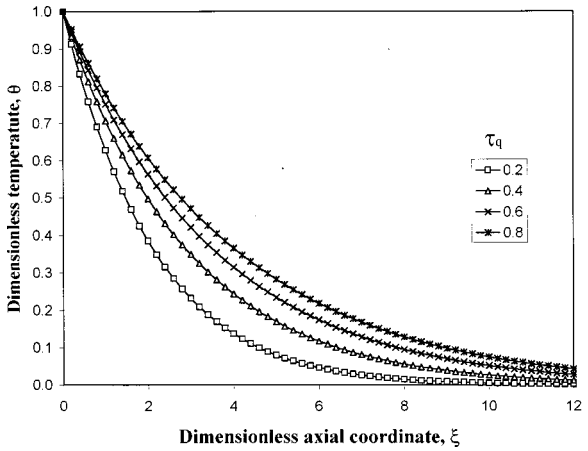

Fig. 3 Effect of the dimensionless heat flux phase-lag on the spatial distribution of the dimensionless temperature for $\eta=2$, $\tau_q/\tau_T=0.05$ and $\theta_w=1.0$

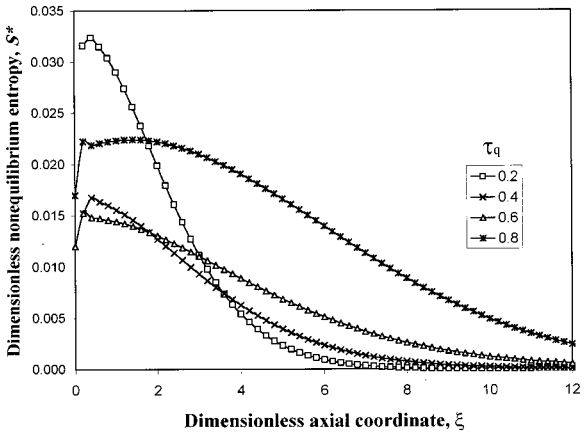

Fig. 6 Effect of the dimensionless heat flux phase-lag on the spatial distribution of the dimensionless nonequilibrium entropy production for $\eta=2$, $\tau_q/\tau_T=0.05$ and $\theta_w=1.0$

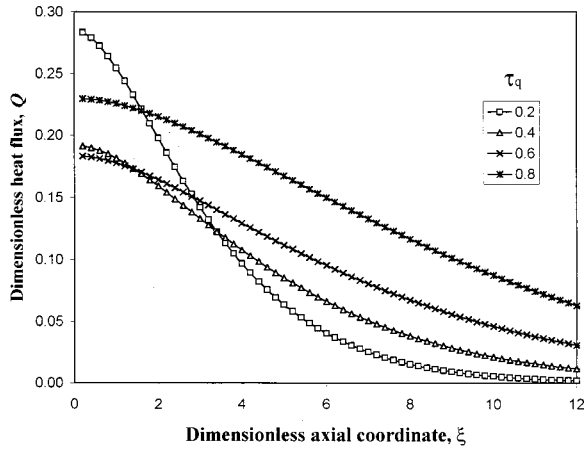

Fig. 4 Effect of the dimensionless heat flux phase-lag on the spatial distribution of the dimensionless heat flux for $\eta=2$, $\tau_q/\tau_T=0.05$ and $\theta_w=1.0$

assumption. This difference increases as the difference $\tau_T-\tau_q$, or the ratio τ_q/τ_T, increases. This is a predicted behavior since the concept of the nonequilibrium behavior in temperature is enhanced as the net phase-lag between heat flux and temperature gradient increases.

The effect of the dimensionless wall temperature on the dimensionless nonequilibrium entropy production is shown in Fig. 9. As θ_w increases, the heat flux into the semi-infinite domain increases and, as a result, the entropy production increases and the maximum entropy production is shifted towards deeper locations within the domain.

Figures 10 and 11 show a comparison between the three models: the Fouriers model, the classical hyperbolic model, and the dual-phase-lag model. Figure 10 shows this comparison for heat flux flow, and Fig. 11 shows the comparison for the nonequilibrium entropy. For both figures, the comparison is conducted at a certain instant of time and, hence, the qualitative and quantitative behavior may change at other times.

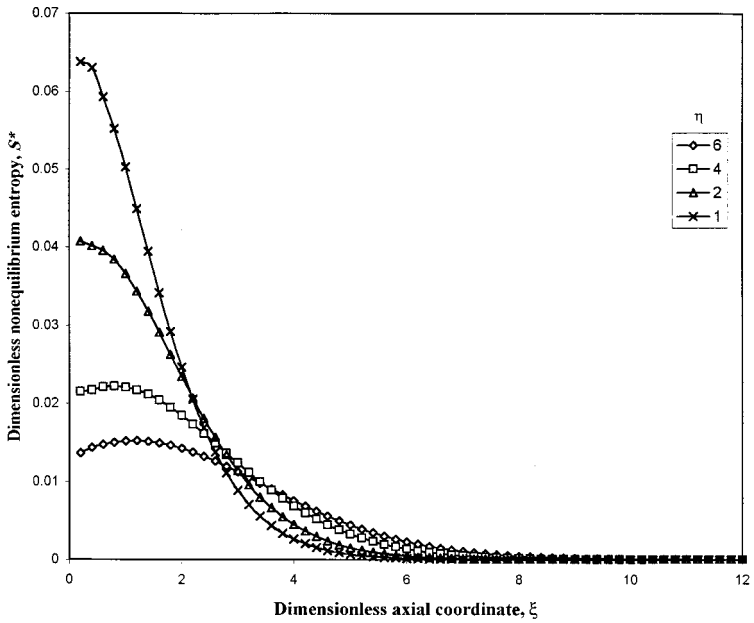

Fig. 5 Spatial distribution of the dimensionless nonequilibrium entropy production at different dimensionless times for $\tau_q=0.01$, $\tau_T=1.0$, and $\theta_w=1.0$

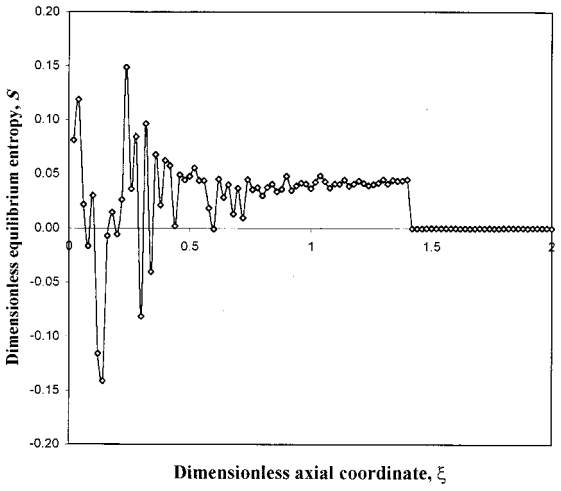

Fig. 7 Spatial distribution of the dimensionless equilibrium entropy production for $\eta=2$, $\tau_q=2$, $\tau_T=1\times10^{-8}$, and $\theta_w=1.0$

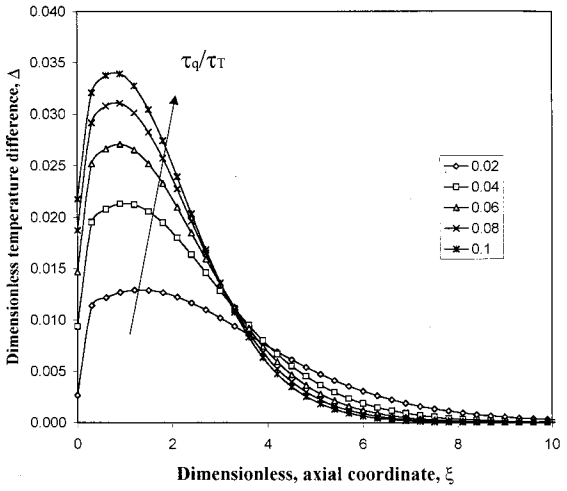

Fig. 8 Effect of the dimensionless phase-lag ratio on the spatial distribution of the dimensionless temperature difference for $\eta=2$, $\tau_q=0.1$, and $\theta_w=1.0$

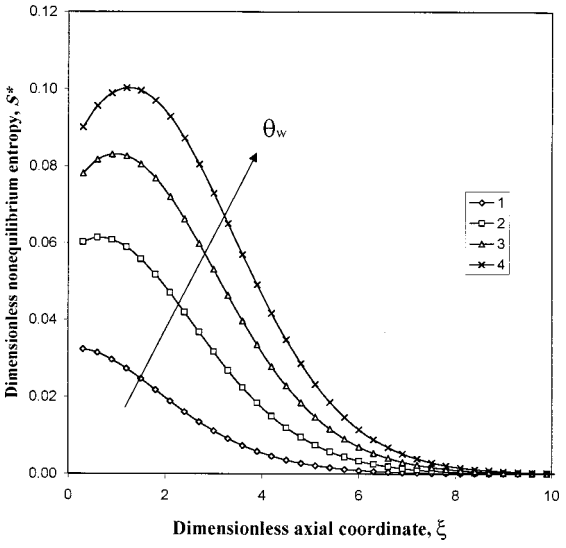

Fig. 9 Effect of the dimensionless wall temperature on the spatial distribution of the dimensionless nonequilibrium entropy production for $\eta=2$, $\tau_q=0.1$, and $\tau_q/\tau_T=0.05$

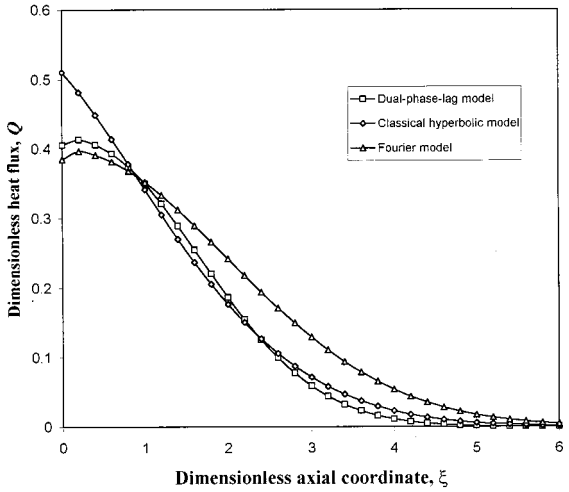

Fig. 10 Spatial distribution of the dimensionless heat flux for the three different models for $\eta=2$, $\tau=\tau_T-\tau_q=1$, $\tau_q=1$, $\tau_T=2$, and $\theta_w=1.0$

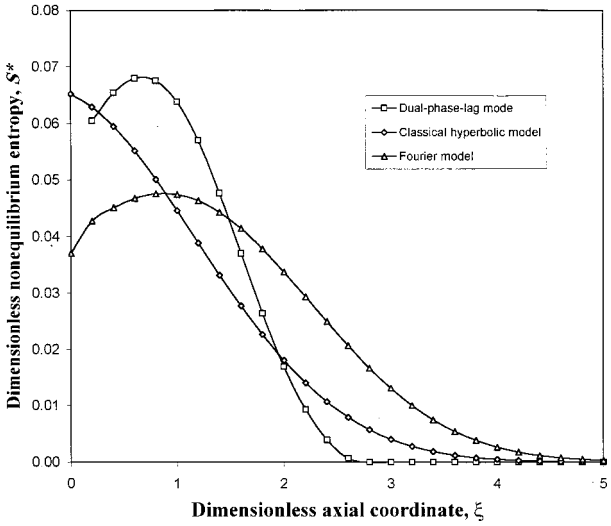

Fig. 11 Spatial distribution of the dimensionless nonequilibrium entropy production for the three different models for $\eta=2$, $\tau=\tau_T-\tau_q=1$, $\tau_q=1$, $\tau_T=2$, and $\theta_w=1.0$

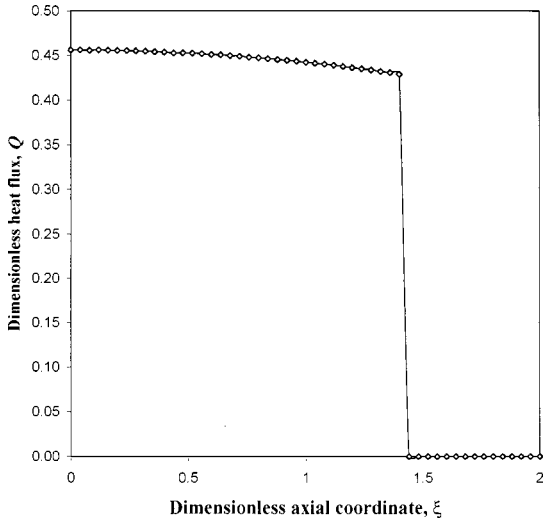

Fig. 12 Spatial distribution of the dimensionless heat flux for $\eta=2$, $\tau_q=2$, $\tau_T=1\times10^{-8}$, and $\theta_w=1.0$

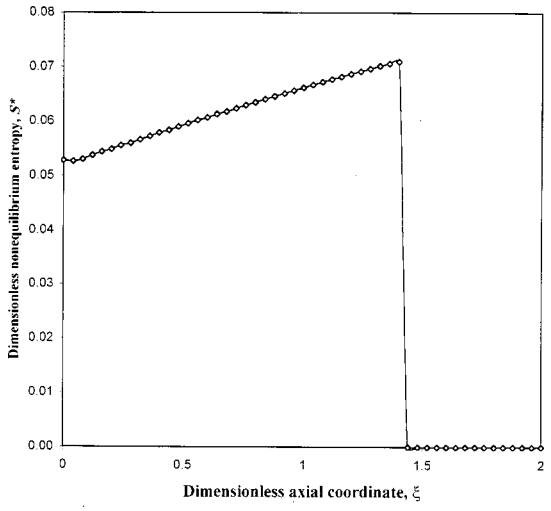

Fig. 13 Spatial distribution of the dimensionless nonequilibrium entropy production for $\eta=2$, $\tau_q=2$, $\tau_T=1\times10^{-8}$, and $\theta_w=1.0$

In Figs. 12 and 13, the spatial distribution for the dimensionless heat flux flow and nonequilibrium entropy is shown, respectively. These figures show the thermal behavior of the semi-infinite domain under the effect of the dual-phase-lag model for $\tau_T \ll \tau_q$. As is clear from these figures, the propagation of heat flux and entropy production behaves in a wavy manner. Also in both figures there is a sharp jump that defines the wave's front.

Conclusion

It is shown in this work that the entropy production under the effect of the dual-phase-lag heat conduction model cannot be described by the classical equilibrium formula. Using the classical formula yields results that violate the thermodynamics second law. The effect of dual-phase-lags in a temperature gradient and in heat flux on the spatial and temporal variation in the nonequilibrium entropy is investigated. It is shown that as the difference $\tau_T-\tau_q$ increases, the propagation of the entropy production shifts from the diffusive type to the wavy type. This is also true for the effect of $\tau_T-\tau_q$ on the temperature and on the heat flux. Also, it is shown that for most practical applications involving the dual-phase-lag model, the nonequilibrium temperature may be replaced by the equilibrium temperature. A case study is presented to demonstrate these results.

Nomenclature

c = specific heat capacity (J/kg.K)
g = heating source per unit volume (W//m^3)
k = thermal conductivity (W/m.K)
p = Laplacian domain
q = conduction heat flux (W/m^2)
Q = dimensionless conduction heat flux, $q\sqrt{\alpha t_o}/kT_i$
$\mathbf{r}$ = spacial vector (m)
s = equilibrium entropy (J/K)
s^* = nonequilibrium entropy (J/K)
S = dimensionless equilibrium entropy production, $\sigma\alpha t_o/k$
S^* = dimensionless nonequilibrium entropy production, $\sigma^*\alpha t_o/k$
t = time (s)
t_o = reference time such as $\overline{\tau_q}$ for copper (s)
T = equilibrium temperature (K)
T_i = initial temperature (K)
T_w = wall temperature (K)
T^* = nonequilibrium temperature (K)
u = specific internal energy (J/kg)
v = specific volume (m^3/kg)
x = axial coordinate (m)

Greek Symbols

α = thermal diffusivity (m^2/s)
η = dimensionless time, t/t_o
ρ = density (kg/m^3)
σ = equilibrium entropy production (W/m^3.K)
σ^* = nonequilibrium entropy production (W/m^3.K)
θ = dimensionless temperature, $T-T_i/T_i$
θ_w = dimensionless wall temperature, T_w-T_i/T_i
τ = dimensionless thermal relaxation time, $\overline{\tau}/t_o$
$\overline{\tau}$ = thermal relaxation time (s)
τ_q = dimensionless phase-lag in the heat flux vector, $\overline{\tau_q}/t_o$
τ_T = dimensionless phase-lag in the temperature gradient, $\overline{\tau_T}/t_o$
$\overline{\tau_q}$ = phase-lag in the heat flux vector (s)
$\overline{\tau_T}$ = phase-lag in the temperature gradient (s)
ξ = dimensionless axial coordinate, $x/\sqrt{\alpha t_o}$

References

[1] Cattaneo, C., 1958, ''A Form of Heat Conduction Equation Which Eliminates the Paradox of Instantaneous Propagation,'' Compte Rendus, **247**, pp. 431–433.
[2] Vernotte, P., 1961, ''Some Possible Complications in the Phenomena of Thermal Conduction,'' Compte Rendus, **252**, pp. 2190–2191.
[3] Tzou, D. Y., 1995, ''A Unified Field Approach for Heat Conduction From Micro-to Macro-Scales,'' ASME J. Heat Transfer, **117**, pp. 8–16.
[4] Tzou, D. Y., 1995, ''The Generalized Lagging Response in Small-Scale and High-Rate Heating,'' Int. J. Heat Mass Transf., **38**, pp. 3231–3240.
[5] Tzou, D. Y., 1995, ''Experimental Support for The Lagging Response in Heat Propagation,'' AIAA J. Thermophys. Heat Transfer, **9**, pp. 686–693.
[6] Brey, J., and Prados, A., 1990, ''Calculation of the Entropy From Master Equations With Time-Dependent Transient Probabilities,'' Phys. Rev. A, **42**, No. 2, p. 765.
[7] Brey, J., and Santos, A., 1992, ''Nonequilibrium Entropy of Gas,'' Phys. Rev. A (15), Statistical Physics, P, **45**, No. 12, p. 8566.
[8] Criado-Sancho, M., and Llebot, J. E., 1993, ''Behavior of Entropy in Hyperbolic Heat Conduction,'' Phys. Rev. E, **47**, No. 6, pp. 4104–4107.
[9] Jou, D., Vazquez, J. C., and Labon, G., 1993, *Extended Irreversible Thermodynamics*, Springer, Berlin.
[10] Sieniutycz, S., and Berry, R. S., 1992, ''Least-Entropy Generation: Variational Principle of Onsager's Type for Transient Hyperbolic Heat and Mass Transfer,'' Phys. Rev. A (15), Statistical Physics, P, **46**, No. 10, pp. 6359–6368.
[11] Sieniutycz, S., and Ratkje, S. K., 1996, ''Variational Principle for Entropy in Electrochemical Transport Phenomena,'' Int. J. Eng. Sci., **34**, No. 5, p. 549.
[12] Sieniutycz, S., and Beris, A. N., 1999, ''A Nonequilibrium Internal Exchange of Energy and Matter and its Onsager's-Type Variational Theory of Relaxation,'' Int. J. Heat Mass Transf., **42**, No. 14, p. 2695.
[13] Tzou, D. Y., 1997, *Macro-to-Microscale Heat Transfer—The Lagging Behavior*, Taylor and Francis, London, pp. 1–46.
[14] Vazquez, J. C., Jou, D., and Labon, G., 1984, *Recent Development in Nonequilibrium Thermodynamics*, Springer, Berlin.
[15] Vazquez, J. C., and Jou, D., 1994, ''Nonequilibrium Temperature Versus Local-Equilibrium Temperature,'' Phys. Rev. E, **49**, No. 2, pp. 1040–1048.

Film Cooling From Shaped Holes

C. M. Bell
Graduate Student

H. Hamakawa[1]
Associate Professor

P. M. Ligrani[2]
Professor, Mem. ASME
e-mail: ligrani@mech.utah.edu

Convective Heat Transfer Laboratory,
Department of Mechanical Engineering,
University of Utah,
Salt Lake City, UT 84112

Local and spatially averaged magnitudes of the adiabatic film cooling effectiveness, the iso-energetic Stanton number ratio, and film cooling performance parameter are measured downstream of (i) cylindrical round, simple angle (CYSA) holes, (ii) laterally diffused, simple angle (LDSA) holes, (iii) laterally diffused, compound angle (LDCA) holes, (iv) forward diffused, simple angle (FDSA) holes, and (v) forward diffused, compound angle (FDCA) holes. Data are presented for length-to-inlet metering diameter ratio of 3, blowing ratios from 0.4 to 1.8, momentum flux ratios from 0.17 to 3.5, and density ratios from 0.9 to 1.4. The LDCA and FDCA arrangements produce higher effectiveness magnitudes over much wider ranges of blowing ratio and momentum flux ratio compared to the three simple angle configurations tested. All three simple angle hole geometries, CYSA, FDSA, and LDSA, show increases of spanwise-averaged adiabatic effectiveness as the density ratio increases from 0.9 to 1.4, which are larger than changes measured downstream of FDCA and LDCA holes. Iso-energetic Stanton number ratios downstream of LDCA and FDCA holes (measured with unity density ratios) are generally increased relative to simple angle geometries for $m \geq 1.0$ when compared at particular normalized streamwise locations, x/D, and blowing ratios, m. Even though this contributes to higher performance parameters and lower protection, overall film cooling performance parameter $\dot{q}''/\dot{q}_o''$ variations with x/D and m are qualitatively similar to variations of adiabatic film cooling effectiveness with x/D and m. Consequently, the best overall protection over the widest ranges of blowing ratios, momentum flux ratios, and streamwise locations is provided by LDCA holes, followed by FDCA holes. Such improvements in protection are partly due to film diffusion from expanded hole shapes, as well as increased lateral spreading of injectant from compound angles. [S0022-1481(00)02202-7]

Keywords: Engines, Film Cooling, Flow, Heat Transfer, Turbines

Introduction

In recent years, designers and manufacturers of turbine components in gas turbine engines have been employing shaped holes (both with and without compound angle orientations), which produce films which provide better thermal protection than round, cylindrical holes. Such efforts have been undertaken simultaneously with only a few experimental and numerical investigations of shaped film cooling hole performance that are published in the open literature.

Existing experimental studies consider a variety of film hole geometries, including conical, diffused holes ([1]), diffused, trapezoidal shaped holes ([2]), square holes ([3]) and shaped, inclined slots ([4]). Schmidt et al. ([5]) present local and spatially averaged adiabatic film cooling effectiveness distributions measured downstream of three hole geometries with $L/D=4$: (i) round, simple angle, (ii) round, compound angle, and (iii) forward diffused, compound angle. The two compound angle arrangements give higher effectiveness magnitudes over a larger range of momentum flux ratios than the simple angle arrangement. Differences in effectiveness magnitudes are especially apparent at high momentum flux ratios and $x/D<15$, where the forward diffused holes give the highest effectiveness magnitudes. Sen et al. [6] present local and spatially averaged iso-energetic Stanton number ratio distributions measured downstream of the same three hole geometries. The two compound angle arrangements give higher spatially averaged Stanton number ratios at momentum flux ratios from 0 to 4. Overall spatially averaged performance parameters measured downstream of the three hole geometries are about same for momentum flux ratios less than about 1.0; however, the best performance at higher momentum flux ratios is produced by the forward diffused, compound angle holes.

Haven and Kurosaka [7] examine film lift-off and present velocity and vorticity distributions downstream of several different hole shapes. According to these authors, film hole vorticity is the source of the counterrotating vorticies which form to the sides of and downstream of ejected film concentrations. Giebert et al. [8] and Thole et al. [9] describe velocity and turbulence flow field measurements made downstream of three simple angle hole configurations: round, laterally diffused (or fan shaped), and forward laterally diffused (or laid-back fan shaped). According to the authors, diffusion shaped holes produce less jet penetration, reduced velocity gradients, and lower turbulence production relative to round holes.

Gritsch et al. [10] present local and spatially-averaged adiabatic effectiveness distributions measured downstream of the same hole geometries investigated by Giebert et al. [8]. The Gritsch et al. study is unique because high-speed compressible flows are investigated experimentally with mainstream Mach numbers of 0.3, 0.6, and 1.2, and coolant passage Mach numbers of 0 and 0.6. With this arrangement, higher effectiveness values are produced by holes with expanded exits, and higher surface effectiveness values are generally measured with a freestream Mach number of 1.2 than when the freestream is subsonic. At blowing ratios from 0.25 to 1.75 (Gritsch et al. [11]) show that the highest spatially averaged Stanton number ratios are generally produced by the round holes, followed by fan shaped holes, and then, by laid-back fan-shaped holes. The best overall film cooling protection at a particular blowing ratio is provided by laid-back fan-shaped holes, followed by fan-shaped holes, and then, by round holes.

Chen et al. [12] compare the performance of conical holes, with different compound angle orientations, and round, simple angle holes. The best overall performance in this study is provided by the conical holes when the compound angle is 0 deg, and the worst performance is produced when the compound angle is 90

[1]Permanent address: Oita University, Oita, Japan.
[2]To whom correspondence should be addressed.

Contributed by the Heat Transfer Division for publication in the JOURNAL OF HEAT TRANSFER. Manuscript received by the Heat Transfer Division, Jan. 21, 1999; revision received, Dec. 2, 1999. Associate Technical Editor: J.-C. Han.

deg. Berger and Liburdy [13] present distributions of velocity, streamwise vorticity, and other film cooling characteristics measured using particle image velocimetry downstream of a single cylindrical hole, a single laterally diffused hole, and a single forward diffused hole. Different flow structures, different vorticity distributions, and different injection coverage and distributions with respect to the test surface are produced which depend upon the hole geometry and direction of injection relative to the freestream.

Of the investigations which employ numerical techniques, Hyams and Leylek [14] examine the behavior of five different hole geometries with simple angle orientations. Heat transfer coefficients, adiabatic film effectiveness values, vorticity distributions, turbulence levels, and other quantities show that flow characteristics at hole exit planes are affected significantly by film hole shape. Of the different simple angle geometries examined, laterally diffused, simple angle holes provide the best coverage and highest surface effectiveness magnitudes. Laterally diffused, simple angle holes produce the highest spanwise-averaged isoenergetic heat transfer coefficients, and forward diffused, simple angle holes produce the lowest spanwise-averaged coefficients. Brittingham and Leylek [15] present distributions of surface adiabatic effectiveness and a number of other quantities downstream of forward diffused and laterally diffused holes with compound angle orientations. According to the authors, the existence, strength, direction of rotation, and locations of the vorticity field at a hole exit are connected to jet/crossflow shear, as well as the shear which originates in the film hole. Higher heat transfer coefficients are produced by the laterally diffused holes with compound angle orientations, than by the cylindrical holes with simple angle orientations at blowing ratios of 1.25 and 1.88, when compared at the same m and x/D. In a later study, McGrath and Leylek [16] employ computational fluid dynamics to investigate the flow physics responsible for hot crossflow ingestion into forward diffused film cooling holes with simple and compound angle orientations. Kohli and Thole [17] numerically investigate the flow field in a diffused film cooling hole and its supply channel.

Here, measured local and spatially averaged adiabatic film cooling effectiveness distributions, Stanton number distributions, and performance parameter distributions are measured downstream of five different film hole geometries, including laterally diffused and forward diffused holes with and without compound angle orientations. The present study thus provides consistent sets of data wherein the performance provided by these different shaped hole geometries can be compared to each other and to the performance provided by round, simple angle holes. To the best of the authors' knowledge, no similar comparisons of experimental data exist in the literature. The only other existing experimental studies of shaped holes which present the same types of surface characteristics ([4–6,10–12]) consider different hole geometries. There is thus a significant need for experimental data measured downstream of shaped holes, like that presented in the present paper, both for the design of gas turbine blade components, as well as for the further development of more widely applicable numerical models and prediction schemes.

Experimental Apparatus and Procedures

The present experiment is conducted on a large scale, with low speeds, flat-plate test sections, and constant property flows to isolate the interactions between the film cooling and the boundary layer, and to allow detailed surface characteristics to be measured.

Wind Tunnel. The wind tunnel is open circuit, subsonic, and located in the Convective Heat Transfer Laboratory of the Department of Mechanical Engineering of the University of Utah. A centrifugal blower is located at the upstream end, followed by a diffuser, a header containing a honeycomb and three screens, and then a 16 to 1 contraction ratio nozzle. The nozzle leads to the test section which is a rectangular duct 3.05 m long, 0.61 m wide, and 0.305 m high (at the inlet) with a top wall having adjustable height to permit changes in the streamwise pressure gradient. The zero-pressure gradient employed here is set to within 0.002 in. of water differential pressure along the length of the test section without film cooling. Flow at the test section inlet shows excellent spatial uniformity and a freestream turbulence level less than 0.1 percent at a freestream velocity of 10 m/s. A 5-mm high, 30-mm wide trip is placed at the beginning of the test surface to insure that the boundary layer is fully turbulent.

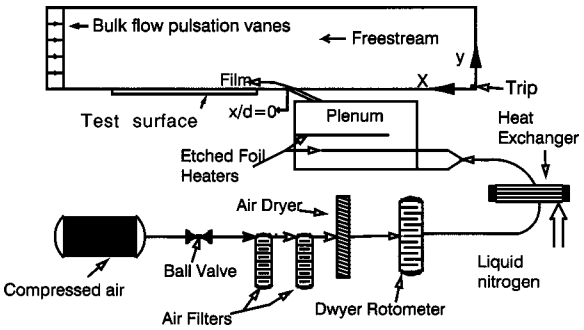

Fig. 1 Coordinate system and experimental apparatus

A schematic of the test section, including the coordinate system and film injection apparatus, is shown in Fig. 1. The downstream edge of the injection holes is 1.050 m downstream of the trip, and surface measurement stations are subsequently located at x/D of 3.87, 8.42, 15.3, 24.4, 36.6, and 42.7. Corresponding freestream Reynolds numbers Re, based on streamwise distance (from the trip) and a freestream velocity of 10 m/s, range from 578,000 to 1,100,000.

Film Cooling Injectant System. The air used for the film first flows through a regulating ball valve, followed by an air filter and dryer system, a Dwyer rotometer, a diffuser, and finally into the injection plenum chamber. From the plenum, the injectant air flows into the film holes, which are installed just upstream of the test surface employed. The film air is cleaned and dried using a Wilkerson high capacity dryer with Wilkerson type DRP-85-060 desiccant and two coalescing filters, PSB Industries 74635-25 and Wilkerson F16-04-FO0B-C97. The regulating valve and rotometer provide means to control the film cooling flow rate, and the injection chamber provides means to heat the injectant above or cool the injectant below ambient temperature. The plenum measures 0.51 m long by 0.51 m wide with a height of 0.38 m. To achieve density ratios greater than 1.0, liquid nitrogen is used to cool the film in a heat exchanger manufactured especially for this purpose by Xchanger Inc.

Adiabatic Film Cooling Effectiveness Measurements. Local magnitudes of the adiabatic film cooling effectiveness are deduced from measurements of coolant static temperature, freestream static temperature, and temperatures measured along an adiabatic test surface. The coolant static temperature is a value which is spatially averaged over the exit planes of the film cooling holes. This is determined from measurements of the coolant plenum temperature and correlations developed especially for this purpose. These correlations are based on film air temperatures measured in separate calibration tests using thermocouples at several hole exit plane locations. Surface temperatures are measured at discrete locations using 150 calibrated Omega, type 5TC-TT-T-36-72, copper-constantan thermocouples, each consisting of a 36-gage wire with a soldered 2-mm-diameter junction. The adiabatic surface is constructed of 101.6-mm thick Dow Chemical Corp. Duramate Styrofoam which has a thermal conductivity of 0.027 W/mK, and a smooth plastic film layer with minimal surface imperfections placed next to the air stream. The thermocouples are oriented into six streamwise rows of 25 thermocouples in each row, with a spanwise spacing of 8.3 mm from

$z/D=-7.5$ to $z/D=1.5$. Each thermocouple is installed from the back of the Styrofoam so that each junction is located about 0.1 mm just beneath the test surface. The upstream edge of the test surface is located five to eight mm from the downstream edges of the film cooling holes.

Voltages produced by the thermocouples are measured and acquired using Hewlett-Packard HP44422T thermocouple cards, installed in an Hewlett-Packard HP3497A data acquisition controller and a Hewlett-Packard HP3498A extender. The data acquisition system is connected to a Hewlett-Packard model A2240B type 362 computer used for collection and processing of data. A Pentium 200 MHz personal computer and the programs DeltaGraph 4.0, Microsoft Excel '97, and Microsoft Word 97 are used for additional processing and plotting of experimental data. As data are acquired, the injectant is heated using the etched foil heaters, with power levels controlled using a variac, to give an average plenum temperature of 50°C. Temperatures as low as −90°C are achieved using the liquid nitrogen heat exchanger system. Twenty-five η values for each of the six streamwise locations are averaged to determine $\overline{\eta}$ ([18]).

Iso-energetic Stanton Number Measurements. The test surface employed for measurements of the iso-energetic Stanton number utilizes a thin, smooth sheet of 0.2-mm-thick stainless steel foil located next to the air stream. 126 copper-constantan thermocouples are located directly beneath the stainless steel foil, arranged in six streamwise rows of 21 per row, spaced spanwise 12.7 mm apart at $z/D=5.87$ to $z/D=-5.87$. Thermocouple wire leads are embedded in a liner under the stainless steel foil. Data reduction procedures include corrections for the temperature drop through the foil and the thermal contact resistance between the foil and the thermocouples. Directly under the liner is an Electrofilm 2.0 kilowatt model P/N 116473-2 etched foil heater encased in Kapton, and used to provide a constant heat flux over the surface. Thus, the foil just next to the air stream is not powered. A 1.27-cm sheet of acrylic supports the smooth foil surface, thermocouples and foil heater. Beneath the acrylic sheet, 10.16 cm of polystyrene foam are used to insulate the surface and reduce conduction losses. All these layers are enclosed in an acrylic case and insulated with Halstead black foam insulation to further minimize conduction losses. The height of the test surface is adjustable to insure that it is flat and level next to the air stream. The upstream edge of this test surface is also located five to eight mm from the downstream edges of the film cooling holes.

For the acquisition of baseline data with no film cooling, injection holes are plugged and covered with thin plastic tape. These baseline values show excellent agreement with the correlation for a fully turbulent, flat plate boundary layer (with unheated starting length) from Kays and Crawford [19]. When data are acquired either with or without film cooling, power is supplied and controlled to the foil heater using a Powerstat type 1368 variac so that the average temperature at the locations of the 126 thermocouples is 55°C. Determination of convective heat flux magnitudes requires: (i) the measurement of power to this heater, (ii) determination of gross conduction losses from the test surface, and (iii) determination of spanwise and streamwise conduction losses and gains along the steel foil. With this arrangement, an iso-energetic condition is produced wherein the freestream and injectant flows are at the same temperature. The same data acquisition and processing system described above is used to acquire and process thermocouple voltages and other measured quantities. Twenty-one St_f/St_o values for each of the six streamwise locations are averaged to determine $\overline{St_f/St_o}$. Additional details are provided by Bell [18].

Experimental Uncertainties. Uncertainty estimates are based on 95 percent confidence levels and determined following

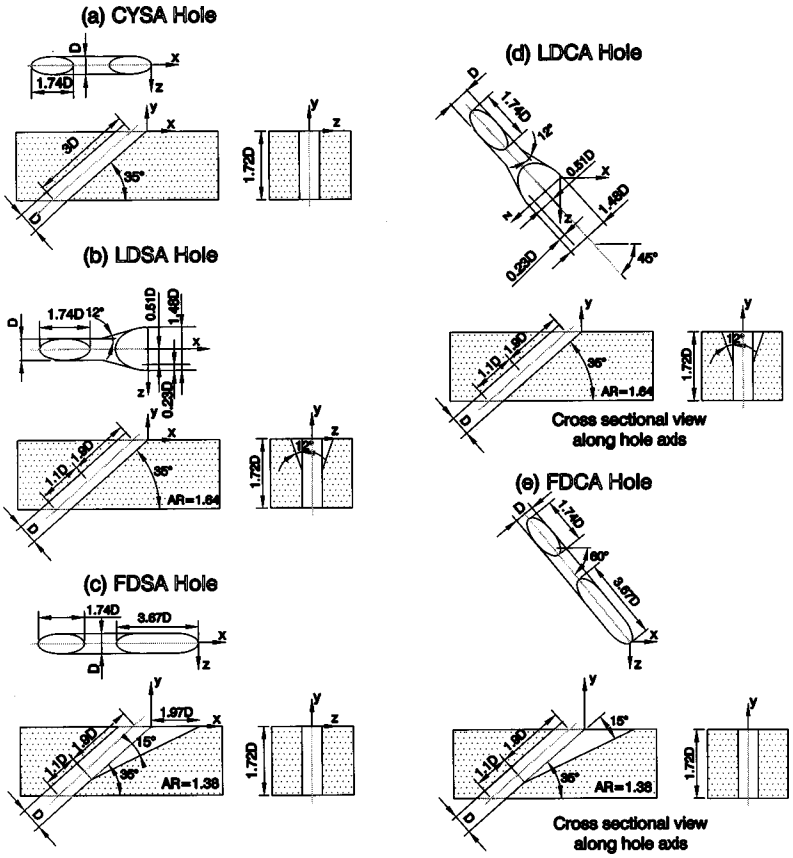

Fig. 2 Film hole configurations

procedures described by Kline and McClintock [20] and Moffat [21]. For each parameter, a range of typical values is given followed by the associated uncertainty: $\overline{\eta}=0.10-0.40\pm0.015$, $\mathrm{Re}_D=2800-6800\pm200$, $x/D=3.87-42.7\pm0.20$, $m=0.40-1.80\pm0.025$, $I=0.17-3.48\pm0.05$, $u_c/u_\infty=0.43-1.94\pm0.02$, $\rho_c/\rho_\infty=0.93-1.40\pm0.005$, $\overline{\mathrm{St}_f/\mathrm{St}_o}=0.95-1.40\pm0.06$, $\dot{q}''/\dot{q}_o''=0.40-1.10\pm0.04$, and $\theta=1.00-2.00\pm0.01$. The $\overline{\eta}$ uncertainty value includes relatively small contributions from errors which may exist due to small amounts of streamwise and spanwise conduction along the test surface. Magnitudes of $\overline{\mathrm{St}_f/\mathrm{St}_o}$ and $\dot{q}''/\dot{q}_o''$ are corrected for spanwise and streamwise conduction losses and gains along the steel foil, as indicated above.

Film Cooling Configurations and Experimental Conditions

Five different film hole geometries, shown schematically in Fig. 2, are investigated: (i) cylindrical round, simple angle (CYSA) holes, (ii) laterally diffused, simple angle (LDSA) holes, (iii) laterally diffused, compound angle (LDCA) holes, (iv) forward diffused, simple angle (FDSA) holes, and (v) forward diffused, compound angle (FDCA) holes. The axis of each hole is oriented at a 35 deg angle from the test surface. Hole entrance (or metering) diameter D is 2.22 cm in each case, giving $L/D=3.0$, and $\delta/D=1.23$ at $x/D=-10.7$ and a freestream velocity of 10 m/s. Ratios of displacement thickness to hole metering diameter, and momentum thickness to hole diameter at the same x/D and u_∞ are then 0.191, and 0.136, respectively. In each case, the holes are placed in a single row with spanwise pitch spacing of $3D$.

Injectant experimental conditions are summarized in Tables 1 and 2. Injection Reynolds number Re_D ranges from 2800 to 12,000, and are thus always high enough to insure that turbulent flow is present at the injection hole exits. All parameters in Tables 1 and 2 are based on inlet metering areas of the film cooling holes.

Table 1 Flow conditions for adiabatic effectiveness measurements

	m	u_c/u_∞	I	ρ_c/ρ_∞
LDSA	0.4	0.43	0.17	0.93
LDSA	0.7	0.75	0.53	0.93
LDSA	0.7	0.58	0.41	1.20
LDSA	0.7	0.54	0.38	1.30
LDSA	1.0	1.08	1.08	0.93
LDSA	1.3	1.40	1.82	0.93
LDSA	1.8	1.94	3.48	0.93
LDCA	0.4	0.43	0.17	0.93
LDCA	0.7	0.75	0.53	0.93
LDCA	0.7	0.52	0.36	1.35
LDCA	1.0	1.08	1.08	0.93
LDCA	1.3	1.40	1.82	0.93
LDCA	1.8	1.94	3.48	0.93
CYSA	0.4	0.43	0.17	0.93
CYSA	0.7	0.75	0.53	0.93
CYSA	0.7	0.56	0.39	1.25
CYSA	0.7	0.50	0.35	1.39
CYSA	1.0	1.08	1.08	0.93
FDSA	0.4	0.43	0.17	0.93
FDSA	0.7	0.75	0.53	0.93
FDSA	0.7	0.58	0.40	1.21
FDSA	0.7	0.53	0.37	1.33
FDSA	1.0	1.08	1.08	0.93
FDSA	1.3	1.40	1.82	0.93
FDSA	1.8	1.94	3.48	0.93
FDCA	0.4	0.43	0.17	0.93
FDCA	0.7	0.75	0.53	0.93
FDCA	0.7	0.58	0.41	1.20
FDCA	0.7	0.52	0.36	1.35
FDCA	1.0	1.08	1.08	0.93
FDCA	1.3	1.40	1.82	0.93
FDCA	1.8	1.94	3.48	0.93

Table 2 Flow conditions for iso-energetic Stanton number measurements

	m	u_c/u_∞	I	ρ_c/ρ_∞
LDSA	0.4	0.40	0.16	1.0
LDSA	0.7	0.70	0.49	1.0
LDSA	1.0	1.00	1.00	1.0
LDSA	1.3	1.30	1.69	1.0
LDSA	1.8	1.80	3.24	1.0
LDCA	0.4	0.40	0.16	1.0
LDCA	0.7	0.70	0.49	1.0
LDCA	1.0	1.00	1.00	1.0
LDCA	1.3	1.30	1.69	1.0
LDCA	1.8	1.80	3.24	1.0
CYSA	0.4	0.40	0.16	1.0
CYSA	0.7	0.70	0.49	1.0
CYSA	1.0	1.00	1.00	1.0
FDSA	0.4	0.40	0.16	1.0
FDSA	0.7	0.70	0.49	1.0
FDSA	1.0	1.00	1.00	1.0
FDSA	1.3	1.30	1.69	1.0
FDSA	1.8	1.80	3.24	1.0
FDCA	0.4	0.40	0.16	1.0
FDCA	0.7	0.70	0.49	1.0
FDCA	1.0	1.00	1.00	1.0
FDCA	1.3	1.30	1.69	1.0
FDCA	1.8	1.80	3.24	1.0

Experimental Results

Effects of Hole Configuration on Adiabatic Film Cooling Effectiveness. Figure 3 shows how spanwise-averaged adiabatic film cooling effectiveness $\overline{\eta}$ varies with normalized streamwise distance for all five hole configurations: LDSA, LDCA, FDSA, FDCA, and CYSA. The figure is divided into five parts, corresponding to blowing ratios of 0.4, 0.7, 1.0, 1.3, and 1.8. All data are given for a density ratio ρ_c/ρ_∞ of 0.93.

Figure 3 shows that the highest magnitudes of $\overline{\eta}$ are measured downstream of LDCA holes for blowing ratios of 0.7, 1.0, 1.3, and 1.8 (when compared at the same x/D). Fairly high magnitudes of $\overline{\eta}$ relative to the other three configurations are also measured downstream of FDCA holes for several of the blowing ratios tested. The three simple hole configurations tested, LDSA, FDSA, and CYSA, show only very small changes of effectiveness magnitudes as the hole configuration is changed at each x/D and m

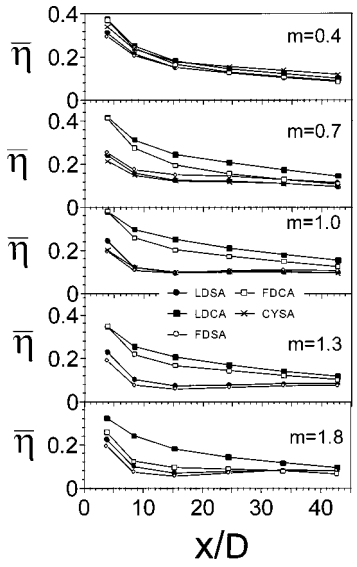

Fig. 3 Spanwise-averaged adiabatic film cooling effectiveness for different blowing ratios and different film hole configurations for $\rho_c/\rho_\infty=0.93$

examined. Overall trends are thus consistent with the numerical predictions of Hyams and Leylek [14] and Brittingham and Leylek [15]. Note that CYSA data are given only for m of 0.4, 0.7, and 1.0 in Fig. 3, and that larger differences between data measured downstream of CYSA, FDSA, and LDSA holes may be present at higher m.

In contrast to the present study, Gritsch et al. [10] present local and spanwise-averaged effectiveness distributions downstream of LDSA holes (called fan-shaped holes) which are significantly higher than values measured downstream of CYSA holes. These differences from the present study illustrate the importance of hole shape, especially the amount of diffusion produced by an individual simple angle hole geometry. The Gritsch et al. fan-shaped holes have a ratio of hole exit width to inlet metering diameter of 3.0 and exit-to-entry area ratio of 2.0 (from a half-expansion angle of 14 deg spread over $4D$ of hole length). The ratio of hole exit width to inlet metering diameter, and exit-to-entry area ratio of the present LDSA holes are 1.48 and 1.64, respectively (from a half-expansion angle of 12 deg spread over $1.9D$ of hole length). Consequently, the LDSA injectant in the present study is less diffused, and less spread out with higher mean exit velocities (when compared at the same average film metering velocity). Greater jetting and increased injectant penetration result (relative to the Gritsch et al. fan hole data) so that performance characteristics of the present shaped, simple angle geometries (FDSA, LDSA) are about the same as or only slightly better than CYSA holes.

Effects of Blowing Ratio and Momentum Flux Ratio on Adiabatic Film Cooling Effectiveness. Figure 4 gives $\overline{\eta}$ as they vary with m and with I for the five different film hole configurations for $x/D=8.42$. From this figure, it is evident that the highest effectiveness magnitudes downstream of the two compound angle configurations, LDCA and FDCA, are produced using blowing ratios from 0.7 to 1.3, and momentum flux ratios from 0.5 to 1.9. In contrast, the highest effectiveness magnitudes downstream of the three simple angle configurations, LDSA, FDSA, and CYSA, are produced using blowing ratios from 0.4 to 0.7, and momentum flux ratios from 0.2 to 0.5. Similar trends are evident at other lower x/D. Such changes with blowing ratio evidence different propensities for film lift-off downstream of the different film hole configurations. The compound angle arrangements are most beneficial in this respect since lift-off generally occurs at higher momentum flux ratios compared to simple angle holes. This is partially because of lateral components of injectant momentum from compound angle holes, which causes the film to be more spread out in the spanwise direction at locations closer to the surface as it is advected downstream ([22]).

Figure 4 thus shows that the best $\overline{\eta}$ distributions over the widest ranges of blowing ratio and momentum flux ratio are produced by the FDCA and LDCA configurations. This is consistent with the measurements of Schmidt et al. [5], who include effectiveness values downstream of one type of compound angle, shaped hole. The present results then also show the LDCA holes to be superior to FDCA holes over a larger range of m and I since consistently higher $\overline{\eta}$ values are produced at $m>0.7$, $I>0.5$, and $x/D=8.42$ in Fig. 4. This is partially a result of lower exit momentum with lateral diffusion (when compared at the same blowing ratio) which causes less penetration into and interaction with the freestream. According to Hyams and Leylek [14], such differences with film hole geometry are also due to the cross flow aligned vorticity from film hole shear layers, which governs the formation of the longitudinal vortices generally located to the sides of the film concentrations. In some cases, altering the strengths of these vortices changes film cooling performance considerably.

Local effectiveness distributions (used to determine $\overline{\eta}$ values) show that the highest local η peaks (at small x/D) are also produced by the LDCA holes, which also give better spreading of injectant along the surface downstream of each hole compared to the three simple angle arrangements. Good lateral injectant spreading is also produced by the FDCA holes, which appear to also give more uniform film coverage than the LDCA holes. Local η distributions measured downstream of the two compound angle hole configurations are also generally higher than values measured downstream of the simple angle hole geometries. The *combination* of less jet penetration, flow diffusion, and lower velocity gradients from shaping ([9] for $m=1.0$), and increased lateral spreading and greater injectant concentrations near the surface from compound angles ([22]) thus results in important local and spatially averaged protection benefits when m ranges from 0.7 to 1.3.

Effects of Density Ratio on Adiabatic Film Cooling Effectiveness. Spanwise-averaged effectiveness data which illustrate the influences of density ratio are presented in Fig. 5. All data are given for the same blowing ratio, $m=0.7$. The figure shows significant $\overline{\eta}$ changes with ρ_c/ρ_∞ at each x/D and m for all three simple angle hole geometries, CYSA, FDSA, and LDSA. In contrast, changes due to variations of the density ratio from 0.93 to 1.3–1.4 are less downstream of the LDCA and FDCA configurations, especially for $x/D>8.42$. The exact density ratio for each data set is given in Table 1.

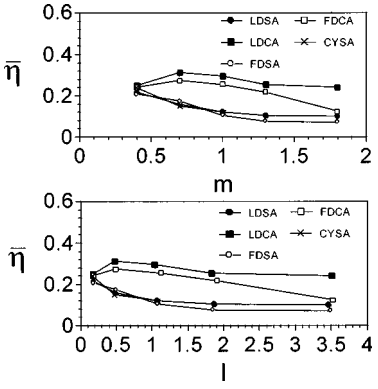

Fig. 4 Spanwise-averaged adiabatic film cooling effectiveness as dependent upon blowing ratio and momentum flux ratio for $x/d=8.42$ and $\rho_c/\rho_\infty=0.93$

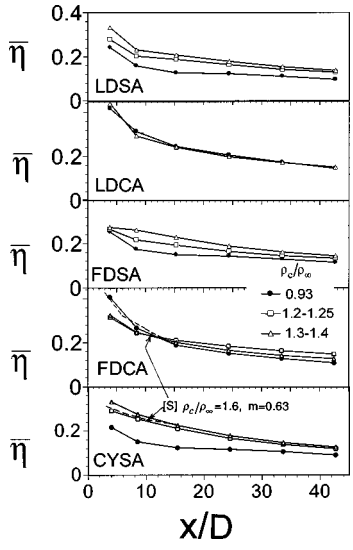

Fig. 5 Spanwise-averaged adiabatic film cooling effectiveness for $m=0.7$ for different film hole configurations and different density ratios, including comparisons with results from [S]: ([5])

The small changes to spanwise-averaged effectiveness downstream of LDCA and FDCA holes as density ratio ranges from 0.9 to 1.3–1.4 are due to film diffusion from expanded hole shapes, and increased lateral spreading of injectant. These act to keep greater injectant concentrations near the surface over a wider range of momentum flux ratios (compared to CYSA holes). This then lessens the influence of decreasing momentum flux ratio, which occurs as density ratio increases at constant blowing ratio. As m increases above 1.4, larger $\overline{\eta}$ changes with ρ_c/ρ_∞ are expected. This is because the influences of density ratio at a particular blowing ratio are probably more important with shaped, compound angle holes when blowing ratios and momentum flux ratios reach values where larger amounts of film lift-off begin to take place.

Effectiveness Comparisons With Other Investigations. As discussed earlier, there are very few experimental results measured downstream of shaped film cooling holes which are published in the open literature. Consequently, only a couple of comparisons with other investigations are possible, and even in these cases, it is not possible to compare at the exact same flow conditions and geometry. In Fig. 5, compared are: (i) CYSA data for $\rho_c/\rho_\infty=1.4$ and $m=0.7$ to CYSA results from Schmidt et al. [5] for $\rho_c/\rho_\infty=1.6$ and $m=0.63$, and (ii) FDCA data for $\rho_c/\rho_\infty=1.36$ and $m=0.7$ to FDCA results from Schmidt et al. [5] for $\rho_c/\rho_\infty=1.6$, $m=0.63$. In both cases, the data from the two sources are in rough agreement. The differences which exist are mostly due to different ρ_c/ρ_∞ and different L/D.

The present CYSA data are compared to results from Pedersen et al. [23] in Fig. 6. The data from the present study are the same data shown in the bottom portion of Fig. 5. Even though the blowing ratios are slightly different, spanwise averaged effectiveness data from both investigations in Fig. 6 are in good agreement as they increase with density ratio at each x/D and m. This further validates the experimental procedures and apparatus employed in the present study.

Effects of Configuration on Stanton Number Ratios. Figure 7 shows how spanwise-averaged iso-energetic Stanton number ratios vary with normalized streamwise distance for all five hole configurations: LDSA, LDCA, FDSA, FDCA, and CYSA. The figure is divided into five parts, corresponding to blowing ratios of 0.4, 0.7, 1.0, 1.3, and 1.8. All data are given for a density ratio ρ_c/ρ_∞ of 1.0.

Magnitudes of $\overline{\mathrm{St}_f/\mathrm{St}_o}$ downstream of the film holes are influenced by levels of turbulence and mixing, and thus, by turbulent transport in the boundary layer. These are then tied to local three-dimensional velocity gradients, shear, and local turbulence production, which can be decreased or increased (relative to no film cooling values) as injectant from the film holes interfaces with and interacts with surrounding boundary layer fluid. In Fig. 7, the simple angle configurations, CYSA, LDSA, and FDSA, consistently produce the lowest $\overline{\mathrm{St}_f/\mathrm{St}_o}$ magnitudes at each x/D and m (for m of 1.0, 1.3, and 1.8) because of hole shaping which gives lower velocity gradients through the film as well as less penetration of the injectant into the flow. As a result, augmentation of shear levels is minimal throughout these film cooled boundary layers even when the blowing ratio is 1.8.

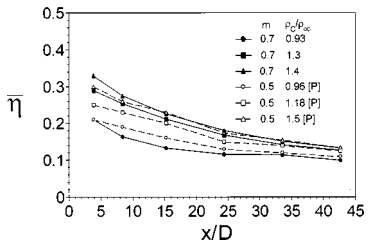

Fig. 6 Comparisons of spanwise-averaged adiabatic film cooling effectiveness distributions for CYSA holes with results from [P]: ([23])

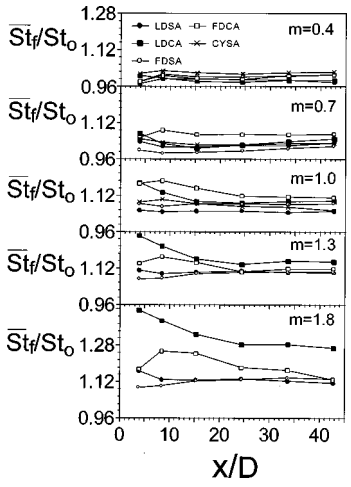

Fig. 7 Spanwise-averaged iso-energetic Stanton number ratios for different blowing ratios and different hole configurations for $\rho_c/\rho_\infty=1.0$

In contrast, boundary layer shear levels and mixing are augmented considerably when the shaped holes are arranged with compound angle orientations. This occurs as injectant with significant spanwise velocity components encounters and interfaces with fluid in the oncoming boundary layer, which moves in the streamwise direction with velocities different from the injectant ([24]). This generally occurs at locations to the sides of metering hole centerlines, and is especially influential in augmenting $\overline{\mathrm{St}_f/\mathrm{St}_o}$ magnitudes because of the diffusion produced by the shaping. $\overline{\mathrm{St}_f/\mathrm{St}_o}$ trends in Fig. 7 indicate that such effects are most pronounced for FDCA holes when $m=0.7$ and $m=1.0$, and for LDCA holes when $m=1.3$ and $m=1.8$, since the highest iso-energetic Stanton number ratios are measured downstream of these holes at these blowing ratios, when compared at the same x/D and m.

From Fig. 7, it is also evident that all five hole geometries give about the same $\overline{\mathrm{St}_f/\mathrm{St}_o}$ magnitudes when $m=0.4$. When $m=0.7$, the same qualitative trends are present, except that the FDCA data are higher than data for the other hole configurations for almost all of the x/D examined (note that CYSA data are given only for m of 0.4, 0.7, and 1.0). In some cases (i.e., FDSA data for $m=0.7$), low speed fluid near the wall reduces turbulence transport below nonfilm cooled values to give $\overline{\mathrm{St}_f/\mathrm{St}_o}$ magnitudes less than 1. In addition, (i) in many cases, little $\overline{\mathrm{St}_f/\mathrm{St}_o}$ variation with x/D is evident for each value of m, and (ii) for each x/D, $\overline{\mathrm{St}_f/\mathrm{St}_o}$ values generally increase with m. Trends (i) and (ii) are then consistent with measurements presented by Ligrani et al. [25].

Figure 7 additionally shows $\overline{\mathrm{St}_f/\mathrm{St}_o}$ which decrease with x/D for each blowing ratio for the LDCA holes (when $x/D<15-25$), and $\overline{\mathrm{St}_f/\mathrm{St}_o}$ values which increase with x/D at each blowing ratio for the FDCA holes (when $x/D<8-10$). Such differences result because of the manner in which injectant is diffused from the shaped holes, and then interfaces and interacts with fluid in the surrounding boundary layer. Of particular importance are injectant velocity distributions at hole exit planes, and streamwise vorticity contours near hole exits. According to Brittingham and Leylek [15], these flow characteristics are significantly different for FDCA holes and LDCA holes. As a result, regions with the largest velocity gradients and the largest shear are at different positions in the flow with respect to metering hole centerlines. The

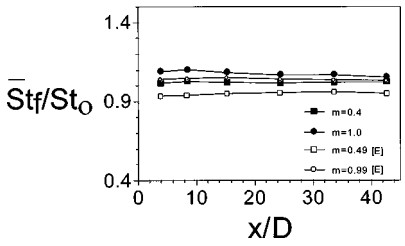

Fig. 8 Comparisons of spanwise-averaged iso-energetic Stanton number ratio distributions for CYSA holes with results from [E]: ([26])

fluid with the highest mixing and highest turbulence, which is also the fluid with the highest thermal transport, then advects to different x/D locations downstream of the two types of holes.

Stanton Number Comparisons With Other Investigations. Figure 8 compares spanwise-averaged iso-energetic Stanton number ratios to CYSA data from Eriksen and Goldstein [26] which, like the present data, are measured using $\rho_c/\rho_\infty = 1$. The two data sets show good trend agreement, with slightly higher magnitudes for the present data, provided the present data for $m = 0.4$ and $m = 1.0$ are compared, respectively, to $m = 0.49$ and $m = 0.99$ data from Eriksen and Goldstein [26].

Effects of Configuration and Blowing Ratio on Overall Film Cooling Performance Parameter. Overall film cooling performance at a particular location on a turbine surface is characterized by $\dot{q}''/\dot{q}_o''$, the ratio of the heat flux with film cooling to the heat flux with no film cooling. This quantity is referred to as the overall film cooling performance parameter, and lower values indicate better film cooling protection. The parameter depends upon the local adiabatic film cooling effectiveness η, iso-energetic Stanton number ratio St_f/St_o, and nondimensional coolant temperature θ. As such, the parameter is given by an equation of the form

$$\dot{q}''/\dot{q}_o'' = (St_f/St_o)[1 - \eta\theta] \quad (1)$$

where θ typically ranges from 1.2 to 2.0, depending upon turbine operating conditions. Here, local η and St_f/St_o, measured at the same blowing ratio m, are used in Eq. (1). Note that when $\rho_c/\rho_\infty = 0.93-1.0$, matching the same m is about the same as matching the same I. The results are then averaged over z/D at each x/D to determine spanwise-averaged magnitudes of $\dot{q}''/\dot{q}_o''$. As in the work of Sen et al. [6], the iso-energetic Stanton number is determined when the coolant and freestream temperatures are about the same and $\rho_c/\rho_\infty = 1$. Corresponding local η values employed in Eq. (1) are then for a slightly different ρ_c/ρ_∞ of 0.93.

Figure 9 shows how spanwise-averaged film cooling performance parameters vary with normalized streamwise distance for all five hole configurations: LDSA, LDCA, FDSA, FDCA, and CYSA. The figure is divided into five parts, corresponding to blowing ratios of 0.4, 0.7, 1.0, 1.3, and 1.8. Note that CYSA data are given for blowing ratios of only 0.4, 0.7, and 1.0. Magnitudes of local $\dot{q}''/\dot{q}_o''$ are deduced from η and St_f/St_o data using Eq. (1) and a θ value of 1.75.

From Fig. 9, it is evident that: (i) the lowest $\dot{q}''/\dot{q}_o''$ magnitudes and best film cooling protection over the widest ranges of x/D are generally provided by LDCA holes at blowing ratios of 0.7, 1.0, 1.3, and 1.8, (ii) the highest values of $\dot{q}''/\dot{q}_o''$ and lowest protection at each x/D and m are generally provided by the simple angle configurations (CYSA, FDSA, LDSA) for blowing ratios of 0.7, 1.0, 1.3, and 1.8, (iii) the differences between the protection provided by the three simple angle configurations (CYSA, FDSA, LDSA) are generally small at each x/D and m, and (iv) all five hole configurations provide about the same level of protection when the blowing ratio is 0.4.

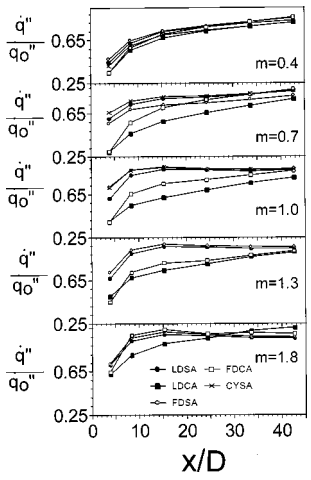

Fig. 9 Spanwise-averaged overall film cooling performance parameters for different blowing ratios and different hole configurations for $\rho_c/\rho_\infty = 0.93-1.0$

From Fig. 9, it is additionally evident that: (i) except for LDSA and FDSA $m \leqslant 0.7$, and LDCA and FDCA $m \leqslant 1.0$, $\dot{q}''/\dot{q}_o''$ values increase with m at each x/D for each hole configuration, (ii) the lowest $\dot{q}''/\dot{q}_o''$ values and best protection from the compound angle, shaped hole arrangements (LDCA, FDCA) are generally produced at blowing ratios from 0.4 to 1.3 (I from 0.16 to 1.69), and (iii) the lowest $\dot{q}''/\dot{q}_o''$ values from the three simple angle arrangements (CYSA, LDSA, FDSA) are present at blowing ratios from 0.4 to 0.7 (I from 0.16 to 0.49).

Spatially averaged magnitudes of the net heat flux reduction, or NHFR, (determined from $\dot{q}''/\dot{q}_o''$ values in Fig. 9) are presented in Fig. 10 as dependent upon momentum flux ratio. This figure shows that the best spatially averaged protection is provided first by LDCA holes, then by FDCA holes, since these give NHFR data which are higher than other data presented at many of the momentum flux ratios examined. NHFR values measured downstream of the three simple angle configurations (FDSA, LDSA, CYSA) have about the same magnitudes at each momentum flux ratio.

Figure 10 additionally shows that trends and quantitative magnitudes of the CYSA data from Sen et al. [6] and from the present study are in fair to very good agreement for the range of I values presented. The present FDCA data also agrees very well with the Sen et al. FDCA data when $I < 0.5$. The present FDCA data then appear to be slightly higher than the Sen et al. data for I near 1.0, and slightly lower for $I > 3.0$. These differences are due to different L/D and different ρ_c/ρ_∞ in the two studies, as well as different averaging schemes used to determine the NHFR. The Sen et al. [6] data represent values averaged over x/D from 3

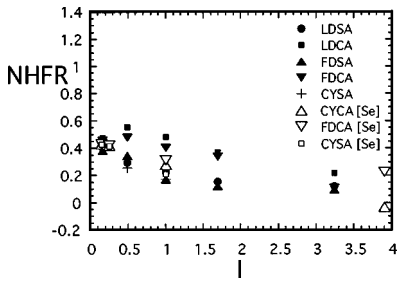

Fig. 10 Spatially-averaged magnitudes of net heat flux reduction (NHFR) at different momentum flux ratios, including comparisons with results from [Se]: ([6])

to 15, whereas the present NHFR data are determined from averages of spanwise-averaged $\dot{q}''/\dot{q}_o''$ at x/D of 3.87, 8.42, and 15.3.

Summary and Conclusions

Local and spanwise-averaged magnitudes of the adiabatic film cooling effectiveness, iso-energetic Stanton number ratios, and film cooling performance parameters are described from measurements downstream of: (i) cylindrical round, simple angle (CYSA) holes, (ii) laterally diffused, simple angle (LDSA) holes, (iii) laterally diffused, compound angle (LDCA) holes, (iv) forward diffused, simple angle (FDSA) holes, and (v) forward diffused, compound angle (FDCA) holes. Data are presented for $L/D=3$, $\delta/D=1.23$, m from 0.4 to 1.8, I from 0.17 to 3.5, and ρ_c/ρ_∞ from 0.9 to 1.4.

The combination of less jet penetration, flow diffusion, and lower velocity gradients from *shaping*, and increased lateral spreading and greater injectant concentrations near the surface from *compound angles*, results in important local and spatially averaged protection benefits. This is evidenced by higher magnitudes of spanwise-averaged performance, globally averaged performance, and spanwise-averaged effectiveness parameters over much wider ranges of blowing ratio and momentum flux ratio downstream of the LDCA and FDCA arrangements compared to the three simple angle configurations tested. This occurs even though the highest spanwise-averaged iso-energetic Stanton number ratios at $x/D=0-20$ are also generally measured downstream of the LDCA and FDCA configurations when m ranges from 0.7 to 1.8. Of these two compound angle configurations, LDCA holes give the highest magnitudes of performance and effectiveness at blowing ratios from 0.7 to 1.8, when compared at the same x/D and ρ_c/ρ_∞. The shaped, compound angle geometries also give better *local* protection along the surface downstream of each hole, and lift-off at higher momentum flux ratios compared to the three simple angle arrangements.

When compared at the same m, ρ_c/ρ_∞, and x/D, *spanwise-averaged* performance differences between the three simple angle configurations, LDSA, FDSA, and CYSA, are small when m ranges from 0.4 to 1.0. Such behavior is different from one other recent study (i.e., [10]) because of significantly less flow diffusion through the shaped hole passages used here. This illustrates the importance of hole shape on the behavior of simple angle film cooling holes.

All three simple angle hole geometries, CYSA, FDSA, and LDSA, show significant increases of spanwise-averaged adiabatic effectiveness as the density ratio ρ_c/ρ_∞ increases from 0.9 to 1.4 when $m=0.7$. In contrast, changes due to increasing ρ_c/ρ_∞ at this blowing ratio downstream of the LDCA and FDCA configurations are much smaller. This is because of the action of these two configurations in keeping greater injectant concentrations near the surface over a wider range of momentum flux ratios. The influences of decreasing momentum flux ratio (which occurs as density ratio increases at constant blowing ratio) are thus diminished for the experimental conditions and hole geometries examined. Different trends are evident when blowing ratio increases at constant density ratio of 0.93. In this case, all five of the configurations tested show that protection often diminishes (as $\dot{q}''/\dot{q}_o''$ values increase) with increasing m at each x/D.

Acknowledgments

This effort is sponsored by the National Science Foundation, Grant number CTS-9615196. Mr. Priyadarshana is acknowledged for some assistance in obtaining a portion of the experimental data reported in this paper.

Nomenclature

c = specific heat
D = diameter of injection hole at inlet
h_f = local iso-energetic heat transfer coefficient, $\dot{q}''/(T_w - T_{aw})$
I = momentum flux ratio, $\rho_c u_c^2/\rho_\infty u_\infty^2$
L = injection hole length
m = blowing ratio, $\rho_c u_c/\rho_\infty u_\infty$
$\dot{q}_0''$ = surface heat flux with no film cooling
$\dot{q}''$ = spanwise-averaged surface heat flux with film cooling
Re_D = coolant Reynolds number, Du_c/ν
Re = freestream Reynolds number, Xu_∞/ν
$\underline{\mathrm{St}}_f$ = local iso-energetic Stanton number, $h_f/\rho_\infty u_\infty c$
St_f = spanwise-averaged iso-energetic Stanton number
St_o = baseline Stanton number with no film cooling
u_∞ = time-averaged freestream velocity
u_c = time-averaged and spatially averaged injectant velocity
$\underline{T}$ = temperature
T = spanwise-averaged temperature
x = streamwise coordinate measured from downstream edge of film cooling holes
X = streamwise coordinate measured from boundary layer trip
y = normal coordinate measured from test surface
z = spanwise coordinate measured from spanwise centerline of test surface

Greek Symbols

$\underline{\eta}$ = local film cooling effectiveness, $(T_{aw}-T_\infty)/(T_{\underline{c}}-T_\infty)$
η = spanwise-averaged film cooling effectiveness, $(T_{aw}-T_\infty)/(T_c-T_\infty)$
ρ = density
θ = dimensionless coolant temperature, $(T_c-T_\infty)/(T_w-T_\infty)$
δ = boundary layer thickness
ν = kinematic viscosity

Subscripts

aw = adiabatic wall value
c = injectant or coolant value
∞ = freestream value
w = wall value

References

[1] Goldstein, R. J., Eckert, E. R. G., and Burggraf, F., 1974, ''Effects of Hole Geometry and Density on Three-Dimensional Film Cooling,'' Int. J. Heat Mass Transf., **17**, pp. 595–607.
[2] Makki, Y. H., and Jakubowski, G. S., 1986, ''An Experimental Study of Film Cooling From Diffused Trapezoid Shaped Holes,'' 24th Aerospace Sciences Meeting & Exhibit, Reno, NV, AIAA Paper No. 86-1326.
[3] Ajersch, P., Zhou, J.-M., Ketler, S., Salcudean, M., and Gartshore, I. S., 1995, ''Multiple Jets in a Crossflow: Detailed Measurements and Numerical Simulations,'' International Gas Turbine and Aeroengine Congress & Exhibition, Houston, TX, ASME Paper No. 95-GT-9.
[4] Farmer, J. P., Seager, D. J., and Liburdy, J. A., 1997, ''The Effect of Shaping Inclined Slots on Film Cooling Effectiveness and Heat Transfer Coefficient,'' International Gas Turbine and Aeroengine Congress & Exhibition, Orlando, FL, ASME Paper No. 97-GT-339.
[5] Schmidt, D. L., Sen, B., and Bogard, D. G., 1996, ''Film Cooling With Compound Angle Holes: Adiabatic Effectiveness,'' ASME J. Turbomach., **118**, pp. 807–813.
[6] Sen, B., Schmidt, D. L., and Bogard, D. G., 1996, ''Film Cooling With Compound Angle Holes: Heat Transfer,'' ASME J. Turbomach., **118**, pp. 800–806.
[7] Haven, B., and Kurosaka, M., 1996, ''The Effect of Hole Geometry on Lift-Off Behavior of Coolant Jets,'' 34th Aerospace Sciences Meeting & Exhibit, Reno, NV, AIAA Paper No. 96-0618.
[8] Giebert, D., Gritsch, M., Schulz, A., and Wittig, S., 1997, ''Film-Cooling From Holes With Expanded Exits: A Comparison of Computational Results With Experiments,'' International Gas Turbine and Aeroengine Congress & Exhibition, Orlando, FL, ASME Paper No 97-GT-163.
[9] Thole, K., Gritsch, M., Schulz, A., and Wittig, S., 1998, ''Flowfield Measurements for Film-Cooling Holes With Expanded Exits,'' ASME J. Turbomach., **120**, pp. 327–336.
[10] Gritsch, M., Schulz, A., and Wittig, S., 1998, ''Adiabatic Wall Effectiveness Measurements of Film-Cooling Holes with Expanded Exits,'' ASME J. Turbomach., **120**, pp. 549–556.

[11] Gritsch, M., Schulz, A., and Wittig, S., 2000, ''Heat Transfer Coefficient Measurements of Film-Cooling Holes with Expanded Exits,'' ASME J. Turbomach., **122**, to appear.
[12] Chen, P.-H., Ai, D., and Lee, S.-H., 1998, ''Effects of Compound Angle Injection on Flat-Plate Film Cooling Through a Row of Conical Holes,'' International Gas Turbine and Aeroengine Congress & Exhibition, Stockholm, ASME Paper No. 98-GT-459.
[13] Berger, P. A., and Liburdy, J. A., 1998, ''A Near-Field Investigation Into the Effects of Geometry and Compound Angle on the Flowfield of a Row of Film Cooling Holes,'' International Gas Turbine and Aeroengine Congress & Exhibition, Stockholm, ASME Paper No. 98-GT-279.
[14] Hyams, D. G., and Leylek, J. H., 1997, ''A Detailed Analysis of Film Cooling Physics, Part III: Streamwise Injection with Shaped Holes,'' International Gas Turbine and Aeroengine Congress & Exhibition, Orlando, FL, ASME Paper No. 97-GT-271.
[15] Brittingham, R. A., and Leylek, J. H., 1997, ''A Detailed Analysis of Film Cooling Physics, Part IV: Compound-Angle Injection with Shaped Holes,'' International Gas Turbine and Aeroengine Congress & Exhibition, Orlando, FL, ASME Paper No. 97-GT-272.
[16] McGrath, E. L., and Leylek, J. H., 1998, ''Physics of Hot Crossflow Ingestion in Film Cooling,'' International Gas Turbine and Aeroengine Congress & Exhibition, Stockholm, ASME Paper No. 98-GT-191.
[17] Kohli, A., and Thole, K. A., 1998, ''Entrance Effects on Diffused Film-Cooling Holes,'' International Gas Turbine and Aeroengine Congress & Exhibition, Stockholm, ASME Paper No. 98-GT-402.
[18] Bell, C. M., 1998, ''Effects of Bulk Flow Pulsations on Film Cooling With Different Density Ratios,'' Master of Science thesis, University of Utah, Salt Lake City, UT.
[19] Kays, W. M., and Crawford, M. E., 1993, *Convective Heat and Mass Transfer*, 3rd Ed, McGraw-Hill, New York.
[20] Kline, S. J., and McClintock, F. A., 1953, ''Describing Uncertainties in Single Sample Experiments,'' Mech. Eng. (Am. Soc. Mech. Eng.), pp. 3–8.
[21] Moffat, R. J., 1982, ''Contributions to the Theory of Single-Sample Uncertainty Analysis,'' ASME J. Fluids Eng., **104**, pp. 250–260.
[22] Ligrani, P. M., Wigle, J. M., Ciriello, S., and Jackson, S. M., 1994, ''Film Cooling From Holes With Compound Angle Orientations: Part 1-Results Downstream of Two Staggered Rows of Holes with 3d Spanwise Spacing,'' ASME J. Heat Transfer, **116**, pp. 341–352.
[23] Pedersen, D. R., Eckert, E. R. G., and Goldstein, R. J., 1977, ''Film Cooling With Large Density Differences Between the Mainstream and the Secondary Fluid Measured by the Heat-Mass Transfer Analogy,'' ASME J. Heat Transfer, **99**, pp. 620–627.
[24] Ligrani, P. M., and Ramsey, A. E., 1997, ''Film Cooling From a Single Row of Holes Oriented in Spanwise/Normal Planes,'' ASME J. Turbomach., **119**, pp. 770–776.
[25] Ligrani, P. M., Wigle, J. M., and Jackson, S. M., 1994, ''Film Cooling From Holes With Compound Angle Orientations: Part 2—Results Downstream of a Single Row of Holes With 6d Spanwise Spacing,'' ASME J. Heat Transfer, **116**, pp. 353–362.
[26] Eriksen, V. L., and Goldstein, R. J., 1974, ''Heat Transfer and Film Cooling Following Injection Through Inclined Circular Holes,'' ASME J. Heat Transfer, **96**, pp. 239–245.

Modal Effects on the Local Heat Transfer Characteristics of a Vibrating Body

K. D. Murphy

T. A. Lambert, Jr.

Department of Mechanical Engineering,
University of Connecticut,
Storrs, CT 06269-3139

This is an experimental investigation of the effects of forced transverse vibrations on the local heat transfer characteristics of a heated, pinned-pinned beam. In particular, the response of a cylindrical beam near its first two natural frequencies, corresponding to the first two vibration modes, is considered. The results show that there is a strong spatial variation in the local Nusselt number and that these variations are closely related to the mode shape of the response. Because the heat transfer measurements were taken at the resonance frequencies, where the structural response was greatest, the measured Nusselt numbers provide an upper bound for the increased convection due to flexible body vibrations, i.e., in the absence of any rigid-body mode. The possibility of large-amplitude nonlinear vibrations are discussed (though they were not witnessed experimentally) in a theoretical framework. [S0022-1481(00)01702-3]

Keywords: Convection, Experimental, Heat Transfer, Vibrating

1 Introduction

Structural/thermal interaction problems are prominent features in many of todays most challenging and relevant engineering applications, such as materials processing, manufacturing (cutting, grinding, etc.), engine development, and electronic components design, to name only a few. In all of these applications, the heat transfer and the mechanical behavior are closely coupled. For example, consider a gas turbine engine. The high-temperature environment produces thermal stresses in the blades which influence their dynamic response. The blade vibrations, in turn, increase the local heat transfer from the blade, changing its temperature profile. From this simple example, it is evident that consideration and knowledge of this thermal/structural coupling is imperative when analyzing or designing new components or processes.

While a wide range of thermal/structural problems have been addressed in the literature ([1–3]), one particularly relevant problem in this field concerns the influence of vibrations on the rate of convective heat transfer from the vibrating body. In particular, most of these studies have focused on the heat transfer from a heated, oscillating wire or cylinder submerged in a fluid. It has been shown that rigid-body oscillations, where the entire structure oscillates but does not deform, can significantly increase the average Nusselt number even at low driving frequencies and amplitudes (see [4] and [5]). This increase in the average Nusselt number due to vibration is typically more pronounced in the presence of a mean cross flow ([6–11]). One common objective in each of these studies has been to correlate the average Nusselt number to some vibration Reynolds number—defined in terms of the driving frequency and amplitude (rather than the response frequency and amplitude), as well as the fluid viscosity. In so doing, these studies ignored the potential for flexible body dynamics to play a significant role in the heat transfer. However, it is well established that flexible bodies subjected to mechanical excitation will experience resonant oscillations (a dramatic amplitude amplification) as the excitation frequency approaches one of the structure's natural frequencies ([12]). Because an increased vibration amplitude is associated with increased convection (see the aforementioned references), it is likely that such resonance behavior will influence the Nusselt number. Similarly, each resonant frequency has an associated spatial mode shape ([12]). These vibration modes should dictate how the Nusselt number varies spatially along the system; e.g., at a vibration node, the amplitude is always zero and there should be no increase in the convection at that point.

The goal of this study is to examine experimentally the influence of the structural dynamic response on the convective heat transfer characteristics of a pinned-pinned cylindrical beam which is heated, submerged in a water bath, and mechanically excited. The specific objectives of this investigation are (i) to measure baseline heat transfer coefficients for a stationary, heated beam submerged in water; (ii) to examine the influence of the excitation frequency and amplitude on the local Nusselt number and, in the process, to make a connection between the heat transfer and the structural response of the beam; (iii) to study the spatial dependence of the heat transfer coefficient for a vibrating beam and correlate it to the vibration modes; and (iv) to determine an upper bound for the Nusselt number and to develop ''rules of thumb'' for how the Nusselt number varies spatially.

2 The Experimental System

Figure 1 shows a schematic of the experimental setup. The system consists of a hollow cylindrical bar made of AISI Type 304L stainless steel mounted on a frame which rests in a 70 gallon fish tank filled with water. The cylindrical beam has an outer diameter of 0.0096 m, an inner diameter of 0.00688 m, and length 0.914 m. A hollow beam was chosen because the reduced cross-sectional area lowers the area moment of inertia and increases flexibility. The ends of the bars were sealed so that the cylinder did not fill with water. Near each end of the beam, through holes were drilled and plastic bushings were pressed into these holes. These bushings served two purposes. First, they acted as low-friction pivot points which closely mimicked the desired pinned-pinned boundary conditions. Second, they electrically isolated the frame from the current which was passed through the bar to produce heating. A steel rod was fit into the bushing to serve as a cross support for the beam, as shown. The ends of the cross support rods were wrapped in insulation and clamped to the frame. A small slot was milled into each end of the beam and a ''pigtail'' of braided copper wire was silver soldered into each slot. The braided wires were sufficiently flexible so as not to hinder the vibration of the beam but thick enough to allow the required current to be delivered. A welding power supply was used to deliver

Contributed by the Heat Transfer Division for publication in the JOURNAL OF HEAT TRANSFER. Manuscript received by the Heat Transfer Division, Jan. 21, 1999; revision received June 25, 1999. Associate Technical Editor: C. Beckerman.

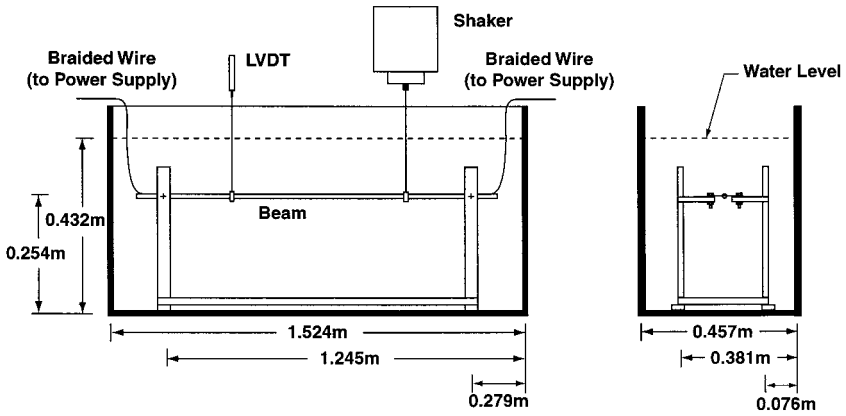

Fig. 1 A schematic of the experimental setup including the beam, frame, water tank, shaker, LVDT, and the relevant dimensions

the current to the beam. This power supply could produce up to 300 Amps of direct current at a maximum of 8 volts.

Not shown in Fig. 1 are a series of copper pipes which were connected to a water chiller by rubber tubing. The copper pipes were placed in the water at the edges of the tank, i.e., approximately one foot from the beam. Cool water was continuously forced through these pipes to help maintain a uniform ambient temperature (T_∞) of the surrounding fluid during extended testing.

An MB Dynamics Model 50A shaker was used to provide periodic excitation to the beam. The shaker was driven by an HP 33120a function generator and an MB dynamics ss250vcf power amplifier. A two-piece stinger was made from a 0.003175-m diameter steel rod and was used to deliver the load from the shaker to the beam. The upper stinger was connected to the (inverted) shaker. A PCB 208b force sensor was attached to the other end of this upper stinger. The other side of the sensor was attached to the lower stinger. The lower stinger was then screwed into a steel swivel pin which was embedded in a nylon coupling attached to the beam. The nonconductive coupling electrically isolated the shaker and the other electrical components while allowing the stinger to pivot when the shaker was used at high force levels. This sensor/stinger configuration allowed for constant monitoring of the periodic force applied to the beam. The force sensor was powered by a small power supply and its signal was output to an HP 3567a dynamic signal analyzer.

The transverse displacement of the beam was measured using a Schaevitz DC-750-200 linear voltage displacement transducer (LVDT). The LVDT was mounted above the beam and the LVDT shaft (its ''core'') was screwed into a nonmagnetic plastic coupling, similar to the one used with the stinger configuration. This coupling was attached to the beam and electrically isolated the LVDT and its components. The LVDT was powered by a HP e3620a DC power supply and its output signal was sent to a data acquisition board connected to a computer.

The temperature of the beam was measured at seven evenly spaced locations along its length using 26-gauge T-type thermocouples. These thermocouples were attached to the beam using aluminum tape that could keep the thermocouples attached to the beam during testing. This approach was used because spot welded thermocouples regularly broke off when the response amplitude was large. The aluminum tape method of attachment was tested against spot welding at both low and high frequencies (away from any structural resonance where the response may become large). The test showed that the aluminum tape and the spot welds rendered almost identical results. In other words, the tape did not affect the response of the thermocouples. Three additional thermocouples were attached to a stand which was placed 6 cm from beam. These thermocouples were arranged such that one lay in the horizontal plane of the beam and the other two were approximately two centimeters above and below that plane, respectively. These three thermocouples were used to measure the vertical temperature gradient of the water near the beam in order to obtain a film temperature to be used as T_∞ in the calculations of the Nusselt number. The voltage output from the thermocouples was sent to a signal conditioning unit (described below) and then to a data acquisition board attached to a computer.

It should also be noted that the time constant for the thermocouples is approximately one second in air, which is much slower than the structural response of the beam. However, the response of the thermocouples did not play a substantial role in the measurements for the following reason. During testing, ten seconds of temperature data would be acquired at a sampling rate of 1 kHz. All of the time traces showed a small but noticeable temperature fluctuation, which is attributed to the time response of the thermocouple. However, the fluctuation was always much less than the uncertainty of the thermocouple (± 1.0°C). In other words, this error was buried down in the noise level. This fact, coupled with the fact that steady-state temperature measurements were desired (not transients), the response of the thermocouple did not play a substantial role.

The data acquisition setup consisted of a data acquisition board with seven National Instruments (NI) 5B37 isolated, nonlinearized, T-type thermocouple signal conditioners and one NI 5B41 isolated voltage input signal conditioner. The LVDT was connected to the isolated voltage input while the seven thermocouples on the beam were connected to the thermocouple signal conditioners. After each test, the first three thermocouples were disconnected from the data acquisition board and the three thermocouples mounted on the remote stand, used to measure T_∞, were connected. The data acquisition board was attached to a 200-MHz Pentium Pro PC and sampling was accomplished using a program developed in LABView. All steady-state temperature measurements were acquired at 1 Hz while the signal from the LVDT was sampled at 1000 Hz.

3 Heat Transfer Calculations and a Structural Model

The following subsections briefly outline the theoretical background for this work. It should be pointed out that there is no detailed description of the fluid mechanics involved even though the structural vibrations disturb the surrounding fluid, producing a flow field. However, this fluid motion is localized around the beam and does not reach into the far field of the fluid bath. As a result, flow effects are negligible (at least compared to the dramatic cross flow effects witnessed by Saxena and Laird [7] and Anatanarayanan and Ramachandran [8] and not considered here. Added mass effects and fluid damping effects *have* been taken into account in the structural model.

3.1 Heat Transfer. As discussed previously, a welding power supply is used to provide a direct current through the cylinder with a maximum current of 300 Amps at 8 volts. The power delivered to the beam, which is converted to heat, may be expressed as

$$q = i^2 R \tag{1}$$

where q is the power, i is the current, and R is the resistance of the beam. Prior to the heat transfer tests, the resistance of the cylinder was found using a sensitive ohmmeter. During testing, the current passed through the beam was measured continuously using a clamp-on ammeter.

At steady state, the heat transfer due to radiation was found to be negligible in this system and, as such, the only mechanisms for appreciable heat transfer was conduction within the beam and convection between the cylinder and the static fluid bath. The local convection coefficient may be defined ([13]) as

$$h(x,\omega) = \frac{q/A}{T_s - T_\infty} \tag{2}$$

where x is position coordinate along the length of the beam, ω is the excitation frequency, q is the input energy, $A = \pi L d_o$ is the beams surface area, d_o is the beams outer diameter. T_s and T_∞ are the local surface temperature of the beam and the film temperature of the water, respectively. T_s was measured at seven points along its length using T-type thermocouples. For these experiments, the temperature of the fluid at infinity, T_∞, is defined as the average of the output from the three remote thermocouples measuring the vertical temperature gradient approximately 6 cm from the beam. For each set of experimental data, the heat transfer coefficient was determined.

The Nusselt number, Nu, is a dimensionless measure of the temperature gradient at the structure/fluid interface. This provides a nondimensional framework for considering the convection coefficient h and is defined ([13]) by

$$\mathrm{Nu} = \frac{h d_o}{k_f} \tag{3}$$

where k_f is the thermal conductivity of the fluid. Because of its nondimensional form, the Nusselt number is used throughout this work rather than the dimensional convection coefficient h.

3.2 Structural Model. The vibrating beam considered in this study may be modeled using nonlinear Euler-Bernoulli beam theory. The governing equation for transverse motion of the beam may be developed using Hamilton's principle ([12]) and leads to

$$m\frac{\partial^2 v}{\partial t^2} + c\frac{\partial v}{\partial t} + EI\frac{\partial^4 v}{\partial x^4} - \frac{\partial}{\partial x}\left(N_x \frac{\partial v}{\partial x}\right) = F\delta(x - x_o)\sin(\omega t) \tag{4}$$

where v is the transverse deflection, m is the combined mass of the beam and the added fluid mass per unit length, c is the combined structural and fluid damping per unit length, t is time, E is Young's modulus, I is the area moment of inertia, x_o is the location of the externally applied point load F, and ω is the excitation frequency. N_x is the axial load imposed on the beam due to (i) quasi-static *axial* deformation of the beam and (ii) compressive loads due to the applied thermal field: $N_x = -EA\alpha T(x) + (EA/2L)\int_0^L (\partial v/\partial x)^2 dx$, where α is the thermal expansion coefficient and $T(x)$ is the spatially varying temperature rise above ambient. For a more detailed discussion, see [14].

This partial differential equation may be transformed to an ordinary differential equation by assuming a separable solution of the form $v(x,t) = a_i(t)\Psi_i(x)$ and applying Galerkin's procedure ([12]). Because the ends of the beam are simply supported, the modes of the linear beam are used as spatial expansion functions: $\Psi_i(x) = \sin(i\pi x/L)$. In this study, only $i = 1,2$ are considered. The ordinary differential equation of motion takes the form

$$m\ddot{a}_i + c_i + \left[EI\left(\frac{i\pi}{L}\right)^4 - EA\alpha\frac{2}{L}\left(\frac{i\pi}{L}\right)^2 C_1 + EA\alpha\frac{2}{L}\left(\frac{i\pi}{L}\right)C_2\right]a_i + \left[\frac{EA}{4}\left(\frac{i\pi}{L}\right)^4\right]a_i^3 = \frac{2F}{L}\sin\left(\frac{i\pi x_o}{L}\right)\sin(\omega t) \tag{5}$$

where $C_1 = \int_0^L T(x)\sin(i\pi x/L)dx$, $C_2 = \int_0^L T'(x)\cos(i\pi x/L)dx$, dots and primes refer to differentiation with respect to time and space, respectively. This is a nonlinear ODE in the modal coefficient a_i and may be solved using a perturbation method (for weakly nonlinear motion) or numerical integration. The specific physical constants (damping, added mass, etc.) for this system were measured and the results are described in the following subsection.

3.3 System Identification. For this study, the cylindrical beam was made of AISI Type 304L stainless steels. This material is an austenitic Cr-Ni stainless steel that has better corrosion resistance than most other stainless steel. This added corrosion resistance was beneficial since the beam would be submerged for extended periods of time. The AISI type 304L stainless steel has an elastic modulus of 193 GPa and a density of 8.00 g/cm^3. The electrical resistivity of the beam is 0.000072 Ohm-cm at 20°C.

To determine the system damping, the bar was ''plucked'' while submerged and the time response of the beam, measured using the LVDT, was recorded. Using the logarithmic decrement method ([12]), the damping ratio was found to be $\zeta = 0.0377$. Since this test was conducted under water, this damping value captures both the structural damping and any added fluid damping.

The added mass of the beam was found by multiplying the added mass of a translating circular cylinder, $m_{\text{added}} = \rho_{\text{fluid}}\pi(d_0/2)^2$, by the appropriate mode shape ([15]). In other words, if a first mode vibration is being considered, the added mass of a cylinder is multiplied by $\Psi_1(x) = \sin(\pi x/L)$ and integrated over the length of the beam.

Finally, the temperature rise above ambient $T(x)$ used to compute N_x in the structural model is assumed to be of the form: $T_i(x) = T_o + T_1\sqrt{\sin^2(i\pi x/L)}$, for vibrations in the ith mode shape as will be discussed in Section 5.3. The coefficients T_1 and T_o are determined in a least squares sense from the measured temperature fields.

4 Experimental Procedure

As discussed in the Introduction, there are four primary objectives to this study. They are (i) to measure baseline heat transfer coefficients for the heated, stationary beam, (ii) to examine how the excitation frequency and amplitude influence the local Nusselt number and relate it to the structural response, (iii) to study the spatial dependence of the Nusselt number of a vibrating, pinned-pinned beam, and (iv) to determine an upper bound for the Nusselt number under specified loading conditions. To accomplish these objectives, the following procedures were developed to obtain the necessary data.

A series of baseline experiments were performed to determine the steady-state temperature distribution along the stationary (non-vibrating) beam for a variety of input current levels. To begin, no current was passed through the beam and the temperature profile was recorded. The current was then increased to 50 Amps. After ten minutes (to allow all thermal transients to decay), the temperature profile was again recorded. This procedure was carried out in 25 Amp increments thereafter to a maximum of 225 Amps. This series of tests provide baseline temperature distributions from which the stationary Nusselt number, $\mathrm{Nu}_s(x)$, could be computed.

To examine the influence of the excitation frequency (amplitude), the excitation amplitude (frequency) was fixed and the frequency (amplitude) was set to a low level. The input current level from the welding power supply was also set to a fixed level of 200 Amps. The temperature distribution along the beam and the am-

bient fluid temperature were then measured after thermal transients were allowed to decay. Simultaneously, the structural response amplitude of the beam at $\xi = x/L = 0.6604$ was reported at the same parameter settings using the LVDT. The frequency (amplitude) was increased and the temperature distribution and structural response were again recorded. After this increasing frequency (amplitude) sweep was completed, a reverse sweep was also undertaken to determine if there were any hysteretic effects.

The frequency sweeps were conducted in two frequency ranges: (i) 17 Hz$<\omega<$40 Hz and (ii) 60 Hz$<\omega<$80 Hz. These ranges were chosen because they captured the first two resonance frequencies of the beam. These resonance frequencies were found experimentally to be approximately $\omega_1 = 22$ Hz and $\omega_2 = 77$ Hz.

The spatial dependence of the Nusselt number could be extracted simply from the frequency (amplitude) sweep experiments at any given input current level. In addition, based on some physical interpretation of the structural response and the thermal response, upper bounds for the Nusselt number may be inferred from the measured frequency (amplitude) sweep data.

5 Results

5.1 Uncertainty Analysis. As with all experimental studies, uncertainties in the measured quantities (temperature, displacement, etc.) are propagated into an uncertainty in the final result. In order to quantify this final uncertainty in the measurements, an uncertainty analysis has been carried out for each experimental data point presented. In all cases, the uncertainty was computed by the procedure suggested by Moffat [16]. Specifically, for a dependent variable R which is a function of j independent variables x_i, each with uncertainty U_{x_i}, the uncertainty in R may be computed by

$$U_R^2 = \left(\frac{\partial R}{\partial x_1} U_{x_1}\right)^2 + \left(\frac{\partial R}{\partial x_2} U_{x_2}\right)^2 + \cdots + \left(\frac{\partial R}{\partial x_j} U_{x_j}\right)^2 .$$

For the specific case of the Nusselt number, the uncertainty is given by

$$U_{\mathrm{Nu}}^2 = \left[\frac{\partial \mathrm{Nu}}{\partial i} U_i\right]^2 + \left[\frac{\partial \mathrm{Nu}}{\partial T_s} U_{T_s}\right]^2 + \left[\frac{\partial \mathrm{Nu}}{\partial T_\infty} U_{T_\infty}\right]^2 + \left[\frac{\partial \mathrm{Nu}}{\partial d_o} U_{d_o}\right]^2 + \left[\frac{\partial \mathrm{Nu}}{\partial d_i} U_{d_i}\right]^2$$

where the partial derivatives are computed by combining Eqs. (1), (2), and (3). Using such a formula, the propagated uncertainty U_{Nu} may be calculated easily.

For this study, the individual uncertainties in the measured quantities, U_{x_i}, include: $U_{d_o} = U_{d_i} = \pm 1.275 \times 10^{-5}$ m, $U_{T_\infty} = U_T = \pm 1.0$°C, $U_i = \pm 0.5$ Amp, $U_{\mathrm{LVDT}} = \pm 1.2 \times 10^{-5}$ m. The propagated uncertainty has been computed for each result, i.e., for each data point. Rather than showing these in table form, the uncertainties are shown in each figure in the form of an error bar. Under certain circumstances, the calculated uncertainties were so small that the associated error bars were much smaller than the symbols used to indicate the data points. In such cases, the error bars have been omitted.

For the results presented, the relative uncertainty in the Nusselt number ranged from $\pm 0.11 < \mathrm{Nu}/\mathrm{Nu}_s < \pm 0.34$. The larger uncertainties almost always occurred where the Nusselt number was the greatest and, hence, where the temperature difference with T_∞ was the smallest. This tended to make the terms $\partial \mathrm{Nu}/\partial T$ large because the denominator contained $(T_s - T_\infty)^2$. These situations occurred at resonance frequencies (in the frequency sweeps) or at the location where the deflection was the greatest (for a fixed frequency).

5.2 Baseline Tests. The results of the baseline tests, with no structural vibration, are shown in Fig. 2 as a function of location along the beam for various current levels. At each current level, the Nusselt number is approximately constant over the entire length of the beam. At low current levels, the slight spatial variation may be attributed largely to the accuracy of the thermocouples. At higher current levels, material imperfections in the beam undoubtedly contribute to a nonconstant electrical resistivity which, coupled with the accuracy limits of the thermocouples, explain the slight spatial variations in the Nusselt number. The trend shows that as the current level is increased the level of heat transfer increases. This is due to the fact that the increased current (and, hence, the increased heat flux into the beam) causes a greater temperature difference between the beam and the water thereby increasing the heat transfer.

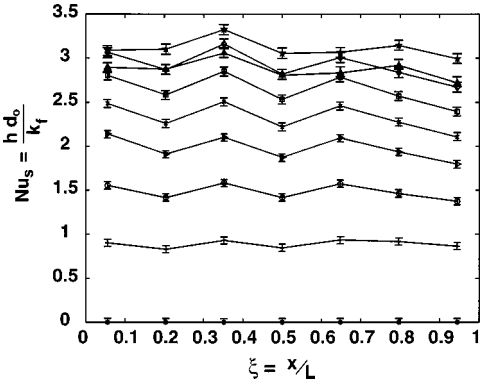

Fig. 2 The Nusselt number as a function of position on the stationary (nonvibrating) beam. The current levels begin at 0 Amps (coincident with the *x*-axis). The next data set is at 50 Amps. Subsequent sets are increased in 25-Amp increments up to 225 Amps.

5.3 Forcing Frequency and Amplitude Effects. Figure 3 shows the amplitude response of the beam at $\xi = 0.6604$ as a function of the excitation frequency in the range of $0.7 < \omega/\omega_1 < 1.8$ (with $\omega_1 = 22$ Hz). The excitation level is $F = 15$ N and the input current is $i = 200$ Amps. The circles represent experimental data points while the solid lines indicate theoretical predictions using the model developed in Section 3.2. For the theoretical results, a temperature profile is assumed in order to compute the thermal stress terms, see Eq. (5). For this work, the temperature profile for the first mode has the form $T(x) = T_o + T_1 \sin(\pi x/L)$. This particular choice for $T(x)$ is based on the Nusselt number distribution along the length of the beam, as will be discussed in Section 5.4.

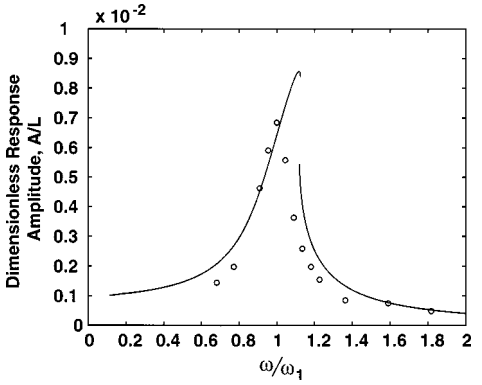

Fig. 3 The amplitude response of the beam at $\xi = x/L = 0.6604$ near the first resonant frequency of the beam with a forcing amplitude of 15 N. The experimental results are indicated by the data points (○) and the theoretical response, based on Eq. (5), is given by the solid line.

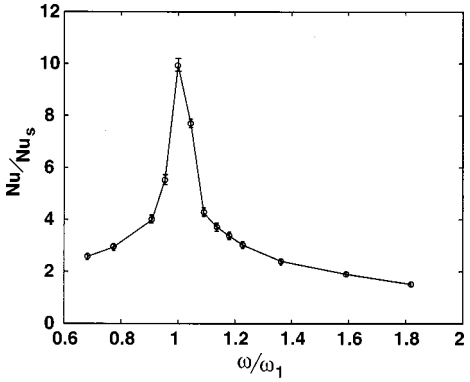

Fig. 4 The response of the Nusselt number (relative to the stationary case) at the center of the beam as a function of excitation frequency near the first resonant frequency of the beam. Here, $F=15$ N and $i=200$ Amps. A peak clearly occurs near resonance matching the amplification of the structural response seen in Fig. 3.

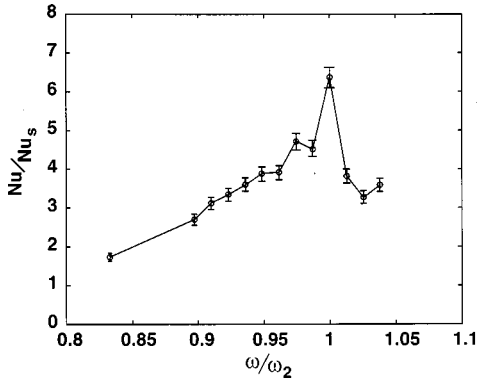

Fig. 5 The response of the Nusselt number (relative to the stationary case) near the quarter cord of the beam as a function of excitation frequency near the second resonant frequency of the beam. The input force and current are $F=15$ N and $i=200$ Amps, respectively. Again a peak occurs near the second resonance in keeping with the structural response.

This amplitude response diagram shows the typical response characteristics associated with a passage through resonance ([12]). Specifically, as the excitation frequency is increased from a low level, the response amplitude gradually increases until a maximum is achieved at $\omega=\omega_1$. As the frequency is increased further, the response amplitude decreases. Frequency sweeps were taken for both increasing and decreasing ω. The experiment did not demonstrate any hysteresis, i.e., there was no noticeable difference between the increasing ω and decreasing ω sweeps. There was a mild hysteresis in the theoretical results. The origin and meaning of the hysteresis, and its implication for the heat transfer, will be explored in more depth in Section 6.

Note that no error bars appear in Fig. 3. For each of these measured amplitudes, the standard error was less than 1/100 of the nondimensional response amplitude. Since the error bars would be dwarfed by the symbols (representing the data points), they were omitted.

Figure 4 shows the ratio of the dynamic to static Nusselt number as a function of the excitation frequency in the vicinity of the first natural frequency of the beam, ω_1. This Nusselt number ratio is one measure of the increased convection from the beam due to vibrations. The dynamic Nusselt number is computed from the temperature reading at the midspan thermocouple ($\xi=x/L=0.5$) where the beams displacement is largest in the first mode. The static value is obtained by averaging the values of Nu_s along the beam at the given current level, see Fig. 2. The excitation parameters correspond exactly to those used in developing Fig. 3. At low frequencies, the Nusselt number is almost two and a half times larger than the static case. Clearly, even mild vibrations lead to a noticeable increase in the rate of heat transfer. As the frequency is increased toward the first natural frequency, the local Nusselt number is increased by an order of magnitude from the static case. This substantial increase is attributed to the increased vibration amplitude associated with resonance, see Fig. 3. As the frequency is increased past resonance, the Nusselt number decreases due to the reduced vibration amplitude, again shown in Fig. 3. Note that the Nusselt number at resonance is an upper bound for all Nusselt numbers in this frequency range. Furthermore, because the Nusselt number was computed at the center of the beam where the deflection is greatest in the first mode, this ''resonant Nusselt number'' serves as an upper bound both in the frequency *and* spatial domains. In other words, it may be concluded that the ratio of Nu/Nu_s may not exceed ten anywhere on the beam at any frequency in the neighborhood of the first resonance.

Figure 5 shows the Nusselt number ratio as a function of excitation frequency in the range of $0.84<\omega/\omega_2<1.05$ (where $\omega_2=77$ Hz), i.e., capturing the second vibration mode. Again, the excitation force level is held constant at $F=15$ N and the current level is fixed at $i=200$ Amps. For this frequency range, the Nusselt number was computed using the thermocouple located at $\xi=x/L=0.2037$. This point was chosen because it is close to the quarter cord which theoretically undergoes the largest deflection in the second mode and, hence, should experience the greatest additional heat transfer. This figure shows similar trends to those found near the first resonant frequency. The Nusselt number ratio is relatively small in the low frequency range but increase steadily as resonance is approached at $\omega=\omega_2$. Above the resonant frequency, the Nusselt number decreases. The maximum Nusselt number ratio of $Nu/Nu_s\approx 6.5$ occurs at the resonant frequency at $\omega/\omega_2=1$. This serves as an upper bound for the Nusselt number for any point along the beam (since all other points experience smaller displacements) in the range of frequencies near ω_2.

One important difference between the first and second mode results should be noted. At resonance in the first mode, the Nusselt number is amplified approximately ten times. At resonance in the second mode, the amplification is approximately six and a half times. This difference arises from the fact that the maximum deflection of the beam (which occurs at $\xi=0.5$ and $\xi=0.25$ for the first and second mode, respectively) is larger in the first mode than in the second. This occurs because the higher spatial frequency of

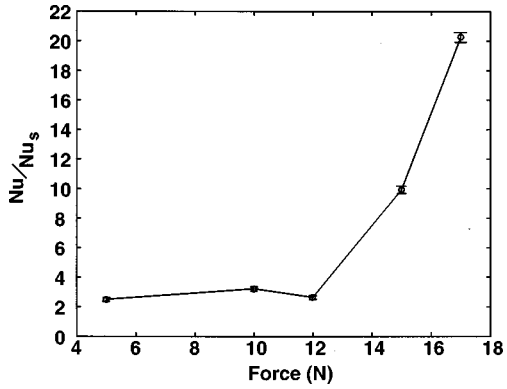

Fig. 6 The response of the Nusselt number (relative to the stationary case) at the center of the beam as a function of the excitation force. Here, $\omega=\omega_1$ and $i=200$ Amps. As the force level increases, the amount of convection increases monotonically.

the second mode prevents the amplitude from becoming as large as the first mode. Therefore it is reasonable to expect that $(\mathrm{Nu}/\mathrm{Nu}_s)|^{\max}_{\text{mode }1} > (\mathrm{Nu}/\mathrm{Nu}_s)|^{\max}_{\text{mode }2}$.

To this point, only the influence of the excitation frequency has been considered. Alternatively, it is useful to examine the influence of the excitation force level. Figure 6 shows the Nusselt number ratio as a function of the forcing amplitude. Here, the current level is $i=200$ Amps and the excitation frequency is $\omega=22$ Hz. These results show that the increase in heat transfer is monotonic with the input force level. This is in stark contrast to the influence of the excitation frequency which had a nonmonotonic effect due to resonance.

5.4 Spatial Effects. Next, consider the spatial variation of the Nusselt number along the beam as it is being excited in its first vibration mode. Figure 7 shows the ratio of the dynamic to static Nusselt number along the length of the beam under a resonant excitation of $\omega=22$ Hz at a load of $F=15$ lbs and a current of $i=200$ Amps. The spatial variation of the Nusselt number follows roughly the symmetric, half sine wave, $\sin(\pi\xi)$, of the first vibration mode for a pinned-pinned beam. This strongly suggests that the increase in the local heat transfer is directly related to local deflection of the beam. However, if this were absolutely true, the ratio of $\mathrm{Nu}/\mathrm{Nu}_s$ would be equal to one at the ends since the deflection is zero. The trend shown in Fig. 7 suggests that at the ends of the beam the Nusselt number ratio is $2.5<\mathrm{Nu}/\mathrm{Nu}_s<3$. This increase in heat transfer—even when there is no deflection—may be attributed to the local flow field induced by the vigorous oscillations of the beam at resonance. Finally, note that the local heat transfer in the center of the beam is approximately ten times greater than the static case as was mentioned in relation to Fig. 4.

Figure 8 shows the spatial variation in the Nusselt number ratio versus position as the system is excited in its second vibration mode. This result corresponds to an excitation frequency of $\omega=77$ Hz at a load of $F=15$ lbs and a current of $i=200$ Amps. At first glance, the spatial variation in the Nusselt number ratio does not resemble a full sine wave, $\sin(2\pi\xi)$, corresponding to the second vibration mode shape. This is explained by the fact that the deflection of the beam, whether above or below the straight equilibrium configuration, always tends to *increase* the Nusselt number. Consequently, this result looks more like a rectified full sine wave: $\sqrt{\sin^2(2\pi\xi)}$. The obvious trends in this figure are that the peaks of the Nusselt number ratio appear near the quarter cord of the beam while there is very little increase in heat transfer at the ends and at the node in the center of the beam. Again, one might expect there to be no increase in $\mathrm{Nu}/\mathrm{Nu}_s$ at the ends or at the central node since the beam deflection is always zero. The mild increase in the Nusselt number ratio may be attributed to the vibration induced flow field near the beam, causing increased local convection.

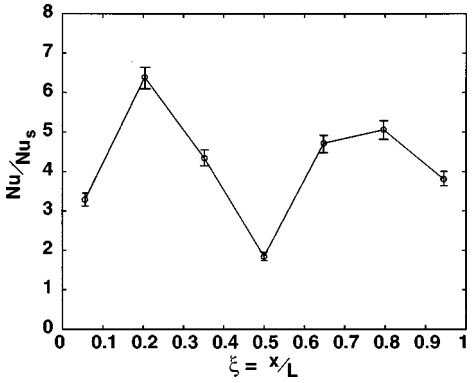

Fig. 8 The spatial distribution of the Nusselt number (relative to the stationary case) as the beam is excited at the second resonant frequency $\omega_2=77$ Hz. Again, $F=15$ N and $i=200$ Amps.

6 Nonlinear and Hysteretic Effects

It has been demonstrated that the structural response and the Nusselt number ratio are sensitive functions of the excitation frequency due to resonance effects. This fact is clearly shown in Figs. 3 and 4. However, this frequency dependence may also be *path dependent* (i.e., initial condition dependent). This is demonstrated in Fig. 9 which shows the response of the beam model at $\xi=0.6604$ for the high excitation amplitude of $F=25$ N. At low excitation frequencies, the response amplitude is small. As the frequency is increased, the response grows along the upper branch until $\omega/\omega_1=1.2721$. At this frequency the response ''jumps down'' to the lower branch as indicated in the figure. Now, consider starting at a high frequency. As the frequency is gradually reduced, the response grows along the lower branch until $\omega/\omega_1=1.1846$. At this frequency, the response amplitude suddenly ''jumps up'' to the upper branch. Clearly, the frequency range $1.1846<\omega/\omega_1<1.2721$ constitutes a hysteresis zone where the response amplitude depends on the path taken. This hysteretic behavior is common in large amplitude, nonlinear structural vibrations and arises from the *hardening spring* characteristics of the beam.

Because it has been shown that the heat transfer is closely tied to the response amplitude, it is thoroughly reasonable to suspect that the Nusselt number ratio will also be multi-valued in this

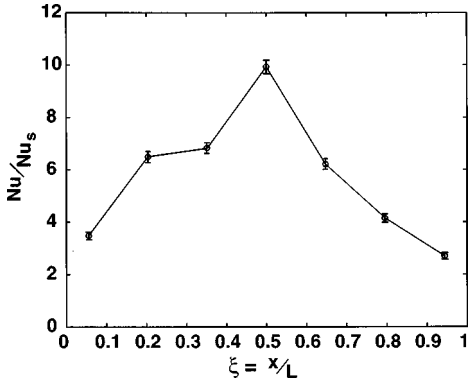

Fig. 7 The spatial distribution of the Nusselt number (relative to the stationary case) as the beam is excited at the first resonant frequency: $\omega_1=22$ Hz. The input force and current are $F=15$ N and $i=200$ Amps, respectively.

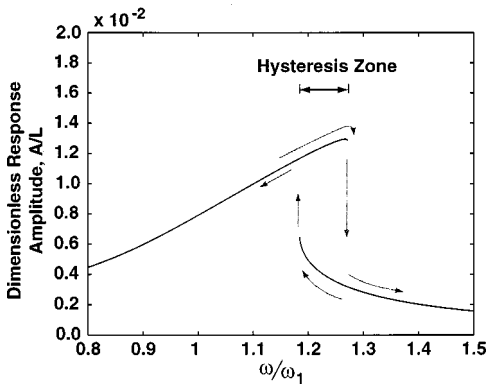

Fig. 9 The amplitude response diagram for the large-amplitude nonlinear response of the beam. The response curve has the typical *hardening* characteristic (bending to the right) and shows a region of hysteresis.

frequency range. Unfortunately, the experimental system developed for this study was unable to produce such large forces. As a result, the displacements achieved were restricted to the linear regime, preventing an experimental verification of this hysteresis effect. Nonetheless, this result serves as an important cautionary note; nonlinear and path-dependent effects may be relevant to heat transfer involving flexible body vibrations.

7 Conclusions

Traditional studies on the convective heat transfer from a vibrating body have focused on wires and cylinders undergoing *rigid-body translations* in either a stationary fluid or in a cross flow. In contrast, this study investigates experimentally the influence of flexible body vibrations on the convective heat transfer. Specifically, the vibrations of a pinned-pinned heated beam are considered. Four subjects related to this problem are addressed and the following conclusions are drawn:

• *Baseline Tests*: A series of baseline tests are performed to determine the static Nusselt number (i.e., no beam vibrations) as a function of position along the length of the beam. These tests show that the static Nusselt number is approximately constant over the length of the beam but increases as the heat flux to the beam is increased.

• *Frequency and Amplitude Dependence*: The Nusselt number is seen to be a sensitive function of excitation frequency. As the excitation frequency is changed and the system passes through a structural resonance, the Nusselt number changes in kind. In other words, the Nusselt number mimics the structural response and, hence, changes nonmonotonically with the input frequency. Nonlinear and hysteretic effects are also witnessed in a theoretical framework but are not verified experimentally. Finally, the Nusselt number is found to be a monotonic function of the applied forcing amplitude. As the excitation level increases, the structural response and the Nusselt number increase.

• *Modal Effects*: For flexible body vibrations, the Nusselt number has strong local tendencies, i.e., it is spatially dependent. For the pinned-pinned beam, it is shown that the spatial dependence of the Nusselt number roughly follows a rectified sine wave. From these results, it may be inferred that the spatial dependence of the Nusselt number for *any* continuous structure will roughly follow a rectified version of that structures mode shapes.

• *Upper and Lower Bounds for the Nusselt Number*: The lower bound is simply the static Nusselt numbers obtained in the baseline tests. An upper bound for the increase in convection from a vibrating body may be obtained by considering the flexible body dynamics and the loading conditions. For a range of operating conditions, the maximum will always occur near the resonant frequency of the structure, e.g., for a range of input frequencies near ω_i, the maximum Nusselt number will occur at ω_i. Furthermore, this maximum will always occur at an antinode of the ith mode, i.e., where the vibration amplitude is always the greatest.

These results indicate that flexible body vibrations can significantly increase the convective heat transfer from a body. Beyond simply demonstrating this fact, this work serves to highlight *how* and *why* the Nusselt number is influenced by the structural vibrations for the particular case of a pinned-pinned beam. While these results are specific to beams with pinned boundaries, they may be extrapolated to provide a more general understanding of heat transfer from any vibrating, flexible structure. Specifically, these results provide a guideline for ''where to look'' for the maximum Nusselt number on any structure. This only requires a knowledge of the input frequencies and the mode shapes; maximums will occur near resonant frequencies and, spatially, at the antinodes of the excited mode.

Acknowledgments

The authors thank Dr. Ranga Pitchumani for his many useful comments. The support of the National Science Foundation, grant number CMS-9625319, is gratefully acknowledged.

Nomenclature

A = cross-sectional area of the beam (m^2)
E = elastic modulus (kg/ms^2)
F = excitation force amplitude (N)
h = convection coefficient (W/m^2 °C)
i = input current (Amps)
I = area moment of inertia (m^4)
k_f = thermal conductivity (W/m °C)
L = length of the beam (m)
m = mass per unit length of the beam (kg/m)
Nu = Nusselt number (dimensionless)
Nu_s = Nusselt number of the stationary beam (dimensionless)
q = input power (W)
R = resistance of the beam (Ω)
T = surface temperature of the beam (the same as T_s) (°C)
T_∞ = film temperature (°C)
v = displacement of the beam (m)
x = spatial coordinate along the beam (m)
x_o = location of the applied force (m)
α = thermal expansion coefficient for the beam (1/°C)
ω = excitation frequency (Hz)
ω_i = ith natural frequency of the beam (Hz)
ξ = nondimensional axial coordinate ($=x/L$) (dimensionless)

References

[1] Richardson, P. D., 1967, ''Effects of Sound and Vibration on Heat Transfer,'' Appl. Mech. Rev., **20**, No. 3, pp. 201–217.
[2] Tauchert, T. R., 1991, ''Thermally Induced Flexure, Buckling, and Vibration of Plates,'' Appl. Mech. Rev., **44**, No. 8, pp. 347–360.
[3] Thornton, E. A., 1993, ''Thermal Buckling of Plates and Shells,'' Appl. Mech. Rev., **46**, No. 10, pp. 485–506.
[4] Deaver, F. K., Penny, W. R., and Jefferson, T. B., 1962, ''Heat Transfer From an Oscillating Horizontal Wire to Water,'' ASME J. Heat Transfer, **84**, pp. 251–254.
[5] Armaly, B. F., and Madsen, D. H., 1971, ''Heat Transfer From an Oscillating Horizontal Wire,'' ASME J. Heat Transfer, **93**, pp. 239–240.
[6] Blevins, R. D., 1977, *Flow Induced Vibrations*, Van Nostrand Reinhold, New York.
[7] Saxena, U. C., and Laird, A. D. K., 1978, ''Heat Transfer From a Cylinder Oscillating in a Cross-Flow,'' ASME J. Heat Transfer, **100**, pp. 684–688.
[8] Anatanarayanan, R., and Ramachandran, A., 1958, ''Effect of Vibration on Heat Transfer From a Wire to Air in Parallel Flow,'' ASME J. Heat Transfer, **80**, pp. 1426–1432.
[9] Faircloth, J. M., and Schaetzle, W. J., 1969, ''Effect of Vibration on Heat Transfer for Flow Normal to a Cylinder,'' ASME J. Heat Transfer, **91**, pp. 140–144.
[10] Cheng, C. H., Chen, H. N., and Aung, W., 1997, ''Experimental Study of the Effect of Transverse Oscillations on Convection Heat Transfer From a Circular Cylinder,'' ASME J. Heat Transfer, **119**, pp. 474–482.
[11] Thrasher, B. H., and Schaetzle, W. J., 1970, ''Instantaneous Measurement of Heat Transfer From an Oscillating Wire in Free Convection,'' ASME J. Heat Transfer, **92**, pp. 439–445.
[12] Meirovitch, L. E., 1967, *Analytical Methods in Vibrations*, Macmillan, New York.
[13] Incropera, F. P., and DeWitt, D. P., 1985, *Introduction to Heat Transfer*, John Wiley and Sons, New York.
[14] Tseng, W. Y., and Dugundji, J., 1970, ''Nonlinear Vibrations of a Beam Under Harmonic Excitation,'' ASME J. Appl. Mech., **37**, pp. 292–297.
[15] Yih, C.-S., 1988, *Fluid Mechanics*, West River Press, Ann Arbor, MI.
[16] Moffat, R. J., 1988, ''Describing the Uncertainties in Experimental Results,'' Exp. Therm. Fluid Sci., **1**, pp. 3–17.

Identification of Dominant Heat Transfer Modes Associated With the Impingement of an Elliptical Jet Array

S. C. Arjocu
Medical University of South Carolina,
Charleston, SC 29403

J. A. Liburdy
Department of Mechanical Engineering,
Oregon State University,
Corvallis, OR 97331
e-mail: liburdy@eng.clemson.edu

The characteristics of the impinging heat transfer of a three-by-three square array of submerged, elliptic impinging jets was studied. Low Reynolds number conditions, 300 to 1500, are considered for two different elliptic jet aspect ratios, with the impingement distance ranging from 1 to 6 jet hydraulic diameters. A transient thermochromic liquid crystal method was used to map the local heat transfer coefficient distribution. The results are reported for the unit cell under the center jet and detail the mean heat transfer as well as the characteristics of the spatial variation of the heat transfer coefficient. The average heat transfer is found to depend inversely on the elliptic jet aspect ratio at these low Reynolds numbers. Distributions of the heat transfer coefficient, h, are also used to obtain proper orthogonal decompositions of h which are used to identify major spatially distributed features. [S0022-1481(00)02102-2]

Keywords: Enhancement, Forced Convection, Heat Transfer, Impingement, Jets

Introduction

Impinging jets, both single jets and jet arrays, have been successfully and extensively used in mass and heat transport applications. The flow and geometrical conditions such as Reynolds number, impingement distance, jet geometry, and jet spacing strongly influence the heat transfer rate. In addition, large scale structures have been shown to exist within the flow and have been considered as a possible mechanism responsible for heat transfer enhancement. Arrays of impinging circular jets have been studied to determine optimal geometric conditions for heat transfer. However, information for very low Reynolds number jets, which are often used in electronic cooling, is not available. For larger Reynolds numbers, 2,500 to 4,000,000, Martin [1] has identified optimum impingement and jet separation distances. Details of circular jet array impingement heat transfer were obtained by Goldstein and Timmers [2] Pan and Webb [3], and Huber and Viskanta [4]. These studies show how heat transfer uniformity and overall magnitude is affected by jet spacing at relatively high Reynolds numbers. Huber and Viskanta show that as Reynolds number is decreased, secondary peaks of the heat transfer coefficient away from the jet centerline are eliminated. These secondary peaks have been attributed to fluid acceleration, boundary layer thinning, and turbulence transition.

Elliptic jets have been studied much less than circular jets, but it is apparent that they have unique flow characteristics in the development region of the jet. The instability of the jet shear layer with a nonuniform distribution of momentum thickness at the jet exit determines different roll-up locations and vortex pairing events in the major and minor axes (Husain and Hussain [5]). The shear layer spreading differs circumferentially (Ho and Gutmark, [6]) and the mass entrainment can be as much as three to eight times larger than circular or planar jets (Lee et al. [7]). The well-documented axis switching phenomena that occurs for single elliptical jets was also shown by Barker and Liburdy [8] for elliptic impinging jets and by Arjocu and Liburdy [9] for an elliptic jet array. The axis switching occurs in the range of three to four jet hydraulic diameters downstream of the exit. The flow field within the same three-by-three elliptic jet array used in this heat transfer study was described by Arjocu and Liburdy [10].

Circular jet flow structures have been studied using proper orthogonal decomposition analysis by Sirovich et al. [11]. They applied this technique to two-dimensional axisymmetric jet field images to identify large scale structures. Similarly, in the mixing layer of an axisymmetric jet, Glauser [12] identified a large-scale structure that transported 40 percent of the turbulent energy, another 40 percent of the energy was carried by the second and third-order structures. The flow field in a three-by-three elliptic jet array similar to that used in this heat transfer study was described by Arjocu and Liburdy [9,10]. They noted that the three-dimensional large-scale elliptic structure developed by the central jet in the array was similar to a single excited elliptic jet ([13]). Arjocu and Liburdy [9] evaluated the vorticity field in the impingement region of the jet array by introducing a modified circulation, Γ^*, which is the integrated squared vorticity in the near wall region of impingement. This measure of the near-wall vorticity field was shown to be strongly Reynolds number dependent at these low jet Reynolds number flows. In the jet array, increasing the Reynolds number or the impingement distance results in a large number of shear layer flow structures generated by the interaction of the returning fluid with the jet flow. At large values of impingement distance the jet sways, where the entire jet column has a wave-like motion, with an amplitude and frequency depending on the Reynolds number.

This experimental study focuses on the identification and quantification of the contribution of the large-scale flow structures on the heat transfer associated with an elliptic jet array impinging on a constant heat flux surface. Low Reynolds number jets, 300 to 1500, are used with applications to low-pressure-driven cooling applications. The relationship between the heat transfer distribution and flow characteristics is considered. Also, dominant modes associated with the local heat transfer coefficient distribution are determined using proper orthogonal decomposition.

Experimental Method

This study considers a three-by-three submerged elliptic jet array impinging on a flat heated surface. The array is square with a

Contributed by the Heat Transfer Division for publication in the JOURNAL OF HEAT TRANSFER. Manuscript received by the Heat Transfer Division, December 30, 1997; revision received, December 2, 1999. Associate Technical Editor: J.-C. Han.

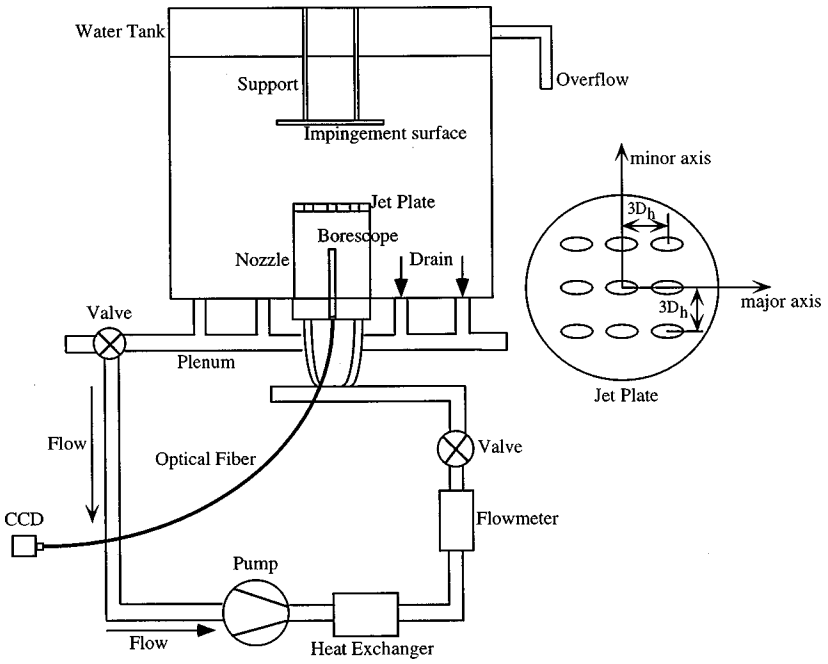

Fig. 1 Experimental flow facility

pitch of three jet hydraulic diameters. Two different jet major-to-minor axes aspect ratios ($r=2$ and 3) were used, with both jets having a hydraulic diameter of $D_h=9$ mm. The impingement distance, normalized by the jet hydraulic diameter, was varied from $H=1$ to 6. The jet exit temperature was kept constant at 20°C. All studies were carried out in water.

The experimental facility is presented in Fig. 1. The jet plate and impingement surface were submerged in a constant head water tank with a closed flow loop. A water-water heat exchanger was used to control the jet temperature to within +/−0.1°C. The jet plenum contained a set of screens used to assure uniform pressure at the array of jet exits. All exit velocities were checked with a miniature pitot tube and were uniform to within +/−1 percent. The impingement surface was adjusted and leveled within the tank to achieve the desired impingement distance. The jet plenum and the impingement surface formed a confined flow region for the jet array.

A transient heating method was used to determine the local heat transfer coefficient distribution. Below the heater surface a 19-cm-thick UHMW polymer substrate was used to establish a semi-infinite solid boundary condition. A one-dimensional conduction heat transfer model was used to determine the local surface heat transfer coefficient. The exact solution for the surface temperature is ([14])

$$(T_s-T_o)/(q''/h)=1-\exp(h^2t/k\rho c_p)\operatorname{erfc}(h\sqrt{t/\lambda\rho c_p}). \quad (1)$$

The one-dimensional model assumption was verified by analyzing the lateral heat transfer based on the temperature difference between two points below the heat transfer surface a distance of one tenth of the substrate thickness. The lateral heat flux was much less than 0.1 percent of the total heat flux.

Details of the impingement surface and data acquisition system are presented in Fig. 2. A stainless steel heating foil covered the substrate with intimate contact provided by a thin layer of high conductive silicon paste. Two copper bars positioned at each end of the foil supplied power to create a uniform heat flux surface. The uniformity of the heat flux was determined using the mea-

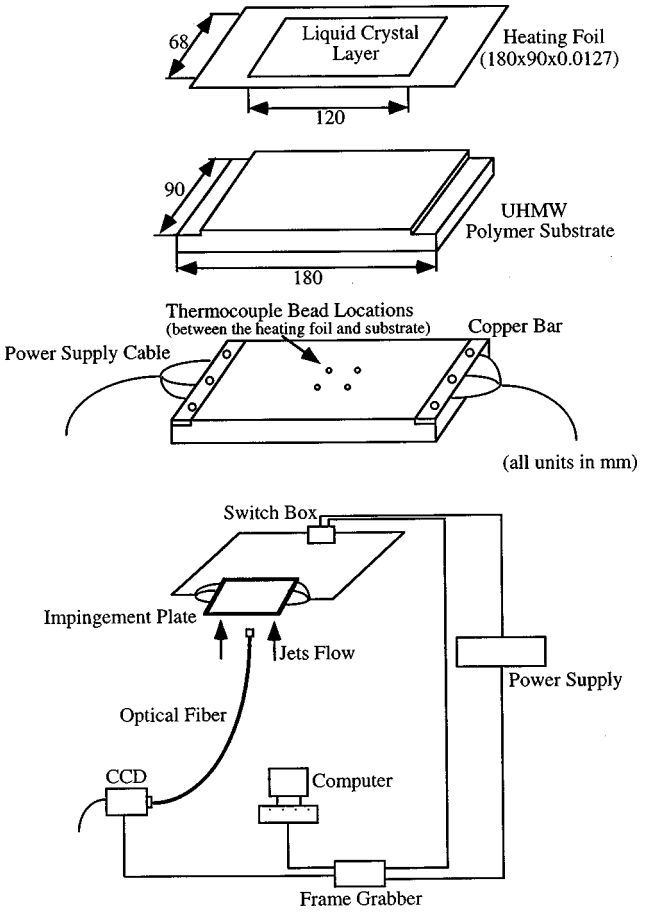

Fig. 2 Heat transfer impingement plate and data acquisition system

sured voltage drop across the heating foil. For ten different locations equally spaced across the foil the standard deviation of the voltage was less than 0.5 percent. A thin layer of black ink was applied on the heating foil on which the liquid crystals were air brushed, layer by layer for a total of three layers. A thin mylar sheet covered the liquid crystals surface protecting it from prolonged water contact.

The liquid crystal was calibrated in place over its operating temperature range of 25–31°C by heating the foil in 0.1°C increments while the jet flow was turned off. The surface temperature was measured during the liquid crystal calibration with four thermocouples positioned just below the heating foil, in the substrate. For visualization an optical fiber and lens system was mounted inside the nozzle, as can be seen in Fig. 2. The field of view was set at approximately 27 mm by 27 mm, using approximately 200 pixels×200 pixels of a three chip CCD camera, surrounding the central jet. The calibration was done using the three RGB camera responses versus temperature to compile a look-up table. Linear interpolation was used between calibration points. Using all three color responses resulted in a lower uncertainty than using a hue-based calibration, (Arjocu [15]). A control circuit activated a trigger that allowed the synchronization of the frame grabber, video camera, and heating foil power supply (Fig. 2). The time for each image was determined to within ± 0.017 s. A total of 40 images were recorded for each condition, over a period of 26 seconds. The impingement surface heat flux was adjusted based on the temperature response of the liquid crystal on the heat transfer surface which was nominally 25°C to 30°C.

The surface temperature data were filtered, passing a 3-by-3 Wiener filter over the surface temperature data, with a linear filter for the corners and edges, for higher accuracy. The temperature difference between the liquid crystal and substrate surface was determined to be negligible based on a one-dimensional conduction model. From the surface temperature distribution, the local convective heat transfer coefficient was obtained using Eq. (1). The uncertainty of the heat flux was the largest contribution to the overall uncertainty of the local heat transfer coefficient which was in the range of 9 to 13 percent (for details see Arjocu [15]).

Lumley [16] introduced the proper orthogonal decompositions (Karhunen-Loeve procedure) method to turbulence by decomposing the velocity vector components into a set of deterministic functions, $\varphi(t)$, by maximizing the scalar product $(\mathbf{u},\varphi)$ (where $\mathbf{u}(t)$ is a square integrable function, and belongs to Hilbert space and the comma represents a scalar product). Based on the Kernel theorem (see Lumley [16]) the analysis reduces to solving the equation

$$\int R(t,t')\varphi_n(t')dt' = \lambda_n \varphi_n(t) \tag{2}$$

which has an infinite number of proper values, λ_n, and orthogonal solutions, $\varphi_n(t)$. In this study, a two-dimensional heat transfer distribution defines the ensemble element with a dependency on the spatial coordinates, *x, y*. The proper orthogonal decomposition basis was obtained solving

$$\int R(x,y,x',y',)\varphi(x',y')dx'dy' = \lambda\varphi(x,y), \tag{3}$$

where $R(x,y,x',y')$ is the autocorrelation matrix for the heat transfer coefficient, *h,* and is given by the expression

$$R(x,y,x',y') = \overline{h(x,y)h(x',y')} = \frac{1}{N}\sum_{1}^{N} h_n(x,y)h_n(x',y'), \tag{4}$$

and *N* is the total number of time sequenced images. The time average, over the *N* spatial heat transfer coefficient distributions, of the total ''energy'' associated with the heat transfer process is

$$\overline{E} = \sum_n \lambda_n . \tag{5}$$

The proper orthogonal decomposition results show that the structure corresponding to the first mode has the highest contribution to the heat transfer ''energy,'' in each of the cases studied. Note that the zero mode corresponds to the spatial mean of the heat transfer coefficient. Since the autocorrelation matrix is based on a spatial correlation of the two-dimensional heat transfer coefficient distribution, the energy of each mode is a measure the ''effectiveness'' of the jet flow structures in cooling the impingement plate.

Results and Discussions

The discussion of the heat transfer results is based on the square unit cell that surrounds the central jet. Results are presented for the instantaneous heat transfer coefficient distribution, the average heat transfer coefficient, and the ''energy'' modes associated with the spatial distribution of the heat transfer coefficient.

Representative heat transfer coefficient distributions, for Re $=300$, $H=2$ and 5, and aspect ratio, $r=3$ are shown in Fig. 3. The consequence of the elliptic orifice are clearly evident at $H=1$ and 2. It should be noted that the variation between the maximum and minimum values of *h* within the unit cell are consistent with the relative variations measured by Huber and Viskanta [4] for a circular jet array at much higher Reynolds numbers. However, the jet spacing used in this study is less than that used by Huber and Vaskanta and it is expected that this maximum-to-minimum range is reduced because of the reduced spacing and also because of the reduced Reynolds numbers. For $H=2$, the time-dependent variation of *h* is evident by a low-frequency oscillation of the peak between one side and the other along the major axis. The peak is shown on one side of the major axis in Fig. 3(*b*). For an impingement distance of $H=3$, the adjacent jet structures tend to move into the central jet unit cell due to significant jet swaying (Arjocu and Liburdy [9]). This intensifies the interaction with adjacent jets and influences entrainment. The results show locally increased heat transfer in the corners of the unit cell. The distribution inside the unit cell becomes closer to a circular shape. At $H=5$, Fig. 3(*c*), the orientation of the elliptical shape has rotated 90 deg. This suggests that axis switching of the central stagnation region structure occurs between $H=3$ and 4, which is consistent with flow visualization studies. At $H=5$, the unit cell distribution of *h* is very uniform, and the small-scale amplitude fluctuations have been reduced. The highest heat transfer coefficients occur at the jet stagnation point and also where the shear layer impinges on the surface. Increasing the impingement distance further, for this low Reynolds number condition results in high local heat transfer coefficients under the shear layer of the return flow, in the corners of the unit cell.

As the Reynolds number is increased to 700 there is still evidence of the bimodal peaks for $H=1$, similar to the lower Reynolds number conditions, shown in Fig. 4(*a*). As *H* increases the bimodal distribution is lost and there is a lateral swaying along the minor axis as shown in Fig. 4(*b*). This movement is consistent with the jet swaying found in flow visualization for $H=3$ and may be a result of pressure oscillations that occur during axis switching (Arjocu and Liburdy [10]).

Shown in Fig. 5 are instantaneous distributions of *h* for Re $=1500$, $H=1$ and $r=2$, where Figs. 5(*a*) and 5(*b*) are for the same conditions but were taken at two different instants in time. There is an increased of the small-scale distribution of *h* over the entire unit cell. The small-scale components are observed to be more prevalent for the higher aspect ratio elliptic jets for the same Reynolds number. Figures 3 and 4 illustrate that the heat transfer coefficient distributions are composed of two primary length scales: the larger scales, which are on the order of the size of the hydraulic diameter of the jets, and the smaller scales, presumable a result of flow instabilities. To document this, power spectra were

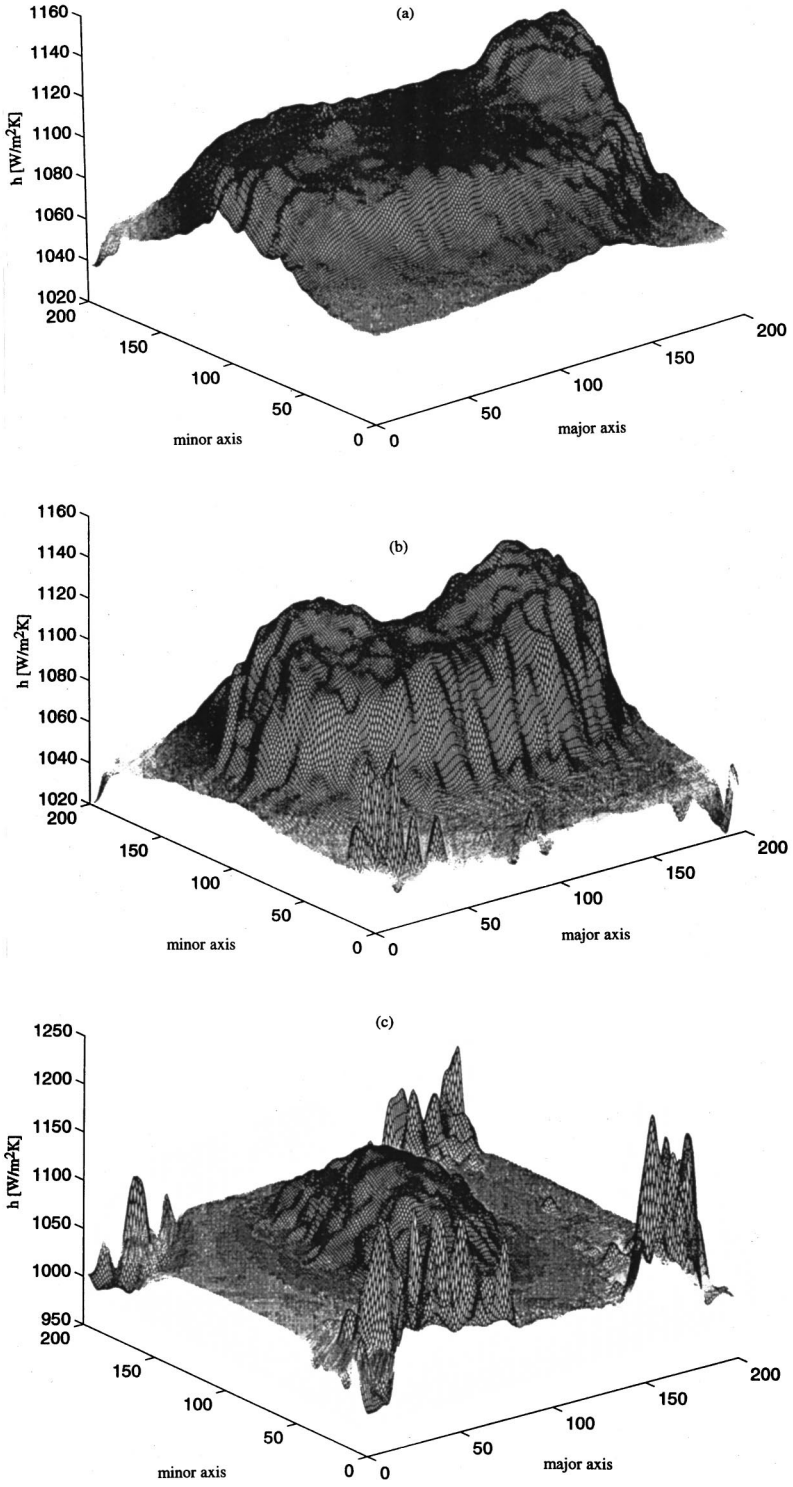

Fig. 3 Spatial heat transfer distribution within the central jet unit cell at Re =300 and $r=3$; (*a*) $H=1$, (*b*) $H=2$, (*c*) $H=5$

determined of the local distributions of the heat transfer coefficients. Associated peaks in the spectrum were used to identify dominant spatial frequencies and the inverse of the frequency was used as an indication of an associated heat transfer length scale. All spectra showed a dominant peak at a frequency of 0.036 pixels/mm which corresponds to a length scale of 27 mm, which is approximately the size of the unit cell. This represents the large scale variation of h over the span of the unit cell. Details of the length scale variation with Reynolds number, impingement distance, and aspect ratio are given in Arjocu [15]. It is found that there is an intermediate length scale of approximately 4 mm that corresponds to the scale of large-scale flow structures at the impingement surface for all conditions studied. This corresponds roughly to one-half of the hydraulic diameter of the jets. Smaller,

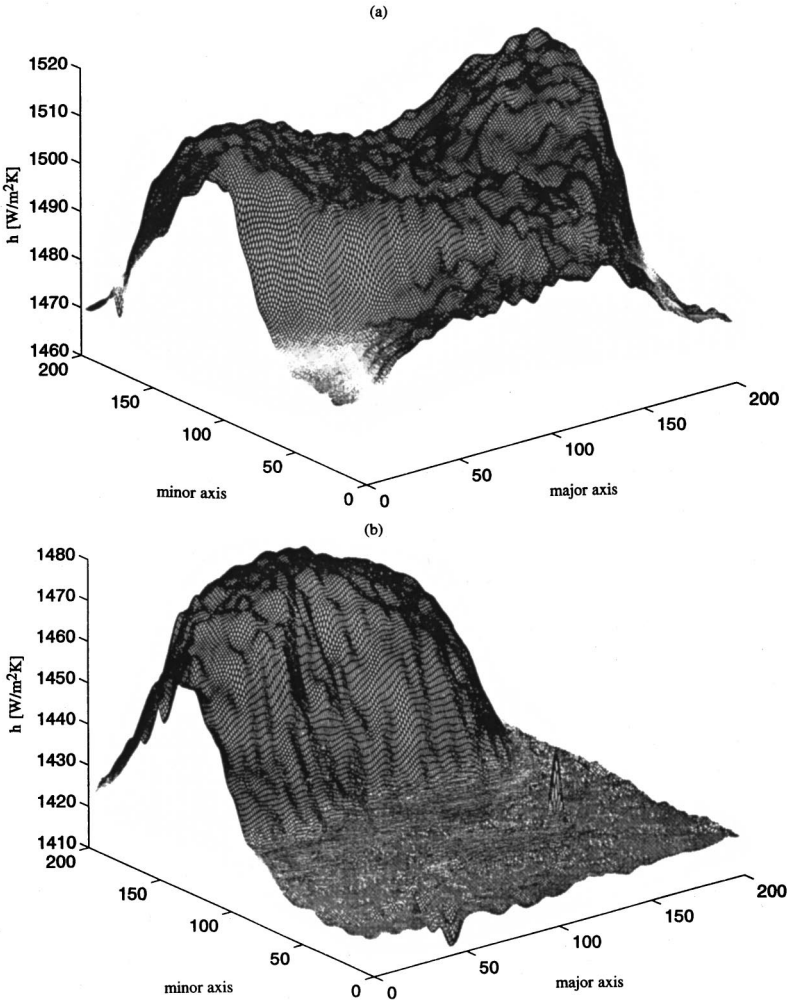

Fig. 4 Spatial heat transfer distribution within the central jet unit cell at Re =700 and $r=3$; (*a*) $H=1$, (*b*) $H=3$

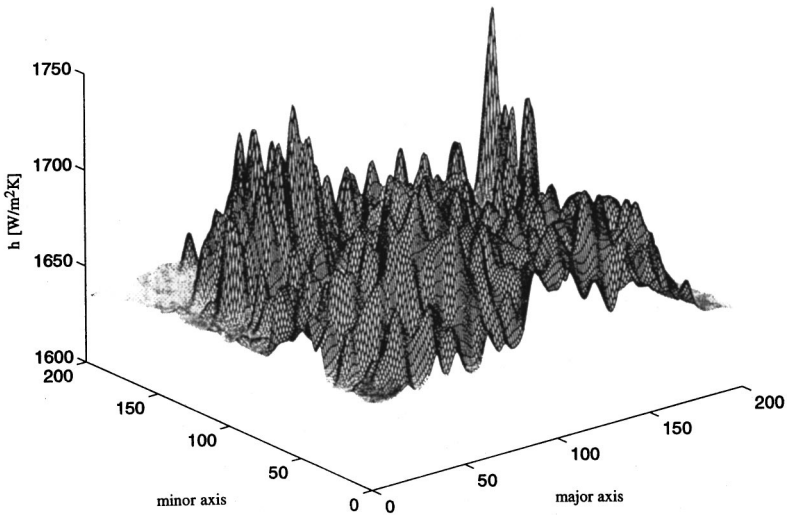

Fig. 5 Spatial heat transfer distribution within the central jet unit cell at Re =1500 and $r=2$, and $H=1$

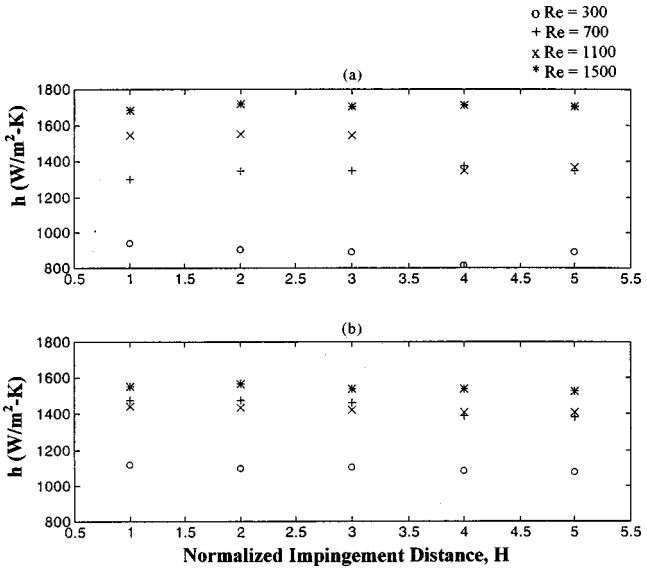

Fig. 6 Average heat transfer coefficient versus impingement distance; (*a*) $r=2$, (*b*) $r=3$

less pronounced, heat transfer and flow length scales were also found at approximately one-quarter and one-eighth of the hydraulic diameter.

Figure 6 shows the variation of the average heat transfer coefficient versus Reynolds number for all of the impingement distances and the two jet aspect ratios. At the lower Reynolds numbers the higher aspect ratio jets achieve more than 16 percent higher heat transfer rates. At the higher Reynolds numbers the lower aspect ratio jets achieve eight percent higher heat transfer. This result indicates that the lower aspect ratio jets have a increased sensitivity to increasing Reynolds number. This higher Reynolds number sensitivity of the lower aspect ratio jets suggests a greater generation of transport producing eddies as the Reynolds number increases; or conversely, a suppression of the large scale enhancing transport properties generated by the higher aspect ratio elliptic jets as the Reynolds number increases. Which if these two mechanism occur is unclear.

To help explain this further the vorticity in the impingement region, defined within the surface layer a distance of 0.5 D_h from

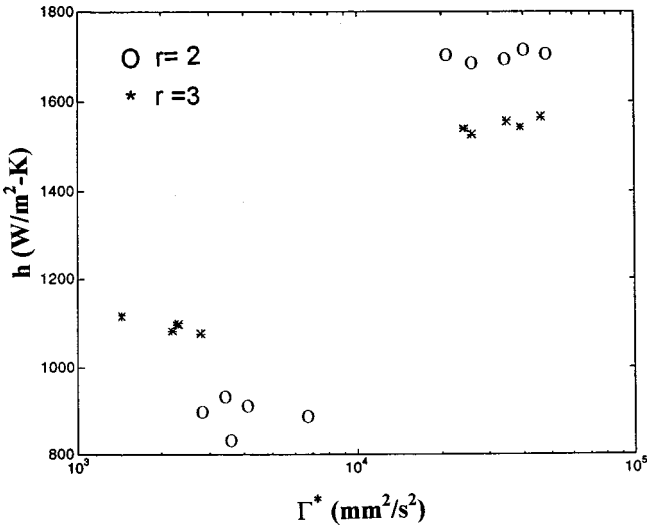

Fig. 7 Average heat transfer coefficient versus modified circulation, Γ*

Table 1 Modal energy distribution of the heat transfer coefficient

Mode Number	$r=2$, $H=2$, Re=1500	$r=2$, $H=4$, Re=1500	$r=3$, $H=2$, Re=300	$r=3$, $H=4$, Re=300
1	85.85%	54.3%	52.55%	54.47%
2	6.57%	22.57%	28.79%	20.56%
3	2.87%	8.71%	4.87%	7.84%
4	2%	5.53%	4.77%	5.07%
5	1.23%	4%	3.19%	4.05%
total energy, [W/m² C]	7.135*10⁵	2.814*10⁵	3.626*10⁵	1.9119*10⁵

the wall, was considered by Arjocu and Liburdy [17]. In that work, a modified circulation Γ* was defined as the integrated vorticity in the surface layer based on the square of the vorticity. The reason the square of the vorticity was used was to characterize a surface renewal property regardless of sign. Figure 7 shows the relationship between the average heat transfer coefficient within the central jet unit cell and the modified circulation, Γ*, (on a semi-logarithmic scale), for jet aspect ratios of 2 and 3. The data are concentrated in two regions of low and high Γ* which also correspond to the low and high Reynolds number conditions between Re = 300 and 1500. The average heat transfer coefficient almost doubles when Γ* increases one order of magnitude. For lower values of Γ* the higher aspect ratio jet results in larger heat transfer while for larger values of Γ* the lower aspect ratio jet provides higher heat transfer rates. This suggests that lower aspect ratio jets generate greater heat transfer contributing vorticity as Reynolds numbers are increased.

To help understand the roles of flow structure on the heat transfer process, proper orthogonal decomposition was applied to the two-dimensional heat transfer coefficient distributions for $H = 2$ and 4. These impingement distances correspond to before and after the jet experiences axis switching. Results are presented for Re=300 and Re=1500, for jet aspect ratio of 3 and 2, respectively, where these aspect ratios correspond to the greatest heat transfer rates for the low and high Reynolds numbers, respectively. Results were obtained using both 30 and 40 images in a time sequence with essentially identical results. This suggests that a sufficiently long time series was used to obtained the decomposition.

The variation of the eigenvalues for the first ten modes of each of the flow conditions shows that beyond ten eigenvalues the energy drops two orders of magnitude, and the remaining modes represents less than 0.5 percent of the total energy. Table 1 shows the energy distribution (in percentages) of the first five modes and the time-averaged total energy as a function of Reynolds number and impingement distance. In the last three cases presented in Table 1, the first two modes have a contribution of nearly 80 percent of the total energy, with the first eigenvalue containing more than 50 percent. For Re = 1500, $H = 2$, and $r=2$, 85 percent of the energy is concentrated in the first mode. In this case, because of the high Reynolds number and low H (before axis switching), the stagnation region flow structure that surrounds the central jet at impingement is very well defined and stable. Beyond the critical impingement distance, for Re=1500 and $H=4$, where axis switching has occurred, there is observed increase in the number of small-scale shear layer structures which increases the overall the turbulence level (Arjocu and Liburdy [9]). The proper orthogonal decomposition analysis illustrates how this effects the heat transfer ''energy'' distribution. The energy of the first mode has dropped to 54 percent of the total with most of the remaining energy contained within the second mode. However, the third, fourth, and fifth modes also show an increased energy content. Therefore, the consequence of increased small-scale flow structures is to divide the heat transfer process into a larger number of energy modes with a more uniform distribution of energy content.

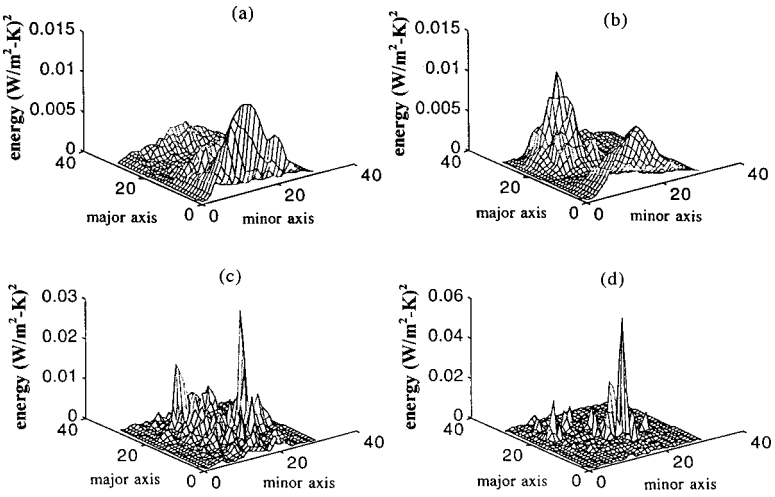

Fig. 8 First-mode proper orthogonal decomposition spatial energy distribution; (*a*) Re=300, *H*=2, *r*=3, (*b*) Re=300, *H*=4, *r*=3, (*c*) Re=1500, *H*=2, *r*=2, (*d*) Re=1500, *H*=4, *r*=2

Figures 8 and 9 show the spatial distribution within the unit cell of the eigenfunction $|\varphi_i|^2$ for the first and second modes, respectively. Note that the orientations of the major and minor axes of both of these figures have been reversed compared to previous figures. The eigenfunctions represents the normalized local energy distribution associated with the various modes. The spatial distributions in Figs. 8(*a*) and 8(*b*) for the first mode at low Reynolds number, strongly resemble the variation of the heat transfer coefficient within the unit cell, seen in Fig. 3. The distributions show regions of high energy near the edges of the major axis, where the flow is accelerated, and a high heat transfer coefficient is induced in the major plane. The second mode shown in Figs. 9(*a*) and 9(*b*) also demonstrates evidence of the bimodal distribution. The local distributions for the high Reynolds number case, in Figs. 8 and 9 are characterized by local oscillations of the modal energy, with a few relative high amplitude peaks for the first two modes. For $H=2$ these oscillations are seen to be superimposed over the bimodal distribution and are more intermittent in nature. This suggests that the average heat transfer coefficient is comprised of dynamic events that occur at both small and large scales and are spatially intermittent.

The average heat transfer results were compared to results for circular jet arrays. There is limited data for the low Reynolds ranges studied, and none available for elliptic jets. However, results were compared with the correlation given by Martin [1] for circular jets over an impingement distance of one to five jet diameters. Martin shows a decrease of Nu with increasing impingement distance, whereas the elliptic jet data is much less sensitive to *H*. Also, the Reynolds number dependence shows a much lower sensitivity (a reduced increase of Nu with increasing Re). When extrapolating Martin's correlation to the Reynolds number range for this study all of the elliptic jet data fall between the extremes of the predictions by Martin for the full range impingement distances. See Arjocu [15] for details.

Conclusions

This study evaluates the local heat transfer distribution in the central unit cell of an array of elliptic impinging jets at relatively low Reynolds numbers. The spatial distribution consists of two types of structures: (i) large-scale structures comparable with the jet hydraulic diameter and (ii) small-scale structures induced pri-

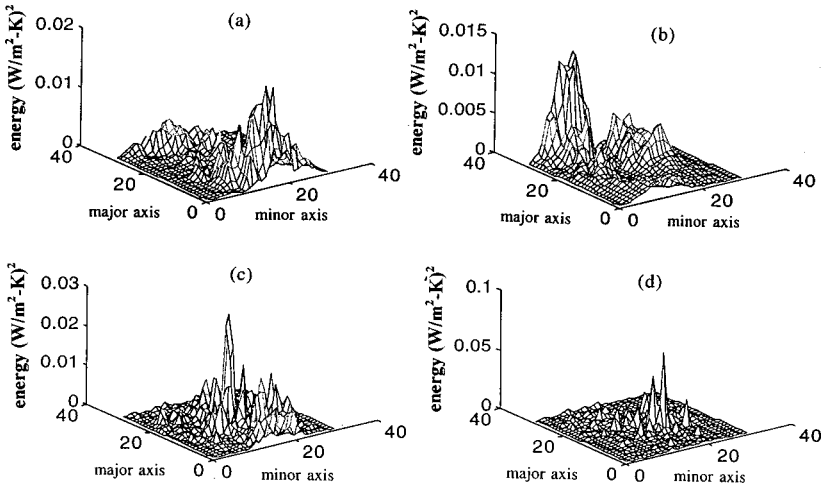

Fig. 9 Second-mode proper orthogonal decomposition spatial energy distribution; (*a*) Re=300, *H*=2, *r*=3, (*b*) Re=300, *H*=4, *r*=3, (*c*) Re=1500, *H*=2, *r*=2, (*d*) Re=1500, *H*=4, *r*=2

marily by adjacent jet interaction and shear layer mixing. The contribution of each of these structures becomes increasingly important at certain values of Reynolds number, impingement distance and aspect ratio. The consequences of the global jet array flow characteristics such as elliptic vortex structure axis switching, jet column instability, and jet swaying are apparent in the detailed surface heat transfer coefficient distribution. Quantitative results of discrete heat transfer modes using proper orthogonal decomposition analysis support the concept of large flow structured dominating the heat transfer distribution. As the Reynolds number is increased higher order modes gain importance suggesting a more broad banded distribution of the heat transfer coefficient based on a decomposition of its ''energy content.''

Nomenclature

c_p = specific heat
D_h = hydraulic diameter
E = total energy content of all modes
h = heat transfer coefficient
H = impingement distance divided by D_h
k = thermal conductivity
Nu = Nusselt number, hD_h/k
q'' = surface heat flux
r = aspect ratio of elliptic jets, major-to-minor axis
R = correlation coefficient
Re = Reynolds number, V_jD_h/ν
t = time
T_s = local surface temperature
T_o = initial surface temperature
V_j = average jet exit velocity

Greek Symbols

Γ^* = modified circulation, area integral of the vorticity squared
λ = eigenvalue
ν = viscosity
ρ = density
φ = eigenfunction

References

[1] Martin, H., 1977, ''Heat and Mass Transfer Between Impinging Gas Jets and Solid Surfaces,'' Adv. Turbulence, **2**, pp. 37–44.
[2] Goldstein, R. J., and Timmers, J. F., 1982, ''Visualization of the Heat transfer From Arrays of Impinging Jets,'' Int. J. Heat Mass Transf., **25**, No. 12, pp. 1857–1868.
[3] Pan, Y., and Webb, B. W., 1994, ''Visualization of Local Heat Transfer Under Arrays of Free-Surface Liquid Jets,'' *Proceedings of the 10th International Heat Transfer Conference*, Vol. 4, Institution of Chemical Engineers, Rugby, UK, pp. 77–82.
[4] Huber, A. M., and Viskanta, R., 1994, ''Effect of Jet-Jet Spacing on Convective Heat Transfer to Confined, Impinging Arrays of Axisymmetric Jets,'' Int. J. Heat Mass Transf., **37**, No. 18, pp. 2859–2869.
[5] Husain, H., and Hussain, F., 1991, ''Elliptic Jets. Part 2. Dynamics of Coherent Structures: Pairing,'' J. Fluid Mech., **233**, pp. 439–482.
[6] Ho, C. M., and Gutmark, E., 1987, ''Vortex Induction and Mass Entrainment in a Small Aspect-Ratio Elliptic Jet,'' J. Fluid Mech., **179**, pp. 383–405.
[7] Lee, S. J., Lee, J. H., and Lee, D. H., 1994, ''Local Heat Transfer Measurements from an Elliptic Jet Impinging on a Flat Plate Using Liquid Crystal,'' Int. J. Heat Mass Transf., **37**, No. 6, pp. 967–976.
[8] Barker, J. M., and Liburdy, J. A., 1999, ''Characterization of the Large-Scale Structures in an Impinging Elliptic Jet,'' *First International Symposium on Turbulence and Shear Flow*, S. Banerjee and J. K. Eaton, eds., Begell House, New York, pp. 653–658.
[9] Arjocu, S. C., and Liburdy, J. A., 1997, ''Flow Structures in an Impinging Elliptic Jet Array,'' *Proceedings of ASME-Fluids Div*, ASME, New York, Vancouver, BC, Canada.
[10] Arjocu, S. C., and Liburdy, J. A., 1999, ''Near Surface Characterization of an Impinging Elliptic Jet Array,'' J. Fluids Eng. **121**, No. 2, pp. 384–390.
[11] Sirovich, L., and Kirby, M., 1990, ''An Eigenfunction Approach to Large Scale Transitional Structures in the Jet Flow,'' Phys. Fluids A, **2**, No. 2, pp. 127–135.
[12] Glauser, M. N., Leib, S. J., and George, W. K., 1987, ''Coherent Structures in the Axisymmetric Turbulent Jet Mixing Layer,'' Turbulent Shear Flow, **5**, pp. 134–145.
[13] Hussain, F., and Hussain, H., 1989, ''Elliptic Jets. Part 1. Characteristics of Unexcited and Excited Jets,'' J. Fluid Mech., **208**, pp. 257–320.
[14] Von Wolfersdorf, J., Hoecker, R., and Sattelmayer, T., 1993, ''A Hybrid Transient Step-Heating Heat Transfer Measurement Technique Using Heater Foils and Liquid-Crystal Thermography,'' ASME J. Heat Transfer, **115**, pp. 319–324.
[15] Arjocu, S. C., 1997, ''Elliptic Jet Flow Structures and Heat Transfer in as Jet Array,'' Ph.D. dissertation, Clemson University, Clemson, SC.
[16] Lumley, L. J., 1970, *Stochastic Tools in Turbulence*, Academic Press, New York.
[17] Arjocu, S. C., and Liburdy, J. A., 1997, ''Analysis of Flow Structures Occurring in Impingement of Elliptic Jet Arrays,'' *28th AIAA Fluid Dynamics Conference*, AIAA, Reston, VA.

Numerical Simulation of Heat Transfer in a Transitional Boundary Layer With Passing Wakes

X. Wu
Wu@transition.stanford.edu

P. A. Durbin
Durbin@vonkarman.stanford.edu

Center for Integrated Turbulence Simulation and
Department of Mechanical Engineering,
Stanford University,
Building 500,
Stanford, CA 94305-3030

Direct numerical simulation (DNS) has been used to investigate heat transfer and provide thermal statistics in a transitional flow in which turbulent wakes traversing the inlet periodically are swept downstream across a constant-temperature flat-plate. The same heat transfer problem was also computed using unsteady Reynolds-averaged Navier-Stokes (RANS) method with the v^2-f turbulence model. During transition, the instantaneous Stanton number field exhibits spotlike structure, which in turn results in a strong streamwise modulation in the phase-averaged Stanton number distribution. At molecular Prandtl number $Pr=0.7$, the Reynolds analogy factor decreases in the transitional region but remains nearly constant afterwards. After the completion of transition, mean and second-order temperature statistics are in good agreement with previous experimental data from slightly heated turbulent flat-plate boundary layers. Throughout the transitional and turbulent regions the turbulent Prandtl number increases sharply as the wall is asymptotically approached. DNS results at a higher wake passing frequency are also presented to illustrate the effect of freestream turbulence. Unsteady RANS predictions of the time- and phase-averaged Stanton numbers as well as the enthalpy thickness are in reasonable agreement with the DNS. [S0022-1481(00)02002-8]

Keywords: Keywords: Heat Transfer, Transitional, Turbines

1 Introduction

Heat transfer over multistage axial turbine and compressor blades is affected by wakes periodically impinging from upstream blade rows. This is well known in the turbomachinery community and has been demonstrated by numerous experiments. Two recent examples are the measurements of Han, Zhang, and Qu [1] in a stationary cascade (Fig. 1(*a*)), and Blair [2] in a rotating turbine. Such modification of heat transfer between blade surface and boundary layer occurs primarily through a bypass transition process promoted by turbulence inside the passing wake. It is unclear to what accuracy an engineering calculation method can predict the true heat transfer coefficient under these complicated conditions, though one pessimistic estimation was discussed in Maciejewski and Moffat [3].

One prevailing approach adopted by academic researchers to address this problem, albeit rather tangentially, is through study of wakes interacting with a flat-plate boundary layer. Orth [4], Funazaki [5], and Funazaki and Koyabu [6] presented experimental investigations on wake-disturbed transitional boundary layer on a flat-plate. The wakes were generated by transversely moving bars upstream of the test plate. Their data confirm that wake passage induces significant changes of flow and heat transfer in the transition region.

Here we consider the fundamental heat transfer problem in a transitional flow in which turbulent wakes traversing the inlet periodically are swept downstream across a constant-temperature flat-plate. The associated fluid mechanics problem was studied in experiments by Liu and Rodi [7], and in DNS by Wu, Jacobs, Hunt, and Durbin [8]. A related theoretical analysis was given in Hunt, Durbin, and Wu [9]. It was shown that near-wall turbulence carried by the wake decays initially under the effect of viscosity. Around the streamwise location where the momentum thickness Reynolds number Re_θ reaches 220, isolated young turbulent spots emerge. These young turbulent spots grow out of the remnants of the upstream decaying inlet wake turbulence through interaction between the boundary layer and freestream turbulence. Jet-like perturbations are spawned in the boundary layer. At preferred spanwise locations they develop rapid, local instabilities, similar to a forced Kelvin-Helmholtz instability. If the wake frequency is increased so that the freestream is continually turbulent, then transition occurs without notable spot formation.

In this paper, we present DNS results of time- and phase-averaged mean and second-order temperature statistics. Using these results we provide answers to the following heat transfer questions: In what manner does the Stanton number depart from the laminar solution? Does the mean Stanton number over shoot classical turbulent correlations in wake-induced transition? How does the Reynolds analogy factor vary in the transitional region? Does it respond to enhanced freestream wake turbulence? How does the turbulent Prandtl number transition from laminar to turbulent? The near-wall asymptotic behavior of the turbulent Prandtl number has been the subject of a major debate since previous simulations give different answers from experimental measurements (see Kays [10] and references therein). Our DNS results agree with the experimental data reviewed by Kays [10]. In this paper, we also present numerical predictions on the same heat transfer problem obtained by unsteady RANS with the v^2-f turbulence model.

2 Mathematical and Numerical Considerations

2.1 Problem Definition. Consider the heat transfer in an incompressible flow over a smooth, slightly heated flat-plate at constant surface temperature ξ_{wall}, with upstream wakes passing periodically (Fig. 1(*b*)). The origin of the coordinate system is at the leading edge of the plate. The wakes are assumed to be generated by imaginary circular cylinders positioned in the plane $x=-L$

Contributed by the Heat Transfer Division for publication in the JOURNAL OF HEAT TRANSFER. Manuscript received by the Heat Transfer Division, Jan. 30, 1999; revision received, Nov. 29, 1999. Associate Technical Editor: R. Douglass.

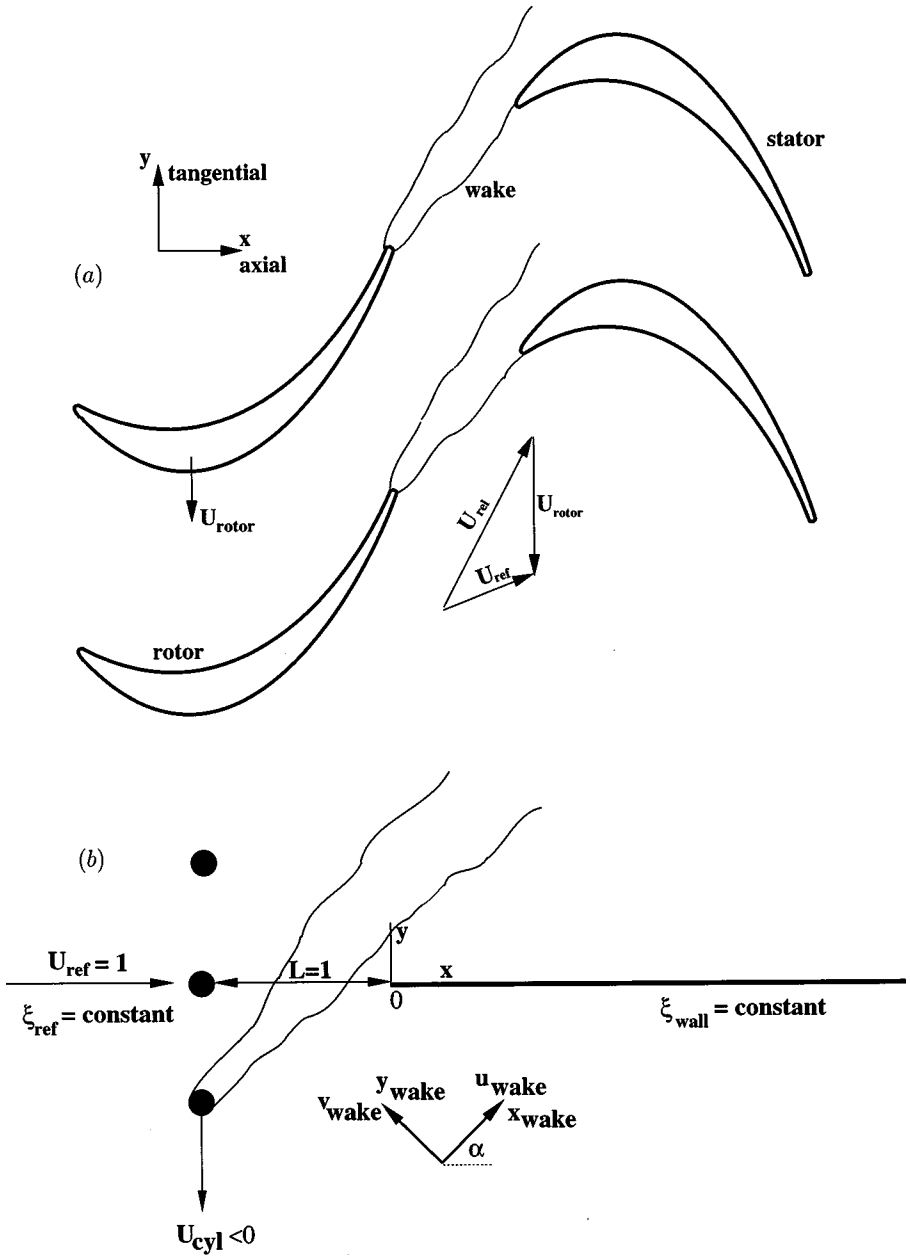

Fig. 1 (*a*) Sketch of turbine rotor wake past a downstream stator passage; (*b*) definition of velocity and length scales in the present simulation

and moving in the $-y$-direction at U_{cyl}. The velocity of the flow far upstream of the cylinder is U_{ref}. Fluid temperature for $x<0$ is uniform, ξ_{ref}, and lower than that of the plate. The cylinders are equally spaced so that they cut through the $y=0$ plane at a specified passing period $\mathcal{T}$. The characteristic velocity scale is U_{ref}, the characteristic length scale is L, the Reynolds number is then $\mathrm{Re}=U_{ref}L/\nu$, where ν is the kinematic viscosity of the fluid. As in Liu and Rodi [7] and Wu et al. [8], $\mathrm{Re}=1.5\times10^5$.

2.2 Governing Equations and Notations. In the DNS, energy conservation is enforced for flow over the flat-plate by solving the full time-dependent energy-conservation equation at every time-step after the mass and momentum transport equations have been solved. We work with the non-dimensional temperature $\phi=(\xi-\xi_{ref})/(\xi_{wall}-\xi_{ref})$. The transport equation for $\phi(x,y,z,t)$ is

$$\frac{\partial\phi}{\partial t}+\mathrm{div}(\mathbf{u}\phi)=\mathrm{div}\left(\frac{\nu}{\mathrm{Pr}}\,\mathrm{grad}\,\phi\right), \tag{1}$$

where $\mathbf{u}$ is the velocity vector with Cartesian components (u,v,w) and Pr the fluid molecular Prandtl number.

In this paper, time-averaging is represented by $\overline{\cdot}$. Averaging at a particular phase, $t^m_{n_\mathcal{T}}=m\mathcal{T}+n_\mathcal{T}\mathcal{T}$, is denoted by $\langle\cdot\rangle$, where m is any integer, $0\leqslant n_\mathcal{T}\leqslant1$ is the fraction of the wake passing period. For example, the phase-averaged mean temperature is evaluated as

$$\langle\phi\rangle(t_{n_\mathcal{T}})=\frac{1}{M}\sum_{m=1}^{M}\phi(t^m_{n_\mathcal{T}}), \tag{2}$$

where M is the total number of periods within which phase-averaging is performed. Averaging over the homogeneous spanwise z-direction is implied in both time-averaging and phase-averaging. Time-averaged and phase-averaged mean temperatures are related via $\overline{\phi}=\overline{\langle\phi\rangle}$. Thus the instantaneous temperature can be decomposed as

$$\phi=\langle\phi\rangle(t_{n_\mathcal{T}})+\phi'(t_{n_\mathcal{T}})=\overline{\phi}+\tilde{\phi}(t_{n_\mathcal{T}})+\phi'(t_{n_\mathcal{T}}), \tag{3}$$

where $\tilde{\phi}(t_{n_\mathcal{T}})=\langle\phi\rangle(t_{n_\mathcal{T}})-\overline{\phi}$ is the periodic temperature fluctuation with respect to the time-averaged mean, and $\phi'(t_{n_\mathcal{T}})$ is the true stochastic turbulence temperature fluctuation. Consequently, the time-averaged heat flux $\overline{\langle u_i'\phi'\rangle}$ can be calculated as

$$\overline{\langle u_i'\phi'\rangle}=\int_0^1\langle[u_i-\langle u_i\rangle(t_{n_\mathcal{T}})][\phi-\langle\phi\rangle(t_{n_\mathcal{T}})]\rangle dn_\mathcal{T}. \tag{4}$$

In the unsteady RANS, energy conservation is enforced by solving the two-dimensional time-dependent energy-conservation equation at every time-step after the mass and momentum transport equations have been solved. The transport equation for the phase-averaged, i.e., ensemble-averaged nondimensional temperature $\langle\phi\rangle(x,y,t)$ is

$$\frac{\partial\langle\phi\rangle}{\partial t}+\mathrm{div}(\langle\mathbf{u}\rangle\langle\phi\rangle)=\mathrm{div}\left\{\left(\frac{\nu}{\mathrm{Pr}}+\frac{\nu_t}{\mathrm{Pr}_t}\right)\langle\phi\rangle\right\}, \tag{5}$$

where ν_t is the turbulent eddy viscosity evaluated using the v^2-f turbulence model (see Parneix, Behnia, and Durbin [11] and Wu and Durbin [12] for details), and Pr_t the turbulent Prandtl number $(=0.9)$.

2.3 Inflow and Other Boundary Conditions. The computational domain is defined as $0.1\leqslant x/L\leqslant 3.5$, $0.0\leqslant y/L\leqslant 0.8$, and $0.0\leqslant z/L\leqslant 0.2$. The length $3.5L$ is the same as used in the experiments of Liu and Rodi [7]. The height of the computational domain $0.8L$ is equivalent to 11.6δ at the exit $x=3.5L$, where δ is the 99 percent boundary layer thickness. The width of the computational domain $0.2L$ is equivalent to 2.9δ at the exit.

Depending upon the passing frequency $1/\mathcal{T}$, at any given instant either one single wake or multiple wakes can be found on the inflow plane. A wake will be found on the computational inflow plane if its centerline is located within the range from $y=-b\cos\alpha$ to $y=0.8L+b\cos\alpha$, where b is wake halfwidth and $\alpha=\tan^{-1}|U_{\mathrm{cyl}}|/U_{\mathrm{ref}}$ is the wake inclination angle (Fig. 1). The total number of such wakes at any time is

$$\mathcal{N}=\mathrm{CEILING}\left(\frac{0.8L+2b\cos\alpha}{|U_{\mathrm{cyl}}|\mathcal{T}}\right), \tag{6}$$

where the function CEILING returns the least integer greater than or equal to its real argument.

In this paper we consider $U_{\mathrm{cyl}}<0$ (Fig. 1). On the inflow plane at the beginning of each wake passing period $(t^m_{n_\mathcal{T}}=0)$, let the origin of the uppermost wake-coordinate system $(x_{\mathrm{wake},1}=0,\ y_{\mathrm{wake},1}=0)$ start to move downwards from $y=0.8L+b\cos\alpha$. This indicates that at $t^m_{n_\mathcal{T}}=0$ the wake starts to enter the top boundary of the inflow plane. At any subsequent time $0<t^m_{n_\mathcal{T}}<\mathcal{T}$ the origin of the wake-coordinate system will be at $y_{\mathrm{centerline}}=0.8L+b\cos\alpha+t^m_{n_\mathcal{T}}U_{\mathrm{cyl}}$. Each point on the inflow plane then has an effective coordinate with respect to the origin of the wake-coordinate system, which is $y_{\mathrm{eff,wake}}(y)=(y-y_{\mathrm{centerline}})/\cos\alpha$.

At the inflow station of the computational domain $x=0.1L$, the velocity components and temperature were prescribed as

$$\begin{aligned}
u&=u_{\mathrm{blasius}}+u_{\mathrm{blasius}}\left(\cos\alpha\sum_{q=1}^{\mathcal{N}}u_{\mathrm{eff,wake},q}-\sin\alpha\sum_{q=1}^{\mathcal{N}}v_{\mathrm{eff,wake},q}\right)\\
v&=v_{\mathrm{blasius}}+u_{\mathrm{blasius}}\left(\sin\alpha\sum_{q=1}^{\mathcal{N}}u_{\mathrm{eff,wake},q}+\cos\alpha\sum_{q=1}^{\mathcal{N}}v_{\mathrm{eff,wake},q}\right)\\
w&=\sum_{q=1}^{\mathcal{N}}w_{\mathrm{eff,wake},q}\\
\phi&=\phi_{\mathrm{blasius}}
\end{aligned} \tag{7}$$

where subscript ''blasius'' denotes the steady Blasius profile for a laminar flat-plate boundary layer. The subscript ''eff, wake,q'' represents the effective instantaneous velocity components in the qth wake coordinate system. The velocities $(u_{\mathrm{eff,wake},q},v_{\mathrm{eff,wake},q},w_{\mathrm{eff,wake},q})$ are the same as the wake velocities $(u_{\mathrm{wake}},v_{\mathrm{wake}},w_{\mathrm{wake}})$ illustrated in Fig. 1 if $|y_{\mathrm{eff,wake},q}|\leqslant b$, and zero otherwise. The wake velocities were multiplied by u_{blasius} so they would satisfy no-slip where the wake intersects the plate.

In the DNS the turbulent wake velocities $(u_{\mathrm{wake}},v_{\mathrm{wake}},w_{\mathrm{wake}})$ appearing in (7) were generated from a separate precomputation of a temporally decaying, self-similar plane wake (Wu et al. [8]). In the unsteady RANS, the wake velocity and turbulence variables were generated from a separate precomputation of a spatially decaying, self-similar plane wake (Wu and Durbin [12]). The maximum inlet wake deficit is 14 percent U_{ref} and the wake half-width is $0.1L$.

At the top of the computational domain, $v=v_{\mathrm{blasius}}$, $\partial u/\partial y=\partial v/\partial x$, $\partial w/\partial y=\partial v/\partial z$ and $\phi=0$ are applied. This is artificial, but given the substantial distance between the top surface and the wall, the effect of the top boundary condition on boundary layer development should be extremely small. At the exit of the computational domain, convective boundary conditions are used. Mass flux at the inflow plane is constant in time, and corrections to the velocities at the exit plane are also made to ensure global mass conservation. Periodic boundary conditions are applied in the homogeneous, spanwise z-direction, $\mathbf{u}=\mathbf{0}$ and $\phi=1$ are applied on the wall.

2.4 Numerical Method. The numerical scheme for the DNS is a parallelized version (by Charles D. Pierce at Stanford) of the method used by Akselvoll and Moin [13]. All spatial derivatives are approximated with a second-order central difference scheme. A third-order Runge-Kutta scheme is used for terms treated explicitly and a second-order Crank-Nicholson scheme is used for terms treated implicitly. The fractional step method is used to remove the implicit pressure dependence in the momentum equations. We added the temperature solver for this study.

The numerical scheme for the unsteady RANS is the artificial compressibility method (INS2D) described in Durbin [14]. The ensemble-averaged momentum and continuity equations are solved simultaneously, as a coupled system for velocity and pressure. Convective derivatives are approximated by third-order, upwind biased flux-splitting and diffusive terms by central differencing. We also added the temperature solver for this study. Both the DNS and RANS exactly produced the laminar Blasius velocity and thermal boundary layer solutions when no wakes are present at the inlet. Transition is allowed to occur naturally in the v^2-f turbulence model. It is known that models bifurcate naturally between laminar and turbulent solution branches (Durbin and Laurence [15]). This is not a numerical artifice; it occurs in steady one-dimensional channel flow where transition can be computed as a function of Reynolds number.

2.5 Computational Details. Two inlet wake passing frequencies are simulated: $\mathcal{T}=1.67L/U_{\mathrm{ref}}$ with $\mathrm{Pr}=0.7$ for case 1; and $\mathcal{T}=0.4175L/U_{\mathrm{ref}}$ with $\mathrm{Pr}=0.7$ or $\mathrm{Pr}=1.0$ for Case 2. In Case 2, at every time-step, the spanwise averaged inlet mean wake velocities are calculated and subtracted from the real wake velocity given in (7). In Case 1 near-wall distortion of the mean velocity at the inlet results in a localized favorable pressure gradient. Eliminating mean wake deficit at the inlet produces shear-free wakes. Absence of an inlet mean flow distortion in Case 2 results in a virtually zero streamwise pressure gradient across the computational domain.

DNS results to be presented in Section 3 were obtained on a $1024\times400\times128$ grid in the streamwise, wall-normal, and spanwise directions, respectively. In terms of viscous wall units based on the Case 1 time-averaged friction velocity at the exit, $\Delta x^+=24$ and $\Delta z^+=11$. At the same location, there are 16 points distributed along the wall-normal direction below $y^+=9$, and 191

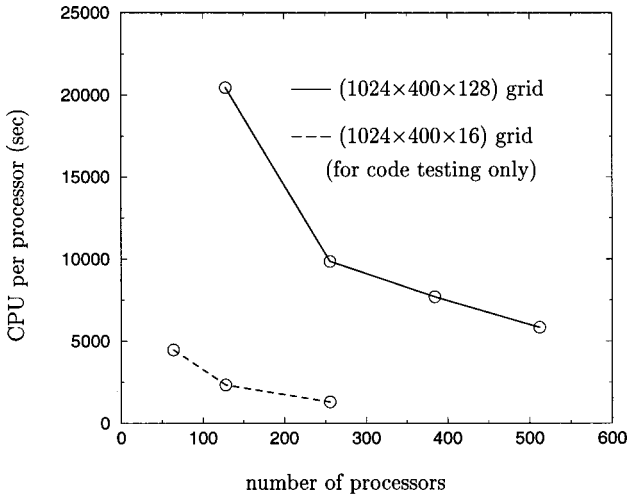

Fig. 2 CPU per processor for simulation of one wake passing period in Case 1

points distributed below $y=\delta$. Adequacy of the spanwise resolution was checked in Wu et al. [8]. The time-step was fixed to be $0.00167L/U_{\text{ref}}$ for the DNS ($1/1000\mathcal{T}$ for Case 1 and $1/250\mathcal{T}$ for Case 2), which is equivalent to $0.59\nu/U_\tau^2$ at the exit. The choice of time-step is primarily constrained by the numerical stability (CFL number < 1.5). The flow was allowed to evolve for 20,000 time-steps; statistics were then collected for another 20,000 time-steps. Phase-averaging was performed by dividing each pass period into 50 equal subdivisions. The computation was carried out on the scalable parallel Cray T3E using up to 512 processors. Figure 2 shows the CPU time consumed by each processor when the code advances one wake passing period $\mathcal{T}$. It is seen from the figure that as the number of processors is incrementally increased from 64 to 512, the CPU time used by each processor decreases nearly proportionally, suggesting very good scalability of the code.

Unsteady RANS results for Case 1 were obtained using three different grids, (201×101), (401×101), and (201×201). The grid spacing in each direction was varied by a factor of two. The time-step was fixed to be $0.00835L/U_{\text{ref}}$ ($1/200\mathcal{T}$ for Case 1 and $1/50\mathcal{T}$ for Case 2). The constraint on the choice of time-step in the RANS is that it should be small enough to capture the unsteady nature of the passing wake. These computations were carried out on an Origin 2000 using a single processor.

3 Results

3.1 Visualization. Pictures of the two boundary layers, drawn using contours of the instantaneous velocity u over one random xy cross section, are shown in Fig. 3. At any instant in Case 1, there is at most one wake present at the computational inflow plane (Fig. 3(a)). Since the passing period is reduced by a factor of four in Case 2, there are at least three full wakes present at the computational inflow station for any instant (Fig. 3(b)). Passing wake-induced transition is evident in Fig. 3(a) for $x>1.75$. Transition occurs much closer to the inlet in Case 2 because the boundary layer is under stronger freestream perturbation, and also because Case 1 has a mild favorable pressure gradient near the inlet. Figure 3(b) shows the gap between neighboring wakes decreases with streamwise distance, and for $x>2.0$ the freestream turbulence is nearly continuous.

As indicated by (7), at the inlet velocity varies with time because of the traversing wake, but the temperature is fixed to be Blasius. Because the inlet wake is isothermal there are no freestream temperature fluctuations as the boundary layers develop downstream. Thus temperature can be used to discriminate the freestream velocity fluctuations due to passing wakes from the velocity fluctuations inside the boundary layer, though this is not explored in the present paper. Figure 4 confirms that the two thermal boundary layers indeed have well-defined boundary layer edge, unlike their velocity counterparts; there the distinction between freestream and boundary layer fluctuations is blurred. Figure 4(a) shows that for $x<1.5$ the temperature field tends to return to laminar after the passage of the turbulent wake. Downstream of this turbulent spots persist behind the wake. Transition is nearly complete at about $x=2.0$. Also evident in the figure is the fact that the computational domain is sufficiently high compared to the boundary layer thickness.

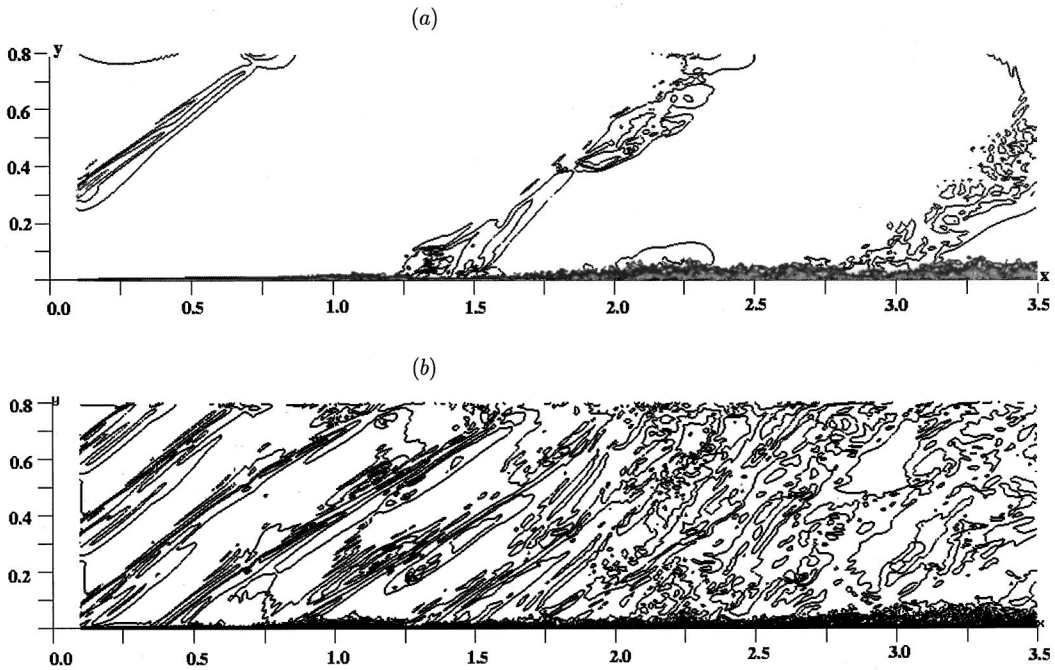

Fig. 3 Instantaneous velocity over a *xy*-plane; (*a*) Case 1; (*b*) Case 2

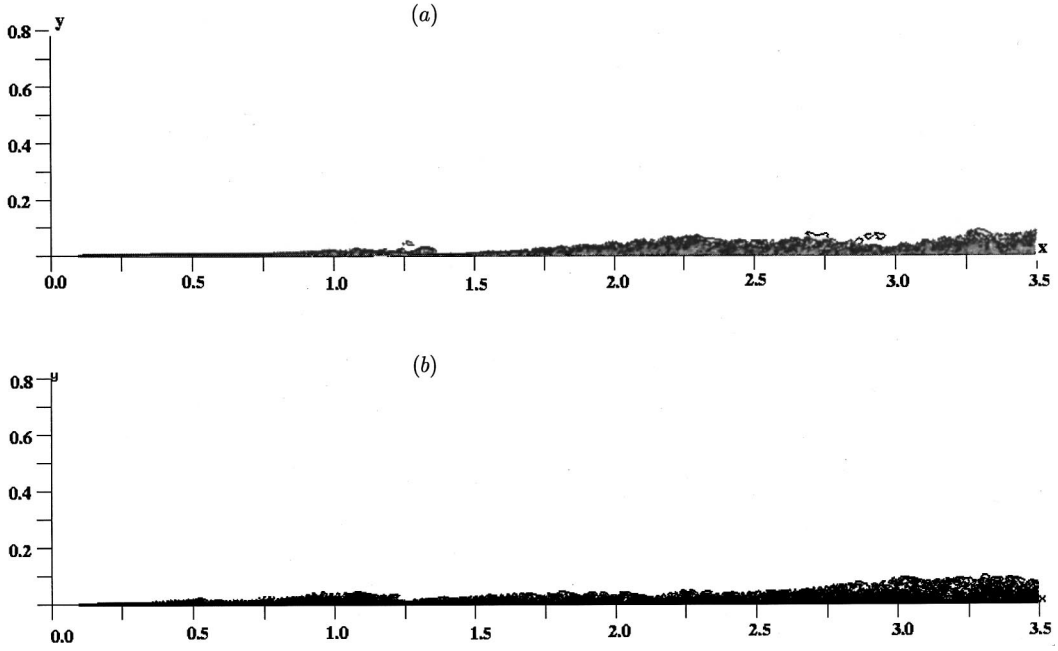

Fig. 4 Instantaneous temperature over a *xy*-plane; (*a*) Case 1; (*b*) Case 2 (Pr=1.0)

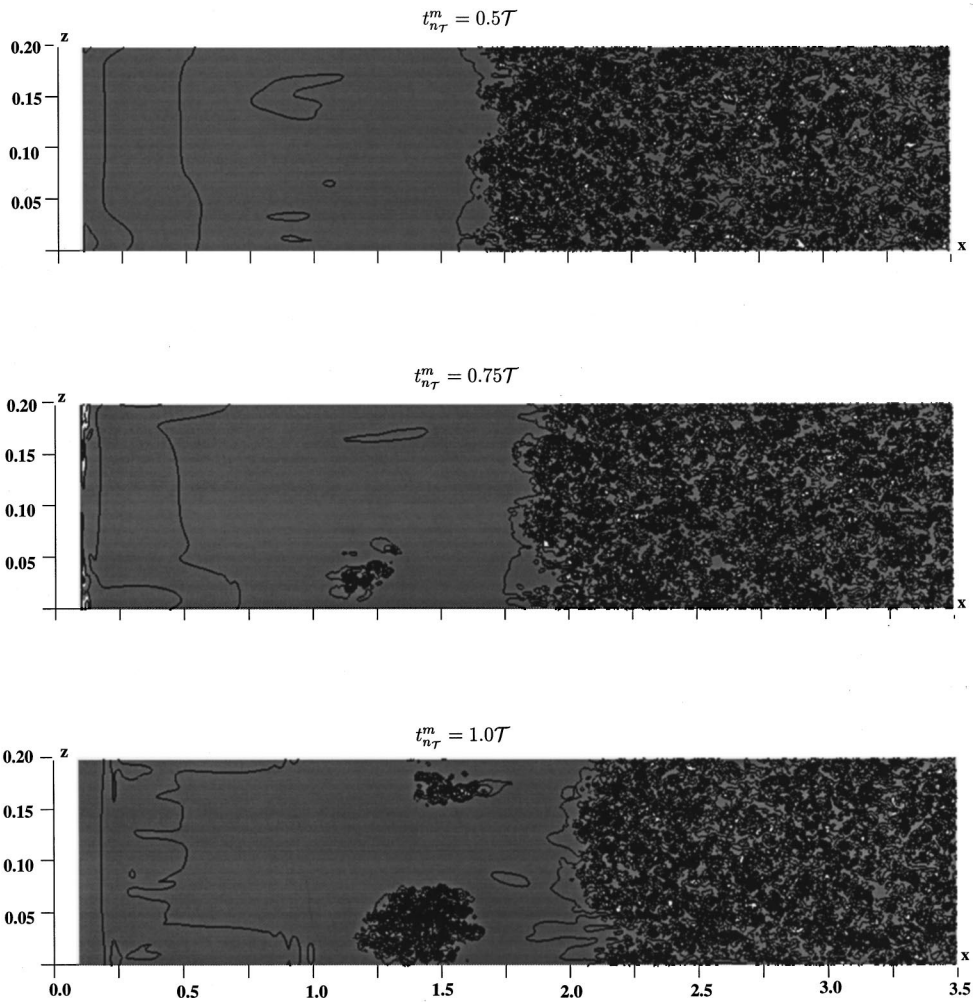

Fig. 5 Instantaneous Stanton number over the *xz*-plane at three consecutive instants in Case 1

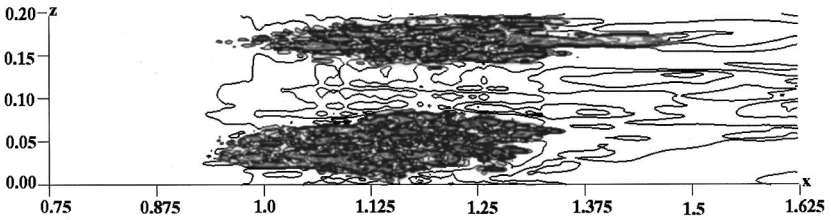

Fig. 6 Contours of near-wall turbulent temperature fluctuation ϕ' in Case 1 over the xz-plane of $y=7.38\times10^{-4}$ ($y^+=5.4$ at $x=1.75$)

The structure of the heat transfer coefficient field in the transitional region is shown in Fig. 5 using the instantaneous Stanton number over the xz-plane. The three subfigures are obtained at three consecutive instants $t^m_{n_\mathcal{T}}=0.5$, 0.75 and 1.0, respectively. After the completion of transition, i.e., $x>2.0$, the instantaneous Stanton number field remains chaotic at all the time. In the transitional region Fig. 5(b) shows that a spot-like structure emerges near $x=1.25$ with a much larger heat transfer coefficient than that of its surrounding. After 0.25 passing period, the young spot-like structure evolves into a large patch in Fig. 5(c). Further growth of this structure and its merger with the retreating downstream turbulent region completes a cycle of the thermal boundary layer transition. This mirrors the spot dynamics seen in the velocity fields (Wu et al. [8]). Note that in Fig. 5 the z-dimension has been artificially enlarged by a factor of four in order to show the entire computational domain. This has an effect of spreading the spot geometry. Figure 6 plots contours of the near-wall instantaneous temperature fluctuations using the correct aspect ratio. Evident from the figure are two turbulent spots. These spots are in good qualitative agreement with the recent liquid crystal experiments of Kittichaikarn et al. [16] on a moving-bar/flat-plate apparatus. The present DNS is designed to replicate such bar/plate experimental configuration. In both the simulation and experiments, the spots taper in the upstream direction.

3.2 Direct Numerical Simulation (DNS) Statistics. Semilogarithmic mean temperature profiles in Case 1 are shown in Fig. 7(a). After transition our DNS results are in excellent agreement with the experimental measurements of Blackwell [17], and the correlation of Kays and Crawford [18] (p. 211). Figure 7(b) gives velocity and temperature profiles in Case 2 at $x=2.75$. One notable change of ϕ^+ from Case 1 to Case 2 is the reduced wake parameter in the outer region. In boundary layers subjected to freestream isotropic grid turbulence, the wake parameter is usually damped substantially (Simonich and Bradshaw [19]). Even though freestream turbulence due to passing wakes and wake/boundary layer interaction is inhomogeneous, similar damping still exists in the present flow.

Figure 8(a) shows the rms temperature fluctuation $\phi'^+_{\rm rms}$ in Case 1. The wall boundary condition is such that $\phi'=0$. After transition the peak of $\phi'^+_{\rm rms}$ at different streamwise locations collapse, in agreement with Subramanian and Antonia [20] for a slightly heated flat-plate boundary layer. However, our peak value of 2.6 is higher than 2.0 in their experiment. The ''shoulder'' in the turbulent profiles of $\phi'^+_{\rm rms}$ is also present in Subramanian and Antonia [20]. The profiles of $\phi'^+_{\rm rms}$ and $u'^+_{\rm rms}$ presented in Fig. 8(b) for Case 2 show that as the boundary layer edge is approached, $\phi'^+_{\rm rms}$ rapidly drops towards zero even though velocity fluctuations persist due to the turbulent passing wake. In Case 2 $u'^+_{\rm rms}=0.55$ in the freestream at $x=2.75$. The time-averaged freestream streamwise intensity decays from 4.2 percent at the inlet to 2.5 percent at $x=2.75$. The relatively strong freestream velocity fluctuations are most evident from Fig. 9 in which the wall-normal intensity from both cases are shown. Note that the freestream turbulence in Case 1 is not continuous because of reduced passing frequency, even though its time-averaged freestream streamwise turbulence intensity is about 1.3 percent at $x=2.75$. Streamwise velocity and temperature correlation $-\overline{\langle u'\phi'\rangle}^+$ is shown in Fig. 10 for Case 1. There is general agreement between DNS and experimental data $-\overline{\langle u'\phi'\rangle}^+$ in the fully turbulent region. In the transitional region $-\overline{\langle u'\phi'\rangle}^+$ exhibits noticeable overshoot compared with the fully turbulent profiles. DNS results on the structure parameter $a_{1\phi}$ are shown in Fig. 11, together with the measurements of Subramanian and Antonia [20]. The figure shows that as the flow develops from laminar to turbulent, the level of temperature-velocity correlation increases downstream. In the turbulent region $a_{1\phi}$ is in reasonable agreement with the flat-plate experiments of Subramanian and Antonia [20].

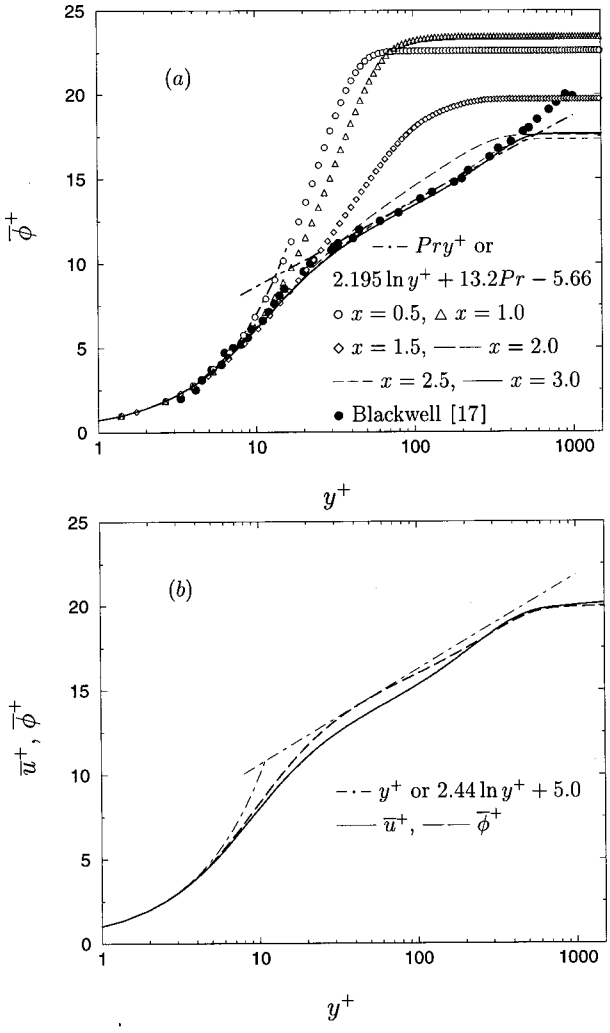

Fig. 7 Time-averaged mean velocity and temperature profiles in wall units; (a) Case 1 at six different streamwise stations; (b) Case 2 (Pr=1.0) at $x=2.75$

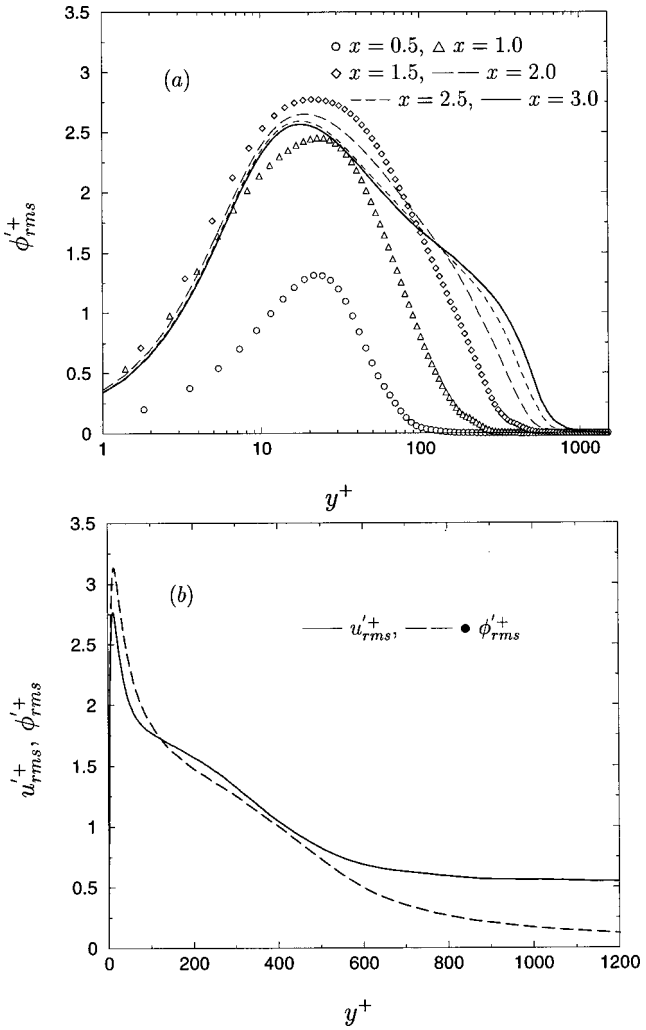

Fig. 8 Rms streamwise velocity and temperature fluctuations; (*a*) Case 1 at six different streamwise stations; (*b*) Case 2 (Pr =1.0) at *x*=2.75

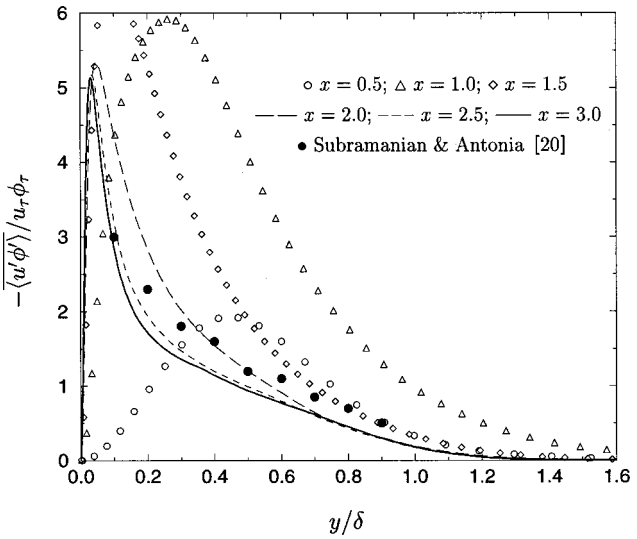

Fig. 10 Streamwise velocity and temperature correlation $-\overline{\langle u'\phi'\rangle}^{+}$ in Case 1

Kays [10] offered a critical review of experimental data on turbulent Prandtl number for the flat-plate boundary layer. He noted a major discrepancy between previous DNS calculations and the experiments. The DNS reviewed by Kays show a peak value of Pr_t at about $y^+ = 40$, whereas all the experiments show no such peak at all but rather a sharp rise to much higher values as the wall is asymptotically approached. Kays noted that the three sets of experiments he reviewed involve two different fluids, two different laboratories and a time span of 17 years (therefore are presumably reliable). In Fig. 12 we present our DNS results of Pr_t. It is seen that after transition our DNS agrees with the experimental data of Blackwell [17] (as well as the other two sets of experimental data in Kays [10]). During transition the profiles of Pr_t systematically approach the fully turbulent profile of Blackwell [17]. We are not aware of any experimental Pr_t data on passing wake-induced transitional boundary layers. It should be remarked, however, that the rapid rise near the wall is in the viscous sublayer, where molecular diffusivity is comparable to turbulent diffusivity. Pr_t becomes the ratio of two small numbers and is quite sensitive to flow conditions.

Simonich and Bradshaw [19] showed that increasing freestream turbulence causes St to increase faster than C_f. This implies that

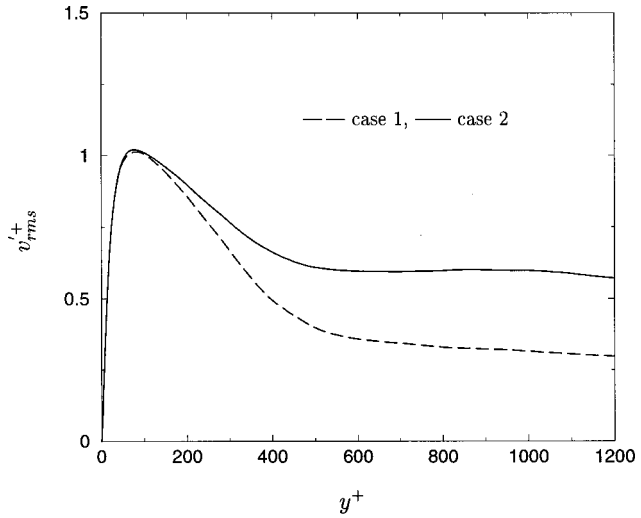

Fig. 9 Rms wall-normal velocity fluctuations at *x*=2.75

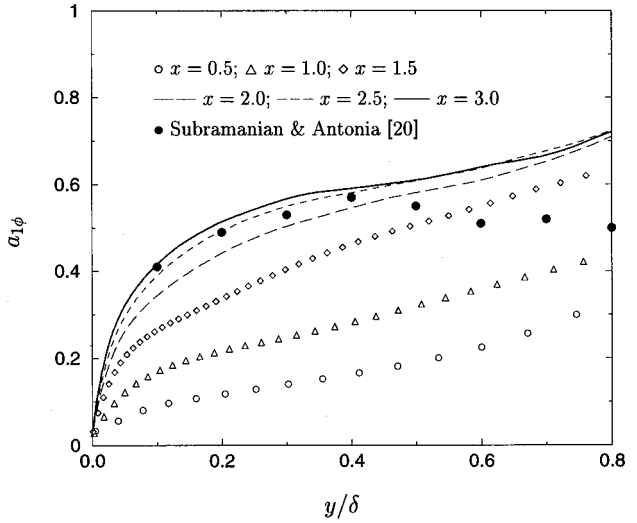

Fig. 11 Structure parameter $a_{1\phi}$ in Case 1

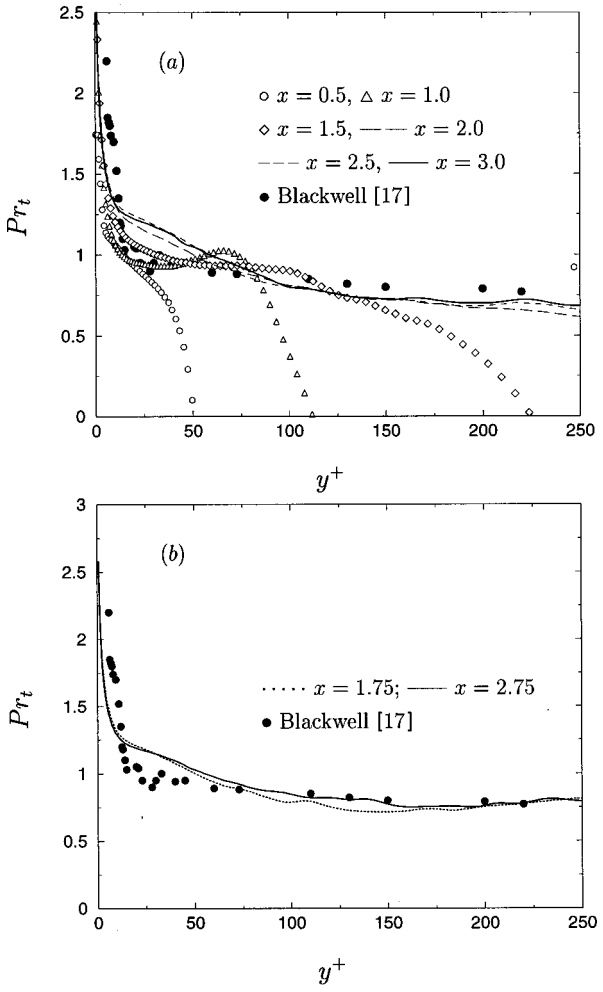

Fig. 12 Turbulent Prandtl number; (*a*) Case 1 at six different streamwise stations; (*b*) Case 2 (Pr=1.0) at two streamwise stations

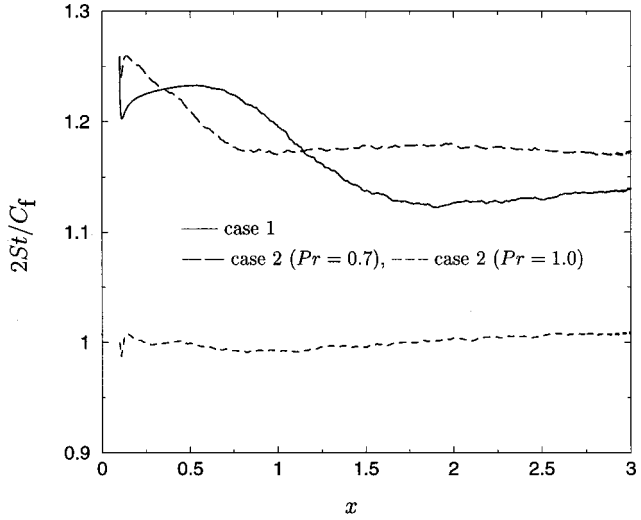

Fig. 13 Reynolds analogy factor

the Reynolds analogy factor $2\mathrm{St}/C_f$ will increase with enhanced freestream turbulence. Figure 13 presents DNS results of the Reynolds analogy factor. Two sets of results are shown. Enhanced freestream turbulence is achieved in this work by reducing the passing period $\mathcal{T}=1.67$ (Case 1) to 1.67/4 (Case 2). Both of these two passing frequencies are typical of those encountered in turbomachinery. Following Zhang and Han [21] a wake-passing Strouhal number can be defined as

$$\text{Strouhal}=(2\pi Nn/60)d/U_{\text{ref}}, \tag{8}$$

where N is wake simulator bar rotation speed (rpm), n the number of wake simulator bars, and d the bar diameter. The corresponding wake-passing Strouhal numbers for $\mathcal{T}=1.67$ and $\mathcal{T}=1.67/4$ are 0.1 and 0.4, respectively (detailed dimensional parameters used for the estimation can be found in Liu and Rodi [7]). Zhang and Han [21] noted that the typical wake-passing Strouhal number in a real gas turbine engine ranges from 0.1 to 0.5, approximately. Their own cascade experiments were conducted in the wake-passing Strouhal number range of 0.0 to 0.9. It is seen from the figure that after transition nearly constant values of $2\mathrm{St}/C_f$ are attained: They are about 1.13 for the low frequency case $\mathcal{T}=1.67$ and 1.17 for the high frequency case $\mathcal{T}=1.67/4$. Therefore increasing passing frequency results in higher Reynolds analogy factor in the turbulent region. The increase can be attributed to the increase of time-averaged freestream turbulence intensity. The values of $2\mathrm{St}/C_f$ in the turbulent region are also in line with the correlation of Simonich and Bradshaw [19]

$$2\mathrm{St}/C_f=1.18/(1-0.098\sqrt{C_f/2}), \quad \text{air only} \tag{9}$$

and the correlation of Kays and Crawford [18]

$$2\mathrm{St}/C_f=\mathrm{Pr}^{-0.4}. \tag{10}$$

Nevertheless, it must be pointed out that the normalization velocity implicitly entering in the Reynolds analogy factor $2\mathrm{St}/C_f$ carries some ambiguity unless the flow is a canonical zero-pressure gradient flat-plate boundary layer. Such ambiguity certainly appears in experiments with wakes because of the wake deficit. It is doubtful, at least in laboratories, that a constant normalization velocity can be maintained when the freestream is highly perturbed and the perturbation level changes. It would therefore be hardly meaningful to discuss the small variation in $2\mathrm{St}/C_f$ with different freestream conditions given this level of uncertainty. In the present work we resolved this ambiguity by fixing the mass flow rate at the inlet of the computational domain corresponding to Blasius. The bulk velocity is then $0.998U_{\text{ref}}$ for both cases. We also discarded the mean wake deficit in the $\mathcal{T}=1.67/4$ case; i.e., the inlet wake only contains turbulence fluctuations with zero mean. Thus our Reynolds analogy factor $2\mathrm{St}/C_f$ is free of the normalization ambiguity.

3.3 Unsteady Reynolds-Averaged Navier-Stokes (RANS) Results. Time-averaged mean enthalpy thickness δ_h is shown in Fig. 14. DNS results show δ_h starts to deviate markedly from the laminar integral solution (Kays and Crawford [18], p. 146) at about $x=0.75$ (x can be easily converted to Re_x by noting $\mathrm{Re}_L=1.5\times10^5$, Section 2.1). By the exit the turbulent thermal boundary layer has an enthalpy thickness about twice as large the local laminar solution. Thus there is a substantial variation in the level of δ_h as the boundary layer transitions from laminar to turbulent. Also presented in the figure are three sets of the unsteady RANS predictions. It is seen that the unsteady RANS with the v^2-f model yields good predictions of the enthalpy thickness δ_h for the present wake-induced transitional thermal boundary layer.

Time-averaged mean Stanton numbers are shown in Fig. 15. Similar to the enthalpy thickness distribution, the mean Stanton number obtained from the DNS departs from the laminar Blasius solution (Kays and Crawford [18], p. 138) at about $x=0.75$, indicating onset of the thermal boundary layer transition. After the completion of transition, $2\mathrm{St}\,\mathrm{Pr}^{2/3}$ still exhibits an overshoot compared to the turbulent correlation (Kays and Crawford [18], p.

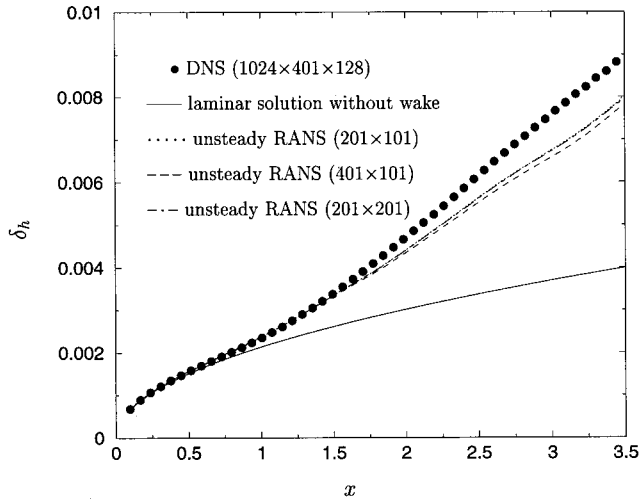

Fig. 14 Time-averaged mean enthalpy thickness in Case 1

213). This overshoot is consistent with experiments on freestream turbulence effects on turbulence boundary layers: one percent of freestream turbulence intensity increases St by about five percent (Simonich and Bradshaw [19]). The 1.3 percent freestream turbulence intensity in Case 1 should increase St by about seven percent.

The second set of the Case 1 results presented in Fig. 15 was indirectly evaluated using the streamwise derivative of δ_h (see Kays and Crawford [18], pp. 56). In general the two sets of results are in good agreement with each other. Figure 15 also shows that the unsteady RANS gives a good prediction of the transition location for the present thermal boundary layer. After the completion of transition, RANS predictions of the mean Stanton number fall on the turbulent correlation of Kays and Crawford without an overshoot. Thus the model is inadequately sensitive to freestream turbulence. The maximum error in the unsteady RANS prediction compared with DNS is about -20 percent found at about $x = 2.2$. Increasing the grid points in the wall-normal direction by a factor of two does not change the RANS prediction of the mean Stanton number. Refining the streamwise resolution by a factor of two does not alter the predicted mean Stanton number in the laminar region ($x < 0.75$) and beyond $x = 2.75$. Within the transitional region RANS predictions of the heat transfer coefficient exhibit a slight dependence on the streamwise resolution.

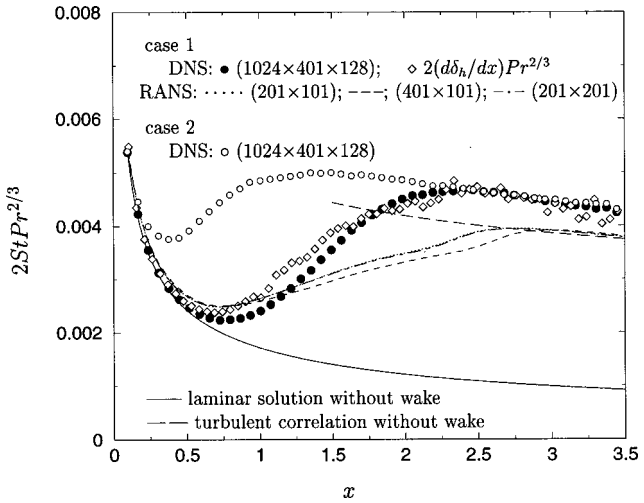

Fig. 15 Time-averaged mean Stanton number St

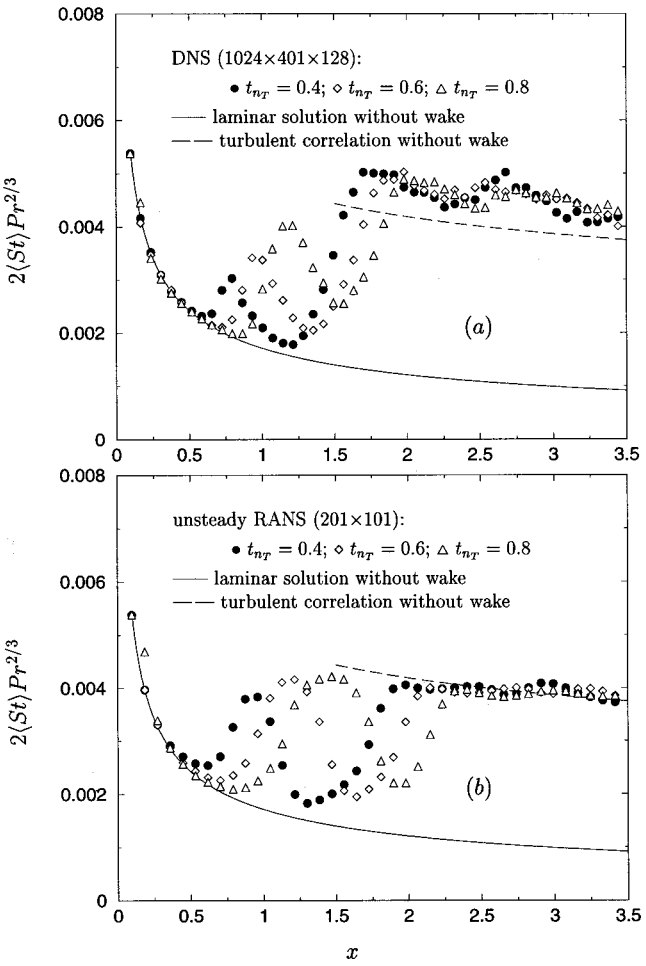

Fig. 16 Phase-averaged mean Stanton number ⟨St⟩ in Case 1

Case 2 data, included in Fig. 15, show that transition takes place near the inlet under the elevated level of external disturbance. Earlier transition results in a thicker boundary layer near the exit, as is evident in Fig. 4. The level of St is the same for both cases when $x > 2$, but Case 2 has a higher Reynolds analogy factor (Fig. 13) indicating that C_f is lower than Case 1. At first this seems an odd effect: Usually St is substantially increased by freestream turbulence, while C_f is much less affected. However, Case 2 has a higher Reynolds number (based on boundary layer thickness) than Case 1 at these locations, so actually it has a higher St for a given Reynolds number. In aggregate, these observations are not inconsistent with the known disproportionate effect of external disturbances on heat transfer; the transition location alters the entire downstream evolution as a function of x.

DNS results on mean Stanton number ⟨St⟩ at various phase angles are shown in Fig. 16(a). Consistent with the growth of the spot-like structure discussed in Fig. 5, ⟨St⟩ exhibits strong streamwise modulation in the transitional region. Remnants of such modulation are still visible in the downstream turbulent region. This is because of the advection of a turbulent strip developed from the mature turbulent spot. These advecting turbulent strips in the region after the wake-induced transition may explain the persistent overshoot of time-averaged mean Stanton number above the conventional correlation. Unsteady RANS predictions of the phase-averaged mean Stanton number are given in Fig. 16(b).

4 Summary

We have used DNS with a grid of $(1024 \times 400 \times 128)$ to perform a numerical experiment on a wake-induced transitional thermal boundary layer. We observed spot-like structures in the in-

stantaneous Stanton number field within the transitional region. Periodic transition of the thermal layer from laminar to turbulent is characterized by the evolution of such structure. Our DNS heat spots are in good qualitative agreement with the recent thermochromic liquid crystal experiments of Kittichaikarn et al. [16], obtained from a moving-bar/flat-plate configuration. Phase-averaged mean Stanton number exhibits strong streamwise modulation before transition. After transition the mean Stanton number overshoots existing turbulent correlations for heated flat-plate boundary layer, possibly because of the advection of the spot- or strip-like structures (containing higher heat transfer coefficient) from the upstream transitional region. The effect of streamwise resolution on overshoot after transition in the turbulent region cannot be entirely ruled out. At $\mathrm{Pr}=0.7$, the Reynolds analogy factor is found to decrease in the transitional region, attaining nearly constant value after transition is completed. Reducing the wake passing period increases the Reynolds analogy factor in the turbulent region. Our DNS results of the turbulent Prandtl number are in good agreement with the experimental data reviewed by Kays [10], showing a sharp rise as the wall is approached. Other mean and second-order temperature statistics are also in good agreement with previous experiments. We also compared our unsteady RANS predictions of the same heat transfer problem to the DNS.

Acknowledgments

We thank C. D. Pierce for the use of his flat-plate code. This work is supported by the Academic Strategic Alliance Program of the U.S. Department of Energy Accelerated Strategic Computing Initiative. The DNS computations were performed on the Cray T3E at the Pittsburgh Supercomputing Center. The computer support from M. Fatica and R. G. Jacobs is also gratefully acknowledged.

Nomenclature

$a_{1\phi}$ = structural parameter $\overline{\langle \phi' v' \rangle}/\{\phi'_{\mathrm{rms}}(-\overline{\langle u' v' \rangle})^{1/2}\}$
b = inlet wake half-width
L = characteristic length scale
m, M = number of periods
$n_{\mathcal{T}}$ = fraction of wake passing period
q = wall heat flux $-k(\partial\phi/\partial y)_{\mathrm{wall}}$
Pr = molecular Prandtl number $\mu c/k$
Pr_t = turbulent Prandtl number $(\overline{\langle u' v' \rangle}\partial\overline{\phi}/\partial y)/(\overline{\langle \phi' v' \rangle}\partial\overline{u}/\partial y)$
Re = $U_{\mathrm{ref}}L/\nu$
Re_θ = momentum thickness Reynolds number
St = Stanton number $q/\rho c_p U_{\mathrm{ref}}(\phi_{\mathrm{wall}}-\phi_{\mathrm{ref}})$
t = time
$t^m_{n_{\mathcal{T}}}$ = phase
u, v, w = instantaneous Cartesian velocity components
$\overline{\langle u' v' \rangle}$ = turbulent shear stress
$-\overline{\langle u' \phi' \rangle}$ = temperature and streamwise velocity correlation
Strouhal = wake passing Strouhal number, as in (8)
U_{ref} = characteristic velocity scale
U_{cyl} = cylinder velocity, inlet wake traversing velocity
U_τ = friction velocity $(\tau_{\mathrm{wall}}/\rho)^{1/2}$
α = wake angle $\tan^{-1} U_{\mathrm{cyl}}/U_{\mathrm{ref}}$
ξ = temperature
ϕ = nondimensional temperature $(\xi-\xi_{\mathrm{ref}})/(\xi_{\mathrm{wall}}-\xi_{\mathrm{ref}})$
ϕ_τ = friction temperature $q/(\rho c_p)/U_\tau$
ϕ^+ = nondimensional mean temperature in wall units $(1-\overline{\phi})/\phi_\tau$
ν, ν_t = molecular and turbulent eddy viscosity
$\mathcal{T}$ = wake passing period
δ_h = enthalpy thickness $\int_0^\infty \overline{u}\,\overline{\phi}\,dy$
$\Delta x, \Delta y, \Delta z$ = grid spacings

Subscripts

blasius = laminar Blasius solution
ref = upstream reference value
wake = in wake coordinate system
wall = surface value
eff, wake = effective components in wake coordinate system

Superscripts

$+$ = normalized by friction velocity or friction temperature
$-$ = time-averaging

Other Symbols

$\langle\,\rangle$ = phase-averaging
$\tilde{}$ = periodic fluctuation

References

[1] Han, J. C., Zhang, L., and Qu, S., 1993, ''Influence of Unsteady Wake on Heat Transfer Coefficient From a Gas Turbine Blade,'' ASME J. Heat Transfer, **115**, pp. 184–189.
[2] Blair, M. F., 1994, ''An Experimental Study of Heat Transfer in a Large-Scalar Turbine Rotor Passage,'' ASME J. Turbomach., **116**, pp. 1–13.
[3] Maciejewski, P. K., and Moffat, R. J., 1992, ''Heat Transfer With Very High Freestream Turbulence: Part I—Experimental Data,'' ASME J. Heat Transfer, **114**, pp. 827–833.
[4] Orth, U., 1993, ''Unsteady Boundary Layer Transition in Flow Periodically Disturbed by Wakes,'' ASME J. Turbomach., **115**, pp. 707–713.
[5] Funazaki, K., 1996, ''Unsteady Boundary Layers on a Flat Plate Disturbed by Periodic Wakes: Part 1—Measurement of Wake Affected Heat Transfer and Wake Induced Transition Model,'' ASME J. Turbomach., **118**, pp. 327–336.
[6] Funazaki, K., and Koyabu, E., 1999, ''Effects of Periodic Wakes Passing Upon Flat Plate Boundary Layers Experiencing Favorable and Adverse Pressure Gradients,'' ASME J. Turbomach., **121**, pp. 333–340.
[7] Liu, X., and Rodi, W., 1991, ''Experiments on Transitional Boundary Layers With Wake Induced Unsteadiness,'' J. Fluid Mech., **231**, pp. 229–256.
[8] Wu, X., Jacobs, R. G., Hunt, J. C. R., and Durbin, P. A., 1999, ''Simulation of Boundary Layer Transition Induced by Periodically Passing Wakes,'' J. Fluid Mech., **398**, pp. 109–153.
[9] Hunt, J. C. R., Durbin, P. A., and Wu, X., 1998, ''Interaction Between Freestream Turbulence and Boundary Layers,'' *Annual Research Briefs*, Center for Turbulence Research, Stanford University, Stanford, CA.
[10] Kays, W. M., 1994, ''Turbulent Prandtl Number—Where Are We?'' ASME J. Heat Transfer, **116**, pp. 284–295.
[11] Parneix, S., Behnia, M., and Durbin, P. A., 1999, ''Predictions of Turbulent Heat Transfer in an Axisymmetric Jet Impinging on a Heated Pedestal,'' ASME J. Heat Transfer, **121**, pp. 43–49.
[12] Wu, X., and Durbin, P. A., 2000, ''Boundary Layer Transition Induced by Periodic Wakes,'' ASME J. Turbomach., in press.
[13] Akselvoll, K., and Moin, P., 1996, ''Large Eddy Simulation of Turbulent Confined Coannular Jets,'' J. Fluid Mech., **315**, pp. 387–411.
[14] Durbin, P. A., 1994, ''Separated Flow Computation With the V2F Model,'' AIAA J., **33**, pp. 659–664.
[15] Durbin, P. A., and Laurence, D., 1996, ''Nonlocal Effects in Single Point Closure,'' *Advances in Turbulence Research—1996*, Korea University, Seoul, Korea, pp. 109–120.
[16] Kittichaikarn, C., Ireland, P. T., Zhong, S., and Hodson, H. P., 1999, ''An Investigation on the Onset of Wake Induced Transition and Turbulent Spot Production Rate Using Thermochromic Liquid Crystals,'' ASME TURBO EXPO'99, Indianapolis, In.
[17] Blackwell, B. F., 1972, ''The Turbulent Boundary Layer on a Porous plate: An Experimental Study of the Heat Transfer Behavior With Adverse Pressure Gradients,'' Ph.D. thesis, Department of Mechanical Engineering, Stanford University, Stanford, CA.
[18] Kays, W. M., and Crawford, M. E., 1980, *Convective Heat and Mass Transfer*, 2nd Ed., McGraw-Hill, New York.
[19] Simonich, J. C., and Bradshaw, P., 1978, ''Effect of Freestream Turbulence on Heat Transfer Through a Turbulent Boundary Layer,'' ASME J. Heat Transfer, **100**, pp. 671–677.
[20] Subramanian, C. S., and Antonia, R. A., 1981, ''Effect of Reynolds Number on a Slightly Heated Turbulent Boundary Layer,'' Int. J. Heat Mass Transf., **24**, pp. 1833–1846.
[21] Zhang, L., and Han, J. C., 1995, ''Combined Effect of Freestream Turbulence and Unsteady Wake on Heat Transfer Coefficients From a Gas Turbine Blade,'' ASME J. Heat Transfer, **117**, pp. 296–302.

Influence of Inflow Disturbances on Stagnation-Region Heat Transfer

S. Bae
Department of Mechanical Engineering,
Korea Advanced Institute of Science
and Technologgy,
Taejon 305-701, Korea

S. K. Lele
Department of Mechanical Engineering,
Stanford University,
Stanford, CA 94309

H. J. Sung[1]
Department of Mechanical Engineering,
Korea Advanced Institute of Science
and Technology,
Taejon 305-701, Korea
e-mail: hjsung@kaist.ac.kr

Numerical simulations of laminar stagnation-region heat transfer in the presence of freestream disturbances are performed. The sensitivity of heat transfer in stagnation-region to freestream vorticity is scrutinized by varying the length scale, amplitude, and Reynolds number. As an organized inflow disturbance, a spanwise sinusoidal variation is superimposed on the velocity component normal to the wall. An accurate numerical scheme is employed to integrate the compressible Navier-Stokes equations and energy equation. The main emphasis is placed on the length scale of laminar inflow disturbances, which maximizes the heat transfer enhancement. Computational results are presented to disclose the detailed behavior of streamwise vortices. Three regimes of the behavior are found depending on the length scale: these are the ''damping,'' ''attached amplifying,'' and ''detached amplifying'' regimes, respectively. The simulation data are analyzed with an experimental correlation. It is found that the present laminar results follow a general trend of the correlation. [S0022-1481(00)01102-6]

Keywords: Computational, Enhancement, Heat Transfer, Impingement, Laminar

Introduction

Heat transfer to a stagnation region is important in many engineering applications. The heat transfer around a turbine blade is a good example among others, where the combustor exit temperature often exceeds the melting point of superalloy turbine blade materials (Yeh et al. [1] and Van Fossen et al. [2]). The highest heat transfer rate on the turbine blade usually occurs at the stagnation point. Thus, an accurate prediction of flow and attendant heat transfer in the stagnation region is of significant importance.

It is known that stagnation-region heat transfer augmentation in the presence of laminar freestream disturbances is caused by the amplification of streamwise vorticity. The streamwise vorticity, which is imposed at the inflow boundary, is convected into the stagnation region, and is amplified by the stretching due to the mean flow (Sutera [3] and Sadeh et al. [4]). A literature survey reveals that there have been many studies on the stagnation-region heat transfer in the presence of laminar freestream disturbances. The sensitivity of heat transfer in the stagnation-region boundary layer to freestream vorticity was studied by Sutera et al. [5]. They proposed a mathematical model to study the vorticity amplification due to the stretching of streamwise vortices in the diverging stagnation-region flow. Rigby et al. [6] imposed numerically a spanwise variation in the laminar freestream to a flow over an elliptical leading edge, and found the increase of wall heat transfer by as much as 25 percent. Hanford et al. [7] investigated the enhancement of wall heat transfer in a flow over a circular cylinder by imposing a pulsation of the incoming velocity and the oscillation of streamlines.

Since often freestream turbulence may contain quasi-organized large-scale structures, it is helpful to study the similarity between heat transfer enhancement in the presence of laminar inflow disturbances and that with the freestream turbulence. Many experiments have been performed to find the influence of turbulence parameters on stagnation-region heat transfer (Kestin [8], Kestin et al. [9], Van Fossen et al. [10], Ames et al. [11], Yeh et al. [1], Ames [12], and Van Fossen et al. [2]). A perusal of relevant literature reveals that the available published data for the length-scale dependence have been inconclusive. Some investigators reported that heat transfer enhancement increases as the length scale increases (Sutera [3] and Sadeh et al. [4]), while reduction of heat transfer enhancement was also noted by some investigators (Van Fossen et al. [10] and Ames et al. [11]) with increasing the length scale. This discrepancy can be attributed to disparity in the length scales examined.

One promising avenue to cope with these discrepancies is to re-evaluate the stagnation-region heat transfer rate in a systematic way. The objective of the present study is to delineate the influence of laminar inflow disturbances on the amplification of vorticity and its heat transfer augmentation in the stagnation region. Toward this end, a series of numerical simulations are conducted. Emphasis is placed on the length scale effect of laminar inflow disturbances which gives the maximum heat transfer augmentation. As an organized inflow disturbance, a simple sinusoidal variation is superimposed on the velocity component normal to the wall. The amplification of vorticity induced by the laminar inflow disturbances is scrutinized by varying the length scale, amplitude, and Reynolds number. In particular, the amplification mechanism of heat transfer enhancement by the streamwise vorticity is investigated in detail. The range of the length scale associated with the disturbances is varied from 2.1δ to 10.6δ, where δ is 99 percent undisturbed laminar boundary layer thickness. The amplitude of the disturbances (A) is varied from 5 percent to 25 percent of the inflow velocity. The Reynolds number based on L, which is a reference length scale, is varied from 5000 to 20,000. The Mach number is set as 0.4 to represent a flow from a combustor. The temperature ratio at the wall is set as $T_w/T_o = 0.8$, where T_w is the wall temperature and T_o is a freestream total temperature.

Numerical Simulation

The governing equations, compressible Navier-Stokes, energy, and continuity equations, are made dimensionless using the following reference values: the reference quantities ρ_∞, U_∞, a_∞, T_∞, L, and t_∞ represent a density, velocity, speed of sound, temperature, length scale, and time scale, respectively. The continuity equation is

[1]To whom correspondence should be addressed.

Contributed by the Heat Transfer Division for publication in the JOURNAL OF HEAT TRANSFER. Manuscript received by the Heat Transfer Division, February 27, 1999; revision received, November 29, 1999. Associate Technical Editor: R. Douglass.

$$\frac{\partial \rho}{\partial t}+\frac{\partial \rho u_i}{\partial x_i}=0, \tag{1}$$

where ρ is the density and x_i $(i=1,2,3)$ denotes three spatial directions in which x is the direction parallel to the wall, y denotes the direction normal to the wall, and z is the spanwise direction.

The Navier-Stokes equations are

$$\frac{\partial \rho u_i}{\partial t}+\frac{\partial \rho u_i u_j}{\partial x_j}+\frac{\partial p}{\partial x_i}-\frac{\partial \sigma_{ij}}{\partial x_j}=0, \tag{2}$$

where u_i is the ith velocity component and p is the pressure. σ_{ij} is the viscous stress tensor defined as

$$\sigma_{ij}=\frac{\mu}{\mathrm{Re/Ma}}\left(2S_{ij}-\frac{2}{3}\frac{\partial u_i}{\partial x_j}\delta_{ij}\right), \tag{3}$$

where μ is the viscosity, Re is the Reynolds number, and Ma is the Mach number. S_{ij} is the strain rate

$$S_{ij}=\frac{1}{2}\left(\frac{\partial u_i}{\partial x_j}+\frac{\partial u_j}{\partial x_i}\right). \tag{4}$$

The energy equation is

$$\frac{\partial \rho e_T}{\partial t}+\frac{\partial \rho u_j(e_T+p)}{\partial x_j}-\frac{\mathrm{Ma}}{\mathrm{Pr\,Re}(\gamma-1)}\frac{\partial}{\partial x_j}\left(k\frac{\partial T_i}{\partial x_j}\right)-\frac{\partial \sigma_{ij}u_j}{\partial x_i}=0, \tag{5}$$

where T is the temperature, Pr is the Prandtl number, k is the thermal conductivity, and γ is the ratio of the specific heat. The total energy per unit mass e_T is

$$e_T=C_v T+\frac{1}{2}u_i u_i, \tag{6}$$

where C_v is the specific heat at constant volume.

A series of simulations are performed by varying Re, λ, and A, where λ and A represent the length scale and amplitude of laminar inflow disturbances, respectively. As shown in Fig. 1, a steady sinusoidal spanwise disturbance is imposed at the inflow boundary

$$v(x,z)=v_m(x)\{1+A\sin(2\pi z/\lambda)\}, \tag{7}$$

where $v_m(x)$ denotes the mean velocity averaged in the spanwise direction at the inflow boundary. Note that only one cycle of the sinusoidal disturbance is retained; the domain size in z is λ. Nonreflecting boundary conditions (Giles [13]) are imposed at the inflow and outflow boundaries. Exit zones (Colonius et al. [14]) are appended to the outflow boundaries, as shown in Fig. 1. In the exit zone, disturbances are smoothly damped by a second-order explicit filter, where the strength of the filter increases to the outflow boundary. For spatial discretization, a fourth-order central differencing scheme is used. A fully implicit second-order scheme is used for time integration. Nonuniform meshes are employed in the x and y-directions, whereas a uniform grid is used in the z-direction. Flow directions are indicated by arrows in Fig. 1 and the wall is located at the bottom $(y=0)$. At the wall, the no-slip boundary condition is imposed for velocities, and the isothermal boundary condition is set for the temperature with $T_w/T_o=0.8$, where T_w is the wall temperature and T_o is the freestream total temperature, respectively.

Several trial calculations are repeated to monitor the sensitivity of the results to grid size, where the grid points are clustered near the wall boundary. The grid independence has been checked, and the outcomes of these tests are found to be satisfactory for the present three-dimensional simulations where $70\times90\times48$ grid points are used in x, y and z-directions respectively. The initial conditions are the solutions for undisturbed laminar flow. The steady-state solutions are obtained by converging unsteady computations when maximum relative variation between two successive iterations is less than 10^{-4}. The computations are implemented on CRAY YMP C-90, and the typical computation time is approximately 40 hours for one set of calculation.

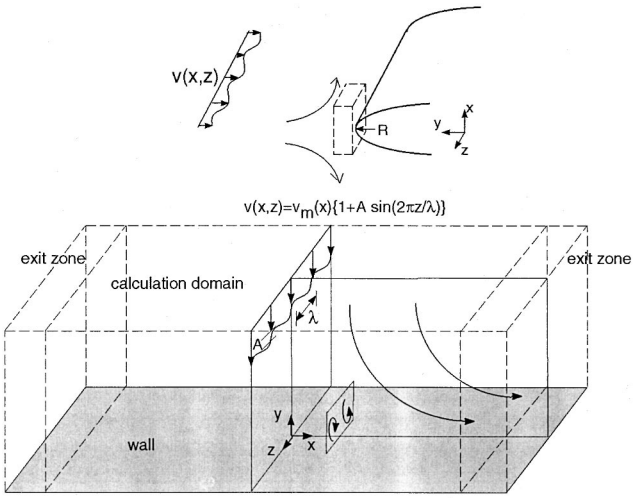

Fig. 1 Schematic diagram of flow configuration with organized inflow disturbances

Results and Discussion

It is important to ascertain the reliability and accuracy of the present numerical simulation. Toward this end, two comparisons are made. First, the present code is compared with a preverified code which uses the sixth-order compact scheme for spatial derivatives (Mahesh et al. [15]). A direct numerical simulation of unsteady three-dimensional homogenous decaying turbulence has been conducted by both codes. The instantaneous results from both codes are compared in Fig. 2(*a*), where the instantaneous w velocity fields are displayed against the z-direction. It is shown that, as the mesh sizes are refined from $80\times80\times80$ to 120×120

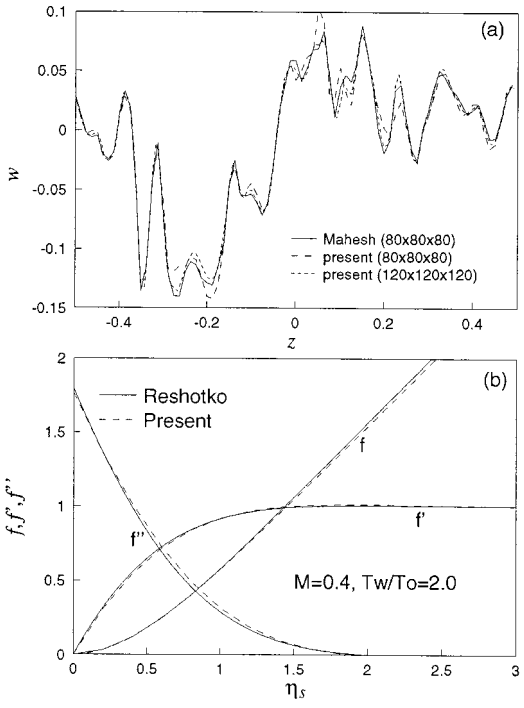

Fig. 2 (*a*) Comparison of the present code with the preverified Mahesh's code. (*b*) Comparison of present results with Reshotko's results. η_s is the self-similar coordinate and $f(\eta_s)$ is the self-similarity solution, after Stewartson's transformation.

$\times 120$, the results from the present code converge to Mahesh's result. Second, a laminar compressible stagnation-point flow without any laminar inflow disturbances has been simulated by using the present numerical code. The solutions of Reshotko et al. [16] are available for comparison. Figure 2(*b*) shows the comparison between the solutions and the computed results for Ma$=0.4$ and $T_w/T_o=2.0$. The solutions are displayed for three functions f, f' and f'', where f is the self-similarity solution for a laminar compressible stagnation flow after Stewartson's transformation. f' is the first derivative and f'' is the second derivative of f, respectively. η_s is the self-similarity coordinate after Stewartson's transformation (Reshotko et al. [16]). As shown in Fig. 2(*b*), the computed values by the present simulation are in good agreement with their solutions.

Effects of the laminar inflow disturbances on the stagnation-region heat transfer are evaluated by varying the length scale (λ), amplitude (A), and Reynolds number (Re), where Re is defined as $\mathrm{Re}=\rho_\infty U_\infty L/\mu_\infty$. L is a reference length scale, which is the distance from the wall to the location where U_∞, ρ_∞, and μ_∞ are estimated. If the strain rate in an external irrotational flow at the bluff body stagnation point is S_∞, the same strain rate generated by specifying the impinging freestream U_∞ at a finite distance L is $S_\infty=U_\infty/L$. Note that S_∞ depends on irrotational flow over the body. In particular, S_∞ is proportional to cU_∞/R, where R is a radius of curvature at the leading edge and c is a constant depending on a body shape, respectively. As shown in Fig. 1, the computational domain of the present study is a zoom of the bluff body stagnation region.

The spanwise variation of wall heat transfer due to the laminar inflow disturbances is characterized by the Stanton number (St), which is defined as

$$\mathrm{St}=\frac{h}{\rho_\infty C_p U_\infty}=\frac{-k\left.\frac{\partial T}{\partial y}\right|_w}{(T_w-T_\infty)\rho_\infty C_p U_\infty}. \tag{8}$$

Here, ρ_∞ and U_∞ represent the reference density and velocity, respectively. The subscript w denotes the wall. h is the heat transfer coefficient and k is the thermal conductivity. C_p is the specific heat at constant pressure. Note that St is constant along x for a given Reynolds number in the present stagnation flow.

First, the influence of the length scale (λ) is scrutinized at a fixed amplitude of laminar inflow disturbances ($A=0.25$). The variations of St are displayed in Fig. 3 for three Reynolds numbers (Re$=5000$, 10,000, and 20,000). A percentage change of St due to the laminar inflow disturbances is calculated, which is defined as $\Delta\mathrm{St}=(\mathrm{St}-\mathrm{St}_{\mathrm{lam}})/\mathrm{St}_{\mathrm{lam}}\times 100$. Here, a reference value $\mathrm{St}_{\mathrm{lam}}$ is the value of St when the laminar inflow disturbances are not imposed on a laminar stagnation-region flow. The averaged value of ΔSt over the z-direction $\overline{\Delta\mathrm{St}}$ is obtained as a function of the length scale (λ/δ). As seen in Fig. 3, the effect of λ/δ on $\overline{\Delta\mathrm{St}}$ is substantial. An overall inspection of Fig. 3 indicates that a specific length scale (λ_s) exists, which maximizes $\overline{\Delta\mathrm{St}}$ at $\lambda_s/\delta\approx 5.3$. This finding is of vital importance in heat transfer designs. For example, the specific length scale λ_s should be avoided in the design of turbine blade. When λ is larger than λ_s, i.e., $\lambda/\delta>5.3$, $\overline{\Delta\mathrm{St}}$ decreases as λ/δ increases. However, when λ is smaller than λ_s ($\lambda/\delta<5.3$), the wall heat transfer increases with the increase of λ/δ. As mentioned in the Introduction, some investigations reported that heat transfer enhancement increases as the length scale increases, whereas reduction of heat transfer enhancement was also noted by some workers with the increase of the length scale. This discrepancy can be attributed to the length scales that were examined.

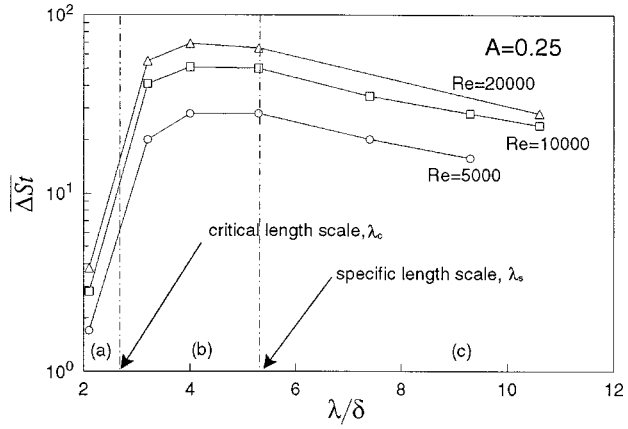

Fig. 3 Variations of $\overline{\Delta\mathrm{St}}$ against λ/δ for $A=0.25$

It is interesting to review the previous studies in a sense of their selected length scale ranges. Ames [12] and Van Fossen et al. [2] conducted experiments, where the heat transfer enhancement is reduced as the length scale increases. When the size of the streamwise vortex is large, the vortex stretching by mean strain rate does not amplify the streamwise vorticity enough to disturb the stagnation boundary layer. Accordingly, the augmentation of heat transfer is attenuated with the larger streamwise vortex in the freestream. Moreover, when the inflow length scale becomes large, the effect of ''blocking'' is increased by the presence of the wall (Hunt [17]). This blocking effect gives the reduction of heat transfer enhancement. Hancock and Bradshaw [18] also addressed the ''blocking'' effect in a flat plate boundary layer.

On the other hand, Sutera [3] investigated the effect of the spanwise length scale in the freestream disturbances when the length scale is smaller than the specific length scale (λ_s). He demonstrated that the heat transfer increases as the length scale increases. It was shown that the amplification of streamwise vorticity enhances the stagnation heat transfer. He also found that if the length scale is larger than a ''critical'' length scale λ_c, the streamwise vorticity is convected toward the wall, stretched by the strain rate and amplified. However, if the length scale is smaller than λ_c, it is damped. Here, the critical length scale is approximately ten times the laminar displacement thickness (δ^*), i.e., $\lambda_c\approx 10\delta^*\approx 2.7\delta$. Sadeh et al. [4] confirmed that if the length scale in freestream turbulence is larger than the critical length scale, the streamwise vorticity is amplified. Figure 3 shows a summary of the aforementioned previous results.

As seen in Fig. 3, three regimes which are dependent on the length scale of the laminar inflow disturbances are observed. When λ/δ is smaller than the critical length scale, a ''damping'' regime is observed, where the streamwise vorticity is damped from the inflow boundary. This regime is denoted by (*a*) in Fig. 3, where a mild heat transfer near the stagnation region is observed. However, as the length scale increases, an ''attached amplifying'' regime is formed. In this regime (*b*), the wall heat transfer increases with the increase of the length scale. When λ/δ increases further, i.e., λ/δ is larger than λ_s, a ''detached amplifying'' regime (*c*) is formed. In the regime (*c*), it is shown that as the length scale increases, the wall heat transfer decreases.

It is known that the enhancement of heat transfer in the stagnation region is caused by the amplification of streamwise vorticity (ω_x) near the stagnation region. To see the detailed amplification mechanism of ω_x, typical isocontours of ω_x in the y-z plane at $x=\delta$ are illustrated in Fig. 4. The negative vorticity is designated by the gray line. In the ''damping'' regime, as shown in Fig. 4(*a*), the magnitude of ω_x decreases as the flow approaches the wall. A sign change of ω_x is captured close to the wall ($y/\delta\approx 0.59$). The countersign vorticity near the wall is formed due to the no-slip condition at the wall. For the ''attached amplifying'' regime shown in Fig. 4(*b*), a pair of peaks of ω_x are observed at $y/\delta\approx 2.4$. The peak locations of ω_x are close to the edge of the boundary layer which is located at $y/\delta=1.0$. A comparison of the magnitude of ω_x discloses that the maximum value of ω_x in the ''attached amplifying'' regime is larger than that in the ''damp-

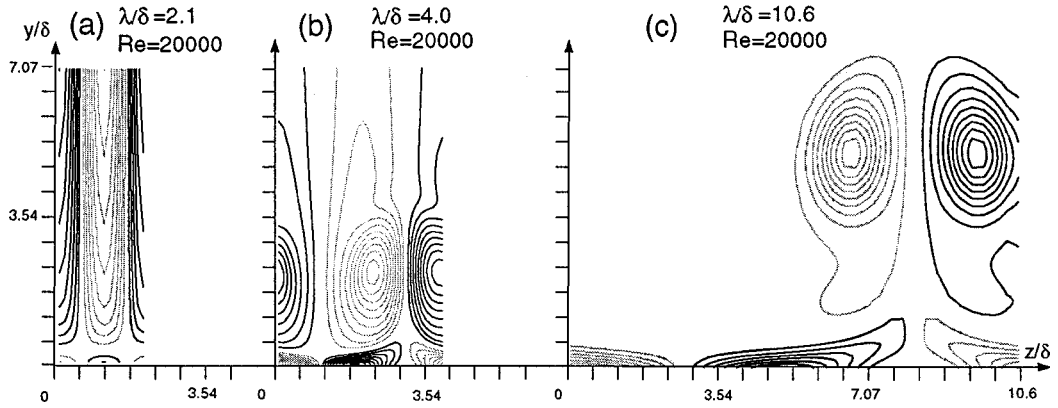

Fig. 4 Contours of streamwise vorticity (ω_x) in *y-z* plane at $x=\delta$ for $A=0.25$ and Re=20,000 (*a*) $\lambda/\delta=2.1$, (*b*) $\lambda/\delta=4.0$, and (*c*) $\lambda/\delta=10.6$. The tick mark spacing is 0.707. (*a*) The maximum contour value is 2.8 and the minimum is −2.8, (*b*) the maximum value is 9.6 and the minimum is −9.6, and (*c*) the maximum value is 12.0 and the minimum is −12.0.

ing'' regime. However, in the ''detached amplifying'' regime in Fig. 4(*c*), the streamwise vorticity is detached from the edge of the boundary layer. The peak locations of ω_x are away from the wall, i.e., $y/\delta\approx 5.3$, whereas the maximum value of ω_x is increased. Van Fossen et al. [10] also showed the role of counterrotating streamwise vortices by a flow visualization, which is consistent with the present observation.

Isocontours of temperature in the *y-z* plane at $x=\delta$ are also shown in Fig. 5 for the three regimes. In the ''damping'' regime, as shown in Fig. 5(*a*), the contours are disturbed mildly. In the ''attached amplifying'' regime of Fig. 5(*b*), the temperature contours are disturbed and a mushroom-shaped region is formed between the pair of streamwise vortices. As λ/δ increases further, i.e., in the ''detached amplifying'' regime (Fig. 5(*c*)), the temperature contours show large distortion. The mushroom-shaped region shows overturned isotherms. These are similar to the temperature contours found in Saric [19] for boundary layer disturbed by Görtler vortices. The height of the mushroom-shaped contour is increased to $y/\delta\approx 7.1$ in Fig. 5(*c*). However, it is important to note that, although the temperature contours in the ''detached amplifying'' regime are shown to be disturbed more vigorously than those in the ''attached amplifying'' regime, the heat transfer rate in the stagnation region shows an opposite result in Fig. 3. This means that $\overline{\Delta St}$ in the ''detached amplifying'' regime is smaller than $\overline{\Delta St}$ in the ''attached amplifying'' regime.

It should be pointed out in the present study that the enhancement of heat transfer in the stagnation region is closely related to the peak location of ω_x and its strength. The streamwise vorticity ω_x in the ''attached amplifying'' regime is displayed in Fig. 6(*a*) for two length scales ($\lambda/\delta=3.2$ and 4.0). The Reynolds number is Re=10,000 and the amplitude is $A=0.25$. To identify the peak location of ω_x, a self-similarity coordinate is employed in the *y*-axis, i.e., $\eta=y\sqrt{\mathrm{Re}}$. As shown in Fig. 6(*a*), as λ/δ increases from 3.2 to 4.0 that are in ''attached amplifying'' regime, the peak value of ω_x increases from 2.7 to 4.8. The corresponding peak location moves from $\eta=2.8$ to $\eta=3.8$. It is recalled from Fig. 3 for Re=10,000 that the heat transfer at $\lambda/\delta=4.0$ is more enhanced than that at $\lambda/\delta=3.2$. When the peak location of ω_x is closer to the wall, larger heat transfer may be expected, but the observed result is opposite to this expectation. Accordingly, another important factor exists, which influences the heat transfer enhancement. As seen in Fig. 6(*a*), the peak value of ω_x at $\lambda/\delta=4.0$ is larger than that at $\lambda/\delta=3.2$.

Figure 6(*b*) represents the profiles of ω_x in the ''detached amplifying'' regime for two length scales $\lambda/\delta=7.4$ and 10.6 at the same Reynolds number as shown in Fig. 6(*a*). From Fig. 3, $\overline{\Delta St}$ for $\lambda/\delta=7.4$ is larger than $\overline{\Delta St}$ at $\lambda/\delta=10.6$. Contrary to Fig. 6(*a*), as λ/δ increases from 7.4 to 10.6, the peak value decreases from 4.7 to 4.2. However, the peak location moves from $\eta=5.7$ to $\eta=6.2$. Since $\overline{\Delta St}$ decreases with the increase of λ/δ in the ''detached amplifying'' regime, both the peak location and the peak value of ω_x act in a mutually cooperating direction. This means that the stagnation heat transfer is more enhanced with the in-

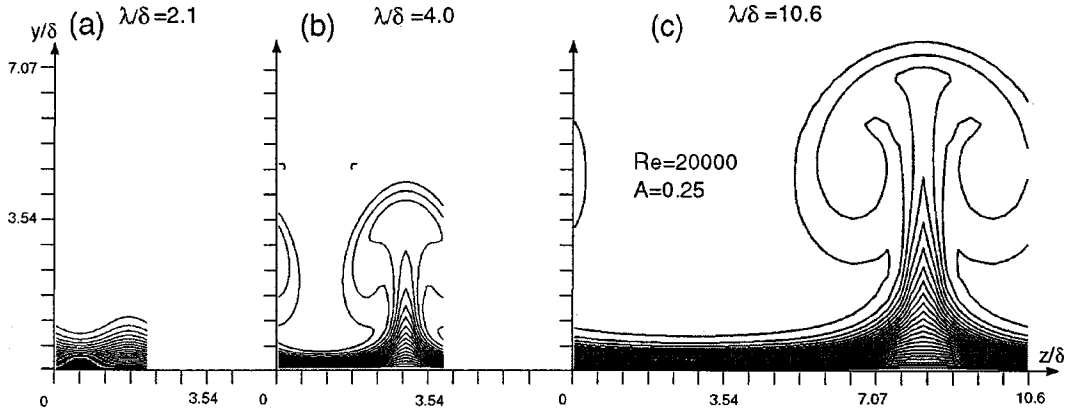

Fig. 5 Contours of temperature in the *y-z* plane at $x=\delta$ for $A=0.25$ and Re=20,000. (*a*) $\lambda/\delta=2.1$, (*b*) $\lambda/\delta=4.0$, and (*c*) $\lambda/\delta=10.6$. The tick mark spacing is 0.707. The maximum value is 1.0 in the freestream and the minimum is 0.8 at the wall.

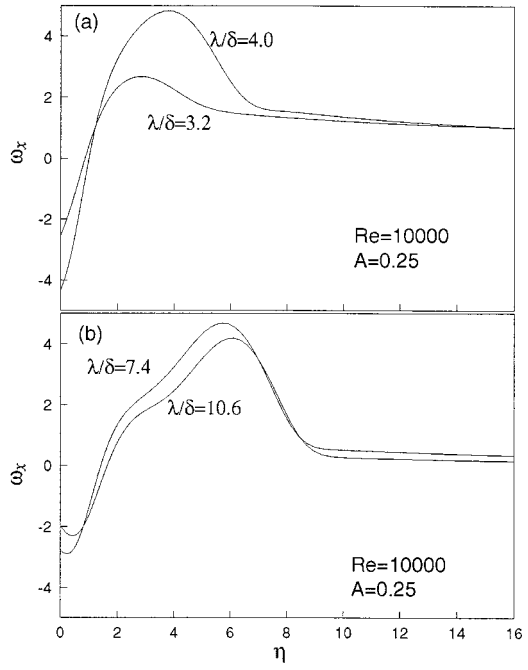

Fig. 6 Variations of streamwise vorticity (ω_x) at the *z*-location where the core of streamwise vortex is located for Re=10,000 and $A=0.25$ ((a) $\lambda/\delta=3.2$ and 4.0; (b) $\lambda/\delta=7.4$ and 10.6)

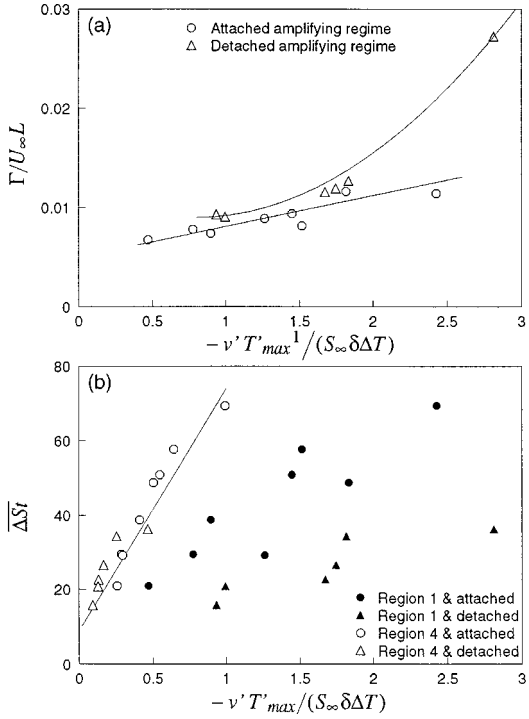

Fig. 8 (a) Variations of Γ against $-v'T'_{max}/(S_\infty\delta\Delta T)$ in region 1. (b) Variations of $\overline{\Delta St}$ against $-v'T'_{max}/(S_\infty\delta\Delta T)$.

crease of the strength of ω_x and the closer peak location of ω_x to the wall. An inflection point can be found in Fig. 6(b) near $\eta \approx 3.7$ for $\lambda/\delta=7.4$ and $\eta\approx 4.0$ for $\lambda/\delta=10.6$, respectively. However, the inflection point is not found in the ''attached amplifying'' regime. Thus, different evolutions of ω_x in the ''attached amplifying'' from ''detached amplifying'' regimes show different behaviors of the enhancement of heat transfer. The negative peaks located very close to the wall are shown inside the boundary layer ($\eta\approx 1.0$). These are not the cores of the streamwise vortices, but are the consequences of the ''lift-up'' distortions of contours as shown in Fig. 4(c).

The aforementioned different evolution of ω_x may be linked to the different evolution of heat flux $\overline{v'T'}$, where v' and T' denote the fluctuations of wall-normal velocity $v'=v-\overline{v}$ and temperature $T'=T-\overline{T}$, respectively. The overbar denotes a spanwise-averaged value. To investigate the effect of $\overline{v'T'}$ on the enhancement of wall heat transfer, the flow and temperature fields are decomposed into four regions shown in Fig. 7. According to the combination of v' and T', four regions are categorized: region 1 ($v'>0$, $T'<0$) represents the mushroom center area of the temperature contours, region 2 ($v'>0$, $T'>0$) the side area of the

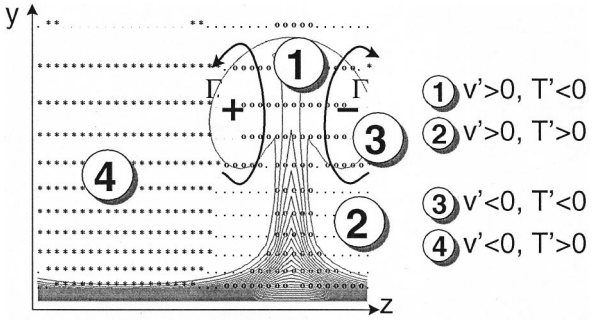

Fig. 7 Schematic diagram for four regions and the circulation Γ

mushroom neck, region 3 ($v'<0$, $T'<0$) the side area of the mushroom head, and region 4 ($v'<0$, $T'>0$) the area where the temperature contours are pushed toward the wall. Γ is the circulation of streamwise vortex.

Figure 8(a) shows the variations of Γ against $-v'T'_{max}/(S_\infty\delta\Delta T)$ in region 1, where ΔT is $\Delta T=T_o-T_w$. The circulation Γ is calculated by integrating ω_x, i.e., $\Gamma=\int\omega_x dydz$. However, the integration domain considered in the present study is not fully covered. This is because ω_x from the domain boundary to infinity is not zero. To compensate for the partial integration, an analytical profile of ω_x outside the domain is extended as (Sutera [3])

$$\omega_x \propto \frac{e^{-0.5\eta^2}}{\eta^{(\lambda_c/\lambda)^2}}, \tag{9}$$

where λ_c is the critical length scale in Fig. 3. It is found that the extended integration value of Γ by the analytical profile does not exceed ten percent of the full circulation Γ. A positive circulation Γ is calculated by only the positive ω_x. As shown in Fig. 8(a), Γ correlates linearly with $-v'T'_{max}/(S_\infty\delta\Delta T)$ in the ''attached amplifying'' regime while Γ does not correlate linearly in the ''detached amplifying'' regime. If the circulation Γ is linearly correlated with $-v'T'_{max}/(S_\infty\delta\Delta T)$, the strength of streamwise vortex is directly correlated to $-v'T'_{max}/(S_\infty\delta\Delta T)$. This implies that vortex dynamics can be applied to estimate the wall heat transfer. The variations of $\overline{\Delta St}$ against $-v'T'_{max}/(S_\infty\delta\Delta T)$ in regions 1 and 4 are displayed in Fig. 8(b). It is shown that $-v'T'_{max}/(S_\infty\delta\Delta T)$ in region 1 is generally larger than that in region 4. Furthermore, $-v'T'_{max}/(S_\infty\delta\Delta T)$ in region 4 at both ''attached amplifying'' and ''detached amplifying'' regimes correlates linearly with $\overline{\Delta St}$. On the contrary, the data in region 1 is shown to be scattered. This suggests that the normal heat flux in region 4 is more directly correlated with the wall heat transfer enhancement than that in region 1. A global inspection of Fig. 8(b) indicates that the overall maximum of $-v'T'_{max}/(S_\infty\delta\Delta T)$ occurs in region 1 among other

Table 1 $\overline{\Delta St}$ (percent) with A and λ/δ at Re=5000

A \ λ/δ	2.1	3.2	4.0	5.3
0.05	0.035	0.91	1.5	1.6
0.10	0.25	3.6	6.0	6.3
0.25	1.7	20	28	28

regions. Accordingly, a simple correlation between $-v'T'_{max}/(S_\infty \delta \Delta T)$ and $\overline{\Delta St}$ is not suitable for representing the wall heat transfer enhancement accurately. In other words, a squeezing motion induced by the counterrotating streamwise vortices in region 4 is more responsible for the wall heat transfer enhancement than a pull-up motion in region 1. Here, the pull-up motion extracts colder fluid out of the thermal boundary layer and pushes it to the hotter region.

Next, the influence of amplitude (A) on $\overline{\Delta St}$ is investigated. As shown in Table 1, A is varied in a range $0.05 \leqslant A \leqslant 0.25$ for four cases of λ/δ, i.e., $\lambda/\delta = 2.1$, 3.2, 4.0, and 5.3. As classified earlier, $\lambda/\delta = 2.1$ belongs to the ''damping'' regime, $\lambda/\delta = 3.2$, 4.0, and 5.3 to the ''attached amplifying'' regime, respectively. An overall inspection of Table 1 indicates that $\overline{\Delta St}$ is increased with increasing A. For $\lambda/\delta = 2.1$ and 3.2, $\overline{\Delta St}$ varies nearly quadratically with A. As A increases from 0.05 to 0.10 and 0.25, $\overline{\Delta St}$ of $A = 0.10$ and 0.25 increase to 4 and 25 times $\overline{\Delta St}$ of $A = 0.05$. Note that the increase from $A = 0.05$ to $A = 0.10$ for $\lambda/\delta = 2.1$ is not quadratic. For other cases, the increase is quadratic at small A, but $\overline{\Delta St}$ from $A = 0.10$ to $A = 0.25$ is no longer quadratic and more gradual.

Efforts are extended to see the influence of A on ω_x near the stagnation region. The profiles of ω_x are displayed for three magnitudes, i.e., $A = 0.05$, 0.10, and 0.25. The length scale $\lambda/\delta = 3.2$ is selected in the ''attached amplifying'' regime for Re=5000. In this regime, as shown in Fig. 9(a), the profiles of $\omega_x/\omega_{x_{in}}$ show the trend in a manner similar to those in Fig. 6. Here, $\omega_{x_{in}}$ is the streamwise vorticity at the inflow boundary. Three profiles of $\omega_x/\omega_{x_{in}}$ are collapsed to one curve. This suggests that the amplification of ω_x is linear with A. However, for $\lambda/\delta = 5.3$ the amplification of ω_x is not linear with A. As shown in Fig. 9(b), three profiles do not coincide, i.e., the enhancement of wall heat transfer saturates as A increases. As A increases, the peak location of ω_x and the peak value of ω_x act in an opposing direction, i.e., the peak location of ω_x moves away from the wall and the peak value of ω_x increases. The nonlinear effects are responsible for the nonquadratic increase of $\overline{\Delta St}$, as shown in Table 1.

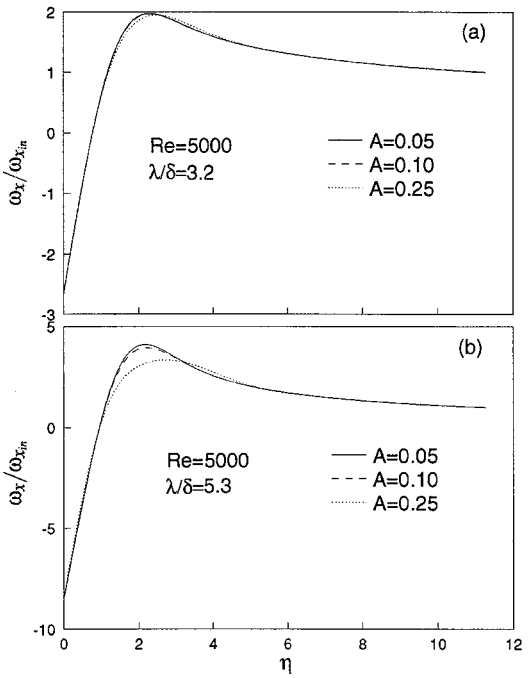

Fig. 9 Variations of normalized streamwise vorticity ($\omega_x/\omega_{x_{in}}$) with three different magnitudes at a z-location where the core of streamwise vortex is located for Re=5000 ((a) $\lambda/\delta = 3.2$; (b) $\lambda/\delta = 5.3$)

As remarked in the Introduction, freestream turbulence may often contain quasi-organized large-scale structures (Van Fossen et al. [10]). It is meaningful to analyze a similarity between the heat transfer enhancement in the presence of the laminar inflow disturbances and the freestream turbulence. For comparison, the formula of Kestin and Wood [9] is adopted, which is a function of Re and Tu where Tu is the turbulence intensity.

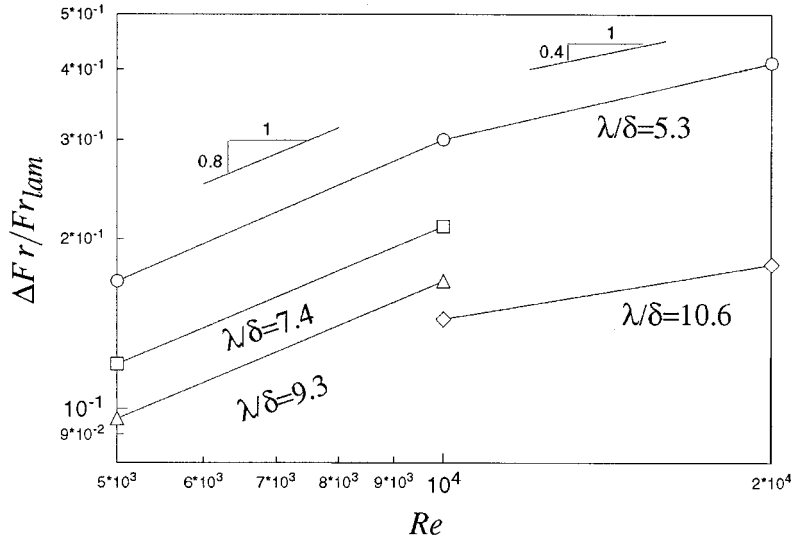

Fig. 10 Plot of $\Delta Fr/Fr_{lam}$ against Re for $A = 0.25$. $\Delta Fr = Fr - Fr_{lam}$.

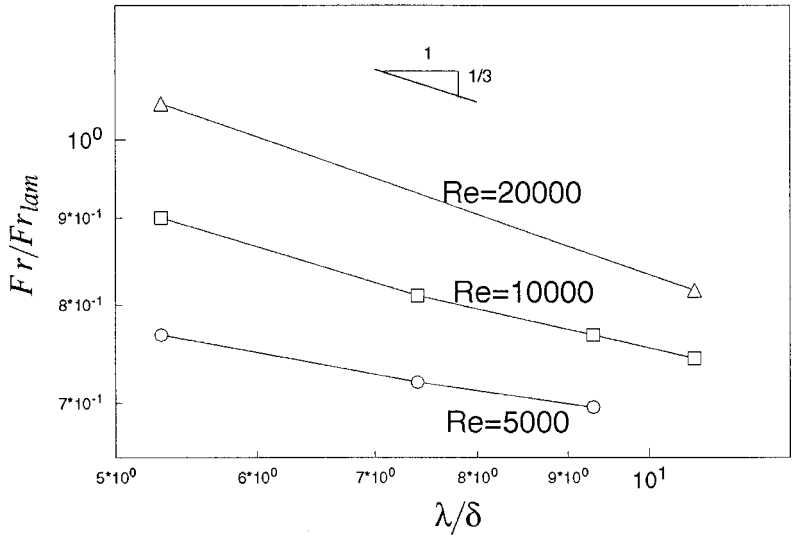

Fig. 11 Plot of Fr/Fr_{lam} against λ/δ for $A=0.25$

$$\mathrm{Fr}=\frac{\mathrm{Nu}}{\sqrt{\mathrm{Re}}}=0.945+3.48\left(\frac{\mathrm{Tu}\sqrt{\mathrm{Re}}}{100}\right)-3.99\left(\frac{\mathrm{Tu}\sqrt{\mathrm{Re}}}{100}\right)^2 \quad (10)$$

Here, Nu is the Nusselt number and Re is the Reynolds number based on the cylinder diameter *D*. The Frössling number is denoted by $\mathrm{Fr}=\mathrm{Nu}/\sqrt{\mathrm{Re}}$. As seen in the above formula, Fr is generally proportional to $\mathrm{Re}^{0.5}$ if $\mathrm{Tu}\sqrt{\mathrm{Re}}$ is small enough to neglect the quadratic term. To see the Re dependence on Fr, $\Delta\mathrm{Fr}/\mathrm{Fr}_{\mathrm{lam}}$ is plotted in Fig. 10. It is noted that the data in Fig. 10 belong to the ''detached amplifying'' regime (data for $\lambda/\delta=5.3$ can be included without loss of generality). ΔFr is defined as $\Delta\mathrm{Fr}=\mathrm{Fr}-\mathrm{Fr}_{\mathrm{lam}}$, where $\mathrm{Fr}_{\mathrm{lam}}$ is the value for the stagnation point flow without the laminar inflow disturbances. For a stagnation-region heat transfer on a circular cylinder, $\mathrm{Fr}_{\mathrm{lam}}$ is known to be $\mathrm{Fr}_{\mathrm{lam}}=1.0$ for Pr=0.72. The constant value $\mathrm{Fr}_{\mathrm{lam}}$ in Eq. (10) is $\mathrm{Fr}_{\mathrm{lam}}=0.945$. As seen in Fig. 10, $\Delta\mathrm{Fr}/\mathrm{Fr}_{\mathrm{lam}}$ is proportional to $\mathrm{Re}^{0.8}$ for lower Reynolds numbers ($\mathrm{Re}\leqslant 10^4$) and to $\mathrm{Re}^{0.4}$ for relatively high Reynolds numbers. Since most prior experiments were conducted for higher Reynolds numbers, it can be said that the present dependence $\Delta\mathrm{Fr}/\mathrm{Fr}_{\mathrm{lam}}$ on Re brackets the observed $\Delta\mathrm{Fr}/\mathrm{Fr}_{\mathrm{lam}}\propto\mathrm{Re}^{0.5}$. The $\mathrm{Re}^{0.5}$ dependence indicates that, as the Reynolds number increases, the boundary layer becomes thin and high mean strain rate impinges on the stagnation region strongly. Consequently, the thermal boundary layer is strongly disturbed and the associated wall heat transfer is augmented accordingly.

Another correlation formula can be found in which the length scale effect is included. Ames et al. [11] proposed a correlation,

$$\mathrm{Fr}=\frac{\mathrm{Nu}}{\sqrt{\mathrm{Re}}}=0.95+0.038\,\mathrm{Tu}\,\mathrm{Re}^{5/12}(\mathrm{Lu}/D)^{-1/3}. \quad (11)$$

In the above, Lu is the integral length scale in free-stream turbulence. In this formula, Fr is seen to be proportional to $\mathrm{Lu}^{-1/3}$. To find the proportional factor in the present data, $\mathrm{Fr}/\mathrm{Fr}_{\mathrm{lam}}$ is plotted in Fig. 11 as a function of λ/δ for different Reynolds numbers. Note that the data in Fig. 11 belong to the ''detached amplifying'' regime (data for $\lambda/\delta=5.3$ can be included without loss of generality). Although some deviations are observed, Fr is proportional to $(\lambda/\delta)^{-1/3}$, i.e., $\mathrm{Fr}\propto\lambda^{-1/3}$. Here, δ is constant for a given Reynolds number. All the present data are compared with Ames' correlation in Fig. 12. In comparison with the correlation of Ames, it should be noted that a conversion is needed between the present plane stagnation flow and the flow over a circular cylinder (Schlichting [20]). The data in the ''damping'' and ''attached amplifying'' regimes are also included in Fig. 12. As seen in Fig. 12, all data are fitted well with Ames' correlation except ''damping'' regime. Moreover, it is interesting to see that the data in the ''attached amplifying'' regime are also well fitted. Recall that the correlation of present study is based on the organized laminar inflow disturbances.

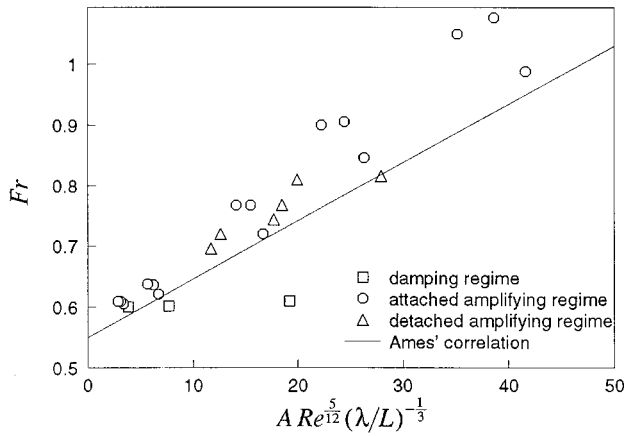

Fig. 12 Plot of Fr against $A\,\mathrm{Re}^{5/12}(\lambda/L)^{-1/3}$

Conclusions

The computational results disclose the prominent features of heat transfer augmentation in the stagnation region. The objective is to depict the influence of laminar inflow disturbances on the amplification of streamwise vorticity and the associated heat transfer augmentation. In the present simulation, the effect of length scale (λ) is significant. When λ is larger than the specific length scale (λ_s), the wall heat transfer decreases as λ increases. However, when λ is smaller than λ_s, the wall heat transfer increases with the increase of λ. Pertaining to the length scale associated with the laminar inflow disturbances, three regimes are classified, which are the ''damping,'' ''attached amplifying,'' and ''detached amplifying'' regimes, respectively. The amplification of streamwise vorticity (ω_x) is scrutinized for the three regimes. The mechanisms of ω_x amplification are analyzed in the ''attached amplifying'' and ''detached amplifying'' regimes, respec-

tively. The enhancement of heat transfer in the stagnation region is closely related to the peak location of ω_x and its strength. It is shown that the squeezing motion induced by the counterrotating streamwise vortices is more responsible for the wall heat transfer enhancement than the pull-up motion. The effect of the amplitude of laminar inflow disturbance (A) is also investigated, where the amplification of ω_x is linear with A for small A and λ. However, for large A and λ, it is not linear with A. The present laminar results are compared with Ames' correlation which is a function of the intensity, integral length scale and Reynolds number of the freestream turbulence. Although some deviations are found, the data are shown to be fitted satisfactorily.

Acknowledgments

Parts of the present study were made while the first author studied at Stanford University and sponsored by Air Force Office of Scientific Research under grant AFOSR-91-0198-D. This work was in part supported by a grant from the National Research Laboratory of the Ministry of Science and Technology, Korea. The computer time for the simulations was provided by NASA Ames Research Center, Pittsburgh Super Computing Center, and KORDIC Supercomputer Center in Korea.

Nomenclature

a = speed of sound
A = amplitude of laminar inflow disturbance
C_p = specific heat at constant pressure
C_v = specific heat at constant volume
e_T = total energy per unit mass
f = Hiemenz solution
Fr = Frössling number, $\mathrm{Fr}=\mathrm{Nu}/\sqrt{\mathrm{Re}}$
h = heat transfer coefficient
k = thermal conductivity
L = reference length scale
Lu = freestream turbulence length scale
Ma = Mach number, $\mathrm{Ma}=U_\infty/a_\infty$
Nu = Nusselt number, $\mathrm{Nu}=hL/k_\infty$
Pr = Prandtl number, $\mathrm{Pr}=\mu_\infty C_p/k_\infty$
R = radius of curvature
Re = Reynolds number, $\mathrm{Re}=\rho_\infty U_\infty L/\mu_\infty$
S_{ij} = strain rate, $S_{ij}=0.5(\partial u_i/\partial x_j+\partial u_j/\partial x_i)$
S_∞ = mean strain rate, $S_\infty=\partial U_\infty/\partial x$
St = Stanton number, $\mathrm{St}=h/\rho_\infty C_p U_\infty$
Tu = freestream turbulence intensity
γ = ratio of specific heat
Γ = circulation
δ = 99 percent boundary layer thickness
δ^* = displacement boundary layer thickness
η = self-similarity coordinate, $\eta=y\sqrt{\mathrm{Re}}$
η_s = self-similarity coordinate after Stewartson's transformation
λ = length scale of laminar inflow disturbance
λ_c = critical length scale
λ_s = specific length scale
σ_{ij} = stress tensor
ω = vorticity

Subscripts

a = analytical value
c = computational value
i = induced value
in = inflow boundary value
lam = laminar value
m = mean value
max = maximum value
o = freestream total value
w = wall value
∞ = freestream value

References

[1] Yeh, F. C., Hippensteele, S. A., Van Fossen, G. J., Poinsatte, P. E., and Ameri, A., 1993, ''High Reynolds Number and Turbulence Effects on Aerodynamics and Heat Transfer in a Turbine Cascade,'' *AIAA paper*, No. 93-225.
[2] Van Fossen, G. J., Simoneau, R. J., and Ching, C. Y., 1995, ''Influence of Turbulence Parameters, Reynolds Number and Body Shape on Stagnation Region Heat Transfer,'' ASME J. Heat Transfer, **117**, pp. 597–603.
[3] Sutera, S. P., 1965, ''Vorticity Amplification in Stagnation-Point Flow and its Effect on Heat Transfer,'' J. Fluid Mech., **21**, pp. 513–534.
[4] Sadeh, W. Z., Sutera, S. P., and Maeder, P. F., 1970, ''An Investigation of Vorticity Amplification in Stagnation Flow,'' Z. Angew. Math. Phys., **21**, pp. 717–741.
[5] Sutera, S. P., Maeder, P. F., and Kestin, J., 1963, ''On the Sensitivity of Heat Transfer in the Stagnation-Point Boundary Layer to Free-Stream Vorticity,'' J. Fluid Mech., **16**, pp. 497–520.
[6] Rigby D. L., and Van Fossen, G. J., 1992, ''Increased Heat Transfer to Elliptical Leading Edges due to Spanwise Variations in the Free-Stream Momentum: Numerical and Experimental Results,'' AIAA Paper No. 92-3070.
[7] Hanford, A. J., and Wilson, D. E., 1994, ''The Effect of a Turbulent Wake on the Stagnation Point: Part II—Heat Transfer Results,'' ASME J. Heat Transfer, **116**, pp. 46–56.
[8] Kestin, J., 1966, ''The Effect of Free-Stream Turbulence on Heat Transfer Rates,'' Adv. Heat Transfer, **3**, pp. 1–32.
[9] Kestin, J., and Wood, R. T., 1970, ''The Influence of Turbulence on Mass Transfer From Cylinders,'' ASME J. Heat Transfer, **92**, pp. 321–327.
[10] Van Fossen, G. J., and Simoneau, R. J., 1987, ''A Study of the Relationship Between Free-Stream Turbulence and Stagnation Region Heat Transfer,'' ASME J. Heat Transfer, **109**, pp. 10–24.
[11] Ames, F. E., and Moffat, R. J., 1990, ''Heat Transfer With High Intensity, Large Scale Turbulence: The Flat Plate Turbulent Boundary Layer and the Cylindrical Stagnation Point,'' Report No. HMT-43, Thermosciences Division of Mechanical Engineering, Stanford University, Stanford, CA.
[12] Ames, F. E., 1994, ''Experimental Study of Vane Heat Transfer and Aerodynamics at Elevated Levels of Turbulence,'' NASA Contractor Report, No. 4633.
[13] Giles, M., 1988, ''Non-reflecting Boundary Conditions for the Euler Equations,'' CFDL-TR-88-1.
[14] Colonius, T., Lele, S. K., and Moin, P., 1993, ''Boundary Conditions for Direct Computation of Aerodynamic Sound Generation,'' AIAA J., **31**, pp. 1574–1582.
[15] Mahesh, K., Lele, S. K., and Moin, P., 1997, ''The Influence of Entropy Fluctuations on the Interaction of Turbulence With a Shock Wave,'' J. Fluid Mech., **334**, pp. 353–379.
[16] Reshotko, E., and Beckwith, I. E., 1958, ''Compressible Laminar Boundary Layer Over a Yawed Infinite Cylinder With Heat Transfer and Arbitrary Prandtl Number,'' NACA Report No. 1379.
[17] Hunt, J. C. R., 1973, ''A Theory of Turbulent Flow around Two-Dimensional Bluff Bodies,'' J. Fluid Mech., **61**, Part 4, pp. 625–706.
[18] Hancock, P. E., and Bradshaw, P., 1983, ''The Effects of Free Stream Turbulence on Turbulent Boundary Layers,'' ASME J. Fluids Eng., **105**, pp. 284–289.
[19] Saric, W. S., 1994, ''Görtler Vortices,'' Annu. Rev. Fluid Mech., **26**, pp. 379–409.
[20] Schlichting, H., 1979, *Boundary Layer Theory*, 7th Ed., McGraw-Hill, New York.

Electrohydrodynamically Enhanced Convective Boiling: Relationship Between Electrohydrodynamic Pressure and Momentum Flux Rate

J. E. Bryan
Outokumpu Copper,
4720 Bowling Green Road,
Franklin, KY 42134

J. Seyed-Yagoobi
Department of Mechanical Engineering,
Texas A&M University,
College Station, TX 77843-3123
e-mail: jyagoobi@mengr.tamu.edu

The relationship between the mean radial electrohydrodynamic (EHD) pressure and the rate of the axial momentum flux and its influence on heat transfer enhancement and pressure drop in EHD-enhanced convective boiling of R-134a in a horizontal smooth tube was investigated in detail. A simple theory, which included the characteristics of two-phase flow, was developed to determine the mean radial EHD pressure. It was shown that the amount of heat transfer enhancement and the pressure drop penalty were dependent upon the size of the mean radial EHD pressure relative to the rate of the axial momentum flux. The influence of the mass flux, change in quality, and saturation temperature on the mean radial EHD pressure relative to the rate of the axial momentum flux was also studied. This study has provided a greater understanding of EHD enhancement of the convective boiling heat transfer. [S0022-1481(00)01802-8]

Keywords: Electric Fields, Enhancement, Heat Transfer, Phase Change, Two-Phase

Introduction

Passive and active enhancement methods for improving convective boiling heat transfer are continuously being developed and researched. An increase in the heat transfer coefficient produced by a new enhancement technique usually results in an increase in the pressure drop as well. It becomes very important to understand the relationship between the heat transfer and pressure drop in order to maximize the heat transfer and minimize the pressure drop. Passive enhancement methods, such as microfin tubes, have resulted in a 100 percent increase in the heat transfer coefficient with less than 25 percent increase in the pressure drop at low mass fluxes and a 50 percent increase in the heat transfer coefficient with 10 percent increase in the pressure drop at higher mass fluxes ([1]).

An active enhancement method which has been recently investigated utilizes the electrohydrodynamic (EHD) phenomena. Only a few researchers, in the last seven years, have investigated EHD-enhanced convective boiling. The limited amount of research is, in part, due to the lack of fundamental knowledge on EHD-enhanced heat transfer. EHD is a promising possibility for enhancing convective boiling heat transfer; however, the enhancement produced by EHD can be offset by potentially high pressure drops.

Yabe et al. [2] reported a 100 percent increase in the heat transfer by applying EHD and they mentioned that the pressure drop was negligible with EHD, but this was not compared to the pressure drop without an electrode in the test section. The reason the pressure drop with EHD was negligible is the electrode, a perforated tube, was 5 mm in diameter and the boiling tube was 10 mm in diameter. Singh [3] increased the heat transfer 260 percent using EHD enhancement on a helical electrode design in a microfin tube, but the pressure drop penalty was 700 percent. However, all of the pressure drop was due to presence of the helical electrode alone; the pressure drop due to the EHD forces was negligible. Salehi et al. [4] increased the heat transfer 80 percent to 100 percent using EHD enhancement on a rod electrode design in a longitudinally finned tube with a pressure drop penalty of 400 percent. Again most of the pressure drop was due to the presence of the electrode.

Bryan and Seyed-Yagoobi [5] have shown that EHD enhanced convective boiling is significantly influenced by quality, flow regime, heat flux, and mass flux. In convective boiling, the EHD force/pressure in many situations will be primarily perpendicular to the bulk fluid motion and the influence of this force will be strongly dependent on the variables mentioned above as well as the fluid electrical properties, electrode geometry, and the applied voltage. This same EHD force which will be acting primarily perpendicular to the fluid flow can also result in increased flow resistance, there by increasing the pressure drop. Therefore, it is important to understand the interdependence of the EHD force and the convective boiling process if an EHD force is to be produced which will maximize the heat transfer and minimize the pressure drop penalty for a given flow condition.

None of the studies reported in the literature has provided a detailed investigation of the relationship between the EHD force/pressure and the convective boiling process and how this relationship influences the heat transfer enhancement and pressure drop. This must be understood if the application of EHD to convective boiling is to become a reality in an industrial environment. The results presented in this study will provide fundamental knowledge of how the EHD force influences both the heat transfer and pressure drop and how this force is affected by the mass flux, change in quality, and flow momentum rate for a given fluid and electrode design.

Electrohydrodynamic Phenomena

The EHD phenomena involve the interaction of electric fields and flow fields in a dielectric fluid medium. This interaction can result in electrically induced fluid motion and interfacial instabilities which are caused by an electric body force. The electric body

Contributed by the Heat Transfer Division for publication in the JOURNAL OF HEAT TRANSFER. Manuscript received by the Heat Transfer Division, December 1, 1997; revision received, November 4, 1999. Associated Technical Editor: M. S. Sohal.

force density acting on the molecules of a dielectric fluid in the presence of an electric field consists of three terms ([6]):

$$\overline{f_e} = q_e\overline{E} - \frac{1}{2}E^2\nabla\varepsilon + \frac{1}{2}\nabla\left[E^2\left(\frac{\partial\varepsilon}{\partial\rho}\right)_T\rho\right]. \quad (1)$$

The three terms in Eq. (1) stand for two primary force densities acting on the fluid. The first term represents the force acting on the free charges in the presence of an electric field and is known as the Coulomb force. The second and third terms represent the polarization force induced in the fluid.

Figure 1 shows four examples of induced forces on a dielectric fluid medium, which can result from the application of a nonuniform electric field. The electric body force density components defined in Eq. (1) are responsible for the induced forces on the dielectric fluid medium. Schematic (*a*) in Fig. 1 is a representation of fluid motion resulting from the Coulomb force. A charged body in a nonuniform or uniform electric field will move along the electric field lines and impart momentum to the surrounding fluid. Free charges can be introduced into the fluid medium by direct injection from an energized sharp electrode resulting in a net charge in the fluid. Free charges can also be induced within the fluid without a net charge buildup. This charge induction takes place in the presence of an electric field due to a nonuniformity in the electric conductivity of the fluid. A nonuniformity in the electric conductivity can be a result of a temperature gradient and/or an inhomogeneous fluid. It is important to note that the motion of the charged body will depend on the strength of the applied electric field and whether it is DC or AC.

Schematic (*b*) in Fig. 1 represents translational motion, often identified as dielectrophoresis, resulting from the generation of the polarization force in a nonuniform electric field. For the fluid to experience a net polarization force over a given region, there must be a relative displacement of positive and negative bound charges in a body by applying an electric field. An induced dipole, resulting from the displacement of the positive and negative bound charges in a neutral body by applying an electric field, will experience a net unidirectional force in a nonuniform electric field. One end (the negative end in the sketch) of this dipole in a nonuniform electric field experiences a higher force than the other end (the positive end in the sketch), resulting in a net translation of the polarized body towards the higher electric field.

There are two ways in which a fluid, which is isotropic both before and after an electric field is applied, can become polarized. The fluid can be inhomogeneous, in the sense that the permittivity is a function of position, or it can vary with density. The second term in Eq. (1) is due to inhomogeneities, while the last term is due to variations in the fluid density. Since the last term provides a coupling between the fluid density and the electric field, it is called the electrostriction force density ([6]). Discussion has persisted over the years with respect to the electrostriction force density term in Eq. (1). It has centered on whether or not the electrostriction force density can be responsible for the translational motion of an induced dipole as shown in schematic (*b*) of Fig. 1. A more detailed discussion on polarization forces and the potential of the electrostriction force density to generate fluid translation is provided by Bryan [7].

The last two schematics, (*c*) and (*d*), in Fig. 1 are additional representations of polarization forces due to the application of a nonuniform electric field. If an interface exists, such as between a liquid and vapor, in a nonuniform electric field, an attraction force is created which draws the fluid of higher permittivity (liquid) toward the region of higher electric field strength, as shown in schematics (*c*) and (*d*) in Fig. 1. The bubble in schematic (*d*), which is of lower permittivity than the surrounding liquid, will be forced to the region of lower electric field strength, as defined by the second term in Eq. (1). It should be noted that the behavior of the bubble, shown in Fig. 1(*d*), has been classified as dielectrophoresis by Jones [8]. The polarization attraction force will occur regardless of whether a DC or AC nonuniform field is applied. However, the potential accumulation of charge at the interface can influence the polarization force. Locally, if the charge accumulation is large enough, space charge effects can become significant and the Coulomb force can be influential.

All three components of the EHD force density can be significant or one can dominate over the others. In convective boiling all

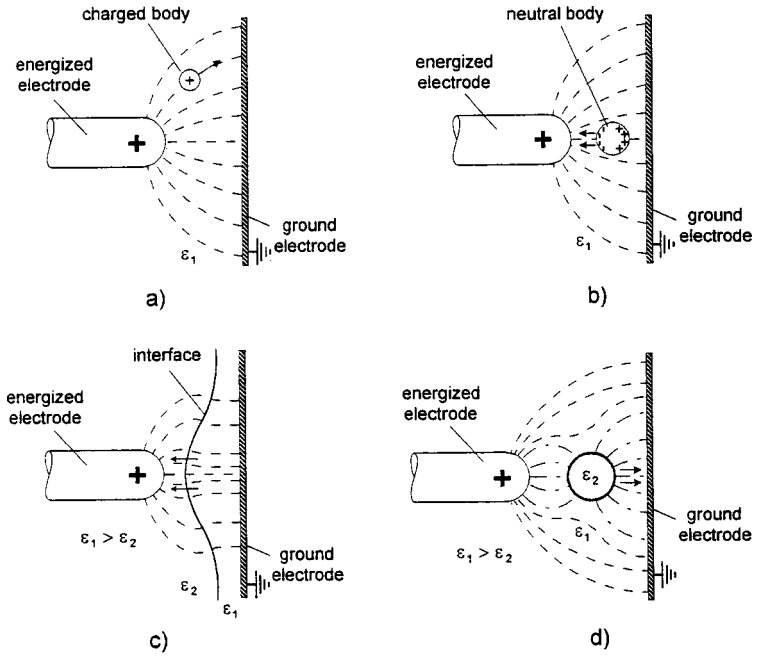

Fig. 1 Simple representations of electric body force density components

three forces will be present, however, the second term of Eq. (1) is expected to dominate as the quality and heat flux increase.

Experimental Apparatus

The experimental apparatus, shown in Fig. 2, is a closed loop in which refrigerant is pumped with a positive displacement gear pump instead of a compressor. The refrigerant flows from the pump through a flow regulating valve and preheat section and then through four evaporator test sections of 10, 20, 30, and 50 cm in length. The refrigerant then flows to the condenser and accumulator where it is condensed and subcooled before reentering the pump. The refrigerant used in all experiments was *R*-134a.

The four test sections, shown in Fig. 2, were connected in series and heat was provided to each by a recirculating hot water loop. The different test sections were used to allow for the measurement of the local heat transfer coefficients and heat fluxes. Each test section, as shown in Fig. 3, consisted of a smooth copper boiling tube (inside diameter=14.1 mm and outside diameter=15.9 mm) surrounded by an acrylic tube (inside diameter 38.1 mm) in which the hot water flowed. T-type thermocouples were soldered to the

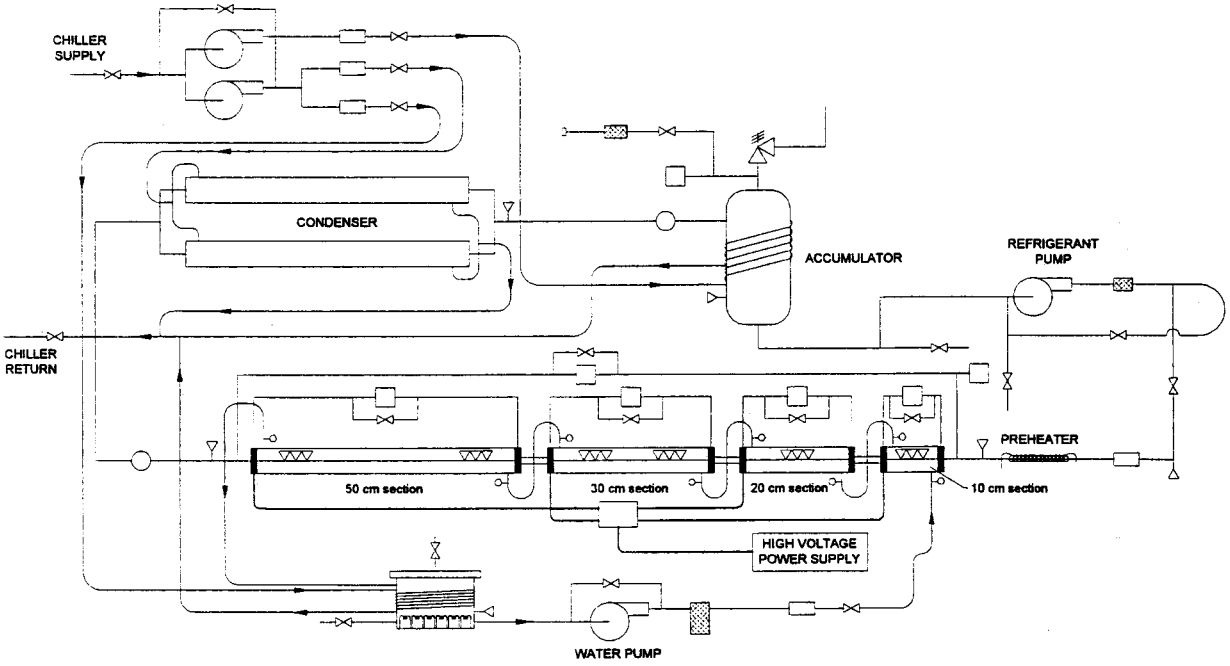

Fig. 2 Schematic of experimental apparatus

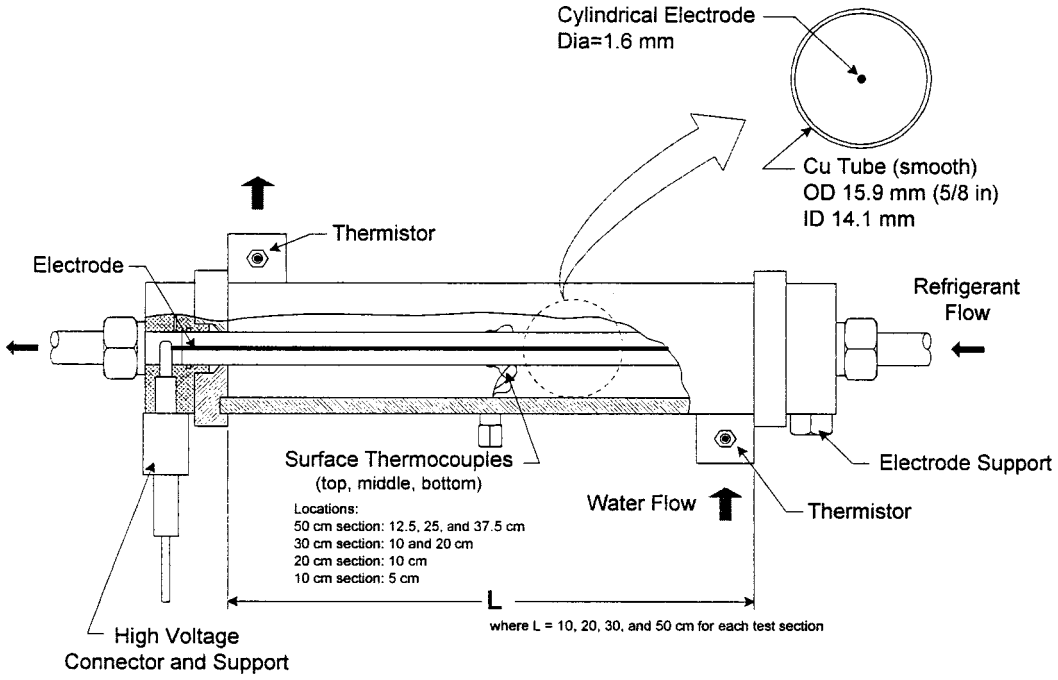

Fig. 3 Drawing of test section

surface of the boiling tubes at the top, middle, and bottom in each test section. In the 10 and 20-cm sections, the surface thermocouples were soldered to the tube surface at the center of the test section. In the 30-cm section they were soldered in two stations at 10-cm intervals and in the 50-cm section in three stations at 12.5 cm intervals. The surface thermocouples allowed for the measurement of the local heat transfer coefficient in each test section. The inlet and outlet water temperature to each test section was measured with thermistors so that in all experiments the temperature difference across each test section could be accurately measured and maintained to 1°C or less. The pressure drop across each test section was measured with a variable reluctance pressure transducer.

The electrode geometry used in the experiments was a brass rod 1.6 mm in diameter (see Fig. 3). The brass electrode was suspended in the center of each test section and held in tension by two electrode supports, one at the entrance and one at the exit of the test section. In all experiments the brass electrode was energized with a positive DC high voltage while the copper boiling tube was grounded. Refer to Bryan and Seyed-Yagoobi [5] for more details on the experimental apparatus.

Experimental Procedure

All experiments began by first starting the recirculating chiller and setting it at an appropriate setpoint temperature. The refrigerant pump was then turned on and then the water heater was set to the desired heat load. The chiller, refrigerant flow rate, and water flow rate were all adjusted for the desired test conditions. Once all adjustments were made, steady state was determined when the accumulator temperature and the inlet and outlet refrigerant temperatures to the test sections had all remained constant for 30 minutes. Four data sets were then taken, each in two-minute intervals at a rate of one sample per two seconds. This resulted in a data file of over 200 points, which were averaged to determine a single test point. Then the high voltage was applied and conditions were adjusted if necessary. Once the system reached steady state and the three temperature probes had remained constant for 30 minutes, another four data sets were taken. The heat load was then changed and the process was repeated. The heat loads were varied randomly and data for one operating condition were acquired over several weeks to insure there was no bias in the test data.

Data Reduction and Uncertainty Analysis

In all experiments the heat transfer coefficient and quality were calculated from direct measurements. The average overall heat transfer coefficient for the four test sections combined was determined from an area average of the local heat transfer coefficients for the 10, 20, 30, and 50-cm sections. The local heat transfer coefficient at each location inside the tube was calculated from

$$h = \frac{\dot{m} c_p (T_{\text{in}} - T_{\text{out}})}{\pi D_i L (T_{w_i} - T_{\text{sat}})}. \tag{2}$$

The local inside wall temperature, T_{w_i}, was calculated through a one-dimensional conduction analysis, knowing the local outside surface temperature, measured at the different locations in each test section as described earlier. The conduction through the wall was accounted for even though its influence was very small. The change in quality was determined from

$$\Delta x = \frac{\left(\dot{m} c_p (T_{\text{in}} - T_{\text{out}})/\dot{m}_{\text{ref}}\right)}{h_{fg}} \tag{3}$$

The change in quality, Δx, is the difference between the exit quality from the last test section and the inlet quality from the first test section. In this study liquid at the saturated condition always enters the first test section, thus the inlet quality is always zero. This means that Δx is the actual quality at the exit of the last test section.

Table 1 Experimental uncertainties

Measurements	Total Uncertainty Average	Total Uncertainty Maximum
Surface temperature	±0.09°C	±0.41°C
Inlet and outlet refrigerant temperature	±0.13°C	±0.17°C
Inlet and outlet water temperature	±0.06°C	±0.09°C
Refrigerant mass flux	±4.2 kg/m^2 s	±4.3 kg/m^2 s
Water mass flow rate	±0.0027 kg/s	±0.0027 kg/s
Pressure drop	±0.056 kPa[a]	±0.074 kPa[a]
Calculated Quantities	Average	Maximum
Quality	±13.8 percent	±20.5 percent
Heat flux	±13.1 percent	±20.0 percent
Heat transfer coefficient	±13.4 percent	±39.2 percent

[a]Uncertainties were smallest on 10-cm section and greatest on 50-cm section and increased as heat load increased

Pressure drop data are difficult to measure in two phase flow, especially over short flow lengths, such as the test sections used in this study. The instantaneous pressure drop measurements in two-phase flow vary significantly; resulting in large standard deviation of the pressure drop measurement. To make a proper pressure drop measurement a large number of samples were taken to obtain an acceptable mean and total uncertainty. In the experiments performed in this study, 240 pressure measurements (at a sample rate of 1 sample per 2 seconds) were obtained for each pressure drop data point. Only 60 samples were required to calculate an acceptable mean pressure drop data point, but the 240 samples were obtained to provide an acceptable total uncertainty.

A total uncertainty analysis was performed for all the measured data and calculated quantities based on methods described by Taylor [9] and Kline and McClintock [10]. The maximum total uncertainties are shown in Table 1 for the different measured and calculated quantities. Great care was taken to properly calibrate all instrumentation, which allowed for a complete uncertainty analysis to be performed with the lowest possible experimental uncertainties.

Results and Discussion

Verification of Experimental Data: No EHD. The heat transfer coefficient data without EHD from this study compared well to existing data from Wattelet et al. [11] and to Kandlikar's [12] correlation. The details are provided in Bryan and Seyed-Yagoobi [5]. Table 2 provides a comparison of some of the pressure drop data in this work without EHD to that of Eckels et al. [1] and Torikoshi and Ebisu [13]. The data in this study, shown in Table 2, compare well to the data of the other researchers.

The experimental data were also compared to an existing two-phase pressure drop correlation for horizontal flow boiling in a constant area smooth tube. This correlation is based on the separated flow model as defined in Carey [14], where the axial pressure gradient is dependent on the frictional losses and the acceleration of the flow due to the heat added to the refrigerant. The axial pressure gradient is defined as

Table 2 Comparison of pressure drop data between this study (electrode in-place and no EHD) and other researchers for conventional horizontal convective boiling with R-134a

Reference	x_{in} kg/kg	x_{out} kg/kg	T_{sat} °C	G kg/m^2 s	D_i mm	L_t m	$\Delta P/L_t$ kPa/m
[1]	0.05	0.85	1	86	8.0	3.7	0.59
[1]	0.05	0.82	1	121	8.0	3.7	1.27
[13]	0.20	1.00	5	91	8.0	4.0	0.90
This study	0.00	0.89	5	102	14.1	1.1[a]	0.9[a]

[a]Summation of the 10, 20, 30, and 50-cm sections.

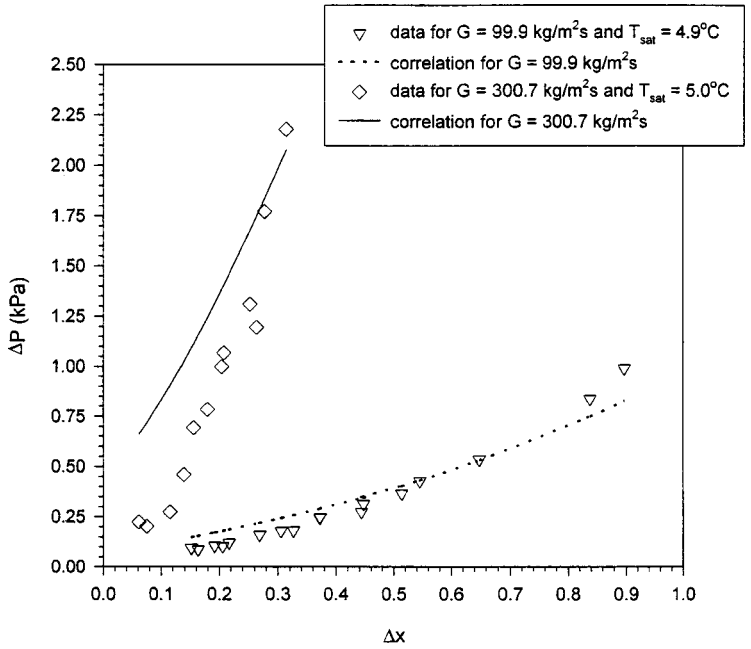

Fig. 4 Comparison of two-phase pressure drop correlation with experimental data at two different mass fluxes (electrode in-place, no EHD)

Table 3 Comparison of pressure drop data from this study without the electrode to the pressure drop correlation

x_{in} kg/kg	x_{out} kg/kg	T_{sat} °C	G kg/m^2 s	ΔP (calculated) kPa	ΔP (measured) kPa
0.05	0.25	4.9	301	1.40	1.19
0.03	0.33	25.2	400	1.67	1.34

$$-\left(\frac{dP}{dz}\right)=\left(\frac{2\,f_{lo}G^2}{\rho_1 D_i}\right)\phi_{lo}^2+G^2\frac{d}{dz}\left[\frac{x^2\nu_v}{\alpha}+\frac{(1-x)^2\nu_1}{1-\alpha}\right] \quad (4)$$

where the first term on the right-hand side represents the pressure gradient due to frictional losses and the second term represents acceleration of the flow. The pressure drop was determined by integrating Eq. (4) over the desired tube length under the assumption that the quality varies linearly with the tube length. The two-phase multiplier, ϕ_{lo}, was calculated using the Friedel [15] correlation, which is recommended as one of the most accurate correlations for horizontal tubes in Collier and Thome [16]. The void fraction, α, was calculated using the Thome [17] correlation which is defined as

$$\alpha=\left[1+\left(\frac{1-x}{x}\right)\left(\frac{\rho_v}{\rho_1}\right)^{0.89}\left(\frac{\mu_1}{\mu_v}\right)^{0.18}\right]^{-1}. \quad (5)$$

The comparison of the correlation to the experimental data is shown in Fig. 4 for an average mass flux of 99.9 and 300.7 kg/m^2 s. The correlation compares well to the experimental data considering the difficulty in predicting two-phase flow pressure drops. It should be noted that the pressure drop data shown in Fig. 4 and Table 2 was measured with the electrode in-place (see Fig. 3). The electrode accounted for about a 25 percent increase in the pressure drop for the two mass fluxes considered in this study. Table 3 shows experimental data from this study for two conditions with no electrode in-place compared to the correlation discussed above. The experimental data are in reasonable agreement with the correlation.

Experimental Results: EHD Enhancement. The results presented in this study include the electrode even when no EHD force is applied. The reason for this is to study the interdependence of the EHD force and the convective boiling process for a given geometrical configuration.

The change in quality and mass flux influence the EHD force and its impact on heat transfer and pressure drop. Experimental evidence of this is shown in Figs. 5 and 6 where the average overall heat transfer coefficient and pressure drop as a function of the change in quality are plotted at a saturated temperature of 5°C for an average mass flux of 99.9 and 300.7 kg/m^2 s, respectively. For all experiments, an increase in Δx was obtained by increasing the heat load (i.e., heat flux) to the test sections. The heat transfer coefficients at 0 kV increase as Δx increases, as shown in Figs. 5 and 6. This is primarily due to the increase in heat flux to the test sections and the fact that the heat transfer is nucleate boiling dominated. However, the flow accelerates as the quality increases and the convective heat transfer also becomes important. The pressure drop increases with an increase in Δx as well, because as more energy is added to the flow the change in frictional losses and the flow momentum rate become larger. The scatter in the heat transfer coefficient data as seen in Figs. 5 and 6 is due to the variation in the active nucleation sites where the heat transfer coefficient was measured. Although these measurements were made at the same location, the experiments were performed randomly, sometimes with increasing heat flux and others with decreasing heat flux, which resulted in variations in the number and location of active nucleation sites.

The EHD force, as seen in Fig. 5, produces some interesting and different results at 5 and 15 kV. From 0 to 5 kV there is a small increase in the heat transfer coefficient and the pressure drop, up to $\Delta x=0.44$. Beyond this point the heat transfer starts being suppressed, but the EHD force is still increasing the pressure drop. From 5 to 15 kV there is a substantial change in the behavior of the heat transfer coefficient and the pressure drop as Δx increases. A 170 percent increase in the heat transfer coefficient at 15 kV and $\Delta x=0.13$ results in almost an order of magnitude increase in the pressure drop. However, at $\Delta x=0.68$, the EHD force at 15 kV is suppressing the heat transfer by 125 percent while generating over 40 percent increase in pressure drop.

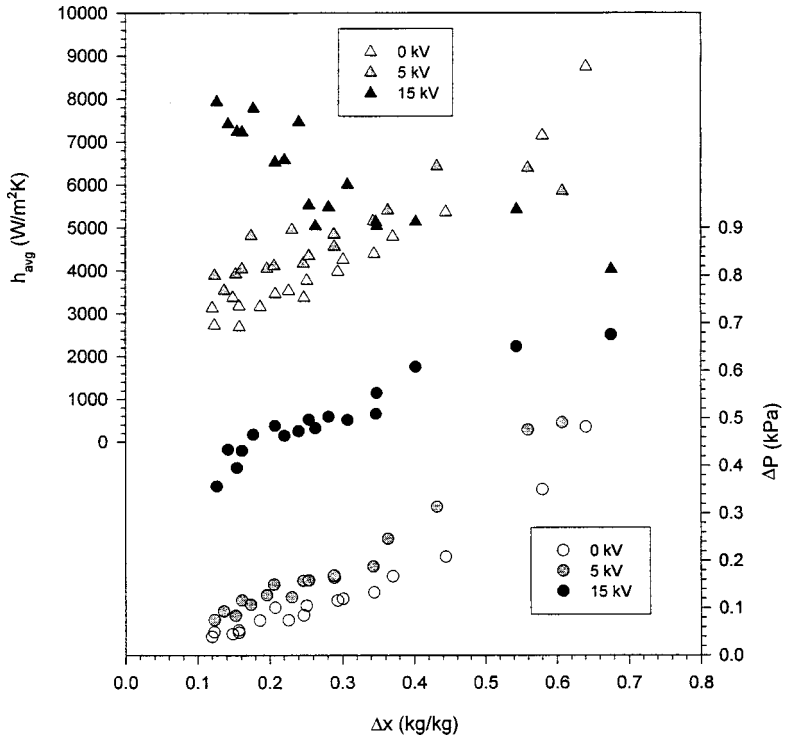

Fig. 5 Heat transfer coefficient and pressure drop versus change in quality at G_{avg}=99.9 kg/m^2 s and T_{sat}=4.9°C

When the mass flux is increased, as shown in Fig. 6, the difference between 5 and 15 kV on the heat transfer-enhancement and pressure drop penalty is not as severe. The prime reason for this is the momentum rate of the flow is greater at 300.7 kg/m^2 s than 99.9 kg/m^2 s, and since the EHD force is applied at the same voltage it is smaller relative to the increase in flow momentum rate. However, the EHD force still produces heat transfer enhancements and an increase in the pressure drop for both 5 and 15 kV. The highest heat transfer enhancement is just over 100 percent and the pressure drop penalty is around 600 percent which

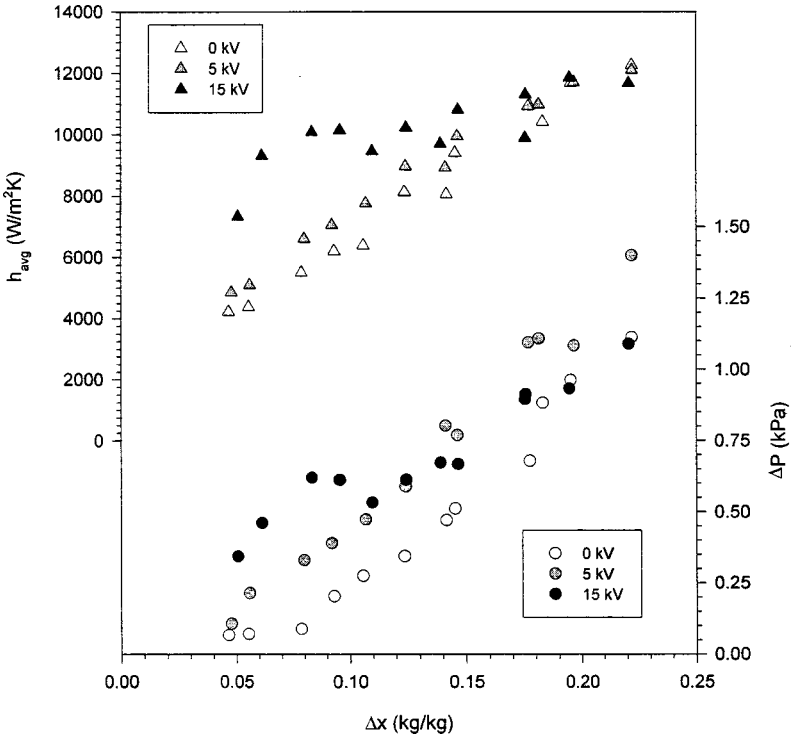

Fig. 6 Heat transfer coefficient and pressure drop versus change in quality at G_{avg}=300.7 kg/m^2 s and T_{sat}=5.0°C

occur at 15 kV and $\Delta x = 0.08$. As Δx increases the heat transfer enhancement and pressure drop penalty decrease at both voltages.

The heat transfer enhancement and suppression occurring over the range of Δx, in both Figs. 5 and 6, is due to several factors as discussed in detail by Bryan and Seyed-Yagoobi [5]. As the flow progresses from the entrance of the test section to the exit, the role and influence of the EHD force density components, defined in Eq. (1), vary depending on the total change in quality. When Δx is small, the Coulomb and polarization forces generate secondary motions in the liquid and the polarization force acts on the liquid-vapor interface. At this point the EHD force components are enhancing the heat transfer, and because their influence is significant they are also generating a substantial increase in the pressure drop. However, when Δx (i.e., heat flux) increases further, the role of the EHD force components change. The Coulomb and polarization forces still generate secondary motions in the liquid, but over the same test section length there is less liquid to act upon since more energy has been added to the flow. The increased energy causes more bubble nucleation to occur along the tube surface resulting in the flow regime transitioning to annular flow. The polarization forces starts to play a more significant role as more energy is added to the flow. The suppression of the heat transfer starts to occur when the influence of the polarization force is still large enough to act at the liquid-vapor interface. This suppression results from the polarization force holding the vapor bubbles on or near the tube wall as they form; and where the flow is annular this force begins to remove the liquid layer from the tube surface. In both cases the resistance to heat transfer increases there by suppressing the heat transfer. The increase in the pressure drop will depend on how significant these EHD force components are with respect to the fluid momentum rate, which increases as more energy is added to the flow.

An interesting result shown in Fig. 6 is that the EHD force at 5 kV is large enough to produce heat transfer enhancement and increase the pressure drop. Conversely, the EHD force at 15 kV is much more substantial and is starting to suppress the heat transfer and produce less pressure drop penalty than occurs at 5 kV. This is especially noticeable between Δx of 0.15 and 0.22, where the pressure drop at 5 kV is greater than at 15 kV. Here the polarization force is forcing the bubbles, which are produced to stay near or on the tube surface and attracting the liquid toward the high voltage electrode in the center of the tube. This reduces the frictional losses at the wall thus reducing the pressure drop at 15 kV compared to 5 kV. The behavior shown in Fig. 6 does not occur in the data shown in Fig. 5 because the flow regime is different. The difference in the flow regime will be discussed later in the paper.

Theoretical Comparison Between EHD Pressure and Flow Momentum. As shown in both Figs. 5 and 6 the EHD force has produced some interesting results and it is evident that the change in quality and mass flux affect the EHD force. There exists a relationship between the EHD force and the convective boiling process and this relationship influences the heat transfer and the pressure drop. This relationship can be better understood by developing a method to compare the mean radial EHD pressure and the rate of the axial momentum flux. To make this comparison, an approximation of the radial EHD pressure is required. This can be accomplished by rewriting the EHD force density in Eq. (1) as a Maxwell stress tensor. By making use of Gauss' law and tensor notation Eq. (1) becomes

$$T_{ij} = \varepsilon E_i E_j - \frac{\varepsilon}{2}\delta_{ij}E_k E_k\left[1 - \frac{\rho}{\varepsilon}\left(\frac{\partial \varepsilon}{\partial \rho}\right)_T\right] \tag{6}$$

where the details of the derivation are discussed by Melcher [6]. Two assumptions can be made to simplify Eq. (6). First, the dominate electric field is in the radial direction with the electrode geometry used in this study (see Fig. 3). Second, the dominant stress component is the normal stress (that is to say pressure) in the radial direction. With these two assumptions the only Maxwell stress component of interest is

$$T_{rr} = \frac{1}{2}\left[\varepsilon E_r^2 + \rho\left(\frac{\partial \varepsilon}{\partial \rho}\right)_T E_r^2\right]. \tag{7}$$

This normal stress component will be used to approximate the radial EHD pressure. A point should be emphasized with respect to Eq. (7). As discussed earlier, the different EHD force density components, defined in Eq. (1), will influence the convective boiling heat transfer and pressure drop. The magnitudes of each component will vary depending on the fluid electric properties, the presence of free and dipole charges, the applied voltage, and electrode geometry.

The radial electric field, shown in Eq. (7), will be highly dependent on the flow regime. To determine an acceptable radial EHD pressure, which can be compared to the axial momentum flux rate, the electric field should be evaluated in a form, which has some relevance to the flow regimes. Two approaches, schematically shown in Fig. 7, will be considered. The first is to assume the flow is a homogeneous mixture of liquid and vapor and the second is to assume the flow is annular with a pure vapor plug surrounded by a pure liquid ring. The electric potential distribution in both approaches can be obtained from a general solution of Laplace's equation applied to the cylindrical geometry and boundary conditions given in Fig. 7. For the homogeneous approach, the solution of Laplace's equation, as shown by Crowley [18], becomes

$$\Phi_H = \frac{V \ln\left(r/r_o\right)}{\ln\left(r_e/r_o\right)}. \tag{8}$$

There are two parts to the electric potential distribution for the annular approach. The potential distribution in the vapor is

$$\Phi_{A,v} = \frac{\varepsilon_1/\varepsilon_v V \ln\left(r/r_e\right)}{\left[\left(\varepsilon_l/\varepsilon_v\right)\ln\left(r_e/r_i\right) + \ln\left(r_i/r_o\right)\right]} + V. \tag{9}$$

The potential distribution in the liquid is

$$\Phi_{A,l} = \frac{V \ln\left(r/r_o\right)}{\left[\left(\varepsilon_l/\varepsilon_v\right)\ln\left(r_e/r_i\right) + \ln\left(r_i/r_o\right)\right]} \tag{10}$$

where the interface radius, r_i, in Eqs. (9) and (10) is defined as

$$r_i = \sqrt{(1-\alpha)r_e^2 + \alpha r_o^2}. \tag{11}$$

The interface radius is determined by use of the void fraction, by assuming the area of vapor grows radially from the electrode toward the tube wall.

The electric field distribution must first be evaluated for both approaches, to determine the radial EHD pressure. The electric field distribution for the homogeneous approach is

$$E_{r,H} = -\frac{\partial \Phi_H}{\partial r} = \frac{V}{r \ln\left(r_o/r_e\right)}; \tag{12}$$

the electric field distribution in the vapor for the annular approach is

$$E_{r,A,v} = -\frac{\partial \Phi_{A,v}}{\partial r} = \frac{\left(\varepsilon_l/\varepsilon_v\right) V}{r\left[\left(\varepsilon_l/\varepsilon_v\right)\ln\left(r_i/r_e\right) + \ln\left(r_o/r_i\right)\right]}; \tag{13}$$

and the electric field distribution in the liquid for the annular approach is

$$E_{r,A,l} = -\frac{\partial \Phi_{A,l}}{\partial r} = \frac{V}{r\left[\left(\varepsilon_l/\varepsilon_v\right)\ln\left(r_i/r_e\right) + \ln\left(r_o/r_i\right)\right]}. \tag{14}$$

The mean radial EHD pressure acting on the flow at a given tube cross section can now be determined by integrating Eq. (7) from r_e to r_o with the appropriate E_r for each approach. Thus, the

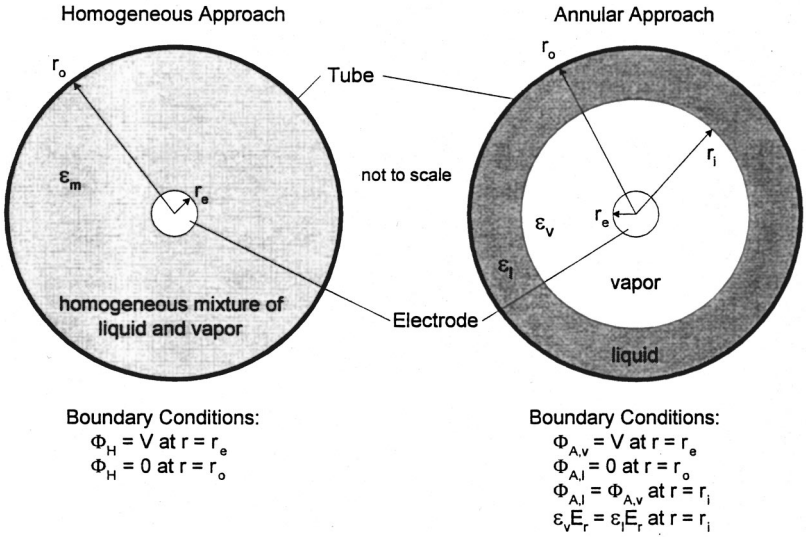

Fig. 7 Schematic of homogeneous and annular approaches for determining EHD force

mean radial EHD pressure for the homogeneous approach is defined as

$$P_{\mathrm{EHD},H}=\frac{1}{\pi(r_o^2-r_e^2)}\int_{r_e}^{r_o}\frac{1}{2}\left\{\varepsilon_m+\left[\rho\left(\frac{\partial\varepsilon}{\partial\rho}\right)_T\right]_m\right\}E_{r,H}^2 2\pi r dr$$

$$=\frac{1}{\pi(r_o^2-r_e^2)}\left\{\varepsilon_m+\left[\rho\left(\frac{\partial\varepsilon}{\partial\rho}\right)_T\right]_m\right\}\frac{\pi V^2}{\ln\left(r_o/r_e\right)} \tag{15}$$

where

$$\varepsilon_m=(1-\alpha)\varepsilon_l+\alpha\epsilon_v \tag{16}$$

and

$$\left[\rho\left(\frac{\partial\varepsilon}{\partial\rho}\right)_T\right]_m=(1-\alpha)\left[\rho\left(\frac{\partial\varepsilon}{\partial\rho}\right)_T\right]_l+\alpha\left[\rho\left(\frac{\partial\varepsilon}{\partial\rho}\right)_T\right]_v. \tag{17}$$

The mixture properties, defined in Eqs. (16) and (17) are effective properties based on the sum of the area proportions of the liquid and vapor at a given tube cross section.

The mean radial EHD pressure for the annular approach becomes

$$P_{\mathrm{EHD},A}=\frac{1}{\pi(r_o^2-r_e^2)}\left[\int_{r_e}^{r_i}\frac{1}{2}\left\{\varepsilon_v+\left[\rho\left(\frac{\partial\varepsilon}{\partial\rho}\right)_T\right]_v\right\}E_{r,A,v}^2 2\pi r dr\right.$$

$$\left.+\int_{r_i}^{r_o}\frac{1}{2}\left\{\varepsilon_l+\left[\rho\left(\frac{\partial\varepsilon}{\partial\rho}\right)_T\right]_l\right\}E_{r,A,l}^2 2\pi r dr\right]$$

$$=\frac{1}{\pi(r_o^2-r_e^2)}\left[\left\{\varepsilon_v+\left[\rho\left(\frac{\partial\varepsilon}{\partial\rho}\right)_T\right]_v\right\}\right.$$

$$\times\frac{\pi\ln\left(\frac{r_i}{r_e}\right)((\varepsilon_l/\varepsilon_v)\,V)^2}{\left[(\varepsilon_l/\varepsilon_v)\ln\left(r_i/r_e\right)+\ln\left(r_o/r_i\right)\right]^2}$$

$$\left.+\left\{\varepsilon_l+\left[\rho\left(\frac{\partial\varepsilon}{\partial\rho}\right)_T\right]_l\right\}\frac{\pi\ln\left(\frac{r_o}{r_i}\right)V^2}{\left[(\varepsilon_l/\varepsilon_v)\ln\left(r_i/r_e\right)+\ln\left(r_o/r_i\right)\right]^2}\right]. \tag{18}$$

The homogeneous approximation will be applied from a quality of 0 to approximately 0.06 or 0.09, for $T_{\mathrm{sat}}=5°\mathrm{C}$ or 25°C, respectively. The point in the flow where the quality is 0.06 or 0.09 was chosen because it represents a value of $X_t\cong 1.6$, where X_t is the Martinelli parameter. Taitel and Dukler [19] established that in the region where $X_t\cong 1.6$ the flow regime transitions from a satisfied wavy and intermittent regime to an annular-dispersed regime. For qualities greater than 0.06 or 0.09, the annular approach will be used. The transition point, defined by X_t, which establishes the approach to be used is based on data without EHD. It is assumed that the flow regime structure does not change much near the transition point when the electric field is applied, so the value $X_t\cong 1.6$ is acceptable. If future research shows that the flow structure will change significantly when the electric field is applied, then a better transition point would have to be defined. It is important to note that the flow regimes will change when the electric field is applied. However, even though the homogeneous and annular approaches are approximations, they do account for some of the fundamental characteristics of two-phase flow with heat transfer. These approaches will produce acceptable results and provide insight into the relationship between the mean radial EHD pressure and the axial momentum flux rate, and the resulting effect on heat transfer and pressure drop. It should also be noted that the homogeneous and annular approaches were chosen and applied based on the electrode geometry used in this work. If a different electrode geometry and or tube geometry were used, then the electric field distribution and the mean EHD pressure would have to be characterized and evaluated relative to the specific geometry and flow regime characteristics.

Now a relationship between the mean radial EHD pressure and the rate of the axial momentum flux can be developed. As stated earlier, the second term in Eq. (4) represents the acceleration, or increase in momentum rate, of the flow due to the energy added to the refrigerant. When energy is added to the flow in the form of heat over a length of tube, the quality will increase and both the radial EHD pressure and the flow momentum rate will change as the refrigerant flows downstream. The mean radial EHD pressure relative to the rate of the axial momentum flux, over this length of tube for a given change in quality (determined from amount of energy added to flow), can be determined from

$$\frac{P_{\mathrm{EHD}}}{M_o}=\frac{1}{L}\int_{z_1}^{z_2}\frac{P_{\mathrm{EHD}}}{G^2\left[\frac{x^2\nu_v}{\alpha}+\frac{(1-x)^2\nu_l}{1-\alpha}\right]}dz. \tag{19}$$

Equation (19) required numerical integration, which was accomplished using the extended trapezoidal rule with a maximum of 51 intervals for the largest change in quality. The large number of intervals is important because the void fraction, α, changes rapidly at low qualities for refrigerants. Also, P_{EHD} in Eq. (19) represents a combination of $P_{EHD,H}$ and $P_{EHD,A}$ applied to the intervals corresponding to the appropriate quality as discussed earlier. The rate of the axial momentum flux, defined in Eq. (19), is determined the same way regardless of whether the homogeneous or annular approach is used. The reason for this is M_o, as originally defined in Eq. (4), is based on the separated flow model. This model provides an adequate estimate for the rate of the axial momentum flux without EHD for the flow regimes of interest in this study. All of the mathematical details leading to Eqs. (15), (18), and (19) are presented and discussed by Bryan [7].

Comparison of Theoretical and Experimental Results. Using the results of the theoretical analysis a more fundamental understanding has been obtained on how the interdependence of the EHD force/pressure and convective boiling process influence the heat transfer and pressure drop. Before the results are discussed, three pieces of information need to be provided, which were used to evaluate Eq. (19). First, the electric fluid properties of R-134a were measured experimentally by various researchers and are shown in Table 4. Second, the void fraction, α, was calculated using the Thome [17] correlation as defined in Eq. (5).

Table 4 Electrical property data from various researchers used to determine EHD force

T_{sat} °C	ε_l[a] pF/m	ε_v[a] pF/m	$(\partial\varepsilon/\partial\rho)_{v,T}$[b] m^3/kg	$(\partial\varepsilon/\partial\rho)_{l,T}$[c] m^3/kg
5	104.6	10.6	0.0044	0.012
25	90.0	11.5	0.0043	0.011

[a]Ref. [7]
[b]Ref. [20]
[c]Ref. [21]

Third, the quality determined from the experiments was used in Eqs. (5) and (19), in order to compare P_{EHD}/M_o with the experimental results.

The results from the theoretical analysis are compared to the experimental data at two values of G and T_{sat}. The experimental data, with no EHD, for these operating parameters are plotted on the flow map by Taitel and Dukler [19] shown in Fig. 8. The data for $G \cong 100\ kg/m^2\ s$, shown in Fig. 8, cover stratified wavy flow through stratified annular flow, and the data for $G \cong 300\ kg/m^2\ s$ cover intermittent flow through annular flow. The region where the homogeneous and annular approaches are applied is marked on the flow map. The data plotted on the flow map in Fig. 8 match, as well as could be determined, the experimental observations made through the sight glasses located at the exit of the individual test sections. It is important to realize when the EHD force is applied the flow structure will change. Future research may show that new flow regimes may have to be defined when the EHD force is present. The point where the change between $P_{EHD,H}$ and $P_{EHD,A}$ occurs, as was defined by X_t, would have to be modified if future research does show that the application of the EHD force produces new flow regimes.

The first comparison to be discussed is for $G = 99.9\ kg/m^2\ s$ and $T_{sat} = 4.9°C$ at an applied voltage of 5 and 15 kV. The experimental results in Fig. 6 were replotted on three different graphs in nondimensional form as shown in Fig. 9. The first two graphs show h_{EHD}/h_o and $\Delta P_{EHD}/\Delta P_o$ both versus Δx, and the third graph shows P_{EHD}/M_o versus the same Δx. The most important result shown in Fig. 9 is P_{EHD}/M_o is directly related to h_{EHD}/h_o and $\Delta P_{EHD}/\Delta P_o$. The trends in the experimental data and the theoretical results are very similar. These results show that if the mean radial EHD pressure is large relative to the rate of the axial momentum flux, as shown at 15 kV in Fig. 9, then large heat transfer enhancements can be obtained, but at a cost of significant pressure drop penalty. As energy is added to the flow the influence of the mean radial EHD pressure on heat transfer and pressure drop decreases rapidly, especially at 15 kV, due to the increase in the rate of the axial momentum flux and change in the flow re-

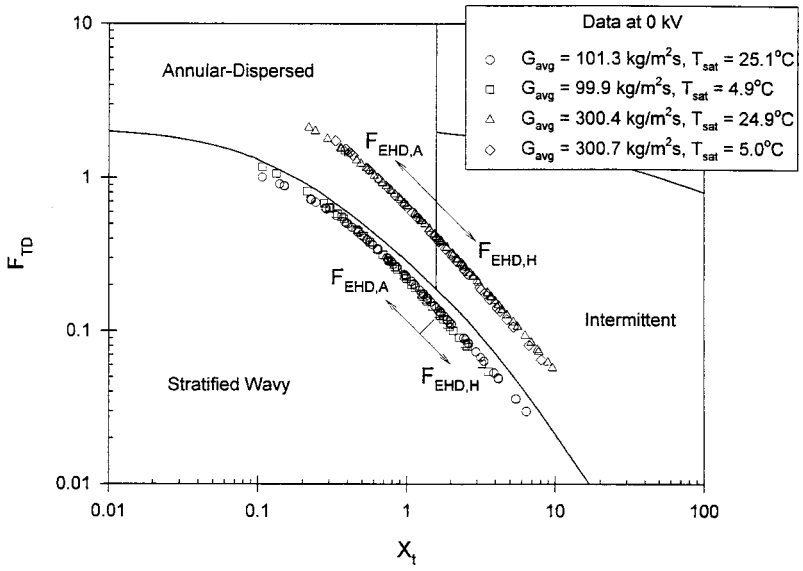

$$F_{TD} = \left[\frac{\rho_v G^2 x^2}{(\rho_l - \rho_v) D_i g}\right]^{0.5} \qquad X_t = \left[\frac{\mu_l^{0.25}\rho_v (1-x)^{1.75}}{\mu_v^{0.25}\rho_l x^{1.75}}\right]$$

Fig. 8 Flow map of Taitel and Dukler [19] showing experimental data for variable G and T_{sat} at 0 kV

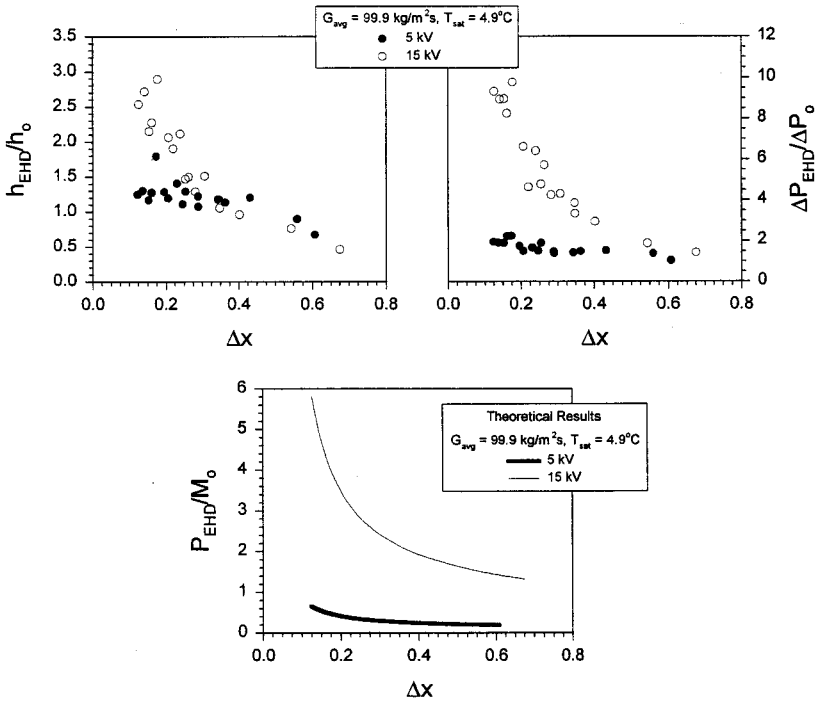

Fig. 9 Nondimensional heat transfer coefficient, pressure drop, and ratio of mean EHD pressure to flow momentum flux rate versus change in quality, all at $G = 99.9$ kg/m^2 s and $T_{sat} = 4.9$°C

gime. If the mean radial EHD pressure is almost the same as the rate of the axial momentum flux of the flow, as shown at 5 kV in Fig. 9, then the heat transfer enhancement and pressure drop penalty are similar. Above $\Delta x = 0.4$ the heat transfer is suppressed at both 5 and 15 kV. In this region, P_{EHD}/M_o is greater than unity at 15 kV but it is around 0.2 at 5 kV. This points out that if the quality and heat flux are large enough only a very small EHD force is needed to potentially suppress the heat transfer.

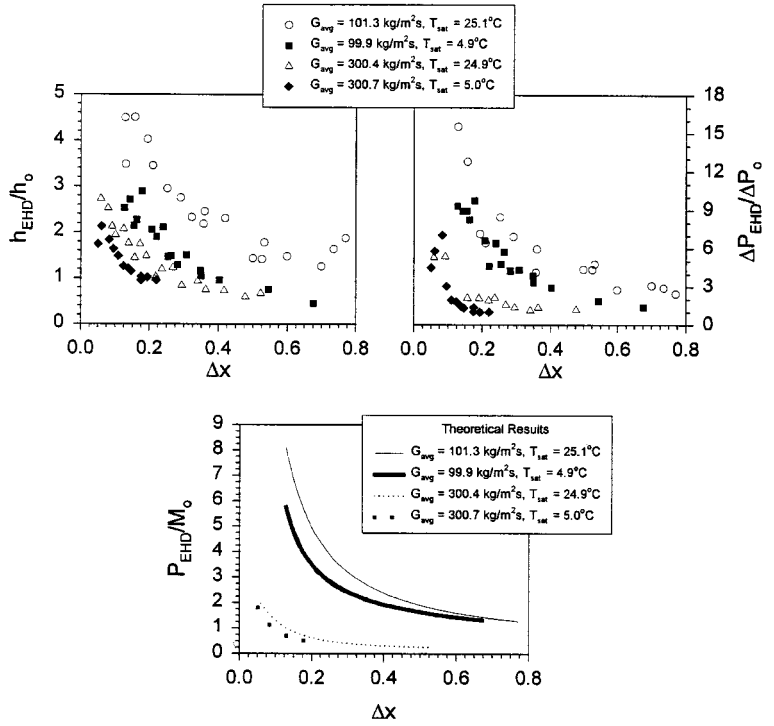

Fig. 10 Nondimensional heat transfer coefficient, pressure drop, and ratio of mean EHD pressure to flow momentum flux rate versus change in quality, all at 15 kV for variable G and T_{sat}

The influence of G and T_{sat} on P_{EHD}/M_o will affect the heat transfer and pressure drop. The same series of graphs are shown in Fig. 10 for two different values of G and T_{sat} at an applied voltage of 15 kV. Again the trend of the experimental data for h_{EHD}/h_o and $\Delta P_{EHD}/\Delta P_o$ and the theoretical calculation for P_{EHD}/M_o are similar and the influence of G and T_{sat} is substantial. The increase in G reduces the influence of the mean radial EHD pressure on the heat transfer and pressure drop by increasing the rate of the axial momentum flux. An increase in T_{sat} has the opposite effect on the mean radial EHD pressure, which results in a greater heat transfer enhancement and a higher pressure drop penalty. This is due to the change in the fluid properties; specifically the relative change between the properties of the liquid and vapor at each T_{sat}. The influence of both G and T_{sat} are predicted by the theoretical analysis and the results shown in Fig. 10 attest to the validity of this analysis.

From the results shown in Figs. 9 and 10, it is evident that the theoretical analysis presented in this study can provide insight into the attainable heat transfer enhancement and the pressure drop penalty for given operating parameters. Furthermore, the existence of a functional relationship between the heat transfer enhancement and P_{EHD}/M_o and between the pressure drop penalty and P_{EHD}/M_o is apparent. One final important point to realize is that the relationship between the mean radial EHD pressure and the rate of the axial momentum flux shown in Figs. 9 and 10 is specific to the electrode design used in this work. A different electrode design and or tube may produce different results.

Conclusion

From the experimental data it is evident that the EHD forces can generate significant enhancements in the convective boiling heat transfer coefficient, but at the same time they can create even greater pressure drop penalties. By developing a simple theory to determine the mean radial EHD pressure, which included the characteristics of two-phase flow, it was shown that the amount of heat transfer enhancement and the pressure drop penalty were dependent upon the size of the mean radial EHD pressure relative to the rate of the axial momentum flux. The theoretical analysis was also able to show the influence of the change in mass flux and saturation temperature on the mean radial EHD pressure relative to the rate of the axial momentum flux.

The EHD enhanced heat transfer will have to be maximized while the pressure drop penalty is minimized, if EHD enhanced convective boiling is to become a potential industrial application. This seems possible if the EHD force can be applied in a fashion where it is of the same order or slightly higher than the rate of the axial momentum flux.

Acknowledgment

The authors gratefully acknowledge the financial support of this research by ASHRAE and NASA Lyndon B. Johnson Space Center (JSC). The authors, also, gratefully acknowledge DuPont for providing the refrigerant used in the experiments and Wolverine Tube, Inc. for providing the boiling tubes.

Nomenclature

c_p = specific heat (J/kg K)
D_i = boiling tube inside diameter (m)
D_o = boiling tube outside diameter (m)
E = electric field strength (V/m)
E_r = electric field strength in radial direction (V/m)
f_e = EHD force density (N/m^3)
P_{EHD} = mean radial EHD pressure (N/m^2)
f_{lo} = Fanning friction factor for liquid
F_{TD} = Taitel and Dukler flow parameter
G = mass flux ($kg/m^2 s$)
h = heat transfer coefficient ($W/m^2 K$)
h_{EHD} = heat transfer coefficient with EHD ($W/m^2 K$)
h_f = saturated liquid enthalpy (J/kg)
h_{fg} = latent heat of vaporization (J/kg)
h_o = heat transfer coefficient without EHD ($W/m^2 K$)
h_s = enthalpy of subcooled liquid (J/kg)
L = length of test section (cm)
m = mass flow rate of water (kg/s)
M_o = rate of momentum flux (N/m^2)
$\dot{m}_{ref}$ = mass flow rate of refrigerant (kg/s)
P = pressure (Pa)
ΔP_{EHD} = pressure drop with EHD (kPa)
ΔP_o = pressure drop without EHD (kPa)
q_e = charge density (C/m^3)
q'' = heat flux (kW/m^2)
r_i = interface radius (m)
r_e = electrode radius (m)
r_o = inside tube radius (m)
T_{ij} = Maxwell stress tensor (N/m^2)
T_{in} = inlet hot water temperature (°C)
T_{out} = outlet hot water temperature (°C)
T_{sat} = refrigerant saturation temperature (°C)
T_{wi} = tube inside surface temperature (°C)
V = applied voltage (V)
x = quality (kg/kg)
Δx = change in quality (kg/kg)
X_t = Martinelli parameter
z = axial length (m)

Greek Symbols

α = void fraction
δ_{ij} = Kronecker delta
ε = permittivity (pF/m)
Φ = electric potential (V)
ϕ_{lo} = two-phase multiplier
ν = specific volume (m^3/kg)
ρ = density (kg/m^3)

Subscripts

A = annular
avg = average
H = homogeneous
i,j,k = tensor notation
l = liquid
m = homogeneous mixture
r = radial direction
t = total
v = vapor

References

[1] Eckels, S. J., Doerr, T. M., and Pate, M. B., 1994, ''In-tube Heat Transfer and Pressure Drop of R-134a and Ester Lubricant Mixtures In a Smooth Tube and a Micro-fin Tube: Part I—Evaporation,'' ASHRAE Transactions, **100**, No. 2, pp. 265–282.
[2] Yabe, A., Taketani, T., Maki, H., Takahshi, K., and Nakadai, Y., 1992, ''Experimental Study of Electrohydrodynamically Enhanced Evaporator for Non-azeotropic Mixtures,'' ASHRAE Transactions, **98**, No. 2, pp. 455–461.
[3] Singh, A., 1995, ''Electrohydrodynamic (EHD) Enhancement of In-Tube Boiling and Condensation of Alternative (NON-CFC) Refrigerants,'' Ph.D. dissertation, University of Maryland, College Park, MD.
[4] Salehi, M., Ohadi, M. M., and Dessiatoun, S., 1996, ''Minimization of Pressure Drop for EHD-Enhanced In-tube Boiling of R-134a,'' *Advances in Energy Efficiency, Heat/Mass Transfer Enhancement*, ASME, New York, pp. 25–31.
[5] Bryan, J. E., and Seyed-Yagoobi, J., 1997, ''Influence of Flow Regime, Heat Flux, and Mass Flux on Electrohydrodynamically Enhanced Convective Boiling,'' *Proceedings of the ASME Heat Transfer Division*, ASME, New York, pp. 187–196.
[6] Melcher, J. R., 1981, *Continuum Electromechanics*, MIT Press, Cambridge, MA.
[7] Bryan, J. E., 1998, ''Fundamental Study of Electrohydrodynamically Enhanced Convective and Nucleate Boiling Heat Transfer,'' Ph.D. dissertation, Texas A&M University, College Station, TX.
[8] Jones, T. B., 1977, ''Bubble Dielectrophoresis,'' J. Appl. Phys., **48**, No. 4, pp. 1412–1417.

[9] Taylor, J. R., 1982, *An Introduction to Error Analysis*, University Science Books, Mill Valley, CA.
[10] Kline, S. J., and McClintock, F. A., 1953, ''Describing Uncertainties in Single Sample Experiments,'' Mech. Eng. (Am. Soc. Mech. Eng.), **75**, pp. 3–8.
[11] Wattelet, J. P., Chato, J. C., Souza, A. L., and Christoffersen, B. R., 1994, ''Evaporative Characteristics of R-12, R-134a, and a Mixture at Low Mass Fluxes,'' ASHRAE Transactions, , **100**, No. 1, pp. 603–615.
[12] Kandlikar, S. G., 1990, ''A General Correlation for Saturated Two-Phase Flow Boiling Heat Transfer Inside Horizontal and Vertical Tubes,'' ASME J. Heat Transfer, **112**, pp. 219–228.
[13] Torikoshi, K., and Ebisu, T., 1993, ''Heat Transfer and Pressure Drop Characteristics of R-134a, R-32, and a Mixture of R-32/R-134a Inside a Horizontal Tube,'' ASHRAE Transactions, , **99**, No. 2, pp. 90–96.
[14] Carey, V. P., 1992, *Liquid-Vapor Phase-Change Phenomena*, Hemisphere, Washington, DC.
[15] Friedel, L., 1979, ''Improved Friction Pressure Drop Correlations for Horizontal and Vertical Two-Phase Pipe Flow,'' presented at The European Two-phase Flow Group, Meeting, Ispra, Italy, Paper E2.
[16] Collier, J. G., and Thome, J. R., 1994, *Convective Boiling and Condensation*, 3rd Ed. Clarendon Press, Oxford, UK.
[17] Thome, J. R., 1964, ''Prediction of Pressure Drop During Forced Circulation Boiling of Water,'' Int. J. Heat Mass Transf., **7**, pp. 709–724.
[18] Crowley, J. M., 1986, *Fundamentals of Applied Electrostatics*, John Wiley and Sons, New York.
[19] Taitel, Y., and Dukler, A. E., 1976, ''A Model for Predicting Flow Regime Transitions in Horizontal and Near Horizontal Gas-liquid Flow,'' AIChE J., **22**, pp. 47–55.
[20] Tanaka, Y., Tsujimoto, T., Matsuo, S., and Makita, T., 1992, ''Dielectic Constant of Environmentally Accepted Refrigerants HFC-134a, HCFC-123, and HCFC-141b Under High Pressures,'' Fluid Phase Equilibria, **80**, pp. 107–117.
[21] Barão, M. T., Mardolcar, U. V., and Nieto de Castro, C. A., 1996, ''The Dielectric Constant of Liquid HFC 134a and HCFC 142b,'' Int. J. Thermophys., **17**, No. 3, pp. 573–585.

The Use of an Organic Self-Assembled Monolayer Coating to Promote Dropwise Condensation of Steam on Horizontal Tubes

A. K. Das[1]
e-mail: ashok_das@amat.com

H. P. Kilty

P. J. Marto

Department of Mechanical Engineering,
Naval Postgraduate School,
Monterey, CA 93943-5100

G. B. Andeen
SRI International,
Menlo Park, PA 94025

A. Kumar
Optigon Technology,
Milpitas, CA 95035

Hydrophobic coatings have been created through self-assembled monolayers (SAMs) on gold, copper, and copper-nickel alloy surfaces that enhance steam condensation through dropwise condensation. The monolayer is formed by chemisorption of alkylthiols on these metal surfaces. Due to their negligible thickness (10–15 Å), SAMs have negligible heat transfer resistance, and involve a minuscule amount of the organic material to pose any contamination problem to the system from erosion of the coating. The coating was applied directly to copper and 90/10 copper-nickel tubes, and to previously gold-sputtered aluminum tubes. The quality of the drops on SAMs, based on visual observation, was found to be similar for the three surfaces, with the gold surface showing a slight superiority. When compared to complete filmwise condensation, the SAM coating increased the condensation heat transfer coefficient by factors of 4 for gold-coated aluminum, and by about 5 for copper and copper-nickel tubes, under vacuum operation (10 kPa). The respective enhancements under atmospheric conditions were about 9 and 14. Comparatively, the heat transfer coefficient obtained with a bare gold surface (with no organic coating) was 2.5 times that of the filmwise condensation heat transfer coefficient under vacuum, and 3.4 at atmospheric conditions. [S0022-1481(00)02502-0]

Keywords: Condensation, Multiphase Flows, Organic Coatings

1 Introduction

Dropwise condensation (DWC), when properly promoted, has been known to produce heat transfer coefficients up to 20 times that of filmwise condensation (FWC). Over the past few decades, considerable attention has been paid toward the development of suitable DWC promoters. Gold and silver have been known to consistently show excellent dropwise characteristics ([1–4]). However, the hydrophobic characteristics of these noble metals as DWC promoters have been controversial in the literature ([5,6]). The noble metals initially have very high surface energy and tend to be completely wet by water. But, on contamination with absorbed carboneous matter, the surfaces, especially gold-plated surfaces, gradually become hydrophobic, exhibiting dropwise characteristics. Woodruff and Westwater [2] have shown that promotion of DWC on gold-plated surfaces was directly related to the carbon-to-gold ratio on the surface.

Organic materials have also received considerable attention for their hydrophobic capabilities to promote DWC. Such studies have generally focused on fluorocarbon or silicone polymers. While several studies were done in the 1950s and 1960s with polytetrafluoroethylene (PTFE), commercially known as Teflon, and silicone, Erb and Thelen [7,8] conducted an extensive investigation of several permanent hydrophobic coatings, including PTFE, sulfide films, parylene-N, and noble metals. However, they concluded that the organic coatings were not as good as a silver-coated surface. Holden et al. [4] conducted experiments on 14 polymer-coated surfaces and an electroplated-silver surface, and showed an increase in condensation heat transfer coefficient of about three to eight relative to filmwise at an operating pressure of 11 kPa, with electroplated silver exhibiting the best performance. In general, the organic coatings exhibited a lack of adherence to the copper tube surface, and were found to be too thick (the thickness of the coating must be less than 1 μm) to obtain any reasonable enhancement. It was concluded that a detailed study of the surface chemistry was needed to improve upon the organic coating technology.

Ma et al. [9] have conducted experiments to study DWC on vertical brass tubes coated with ultra-thin polymers which were created by plasma polymerization and dynamic ion-beam mixed implantation methods. They concluded that while the heat transfer enhancements were as high as 20, the enhancement and the adhesion of the film were strongly dependent on the process conditions of the two methods, which needed to be further studied to optimize the performance. The ion-implantation technique was also reported by Zhao and Burnside [10] to implant Cr^+ onto PTFE-coated surfaces to further enhance the DWC heat transfer coefficient by increasing the thermal conductivity of the coating, and thus reducing the film resistance. While an enhancement of about 1.8 times that of an untreated surface was reported for the PTFE-coated surface, the value increased to five with Cr^+ implanted surface. However, once again, the treatment involved considerable uncertainties, and further study was needed to establish the best treatment conditions and the best polymer. Zhao and Burnside [11] also successfully used these coated surfaces in a utility condenser. Further, Bonnar et al. [12–14] utilized glow-discharge methods to coat silicon organic polymers to obtain DWC.

Taniguchi and Mori [15] studied the effectiveness of an expensive composite formed with copper (Cu) and graphite fluoride $(CF)_n$ on DWC on a vertical copper surface. They concluded that despite being much more hydrophobic than electroplated gold and

[1]Present address: Applied Materials, Inc., 3100 Bowers Avenue, M/S 0225, Santa Clara, CA 95054.

Contributed by the Heat Transfer Division for publication in the ASME JOURNAL OF HEAT TRANSFER. Manuscript received by the Heat Transfer Division Apr. 3, 1997; revision received Dec. 23, 1999. Associate Technical Editor: M. S. Sohal.

many other noble metals for water in air, the Cu/$(CF)_n$ surface did not thermally outperform the gold surface, but rather decreased it. They speculated that the hydrophobicity of $(CF)_n$ in air is not necessarily relevant to the hydrophobicity of the surface in a condensing steam atmosphere.

The use of fluorinated organics for creating a hydrophobic surface has been investigated as early as 1975, when Deronzier et al. [16] used several organic compounds injected directly into the steam to react with the condenser surface to yield a hydrophobic coating. For example, $CF_3-(CF_2)_n-C_2H_4-SH$ was used successfully with a copper surface. Recently, Gavrish et al. [17,18] tested fluorinated carbon sulfide as an additive to the boiler feed water to obtain DWC. The hydrophobic coatings were generated in about 24 hours and were retained for about 4200 hours of operation. The heat transfer coefficients were enhanced by three to ten times. However, the coating underwent an oxidizing process and the condensation converted back to filmwise. The oxide film needed to be removed and the process had to be started again to return to the dropwise mode.

In general, organic coatings are difficult to maintain, and require strong, long-term adhesion forces between the coating and the metal substrate. Usually, the thicker the coating, the better its resistance to corrosion/erosion. However, due to very low thermal conductivity, thick organic coatings add to the heat transfer resistance that deteriorates the DWC performance ([5]). Moreover, the coating material, if inadvertently removed from the condenser surface, may contaminate the system, e.g., as impurities in the boiler feedwater of a power plant.

1.1 Self-Assembled Monolayer Coatings. Self-assembled monolayers (SAMs) are composed of a single layer of organic molecules adsorbed onto a surface to form a coating. Such coatings form upon chemisorption of alkylthiols on gold, silver, copper, or copper-nickel surfaces ([19,20]). A strong *covalent bond* is formed between the sulfur of alkylthiol and the metal (M):

$$M+HS\text{-}(CH_2)_n\text{-}R \rightarrow MS\text{-}(CH_2)_n\text{-}R.$$

By appropriately choosing the terminal group (R) on these alkylthiol molecules, one can predetermine the chemical and physical properties of the resulting SAM. For example, a SAM formed from $HS(CH_2)_{15}CH_3$ exhibits hydrophobic characteristics with water. Such coatings have been used as model surfaces for studies in tribology, adhesion, wetting, and biocompatibility ([21–23]), but they have not been used in condensation heat transfer prior to this study.

These self-assembled monolayers are very resilient and form easily. The SAMs formed from hexadecylthiol $[HS(CH_2)_{15}CH_3]$ are extremely low free-energy surfaces, exhibiting large advancing contact angles of 110–112 deg (Fig. 1) with water and hence have good DWC characteristics. In addition, they are very stable and should last over long periods of time. Being only a monolayer-thick (10–15 Å), these coatings give negligible heat transfer resistance, and the total amount of coating material involved is minuscule ($\sim 5\times 10^{-11}$ gm/cm^2, or 0.05 gm for a condenser with a million square foot surface area) to pose any contamination problem. These monolayers, therefore, appear to offer a strong potential for long-term DWC promoters, although durability tests have yet to be conducted.

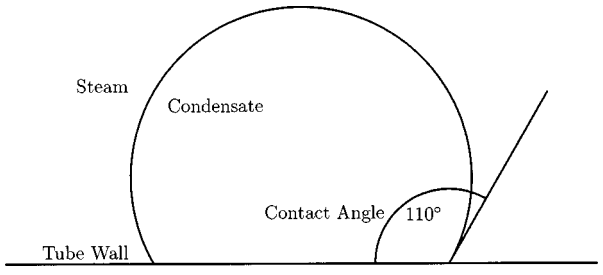

Fig. 1 Sketch of a condensate drop on a flat surface, and definition of contact angle

During this study, SAMs were formed on gold-coated-aluminum, copper, and copper-nickel condenser tubes to study their condensation characteristics. Since SAMs formed on gold surfaces are the most resilient and hydrophobic, the aluminum tube was first sputter-coated with titanium for adhesion and then with gold before applying the SAM coating. The copper and copper-nickel tube could be directly coated with SAM, and eliminated the expensive gold-sputtering step. The steps were exactly the same as that used in our study of the effect of SAM coating on Korodense tubes ([24]). As in our previous study ([24]), the experiments were conducted in a horizontal single-tube condensation apparatus. A brief description of the experimental program and the apparatus follows.

2 Experimental Apparatus

Figure 2 shows a general schematic of the overall system. Steam is generated in a Pyrex glass cylindrical boiler of 0.3-m diameter and 0.5-m height at a maximum working pressure of 72.6 kPa gage. The boiler contains ten vertically mounted 4 kW, 440 VAC stainless-steel clad immersion heaters connected in parallel. Steam from the boiler passes up through a cylindrical section of foam-covered Pyrex glass with an inside diameter of 0.15 m and a length of 2.13 m. Two 90-deg Pyrex glass elbows redirect the steam back down a second similar cylindrical section of 1.52 m in length. Steam then enters a stainless steel test section, flowing downwards over the horizontal condenser tube mounted, as shown in Fig. 3. The test section is fitted with openings for Teflon and nylon inserts that support the horizontal tube and provide a coolant flow path through the system. These inserts contain O-rings to seal the condenser from the ambient atmosphere and the coolant. The test section also contains a double pane viewing port so that the condensation process can be observed, and video-recorded. The inner glass and outer plastic panes are separated with a spacer through which heated air can be blown to defog the inner glass. A smaller port in the test section allows connection of a pressure gage and thermocouple well.

Steam not condensed in the test section passes into a final Pyrex glass cylinder containing an auxiliary condenser. The auxiliary condenser, constructed of a single helically wrapped water-cooled copper coil mounted to a stainless-steel base, condenses the balance of the steam, collects all the condensate and returns it to the boiler through a gravity drain in the base plate. Two stainless-steel side plates are mounted to the auxiliary condenser with penetrations for a pressure bleed valve, a vacuum line, and a pressure transducer. The auxiliary condenser cooling water is supplied directly from the building water main and passes through a pressure regulator that eliminates any pressure fluctuations. Saturation temperature in the test apparatus is controlled by adjusting a throttle valve in the auxiliary condenser coolant flow line. Cooling water exiting the auxiliary condenser is discharged to the building drain.

Cooling water for the test section originates in a stainless steel sump tank. Two centrifugal pumps connected in series draw suction from the sump. A throttle valve and calibrated rotameter on the discharge side of the pumps allow control of the cooling water flow. After flowing through the test tube, cooling water flows into a Nylon mixing chamber (Fig. 3) so that an average outlet temperature can be accurately measured. This chamber alternately forces the flow to occur between the center region and the outer edges of the block to promote turbulent mixing. Thermocouples and quartz thermometer probes are installed on the coolant lines prior to the test section and following the mixing chamber. The warm coolant exiting the test section is drained into the sump tank with an overflow where it mixes with the filtered cold water flowing into the sump, before being recycled to the test section through the pumps.

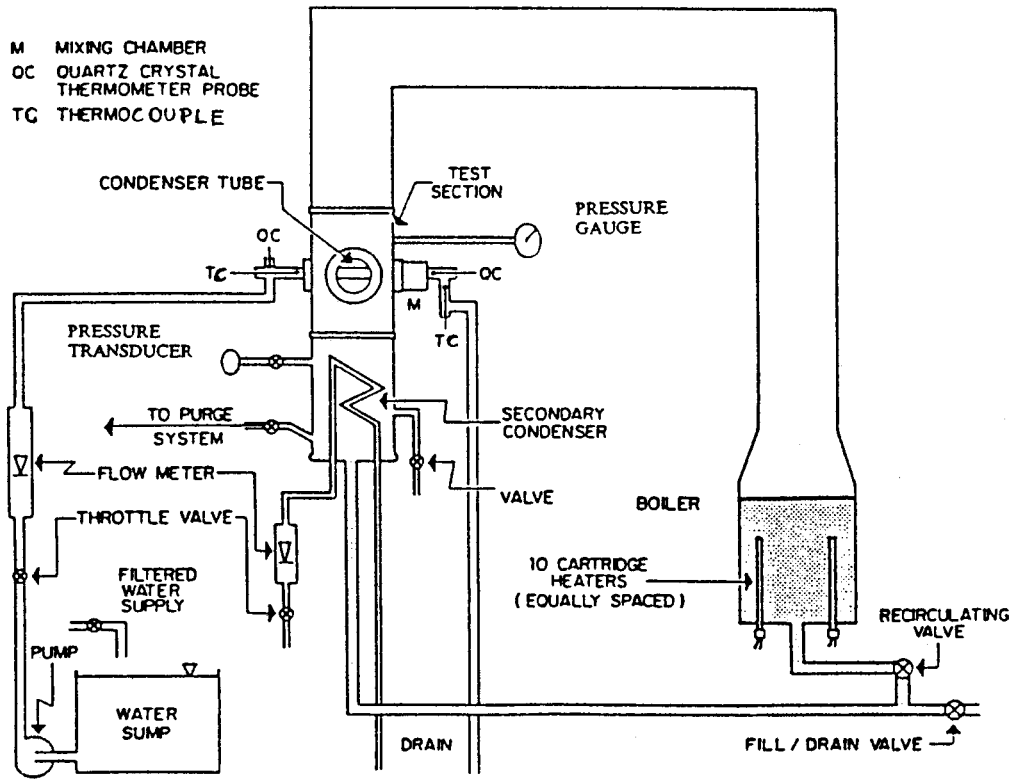

Fig. 2 Schematic of the experimental setup

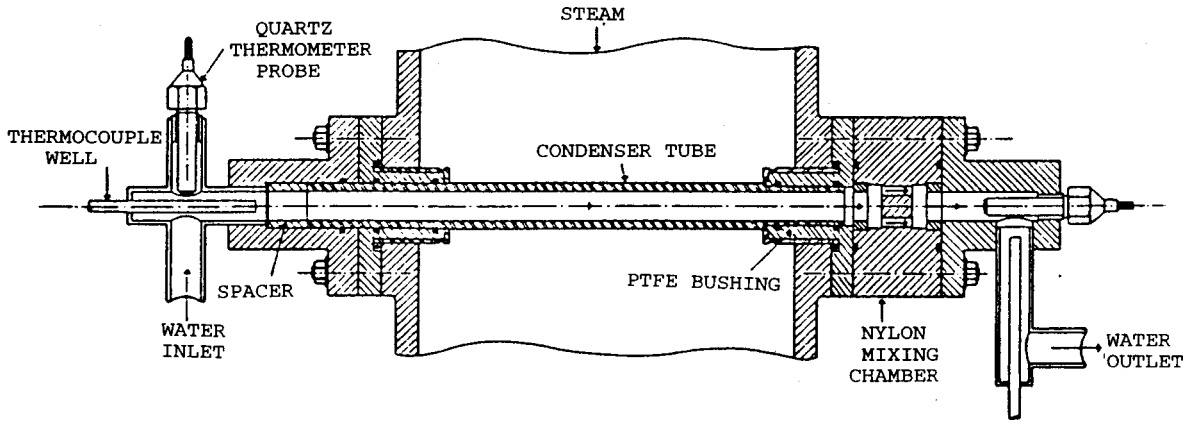

Fig. 3 Schematic of the test section

The vapor velocities across the test tubes are determined to be approximately 1 m/s at atmospheric pressure and 2 m/s under vacuum conditions. These velocities carry away any noncondensible gas from the test tubes. The noncondensible gases are removed by a vacuum system through a suction port at the base of the auxiliary condenser section. The vapor-gas mixture passes through an internal condensing coil located in the cooling sump where any steam is condensed and collected in a Plexiglas vacuum chamber. The noncondensibles are passed through a vacuum pump and expelled to the atmosphere. The pump can draw a vacuum down to an absolute pressure of 130 mm Hg (17 kPa). A check valve is installed to prevent back flow of air into the test section when the pump is stopped. The apparatus had a mean pressure leak rate of 0.4 kPa per day.

2.1 System Instrumentation. Steam temperature in the test condenser is measured by two thermocouples positioned in a well whose tip is located in the steam flow just upstream of the test tube. Ambient temperature is measured with a similar thermocouple located in the proximity of the apparatus. The inlet and outlet test tube coolant temperatures are measured with a quartz crystal thermometer, and are checked by two thermocouples at the coolant inlet and outlet. Test condenser pressure is monitored by both a 0–103.4 kPa Bourdon pressure gage and a vacuum pressure transducer. Both devices measure gage pressure relative to atmospheric, and require a local atmospheric pressure valve, supplied externally by reading from a barometer, to convert from gage to absolute pressure. For calculations, we have used the steam-side temperature, rather than the saturation temperature ob-

tained from the pressure. This was done in order to simplify the calculations and to reduce the error due to higher uncertainty in pressure measurement. Coolant flow is measured by a calibrated rotameter installed on the discharge side of the coolant pumps.

Power for the boiler heaters is controlled by an electronic system. 440-VAC line voltage is reduced by a factor of 100 in a differential input precision voltage attenuator and then passed through a true-root-mean-square (TRMS) converter. The output of the TRMS converter is accurately recorded by comparing to a reference voltage from a panel-mounted potentiometer. The power input is computed from this voltage and the known total electrical resistance of the heaters.

A data acquisition system collects the voltage readings from the thermocouples, pressure transducer, and heater switchboard. The data acquisition system and quartz thermometer unit are linked to a computer. The rotameter, pressure gage, and local atmospheric pressure readings are manually entered into the computer.

3 Experimental Procedure

Although the most accurate way to obtain inside and outside heat transfer coefficients is to directly measure the vapor temperature, mean inside and outside wall temperatures, and the coolant temperature, the measurement of tube wall temperatures requires the use of an instrumented tube (with numerous thermocouples embedded in the walls), which unfortunately is expensive to manufacture. Therefore, during these tests, the experimental data were reduced using the ''Modified Wilson Plot'' technique ([25]).

3.1 Modified Wilson Plot Technique. The Modified Wilson Plot technique reduces the data using an iterative procedure which relies on the fact that the overall heat transfer coefficient can be reliably measured from experimental data using the expression

$$U_o = \frac{\dot{m} C_p (T_{co} - T_{ci})}{A_o (\mathrm{LMTD})} \tag{1}$$

where

$$\mathrm{LMTD} = (T_{co} - T_{ci}) / \ln\left[\frac{T_s - T_{ci}}{T_s - T_{co}}\right],$$

and, where the overall heat transfer coefficient U_o is related to the inside and outside heat transfer coefficients, h_i and h_o, by

$$\frac{1}{U_o A_o} = \frac{1}{h_i A_i} + \frac{\ln(D_o/D_i)}{2\pi L k_w} + \frac{1}{h_o A_o}. \tag{2}$$

The inside heat transfer coefficient was calculated by the Petukhov-Popov ([26]) correlation which gives

$$h_i = C_i \Omega, \tag{3}$$

where

$$\Omega = \frac{k_{cw}}{D_i} \frac{(\xi/8)\mathrm{Re}\,\mathrm{Pr}}{K_1(\xi) + K_2(\mathrm{Pr})(\xi/8)^{1/2}(\mathrm{Pr}^{2/3} - 1)}, \tag{4}$$

with

$$\xi = (1.82 \log \mathrm{Re} - 1.64)^{-2}, \tag{5}$$

$$K_1(\xi) = 1 + 3.4\xi, \tag{6}$$

$$K_2(\mathrm{Pr}) = 11.7 + 1.8\,\mathrm{Pr}^{-1/3}. \tag{7}$$

The Petukhov-Popov correlation is valid for fully developed *turbulent* flow inside a *smooth* tube. The range of validity includes $\mathrm{Re} = 10^4 - 10^6$ and $\mathrm{Pr} = 0.5 - 2000$. For the tests in this study, turbulent flow of the coolant was ensured by using a Heatex insert[2] and by keeping $\mathrm{Re} > 10^4$. For all tests in this study, $1.5 \times 10^4 < \mathrm{Re} < 8 \times 10^4$ and $4 < \mathrm{Pr} < 7$.

[2]A Heatex insert consists of a series of wire loops large enough to tightly touch the inner wall of the tube and break up the boundary layer near the tube wall.

A ''floating'' leading coefficient C_i was introduced into Eq. (3) to account for the use of the Heatex insert, and also to allow for any deviations from the ideal Petukhov-Popov conditions due to the short length of the test tube. The Heatex insert also helps to boost the inside heat transfer coefficient, thus lowering the inside thermal resistance and improving the accuracy of the outside heat transfer coefficient.

During this study, with dropwise condensation occurring on the outside of the tube, the outside heat transfer coefficient h_o may be assumed to be constant over the measured heat flux range ([27]):

$$h_o = C_o = \text{constant}. \tag{8}$$

The values for h_o and h_i from Eqs. (8) and (3) can be inserted into Eq. (2) which can then be rearranged to get

$$Y = \frac{1}{C_i} X + \frac{1}{C_o} \tag{9}$$

where

$$X = \frac{A_o}{A_i \Omega}, \tag{10}$$

and

$$Y = \left[\frac{1}{U_o} - A_o \frac{\ln(D_o/D_i)}{2\pi L k_w}\right]. \tag{11}$$

Due to the temperature dependence of the properties contained in Ω, the method utilizes an iterative procedure in the solution for each data point. In the present study, 14 sets of data were collected for each test-run. The coolant flow rate was varied from 80 percent down to 20 percent of the rotameter scale and then back up to 80 percent in steps of 10 percent, thus obtaining 14 sets of data—one for each of these settings. A least-squares fit of Eq. (9) with respect to X and Y for each data set determines C_i and C_o for each test-run, which are, respectively, the inverse of the slope and the intercept on the Y-axis. The value of C_i is then used in Eq. (3) to compute h_i. The value of h_o is equal to C_o. Once h_o is known, the temperature difference, ΔT, can be calculated as

$$\Delta T = \frac{\dot{m} C_p (T_{co} - T_{ci})}{\pi D_r L h_o}. \tag{12}$$

3.2 Definition of Enhancement Ratio. The heat transfer enhancement $\epsilon_{\Delta T}$ is defined as the ratio of the condensing heat transfer coefficient during DWC, to the heat transfer coefficient with FWC, for the same subcooling, $\Delta T = (T_s - T_{wo})$. Mathematically,

$$\epsilon_{\Delta T} = \left(\frac{h_{o,\mathrm{DWC}}}{h_{o,\mathrm{FWC}}}\right)_{\Delta T}. \tag{13}$$

3.3 Repeatability and Uncertainty. Two tests were conducted for each tube—one at atmospheric pressure, and the other at a vacuum of around 8.3–10.3 kPa. The data for each test were repeated for the same tubes under the same pressure conditions in order to obtain repeatability and achieve confidence in the data. The difference in the values of C_o, as defined above in Eq. (8), for the repeated data were less than ten percent for the tests.

The uncertainty in the reduced data and calculated quantities were also determined. The uncertainty in the independent variables was measured/estimated to be two percent in the rotameter reading, four percent in the thermal conductivity, 0.05°C in the quartz thermometer temperatures, and 0.2°C and 0.4°C in the steam thermocouple temperatures for vacuum and atmospheric conditions, respectively. The uncertainty in the calculated quantities was obtained by the Kline and McClintock ([28]) analysis. Since the values of C_i and C_o are determined from a least-squares line fit in the modified Wilson procedure, the uncertainties in

Table 1 Geometry and surface finish of coated and uncoated tubes

Tube Label	D_i (mm)	D_o (mm)	Substrate Material	Surface Finish	Coatings Applied
Bare Gold	12.7	13.3	Al	Machine	50 Å Ti and 500 Å Au
SAM-on-Gold	12.7	13.3	Al	Machine	50 Å Ti, 500 Å Au, and SAM
SAM-on-Copper	12.7	13.3	Cu	Mirror	SAM
SAM-on-Cu-Ni	12.7	13.9	90/10 Cu-Ni	Mirror	SAM
FWC	12.5	13.2	Al	Machine	Oxidation

these quantities were calculated by assuming that the Wilson *X-Y* data points are normally and independently distributed. A t-distribution is assumed with a 95 percent confidence interval for the 14 data points for each test condition, to compute the uncertainties in C_i and C_o. Typical uncertainties in h_o ranged between 8 and 30 percent, with copper-nickel tubes showing the largest values.

4 Tube Geometry and Coating Procedures

A series of experiments were conducted with tubes made of aluminum, copper, and copper-nickel. The length of each tube was 228.6 mm, with an active condensation length (L) of 133.4 mm. The tube-outer diameter at the ends was machined to a standard tube size of 15.88 mm, whereas the outer nominal diameter (D_o) over the active condensing length was 13.3 mm. The tubes had an inside nominal diameter (D_i) of 12.7 mm. The thermal conductivity of the aluminum tube was 209 W/m-K, and was assumed not to have been altered by the thin titanium and gold coatings. For copper and 90/10-copper-nickel, the conductivities were 385 W/m-K and 55 W/m-K, respectively. The basic dimensions and surface properties of the tubes are given in Table 1.

For the bare gold and SAM-on-gold surfaces, the ''machine-finish'' aluminum tubes were first sputter-coated with a layer of titanium (~50 Å) for adherence of gold to the metal surface. The gold coating (~500 Å) was then deposited onto the titanium by subsequent sputtering. While one tube was tested only with the gold coating on it, two others were further coated with the hydrophobic monolayer (SAM). The bare-gold tube was tested to compare the hydrophobic characteristics of the bare gold surface with that of SAM on gold. To eliminate the required sputtering for Au surfaces, copper and copper-nickel tubes were also used, especially since copper alloys are common in the condenser industry. On copper and copper-nickel tubes, SAM coatings could be directly applied to the surface without any prior sputtered coating. On the copper and copper-nickel surfaces, the SAMs were formed on ''polished'' tube surfaces. These tubes were polished to a mirror finish on the smallest emery paper size of P4000 followed by polishing with a commercial Pol metal polish. The SAM coatings were applied manually with special small-tipped felt pens.

Tests were also conducted for filmwise condensation on oxidized aluminum tubes for baseline FWC data. The surface for FWC was obtained by oxidation of the tube surface with a mixture of sodium hydroxide and ethanol in a steam bath. The mixture was applied on the tube surface with a brush, while rotating the tube around for better uniformity. The details of all these procedures are provided by Kilty [29].

5 Results and Discussion

A series of tests were carried out, at both atmospheric and vacuum conditions, for various combinations of tubes and coatings; namely, bare-gold on aluminum (Al/Ti/Au), SAM-on-gold-coated aluminum (Al/Ti/Au/SAM), SAM-on-copper (Cu/SAM) and SAM-on-copper-nickel (Cu-Ni/SAM). Tests were also conducted for the case of filmwise condensation on aluminum tubes to establish a baseline.

5.1 Overall Heat Transfer Coefficients. The overall heat transfer coefficient (U_o), as defined in Eq. (1), is plotted in Fig. 4 as a function of the coolant velocity, V_{cw} (or coolant flow rate). Figure 4(*a*) shows data for atmospheric conditions while Fig. 4(*b*) shows data during vacuum conditions. Data collected for filmwise condensation are also presented.

The plots in Fig. 4 show a parabolically increasing U_o with increasing V_{cw}. The SAM-coated tubes and the gold-only tubes with DWC show higher U_o compared to the FWC case. The ratio of the value of the overall heat transfer coefficient for DWC compared to FWC increases with increasing V_{cw} since, as V_{cw} increases, the outside resistance becomes more important. The ratio increases significantly more for the case of SAM-on-Cu and SAM-on-gold-coated-aluminum tubes, than for SAM-on-copper-nickel or bare-gold-on-aluminum tubes, as summarized in Table 2. For example, compared to FWC, the ratio of U_o for Cu/SAM increases from 2.5 for the minimum coolant flow to 4.6 for the maximum flow at atmospheric pressure. The respective increase under vacuum conditions range from 1.9 to 3. These ratios range from 2.5 to 4.1 at atmospheric pressure, and 1.9 to 2.3 under vacuum conditions for Al/Ti/Au/SAM; 2.0 to 3.2 at atmospheric

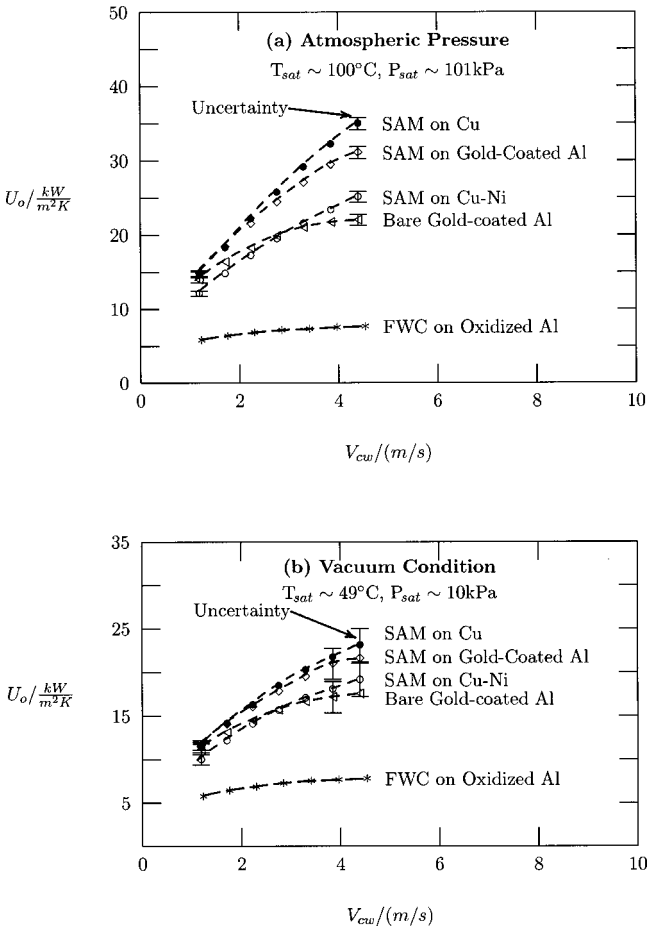

Fig. 4 Overall heat transfer coefficient (U_o) versus coolant velocity during dropwise condensation (DWC) of steam on coated tubes

Table 2 Increase in overall heat transfer coefficient for coated tubes compared to FWC at minimum and maximum coolant flow rates

Tube Label	Substrate Material	Atmospheric Pressure		Vacuum Condition	
		Min. V_{cw}	Max. V_{cw}	Min. V_{cw}	Max. V_{cw}
SAM-on-Cu	Cu	2.5	4.6	1.9	3.0
SAM-on-Gold	Al/Ti	2.5	4.1	1.9	2.3
SAM-on-Cu-Ni	Cu-Ni	2.0	3.2	1.7	2.5
Bare Gold	Al/Ti	2.4	2.9	1.8	2.0

pressure, and 1.7 to 2.5 under vacuum conditions for Cu-Ni/SAM; and 2.4 to 2.9 at atmospheric pressure, and 1.8 to 2.0 under vacuum conditions for Al/Ti/Au. The results not only show the effect of the DWC coating, but also the effect of thermal conductivity of the tubes on the heat transfer enhancement, with higher thermal conductivity tubes yielding higher heat transfer aids. It is interesting to note that the overall heat transfer coefficient U_o for bare-gold tubes are initially higher than that for SAM-on-Cu-Ni tubes, but as V_{cw} increases, U_o for Cu-Ni tubes crosses above the bare-gold values. This could be due to the fact that the wall-thermal resistance of Cu-Ni is 1/10th of Al tubes, and for lower V_{cw}, U_o is dominated by thermal resistance. However, at higher flow rates, U_o gets dominated by h_o which is much higher for Cu-Ni than that for bare-gold. In addition, the overall heat transfer coefficient, and hence the enhancements, are more pronounced at atmospheric operating pressures than at low pressures.

5.2 Condensation Heat Transfer Coefficients and Enhancements. The steam-side heat transfer coefficient (h_o) is tabulated in Table 3 and plotted in Fig. 5 as a function of the subcooling, ΔT, the temperature difference between steam and outer tube wall, obtained by data reduction (Eq. (12)). The figure shows plots of h_o for both (a) atmospheric and (b) vacuum condition. The FWC data is also plotted for comparison, along with the Nusselt theory results for FWC of quiescent vapor. The FWC data lie above Nusselt theory due to a small effect of vapor shear. The plots also show ''high,'' ''low,'' and ''maximum'' uncertainty for each tube-type as error bars. The error bar on SAM-on-copper-nickel is the highest of all, and if taken properly into account, it is hard to distinguish h_o for SAM-on-copper and SAM-on-copper nickel. The values for SAM-on-gold-coated-aluminum is significantly lower than that for SAM-on-copper or SAM-on-copper-nickel, with bare-gold-on-aluminum (without SAM) being the lowest of all the DWC cases.

All of the SAM-coated tubes exhibit large increases in condensing coefficients, compared to FWC case. The SAM-on-copper and SAM-on-copper-nickel tubes show enhancements of 14–15 at atmospheric pressure and 5–6 under vacuum conditions. The enhancement values for SAM-on-gold-coated-aluminum tubes are approximately 9 and 4, respectively, at atmospheric and vacuum conditions. The gold-coated-aluminum without SAM coating gave enhancements of about 3 at atmospheric and 2 under vacuum. The improvement during DWC results primarily from the presence of numerous microscopic-sized drops on the hydrophobic surfaces that do not exist during FWC. Active sweeping of larger drops from above help continue the nucleation of small droplets on the surface, after a larger drop sweeps off the surface; the DWC cycle then repeats itself. This sweeping effect controls the size of drops on the lower part of the tube, as they are prevented from growing too large due to their coalescence into the sweeping drop.

The heat transfer coefficients for atmospheric condition for all the runs were found to be greater than those under vacuum condition. In general, the ratio of atmospheric (101 kPa) values to those under vacuum (10 kPa) were approximately 2.9 for SAM-on-copper, 2.2 for SAM-on-copper-nickel, 2.3 for SAM-on-gold-coated aluminum, and 1.3 for bare-gold-on-aluminum, for the same amount of subcooling. For vertical copper surfaces, Tanasawa [6] reported a similar increase in the dropwise heat transfer coefficient with increasing pressure, with ratios of about 2.2 to 2.8 for a pressure increase from 10 kPa to 100 kPa. One possible explanation for the smaller values at lower pressures may be the fact that at lower pressures, and hence lower temperature and heat flux, the drop departure diameter is larger due to a larger surface tension force. This trend may further be affected by the interphase mass transfer resistance, as pointed out by Briggs and Rose [30].

5.3 Effect of Substrate Material, Surface Roughness, and Metal-SAM Bond. Table 3 summarizes the experimentally determined enhancement ratio for each experimental run. As evident from this table, DWC on a SAM-on-Cu tube gives the highest enhancement value of about 14 above the complete FWC case at atmospheric pressure, and about 6 at vacuum. There is an approximate 24 percent decrease in the outside heat transfer coefficient of aluminum tubes over that of copper tubes at vacuum and about a 40 percent decrease at atmospheric pressure. The enhancement values with the bare-gold coating on aluminum further decrease by 30 percent under vacuum, and by about 53 percent at atmosphere. The enhancement for Cu-Ni tube is as good as copper under vacuum and atmospheric condition, within the experimental error. To explain these trends, we need to consider three factors influencing the DWC characteristics, namely, the substrate material, the surface finish, and the hydrophobicity of the metal-SAM bond for different substrates.

Two schools of thought exist on the effect of substrate material on the heat transfer coefficient. One theory, held by Aksan and Rose [31], suggests that the type of substrate has no effect on the

Table 3 Comparison of DWC enhancements with SAM coatings on copper, copper-nickel, and gold-coated-aluminum tubes. (Values of h_o for FWC were taken at $\Delta T=52$°C at atmospheric pressure and $\Delta T=17$°C under vacuum conditions.)

Tube Label	Substrate Material	Surface Finish	Atmospheric Pressure			Vacuum Condition		
			h_o kW/m^2 K	Δh_o %	$\epsilon_{\Delta T}$	h_o kW/m^2 K	Δh_o %	$\epsilon_{\Delta T}$
FWC	Al	Machined	10	10%	1	11	15%	1
Bare Gold	Al/Ti	Machined	35	10%	3.5	26	12%	2.4
SAM-on-Gold	Al/Ti	Machined	88	11%	8.8	41	16%	3.8
SAM-on-Cu	Cu	Polished	141	13%	14.1	50	19%	5.0
SAM-on-Cu-Ni	Cu-Ni	Polished	144	22%	14.4	60	30%	5.5

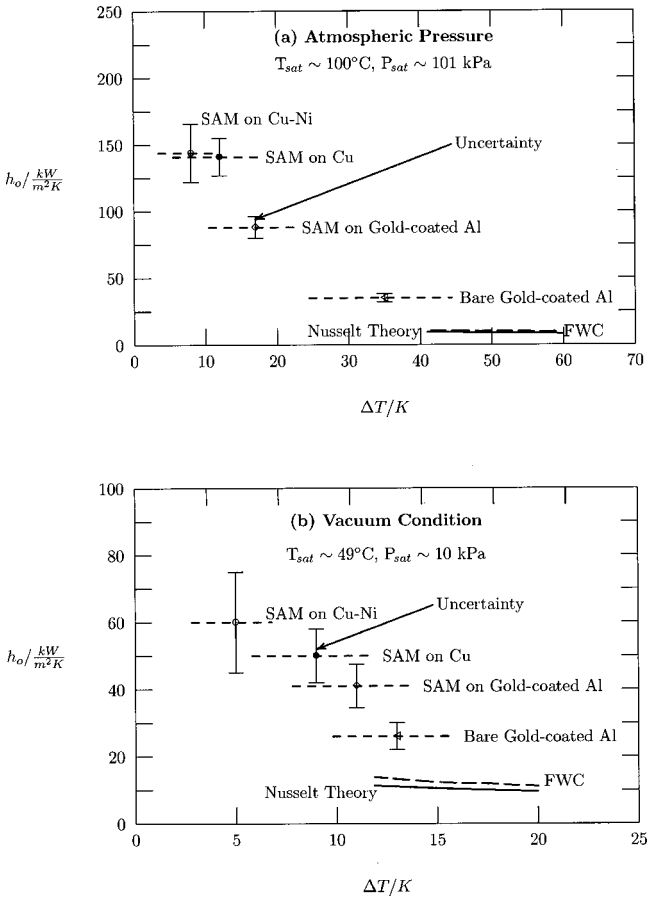

Fig. 5 Heat transfer coefficient versus vapor to tubewall temperature difference during dropwise condensation (DWC) of steam on coated tubes

DWC heat transfer behavior. The differences in the heat transfer between different substrates can be attributed to discrepancies in how a promoter bonds to a substrate and in the resulting surface conditions. In addition, Holden et al. [4], through their evaluation of organic coatings, came to a similar conclusion. The other theory, held by Tanasawa [6] and Mikic [32], states that at a given subcooling, the DWC heat transfer rate must be lower on a poorly conducting surface. Tsuruta and Tanaka [33] carefully measured DWC heat transfer coefficients on quartz glass, stainless steel, and carbon steel, and found that, in fact, the heat transfer coefficient does decrease with decreasing surface thermal conductivity.

The trend observed in the present study seems consistent with and adds credence to the theory that substrate conduction plays an important role in DWC. The thermal conductivity of aluminum is about half that of copper, and hence, the aluminum tube should produce lower heat transfer coefficients. When one realizes that SAM-coated-gold surfaces are much more resilient and hydrophobic than SAM-coated-copper surfaces (as exhibited by the quality of the drops seen on the video recordings), one would expect better heat transfer performance on the gold-coated aluminum tubes. However, the experimental results show the contrary, indicating that the effect of substrate thermal conductivity is significant.

Another possible reason for the reduction in heat transfer of aluminum DWC tubes may be due to surface roughness. The aluminum DWC tubes were not polished prior to the coating of titanium, gold, and SAM. They had an ''as-machined'' finish. On the other hand, the copper and Cu-Ni tubes were polished in a five-step polishing procedure to a mirror finish ([29]). Roughness on a surface tends to decrease DWC heat transfer ([34]), as the drops experience additional drag and greater retention on rough surfaces compared to smooth ones. One way to eliminate the ambiguity of the results is, of course, to polish aluminum tubes using the same five-step procedure and retest.

In the case of the results for SAM-on-Cu-Ni tubes, the above reasons take a different direction. SAM-on-Cu-Ni has an enhancement almost similar to SAM-on-Cu. Both these tubes were polished to the same mirror finish following the same procedure, so that surface roughness of both tubes was nearly the same. However, while the thermal conductivity of Cu-Ni is almost eight times lower than that for copper, there is no decrease in the enhancement, contradicting the conductivity theory. Nevertheless, the overall heat transfer (Fig. 4) for SAM-on-Cu-Ni does show values lower than SAM-on-Al/Ti, which is lower than SAM-on-Cu, and this conforms to the conductivity theory. On the other hand, compared to the enhancement obtained for SAM-coated Cu-Ni Korodense tubes ([24]), the condensation heat transfer coefficient for SAM-on-Cu-Ni tube is almost three times higher in case of the smooth tubes. Given the fact that Korodense tubes have higher internal enhancements, there are only two possible reasons for this lower external enhancement on Korodense tubes: (1) the grooves in the Korodense tube have thick films which reduce the effect of dropwise enhancement, and (2) the smooth tube was highly polished, whereas the Korodense tube was not, exhibiting a strong effect of roughness.

5.4 Condensate Dynamics. The condensation dynamics for all the tubes and test-runs were video recorded. For the bare-gold tube, patches of filmwise and dropwise zones throughout the axial length of the tube were present. The bottom part of the tube, however, was observed to be almost complete filmwise for most condensation rates and most of the runs, except at high heat flux when the bottom was completely filmwise in appearance. The video also showed a transition from larger filmwise zones to smaller filmwise zones with subsequent runs. The drops at the top of the tube were mostly flat and showed very low contact angles. The drops were observed to be less flat in the later runs, indicating stronger dropwise characteristics.

The SAM-coated gold, copper, and copper-nickel tubes showed very discrete drops/droplets all across the tube. Figure 6 shows a still frame from the video-recording of SAM-coated copper tube. The contact angles were larger than 100 deg, and no patches of any filmwise zone were observed. The contact angle for the SAM-on-gold tube appeared larger than that on SAM-on-Cu and SAM-on-Cu-Ni tubes, which is expected since the strongest SAM is formed on gold surfaces ([21–22]). However, the drop sizes were

Fig. 6 Photograph of dropwise condensation on self-assembled monolayer (SAM) coated copper tube under atmospheric condition. Captured from condensation video.

about the same for all three surfaces. The droplets coalesced very rapidly into larger drops, with coalescence effect being so strong in some regions that a few droplets were observed to even *move up against gravity* in order to merge into larger drops. The drops at the top of the tube were still quite large, but had much larger contact angles than observed for the bare-gold tube.

5.5 Some Issues in DWC and Future Work. Even though the hydrophobic coatings enhanced the heat transfer by about a factor of 3 to 10 depending on the pressure and substrate material (surface characteristics), these enhancements are much lower than reported values on vertical surfaces. The main reason for this lower enhancement for horizontal tubes can be attributed to the relatively large size of the drops at the top and bottom of the horizontal tubes which do not occur on vertical surfaces. In the case of vertical surfaces, drops depart easier and sweep the surface at higher frequencies. For horizontal tubes, therefore, a few fundamental issues must still be resolved. For example, how can one remove large ''dead'' drops at the top and bottom of horizontal tubes? How can drop departure diameters be kept small? How can the drainage at the top, sides and bottom of the tubes be controlled? These issues are not very easy to resolve, and require additional research.

6 Conclusions

Organic self-assembled-monolayer (SAM) coatings have been used, for the first time, to enhance steam condensation on horizontal tubes through dropwise condensation. SAMs are formed on tube-metal surfaces to create a hydrophobic surface. SAMs have negligible heat transfer resistance, and pose no contamination threat to the system. The coating is characterized by strong covalent bonds between alkylthiol and metal. In addition to gold-coated aluminum tubes, the coating has been applied directly to copper and copper-alloy (90/10 Cu-Ni) tubes, with equally effective results. Although the coating looks promising due to strong covalent bond, the durability needs to be determined before it can be commercialized. The highlights of this study can be summarized as follows:

1 The quality of the drops was similar for the three different SAM surfaces: SAM-on-gold, SAM-on-copper, and SAM-on-copper-nickel, with contact angles greater than 100 deg. The gold-coated aluminum surface, however, exhibited slightly better quality in the video-recording. In comparison, the quality of drops on the bare-gold surface (i.e., with no SAM present) was inferior, with contact angles less than 90 deg.

2 The size of the drops was observed to be relatively large (2–3 mm) at the top and bottom of the tube. The drops were much smaller around the vertical side of the tube. These smaller drops were generally swept away by the larger drops departing from the top.

3 The SAM coating was found to increase the DWC condensation heat transfer coefficient over the FWC case, under atmospheric operating conditions, by a factor of 14 for SAM-on-copper tubes, nine for SAM-on-gold-coated-aluminum tubes, and 14 for SAM-on-copper-nickel tubes. The enhancement values under vacuum conditions were 5 for Cu and Cu-Ni and 3.8 for SAM-on-gold-coated-aluminum. Comparatively, the heat transfer coefficient obtained with a bare-gold-coated aluminum tube was about 3.5 times that of the FWC case, under atmospheric conditions, and about 2.4 times under vacuum operation.

4 Variations in the measured enhancement with the SAM-coated tubes may be due to the thermal conductivity of the substrate metal, the surface roughness, or to the surface chemistry of the SAM-metal bond. Additional testing is therefore required to elucidate which mechanisms are most important.

Acknowledgment

Funding for a major portion of this work was provided by National Science Foundation Grant CTS-9624060.

Nomenclature

A = area
C_i, C_o = leading coefficients in Eqs. (3) and (8)
C_p = specific heat
D = diameter
g = gravitational acceleration
h = heat transfer coefficient
h_{fg} = latent heat of vaporization
k = thermal conductivity
L = active condensation length
$\dot{m}$ = coolant mass flow rate
Pr = Prandtl number
Re = Reynolds number
T = temperature
ΔT = temperature difference between saturated steam and tube outer surface, $(T_s - T_w)$
U_o = overall heat transfer coefficient, Eq. (1)
X,Y = variables defined in Eqs. (10) and (11)

Greek Symbols

ϵ = heat transfer enhancement, as defined in Eq. (13)
μ = viscosity
Ω = variable defined in Eq. (4)
ρ = density
σ = surface tension
ξ = variable in Petukhov-Popov correlation, Eq. (5)

Subscripts

ci = cooling water in
co = cooling water out
cw = cooling water
DWC = dropwise condensation
f = condensate
FWC = filmwise condensation
i = inside
o = outside
s = saturation state
w = tube-wall
wo = tube-wall outer surface

References

[1] Woodruff, D. W., and Westwater, J. W., 1979, ''Steam Condensation on Electroplated Gold: Effect of Plating Thickness,'' Int. J. Heat Mass Transf., **22**, pp. 629–632.
[2] Woodruff, D. W., and Westwater, J. W., 1981, ''Steam Condensation on Various Gold Surfaces,'' ASME J. Heat Transfer, **103**, pp. 685–692.
[3] O'Neill, G. A., and Westwater, J. W., 1984, ''Dropwise Condensation of Steam on Electroplated Silver Surfaces,'' Int. J. Heat Mass Transf., **27**, pp. 1539–1549.
[4] Holden, K. M., Wanniarachchi, A., Marto, P. J., Boone, D. H., and Rose, J. W., 1987, ''The Use of Organic Coatings to Promote Dropwise Condensation of Steam,'' ASME J. Heat Transfer, **109**, pp. 768–774.
[5] Marto, P. J., Looney, D. J., Rose, J. W., and Wanniarachchi, A., 1986, ''Evaluation of Organic Coatings for the Promotion of Dropwise Condensation of Steam,'' Int. J. Heat Mass Transf., **29**, No. 8, pp. 1109–1117.
[6] Tanasawa, I., 1991, ''Advances in Condensation Heat Transfer,'' Adv. Heat Transfer, **21**, pp. 55–139.
[7] Erb, R., and Thelen, E., 1965, ''Dropwise Condensation,'' *Proceedings of the First International Symposium on Water Desalination*, Washington, D.C., pp. 18–24.
[8] Erb, R., and Thelen, E., 1965, ''Promoting Permanent Dropwise Condensation,'' Ind. Eng. Chem., **57**, pp. 49–52.
[9] Ma, X., Xu, D., and Lin, J., 1994, ''A Study of Dropwise Condensation on the Ultra-Thin Polymer Surfaces,'' *Heat Transfer 1994*, Vol. 3, IChemE, Rugby, UK, pp. 359–364.
[10] Zhao, Q., and Burnside, B., 1994, ''Dropwise Condensation of Steam on Ion Implanted Condenser Surfaces,'' Heat Recovery Syst. CHP, **14**, No. 5, pp. 525–534.
[11] Zhao, Q., and Burnside, B., 1996, ''Dropwise Condensation of Steam at High Velocity and Vacuum Pressures Over a Small Tube Bank,'' *Heat Transfer in*

Condensation, Process Eurotherm Seminar, No. 47, Marvillet and Vidil, eds., Elsevier, New York, pp. 196–204.
[12] Bonnar, M., Burnside, B., Hadi, H., Reuben, R., and Wilson, J., 1995, ''New Plasma Deposition Technology Revives Interest in Designing Utility Condensers for Dropwise Condensation,'' *Transactions of the 4th UK Conference on Heat Transfer*, Institute of Mechanical Engineers, London, pp. 329–333.
[13] Bonnar, M., Burnside, B., Little, A., Reuben, R., Sceal, E., and Wilson, J., 1997, ''Plasma Polymer Coatings for Hydrophobic Surfaces,'' *Proceedings of the 5th European Conference on Advanced Materials and Applications*, Netherlands Society for Materials Science, Maastricht, The Netherlands, **3**, pp. 201–204.
[14] Bonnar, M., Burnside, B., Reuben, R., Wilson, J., and Liehr, M., 1995, ''Hydrophobic Fluorocarbon and Organo-Silicon Condenser Tube Coatings Deposited by Plasma Enhanced CVD,'' *Proceedings of the 12th International Symposium on Plasma Chemistry*, J. V. Heberlein, ed., pp. 99–104.
[15] Taniguchi, A., and Mori, Y. H., 1994, ''Effectiveness of Composite Copper/Graphite Fluoride Platings for Promoting Dropwise Condensation of Steam: A Preliminary Study,'' Int. Commun. Heat Mass Transfer, **21**, No. 5, pp. 619–627.
[16] Deronzier, J. C., Foulletier, L., Huyghe, J., and Niezborala, J. M., 1975, ''Method for Causing Condensation in Drops on Heat Exchanger Tubes,'' Apr. 22, U.S. Patent No. 3,878,885.
[17] Gavrish, A. S., Reifert, V. G., Sardak, A. I., and Podbereznyy, V. L., 1993, ''A New Dropwise Condensation Promoter For Desalination and Power Plants,'' Heat Transf. Res., **25**, No. 1, pp. 82–86.
[18] Gavrish, A. S., and Reifert, V. G., 1996, ''Investigation of Water Vapor Dropwise Condensation Stimulated by Fluorine-Containing Disulphide,'' *2nd European Thermal-Sciences and 14th UIT National Heat Transfer Conference*, G. P. Celata, P. Di Marco, and A. Mariani, eds., Edizioni, pp. 1257–1261.
[19] Bain, C. D., Evall, J., and Whitesides, G. M., 1989, ''Formation of Monolayer by the Co-adsorption of Thyl on Gold: Variation in Head Group, Tail Group, and Solvent,'' J. Am. Chem. Soc., **111**, pp. 7155–7169.
[20] Dubois, L. H., and Nuzzo, R. G., 1992, ''Synthesis, Structure, and Properties of Model Organic Surfaces,'' Annu. Rev. Phys. Chem., **43**, pp. 437–463.
[21] Kumar, A., and Whitesides, G. M., 1994, ''Patterned Condensation Figures as Optical Diffraction Gratings,'' Science, Washington, DC, **263**, pp. 60–62.
[22] Kumar, A., Biebuyck, H. A., and Whitesides, G. M., 1994, ''Patterning Self-Assembled Monolayers: Applications in Materials Science,'' Langmuir, **10**, No. 5, pp. 1498–1511.
[23] Kumar, A., Abott, N. L., Kim, E., Biebuyck, H. A., and Whitesides, G. M., 1995, ''Patterned Self-Assembled Monolayers and Meso-Scale Phenomena,'' Acc. Chem. Res., **28**, No. 5, pp. 219–226.
[24] Das, A. K., Kilty, H. P., Marto, P. J., Kumar, A., and Andeen, G. B., 2000, ''Dropwise Condensation of Steam on Horizontal Corrugated Tubes Using an Organic Self-Assembled Monolayer Coating,'' J. Enhanced Heat Transf., to be published.
[25] Briggs, D. E., and Young, E. H., 1968, ''Modified Wilson Plot Techniques for Obtaining Heat Transfer Correlations for Shell and Tube Heat Exchangers,'' Chem. Eng. Prog., Symp. Ser., **65**, No. 92, pp. 35–45.
[26] Petukhov, B. S., 1970, ''Heat Transfer and Friction in Turbulent Pipe Flow With Variable Physical Properties,'' Adv. Heat Transfer, **6**, pp. 503–564.
[27] Rose, J. W., 1998, ''Condensation Heat Transfer Fundamentals,'' Trans. IChem E., **5**, Part A, pp. 143–152.
[28] Kline, S. J., and McClintock, F. A., 1953, ''Describing Uncertainties in Single-Sample Experiments,'' Mech. Eng. (Am. Soc. Mech. Eng.), **74**, pp. 3–8.
[29] Kilty, H. P., 1996, ''The Effect of a Novel Coating Technique on Filmwise and Dropwise Condensation of Steam on Horizontal Tubes,'' Master's Thesis, Naval Postgraduate School, Monterey, CA.
[30] Briggs, A., and Rose, J. W., 1996, ''Condensation on Low-Fin Tubes: Effects of Non-Uniform Wall Temperature and Interphase Matter Transfer,'' *Process, Enhancement, and Multiphase Heat Transfer*, R. M. Manglik and A. D. Krause, eds., Spiegel Homes, pp. 455–460.
[31] Aksan, S., and Rose, J. W., 1973, ''Dropwise Condensation—The Effect of Thermal Properties of the Condenser Material,'' Int. J. Heat Mass Transf., **16**, p. 461.
[32] Mikic, B., 1969, ''On Mechanism of Dropwise Condensation,'' Int. J. Heat Mass Transf., **12**, pp. 1311–1323.
[33] Tsuruta, T., Tanaka, H., and Togashi, S., 1991, ''Experimental Verification of Constriction Resistance Theory in Dropwise Condensation Heat Transfer,'' Int. J. Heat Mass Transf., **34**, No. 11, pp. 2787–2796.
[34] Izumi, M., and Yamakawa, N., 1993, ''Dropwise Condensation on Rough Surfaces,'' *Condensation & Condenser Design*, ASME, New York, pp. 143–154.

The Numerical and Experimental Study of Non-Premixed Combustion Flames in Regenerative Furnaces

C. Zhang[1]
Assoc. Mem. ASME

T. Ishii[2]
e-mail: tishii@lab.fukuyama.nkk.co.jp

Y. Hino

S. Sugiyama

Materials and Processing Research Center,
NKK Corporation,
Fukuyama, Hiroshima 721, Japan

A numerical procedure is presented to predict the turbulent non-premixed combustion flames in regenerative furnaces. A moment closure method with the assumed β probability density function (PDF) for the mixture fraction is used in the present work. The procedure is applied to an experimental regenerative slab reheat furnace developed in NKK to demonstrate its predictive capability. The predictions are compared with the experimental data. The comparison is favorable. [S0022-1481(00)01302-5]

Keywords: Combustion, Computational, Heat Transfer, Turbulence

1 Introduction

Fuel consumption in industrial furnaces represents a significant percentage of the total processing cost. In order to increase the furnace thermal efficiency and reduce the fuel consumption, it is important and necessary to understand the physical phenomena of the combustion process in furnaces. The flow, heat, and mass transfer in gas-fired reheat furnaces are complicated by the interaction of turbulence and chemical reactions. A considerable amount of research has been conducted in modeling turbulent combustion flames, such as the works of Magnussen and Hjertager [1], Spalding [2], Janicka and Kollmann [3], Pope [4], Cook [5], Chen and Kollmann [6], Buch et al. [7], Gaffney et al. [8], Smith et al. [9], Boardman et al. [10], Chen et al. [11] and Peters and Weber [12]. However, the open literature has given little attention to the predictive capability of numerical models for the simulations of the flow and composition fields in gas-fired reheat furnaces with moving slabs. The present work is a step forward to fill this gap. This work is a further extension of the recent work by Zhang et al. [13] in which the numerical predictions of the experimental furnace were accessed by comparison to the preliminary experimental data.

In this work, the moment closure method is used to simulate the turbulent non-premixed combustion processes in regenerative furnaces. Since fluctuations appear in the temperature and species concentrations, which in turn introduce fluctuations in the reaction rate coefficients and species production term, the assumed-shape PDF method is applied to account for the effects of turbulent fluctuations on combustion. The combustion model based on the chemical equilibrium concept is employed to specify the instantaneous thermochemical state of the combustion mixture and to take into account the intermediate species formation and dissociation. The standard $k-\varepsilon$ model with a wall function is used to model the turbulence behavior. The moving steel slabs in the furnace are modeled by solving an additional conduction equation. The radiation heat transfer rate is determined by the $P-1$ model. The predicted temperature distributions inside the experimental furnace are compared with the experimental data to evaluate the predictive capability of the numerical model.

2 Turbulent Combustion Model

2.1 Conservation Equations. Since the flows in furnaces are turbulent and reactive, the Favre-averaged form of conservation equations is used in this study to account for the effects of density change. The steady three-dimensional conservation equations of mass, momentum, and energy can be expressed as ([14], [12])

$$\frac{\partial}{\partial x_i}(\overline{\rho}\tilde{u}_i)=0 \tag{1}$$

$$\frac{\partial}{\partial x_i}(\overline{\rho}\tilde{u}_i\tilde{u}_j)=\frac{\partial}{\partial x_j}\left[\mu_e\left(\frac{\partial\tilde{u}_i}{\partial x_j}+\frac{\partial\tilde{u}_j}{\partial x_i}\right)-\left(\frac{2}{3}\mu_e\frac{\partial\tilde{u}_l}{\partial x_l}\right)\right]-\frac{\partial\overline{p}}{\partial x_i} \tag{2}$$

where $\mu_e=\mu+\mu_t$, $\mu_t=\overline{\rho}C_\mu k^2/\varepsilon$ and $C_\mu=0.09$

$$\frac{\partial}{\partial x_i}(\overline{\rho}\tilde{u}_i\tilde{h})=\frac{\partial}{\partial x_i}\left(\frac{\mu_t}{\sigma_h}\frac{\partial\tilde{h}}{\partial x_i}\right)+\tilde{S}_h \tag{3}$$

where S_h consists of sources of enthalpy due to chemical reaction and radiation.

Besides the above conservation equations, the moving steel slabs in the furnace are modeled by solving the following conduction equation:

$$\frac{\partial}{\partial x_i}(\rho_s u_{i,s}C_{ps}T_s)=\frac{\partial}{\partial x_i}\left(\lambda_s\frac{\partial T_s}{\partial x_i}\right). \tag{4}$$

2.2 Turbulent Model. For the standard $k-\varepsilon$ model ([15]), k and ε transport equations are expressed as

$$\frac{\partial}{\partial x_i}(\overline{\rho}\tilde{u}_i k)=\frac{\partial}{\partial x_i}\left(\frac{\mu_t}{\sigma_k}\frac{\partial k}{\partial x_i}\right)+G_k-\overline{\rho}\varepsilon \tag{5}$$

$$\frac{\partial}{\partial x_i}(\overline{\rho}\tilde{u}_i\varepsilon)=\frac{\partial}{\partial x_i}\left(\frac{\mu_t}{\sigma_\varepsilon}\frac{\partial\varepsilon}{\partial x_i}\right)+C_1\frac{\varepsilon}{k}G_k-C_2\overline{\rho}\frac{\varepsilon^2}{k} \tag{6}$$

where

$$G_k=\mu_t\left(\frac{\partial\tilde{u}_j}{\partial x_i}+\frac{\partial\tilde{u}_i}{\partial x_j}\right)\frac{\partial\tilde{u}_i}{\partial x_i}$$

$C_1=1.44$, $C_2=1.92$, $C_\mu=0.09$, $\sigma_k=1.0$, and $\sigma_\varepsilon=1.3$.

As near-wall boundary conditions, values of k and ε at the first grid node are related to the wall shear stress by assuming local equilibrium in the near-wall layer.

[1]Permanent address: Department of Mechanical and Materials Engineering, University of Western Ontario, London, Ontario N6A 5B9, Canada.

[2]To whom correspondence should be addressed.

Contributed by the Heat Transfer Division for publication in the JOURNAL OF HEAT TRANSFER. Manuscript received by the Heat Transfer Division, Aug. 29, 1997; revision received, Dec. 19, 1999. Associate Technical Editor: S. Ramadhyani.

2.3 Combustion Model. For turbulent non-premixed combustion, the time scales of turbulent mixing are large as compared with the time scales of the conversion of fuel. Thus, a widely used approach in the modeling of non-premixed turbulent reacting flows is to assume fast chemistry. It results in a considerable simplification for modeling and does allow a reasonably accurate description of many features, including the fields of temperature and concentrations of major species ([14]). Also, it is reasonable to assume that all species and enthalpy have equal diffusion coefficients for turbulent flows. Under these assumptions, the instantaneous thermochemical state of the mixture in a turbulent non-premixed combustion system is a function of the instantaneous mixture fraction and enthalpy only, i.e.,

$$\phi = \phi(f,h) \tag{7}$$

where ϕ may denote an instantaneous species concentration, temperature or fluid density, and f is the mixture fraction which is defined as

$$f = \frac{Z_k - Z_{ko}}{Z_{kf} - Z_{ko}}. \tag{8}$$

Based on the assumption that chemistry is fast enough for chemical equilibrium always to exist, the function $\phi(f,h)$ can be determined by minimizing the Gibbs free energy. Temporal fluctuations can be accounted for by using a joint PDF, $P(f,h)$. However, the computation of $P(f,h)$ is not practical for engineering applications. If we assume that the heat losses do not significantly affect the turbulent enthalpy fluctuations, we have $P = P(f)$. Then, the Favre-averaged values of ϕ can be calculated by

$$\tilde{\phi} = \int_0^1 P(f)\phi(f,\tilde{h})df. \tag{9}$$

The fluid density in the Favre-averaged equations is evaluated by

$$\overline{\rho} = \left[\int_0^1 \frac{P(f)}{\rho(f,\tilde{h})} df \right]^{-1}. \tag{10}$$

The β-PDF is widely used in turbulent combustion simulations [11]. So, the β-function is selected as the PDF of the mixture fraction.

$$P(f) = \frac{f^{\alpha-1}(1-f)^{\beta-1}}{\int f^{\alpha-1}(1-f)^{\beta-1}df} \tag{11}$$

where

$$\alpha = \tilde{f}\left(\frac{\tilde{f}(1-\tilde{f})}{\widetilde{f'^2}} - 1 \right) \quad \text{and} \quad \beta = (1-\tilde{f})\left(\frac{\tilde{f}(1-\tilde{f})}{\widetilde{f'^2}} - 1 \right).$$

$\tilde{f}$ and $\widetilde{f'^2}$ can be obtained by solving their corresponding transport equations as given below ([14]):

$$\frac{\partial}{\partial x_i}(\overline{\rho}\tilde{u}_i\tilde{f}) = \frac{\partial}{\partial x_i}\left(\frac{\mu_t}{\sigma_t}\frac{\partial \tilde{f}}{\partial x_i} \right) \tag{12}$$

$$\frac{\partial}{\partial x_i}(\overline{\rho}\tilde{u}_i\widetilde{f'^2}) = \frac{\partial}{\partial x_i}\left(\frac{\mu_t}{\sigma_t}\frac{\partial \widetilde{f'^2}}{\partial x_i} \right) + C_g\mu_t\left(\frac{\partial \tilde{f}}{\partial x_i} \right)^2 - C_d\overline{\rho}\frac{\varepsilon}{k}\widetilde{f'^2} \tag{13}$$

where $\sigma_t = 0.7$, $C_g = 2.86$, and $C_d = 2.0$.

The mean mixture fraction, $\tilde{f}$, is 1 at the fuel inlet and 0 at the oxidizer inlet. The mean mixture fraction variances, $\widetilde{f'^2}$, are 0 at both fuel and oxidizer inlets.

2.4 Radiation Model. In this work, the $P-1$ radiation model [16] is used to calculate the radiation transfer source terms in the enthalpy equation. The mean radiation flux, $\tilde{q}$, is determined by the following equation:

$$-\nabla\tilde{q} = a\theta - 4a\sigma\tilde{T}^4 \tag{14}$$

where θ is calculated by the following transport equation:

$$\nabla(\Gamma\nabla\theta) - a\theta + 4a\sigma\tilde{T}^4 = 0 \tag{15}$$

where $\Gamma = 1/(3(a+\sigma_s))$. A variable absorption coefficient model, weighted-sum-of-Gray-Gases model, is used to determine the absorption coefficient, a. Since the scattering coefficient σ_s is very small in most clear gas combustion systems, a very small value, 10E-6, suggested by FLUENT is used. This is clear gas combustion. Therefore, there is no soot generated.

3 Experimental Furnace

The furnace selected for this study is an experimental regenerative continuous slab reheat furnace with the inner dimensions of $8\times4\times3$ m^3. The configuration of the furnace is depicted in Fig. 1. The origin of the coordinate system is located at the front-left-bottom corner of the furnace. The geometrical parameters are listed in Table 1. Regenerative burners are used in this furnace to increase the furnace thermal efficiency. By using regenerative burners, the combustion air is preheated by utilizing the heat in the exhaust gases that is normally discharged to the atmosphere in conventional furnaces. So, the fuel consumed to heat the combustion air can be reduced and the furnace thermal efficiency can be increased. In this furnace, there are four pairs of regenerative burners in which one burner of a pair is placed on the front wall and the other one is on the back wall of the furnace as shown in Fig. 1. Each regenerative burner contains a ceramic honeycomb regenerator that absorbs heat from the exhaust gases during the exhaust cycle and releases heat to the combustion air during the firing cycle. One burner of a pair serves as an exhaust gas heat extractor and storage bed while the other one is in a firing mode. The exhaust/firing cycles are reversed every 30 seconds. When the combustion air passes through the honeycomb regenerator, it is preheated to a temperature close to the flue gas temperature before it enters the furnace. Exhausting 80 percent of the flue gases through the burner outlets is sufficient to preheat the combustion air. So, the furnace also contains an auxiliary exhaust outlet of diameter 450 mm on the left-hand side of the furnace wall as

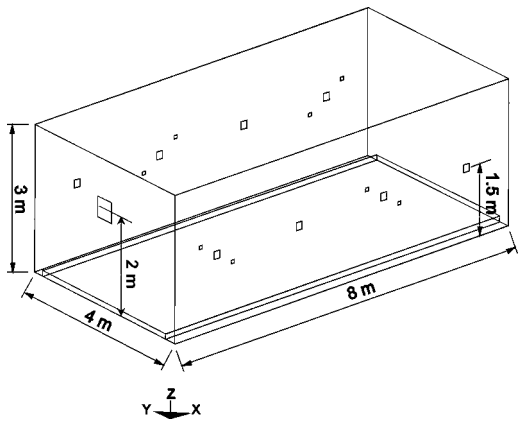

Fig. 1 Configuration of the furnace

Table 1 Geometrical parameters of the furnace

Furnace length	8 m
Furnace width	4 m
Furnace height	3 m
Slab width	3.5 m
Slab thickness	110 mm
Air nozzle diameter	151 mm
Fuel nozzle diameter	28 mm

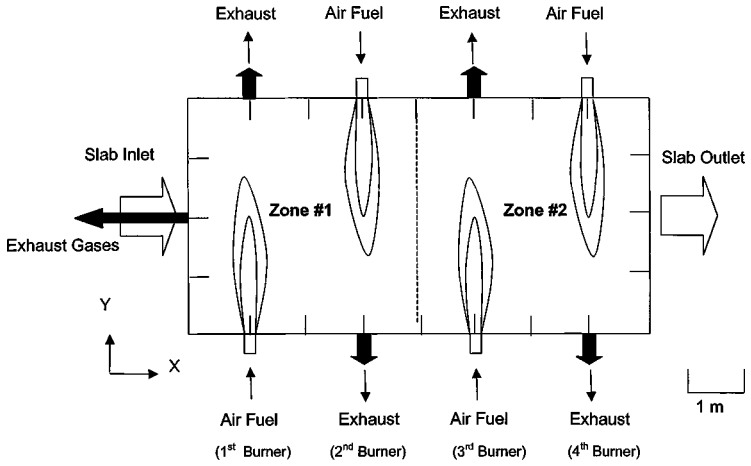

Fig. 2 Top view of the furnace

Table 2 Operating conditions of the furnace

	Zone #1	Zone #2
Fuel thermal input rate	1791 kW	1128 kW
Combustion air inlet temperature	1455 K	1358 K
Combustion air inlet velocity	69.5 m/s	41.0 m/s
Fuel inlet temperature	303 K	303 K
Fuel inlet velocity	70.8 m/s	44.6 m/s
Excess air ratio	1.143	1.147
Slab inlet temperature	296 K	
Slab speed	0.000833 m/s	
Combustion air composition (vol.%)	N_2: 79%; O_2: 21%	
Fuel composition (vol.%)	CH_4: 12.9%; C_2H_2: 1.2%; CO:23.7%; CO_2: 10.6%; H_2: 25.5%; H_2O: 1.3%; N_2: 24.8%;	

shown in Fig. 1. The center of the exhaust outlet is located at 2 m from the bottom of the furnace wall and 2 m from the front of the furnace wall. The combustion air, fuel, and exhaust gases flow directions, and the slab moving direction are shown in Fig. 2. For the convenience of description, the furnace is divided into two zones as shown in Fig. 2. The left-hand half of the furnace is named as Zone #1 and the right-hand half is named as Zone #2.

The operating conditions are listed in Table 2, which are obtained from the measurements. The burner capacity is 1163 kW (i.e., 10^6 kcal/h) per burner. Under the selected operation conditions, the burners in Zone #1 and Zone #2 are operated at 77.0 percent load and 48.5 percent load, respectively. The total fuel thermal input rate to the furnace is 2919 kW, i.e., 1791 kW to Zone #1 and 1128 kW to Zone #2.

Figure 3 sketches the configuration of the burners used in this experimental furnace. Each burner consists of one air injection nozzle and two fuel injection nozzles. The air injection nozzle is located in the center of the burner and the two fuel injection nozzles are placed on the corners. The combustion air and fuel are injected separately along the *y*-direction into the furnace at high velocities in order to achieve good mixing of the combustion air with the flue gases before combustion occurs. The center of the burner, which is also the center of the air nozzle, is located at 1.5 m from the bottom of the furnace as shown in Fig. 1. The distance between the centers of two adjacent burners is 2 m and the distance between the center of the burner and the furnace wall is 1 m as shown in Fig. 2.

Water-cooled skids are placed on the bottom of the furnace, which are not shown in Fig. 1. There are four cooling pipes equally located along the *x*-direction and three cooling pipes equally located along the *y*-direction in order to cool the skids. These cooling pipes extract heat at a rate of 271 kW. Low-carbon steel slabs are fed into the top of the skids continuously at an average speed of 0.000833 m/s along the *x*-direction. The slab is located at $z=0$ in Fig. 1. The density, thermal conductivity, specific heat, and surface emissivity of the slabs are 7600 kg/m^3, 27.0 W/mK, 0.749 kJ/kgK, and 0.8, respectively.

The furnace walls consist of three layers. The outer layer is a steel cover layer of thickness 4.5 mm. The middle layer is a refractory layer with thickness of 200 mm and thermal conductivity of 0.14 W/mK. The inner layer is a coating layer with thickness of 50 mm and thermal conductivity of 0.24 W/mK.

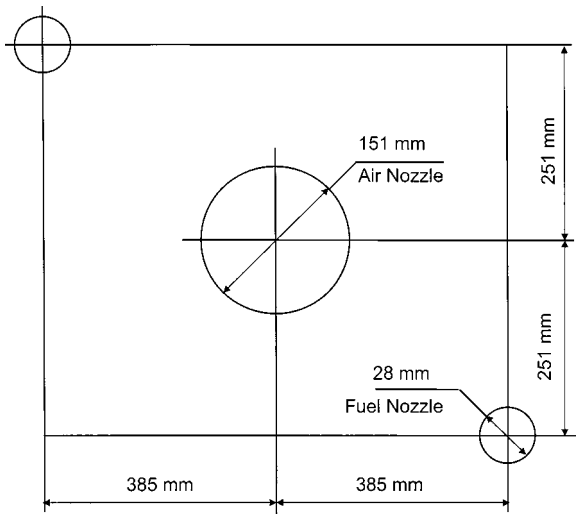

Fig. 3 Configuration of the burner

4 Numerical Simulations

The code, FLUENT, is used for the simulations in the present work. A control volume approach ([17]) is used in which a nonstaggered grid arrangement is employed to discretize the differential governing equations. The interpolations between the grid points are accomplished via a first-order power-law scheme. The velocity and pressure fields are linked by the SIMPLEC algorithm proposed by van Doormaal and Raithby [18]. The discretized governing equations are solved by sweeping plane by plane in one of the three directions. An iterative line-by-line matrix solver with a multigrid acceleration scheme is used on each plane.

The numerical simulations are carried out on a nonuniform grid of $89\times25\times31$ nodes along the *x*-, *y*- and *z*-coordinates to accommodate the locations and sizes of the slab, air and fuel injection nozzles, and auxiliary exhaust tube. The grid independence test from the previous work ([13]) indicated that the grid of $89\times25\times31$ can give essentially grid independent results (i.e., the maximum temperature difference between the results obtained using the grid of $89\times25\times31$ and a finer grid was less than one percent).

The combustion process in the experimental regenerative furnace is a periodical process since the exhaust/firing cycles are reversed every 30 seconds. Nevertheless, the previous simulations using periodical boundary conditions indicated that, during each cycle, the combustion process would reach steady state after three to four seconds. In other words, the process has already reached steady state long before the cycle is reversed. So, in this work, the steady-state turbulent combustion process is simulated in which the exhaust/firing cycles will not be reversed. The numerical simulations are performed when the first and third burners on the front wall and the second and fourth burners on the back wall are in the firing mode.

In the simulations, the top and side of the furnace walls are treated as convection/radiation walls. The overall external heat transfer coefficient, h_o, is determined based on the thermal resistances of the refractory and coating layers, and the thermal resistance of the convection heat transfer between the wall and the surroundings, i.e.,

$$h_o=\left(\frac{1}{\alpha}+\frac{L_r}{\lambda_r}+\frac{L_c}{\lambda_c}\right)^{-1} \tag{16}$$

where α is the convection heat transfer coefficient between the furnace walls and the surroundings. The temperature of the surroundings is 23°C. The thermal resistance of the steel cover of the furnace is neglected. The convection between the furnace walls and surroundings is treated as free convection. A typical value of free convection heat transfer coefficient between gases and solid surfaces is 2–25 W/m^2K ([19]). A value of 10 W/m^2K is taken in the simulations. This value was not adjusted to get the results to agree with the experiments since it accounts for only a small portion in the overall thermal resistance. A value of 0.58 W/m^2K is obtained for h_o using Eq. (16). The bottom wall of the furnace is considered as a wall with a constant heat flux of 8.47 kW/m^2. This value is determined from the heat rate extracted by the cooling pipes in the bottom of the furnace.

5 Experimental Measurement

5.1 Measurement Program. The measurement program includes flue gas temperatures at 90 locations inside the experimental furnace. A computerized data acquisition and process control system is installed on the experimental furnace. The *B*-type thermocouples are used to measure the flue gas temperature inside the furnace. The diameter of each thermocouple probe is 1.6 mm. The probes are shielded against radiation. The accuracy of the temperature measurement system is ±10°C at 1300°C, which is supplied by the manufacturer. The measurements of the flue gas temperature are made at 18 fixed locations on the horizontal plane as shown in Fig. 4. The thermocouples are inserted into the furnace from the top of the furnace and they can be moved vertically

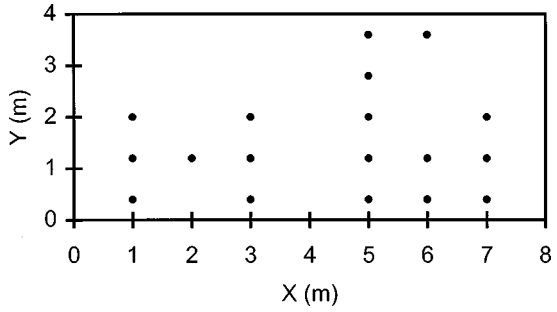

Fig. 4 Locations of temperature measurement

(*z*-direction). The uncertainties associated with the probe positions are ±10 mm in the *x*- and *y*-directions, and ±2 mm in the *z*-direction. The measurements are performed for five horizontal planes at the vertical distances from the bottom of the furnace of $z=0.5$, 1.0, 1.5, 2.0, and 2.5 m.

5.2 Experimental Uncertainty Analysis. The uncertainty of the experimental measurements is calculated based on the combination of the bias error limit, *B*, and precision error limit, *P*.

$$U=\sqrt{(B^2+P^2)} \tag{17}$$

The precision error limit, which can be determined by repeated measurements of the variable of interest, is related to the standard deviation of the measurements. The standard deviation of the temperature measurements, S_T, is given as

$$S_T=\sqrt{\frac{\sum_{i=1}^{n}(T_i-\bar{T})^2}{n-1}}. \tag{18}$$

The standard deviation of the mean temperature is related to the standard deviation of the measurements by ([20])

$$S_{\bar{T}}=\frac{S_T}{\sqrt{n}}. \tag{19}$$

The precision error limit in the mean value can be determined by ([20])

$$P=tS_{\bar{T}} \tag{20}$$

where *t* is a function of the confidence level and the degrees-of-freedom. At a 95 percent confidence level with a large number of samples (over 30), $t=2.0$ ([20]). The number of samples taken in this experiment is more than 60. Therefore, the value of *t* is taken as 2.0.

In this work, the average precision error at all temperature measurement locations is 4.03°C for a confidence level of 95 percent. The maximum and minimum values of the precision error limits are 9.26°C and 0.84°C, respectively. As suggested by Wheeler and Ganji [20] the accuracy of the measurement system supplied by the manufacturer should be treated as the bias error limit. Thus the value of *B* is 10°C. The uncertainty can be determined using Eq. (17). The average uncertainty is 10.8°C. The maximum and minimum uncertainties are 13.6°C and 10.0°C, respectively.

6 Predicted Results

The variation of the temperature on the slab that is located on the bottom of the furnace is shown in Fig. 5. The slab temperature along the slab moving direction (*x*-direction) increases gradually due to the heat transfer to the slab and it is fairly uniform in the cross-sectional direction (*y*-direction). The temperature distribution on the horizontal plane that cuts through the combustion air injection ports ($z=1.5$ m) is also depicted in Fig. 5. This figure shows the four main reaction regions characterized by a high level

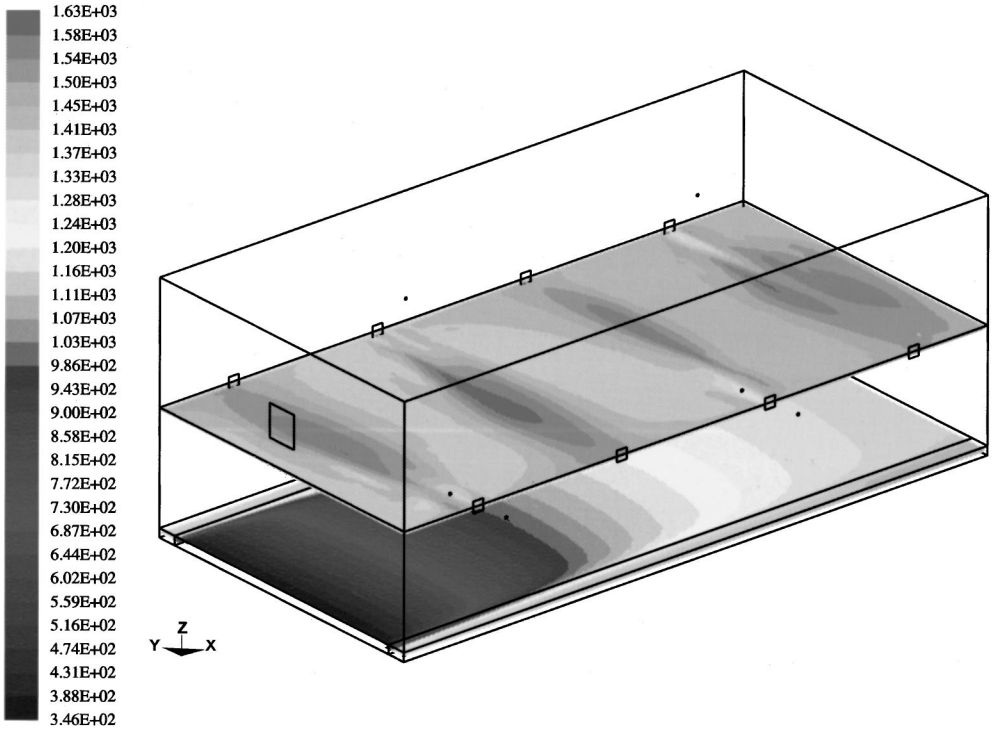

Fig. 5 Temperature distribution (K)

of temperature. It is noticed that the centers of the two main reaction regions in Zone #1 have slightly higher temperatures in comparison with the centers of the other two main reaction regions in Zone #2. This may be attributed to the fact that the fuel and combustion air input rates to Zone #1 are higher than these to Zone #2. The combustion in Zone #1 occurs at a higher rate which results in a higher temperature. On the other hand, the temperature outside of the main reaction regions in Zone #2 is slightly higher than that in Zone #1 since the slab temperature is higher in Zone #2. The results also indicate that 98 percent of the heat transferred to the slab is by radiation and only two percent of the heat is transferred to the slab by convection.

7 Comparisons and Discussion

Since the numerical simulations are performed when the first and third burners on the front wall and the second and fourth burners on the back wall are in the firing mode, the experimental data used here are time-mean values obtained during the cycles when the first and third burners on the front wall and the second and fourth burners on the back wall are in the firing mode. Typically, the time-mean values are average values over five to six cycles.

Comparisons for the flue gas temperature distributions are made for $y=0.4$ m at $z=1.5$ and 2.5 m, $y=1.2$ m at $z=1.5$ and 2.5 m, and $y=2$ m at $z=0.5$, 1.0, 1.5, 2.0, and 2.5 m along the x-direction, respectively, as shown in Fig. 6. The overall agreement is good considering the complexity of the turbulent combustion process in the furnace and the uncertainty of the experimental data.

The temperature distributions at $z=2.5$ m which is close to the top of the furnace are relatively uniform. The temperature at $z=0.5$ m increases in the x-direction due to the effect of the slab temperature distribution. The agreement between the prediction and experiment is very good at $z=2.5$ m. The agreement is also very good at $z=0.5$ m except the point close to the slab exit end of the furnace where the temperature is overpredicted. Since $z=0.5$ m is close to the bottom of the furnace, the heat loss through the gap between the slab outlet and the furnace wall may cause the lower flue gas temperature at the slab exit end of the furnace.

The numerical predictions show that the highest temperature on the horizontal plane of $z=1.5$ m occurs in the center of the second main combustion region as shown in Fig. 5. The experimental data confirmed this result. At $y=0.4$ and 1.2 m, and $z=1.5$ m, both the predicted and experimental results show that the highest temperatures occur in the center of the second main combustion region. The agreement is good in these regions. However, a relatively large discrepancy between the predicted and experimental results occurs at $y=2$ m, and $z=1.5$ and $z=2$ m. At the horizontal plane of $z=1.5$ m, the peak temperatures at the centers of the main combustion regions are overpredicted. Since the combustion air injection nozzles are located at $z=1.5$ m and the combustion air is injected into the furnace in the y-direction, the predicted peak temperatures occur at $z=1.5$ m. But, the measured peak temperature at $y=2.0$ m occurs at the second main reaction region on $z=2.0$ m. A possible explanation for the large difference may be attributed to the inlet combustion air flow distribution which, unfortunately, at this stage of the experimental program, there is as yet no available information. In the simulations, the inlet velocity profile of the combustion air is assumed to be uniform and in the y-direction only. In the experiment, however, the combustion air from the second burner may flow into the furnace with an upward vertical velocity component. It is also noticed that the predicted temperatures at the first and fourth main reaction regions at $y=2$ m and $z=2$ m agree well with the measured values. Nevertheless, the measured values in the first and fourth main reaction regions at $z=1.5$ m are much lower than the predicted data. This may be due to the heat loss through the gaps between the furnace walls and slab inlet and outlet.

8 Conclusions

The numerical simulations of turbulent non-premixed combustion process for a regenerative slab reheat furnace have been carried out using the conserved scalar/PDF approach and the chemical equilibrium concept. The numerical simulations have provided

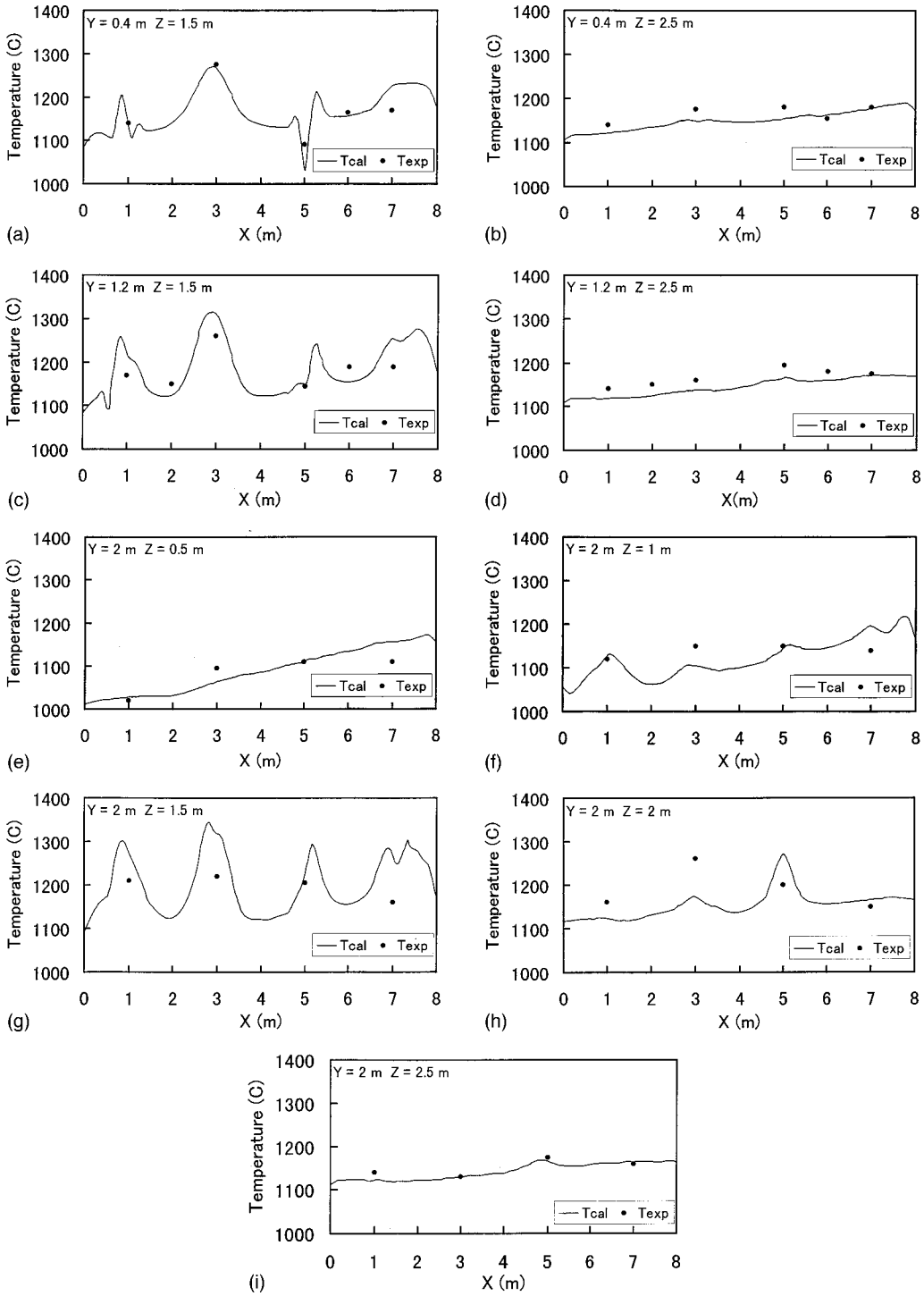

Fig. 6 Comparison of temperature distribution

detailed information on the flow and heat transfer fields in the furnace, which is of primary importance in performing the design analysis of furnaces. The comparisons with the experimental data indicate that the predictive capability of the numerical model used in this study is very encouraging and can be used as an analytical and design tool.

Acknowledgments

This work has been supported by the New Energy and Industrial Technology Development Organization (NEDO) under the contract of the Development of Higher Thermal Efficiency New Industrial Furnaces. The authors would also like to acknowledge the support from the NKK Corporation for the Research Fellowship (for C. Z.).

Nomenclature

a = absorption coefficient
B = bias error limit
C_g, C_d = constants in the equations for the mixture fraction and its variance
C_p = specific heat
C_1, C_2, C_μ = constants in the $k-\varepsilon$ model

f = mixture fraction
f'^2 = mixture fraction variance
h = enthalpy
h_o = overall external heat transfer coefficient
k = turbulent kinetic energy
L = thickness of the furnace wall layer
n = number of measurements
P = precision error limit
$P()$ = probability density function
p = pressure
q = radiation flux
S = source term in the governing equation
S_T = standard deviation of the temperature measurement
$S_{\bar{T}}$ = standard deviation of the mean temperature
T = temperature
$\bar{T}$ = mean temperature
U = uncertainty
u_i = velocity component in i-direction
x, y, z = Cartesian coordinates
x_i = Cartesian coordinate in i-direction
Z_k = mass fraction of element k

Greek Symbols

α = convection heat transfer coefficient
α, β = parameters in β-function
ε = turbulent kinetic energy dispassion rate
ϕ = general dependent variable
λ = thermal conductivity
μ = dynamic viscosity
ρ = density
σ = Stefan-Boltzmann constant
$\sigma_h, \sigma_k, \sigma_\varepsilon, \sigma_t$ = turbulent Prandtl/Schmidt number for h, k, ε, and f, f'^2
σ_s = scattering coefficient

Subscripts

c = coating layer
e = effective
f = fuel inlet
h = property for h
i, j = coordinate direction identifiers
o = oxidizer inlet
r = refractory layer
s = slab
t = turbulent

Subscripts

$-$ = conventional mean (Reynolds-averaged value)
$\sim$ = density-weighted mean (Favre-averaged value)
$'$ = Favre fluctuation variable

References

[1] Magnussen, B. F., and Hjertager, B. H., 1976, ''On Mathematical Models of Turbulent Combustion With Special Emphasis on Soot Formation and Combustion,'' *Proc. 16th Symposium (International) on Combustion*, The Combustion Institute, Pittsburgh, PA, pp. 719–729.

[2] Spalding, D. B., 1977, ''Development of the Eddy-Break-Up Model of Turbulent Combustion,'' *Proc. 16th Symposium (International) on Combustion*, The Combustion Institute, Pittsburgh, PA, pp. 1657–1663.

[3] Janicka, J., and Kollmann, E., 1978, ''A Two-Variables Formalism for the Treatment of Chemical Reactions in Turbulent H_2–Air Diffusion Flames,'' *Proc. 17th Symposium (International) on Combustion*, The Combustion Institute, Pittsburgh, PA, pp. 421–430.

[4] Pope, S. B., 1981, ''A Monte Carlo Method for the PDF Equations of Turbulent Reactive Flow,'' Combust. Sci. Technol., **25**, pp. 159–174.

[5] Cook, D. K., 1990, ''An Integral Model of Turbulent Non-Premixed Jet Flames in a Cross Flow,'' *Proc. 23rd Symposium (International) on Combustion*, The Combustion Institute, Pittsburgh, PA, pp. 653–660.

[6] Chen, J., and Kollmann, W., 1990, ''Chemical Models for PDF Modeling of Hydrogen-Air Nonpremixed Turbulent Flames,'' Combust. Flame, **79**, pp. 75–99.

[7] Buch, K. A., Dahm, W. J. A., Dibble, R. W., and Barlow, R. S., 1992, ''Structure of Equilibrium Reaction Rate Fields in Turbulent Jet Diffusion Flames,'' *Proc. 24th Symposium (International) on Combustion*, The Combustion Institute, Pittsburgh, PA, pp. 295–301.

[8] Gaffney, Jr., R. L., Girimaji, S. S., and Drummond, J. P., 1992, ''Modeling Turbulent/Chemistry Interactions Using Assumed PDF Methods,'' *AIAA/SAE/ASME/ASEE, 28th Joint Propulsion Conference and Exhibit*, July 6–8, Nashville, TN.

[9] Smith, N. S. A., Bilger, R. W., and Chen, J., 1992, ''Modelling of Nonpremixed Hydrogen Jet Flames Using a Conditional Moment Closure Method,'' *Proc. 24th Symposium (International) on Combustion*, The Combustion Institute, Pittsburgh, PA, pp. 263–269.

[10] Boardman, R. D., Eatough, C. N., Germane, G. J., and Smoot, L. D., 1993, ''Comparison of Measurements and Predictions of Flame Structure and Thermal NO_x in a Swirling, Natural Gas Diffusion Flame,'' Combust. Sci. Technol., **93**, pp. 193–210.

[11] Chen, C., Chang, K., and Chen, J., 1994, ''Application of a Robust β-pdf Treatment to Analysis of Thermal NO Formation in Nonpremixed Hydrogen-Air Flame,'' Combust. Flame, **98**, pp. 375–390.

[12] Peters, A. A. F., and Weber, R., 1995, ''Mathematical Modeling of a 2.25 MW_t Swirling Natural Gas Flame. Part1: Eddy Break-up Concept for Turbulent Combustion; Probability Density Function for Nitric Oxide Formation,'' Combust. Sci. Technol., **110–111**, pp. 67–101.

[13] Zhang, C., Ishii, T., and Sugiyama, S., 1997, ''Numerical Modeling of the Thermal Performance of Regenerative Slab Reheat Furnaces,'' Numer. Heat Transfer, Part A, **32**, No. 6, pp. 613–631.

[14] Jones, W. P., and Whitelaw, J. H., 1982, ''Calculation Methods for Reacting Turbulent Flows: A Review,'' Combust. Flame, **48**, pp. 1–26.

[15] Launder, B. E., and Spalding, D. B., 1974, ''The Numerical Computation of Turbulent Flows,'' Comput. Methods Appl. Mech. Eng., **3**, pp. 269–289.

[16] Cheng, P., 1964, ''Two Dimensional Radiating Gas Flow by a Moment Method,'' AIAA J., **2**, pp. 1662–1664.

[17] Patankar, S. V., 1980, *Numerical Heat Transfer and Fluid Flow*, Hemisphere, Washington, DC.

[18] van Doormaal, J. P., and Raithby, G. D., 1984, ''Enhancements of the SIMPLE Method for Predicting Incompressible Fluid Flows,'' Numer. Heat Transf., **17**, pp. 147–163.

[19] Incropera, F. P., and DeWitt, D. P., 1996, *Fundamentals of Heat and Mass Transfer*, 4th Ed., John Wiley and Sons, New York.

[20] Wheeler, A. J., and Ganji, A. R., 1996, *Introduction to Engineering Experimentation*, Prentice-Hall, Englewood Cliffs, NJ.

Surface Tension Effects on Post-Nucleation Growth of Water Microdroplets in Supersaturated Gas Mixtures

V. P. Carey
Mechanical Engineering Department,
University of California,
Berkeley, CA 94720-1740
e-mail: vcarey@me.berkeley.edu

Immediately after nucleation in a superheated gas mixture, the very small size of liquid droplets affects the condensation growth of the droplets in two ways: (1) The droplet size may be comparable to the mean free path of the gas molecules, resulting in noncontinuum transport effects, and (2) surface tension effects may strongly alter the conditions at the interface of the droplet. In the study reported here, a direct simulation Monte Carlo scheme was used to model the molecular transport during quasi-equilibrium condensation growth of water microdroplets in a supersaturated mixture of water vapor and a noncondensable gas. In the simulation, the boundary condition at the droplet surface is treated in a manner that allows us to model surface tension effects on transport. Results of calculations are presented for water vapor and argon mixtures for which some experimental data on droplet growth rates exists. The simulation results indicate that surface tension effects play a significant role in the determination of droplet growth rates during early stages of droplet growth. In particular, the results indicate that the droplet growth rate, droplet temperature, and the temperature slip at the interface pass through maxima as the droplet grows. These trends are a consequence of the shift in equilibrium vapor pressure due to surface tension effects at small droplet radii. [S0022-1481(00)02702-X]

Keywords: Condensation, Droplet, Microscale, Monte Carlo, Surface Tension

Introduction

Condensation of liquid microdroplets in a supersaturated mixture of its vapor and a noncondensable gas is an important fundamental process during cloud formation in the atmosphere and in a variety of technological applications. For the initial stage of droplet growth in such circumstances, the size of the droplets is often comparable to the mean free path of the surrounding gas molecules. As the droplet grows, the heat and mass transfer associated with the process traverses the transition regime between free molecular and continuum transport. Since neither free molecular theory nor continuum theory is accurate in the transition regime, prediction of the condensation growth of microdroplets in this size range is particularly challenging.

There have been a number of investigations of noncontinuum effects on condensation growth of droplets. In an early studies, Kang [1], Sampson and Springer [2], Shankar [3], Gajewski et al. [4], and Lou [5] developed kinetic-theory based analyses of droplet condensation growth. More recent investigations by Loyalka [6], Lang [7], Chernayak and Margilevskiy [8], Young [9–10], Peters and Paikert [11], and Peters and Meyer [12] also explored analytical extensions of kinetic theory as means of predicting heat and mass transfer between a condensing droplet and a surrounding gas at arbitrary Knudsen numbers. Widder and Titulaer [13] formulated an analysis of transport to a condensing droplet in a supersaturated mixture of a light noncondensable gas and a heavy vapor species. Their analysis was constructed in terms of the Navier-Stokes equations and the Klien-Kramers equation for Brownian motion of the vapor molecules. The governing equations were solved numerically to predict the droplet temperature and growth rate for specified ambient conditions.

An alternate approach to the kinetic theory based models used in the above studies is to use a molecular simulation model. This type of approach has been used by El-Afify and Corradini [14] to model low-pressure transient condensation of mercury vapor on a vertical flat surface. In a subsequent paper, El-Afify and Corradini [15] extended their simulation model to transient condensation of mercury vapor on a flat vertical surface in the presence of a monoatomic noncondensable gas. More recently, a molecular simulation model has been used by Carey et al. [16] to model condensation growth of water microdroplets in supersaturated mixtures of water vapor and a noncondensable gas. Droplet condensation in a supersaturated gas is fundamentally different from the process of condensation on a flat surface studied by El-Afify and Corradini [14–15]. These investigators considered condensation in the absence of forced or free convection. Except for the limiting case of free molecular transport in the surrounding gas, condensation on a flat surface is an intrinsically time-varying process in which the thermal and mass concentration layers in the gas grow progressively thicker with time. In contrast, for any specified supersaturated ambient conditions, steady temperature and concentration profiles are established in the gas for condensation on a spherical droplet of fixed size.

For most circumstances of interest, the size of the droplet increases significantly during the condensation growth over a time interval that is relatively long compared to the time required to achieve steady temperature and concentration fields in the surrounding gas. In such circumstances, the transport in the gas at any instantaneous radius r_d during the droplet growth is well approximated by the steady-state quasi-equilibrium transport that results for a droplet of fixed r_d condensing at the specified ambient conditions.

The microphysics of condensation in the presence of a noncondensable gas is significantly more complex than condensation of the pure vapor phase of the liquid in the droplet. Condensation removal of vapor at the droplet interface and mass diffusion result in a water vapor concentration at the interface which can be significantly different from that in the far ambient. For a quasi-

Contributed by the Heat Transfer Division for publication in the JOURNAL OF HEAT TRANSFER. Manuscript received by the Heat Transfer Division, June 7, 1999; revision received, Jan. 13, 2000. Associate Technical Editor: T. Avedisian.

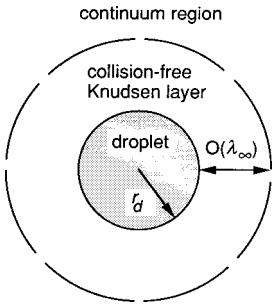

Fig. 1 Transport domains near a droplet under transition regime conditions

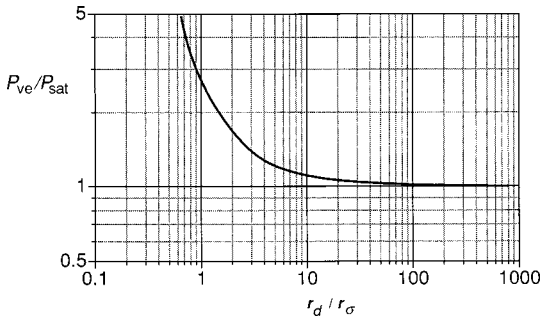

Fig. 2 Variation of equilibrium vapor pressure with droplet radius

equilibrium process, the interface temperature must equal the saturation temperature of the liquid species at the partial pressure of the vapor in the gas at the interface. Thus, the droplet surface temperature cannot be specified a priori. Any transport analysis scheme for this type of droplet condensation process must therefore include a means of determining the interface temperature as an integral part of the analysis. Also, to handle an arbitrary mixture, treatment of molecules that store energy by rotation as well as translation must be incorporated into the model.

Two conditions must be satisfied for the quasi-equilibrium model to accurately predict transport at any instant during the droplet growth process. First, the time scale associated with internal conduction inside the droplet must be small compared to the characteristic time associated with transport in the gas. Since the liquid thermal conductivity is large compared to that of the vapor, this condition is satisfied for the systems of interest here. This line of reasoning implies that the temperature is essentially uniform within the droplet but may vary slowly with time as the droplet grows. In addition, the quasi-equilibrium model treats the radius as fixed during the simulation, even though the droplet is actually growing during the condensation process. This is a good approximation if the characteristic time of the droplet growth process $(r_d/(dr_d/dt))$ is large compared with the characteristic time for transport in the gas. This requirement is met for the systems studied here. The droplet size changes significantly over milliseconds while times on the order of microseconds are required to establish steady transport in the gas.

In the very early stages of growth, immediately after nucleation, the droplet size is comparable to or smaller than the mean free path of the molecules in the surrounding gas. For such circumstances, the Knudsen layer region within about one mean free path of the droplet surface is essentially a collision-free zone. This is shown schematically in Fig. 1. Immediately after nucleation, the droplet size may be so small that the extent of the Knudsen layer is large compared to the droplet and the transport is in the free-molecular regime. As the droplet grows, the size of the droplet becomes comparable to and then larger than the thickness of the Knudsen layer with the associated changes from free molecular transport to the transition regime and then to continuum transport.

For very small droplets, the surface tension shifts the equilibrium vapor pressure from the flat interface value. Classical thermodynamics dictates that this shift is given by

$$P_{ve} = P_{\text{sat}}(T_d)\exp(r_\sigma/r_d) \tag{1}$$

where

$$r_\sigma = \frac{2\sigma_{lv}}{\rho_l R T_d}. \tag{2}$$

In the above relation, T_d is the droplet temperature, r_d is the droplet radius, and $P_{\text{sat}}(T_d)$ is the flat-interface saturation pressure for water at T_d. When the radius of the droplet is large compared to r_σ, the equilibrium vapor pressure at the droplet surface is that for a flat interface, assuming that local thermodynamic equilibrium exists there. As seen in Fig. 2, r_d must be smaller than $10\,r_\sigma$ before the departure from the flat-interface vapor pressure is significant. In general, however, the departure from the flat interface vapor pressure can be substantial for conditions immediately following water droplet nucleation in water-vapor and noncondensable gas mixtures. A major objective of this study was to determine quantitatively the effect of this shift in equilibrium vapor pressure on the transport in the gas and the droplet growth rate.

The investigation summarized in this paper used a stochastic, Monte Carlo direct simulation scheme as a method for predicting the molecular transport to a condensing microdroplet in the presence of a second noncondensable species. The simulation was specifically applied to microdroplets condensing under free molecular and transition regime conditions. The simulation method used in this study is similar to that used by Carey et al. [16], incorporating modifications to account for condensation and to allow determination of the initially unknown temperature at the droplet surface.

In the study of Carey et al. [16], the accuracy of the simulation method used in this study was assessed by comparing its predictions with previously obtained data for droplet condensation in supersaturated argon-water gas mixtures. For an accommodation coefficient value of 1.0, the simulation predictions were found to agree well with droplet growth rates inferred from measurements in a supersaturated mixture of argon and water vapor for droplet radii greater than 0.4 μm. In that study no efforts were made to explore the transport or droplet growth rate trends at smaller radius values which characterize droplet immediately after nucleation. In the study summarized here, the simulation scheme used by Carey et al. [16] was extended to examine transport at the small droplet radii which arise immediately following droplet nucleation where surface tension may significantly alter the equilibrium vapor pressure. The simulation results for such conditions in an argon-water vapor mixture were examined to assess the effects of surface tension on transport in the surrounding gas and the associated droplet growth rate.

Application of the Particle Simulation Method

The particle simulation method used here is a derivative of the direct simulation Monte Carlo technique pioneered by Bird [17]. Some of the refinements developed by McDonald [18] and Baganoff and McDonald [19] have also been incorporated into the scheme used here. The main features of the particle simulation method are described briefly in the Appendix. The special features added in our investigation to model the condensation growth of a spherical droplet in a supersaturated mixture of vapor and a noncondensable gas are described in detail below.

To minimize memory requirements and computational time, the simulation domain was limited to one octant around the droplet, as shown in Fig. 3. In addition, to avoid the computational costs of extending the simulation out to large radial distances, in this study the simulation domain was limited to a radial distance of

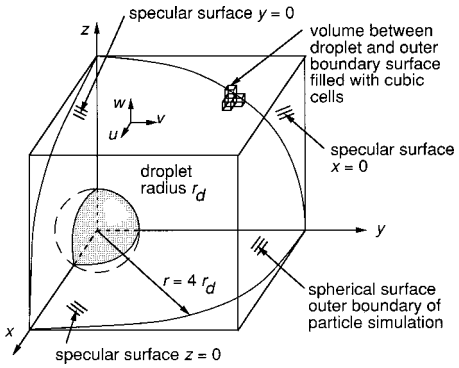

Fig. 3 Boundaries and cell grid for the simulation domain

four sphere radii. For free molecular conditions, the simulation boundary condition was set to the ambient conditions at $r=4r_d$. For transition regime conditions, the simulation boundary condition was matched to the continuum transport solution beyond $r=4r_d$.

For transition regime conditions, the temperature and water vapor concentration gradients decrease rapidly with distance from the sphere, approximately proportional to r^2. Consequently, while the temperature may drop and the water concentration may rise significantly over a few mean free paths near the sphere, beyond $r=4r_d$ it will take many free paths for the temperature to change significantly. The local Knudsen number $\lambda(dT/dr)/(T_d-T_\infty)$ decreases rapidly with distance from the sphere, causing the temperature and concentration profiles to approach those for continuum transport at large r. This line of reasoning, which divides the region near the sphere into a noncontinuum region close to the body and a continuum transport region farther away was first used by Langmuir [20] to facilitate the analysis of transition regime transport to a cylindrical body. The matching process for transition regime conditions used in the simulation scheme is therefore consistent with Langmuir's model which has been widely used for problems of this nature.

The octant simulation region shown in Fig. 3 was bounded by the surface of the sphere at $r=r_d$, the outer boundary at $r=4r_d$, and specularly reflecting planar surfaces at $x=0$, $y=0$ and $z=0$. The specular surfaces which lie along planes of symmetry have the effect of giving the octant the same statistical behavior as a complete sphere surrounded by particles. Each particle in the simulation represents N_{mpp} molecules. The region bounded by these surfaces was filled with cubic cells which were used to collect collision candidate pairs and define regions over which particle properties were averaged to obtain macroscopic thermodynamic characteristics of the gas adjacent to the droplet.

Particles that move beyond the outer boundary when the particles are advanced along their trajectory were simply removed from the simulation. During each time-step, particles of each species are added to the simulation just inside the $r=4r_d$ boundary. The rate of water particle addition $\dot{n}_w$ and the rate of nitrogen particle addition $\dot{n}_n$ are computed as

$$\dot{n}_w = N_{\mathrm{mpp}}(\pi/2)(4r_d)^2 j_w \tag{3}$$

$$\dot{n}_n = N_{\mathrm{mpp}}(\pi/2)(4r_d)^2 j_n \tag{4}$$

where j_w and j_n are the fluxes of water and nitrogen molecules across a surface predicted by kinetic theory for a mixture at a pressure P_∞, temperature T_4 and water mole fraction of $X_{w,4}$.

$$j_w = \left(\frac{k_B T_4}{2\pi m_w}\right)^{1/2}\left(\frac{X_{w,4}P_\infty}{k_B T_4}\right) \tag{5}$$

$$j_n = \left(\frac{k_B T_4}{2\pi m_n}\right)^{1/2}\left(\frac{(1-X_{w,4})P_\infty}{k_B T_4}\right) \tag{6}$$

This treatment allows the simulation domain to establish whatever mean particle density is necessary to balance the inward and outward fluxes at the outer boundary. Equations (5) and (6) are derived from equilibrium kinetic theory. Implicit in their use here is the idealization that equilibrium Boltzmann distributions are valid at $r=4r_d$. This idealization is justified because bulk motion of the gas induced by condensation at the droplet surface is small compared to mean molecular velocities, and because temperature and concentration gradients are low at this location.

Based on the observation that the liquid thermal conductivity is large compared to that of the vapor, conduction inside the droplet was idealized as being very fast. The droplet Biot number, which essentially equals the ratio of the gas conductivity to the liquid conductivity, is approximately 0.27. For the conditions of interest in this study, temperature variation inside the droplet is estimated to be less than 0.6 K. The temperature was therefore taken to be uniform within the droplet and transient conduction effects in the liquid droplet were not considered in the energy balance at the droplet surface.

When molecules from a surrounding gas enter the interfacial region near a solid or liquid phase, experimental evidence and molecular simulation studies indicate that only a fraction of the incident molecules thermally interact with the molecules of the condensed phase (see, for example, references by Paul [21] and Yasuoka et al. [22]. It is generally acknowledged that the exact value of this fraction may vary from one system to another. In our simulations, this behavior is stochastically represented by specifying an accommodation coefficient σ_t which is taken to equal the fraction of incident molecules that thermally interact with the droplet surface.

If a particle strikes the droplet surface during a given time-step, a random number $\Re$ uniformly distributed on [0,1] is compared to the specified accommodation coefficient. If $\Re > \sigma_t$, the particle is diffusely scattered from the surface. Its speed and rotational energy are left unchanged, but its direction is randomly set by sampling a distribution that, on the average, isotropically scatters particles from the surface. If $\Re \leq \sigma_t$, the particle interacts thermally with the surface.

Each thermally interacting particle is treated as if it merges into the liquid droplet, delivering its energy, including an energy of vaporization, to the droplet. Computationally, particles that merge into the droplet are removed from the simulation. The number of particles absorbed in this manner is counted, and the energy delivered to the droplet by these particles is summed.

In a subsequent portion of the time-step calculations, particles are added to the simulation domain just beyond $r=r_d$. Before executing the emission of particles from the droplet surface, the temperature of the droplet surface is computed. Kinetic theory predicts that for an interface at equilibrium, the flux of emitted water vapor molecules is given by

$$j_w = \sigma_t \frac{P_{ve}(T_d)}{(2\pi m_w k_B T_d)^{1/2}}. \tag{7}$$

For the spherical microdroplets considered here, the equilibrium vapor pressure P_{ve} in the above relation is a function of the droplet temperature T_d and the droplet radius r_d as given by Eqs. (1) and (2). The surface tension is determined from the relation

$$\sigma_{lv} = 0.07583 - 0.0001477(T_d - 273.2) \tag{8}$$

where T_d is in K and σ_{lv} is in N/m. This relation is an established surface tension relation for a water liquid-vapor interface at equilibrium (see Carey [23]) which is extrapolated here to nonequilibrium conditions. For the smallest droplets considered in this study, the interfacial tension is more properly interpreted as the mean interfacial free energy per unit area of the droplet. Its use in this model analysis is consistent with this interpretation.

In the limit of long times, the steady-state energy exchange at the interface must satisfy conservation of energy

$$\sum_{i=1}^{N_{\text{steps}}} (E_{\text{gain}})_i = 3k_B T_d N_{\text{mpp}} \sum_{i=1}^{N_{\text{steps}}} (N_{\text{non}})_i + \frac{\pi}{2} r_d^2 j_w \times \Delta t \left(\hat{u}_{lv} + \frac{1}{2} k_B T_d \right) \tag{9}$$

In the above equation, $(N_{\text{non}})_i$ is the number of noncondensable molecules which thermally interact with the surface and then are re-emitted into the gas and $(E_{\text{gain}})_i$ is the energy delivered by molecules colliding with the droplet surface in time-step *i*. The left side of the above equation is the total energy delivered by molecules colliding with the surface through N_{steps} time-steps of the simulation. The right side is the energy carried away by molecules leaving the droplet surface. The first term on the right represents energy carried away by noncondensable gas molecules re-emitted to the gas, and the second represents energy removed by water molecules. Combining Eqs. (7) and (8) and substituting into Eq. (9) yields

$$\sum_{i=1}^{N_{\text{steps}}} (E_{\text{gain}})_i = 3k_B T_d N_{\text{mpp}} \sum_{i=1}^{N_{\text{steps}}} (N_{\text{non}})_i + \frac{\pi r_d^2 \sigma_t P_{\text{sat}}(T_d)}{2(2\pi m_w k_B T_d)^{1/2}} \times \Delta t \left(\hat{u}_{lv} + \frac{1}{2} k_B T_d \right) \exp\left(\frac{2\sigma_{lv}}{\rho_l r_d R T_d} \right). \tag{10}$$

In Eq. (10) P_{sat} and $\hat{u}_{lv}$ are functions of temperature. For the purposes of our simulation calculations P_{sat} was computed using the following relation which is a curve fit to data for water between 10°C and 70°C based on the Clapeyron equation.

$$P_{\text{sat}}(T_d) = e^{(A - B/T_d)} \tag{11}$$

In Eq. (9), $A = 18.71$ and $B = 5240$ for T_d in *K* and P_{sat} in kPa. Values of $\hat{u}_{lv}$ were determined using the following linear fit to data for water between 10°C and 70°C:

$$\hat{u}_{lv} = 7.016 \times 10^{-20} [1 - (T_d - 283.2)/825.4] \tag{12}$$

where $\hat{u}_{lv}$ is in J/molecule and T_d is in K. In the simulation, the summations of incident energy and number of incident noncondensable molecules were updated at each time-step. The droplet temperature was computed at each time-step by iteratively solving Eqs. (10), (11), and (12) simultaneously. A guess of the surface temperature was provided to initiate the simulation. As the number of time-steps increases, the surface temperature computed in this manner converges to a value which is interpreted as being the actual physical temperature of the droplet for the quasi-steady process being modeled in the simulation.

Once the surface temperature of the droplet was determined for a given time-step, particles were computationally emitted from the droplet surface. First, N_{non} noncondensable particles were emitted, so that there is no net transfer of the noncondensable species to the droplet during the time-step. Then, particles of the condensable species were emitted from the droplet surface until an energy balance was achieved.

Each time a particle was emitted from the droplet surface, the energy carried away from the droplet by the particle was added to a cumulative total for the time-step. When this total just exceeded the amount delivered to the sphere during the time-step, the particle addition process was stopped. The amount by which the energy for the added particles exceeded that for the incoming particles was subtracted from the energy of the incoming particles in the next time-step. This imposed a zero-net energy flux condition on the droplet interface. However, the number of incident condensable particles exceeded the number of emitted condensable particles, resulting in a finite net mass flux to the droplet surface.

For both condensable and noncondensable particles, the location at which a particle is added to the simulation was determined by randomly sampling a distribution function which produces a uniform flux of particles over the spherical surface of the droplet. The velocity components and rotational energy were randomly sampled from appropriate Boltzmann distributions for molecules crossing a fixed surface in a gas at the specified sphere temperature T_d. The distributions used are defined in Eqs. (*A*1)–(*A*3) in the Appendix.

The energy of saturated water vapor molecules, on average, exceeds that of saturated liquid molecules by $\hat{u}_{lv}$. At temperature T_d, the mean energy of a water vapor molecule is $3k_B T_d$. The energy of an arbitrary water molecule in the gas with translational energy ε_{tr} and rotational energy ε_{rot} thus exceeds the mean energy of the liquid water molecules in the droplet by $\varepsilon_{\text{tr}} + \varepsilon_{\text{rot}} - 3k_B T_d + \hat{u}_{lv}$. In the energy balance calculations at the droplet interface, the mean energy of the saturated liquid molecules was taken as the level of zero energy for water molecules. The energy delivered to the droplet by one interacting water particle from the surrounding gas is therefore given by

$$\Delta E_{w,\text{in}} = N_{\text{mpp}} (\varepsilon_{\text{tr}} + \varepsilon_{\text{rot}} - 3k_B T_d + \hat{u}_{lv}) \tag{13}$$

where N_{mpp} is the number of molecules per particle in the simulation. This relation was used to compute the energy delivered to the droplet by a water particle striking and interacting with the droplet. The energy delivered by one nitrogen particle is given by $N_{\text{mpp}}(\varepsilon_{\text{tr}} + \varepsilon_{\text{rot}})$. Based on similar reasoning, the following relation was used to compute the energy removed from the droplet by an emitted water particle

$$\Delta E_{w,\text{em}} = N_{\text{mpp}} (\varepsilon_{\text{tr}} + \varepsilon_{\text{rot}} - 3k_B T_d + \hat{u}_{lv}) \tag{14}$$

where ε_{tr} and ε_{rot} were obtained by sampling the appropriate Boltzmann distributions at T_d.

In the simulation calculations in this study, the simulation domain shown in Fig. 3 was filled with cubic cells which formed a uniform Cartesian mesh. The radius of the droplet in the simulations ranged from 0.7 nm to 1.0 μm. The effects of cell and time-step sizes on the results of the simulation were explored and consequently the cell size was chosen to be on the order of one mean free path. The mean free path for the system considered here is on the order of 0.09 μm. For the droplet sizes considered here this corresponds to a range of Knudsen number Kn_D from 0.045 to 64. The time-step was chosen so a particle with average speed traveled approximately half a mean free path in one time-step. Generally, the results were found to be insensitive to the choice of these parameters as long as they were close to the values indicated by these guidelines. The side of the cell varied from 0.7 nm for the smallest droplets to 0.125 μm for the largest droplets considered in this study. The number of cells used was a compromise between accuracy and computational effort. The ratio of the number of molecules per particle N_{mpp} was chosen in each simulation to compromise between computational accuracy and storage limitations on the computer. The values used in the calculations reported here ranged from 0.0003 to 1784 molecules per particle. Simulations were typically run for 16,000 to 240,000 time-steps, with a time-step typically being 20–200 picoseconds. For the smallest droplets, time-steps were on the order of 20 picoseconds. Altering the time-step by ± 50 percent had a negligible effect (<0.1 percent) on transport parameters predicted by the simulation.

After running the simulation for a sufficiently long time, the simulation predicts the equilibrium temperature and concentration fields adjacent to the surface of the droplet for arbitrarily specified values of the ambient pressure and the temperature and water vapor concentration at $r = 4r_d$. For transition regime conditions, the matching procedure mentioned above was then used to determine the corresponding values of the temperature and water vapor concentration in the far ambient. To do so, the net heat flux from the droplet surface (carrying away the latent heat of the net condensation effect) is first computed from the simulation results using the following relation:

$$q_d'' = \frac{\Delta N_{\text{net}} \hat{u}_{lv} N_{\text{mpp}}}{(4\pi r_d^2/8) N_{\text{steps}} \Delta t} \tag{15}$$

where N_{steps} is the number of time-steps in the simulation and ΔN_{net} is the net number of water particles transferred to the droplet due to particle interactions during the simulation to that time-step. Conservation of energy requires that at steady state, the heat flux through the spherical surface at $r/r_d=4$ must be given by

$$q''_4=(4)^{-2}q''_d=q''_d/16. \tag{16}$$

For transition range conditions, transport of energy and mass beyond $r=4r_d$ are treated as continuum transport from an evaporating sphere with radius $4r_d$ for a surface temperature of T_4 and a heat flux of q''_4. The outward velocity due to the net generation of molecules at the droplet surface is negligible at $r=4r_d$ and transport in the outer continuum region is, to a good approximation, by conduction only. It follows from the well-known continuum solution for steady conduction from a sphere that

$$T_\infty=T_4+\frac{r_d q''_d}{4k_v}. \tag{17}$$

For transition regime conditions ($0.01<\mathrm{Kn}_D<2$), Eqs. (15) and (17) were used to determine the ambient temperature T_∞. A completely analogous analysis of mass diffusion allows matching of the particle simulation to a continuum concentration field in the region beyond $r=4r_d$. Following the same line of analysis as for the conduction heat transfer yields the following relations for the net mass flux of water vapor at the droplet surface m''_d and the ambient water vapor concentration $X_{w,\infty}$.

$$m''_d=\frac{\Delta N_{\mathrm{net}} N_{\mathrm{mpp}}}{(4\pi r_d^2/8)N_{\mathrm{steps}}\Delta t} \tag{18}$$

$$X_{w,\infty}=X_{w,4}+\frac{r_d m''_d}{4\rho_v D_v} \tag{19}$$

When required, the thermal conductivity of the mixture was computed using the method of Mason and Saxena [24] and the diffusion coefficient for water vapor was determined using the empirical correlation of Wilke and Lee [25]. Note that for free molecular transport ($\mathrm{Kn}_D>2$), calculations to determine the water vapor concentration and temperature in the far field were unnecessary since the ambient conditions are those specified at the edge of the simulation ($r=4r_d$). For free molecular transport or transition regime transport, the growth rate of the droplet can be computed as

$$\frac{dr_d}{dt}=\frac{m''_d}{\rho_l} \tag{20}$$

where m''_d is computed using Eq. (18).

Simulation Predictions for Argon-Water Mixtures

In their recent study, Peters and Paikert [11] experimentally determined the variation of water microdroplet size with time for droplets in supersaturated and superheated gas mixtures in a shock tube apparatus. These experiments produced a low-volume concentration of virtually monodisperse droplets which grew through condensation while the gas was supersaturated and decreased in size when the gas was superheated. In this study, the intensity of scattered laser light was analyzed using Mie scattering theory to determine the variation of radius with time. These investigators presented plots of the measured radius versus time for droplet growth in water-argon mixtures. To evaluate the molecular simulation scheme described above, Carey et al. [16] determined the mean growth rate of the droplet between successive measured points in the Peters and Paikert [11] data and compared the values to the simulation predictions for the same conditions.

To conduct the comparison described above, it is necessary to choose a value of the thermal accommodation coefficient for use in the simulation. The value of the accommodation coefficient σ_t for a condensing or evaporating interface has been the subject of much debate. The tabulation assembled by Paul [21] lists values ranging from 0.02 to 0.04 for some liquids to values very near 1.0 for others. Mills [26] has suggested that molecular accommodation should be imperfect only when the interface is impure. Paul [21] notes that in almost every case where σ_t was found to be appreciably less than one, the average condition of the vapor molecules was different from that for the liquid phase because of association, disassociation or polymerization. This suggests that if the water in this study is assumed to be virtually pure and that association, disassociation and polymerization do not occur to any significant degree, the accommodation coefficient should be close to unity. On the other hand, recent deterministic molecular simulation studies by Yasuoka et al. [22] imply that the accommodation coefficient for a pure water interface should be near 0.4. In the analysis of their data, Peters and Paikert [11] suggested a value of 1.0 for the accommodation coefficient as best fitting their data in an analytical kinetic-theory model.

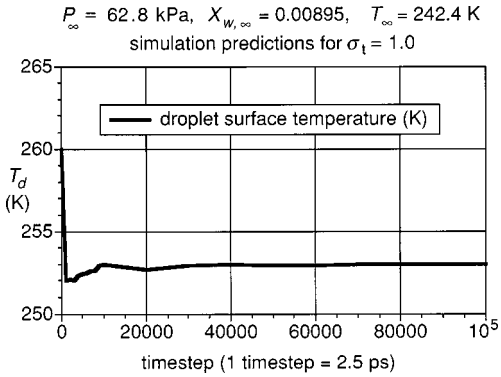

Fig. 4 Variation of droplet temperature at 1000 step intervals during the simulation for a water droplet with a radius of 0.4 μm surrounded by an argon-water vapor mixture

Carey et al. [16] found that simulation calculations for $\sigma_t=1.0$ best fit the droplet growth rate data from the experiment of Peters and Paikert [11]. The accommodation coefficient was therefore set at 1.0 in the simulation calculations in this study. In the study summarized here, simulation calculations were performed for one of the argon-water vapor mixtures tested experimentally by Peters and Paikert [11]. These calculations span the range of droplet radius from values near the critical radius r_c where nucleation occurs, to 1 μm where transition conditions merge into the continuum transport regime. Figure 4 shows the variation of the droplet temperature with time during the simulation calculation for a droplet radius of 0.4 μm, based on samples at 1000 step intervals. It can be seen that the iteration of the droplet temperature achieved by solving Eq. (10) at successive time-steps does converge quickly to a value that remains steady with time. This steady value is interpreted as the droplet temperature that corresponds to the droplet size in the simulation during the growth process.

The simulation predictions of the variation of droplet growth rate with droplet size for one of the argon-water vapor mixtures studied by Peters and Paikert [11] are plotted in Fig. 5. Results are shown for droplet radii ranging from just above the critical radius (for homogeneous nucleation, see Carey [23]) to droplets with a radius of 1 μm. Simulation results are shown with the effect of surface tension included and with it artificially removed (σ_{lv} set to zero). It can be seen that these predictions of the growth rate variation with radius are the same except at very low radii. The surface tension effect on equilibrium vapor pressure results in a strong reduction in the droplet growth rate as the critical radius is approached. Also shown in Fig. 5 is the prediction of standard continuum theory using Fourier's law and Fick's law to predict the simultaneous heat and mass transfer associated with quasi-

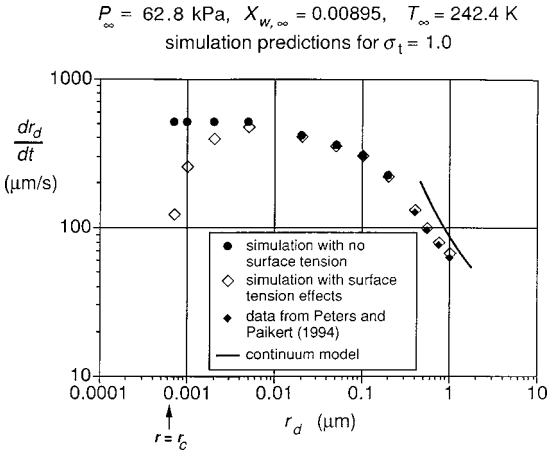

Fig. 5 Comparison of simulation predictions of droplet growth rates with and without surface tension effects on vapor pressure for the droplet growth conditions in the experiment of Peters and Paikert [11]. Continuum theory predictions and growth rates determined from the data of Peters and Paikert [11] are also shown.

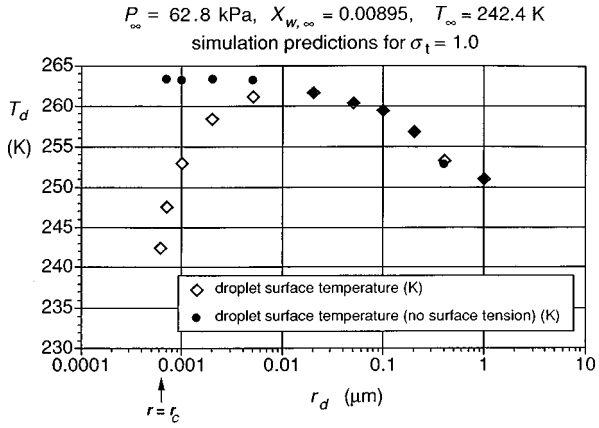

Fig. 6 Comparison of simulation predictions of T_d with and without surface tension effects on vapor pressure for the droplet growth conditions in the experiment of Peters and Paikert [11]

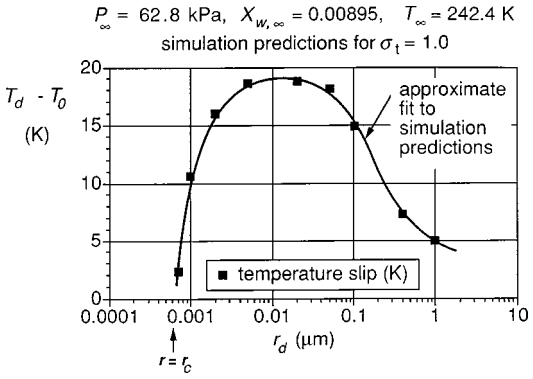

Fig. 7 Simulation predictions of the variation of temperature slip at the droplet surface for growth conditions in the experiment of Peters and Paikert [11]

steady condensation at the indicated conditions. For the continuum model, the governing equation and boundary conditions are

$$r^{-2}\frac{d}{dr}(r^2 u_r) = 0 \tag{21}$$

$$u_r\frac{du_r}{dr} = -\frac{1}{\rho_v}\frac{dP}{dr} + \left(\frac{\nu_v}{r^2}\right)\frac{d}{dr}\left(r^2\frac{du_r}{dr}\right) - \left(\frac{2\nu_v u_r}{r^2}\right) \tag{22}$$

$$\rho_v c_p u_r\frac{dT}{dr} = r^{-2}\frac{d}{dr}\left(r^2 k_v\frac{dT}{dr}\right) \tag{23}$$

$$u_r\frac{dX_w}{dr} = r^{-2}\frac{d}{dr}\left(r^2 D_v\frac{dX_w}{dr}\right) \tag{24}$$

$$r = r_d:\ u_r = -\left(\frac{k_v}{\rho_v h_{lv}}\right)\left(\frac{dT}{dr}\right)_{r=r_s},\quad T = T_{\text{sat}}(X_w P_\infty, r_d) \tag{25}$$

$$r \to \infty:\ u_r \to 0,\quad T \to T_\infty,\quad X_w \to X_{w,\infty}. \tag{26}$$

Equations (21), (22), (23), and (24) represent conservation of total mass, momentum, energy and water vapor, respectively. In this formulation, $T_{\text{sat}}(X_w P_\infty, r_d)$ is the saturation temperature of water at the partial pressure $X_w P_\infty$, corrected for the effect of surface tension at the droplet radius r_d. For these circumstances, the continuity Eq. (21) dictates that the radial velocity decays from its value at the droplet surface proportional to r^{-2}. The continuity, water vapor transport, and energy transport equations can be solved together with the boundary conditions to obtain the velocity, concentration, and temperature fields. The momentum equation can then be solved for the pressure field if desired. The continuum analysis used here is similar to that described by Mills [27] for evaporating droplets, with the thermal conductivity and diffusivity evaluated using the methods described by Mason and Saxena [24] and Wilke and Lee [25].

The above system of equations and boundary conditions was solved to produce the continuum curve indicated in Fig. 5. The simulation predictions of droplet growth rate are seen to agree well with the experimentally determined growth rates and to approach the continuum predictions at larger droplet sizes. Of particular interest is that the simulation model predicts that the droplet growth rate achieves a maximum value in the transition regime which is attributable to the interaction of surface tension effects and transport variation with droplet size. The extremum in the growth rate is a consequence of the variations of the heat transfer coefficient and equilibrium vapor pressure with droplet size. For the small droplet sizes characteristic of conditions immediately after onset of nucleation, the heat transfer coefficient is large, but the driving temperature difference is small because of the surface-tension-induced vapor pressure shift at small droplet sizes. As the droplet grows in size, the vapor pressure shift diminishes and the driving temperature difference increases faster than the heat transfer coefficient decreases. This initially produces an increase in the growth rate as the droplet grows. Eventually the reduction in the heat transfer coefficient dominates, causing the droplet growth rate to peak and then decline with increasing droplet size. It is noteworthy that these results are consistent with the predictions of the kinetic theory model of Peters and Meyer [12], which also predicts a maximum in the droplet growth rate with increasing size for water droplets growing in supersaturated pure steam.

This investigation also examined other microscale features of the droplet growth process predicted by the simulation for the experimental conditions of Peters and Paikert [11]. Simulation predictions of the droplet temperature at different droplet radii are shown in Fig. 6. Predictions are shown for simulations with the effect of surface tension included and with it artificially removed (σ_{lv} set to zero). Surface tension effects are seen to strongly affect the droplet temperature at the smallest radius values immediately following nucleation. A peak in the droplet temperature occurs in the transition regime.

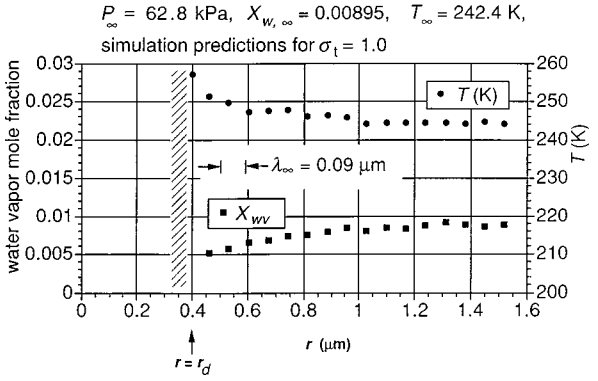

Fig. 8 Simulation prediction of the concentration and temperature profiles near the droplet at a radius of 0.4 μm for the growth conditions in the experiment of Peters and Paikert [11]

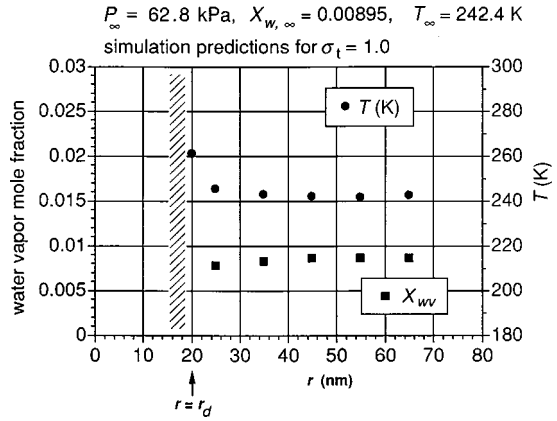

Fig. 9 Simulation prediction of the concentration and temperature profiles near the droplet at a radius of 20 nm for the growth conditions in the experiment of Peters and Paikert [11]

The variation of the temperature slip at the droplet surface predicted by the simulation for the conditions in the Peters and Paikert [11] experiment is shown in Fig. 7. As expected, the slip decreases towards zero as the droplet size increases and the transport approaches continuum behavior. The results also indicate that the slip tends towards zero as the radius approaches r_c, which is a consequence of the fact that the droplet is in unstable equilibrium with the surrounding supersaturated gas at the critical radius. The result is that a maximum level of temperature slip occurs in the transition regime.

The temperature and concentration profiles near the droplet predicted by the simulation for a 0.4 μm radius droplet under the conditions in Peters and Paikert [11] experiment are shown in Fig. 8. The profiles for a droplet with a radius of 20 nm are similarly shown in Fig. 9. These profiles exhibit the expected asymptotic approach to the ambient temperature and concentration at large r. The temperature slip is larger for the smaller droplet size which corresponds to free molecular transport conditions.

Concluding Remarks

This study explored the use of a direct simulation Monte Carlo technique to predict the effects of surface tension on transport during post-nucleation quasi-equilibrium growth of water microdroplets in supersaturated gas mixtures. The simulation employed a treatment of the droplet interface boundary condition which makes it possible to compute the droplet surface temperature as part of the simulation calculation. This appears to be the first time such a simulation model has been employed to model transport near a droplet during the early stages of condensation growth from the critical radius through sizes that correspond to continuum transport. At the largest droplet sizes considered in this study, the growth rates predicted by the simulation are consistent with experimental measurements and with trends indicated by the continuum transport model.

At droplet sizes between 0.7 nm and 0.4 μm, which correspond to free molecular and transition transport rages, the results of the simulation reveal interesting features of the variation of droplet temperature and growth rate as the droplet grows. The observed maxima in the droplet growth rate, the droplet temperature and the temperature slip as the droplet grows through these regimes are somewhat unexpected consequences of surface tension effects on the equilibrium vapor pressure as the droplet grows. This trend can be understood in terms of changes in the vapor pressure shift and variation of the heat transfer coefficient with droplet size. At the smallest radius values, the heat transfer coefficient associated with the droplet growth process is large, but the driving temperature difference is small because of the vapor pressure shift at small droplet sizes. As the droplet becomes larger, the vapor pressure shift becomes negligible faster than the heat transfer coefficient decreases, resulting in a net increase in the droplet growth rate. Eventually the reduction in the heat transfer coefficient dominates and the droplet growth rate peaks and then declines with increasing size.

Example calculations presented in this paper provide considerable insight into the transport associated with microdroplet evaporation in the free molecular and transition regimes. As expected, in the transition regime, condensation of water vapor at the droplet surface reduces the water vapor concentration there below that in the ambient. The percentage change in water vapor concentration is very significant at low ambient concentration levels. For transport in the free molecular regime, the temperature and concentration profiles near the droplet are virtually flat, with a jump in temperature at the droplet surface, as expected.

The results of this study indicate that noncontinuum effects, and surface tension effects play import roles in the transport associated with quasi-equilibrium post-nucleation growth of water microdroplets in water-argon mixtures. These results clearly indicate that theoretical treatments of this type of transport problem must have the capability to handle these complexities if they are to provide accurate predictions of the droplet growth rates.

Acknowledgments

Support for this research by the Alcoa Foundation is gratefully acknowledged.

Nomenclature

c_p = specific heat at constant pressure
c_v = specific heat at constant volume
D_d = diameter of droplet
D_m = effective diameter of molecules
D_v = mass diffusion coefficient in vapor
h_{lv} = latent heat of vaporization
j = molecular number flux
k_v = gas thermal conductivity
k_B = Boltzmann constant
Kn_D = Knudsen number, $\lambda/2r_d$
m = mass of a molecule
n_m = number density of molecules
P = pressure
q'' = energy flux
r_d = radius of droplet
r_σ = length scale defined by Eq. (2)
$\Re$ = a random number uniformly distributed on [0,1]
T = absolute temperature
$\hat{u}_{lv}$ = latent energy per water molecule merged into droplet

$\mathbf{v}_r$ = relative velocity vector for collision pair
X_w = mole fraction of water vapor in gas mixture

Greek

α = thermal diffusivity,
Δt = time interval for one time-step of simulation
ε = molecular energy component
λ = molecular mean free path
ρ = density
σ_{lv} = liquid-vapor interfacial tension
σ_t = energy accommodation coefficient

Subscripts

d = corresponding to the liquid droplet surface
em = corresponding to particles emitted by the droplet
in = corresponding to particles incident on the droplet
l = liquid
rot = rotational
tr = translation
v = vapor
∞ = corresponding to far ambient conditions
0 = corresponding to conditions in the gas adjacent to the droplet surface
4 = corresponding to $r/r_d=4$

Appendix

To initiate the particle simulation calculation, the cells in the simulation domain are initially loaded with particles, each of which represents a fixed number of molecules of a given type. The number of particles initially loaded into the cells is arbitrarily set to correspond to the ambient number density of molecules. The mean number of particles in each cell is subsequently determined as the calculation is marched forward in time.

The particles initially loaded into the cells are randomly given translational and internal (rotational) energies by randomly sampling values from the Boltzmann distribution for the gas (at equilibrium) at the outer boundary temperature. The particle simulation method marches the computation forward in time. For each time-step Δt, the following operations were executed:

1 Statistical information on particles in each cell was gathered at the beginning of each time-step.

2 All particles were transported in space at constant velocity along their current velocity vectors for time Δt, ignoring possible collisions.

3 Each particle was checked to determine if it hit the droplet or hit a boundary of the simulation domain. If it had, appropriate actions were taken, based on the nature of the boundary. Specular surfaces only reverse the normal component of velocity of the particles that strike them. Particles striking the sphere or going beyond the outer boundary were removed from the simulation.

4 Particles were randomly added to cells along the outer boundary surface $r=4r_d$ to simulate the molecular flux (from the ambient) across this surface. The velocities and rotational energies were sampled from appropriate Boltzmann distributions for the outer boundary temperature.

5 Particles were randomly added to cells along the droplet surface $r=r_d$ using the appropriate surface interaction model.

6 Candidate collisions pairs were randomly selected in each cell until approximately $n_p/2$ candidate collision pairs were formed per cell, where n_p is the particle number density in each cell. A selection rule (based on the statistical probability of collision) was used to determine whether the pair actually executed a collision.

7 For each of the candidate pairs accepted for collision, the collision is executed, conserving energy and momentum. The orientation of the post-collision relative velocity vector was chosen randomly.

8 For particles added to the domain at the droplet surface or at the outer boundary, the surface normal velocity component ($c_\perp$) and the tangential velocity components ($c_=$) were sampled from the distributions

$$\mathfrak{J}(c_\perp)dc_\perp=\frac{mc_\perp}{k_BT}e^{-mc_\perp^2/2k_BT}dc_\perp \tag{A1}$$

$$\mathfrak{J}(c_=)dc_==\left(\frac{m}{2\pi k_BT}\right)^{1/2}e^{-mc_=^2/2k_BT}dc_= . \tag{A2}$$

For water, which is triatomic and nonlinear, the rotational energy was sampled from

$$\mathfrak{J}(\varepsilon_{\rm rot})d\varepsilon_{\rm rot}=\frac{2\varepsilon_{\rm rot}^{1/2}}{\sqrt{\pi}(k_BT)^{3/2}}e^{-\varepsilon_{\rm rot}/k_BT}d\varepsilon_{\rm rot} . \tag{A3}$$

In using the above distributions, T was set equal to either T_d or T_4, as appropriate. At the droplet surface $c_\perp$ was taken to be an outward normal velocity whereas at the outer boundary it was taken to be an inward normal velocity. Sampled velocity components were subsequently converted to u, v, and w components associated with the x-y-z coordinate system.

The selection rule used in Step 6 above was essentially that recommended by Baganoff and McDonald [19]. For the hard sphere interaction model used in this study, this amounts to picking the number of potential collision pairs S for the cell equal to $\langle n_p\rangle/2$, where $\langle n_p\rangle$ is the mean particle number density in the cell, and selecting collision pairs with probability $\tilde{P}_s$ given by

$$\tilde{P}_s=1.5\frac{\langle n_p\rangle|\mathbf{v}_r|\Delta t}{\sqrt{2}\overline{n}_{p,4}\lambda_4} \tag{A4}$$

where $\overline{n}_{p,4}$ and λ_4 are the mean particle density and mean free path for the reference condition at $r=4r_d$, and $|\mathbf{v}_r|$ is the magnitude of the pre-collision relative velocity of the particles being considered as a possible collision pair. The value of the multiplier 1.5 in Eq. (*A*4) was chosen to match simulation collision frequencies with collision frequency predictions of kinetic theory for the conditions considered in this study.

Molecular collisions within the vapor were modeled with a simple hard sphere interaction model. For hard-sphere collisions, post-collision relative velocities must be isotropically scattered. The method used in this study to randomly select post-collision velocities with isotropic scattering has been widely used in direct molecular simulation calculations. A detailed description of this methodology can be found in Bird [17] or McDonald [18].

If the collision is elastic (no exchange of energy in internal modes), the magnitude of the post-collision relative velocity vector is set equal to the value dictated by the pre-collision velocities of the particles. If the collision is inelastic, however, the post-collision fraction of relative translational energy to total collision energy is sampled from the distribution for an equilibrium gas. For molecules obeying a hard-sphere potential and having rotational internal storage only, a relation for this fraction f_{rt} which is applicable to different molecular species with different intermolecular force potentials has been derived by Borgnakke and Larsen [28]. In the simulation scheme described in this paper, the molecules have a hard-sphere force interaction potential and have rotational internal storage only. The relation developed by Borgnakke and Larsen [28] then prescribes that f_{rt} obeys the distribution (*A*5) below for water-water collisions.

$$\mathfrak{J}(f_{rt})df_{rt}=12f_{rt}(1-f_{rt})^2df_{rt} \tag{A5}$$

In our calculations, the appropriate distribution for each type of molecular collision was randomly sampled to determine the f_{rt} value for each collision.

Following McDonald [18] an effective rotational collision number of 5 was used in our calculations with the result that one in five collisions was treated as inelastic. The method used to partition the collision energy in the post-collision state using the sto-

chastically determined f_{rt} value is similar to that used by Carey et al. [16] for droplet evaporation in water-vapor and noncondensable gas mixtures and by McDonald [18] for high-speed rarefied gas flows.

In our simulation calculations, the post-collision partitioning of internal energy between the two molecules is assumed to obey the distribution relation cited by Bird [17] for f_{r1}, the fraction of the post-collision internal energy allocated to molecule 1. For water-water collisions involving only rotational internal storage, the distribution function for the fraction of the internal energy allocated to molecule 1 is given by

$$\Im(f_{r1})df_{r1}=\left(\frac{8}{\pi}\right)f_{r1}^{1/2}(1-f_{r1})^{1/2}df_{r1}. \qquad (A6)$$

For water-water collisions either molecule can be designated as molecule 1. In our calculations, the above distribution was randomly sampled to determine the f_{r1} value for each water-water collision.

To evaluate the mean free path for each species *i* in the mixture with the other species *j*, the following relation from kinetic theory was used:

$$\lambda_i=[n_{m,i}(D_m)_{ii}^2\sqrt{2}+n_{m,j}(D_m)_{ij}^2\sqrt{1+m_i/m_j}]^{-1}. \qquad (A7)$$

The mean free path for the mixtures was computed as a mole-fraction-weighted average

$$\lambda=X_w\lambda_w+(1-X_w)\lambda_a \qquad (A8)$$

where λ_w and λ_a are the mean free path for water and argon molecules, respectively, computed using Eq. (*A*7).

References

[1] Kang, S.-W., 1967, ''Analysis of Condensation Droplet Growth in Rarefied and Continuum Environments,'' AIAA J., **5**, pp. 1288–1295.

[2] Sampson, R. E., and Springer, G. S., 1969, ''Condensation on and Evaporation From Droplets by the Moment Method,'' J. Fluid Mech., **36**, pp. 577–584.

[3] Shankar, P. N., 1970, ''A Kinetic Theory of Steady Condensation,'' J. Fluid Mech., **40**, pp. 385–400.

[4] Gajewski, P., Kulicki, A., Wisniewski, A., and Zgorzelski, M., 1974, ''Kinetic Theory Approach to the Vapor Phase Phenomena in Non-equilibrium Condensation Process,'' Phys. Fluids, **17**, pp. 321–327.

[5] Lou, Y. S., 1978, ''On the Nonlinear Droplet Condensation and Evaporation Problem,'' J. Appl. Phys., **49**, pp. 2350–2356.

[6] Loyalka, S. K., 1982, ''Condensation on a Spherical Droplet, II,'' J. Colloid Interface Sci., **87**, pp. 216–224.

[7] Lang, H., 1983, ''Heat and Mass Exchange of a Droplet in a Polyatomic Gas,'' Phys. Fluids, **26**, pp. 2109–2114.

[8] Chernyak, V. G., and Margilevskiy, A. Y., 1989, ''The Kinetic Theory of Heat and Mass Transfer From a Spherical Particle in a Rarefied Gas,'' Int. J. Heat Mass Transf., **32**, pp. 2127–2134.

[9] Young, J. B., 1991, ''The Condensation and Evaporation of Liquid Droplets in a Pure Vapor at Arbitrary Knudsen Number,'' Int. J. Heat Mass Transf., **34**, pp. 1649–1661.

[10] Young, J. B., 1993, ''The Condensation and Evaporation of Liquid Droplets at Arbitrary Knudsen Number in the Presence of an Inert Gas,'' Int. J. Heat Mass Transf., **36**, pp. 2941–2956.

[11] Peters, F., and Paikert, B., 1994, ''Measurement and Interpretation of Growth and Evaporation of Monodispersed Droplets in a Shock Tube,'' Int. J. Heat Mass Transf., **37**, pp. 293–302.

[12] Peters, F., and Meyer, K. A. J., 1995, ''Measurement and Interpretation of Growth and Evaporation of Monodispersed Water Droplets Suspended in Pure Vapor,'' Int. J. Heat Mass Transf., **38**, pp. 3285–3293.

[13] Widder, M. E., and Titulaer, U. M., 1993, ''Kinetic Boundary Layers in Gas Mixtures: Systems Described by Nonlinearly Coupled Kinetic and Hydrodynamic Equations and Applications to Droplet Condensation and Evaporation,'' J. Stat. Phys., **70**, pp. 1255–1279.

[14] El-Afify, M. M., and Corradini, M. L., 1989, ''Transient Condensation of Vapor Using a Direct Simulation Monte Carlo Method,'' Fusion Technol., **15**, pp. 783–790.

[15] El-Afify, M. M., and Corradini, M. L., 1990, ''Condensation of Vapor in the Presence of a Noncondensable Gas at Low Pressures,'' Nucl. Eng. Des., **121**, pp. 103–111.

[16] Carey, V. P., Oyumi, S. M., and Ahmed, S., 1997, ''Post Nucleation Growth of Water Microdroplets in Supersaturated Gas Mixtures: A Molecular Simulation Study,'' Int. J. Heat Mass Transf., **40**, pp. 2393–2406.

[17] Bird, G. A., 1994, *Molecular Gas Dynamics and the Direct Simulation of Gas Flows*, Oxford University Press, Oxford, UK.

[18] McDonald, J. D. 1989, ''A Computationally Efficient Particle Simulation Method Suited to Vector Computer Architectures,'' Report SUDAAR 589, Department of Aeronautics and Astronautics, Stanford University, Stanford, CA.

[19] Baganoff, D., and McDonald, J. D., 1990, ''A Collision-Selection Rule for a Particle Simulation Method Suited to Vector Computers,'' Phys. Fluids A, **2**, pp. 1248–1259.

[20] Langmuir, I., 1915, ''The Dissociation of Hydrogen Into Atoms, Part II,'' J. Am. Chem. Soc., **37**, pp. 417–458.

[21] Paul, B., 1962, ''Compilation of Evaporation Coefficients,'' ARS J., **32**, pp. 1321–1328.

[22] Yasuoka, K., Matsumoto, M., and Kataoka, Y., 1995, ''Molecular Simulation of Evaporation and Condensation I. Self Condensation and Molecular Exchange,'' *Proc. ASME/JSME Thermal Engineering Joint Conf.*, Vol. 2, ASME, New York, pp. 459–464.

[23] Carey, V. P., 1992, *Liquid-Vapor Phase Change Phenomena*, Taylor and Francis, New York.

[24] Mason, E. A., and Saxena, S. C., 1958, ''Approximate Formula for the Thermal Conductivity of Gas Mixtures,'' Phys. Fluids, **1**, pp. 361–369.

[25] Wilke, C. R., and Lee, C. Y., 1955, ''Estimation of Diffusion Coefficients for Gases and Vapors,'' Ind. Eng. Chem., **47**, pp. 1253–1257.

[26] Mills, A. F. 1965, ''The Condensation of Steam at Low Pressures,'' Technical Report NSF GP-2520, Series No. 6, Issue No. 39, Space Sciences Laboratory, University of California, Berkeley, CA.

[27] Mills, A. F. 1995, *Heat and Mass Transfer*, Richard D. Irwin, Chicago, IL, Chapters 9–10.

[28] Borgnakke, C., and Larsen, P. S., 1975, ''Statistical Collision Model for Monte Carlo Simulation of a Polyatomic Gas Mixture,'' J. Comput. Phys., **18**, pp. 405–420.

Analysis of Variants Within the Porous Media Transport Models

B. Alazmi

K. Vafai
e-mail: Vafai.1@osu.edu

Department of Mechanical Engineering,
The Ohio State University,
Columbus, OH 43210

An investigation of variants within the porous media transport models is presented in this work. Four major categories in modeling the transport processes through porous media, namely constant porosity, variable porosity, thermal dispersion, and local thermal nonequilibrium, are analyzed in detail. The main objective of the current study is to compare these variances in models for each of the four categories and establish conditions leading to convergence or divergence among different models. To analyze the effects of variants within these transport models, a systematic reduction and sensitivity investigation for each of these four aspects is presented. The effects of the Darcy number, inertia parameter, Reynolds number, porosity, particle diameter, and the fluid-to-solid conductivity ratio on the variances within each of the four areas are analyzed. It is shown that for some cases the variances within different models have a negligible effect on the results while for some cases the variations can become significant. In general, the variances have a more pronounced effect on the velocity field and a substantially smaller effect on the temperature field and Nusselt number distribution. [S0022-1481(00)02602-5]

Keywords: Convection, Heat Transfer, Modeling, Porous Media

1 Introduction

Modeling of the non-Darcian transport through porous media has been the subject of various recent studies due to the increasing need for a better understanding of the associated transport processes. This interest stems from the numerous practical applications which can be modeled or can be approximated as transport through porous media such as thermal insulation, packed bed heat exchangers, drying technology, catalytic reactors, petroleum industries, geothermal systems, and electronic cooling. The work of Vafai and Tien [1] presented and characterized the boundary and inertial effects in forced convective flow through a porous medium. Later, Vafai and Tien [2] investigated the boundary and inertial effects on convective mass transfer in porous media. Vafai and Kim [3] used the Brinkman-Forcheimer-extended Darcy model to obtain a closed-form analytical solution for fully developed flow in a porous channel subject to constant heat flux boundary conditions. Hadim [4] performed a numerical study to analyze steady forced convection in a channel filled or partially filled with a porous medium and containing discrete heat sources. Kaviany [5] studied the flow through a constant porosity medium bounded by isothermal parallel plates using the Brinkman-extended flow model and constant matrix porosity. Lauriat and Vafai [6] presented a comprehensive study of forced convective heat transfer in porous media through a channel or over a flat plate.

Other research works consider various problems of the flow and heat transfer through a constant porosity medium (Beckerman and Viskanta [7], Kim and Choi [8], Kladias and Prasad [9], Nield et al. [10], Sung et al. [11], You and Chang [12,13], Neale and Nader [14], Poulikakos and Kazmierczak [15], Kim et al. [16], Chen and Vafai [17], Nakayama et al. [18], Hong et al. [19], Kaviany [20], Kuznetsov [21], Lan and Khodadadi [22], Nakayama et al. [23], Ould-Amer et al. [24], Vafai and Kim [25,26]). A synthesis of various aspects of modeling of transport processes in porous media was given in Tien and Vafai [27]. Recent monographs in which some aspects of transport in porous media were discussed have been presented by Kaviany [28] and Nield and Bejan [29].

A number of experimental and theoretical studies have shown that variation of porosity near a solid boundary has a significant effect on the velocity fields in packed beds resulting in an appreciable flow maldistribution, which appears as a sharp peak near the solid boundary and decreases to nearly a constant value at the center of the bed. This phenomenon is known as the channeling effect. Vafai [30,31] and Vafai et al. [32] investigated analytically and experimentally the channeling effect on an external forced convective flow and heat transfer. Poulikakos and Renken [33] presented a numerical study of the variable porosity effects in a channel bounded by two isothermal parallel plates and in a circular pipe. A number of investigations have considered the effect of variable porosity on fluid flow and heat transfer in porous media (Renken and Poulikakos [34], Hunt and Tien [35,36], and Hsiao et al. [37]).

It is well documented in the literature that the effect of thermal dispersion is essential for a number of applications in the transport processes through porous media. As such, a number of investigations have considered the effects of both thermal dispersion and variable porosity (Hunt and Tien [35,36], Hsiao et al. [37], Hong et al. [38], Chen [39–41], David et al. [42], Hsu and Cheng [43], Cheng et al. [44], Fu et al. [45], and Chen et al. [46]). On the other hand, some other investigations considered only the effect of thermal dispersion (Jang and Chen [47], Hunt and Tien [35,36], and Hong and Tien [48]). Cheng and Hsu [49] analyzed the wall effect of the thermal dispersion process in the forced convective flow through an annular packed-sphere bed. Cheng and Zhu [50] studied the effects of radial thermal dispersion on fully developed forced convection in cylindrical packed tubes. Later, Cheng and Vortemeyer [51] studied the effect of transverse thermal dispersion on fully developed forced convection in packed beds. Vafai and Amiri [52] have shown that the effect of longitudinal dispersion is insignificant for $Pe>10$. Their results show that the effect of transverse dispersion is much more important than the longitudinal dispersion.

The assumption of local thermal equilibrium (LTE) is widely used in analyzing transport processes through porous media. However, this assumption is not valid for some applications where a substantial temperature difference exists between the solid phase and the fluid phase. Amiri and Vafai [53] and Amiri et al. [54] employed a fully general model for the momentum equation and a two-phase model for the energy equation, including axial and transverse thermal dispersion to investigate forced convection in a channel. They presented detailed error maps for assessing the importance of various simplifying assumptions that are commonly used. In addition, Amiri and Vafai [55] presented a comprehensive numerical study for the problem of transient incompressible

Contributed by the Heat Transfer Division for publication in the JOURNAL OF HEAT TRANSFER. Manuscript received by the Heat Transfer Division, Sept. 30, 1999; revision received, Dec. 16, 1999. Associate Technical Editor: J. Howell.

flow through a packed bed including inertia and boundary effects in the momentum equation and the effects of thermal dispersion and local thermal nonequilibrium (LTNE) in the energy equation. Hwang et al. [56] investigated the non-Darcian forced convection taking into account the effects of boundary, inertia, and transverse thermal dispersion. Dixon and Cresswell [57] investigated the problem of LTNE between the fluid and solid phases and obtained a correlation for the fluid-to-solid heat transfer coefficients. Kuznetsov [58] presented an analytical solution for the simplified version of LTNE in a parallel plate channel subject to constant heat flux boundary conditions.

Four major categories in modeling the transport processes through porous media are analyzed in detail in this work. These four categories are related to transport aspects for constant porosity, variable porosity, thermal dispersion, and LTNE. As such, many different pertinent research works are systematically analyzed in the present investigation. For each category, a number of research works are found to be relevant to the present investigation. In all the above-mentioned investigations, variants of Darcy, Forchheimer, and Brinkman terms in the momentum equation as well as variants of thermal dispersion terms and the LTNE presentations were utilized. The main objective of the present work is to investigate and compare variances in models for each of the four categories and establish conditions leading to convergence or divergence among different models.

2 Problem Formulation

To analyze the four major categories in modeling the transport processes through porous media, a fundamental configuration shown in Fig. 1 is selected. This configuration consists of a parallel plate channel with constant heat flux q_w or constant wall temperature T_w. The height and the width of the channel are $2H$ and L, respectively. The velocity of the upstream flow is u_c and its temperature is T_e. This configuration allows an investigation of all the major aspects described earlier. The main assumptions for this investigation are summarized as follows:

1 The flow is steady and incompressible.
2 The properties of the porous medium and the fluid are isotropic and homogeneous.
3 The thermophysical properties of the fluid and the porous matrix are assumed to be constant.
4 Only the effect of transverse thermal dispersion is included, i.e., the effect of longitudinal dispersion is neglected. This is justified in light of the analysis by Amiri and Vafai [53].

The governing equations for the present investigation assuming fully developed conditions, can be written as given in Vafai [30], Vafai and Kim [3], and Amiri and Vafai [53]:

(a) Momentum Equation.

$$\frac{\rho_f}{\varepsilon}\langle (V\cdot\nabla)V\rangle = -\frac{\mu}{K}\langle V\rangle - \frac{\rho_f F\varepsilon}{\sqrt{K}}[\langle V\rangle\cdot\langle V\rangle]J + \frac{\mu}{\varepsilon}\nabla^2\langle V\rangle - \nabla\langle P\rangle \tag{1}$$

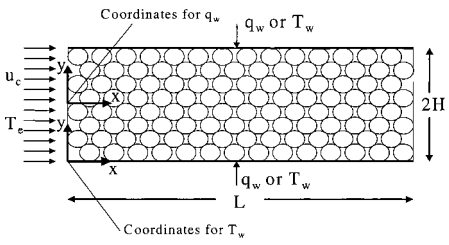

Fig. 1 Schematic diagram of the problem and the corresponding coordinate systems

For variable porosity case, the permeability of the porous medium K and the geometric function F can be represented as in Ergun [59] and Vafai [30,31]:

$$K = \frac{\varepsilon^3 d_P^2}{150(1-\varepsilon)^2} \tag{2}$$

$$F = \frac{1.75}{\sqrt{150\varepsilon^3}} \tag{3}$$

According to Benenati and Brosilow [60] and Vafai [30,31], the porosity distribution throughout the porous medium can be presented by the following equation:

$$\varepsilon = \varepsilon_\infty\left[1 + b\exp\left(\frac{-cy}{d_p}\right)\right]. \tag{4}$$

(b) Energy Equation.

$$(\rho C_P)_f\langle V\rangle\cdot\nabla\langle T\rangle = \nabla\cdot\left[\frac{k_{\text{eff}}}{\varepsilon}\cdot\nabla\langle T\rangle\right] \tag{5}$$

For thermal dispersion (Amiri and Vafai [53] and Amiri et al. [54])

$$k_{\text{eff}} = k_o + k_d \tag{6}$$

where k_o is the stagnant thermal conductivity and k_d is the dispersion conductivity.

For LTNE, two separate energy equations are required (Vafai and Amiri [52], Amiri and Vafai [53], and Amiri et al. [54]):

Fluid-Phase Energy Equation.

$$(\rho C_P)_f\langle V\rangle\cdot\nabla\langle T_f\rangle = \nabla\cdot\{k_{f\,\text{eff}}\cdot\nabla\langle T_f\rangle\} + h_{sf}a_{sf}(\langle T_s\rangle - \langle T_f\rangle) \tag{7}$$

Solid-Phase Energy Equation.

$$0 = \nabla\cdot\{k_{s\,\text{eff}}\cdot\nabla\langle T_s\rangle\} - h_{sf}a_{sf}(\langle T_s\rangle - \langle T_f\rangle) \tag{8}$$

where

$$k_{f\,\text{eff}} = \varepsilon k_f \tag{9}$$

and

$$k_{s\,\text{eff}} = (1-\varepsilon)k_s\,. \tag{10}$$

3 Problem Setup and Validation

An implicit method was used to solve the fully developed velocity field. The nonlinear term (Forchheimer term) was linearized by using the prior iteration values of the velocity. Convergence was considered to have been achieved when the absolute error between two successive iterations was less than 10^{-6}. The successive over relaxation method (SOR) was used to accelerate the convergence rate. The energy equation was solved by applying a central differencing for the diffusion term and upwind differencing for the convection term.

Numerical investigations were performed using different number of grid points to assess and ascertain grid independence results for the field variables. It was found that any increase beyond a set given by 500×1000 results in less than 0.2 percent change in the results. The local Nusselt number distribution was found using a three point differencing. Due to symmetry considerations, the solution is found for the upper half of the channel for the constant porosity category and for the lower half of the channel for the other three categories.

4 Results and Discussion

The numerical results for the constant porosity category were compared with the exact solution given by Vafai and Kim [3] as shown in Fig. 2, and an excellent agreement was found. The accuracy of the simulation of the variable porosity effects were

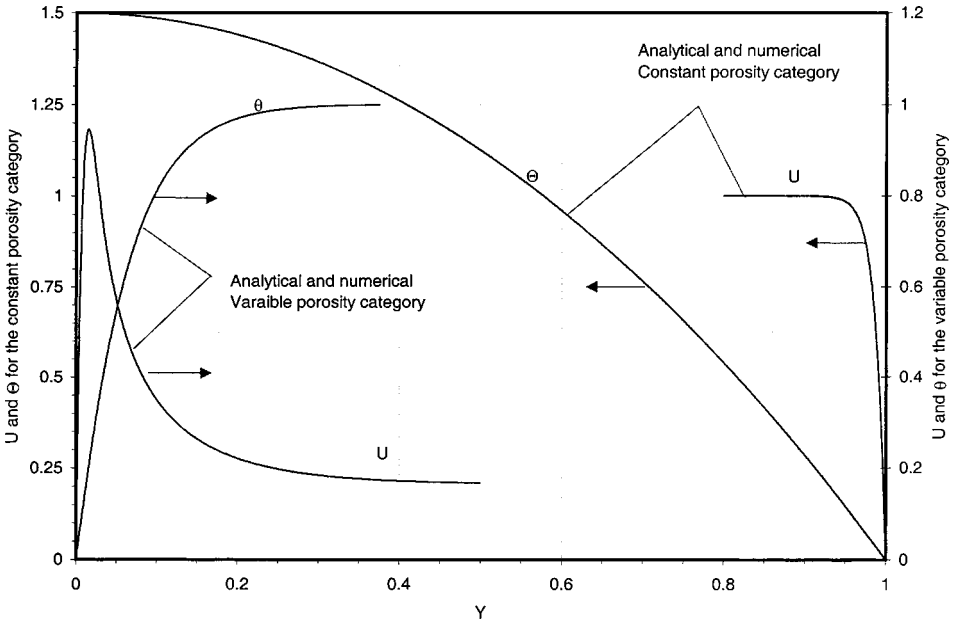

Fig. 2 Comparisons between the numerical results of the present study and the analytical solutions of Vafai and Kim [3] and Vafai [30]. The constant porosity category [$\varepsilon=0.9$, $\Lambda=100$, Da=0.001 and Re=100]. The variable porosity category [$dp/dx=-1493$, $d_p=0.008$, $b=0.98$, $c=2.0$, and $\varepsilon_\infty=0.5$].

checked against the analytical solution given in Vafai [30] and are presented in Fig. 2. An excellent agreement was found between the numerical results and the analytical solution given in Vafai [30]. In what follows, the results for each category are presented separately. Figure 1 describes the coordinate system and schematic of the fundamental configuration for the case of constant porosity as well as the fundamental configuration for the other

Table 1 Relationship between various models and the pertinent literature

Model	References
C1	Vafai and Tien [1,2], Vafai and Kim [3], Kaviany [5], Lauriat and Vafai [6], Hong et al. [19], Kaviany [20], Kuznetsov [21], Lan and Khodadadi [22], Nakayama et al. [23], Ould-Amer et al. [24], Vafai and Kim [25,26]
C2	Kim et al. [16], Chen and Vafai [17], Nakayama et al. [18]
C3	Hadim [4], Beckermann and Viskanta [7], Kim and Choi [8], Kladias and Prasad [9], Nield et al. [10], Sung et al. [11], You and Chang [12,13], Neale and Nader [14], Poulikakos and Kazmierczak [15]
V1	Vafai [30], Vafai [31], Vafai et al. [32], Vafai and Amiri [52], Amiri and Vafai [53], Amiri et al. [54], Amiri and Vafai [55]
V2	Lauriat and Vafai [6], Poulikakos and Renken [33], Renken and Poulikakos [34]
V3	Hunt and Tien [36], Hong et al. [38], Chen [39–41], Cheng et al. [44], Chen et al. [46]
V4	Hsiao et al. [37], David et al. [42], Hsu and Cheng [43], Fu et al. [45]
D1	Hong et al. [38], Hong and Tien [48], Vafai and Amiri [52], Amiri and Vafai [53], Amiri et al. [54], Amiri and Vafai [55]
D2	Chen [39–41], David et al. [42], Hsu and Cheng [43], Jang and Chen [47]
D3	Hsu and Cheng [43], Cheng et al. [44], Fu et al. [45], Vafai and Amiri [52], Hwang et al. [56]
D4	Chen et al. [46]
D5	Hunt and Tien [35,36]
E1	Vafai and Amiri [52], Amiri and Vafai [53], Amiri et al. [54], Amiri and Vafai [55]
E2	Hwang et al. [56]
E3	Dixon and Cresswell [57]

Table 2 Different models of constant porosity

Model	Darcy	Forchheimer	Brinkman
C1**	$\frac{\mu}{K}u$	$\rho\frac{F\varepsilon}{\sqrt{K}}u^2$	$\frac{\mu}{\varepsilon}\nabla^2 u$
C2	$\frac{\mu}{K}u$	$\rho\frac{F}{\sqrt{K}}u^2$	$\frac{\mu}{\varepsilon}\nabla^2 u$
C3*	$\frac{\mu}{K}u$	$\rho\frac{F}{\sqrt{K}}u^2$	$\mu\nabla^2 u$

*References [14] and [15] did not include the Forchheimer term. In comparisons, to properly concentrate on the difference with other models, a Forchheimer term was used within each of the categories.
**This model was used in the exact solution of Vafai and Kim [3].

Table 3 Different models of variable porosity (modified models)

Model	Darcy	Forchheimer	Brinkman
V1	$\mu\frac{150(1-\varepsilon)^2}{\varepsilon^3 d_p^2}u$	$\rho\frac{1.75(1-\varepsilon)}{\varepsilon^2 d_p}u^2$	$\frac{\mu}{\varepsilon}\nabla^2 u$
V2*	$\mu\frac{150(1-\varepsilon)^2}{\varepsilon^3 d_p^2}u$	$\rho\frac{1.75(1-\varepsilon)}{\varepsilon^3 d_p}u^2$	$\mu\nabla^2 u$
V3*	$\mu\frac{150(1-\varepsilon)^2}{\varepsilon^3 d_p^2}u$	$\rho\frac{1.75(1-\varepsilon)}{\varepsilon^3 d_p}u^2$	$\frac{\mu}{\varepsilon}\nabla^2 u$
V4	$\mu\frac{150(1-\varepsilon)^2}{\varepsilon^2 d_p^2}u$	$\rho\frac{1.75(1-\varepsilon)}{\varepsilon^2 d_p}u^2$	$\mu\nabla^2 u$

*In these models, the Darcy's term constant was changed from 175 into 150 for the purpose of comparison.

Table 4 Different models of transverse thermal dispersion

Model	Dispersion Conductivity	Notes
D1	$\gamma\rho C_P U d_p$	$\gamma=0.1$ $\gamma=0.2$
D2	$\gamma\frac{1-\varepsilon}{\varepsilon}\rho C_p U d_p$	$\gamma=0.04$ $\gamma=0.02$
D3	$\gamma\rho C_P U d_p\left(1-\exp\left(\frac{-y}{wH}\right)\right)$	$\gamma=0.17$, w=1.5 $\gamma=0.12$, w=1.0 $\gamma=0.3$, w=3.5 $\gamma=0.375$, w=1.5
D4	$0.01\frac{1-\varepsilon}{\varepsilon^2}\rho C_P U d_p$	
D5	$0.025\rho C_P U\sqrt{K}$	

Table 5 Different models of the fluid to solid heat transfer coefficient and the fluid to solid specific area

Model	h_{sf}	a_{sf}	Notes
E1	$\frac{k_f(2+1.1\mathrm{Pr}^{1/3}\mathrm{Re}^{0.6})}{d_p}$	$\frac{6(1-\varepsilon)}{d_p}$	
E2	$0.004\left(\frac{d_V}{d_p}\right)\left(\frac{k_f}{d_p}\right)\mathrm{Pr}^{0.33}\mathrm{Re}^{1.35}$	$\frac{20.346(1-\varepsilon)\varepsilon^2}{d_p}$	Re<75
	$1.064\left(\frac{k_f}{d_p}\right)\mathrm{Pr}^{0.33}\mathrm{Re}^{0.59}$		Re>350
E3*	$\left[\frac{d_p\varepsilon}{0.2555\mathrm{Pr}^{1/3}\mathrm{Re}^{2/3}k_f}+\frac{d_p}{10k_s}\right]^{-1}$	$\frac{6(1-\varepsilon)}{d_p}$	

*In this model, a_{sf} was taken similar to model E1 for the purpose of comparison, where $d_V=4\varepsilon/a_{sf}$.

three cases namely variable porosity, thermal dispersion and LTNE. A very large body of research works were analyzed and categorized for each of these areas.

The pertinent works within each area resulting in a true variance were selected within each category. The association between various models and the pertinent literature is given in Table 1. This comprehensive analysis resulted in Tables 2, 3, 4, and 5 for each of the presented categories. In the discussion of the results, the concentration is placed directly on the variances and mechanisms involved in creating these variances within each category. The physics of the two fundamental configurations considered here have been analyzed in detail in Vafai and Kim [3] and Amiri et al. [54] and will not be considered here.

4.1 Constant Porosity. Table 2 shows three variant models related to this category. Again, the corresponding references which form the variant models for this category as well as other categories are given in Table 1. The velocity and temperature profiles of the three different models are produced by solving the momentum and energy equations for the fundamental configuration shown in Fig. 1. As a result of using different variants of the Forchheimer and Brinkman terms in the momentum equation, the resultant velocity profiles for these models are expected to be different and consequently the heat transfer rate will also differ since the solution of the energy equation depends on the solution of the momentum equation.

A comprehensive study is performed to show the variations between the three different models by comparing the corresponding differences in velocity, temperature, and local Nusselt number distributions. The pertinent controlling parameters used for this category are porosity, inertia parameter, Darcy number, and Reynolds number. Figures 3–10 present a synthesis of variants for the models utilized within this category. The variations between the three variant models are found to be more visible in the velocity profiles which are shown in Figs. 3, 5, 7, and 9. The three models have an insignificant effect on the variations for the temperature and Nusselt number distributions as can be seen in Figs. 3–10. As such, the velocity profiles are used for comparing the three variant models within this category. The results reveal that the inertia parameter, porosity and the Darcy number have more a pro-

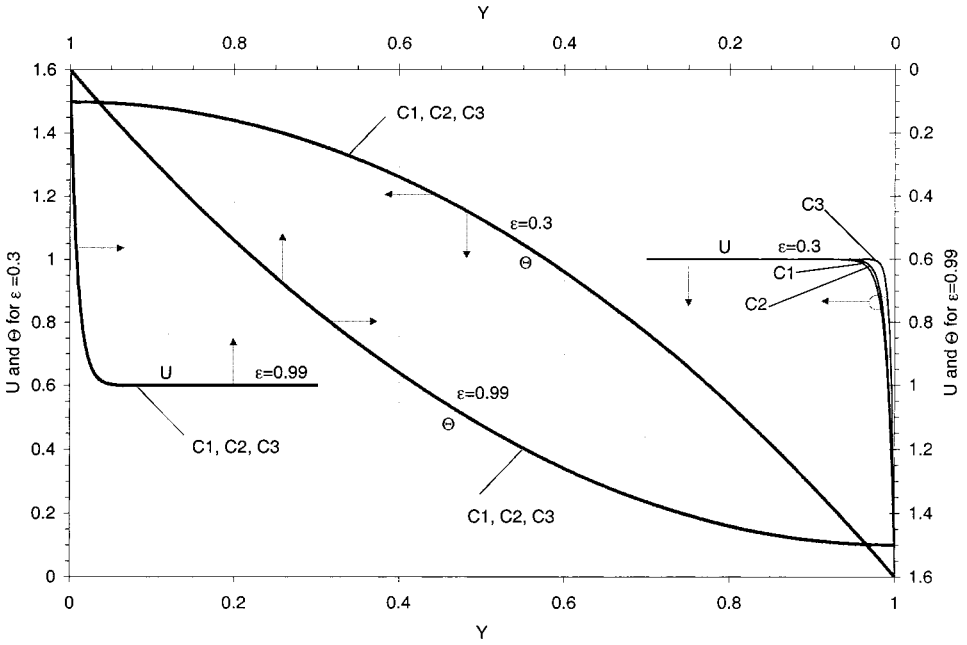

Fig. 3 Effect of porosity variations on velocity and temperature distributions for the constant porosity category [$\Lambda=10$, $\mathrm{Da}=10^{-4}$ and $\mathrm{Re}_H=100$]; (*a*) $\varepsilon=0.3$, (*b*) $\varepsilon=0.99$

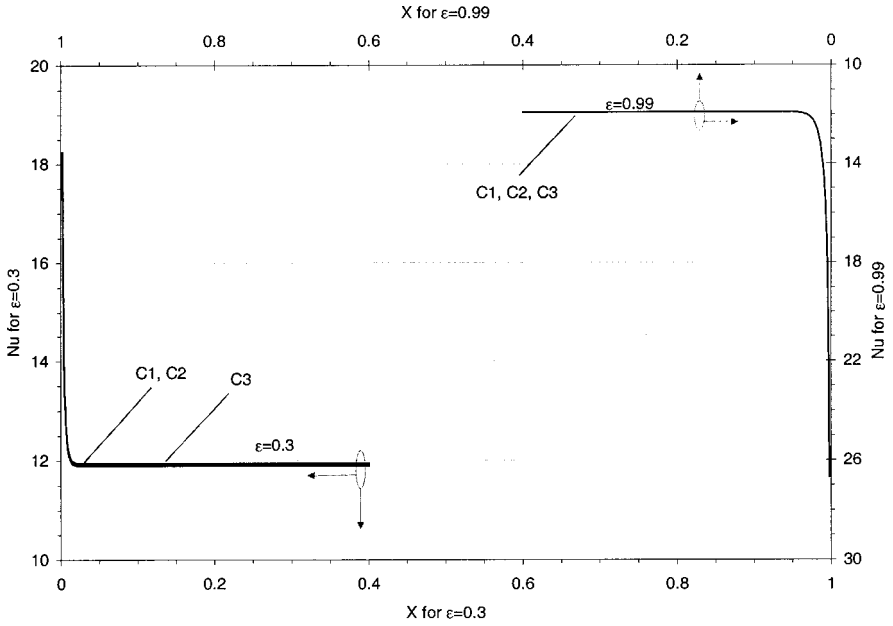

Fig. 4 Effect of porosity variations on Nusselt number distributions for the constant porosity category [$\Lambda=10$, $Da=10^{-4}$, and $Re_H=100$]; (*a*) $\varepsilon=0.3$, (*b*) $\varepsilon=0.99$

nounced effect on the convergence and the divergence of these models from each other even though the overall variations are relatively very small.

For the case of Darcy numbers corresponding to almost all practical applications, the three models are found to result in velocity and temperature fields which are quite close to each other for a given porosity or inertia parameter. Figure 5 shows that for a higher inertia parameter, the velocity profiles for the three models become closer to each other. It can be seen that models C1 and C2 become identical when the fluid inertia is negligible, i.e., $\Lambda=0$. This occurs because models C1 and C2 have the same Darcy and Brinkman terms which makes them the same when the

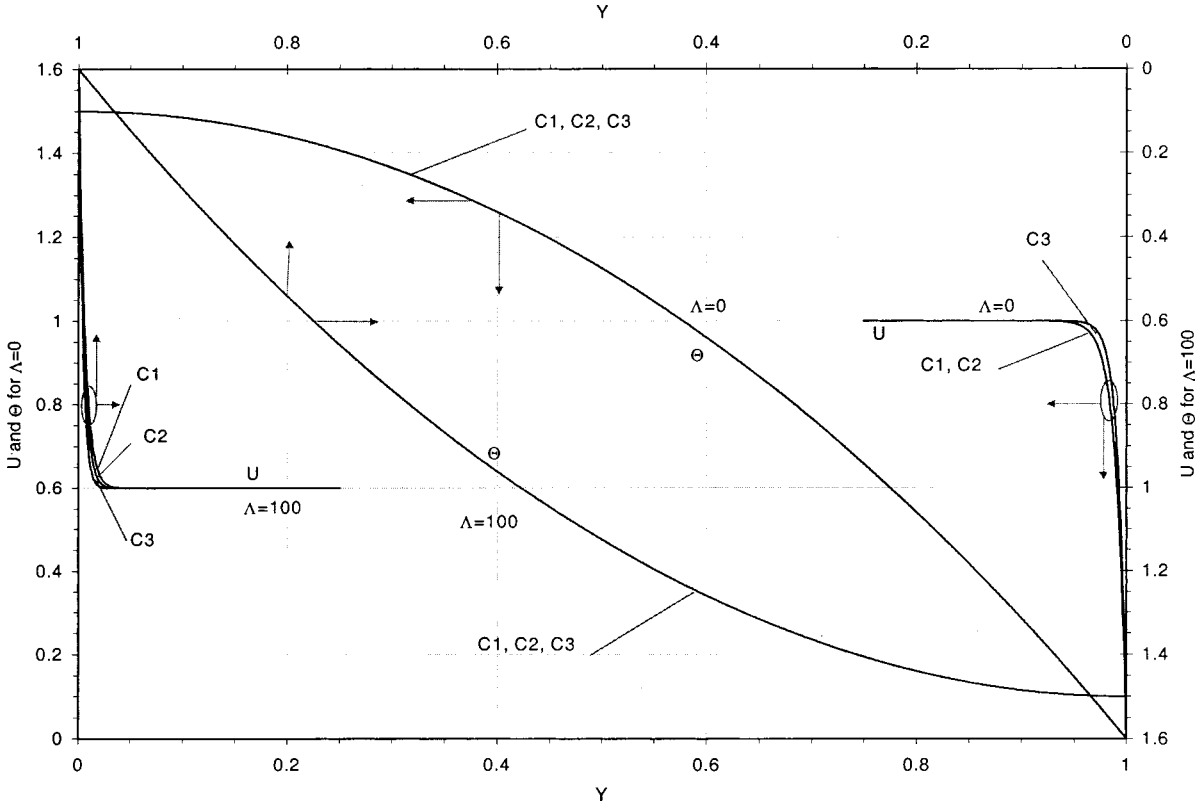

Fig. 5 Effect of the inertia parameter on velocity and temperature distributions for the constant porosity category [$\varepsilon=0.6$, $Da=10^{-4}$, and $Re_H=100$]; (*a*) $\Lambda=0$, (*b*) $\Lambda=100$

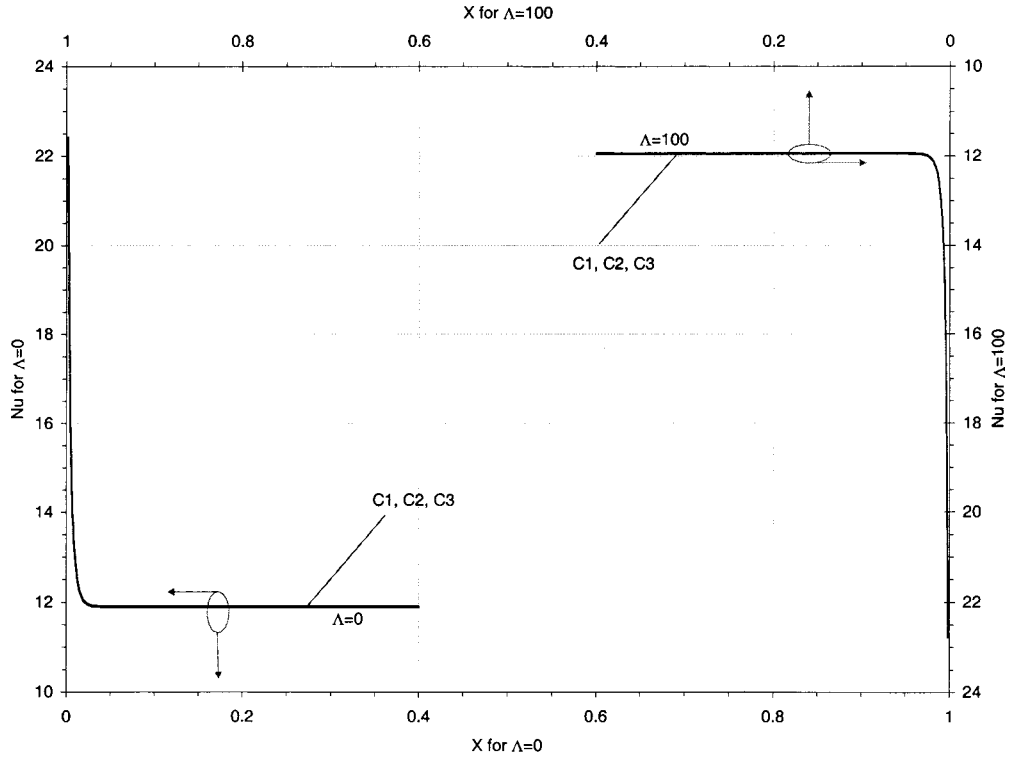

Fig. 6 Effect of the inertia parameter on Nusselt number distributions for the constant porosity category [ε=0.6, Da=10^{-4}, and Re_H=100]; (*a*) Λ=0, (*b*) Λ=100

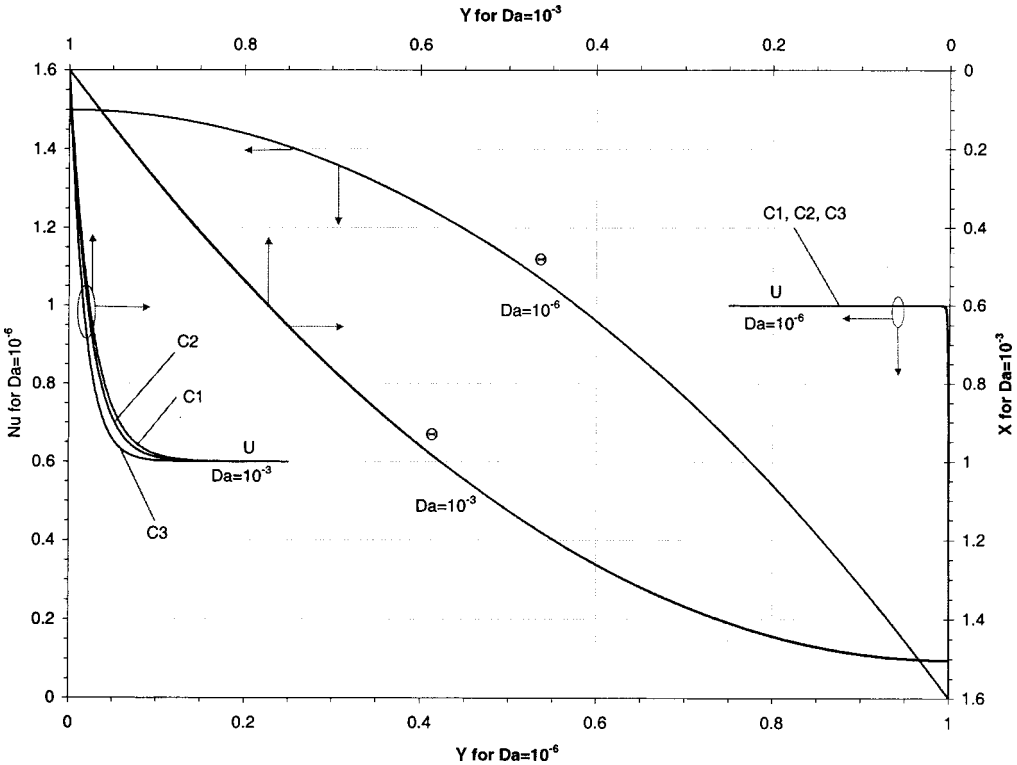

Fig. 7 Effect of Darcy number variations on velocity and temperature distributions for the constant porosity category [ε=0.6, Λ=10, and Re_H=100]; (*a*) Da=10^{-6}, (*b*) Da=10^{-3}

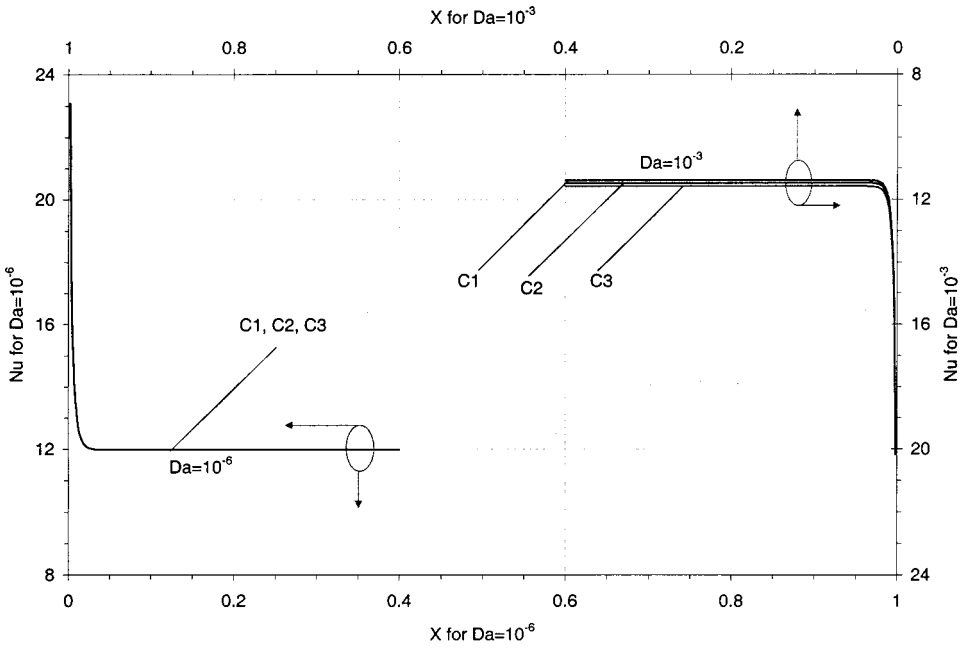

Fig. 8 Effect of Darcy number variations on Nusselt number distributions for the constant porosity category [ε=0.6, Λ=10, and Re_H=100]; (*a*) Da=10^{-6}, (*b*) Da=10^{-3}

Forchheimer term is ignored. It is relevant to mention that for high inertia parameter, the Forchheimer terms for models C2 and C3 are of the same order of magnitude as the Forchheimer term for model C1, while for low inertia parameters, the difference becomes more significant. It can be seen that for the case when the porosity of the porous medium approaches unity, the three models presented in Table 2 overlap and become identical as shown in Figs. 3–4. This happens because the presentations of the Darcy, Forchheimer, and Brinkman terms approach the same limit for all the three models when the porosity approaches unity.

It is clear that model C3 results in the thinnest momentum boundary layer while model C1 results in the thickest momentum

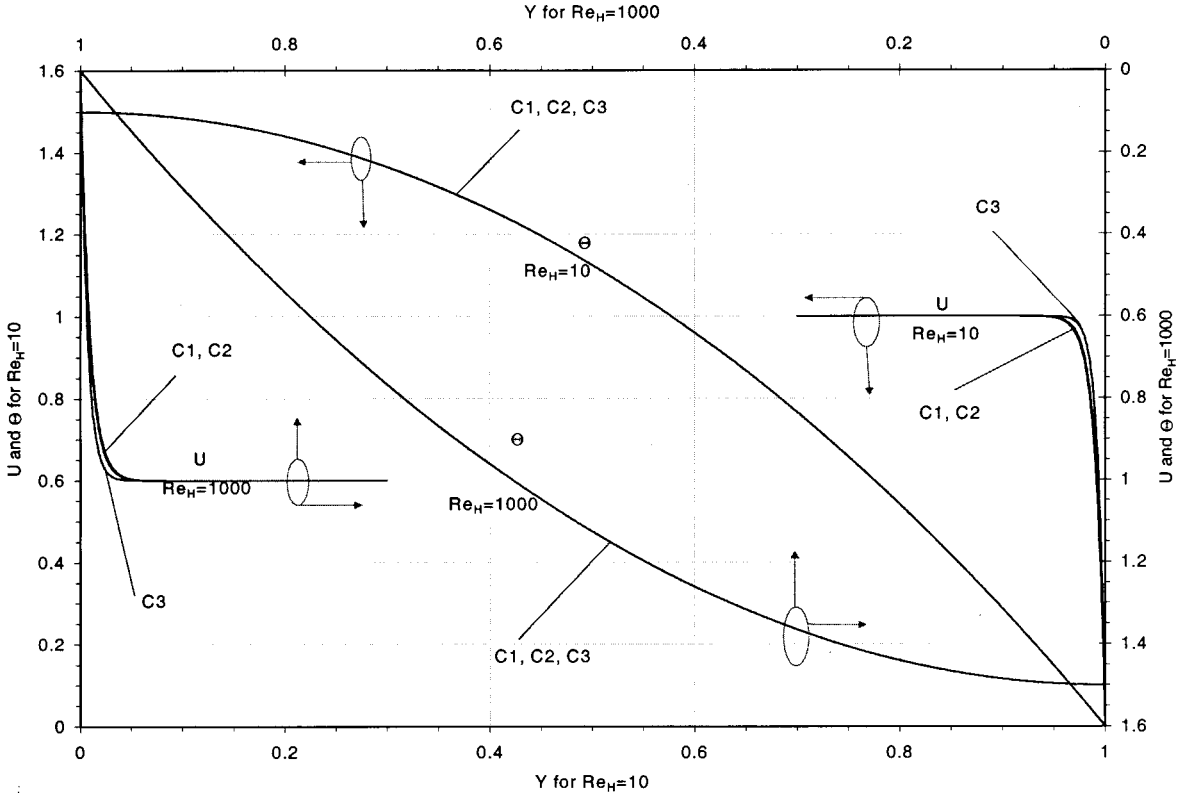

Fig. 9 Effect of Reynolds Number variations on velocity and temperature distributions for the constant porosity category [ε=0.6, Λ=10, and Da=10^{-4}]; (*a*) Re_H=10, (*b*) Re_H=1000

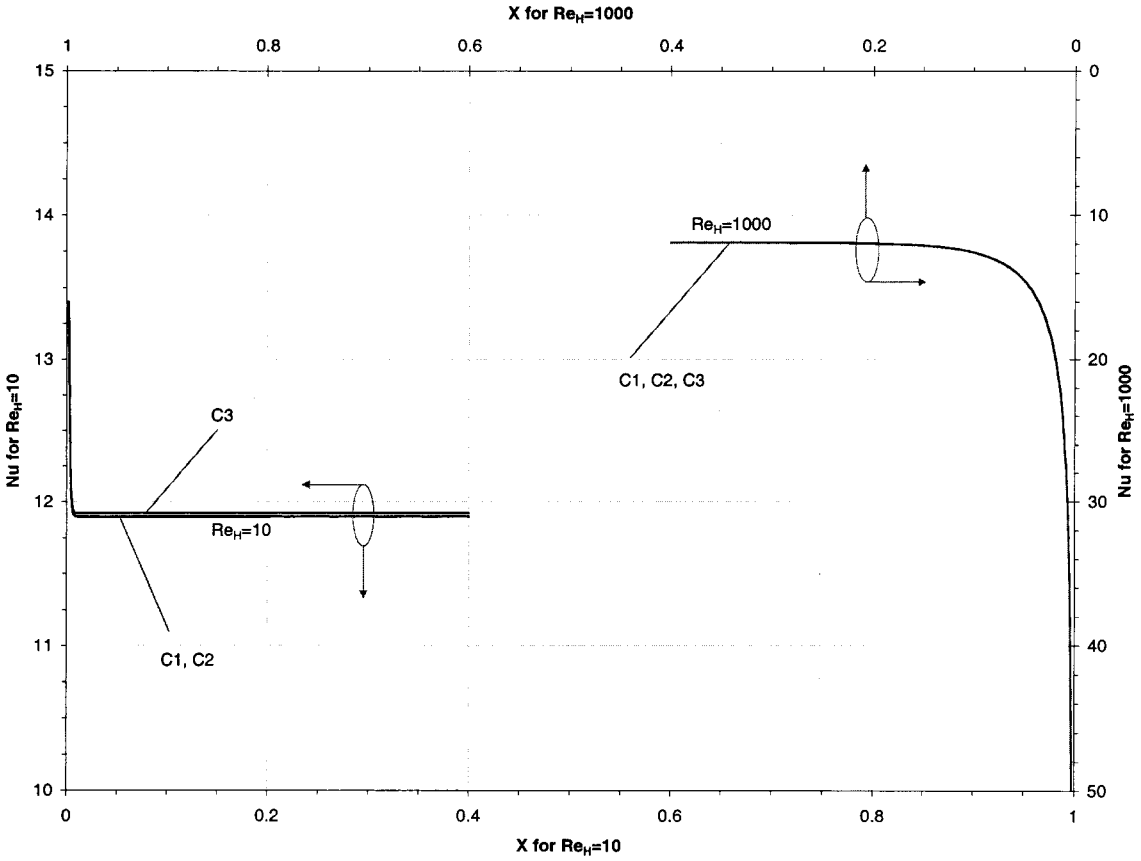

Fig. 10 Effect of Reynolds Number variations on Nusselt number distributions for the constant porosity category [ε=0.6, Λ=10, and Da=10^{-4}]; (*a*) Re$_H$=10, (*b*) Re$_H$=1000

boundary layer. This can be explained by first realizing that the Darcy terms are the same for the three variant models. Next, it should be noted that models C2 and C3 have similar Forchheimer terms; models C1 and C2 have similar Brinkman terms, while models C1 and C3 have different Forchheimer and Brinkman terms. Therefore, model C2 should fall in between the two other models as can be seen in Figs. 3–10. The reason that model C3 has the thinnest momentum boundary layer can be explained in terms of its Brinkman term formation which results in a smaller effective viscosity and a reduction in the shear stress between the fluid layers. On the other hand, model C1 has a smaller Forchheimer term which translates into less inertia than the other two models and as a result, the overall velocities of this model will be smaller. Therefore, the velocity profile for model C3 will appear as the upper bound; the velocity profile for model C1 will be the lower bound while model C2 will be in between for any condition.

Figures 3, 5, 7, and 9 show the velocity and temperature profiles for this category. It is clear that using different models has a substantially less impact on the temperature fields. Likewise, the Nusselt number profiles, as shown in Figs. 4, 6, 8, and 10 reveal that the three models result in very close agreements.

4.2 Variable Porosity. Four variant models have been found in literature for variable porosity media category as shown in Table 3. It can be seen that models V2 and V3 have the same Darcy and Forchheimer terms while the only difference between them is the presentation of the Brinkman terms. Models V1 and V4 have the same Forchheimer term, models V1 and V3 have the same Brinkman term while models V1, V2, and V3 have the same formation for the Darcy term. The pertinent parameters in this category are similar to those used by Vafai [30]. These parameters are the pressure gradient, the particle diameter, the freestream porosity, and the constants *b* and *c* in Eq. (4). Models V2 and V3 are closer to each other due to their similar representations for the Darcy and Forchheimer terms. On the other hand, models V1 and V4 are closer to each other due to similar Forchheimer terms. Figures 11–16 describe a synthesis of variants for the models utilized within the variable porosity category. Velocity profiles, temperature profiles, and Nusselt number profiles for this category are all shown in Figs. 11–16.

It has been shown in the literature (Vafai [30]) that an increase in the pressure gradient increases the centerline velocity and decreases the dimensionless velocity which is the ratio of the actual velocity to the centerline velocity. Also, an increase in the pressure gradient has been shown to form a thinner thermal boundary layer which leads to a higher Nusselt number. Figure 11 shows the effect of the pressure gradient on these four models for the variable porosity category. It can be seen that increasing the pressure gradient results in a closer agreement between models V1 and V4. Increasing the particle diameter causes the channeling effect to be more pronounced due to a reduction in fluid flow resistance near the solid boundary. These higher velocities increase the convected energy and form a thinner thermal boundary layer which leads to higher values of Nusselt number (Vafai [30]). The effect of the particle diameter on the nature of the four models can be seen in Fig. 12. It can be seen that an increase in the particle diameter causes a better agreement between models V1 and V4. The temperature profiles given in Fig. 12 show that an increase in the particle diameter results in closer agreement between all four models for the variable porosity category. This is due to the development of a thinner boundary layer which, in effect, masks out the variants within these four models.

Increasing the porosity causes the Darcy and Forchheimer terms within these models to approach the same limiting forms. Figure 13 shows that an increase in the freestream porosity results

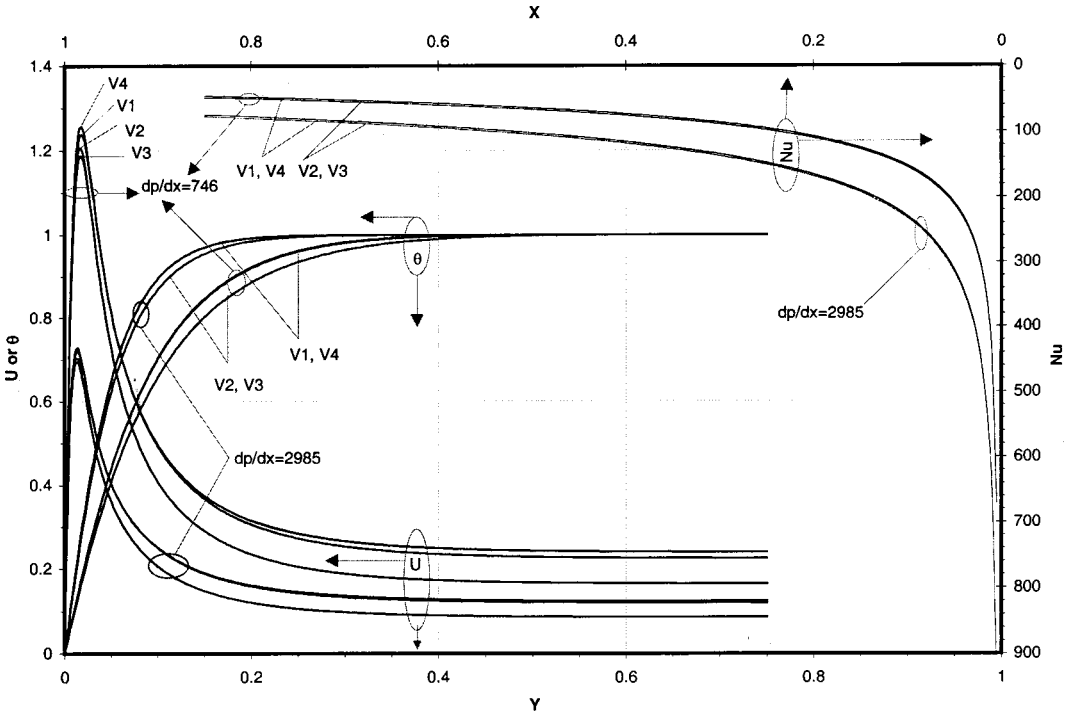

Fig. 11 Effect of pressure gradient on velocity, temperature and Nusselt number distributions for the variable porosity category [d_p=0.008, b=0.98, c=2.0, ε_∞=0.5]; (*a*) dp/dx=746, (*b*) dp/dx=2985

in a better agreement between these four models. That is, the overall difference between these four models diminishes as the freestream porosity increases. The effects of the constants b and c were discussed in Vafai [30]. It was found that an increase in b boosts the porosity near the walls while an increase in c causes more rapid decaying in the porosity resulting in a faster approach towards the freestream porosity value. Since increasing b and decreasing c increases the overall porosity, this effect is similar to increasing the freestream porosity. Therefore, increasing b and decreasing c creates a better agreement between these models. Figure 14 shows the effect of the constant c while Fig. 15 shows the effect of the constant b on the velocity profiles. A worse-case scenario for the divergence between these models is presented in Fig. 16 by combining the effects of a lower pressure gradient, lower freestream porosity, and smaller b and larger c, all of which enlarge the divergence between these four models. In contrast, the

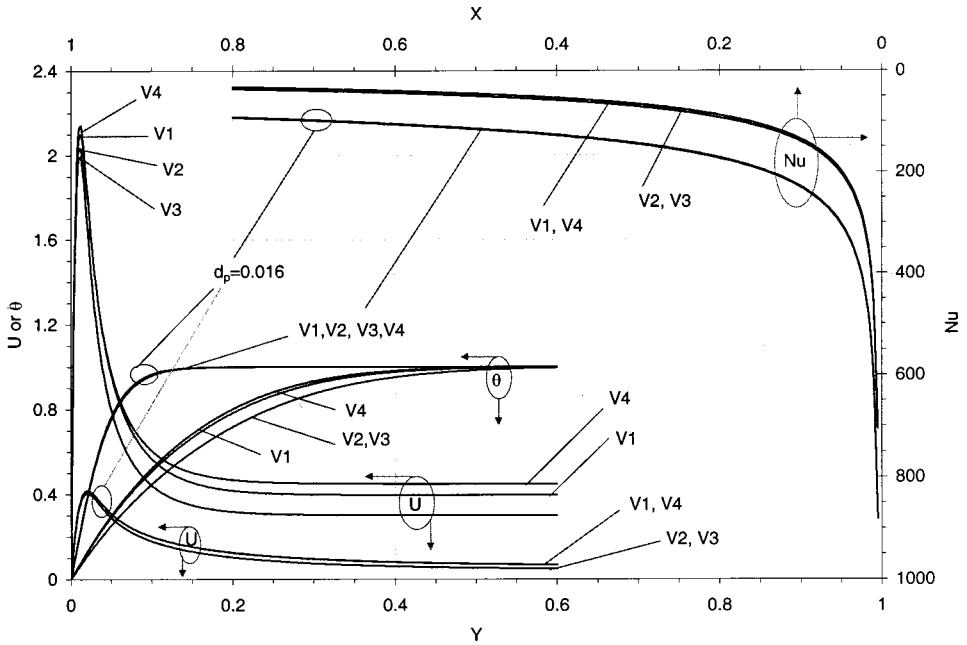

Fig. 12 Effect of particle diameter on velocity, temperature, and Nusselt number distributions for the variable porosity category [dp/dx=1493, b=0.98, c=2.0, ε_∞=0.5]; (*a*) d_p=0.004, (*b*) d_p=0.016

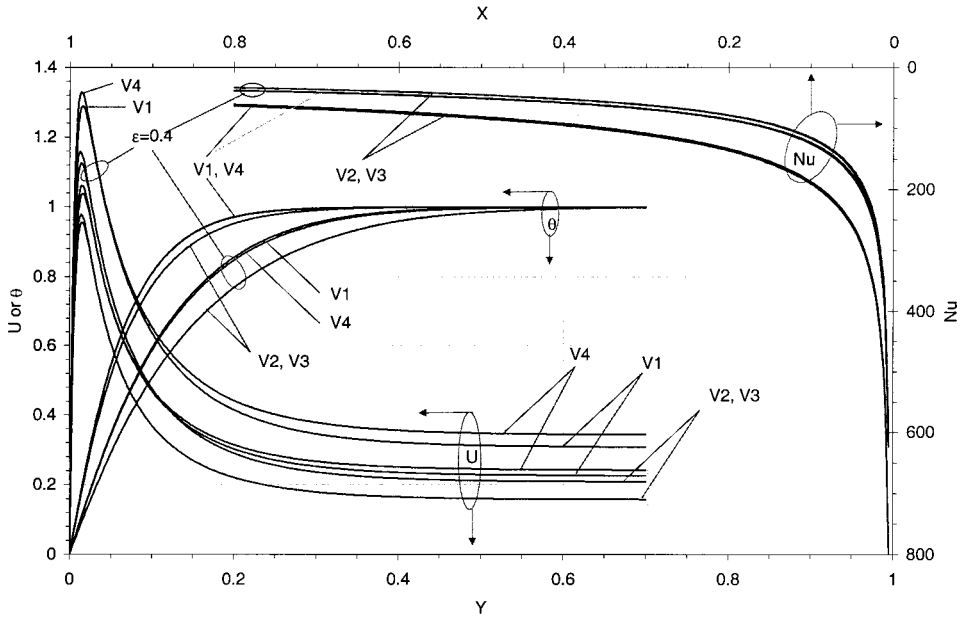

Fig. 13 Effect of freestream porosity on velocity, temperature, and Nusselt number distributions for the variable porosity category [$dp/dx=1493$, $d_p=0.008$, $b=0.98$, $c=2.0$]; (*a*) $\varepsilon_\infty=0.4$, (*b*) $\varepsilon_\infty=0.45$

effects of a higher pressure gradient, larger particle diameter, higher freestream porosity, larger b and smaller c, create a closer agreement between these four models, as seen in Fig. 16.

In general, models V2 and V3 result in velocity distributions which are quite close to each other except at the peak where V2 has a higher peak than model V3. This happens because model V2 has a lower effective viscosity than model V3 which translates to a lower resistance to fluid flow and consequently a higher peak. In general, models V1 and V4 are more similar and result in a larger freestream velocity when compared to models V2 and V3. This occurs because the Forchheimer term for the V2 and V3 models are larger than the corresponding one in the V1 and V4 models.

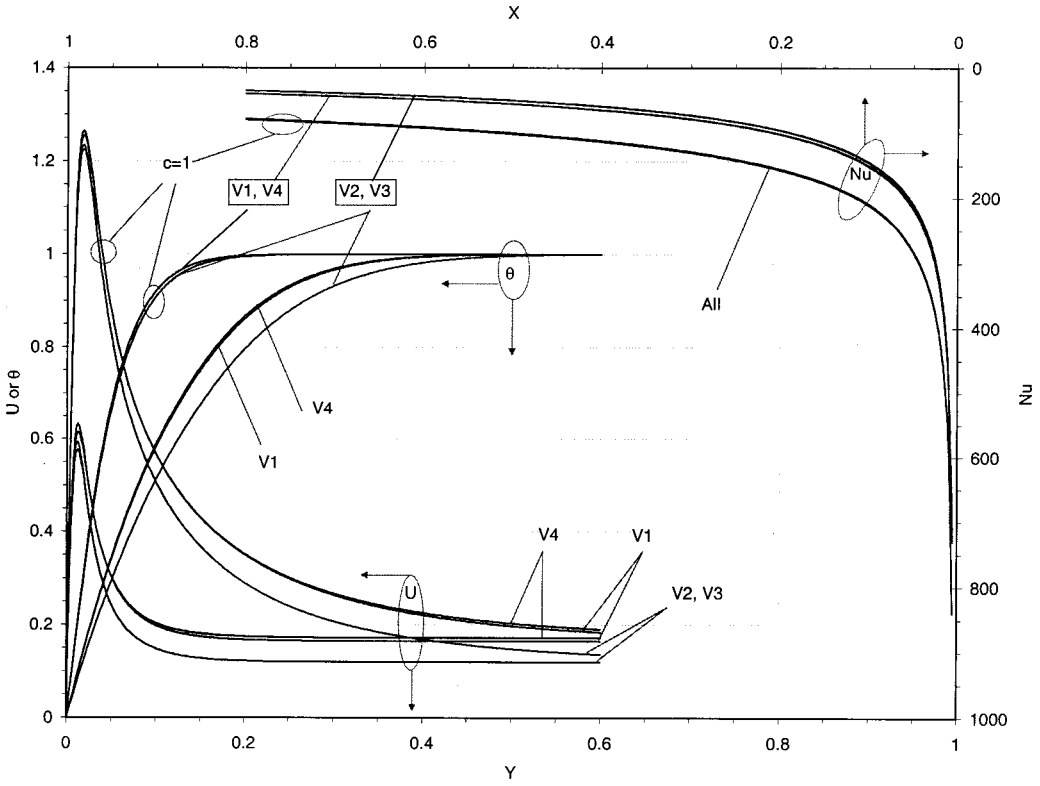

Fig. 14 Effect of constant c on velocity, temperature, and Nusselt number distributions for the variable porosity category [$dp/dx=1493$, $d_p=0.008$, $b=0.98$, $\varepsilon_\infty=0.5$]; (*a*) $c=1.0$, (*b*) $c=5.0$

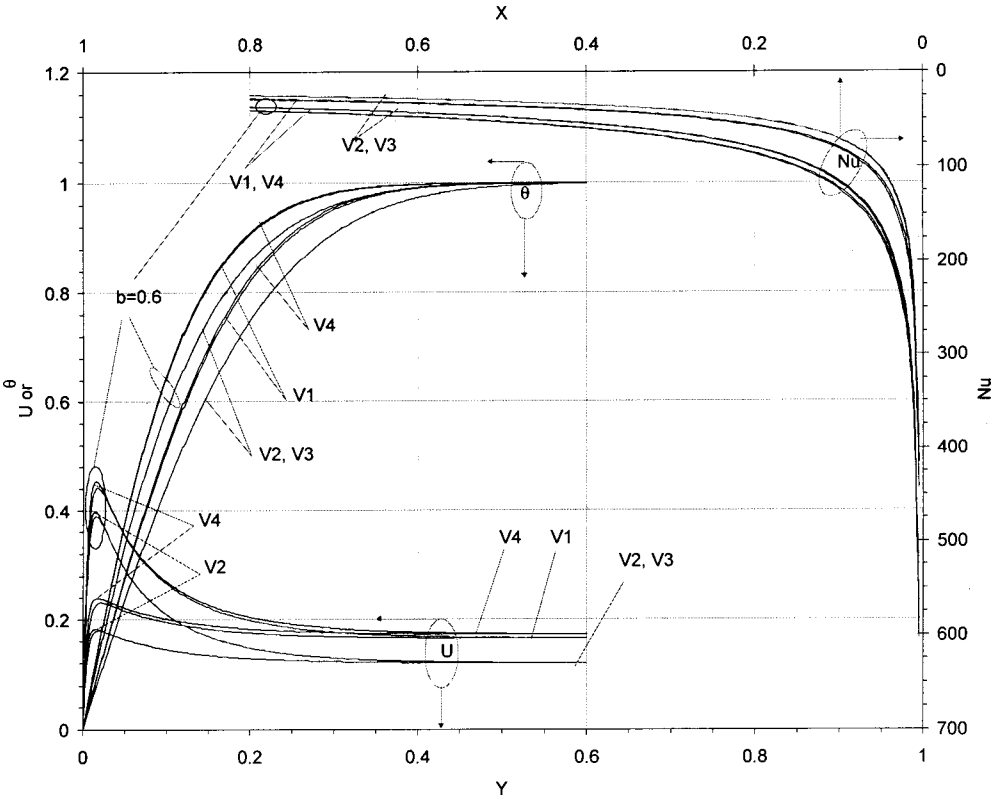

Fig. 15 Effect of constant *b* on velocity, temperature, and Nusselt number distributions for the variable porosity category [$dp/dx=1493$, $d_p=0.008$, $c=2.0$, $\varepsilon_\infty=0.5$]; (*a*) $b=0.2$, (*b*) $b=0.6$

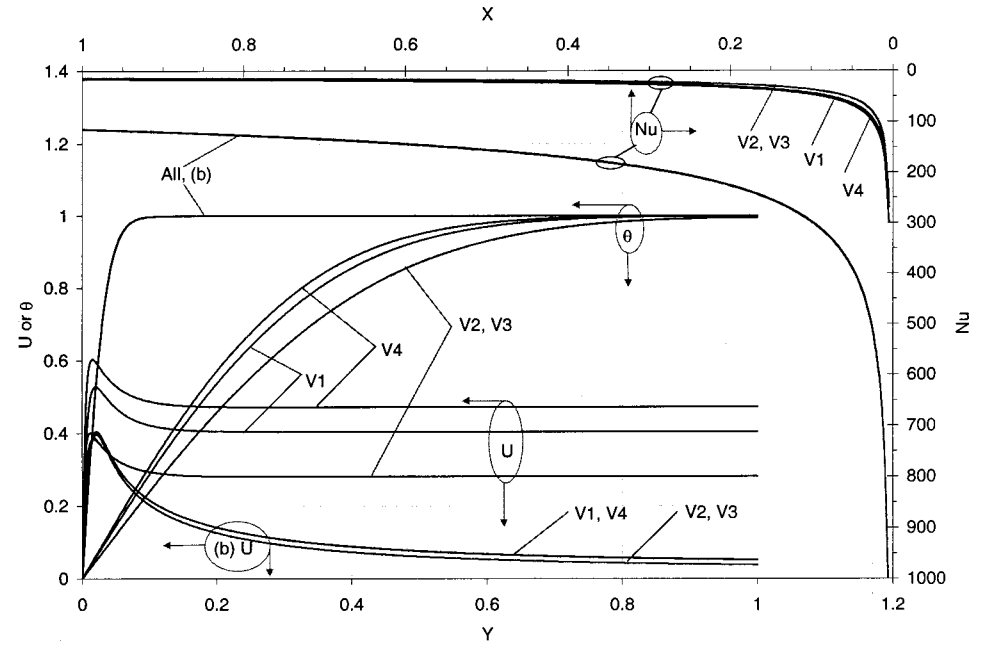

Fig. 16 Velocity, temperature, and Nusselt number distributions for the variable porosity category (*a*) $dp/dx=746$, $d_p=0.008$, $b=0.2$, $c=5.0$, $\varepsilon_\infty=0.4$; (*b*) $dp/dx=2985$, $d_p=0.016$, $b=0.98$, $c=1.0$, $\varepsilon_\infty=0.5$

4.3 Thermal Dispersion. The effect of thermal dispersion has been studied by a number of researchers in the past few years and has been shown to enhance the heat transfer process. These studies have tried to correlate the experimental data to a formulation for the thermal dispersion conductivity or diffusivity. A detailed analysis of the research works in this area reveals the existence of five pertinent models as displayed in Table 4. The present section considers the effects of using these five variant models for the transverse thermal dispersion conductivity on the transport processes in porous media. For this category, a constant porosity assumption was invoked since the variable porosity category was analyzed earlier.

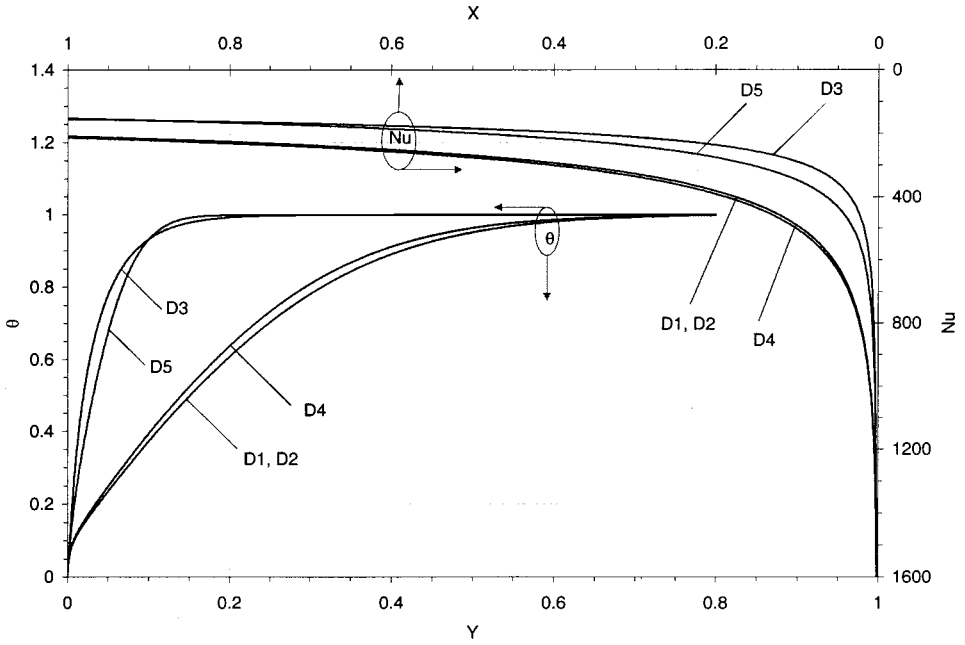

Fig. 17 Effect of porosity variations on temperature and Nusselt number distributions for the thermal dispersion category [ε=1/3.5, Λ=10, Da=10^{-4}, Re_p=100, and d_p=0.008]

Figures 17–24 present the effect of variations within the models utilized for the thermal dispersion category. Models D1 and D2 will be identical when the porosity equals 1/3.5 while models D1 and D4 will be identical when the porosity equals 0.27. Moreover, models D2 and D4 will be the same if the porosity of the porous medium is 0.25 as indicated in Fig. 19. In the present investigation, γ=0.1 was used for model D1, γ=0.04 was used for model D2, and γ=0.17 and w=1.5 were used for model D3. It is easier to observe the differences between models D1, D2, and D4. However, models D3 and D5 have different structures requiring a more careful set of comparisons. A comprehensive numerical study was performed to analyze the variances between the five cited models.

The effects of porosity, inertia parameter, Darcy number, Reynolds number, and the particle diameter on the variances within the thermal dispersion category are best illustrated in terms of their effects on the temperature and the local Nusselt number profiles. Changing the porosity has a significant effect on models D1, D2, and D4, while changing the Darcy number has a greater impact on model D5 since the permeability is directly a function of

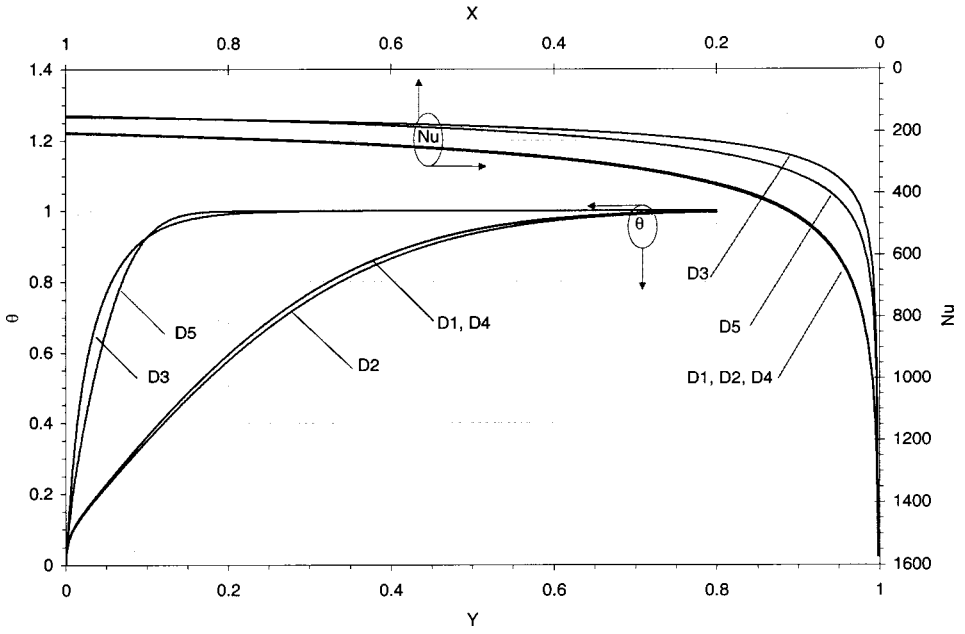

Fig. 18 Effect of porosity variations on temperature and Nusselt number distributions for the thermal dispersion category [ε=0.27, Λ=10, Da=10^{-4}, Re_p=100, and d_p=0.008]

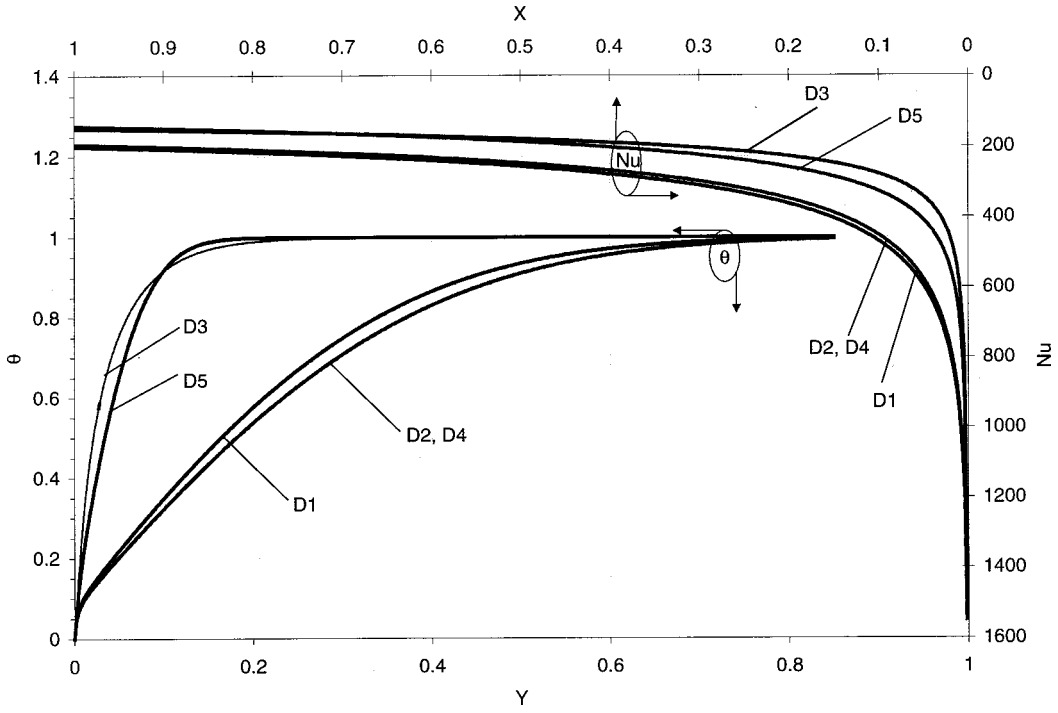

Fig. 19 Effect of porosity variations on temperature and Nusselt number distributions for the thermal dispersion category [ε=0.25, Λ=10, Da=10^{-4}, Re_p=100, and d_p=0.008]

the Darcy number. In general, model D3 has the thinnest thermal boundary layer while model D1 has the thickest boundary layer. Figures 17–20 show the effect of porosity on the temperature profiles and the Nusselt number profiles for the five dispersion models. It can be seen that models D1, D2, and D4 are affected by changing the porosity while the effect of porosity on models D3 and D5 is insignificant. The effect of the inertia parameter Λ is shown in Fig. 21, it can be seen that an increase in the inertia parameter causes a reduction in the disparity between the five models without changing the orders. This happens because the inertia parameter affects the velocity distribution and consequently affects the temperature and Nusselt number profiles. Since a velocity term appears in the expressions for the dispersion conductivity in all the five models, a change in the inertia parameter has an effect of the same order on the thermal dispersion for all of the five variant models.

As mentioned above, the Darcy number has a significant effect on model D5. This effect is shown in Fig. 22. Also, it can be seen

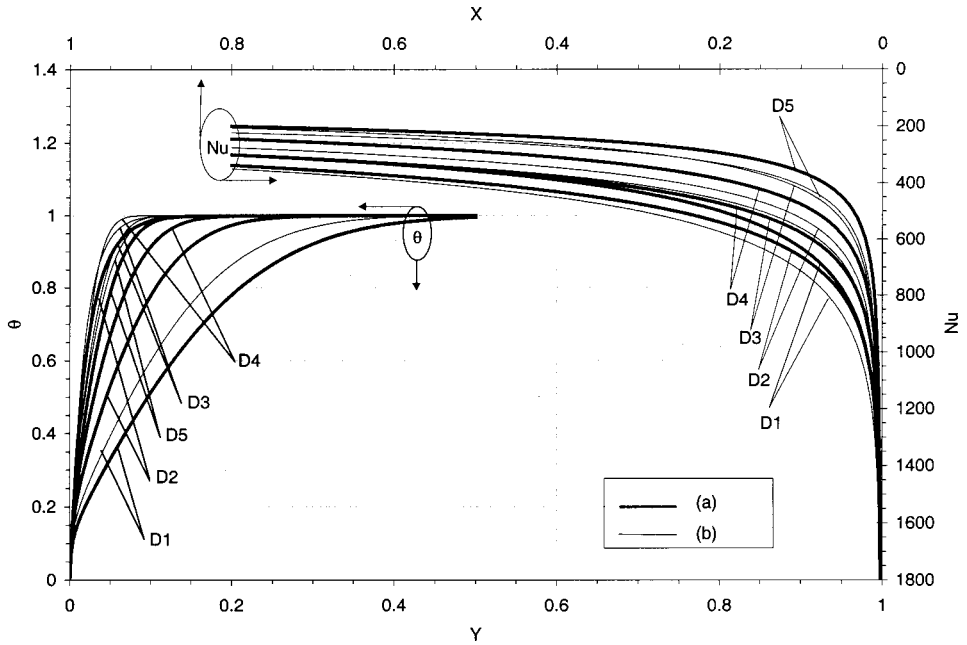

Fig. 20 Effect of porosity variations on temperature and Nusselt number distributions for the thermal dispersion category [Λ=10, Da=10^{-4}, Re_p=100, and d_p=0.008]; (*a*) ε=0.6, (*b*) ε=0.9

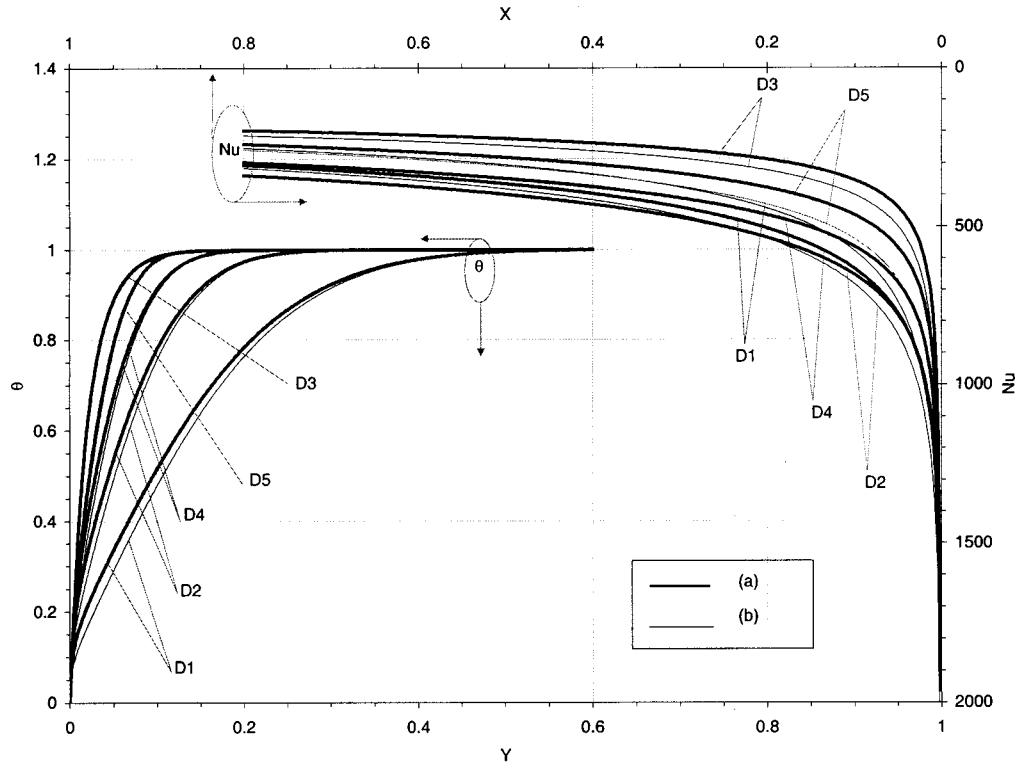

Fig. 21 Effect of inertia parameter variations on temperature and Nusselt number distributions for the thermal dispersion category [ε=0.6, Da=10^{-4}, Re_p=100, and d_p=0.008]; (*a*) Λ=0, (*b*) Λ=100

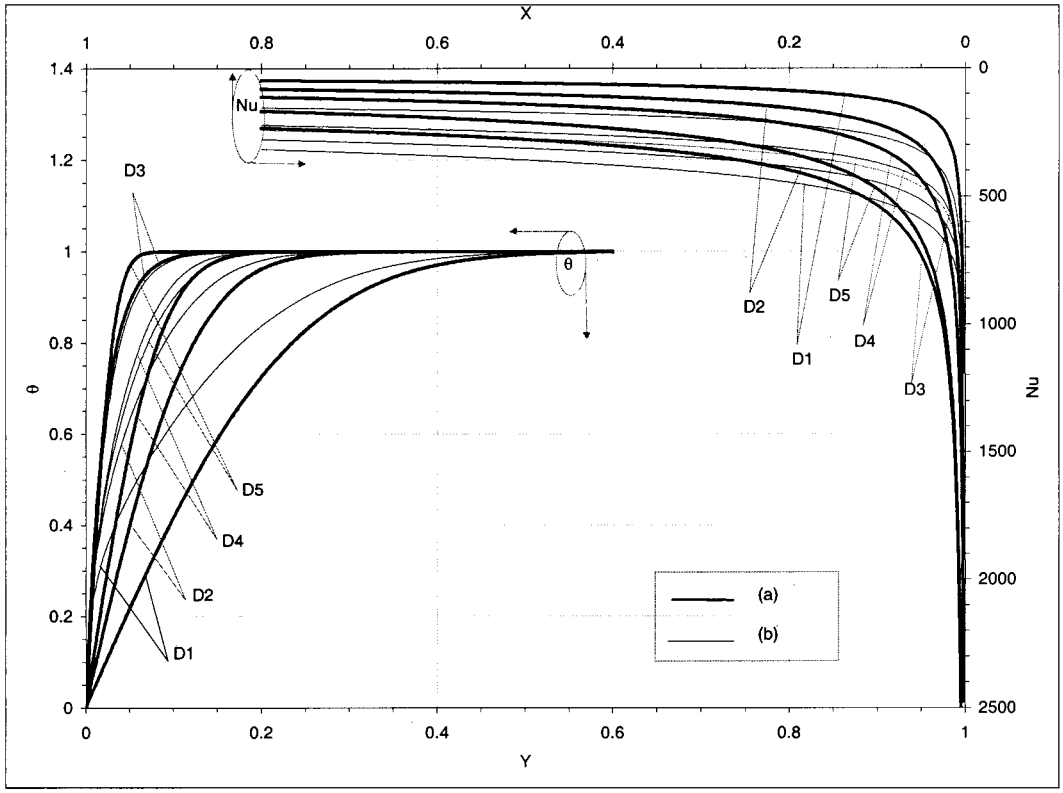

Fig. 22 Effect of Darcy number variations on temperature and Nusselt number distributions for the thermal dispersion category [ε=0.6, Λ=10, Re_p=100, and d_p=0.008]; (*a*) Da=10^{-7}, (*b*) Da=10^{-3}

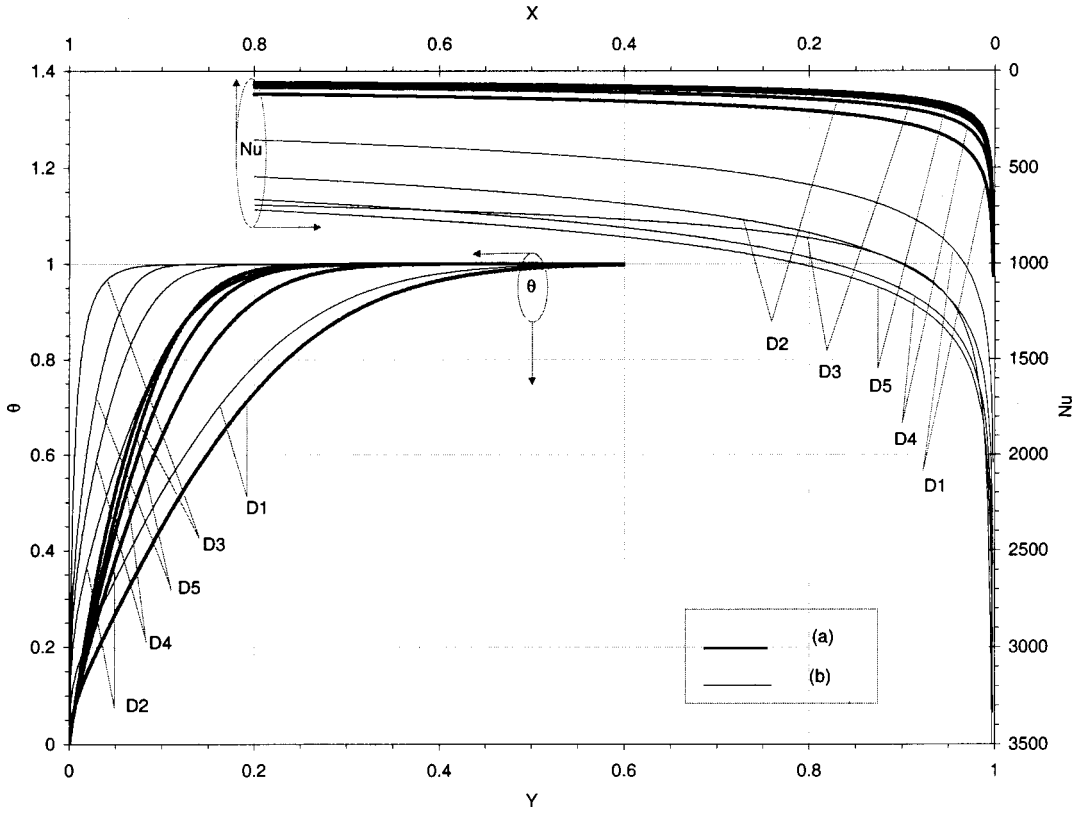

Fig. 23 Effect of Reynolds number variations on temperature and Nusselt number distributions for the thermal dispersion category [ε=0.6, Λ=10, Da=10^{-6}, and d_p=0.008]; (*a*) Re_p=10, (*b*) Re_p=1000

that an increase in the Darcy number, which is equivalent to an increase in the permeability, increases the thermal dispersion conductivity of model D5. The effect of increasing the Reynolds number on the thickness of the thermal boundary layers is shown in Fig. 23. Figure 23 shows the effect of Reynolds number on the Nusselt number distribution for the five dispersion models. It can be seen that at low Reynolds numbers model D3 establishes the lower bound for the heat transfer rate, while models D1 and D2 establish the upper bound. However, at high Reynolds numbers, models D1 and D2 establish the lower bound for the heat transfer rates. Finally, the effect of the particle diameter is found to be significant only for the first four models. This is due to the appearance of the particle diameter in the expressions for the thermal dispersion conductivity for these models. It can be seen from

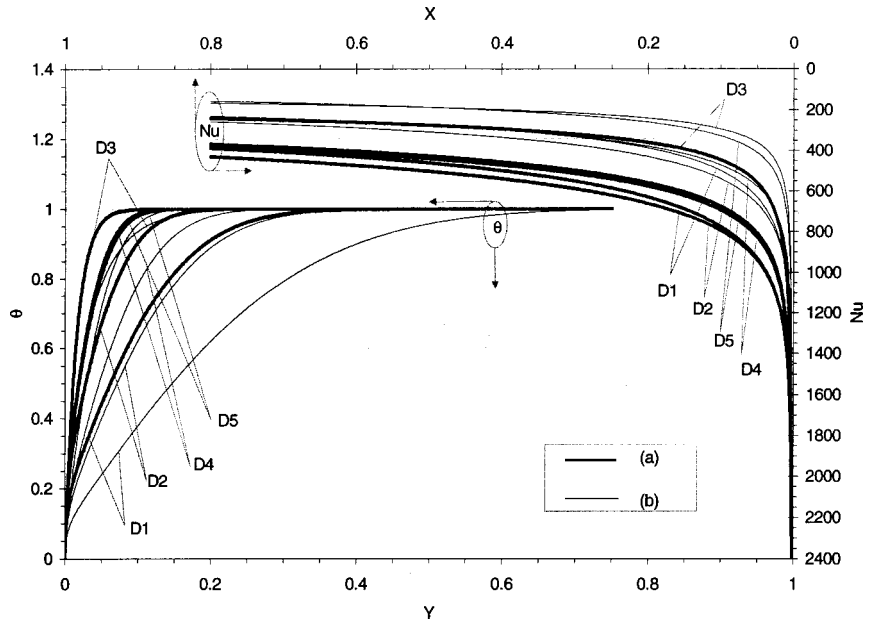

Fig. 24 Effect of particle diameter variations on temperature and Nusselt number distributions for the thermal dispersion category ε=0.6, Λ=10, Da=10^{-6}, and Re_p =100; (*a*) d_p=0.004, (*b*) d_p=0.016

Fig. 24 that model D5 is almost unaffected by changing the particle diameter while the other four models are significantly affected. Increasing the particle diameter enhances the thermal dispersion conductivity and consequently increases the heat transfer rate by causing a formation of a thinner thermal boundary layer.

4.4 Local Thermal Nonequilibrium. Table 5 shows three variant models for the fluid to solid heat transfer coefficient h_{sf} and for the specific surface area of the packed bed a_{sf}, corresponding to the pertinent investigations in the LTNE area. The effects of porosity, inertia parameter, Darcy number, Reynolds number, particle diameter, and ratio of fluid-to-solid conductivities on temperature and Nusselt number profiles for the models shown in Table 5 are analyzed.

Effects of porosity, inertia parameter, Darcy number, Reynolds number, particle diameter, and solid-to-fluid thermal conductivity changes on variances among these models are shown in Figs. 25–31. Porosity is expected to have an effect on the temperature distribution since a porosity term appears in a_{sf} for all the three models. Figure 25 shows the effect of porosity on the temperature distributions as well as the Nusselt number distributions for this category. The higher the porosity the smaller the variances among the three models. At low porosities models E2 and E3 are closer to each other. It is clear from the temperature profiles that the effect of the inertia parameter has an insignificant effect on the order of the thermal boundary layer for these models. However, a lower inertia parameter results in a closer agreement among the three models. Figure 26 shows the effect of the inertia parameter on the Nusselt number profiles. It is also found that the Darcy number also has an insignificant effect on the results. However, higher Darcy numbers cause slightly closer agreement among the models as seen in Fig. 27.

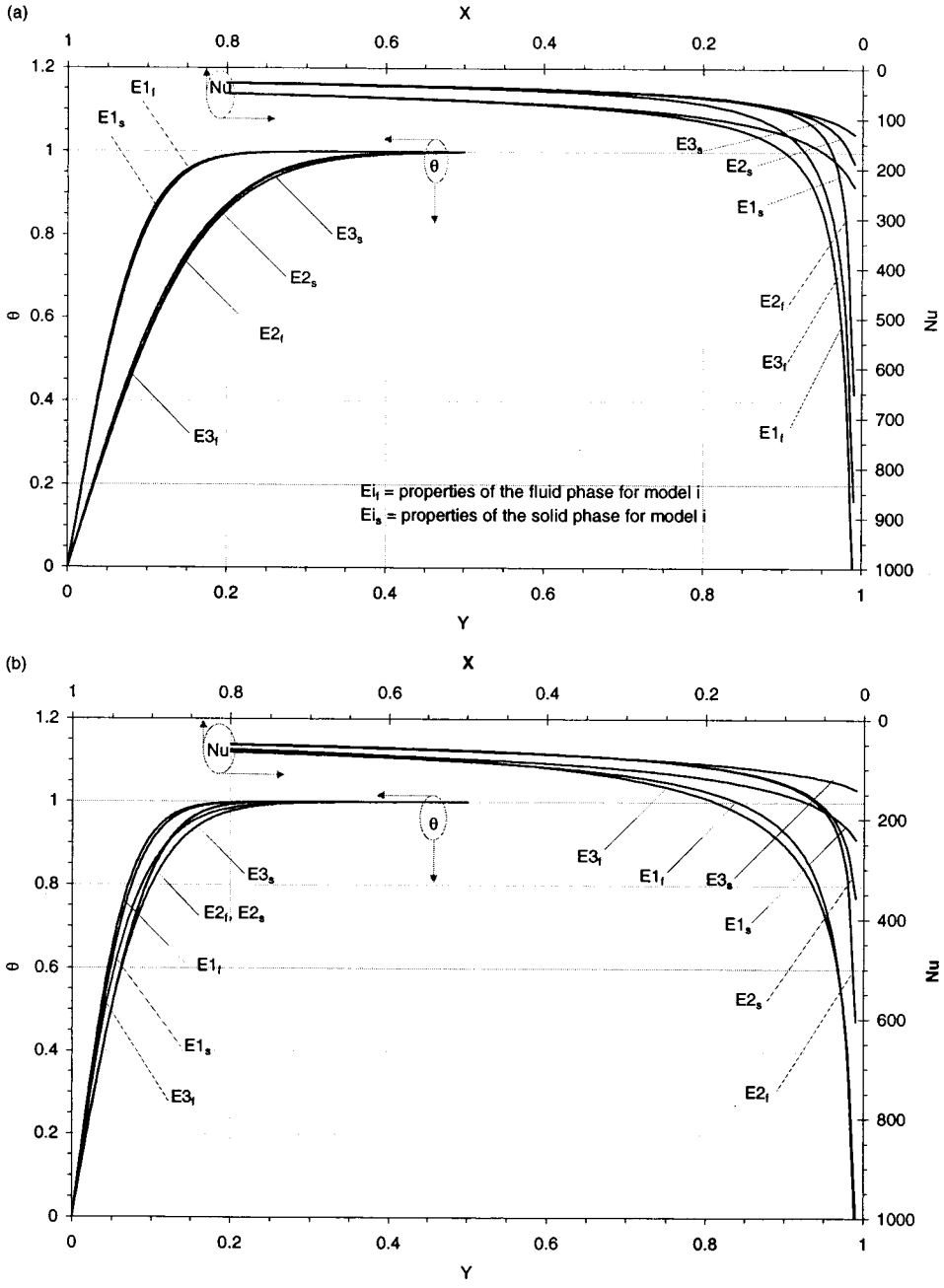

Fig. 25 Effect of porosity variations on temperature and Nusselt number distributions for the LTNE category [Λ=10, Da=10^{-4}, Re_P=100, d_P=0.008, k_s/k_f=25]; (*a*) ε=0.3, (*b*) ε=0.6

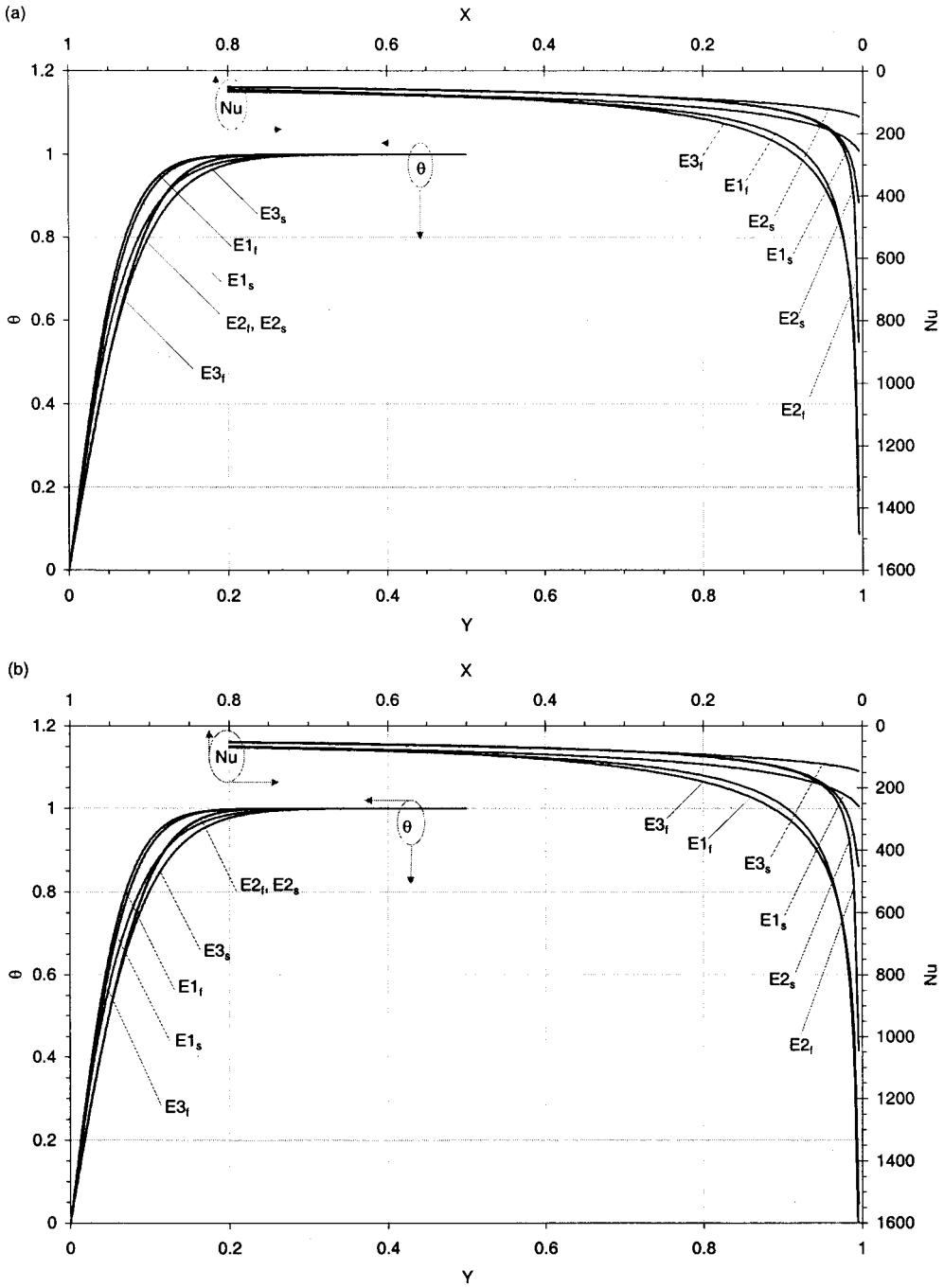

Fig. 26 Effect of inertia parameter variations on temperature and Nusselt number distributions for the LTNE category [ε=0.6, Da=10^{-4}, Re_P=100, d_P=0.008, k_s/k_f=25]; (*a*) Λ=0, (*b*) Λ=100

The Reynolds number is found to have a substantial effect on the variances among the three models. For higher Reynolds numbers the temperature profiles as well as Nusselt number distributions for the three models become closer to each other as shown in Fig. 28. The particle diameter appears in the expressions for h_{sf} and a_{sf} within all of the three models. Therefore, the effect of the particle diameter is expected to be critical. Smaller particle diameters encourage the LTE in models E1 and E3 while minimizing the variances among the three models. Larger particle diameters enhance the LTNE in models E1 and E3 while increasing the variances among the three models as seen in Fig. 29.

It should be noted that the thermal conductivities of the solid and fluid appear in the relationship for h_{sf} for model E3 while only the fluid phase conductivity appears in the h_{sf} equation for models E1 and E2. As such, the solid to fluid thermal conductivity ratio will have a significant effect on the variances among the three models. As seen in Fig. 30, a lower conductivity ratio enhances the LTE and reduces the variances among the three models. Figure 31 demonstrates two extreme conditions. In Fig. 31(*a*), all of the three models tend to be in local thermal equilibrium with very little variances among them, thus resulting in almost a single temperature profile. On the other hand, Fig. 31(*b*) shows conditions under which the LTNE as well as variances among the three models are substantially enhanced.

Recent investigations have made it possible to look at some additional physical effects regarding the thermal nonequilibrium. As such the works by Lee and Vafai [61] and Kuznetsov [62,58,63] can be cited. For example, in Kuznetsov [62–63] it

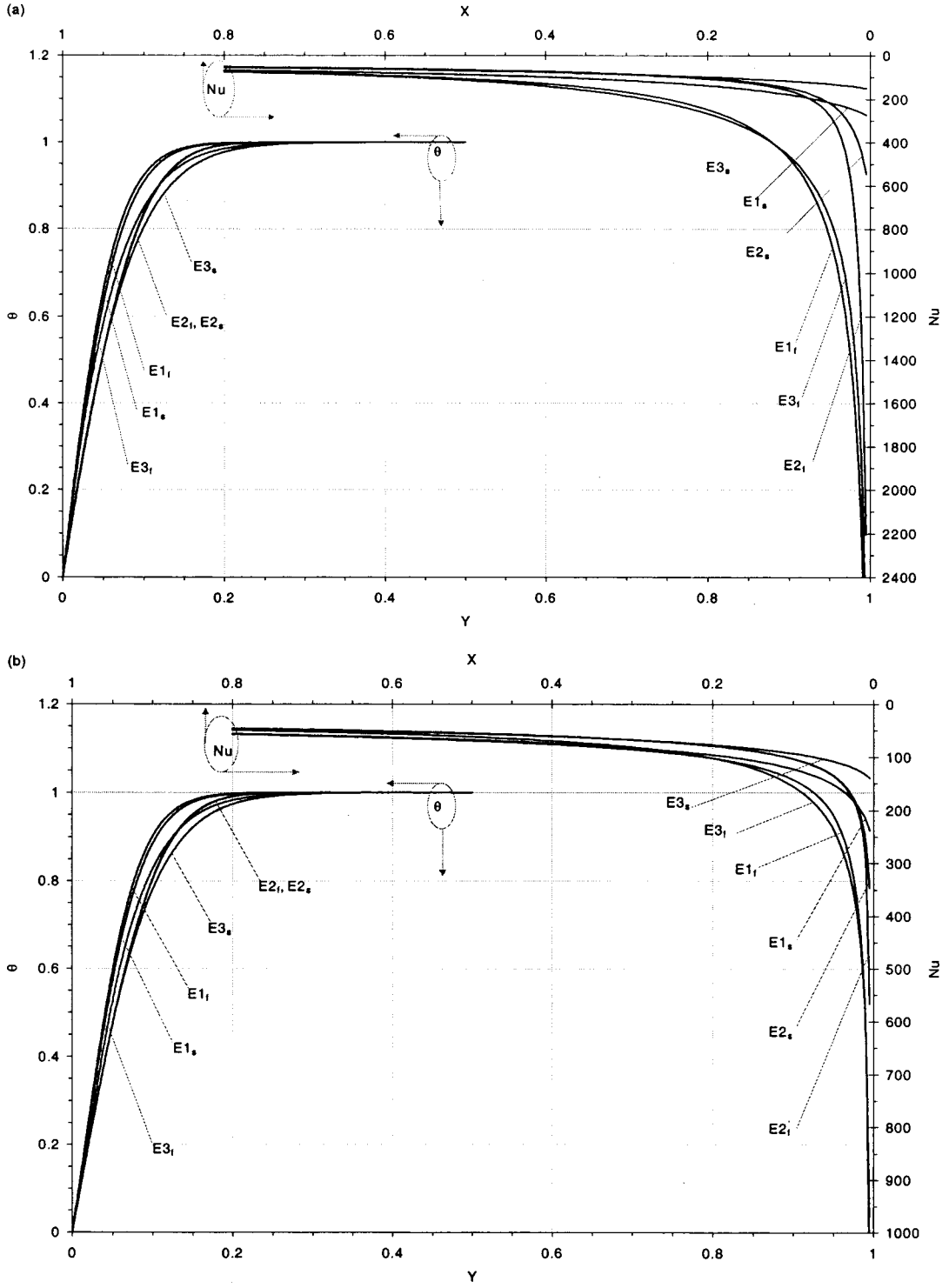

Fig. 27 Effect of Darcy number variations on temperature and Nusselt number distributions for the LTNE category [ε=0.6, Λ=10, Re_P=100, d_P=0.008, k_s/k_f=25]; (*a*) Da=10^{-8} (*b*) Da=10^{-3}

was shown that the temperature difference between the fluid and solid phases in forced convection flow through porous packed bed forms a wave whose amplitude is decreasing while propagating downstream.

A useful set of correlations for conversion of different models within each category is provided as follows.

$$\mathrm{Nu}_{C2}=0.9998\ \mathrm{Nu}_{C1}+0.23\varepsilon^{-1.173}\Lambda^{0.2812}\mathrm{Da}^{0.5357}\mathrm{Re}_H^{0.0636} \quad (11)$$

$$\mathrm{Nu}_{C3}=0.0002\ \mathrm{Nu}_{C1}+0.3664\varepsilon^{-1.2582}\mathrm{Da}^{0.45}\mathrm{Re}_H^{0.1788} \quad (12)$$

$$\mathrm{Nu}_{V2}=-3.927+1.2366\ \mathrm{Nu}_{V1}\left(\frac{dp}{dx}\right)^{-0.0041051} \times d_p^{0.0092769}(\varepsilon_\infty)^{0.1534}b^{0.0348}c^{-0.0218} \quad (13)$$

$$\mathrm{Nu}_{V3}=-4.6447+1.2441\ \mathrm{Nu}_{V1}\left(\frac{dp}{dx}\right)^{-0.005978} \times d_p^{0.0058872}(\varepsilon_\infty)^{0.1621}b^{0.0363}c^{-0.0228} \quad (14)$$

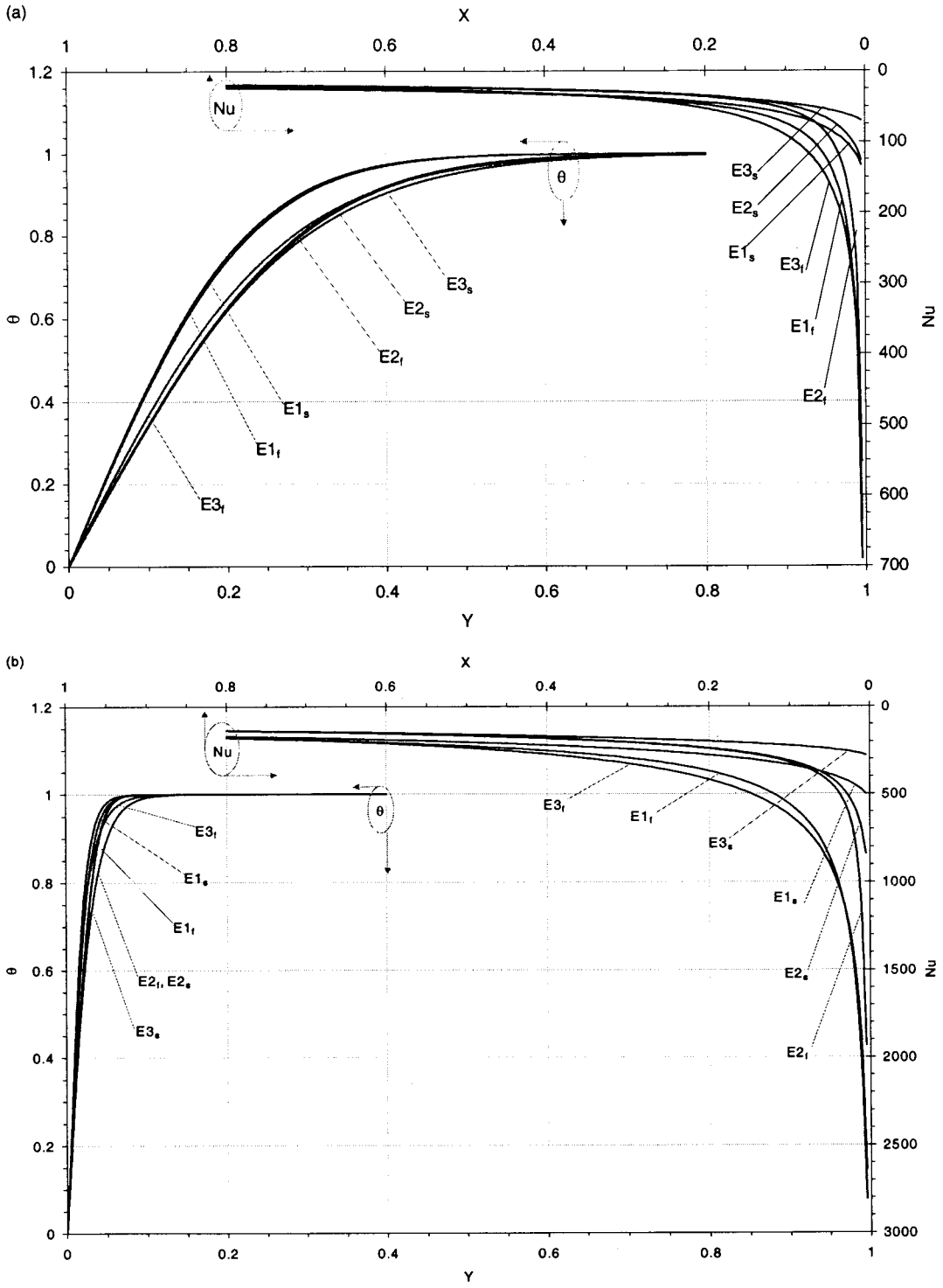

Fig. 28 Effect of Reynolds number variations on temperature and Nusselt number distributions for the LTNE category [ε=0.6, Λ=10, Da=10^{-4}, d_P=0.008, k_s/k_f=25]; (*a*) Re_P=10, (*b*) Re_P=1000

$$\mathrm{Nu}_{V4}=4.7358+0.9921\ \mathrm{Nu}_{V1}\left(\frac{dp}{dx}\right)^{0.0125}\times d_p^{0.0152}(\varepsilon_\infty)^{0.0578}b^{0.0253}c^{-0.01} \quad (15)$$

$$\mathrm{Nu}_{D2}=4.8126+0.9898(4.8132+\mathrm{Nu}_{D1})^{0.9983}+0.9581\varepsilon^{0.0634}\Lambda^{1.0442}\mathrm{Da}^{0.7976}\mathrm{Re}_p^{1.2389}d_p^{0.9967}\mathrm{Nu}_{D1}^{1.0593} \quad (16)$$

$$\mathrm{Nu}_{D3}=29.5369+0.3445\varepsilon^{0.2447}(61.4249+\Lambda)^{0.1497}\mathrm{Da}^{-0.1152}\times\mathrm{Re}_p^{0.511}d_p^{-0.2456}\mathrm{Nu}_{D1}^{0.2314} \quad (17)$$

$$\mathrm{Nu}_{D4}=45.8467+0.8801\,\mathrm{Nu}_{D1}^{0.9983}+0.721\varepsilon^{-0.3152}\Lambda^{0.8653}\times\mathrm{Da}^{0.7076}\mathrm{Re}_p^{1.3521}d_p^{1.05}\mathrm{Nu}_{D1}^{1.0548} \quad (18)$$

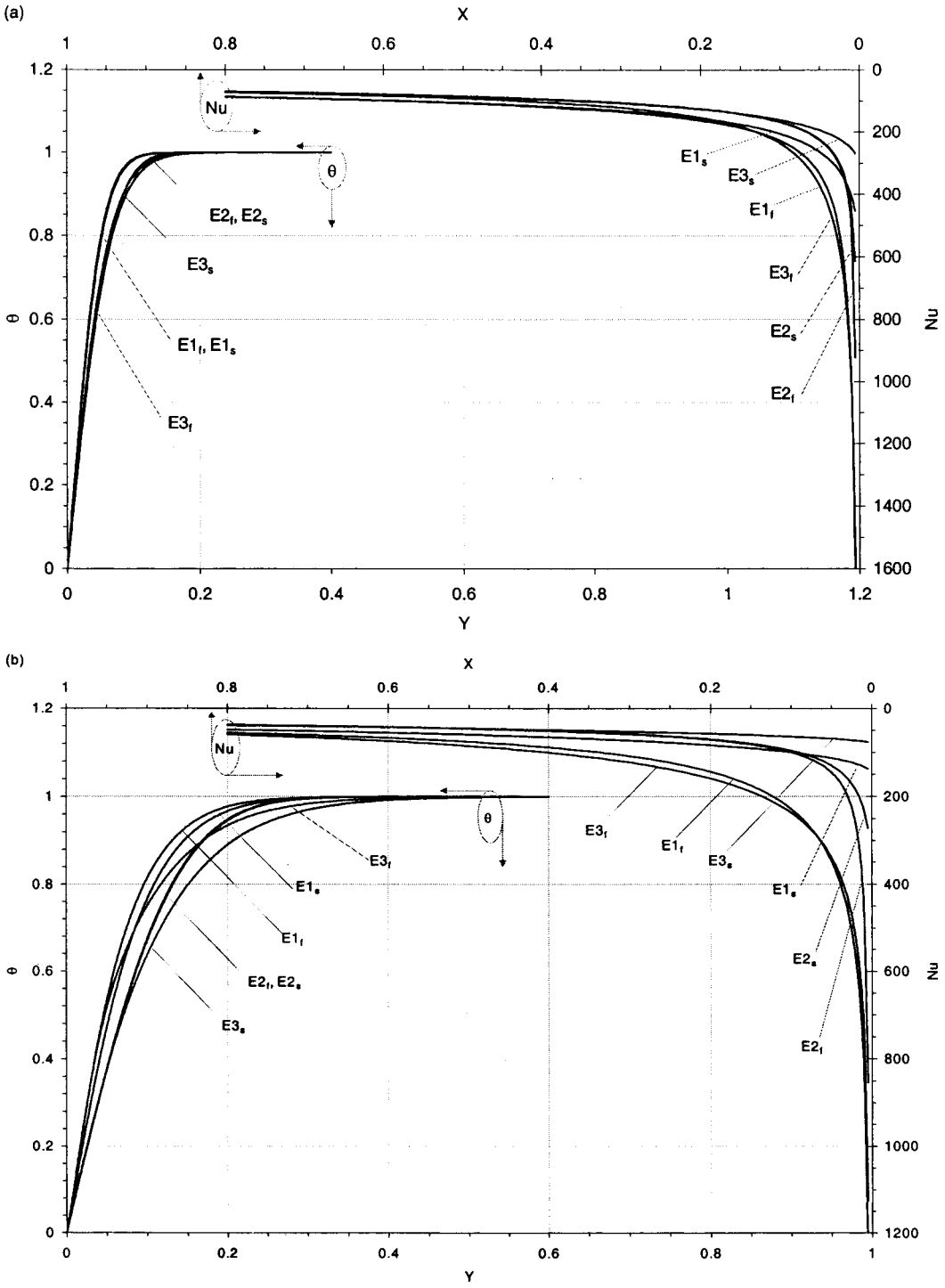

Fig. 29 Effect of particle diameter variations on temperature and Nusselt number distributions for the LTNE category [ε=0.6, Λ=10, Da=10^{-4}, Re_P=100, k_s/k_f=25]; (*a*) d_P=0.004, (*b*) d_P=0.016

$$Nu_{D5} = -71.2195 + 0.137\varepsilon^{0.2971}(389.0253+\Lambda)^{0.4933} \times Da^{-0.0354} Re_p^{0.3744} d_p^{-0.3873} Nu_{D1}^{0.2098} \quad (19)$$

$$Nu_{E2f} = 2.4262 + 1.2043(Nu_{E1f})^{0.8152} + 0.7792\varepsilon^{0.2.2892}\Lambda^{0.0485} \times Da^{0.1749} Re_p^{0.1567} d_p^{-0.0531} \left(\frac{k_s}{k_f}\right)^{-0.4402} (Nu_{E1f})^{1.268} \quad (20)$$

$$Nu_{E3f} = -77.5642 + 0.2554(Nu_{E1f})^{1.1645} + 81.2051\varepsilon^{0.5343}(0.3576+\Lambda)^{0.0139} Da^{-0.0201} \times Re_p^{0.1605} d_p^{0.0328} \left(\frac{k_s}{k_f}\right)^{-0.0019348} \quad (21)$$

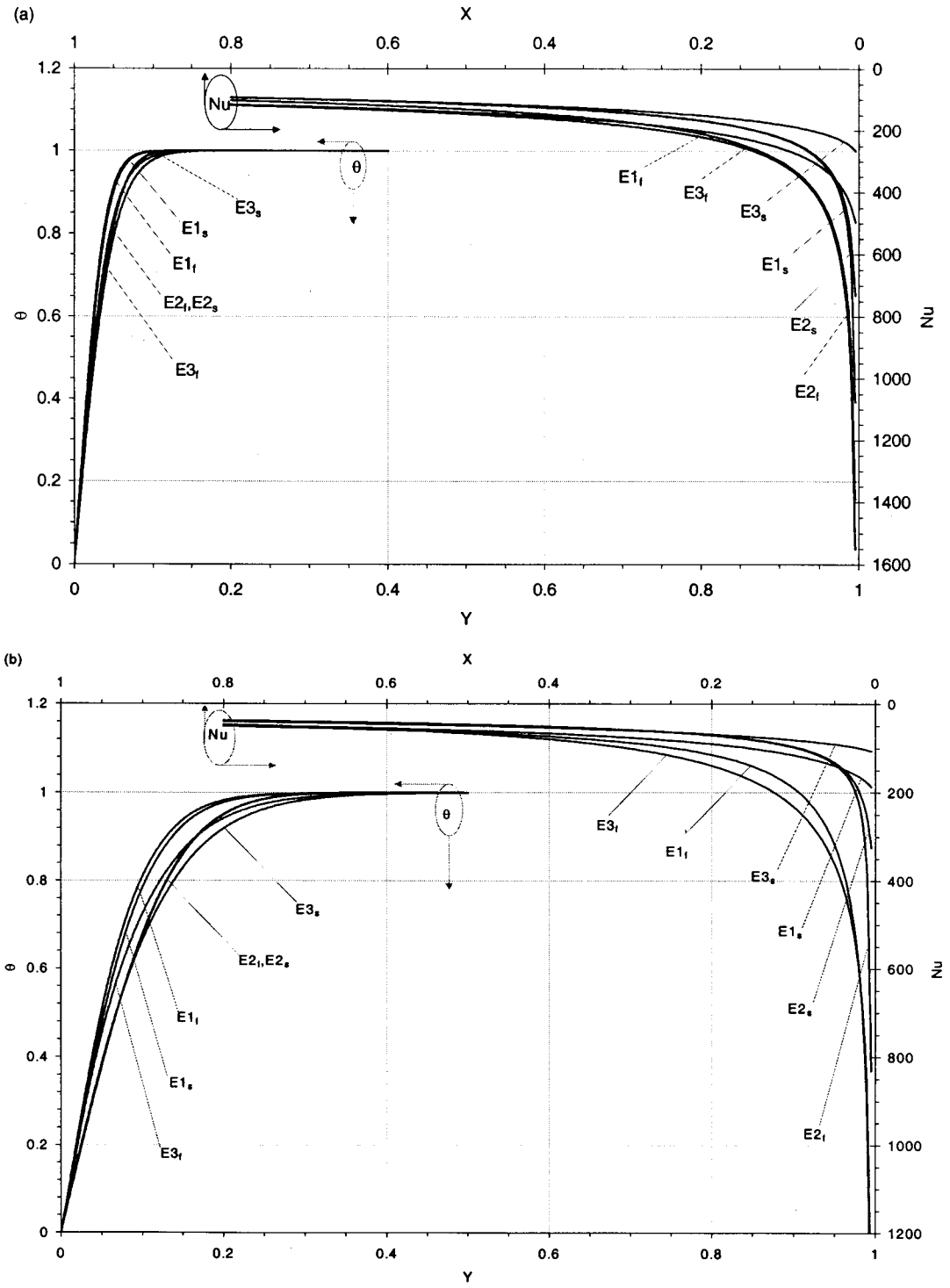

Fig. 30 Effect of solid-to-fluid thermal conductivity ratio variations on temperature and Nusselt number distributions for the LTNE category [ε=0.6, Λ=10, Da=10^{-4}, Re_P=100, d_P=0.008]; (*a*) k_s/k_f=5, (*b*) k_s/k_f=50

$$\mathrm{Nu}_{\mathrm{E2}s} = -10.5362 + 1.7505(\mathrm{Nu}_{\mathrm{E1}s})^{0.8054} + 0.0515\varepsilon^{1.469}\mathrm{Da}^{0.0187}\mathrm{Re}_p^{-0.3453} \times d_p^{0.6346}\left(\frac{k_s}{k_f}\right)^{0.3848}(\mathrm{Nu}_{\mathrm{E1}s})^{2.2807} \quad (22)$$

$$\mathrm{Nu}_{\mathrm{E2}s} = -9.566 + 0.7751(\mathrm{Nu}_{\mathrm{E1}s})^{0.9753} + 28.018\varepsilon^{1.6719} \times (0.0463+\Lambda)^{0.0154}\mathrm{Da}^{-0.011}\mathrm{Re}_p^{0.7615}d_p^{-1.1829}\left(\frac{k_s}{k_f}\right)^{-0.6435} \times (\mathrm{Nu}_{\mathrm{E1}s})^{-1.5} \quad (23)$$

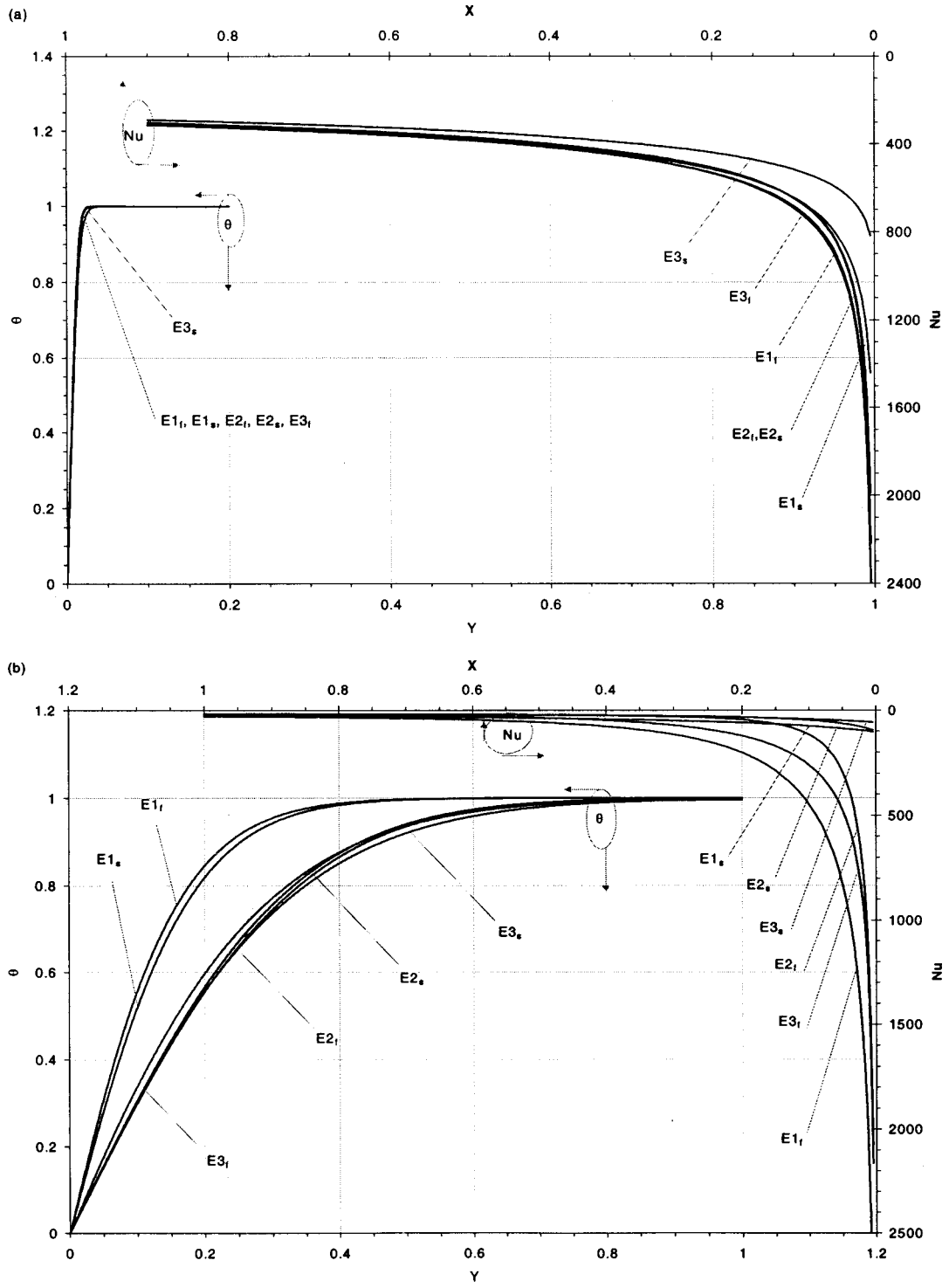

Fig. 31 Temperature and Nusselt number distributions for the LTNE category; (*a*) $\varepsilon=0.9$, $\Lambda=0$, Da $=10^{-3}$, $Re_P=1000$, $d_P=0.004$, $k_s/k_f=5$, (*b*) $\varepsilon=0.3$, $\Lambda=100$, $Da=10^{-8}$, $Re_P=100$, $d_P=0.016$, $k_s/k_f=50$

Equations (11) and (12) convert the results from models C2 and C3 to model C1 for the constant porosity category. Equations (13), (14) and (15) convert the results from models V2, V3, and V4 to model V1 for the variable porosity category. Equations (16), (17), (18), and (19) convert the results from models D2, D3, D4, and D5 to model D1 for the thermal dispersion category. Finally, Eqs. (20), (21), (22), and (23) convert the results from models E2 and E3 to model E1 for the local thermal nonequilibrium category.

5 Conclusions

A comprehensive comparative study of the models for transport processes through a porous medium was performed. Four major categories namely constant porosity, variable porosity, thermal dispersion, and local thermal nonequilibrium were analyzed in detail. The main objective of the present study was to analyze the variances among these models within each category. The results of this investigation systematically quantify and characterize the

effects of the pertinent controlling parameters on the variances among different models. It is shown that for some cases the variances within different models have a negligible effect on the results, while for some cases the variations can become significant. In general, the variances have a more pronounced effect on the velocity field and a substantially smaller effect on the temperature field and Nusselt number distribution.

The variants among models for the constant porosity and the variable porosity categories are generally small and are anticipated to be well within experimental uncertainties. As such, these models can be considered to have negligible variances amongst them. On the other hand, the variants among models for the thermal dispersion category are found to be more pronounced. For small porosities, models D1, D2, and D4 are close to each other while for large porosities, models D2, D3, D4, and D5 are close to each other. For small inertia parameters, model D1 and D4 are found to be close to each other while for large inertia parameters, models D1 and D5 are closer to each other. For low Reynolds numbers, models D3 and D5 are close to each other. For small particle diameters, models D1, D4, and D5 are found to be closer to each other. Finally, the variants among models for the local thermal nonequilibrium category are not substantial and are generally more pronounced within the entry region and well within experimental uncertainties. However, model E1 differs from models E2 and E3 for the cases of small porosities and low Reynolds numbers. It should be noted that a detailed analysis of different types of interfacial conditions between a porous medium and a fluid layer was also recently investigated by Alazmi and Vafai [64].

Nomenclature

a_{sf} = specific surface area of the packed bed, m^{-1}
b, c = porosity variation parameters, Eq. (4)
C_p = specific heat at constant pressure, J kg^{-1} K^{-1}
d_p = particle diameter, m
d_v = parameter defined in Table 5
Da = Darcy number, K/H^2
F = geometric function defined in Eq. (3)
h_{sf} = fluid-to-solid heat transfer coefficient, W m^{-2} K^{-1}
H = half the height of the packed bed, m
k = thermal conductivity, W m^{-1} K^{-1}
K = permeability, m^2
L = length of the packed bed, m
Nu = local Nusselt number, hD_h/k_{eff}
Nu = average Nusselt number
Pe = Peclet number, $u_c d_p/\alpha_f$
Pr = Prandtl number, $\mu C_{Pf}/k_f$
Re_H = Reynolds number, $u_c H/\nu$
Re_p = particle Reynolds number, $u_c d_p/\nu$
T = temperature, K
u = velocity in x-direction, m s^{-1}
U = nondimensional velocity, u/u_c
x, y = Cartesian coordinates, m
X, Y = nondimensional coordinates, x/H and y/H

Greek Symbols

α = thermal diffusivity, m^2 s^{-1}
γ = dispersion coefficient parameter
ε = porosity
Λ = inertia parameter, $\varepsilon^{3/2} F u_\infty H/\nu_f$
μ = kinematics viscosity, kg m^{-1} s^{-1}
ν = dynamic viscosity, m^2 s^{-1}
θ = dimensionless temperature, $(T_w - T)/(T_w - T_e)$
Θ = dimensionless temperature, $h(T_w - T)/q_w$

Subscripts

c = convective component
d = dispersion
e = inlet
eff = effective property
f = fluid
s = solid
w = wall
∞ = freestream

References

[1] Vafai, K., and Tien, C. L., 1981, ''Boundary and Inertia Effects on Flow and Heat Transfer in Porous Media,'' Int. J. Heat Mass Transf., **24**, pp. 195–203.
[2] Vafai, K., and Tien, C. L., 1982, ''Boundary and Inertia Effects on Convective Mass Transfer in Porous Media,'' Int. J. Heat Mass Transf., **25**, pp. 1183–1190.
[3] Vafai, K., and Kim, S. J., 1989, ''Forced Convection in a Channel Filled With a Porous Medium: An Exact Solution,'' ASME J. Heat Transfer, **111**, pp. 1103–1106.
[4] Hadim, A., 1994, ''Forced Convection in a Porous Channel With Localized Heat Sources,'' ASME J. Heat Transfer, **116**, pp. 465–472.
[5] Kaviany, M., 1985, ''Laminar flow through a porous channel bounded by isothermal parallel plates,'' Int. J. Heat Mass Transf., **28**, pp. 851–858.
[6] Lauriat, G., and Vafai, K., 1991, ''Forced Convective Flow and Heat Transfer Through a Porous Medium Exposed to a Flat Plate or a Channel,'' *Convective Heat and Mass Transfer in Porous Media*, S. Kacac, B. Kilikis, F. A. Kulacki, and F. Arnic, eds., Kluwer Academic, Dordrecht, pp. 289–328.
[7] Beckermann, C., and Viskanta, R., 1987, ''Forced Convection Boundary Layer Flow and Heat Transfer Along a Flat Plate Embedded in a Porous Medium,'' Int. J. Heat Mass Transf., **30**, pp. 1547–1551.
[8] Kim, S. J., and Choi, C. Y., 1996, ''Convective Heat Transfer in Porous and Overlying Fluid Layers Heated From Below,'' Int. J. Heat Mass Transf., **39**, pp. 319–329.
[9] Kladias, N., and Prasad, V., 1990, ''Flow Transitions in Buoyancy-Induced Non-Darcy Convection in a Porous Medium Heated From Below,'' ASME J. Heat Transfer, **112**, pp. 675–684.
[10] Nield, D. A., Junqueira, S. L. M., and Lage, J. L., 1996, ''Forced Convection in a Fluid-Saturated Porous-Medium Channel With Isothermal or Isoflux Boundaries,'' J. Fluid Mech., **322**, pp. 201–214.
[11] Sung, H. J., Kim, S. Y., and Hyun, J. M., 1995, ''Forced Convection From an Isolated Heat Source in a Channel With Porous Medium,'' Int. J. Heat Fluid Flow, **16**, pp. 527–535.
[12] You, H. I., and Chang, C. H., 1997, ''Determination of Flow Properties in Non-Darcain Flow,'' ASME J. Heat Transfer, **119**, pp. 840–843.
[13] You, H. I., and Chang, C. H., 1997, ''Numerical Prediction of Heat Transfer Coefficient for a Pin-Fin Channel Flow,'' ASME J. Heat Transfer, **119**, pp. 840–843.
[14] Neale, G., and Nader, W., 1974, ''Practical Significance of Brinkman's Extension of Darcy's Law: Coupled Parallel Flows Within a Channel and a Bounding Porous Medium,'' Can. J. Chem. Eng., **52**, pp. 475–478.
[15] Poulikakos, D., and Kazmierczak, M., 1987, ''Forced Convection in a Duct Partially Filled With a Porous Material,'' ASME J. Heat Transfer, **109**, pp. 653–662.
[16] Kim, S. Y., Kang, B. H., and Hyun, J. M., 1994, ''Heat Transfer From Pulsating Flow in a Channel Filled With Porous Media,'' Int. J. Heat Mass Transf., **37**, pp. 2025–2033.
[17] Chen, S. C., and Vafai, K., 1996, ''Analysis of Free Surface Momentum and Energy Transport in Porous Media,'' Numer. Heat Transfer, Part A, **29**, pp. 281–296.
[18] Nakayama, A., Kokudai, T., and Koyama, H., 1990, ''Non-Darcian Boundary Layer Flow and Forced Convection Heat Transfer Over a Flat Plate in a Fluid-Saturated Porous Medium,'' ASME J. Heat Transfer, **112**, pp. 157–162.
[19] Hong, J. T., Tien, C. L., and Kaviany, M., 1985, ''Non-Darcain Effects on Vertical-Plate Natural Convection in Porous Media With High Porosities,'' Int. J. Heat Mass Transf., **28**, pp. 2149–2157.
[20] Kaviany, M., 1987, ''Boundary layer treatment of forced convection heat transfer from a semi-infinite flat plate embedded in porous media,'' ASME J. Heat Transfer, **109**, pp. 345–349.
[21] Kuznetsov, A. V., 1996, ''Analytical Investigation of the Fluid Flow in the Interface Region Between a Porous Medium and a Clear Fluid in Channels Partially Filled With a Porous Medium,'' Appl. Sci. Res., **56**, pp. 53–67.
[22] Lan, X. K., and Khodadadi, J. M., 1993, ''Fluid Flow and Heat Transfer Through a Porous Medium Channel With Permeable Walls,'' Int. J. Heat Mass Transf., **36**, pp. 2242–2245.
[23] Nakayama, A., Koyama, H., and Kuwahara, F., 1988, ''An Analysis on Forced Convection in a Channel Filled With a Brinkman-Darcy Porous Medium: Exact and Approximate Solutions,'' Wearme-und Stoffeubertragung, **23**, pp. 291–295.
[24] Ould-Amer, Y., Chikh, S., Bouhadef, K., and Lauriat, G., 1998, ''Forced Convection Cooling Enhancement by use of Porous Materials,'' Int. J. Heat Fluid Flow, **19**, pp. 251–258.
[25] Vafai, K., and Kim, S. J., 1995, discussion of ''Forced Convection in a Porous Channel With Localized Heat Sources,'' ASME J. Heat Transfer, **117**, pp. 1097–1098.
[26] Vafai, K., and Kim, S. J., 1995, ''On the Limitations of the Brinkman-Forchheimer-Extended Darcy Equation,'' Int. J. Heat Fluid Flow, **16**, pp. 11–15.

[27] Tien, C. L., and Vafai, K., 1989, ''Convective and Radiative Heat Transfer in Porous Media,'' Adv. Appl. Mech., **27**, pp. 225–282.
[28] Kaviany, M., 1995, *Principles of Heat Transfer in Porous Media*, 2nd Ed., Springer-Verlag, New York.
[29] Nield, D. A., and Bejan, A., 1995, *Convection in Porous Media*, 2nd Ed., Springer-Verlag, New York.
[30] Vafai, K., 1984, ''Convective Flow and Heat Transfer in Variable-Porosity Media,'' J. Fluid Mech., **147**, pp. 233–259.
[31] Vafai, K., 1986, ''Analysis of the Channeling Effect in Variable Porosity Media,'' ASME J. Energy Resour. Technol., **108**, pp. 131–139.
[32] Vafai, K., Alkire, R. L., and Tien, C. L., 1985, ''An Experimental Investigation of Heat Transfer in Variable Porosity Media,'' ASME J. Heat Transfer, **107**, pp. 642–647.
[33] Poulikakos, D., and Renken, K., 1987, ''Forced Convection in a Channel Filled With Porous Medium, Including the Effects of Flow Inertia, Variable Porosity, and Brinkman Friction,'' ASME J. Heat Transfer, **109**, pp. 880–888.
[34] Renken, K., and Poulikakos, D., 1988, ''Experiment and Analysis of Forced Convective Heat Transport in a Packed Bed of Spheres,'' Int. J. Heat Mass Transf., **25**, pp. 1399–1408.
[35] Hunt, M. L., and Tien, C. L., 1988, ''Effects of Thermal Dispersion on Forced Convection in Fibrous Media,'' Int. J. Heat Mass Transf., **31**, pp. 301–309.
[36] Hunt, M. L., and Tien, C. L., 1988, ''Non-Darcian Convection in Cylindrical Packed Beds,'' ASME J. Heat Transfer, **110**, pp. 378–384.
[37] Hsiao, S. W., Cheng, P., and Chen, C. K., 1992, ''Non-uniform Porosity and Thermal Dispersion Effects on Natural Convection About a Heated Horizontal Cylinder in an Enclosed Porous Medium,'' Int. J. Heat Mass Transf., **35**, pp. 3407–3418.
[38] Hong, J. T., Yamada, Y., and Tien, C. L., 1987, ''Effect of non-Darcian Non-Uniform Porosity on Vertical-Plate Natural Convection in Porous Media,'' ASME J. Heat Transfer, **109**, pp. 356–362.
[39] Chen, H., 1996, ''Technical Note: Non-Darcy Mixed Convection From a Horizontal Surface With Variable Surface Heat Flux in a Porous Medium,'' Numer. Heat Transfer, Part A, **30**, pp. 859–869.
[40] Chen, H., 1997, ''Non-Darcy Mixed Convection Over a Vertical Flat Plate in Porous Media With Variable Wall Heat Flux,'' Int. Commun. Heat Mass Transfer, **24**, pp. 427–437.
[41] Chen, H., 1997, ''Analysis of Non-Darcian Mixed Convection From Impermeable Horizontal Surface in Porous Media: The Entire Regime,'' Int. J. Heat Mass Transf., **40**, pp. 2993–2997.
[42] David, E., Lauriat, G., and Cheng, P., 1991, ''A Numerical Solution of Variable Porosity Effects on Natural Convection in a Packed-Sphere Cavity,'' ASME J. Heat Transfer, **113**, pp. 391–399.
[43] Hsu, T., and Cheng, P., 1990, ''Thermal Dispersion in a Porous Medium,'' Int. J. Heat Mass Transf., **33**, pp. 1587–1597.
[44] Cheng, P., Hsu, C. T., and Chowdary, A., 1988, ''Forced Convection in the Entrance Region of a Packed Channel With Asymmetric Heating,'' ASME J. Heat Transfer, **110**, pp. 946–954.
[45] Fu, W., Huang, H. C., and Liou, W. Y., 1996, ''Thermal Enhancement in Laminar Channel Flow With a Porous Block,'' Int. J. Heat Mass Transf., **39**, pp. 2165–2175.
[46] Chen, H., Chen, T. S., and Chen, C. K., 1996, ''Non-Darcy Mixed Convection Along Non-isothermal Vertical Surface in Porous Media,'' Int. J. Heat Mass Transf., **39**, pp. 1157–1164.
[47] Jang, J. Y., and Chen, J. L., 1992, ''Forced Convection in a Parallel Plate Channel Partially Filled With a High Porosity Medium,'' Int. Commun. Heat Mass Transfer, **19**, pp. 263–273.
[48] Hong, J. T., and Tien, C. L., 1987, ''Analysis of Thermal Dispersion Effect on Vertical-Plate Natural Convection in Porous Media,'' Int. J. Heat Mass Transf., **30**, pp. 143–150.
[49] Cheng, P., and Hsu, C. T., 1986, ''Fully-Developed, Forced Convective Flow Through an Annular Packed-Sphere Bed With Wall Effects,'' Int. J. Heat Mass Transf., **29**, pp. 1843–1853.
[50] Cheng, P., and Zhu, C. T., 1987, ''Effect of Radial Thermal Dispersion on Fully Developed Forced Convection in Cylindrical Packed Tubes,'' Int. J. Heat Mass Transf., **30**, pp. 2373–2383.
[51] Cheng, P., and Vortmeyer, D., 1988, ''Transverse Thermal Dispersion and Wall Channeling in a Packed Bed With Forced Convective Flow,'' Chem. Eng. Sci., **43**, pp. 2523–2532.
[52] Vafai, K., and A. Amiri, 1998, ''Non-Darcian Effects in Confined Forced Convective Flows.'' *Transport Phenomena in Porous Media*, D. B. Ingham and I. Pop, eds., Pergamon, England, pp. 313–329.
[53] Amiri, A., and Vafai, K., 1994, ''Analysis of Dispersion Effects and Non-thermal Equilibrium, Non-Darcian, Variable Porosity, Incompressible Flow Through Porous Media,'' Int. J. Heat Mass Transf., **37**, pp. 939–954.
[54] Amiri, A., Vafai, K., and Kuzay, T. M., 1995, ''Effects of Boundary Conditions on Non-Darcian Heat Transfer Through Porous Media and Experimental Comparisons,'' Numer. Heat Transfer, Part A, **27**, pp. 651–664.
[55] Amiri, A., and Vafai, K., 1998, ''Transient Analysis of Incompressible Flow Through a Packed Bed,'' Int. J. Heat Mass Transf., **41**, pp. 4259–4279.
[56] Hwang, G. J., Wu, C. C., and Chao, C. H., 1995, ''Investigation of Non-Darcian Forced Convection in an Asymmetrically Heated Sintered Porous Channel,'' ASME J. Heat Transfer, **117**, pp. 725–732.
[57] Dixon, A. G., and Cresswell, D. L., 1979, ''Theoretical Prediction of Effective Heat Transfer Parameters in Packed Beds,'' AIChE J., **25**, pp. 663–676.
[58] Kuznetsov, A. V., 1997a, ''Thermal Non-equilibrium, Non-Darcian Forced Convection in a Channel Filled With a Fluid Saturated Porous Medium–A Perturbation Solution,'' Appl. Sci. Res., **57**, pp. 119–131.
[59] Ergun, S., 1952, ''Fluid Flow Through Packed Columns,'' Chem. Eng. Prog., **48**, pp. 89–94.
[60] Benenati, R. F., and Brosilow, C. B., 1962, ''Void Fraction Distribution in Beds of Sphere,'' AIChE J., **8**, pp. 359–361.
[61] Lee, D. Y., and Vafai, K., 1999, ''Analytical Characterization and Conceptual Assessment of Solid and Fluid Temperature Differentials in Porous Media,'' Int. J. Heat Mass Transf., **42**, pp. 423–435.
[62] Kuznetsov, A. V., 1994, ''An Investigation of Wave of Temperature Difference Between Solid and Fluid Phases in a Porous Packed Bed,'' Int. J. Heat Mass Transf., **35**, pp. 3030–3033.
[63] Kuznetsov, A. V., 1997b, ''A Perturbation Solution for Heating a Rectangular Sensible Heat Storage Packed Bed With a Constant Temperature at the Walls,'' Int. J. Heat Mass Transf., **40**, pp. 1001–1006.
[64] Alazmi, B., and Vafai, K., 2000, ''Analysis of Fluid Flow and Heat Transfer Interfacial Conditions Between a Porous Medium and a Fluid Layer,'' Int. J. Heat Mass Transf., to appear.

Heat Transfer and Fluid Flow in a Square Duct With 12 Different Shaped Vortex Generators

T.-M. Liou[1]
Professor,
Fellow ASME
e-mail: tmliou@pme.nthu.edu.tw

C.-C. Chen
Ph.D. Candidate,

T.-W. Tsai
Graduate Student

Department of Power Mechanical Engineering,
National Tsing Hua University,
Hsinchu, Taiwan 30043, R.O.C.

Detailed local Nusselt number distributions in the first pass of a sharp turning two-pass square channel with various configurations of longitudinal vortex generator arranged on one wall were measured using transient liquid crystal thermography. Flow patterns and friction factors were measured by the use of laser-Doppler velocimeter and pressure transducer, respectively. The Reynolds number, based on channel hydraulic diameter and bulk mean velocity, was fixed at 1.2×10^4. The vortex generator height-to-hydraulic diameter ratio and pitch-to-height ratio were 0.12 and 10, respectively. Comparisons in terms of heat transfer augmentation and uniformity and friction loss are first performed on 12 configurations of single longitudinal vortex generator. The fluid dynamic mechanisms and wall confinement relevant to heat transfer enhancement are then documented for three-selected vortex generator models. In addition, the differences in fluid flow and heat transfer characteristics between a single vortex generator and a vortex generator array are addressed for the delta wing I and 45 deg V (with tips facing upstream) models which provide better thermal performance among the 12 configurations examined. The direction and strength of the secondary flow with respect to the heat transfer wall are found to be the most important fluid dynamic factors affecting the heat transfer promotion through the channel wall, followed by the convective mean velocity, and then the turbulent kinetic energy. [S0022-1481(00)01202-0]

Keywords: Augmentation, Channel Flow, Heat Transfer, Image Processing, Nonintrusive Diagnostics

Introduction

Rib arrays inside an internal cooling channel are often used in heat exchanger systems to enhance the heat transfer rate. In the second generation of internal channel cooling ([1]), spanwise vortices induced by the square cross-sectioned right-angled ribs break up the boundary layer to reduce the heat resistance between coolant flow and hot walls. Turbulence, generated from separation and flow reattachment, provides good mixing to increase heat exchange. In the third generation of internal channel cooling ([1]), longitudinal vortices generated by protuberances are receiving more and more attention both in laminar ([2,3]) and turbulent flow regimes ([4,5,6]), not only because they are capable of strongly perturbing the boundary layer by the associated secondary flow, but also longitudinal vortices usually maintain over longer streamwise distances ([7]).

The Laser-Doppler velocimetry (LDV) measurements of Liou et al. [8] showed that right-angled ribs also generate a pair of longitudinal vortices. These vortices are relatively small and are located near side walls due to the interaction of the rib with the flow near the side wall. They have thus a minor effect on heat transfer. When ribs are oblique to the channel, i.e., the rib has a partial streamwise direction, the main flow can more easily climb over the ribs and generate stronger secondary flows, as depicted in Fig. 1. Han et al. [9] examined the effect of rib angle orientation on the heat transfer distributions and pressure drop in a square duct. The results showed that V-shaped angled rib produces the highest heat transfer augmentation and the greatest pressure drop. The large pressure drop generally results from flow separation behind the square cross-sectioned ribs. With a proper design, a vortex generator, such as a delta wing, could generate strong longitudinal vortices without a recirculation zone behind it and, therefore, lower pressure drop ([3,10]). Hibbs et al. [11] examined the effect of additional cylindrical vortex generators on the heat transfer from the right-angle-ribbed passage. Their results indicated that the presence of vortex generators not only led to high local heat transfer rates, but also made the inter-rib heat transfer distributions more uniform. Eibeck and Eaton [4] studied the heat transfer effect of a vortex introduced by a half-delta wing. Pauley and Eaton [6] further examined a pair of half-delta wings. Both results showed that heat transfer is enhanced where secondary flow is directed toward the primary (bottom) wall and reduced where the secondary flow is directed away from the primary wall. Their duct has a larger aspect ratio (span-to-height ratio=4.8), and the size of vortex generators is much smaller than the channel width. In a turbine blade internal cooling channel, the spanwise width of ribs or vortex generators is comparable to the channel width. In addition, though the aspect ratios range from 1:4 to 4:1 for the turbine blade internal cooling channels, most researchers ([12,13,14,15,16]) chose the simplest case 1:1 in their investigations. The side walls in the turbine blade internal cooling passage could thus restrict and largely modify the longitudinal vortex structure reported by the aforementioned researchers who adopted vortex generators having sizes much smaller than the channel width ([4,6]) and, in turn, modify the heat transfer characteristics. Han's research group ([9,17,18,19]) had made comprehensive studies on the heat transfer enhancement of vortex generators with different shapes and configurations by using thermocouple techniques. Similar to other previous thermocouple measurements on heat transfer augmentation using vortex generators ([20,5,6,14]), these experimental results provided discrete regional averaged heat transfer coefficients. Recently, Ekkad and Han [13] reported Nusselt number distributions for a two-pass square channel with one ribbed wall using a transient liquid crystal technique. Chyu et al. [21] investigated heat transfer enhancement of ducts with multiple delta wing pair arrays by using a transient liquid crystal

[1]To whom correspondence should be addressed.

Contributed by the Heat Transfer Division for publication in the JOURNAL OF HEAT TRANSFER. Manuscript received by the Heat Transfer Division, March 27, 1999; revision received December 1, 1999. Associate Technical Editor: J. Han.

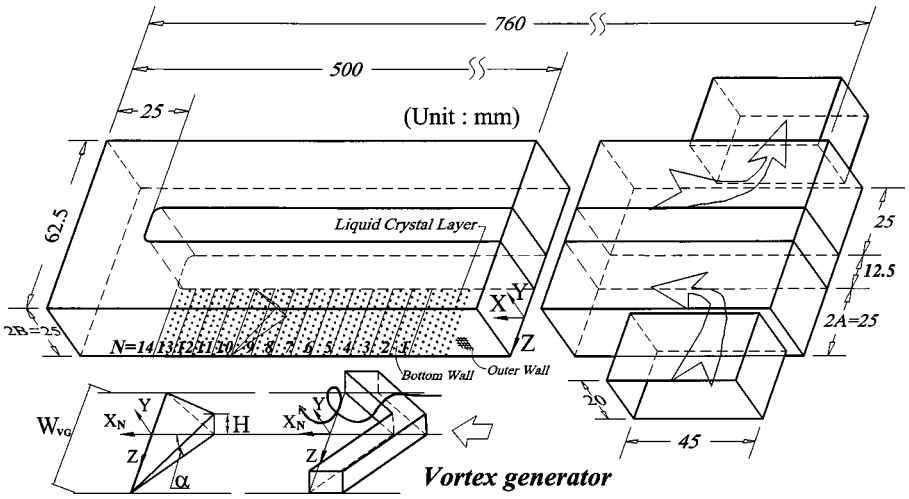

Fig. 1 Sketch of configuration, coordinate system, and dimensions of vortex generator and test section

technique as well. In general, the transient liquid crystal technique is able to provide detailed local heat transfer distribution maps; nevertheless, its applications to study heat transfer augmentation associated with longitudinal vortex generators are still less in comparison with the thermocouple technique.

One of the goals of the present research is to make a comparison of the level of heat transfer augmentation of 12 differently shaped longitudinal vortex generators in a square channel by using the transient liquid crystal thermography. Both detailed and regional averaged Nusselt number distributions are presented. The uniformity of heat transfer distribution is examined by comparing the calculated standard deviations of Nusselt number distributions. To the authors' knowledge, no previous work investigated the nonuniformity of rib-enhanced internal channel cooling in terms of a quantitative comparison. In general, previous studies based on thermocouple measurements ([9,14]) could provide the nonuniformity information of the regional-averaged values rather than the local values within each averaged region. The pressure drop across vortex generators is presented to evaluate the friction factor and thermal performance. More importantly and uniquely, LDV measurements in the near fields of selected vortex generators with better heat transfer enhancement are presented to relate the mean flow patterns and turbulent kinetic energy distribution to the heat transfer distributions, an approach lacking in pertinent open literature. In addition, the heat transfer and fluid flow over the periodic vortex generator array are studied and compared with those over the single vortex generator.

Test Apparatus

Figure 2 schematically illustrates the transient thermochromic liquid crystal thermography and LDV experimental setup. The liquid crystal thermography system ([15]) consisted of a digital video camera used to record the color change of the liquid crystal coating, a thermocouple recorder measuring the main flow temperatures during the test, and a micro-differential transducer with pressure taps measuring the static pressure drop. For the case of single vortex generator, two thermocouple probes were placed at $X=325$ mm and $X=400$ mm, i.e., 10 H in front of and 15 H in back of the vortex generator's rear edge for main flow temperature measurements. For multiple vortex generator array, two thermocouple probes were placed at $X=55$ mm and $X=475$ mm. The in-between main flow temperature could be estimated by the linear interpolation of two measured temperatures. The two-dimensional LDV system adopted was a two-color four-beam system using a 4-W argon-ion laser with 488 nm (blue) and 514.5 nm (green) lines ([23,22]). A forward scattering configuration provided a probe ([23]) volume of about 1.69 mm in length and 0.164 mm in diameter, and an off-axis scattering configuration 0.74 mm in length and 0.164 mm in diameter, based on $1/e^2$ extent of light intensity. The LDV system was mounted on a vibration-isolated milling machine, providing a probe-volume-position resolution of 0.01 mm. The scattered light from particles with a nominal size of 0.8 μm was collected into the photomultiplier and then down-mixed to the adequate frequency shift of 0.1 to 10 MHz. The two counter processors (1-ns resolution) were used to process the Doppler signals and feed the digital data into a PC-586 for storage and analysis. A 2.2-kW turbo blower at downstream end of the flow circuit drove the fluid flow in the suction mode. The working medium, air, was drawn into a rectangular duct with an aspect ratio of 2.25:1, passing through a quick response heater mesh, and turned 90 deg into the two-pass test duct with a square cross section. Downstream of the test section, the air flowed through a flowmeter, a bellows, and then exhausted.

Theory of Heat Transfer Analysis

Equation (1) is the analytical solution of a one-dimensional transient heat transfer conduction model over a semi-infinite solid wall with a convective boundary condition ([12]):

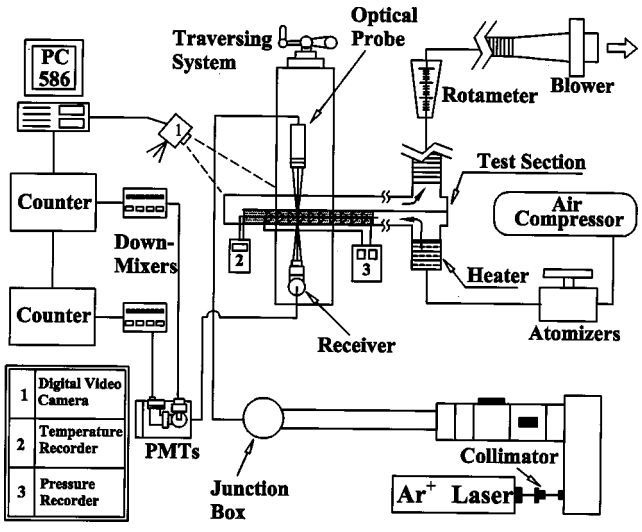

Fig. 2 Schematic drawing of overall experimental system

$$\frac{T_w - T_i}{T_r - T_i} = 1 - \exp\left(\frac{h^2 \alpha_w t}{k_w^2}\right) \operatorname{erfc}\left(\frac{h\sqrt{\alpha_w t}}{k_w}\right) \quad (1)$$

which is used to evaluate the local heat transfer coefficient (h) over the test surface coated with liquid crystals. The thermochromic liquid crystal has a color-changing range of 5 K. The calibrated value of the green point temperature (T_w) under fixed lighting environment is 312.4 K. When initial temperature of the test surface (T_i), bulk mean temperature of main flow (T_r), and the time (t) for wall temperature reaching the green point (T_w) are given, h can be calculated from Eq. (1). Thermal performance evaluation is accomplished by assuming that heat transfer area and pumping power are constant. The relation can be written as

$$\mathrm{Re}^* = (f \cdot \mathrm{Re}^3 / 0.316)^{1/2.75} \quad (2)$$

where Re* represents Reynolds number in the corresponding smooth duct. The thermal performance is determined by the ratio of average Nusselt number $\overline{\mathrm{Nu}}$ of the roughened ducts to Nu_0^* of a smooth duct at the condition of constant pumping power, $\overline{\mathrm{Nu}}/\mathrm{Nu}_0^*$, where Nu_0^* is obtained from the Dittus-Boelter correlation ([24]) for a smooth circular tube under fully developed condition and has the following form:

$$\mathrm{Nu}_0^* = 0.023 \cdot \mathrm{Re}^{*0.8} \cdot \mathrm{Pr}^{0.4}. \quad (3)$$

Test Section and Vortex Generators

Figure 1 shows the configuration, coordinate system, and dimensions of the test section. The test section was made of 10-mm to 15-mm thick acrylic sheets for optical access. The flow path has a square cross section with a hydraulic diameter of $D_H = 25$ mm. The lengths of the first pass, sharp turn, and second pass are $30.4\,D_H$, $0.5\,D_H$, and $30.4\,D_H$, respectively. At the turn, the clearance between the tip of the divider wall and the duct outer wall is equal to $1\,D_H$ (or 25 mm). The divider-wall thickness is $0.5\,D_H$. The geometric parameters of a vortex generator (hereafter also referred to as VG) are also defined in Fig. 1. Table 1 shows the 12 configurations of the vortex generators investigated. The vortex generator height, H, is fixed at 3 mm and width, W_{VG}, at 25 mm (except the models (B), (K), and (L) in Table 1). Two facing directions, i.e., with the tip of the vortex generator facing upstream (denoted as U) or downstream (denoted as D), were investigated for V-shaped angled ribs ((C)–(F)) and delta wings ((G)–(J)). The inlet reference station ($X = 0$) is chosen at 475 mm or $19\,D_H$ upstream of the turn. To facilitate the description of the fluid flow and heat transfer around the vortex generator, the streamwise coordinate X_N with $X_N = 0$ located at vortex generator's rear edge is used, where N is the position index of the Nth vortex generator in the array. In the multiple vortex generator array study, the first vortex generator's rear edge is placed at $X = 3.4\,D_H$ or $X = 85$ mm. There are 14 vortex generators evenly placed in the first pass with a pitch of $Pi = 30\,\mathrm{mm} = 10\,H$. In the single vortex generator study, the vortex generator's rear edge is placed at X_{10} or $X = 355$ mm. X_{10} is chosen since the fluid flow in a vortex generator array attains spatially periodic condition typically at $X > X_{10}$ ([8,22,23]). One can then compare fluid flow and heat transfer characteristics under spatially periodic (i.e., multiple vortex generators) and nonperiodic (i.e., single vortex generator) conditions.

Test Conditions and Uncertainty Estimation

The Reynolds number, based on the channel bulk mean velocity of $U_b = 7.3$ m/s and hydraulic diameter, was fixed at 1.2×10^4, and the inlet air temperature was maintained at 330 K. The heat transfer measurements were made in the region of 8 H upstream to 15 H downstream of $X_N = 0$ for the case of single vortex generator study, models (A)–(L) in Table 1, and 25 H upstream to 25 H downstream of $X_N = 0$ for the case of multiple vortex generator array, models (C) and (G) in Table 1. The nondimensional uncertainty intervals for the variables in Eq. (1) are listed as follows:

Time of color change	t	±3 percent
Thermal diffusivity of wall	$\sqrt{\rho_w C p_w k_w}$	±5 percent
Thermal conductivity of wall	k_w	±5 percent
Bulk mean temperature of main stream	T_r	±1 percent
Green-point temperature	T_w	±1 percent
Initial temperature of wall	T_i	±0.3 percent

According to the root-sum-square method, the most proper uncertainty is estimated to be ±8 percent. The maximum uncertainty, 23 percent, occurs on the surface of the vortex generators, where one-dimensional model is not valid. In general, the uncertainty can be higher on and very near the edge of the vortex generator due to potential two-dimensional effect. Vedula et al. [25] also found that effects of lateral and anisotropic conduction are not very significant except in very small regions of protrusions. Conduction losses are relatively small because the transient test period is short (less than 60 seconds for 90 percent of test areas) and the

Table 1 A list of configurations, regional averaged Nusselt number ratios, standard deviations of regional averaged Nusselt number ratios, and friction factors for 12 different vortex generators at Re=1.2×10⁴

VG Type	Configuration D_h=25mm H/D_h=0.12	$\mathrm{Nu}_{r2}/\mathrm{Nu}_0$ △X/H ~20	$\mathrm{Nu}_{r2}/\mathrm{Nu}_0$ △X/H ~10	$(\mathrm{Nu}/\mathrm{Nu}_0)_{\mathrm{Std}}$ △X/H~20	f/f$_0$	$\mathrm{Nu}_{rg}/\mathrm{Nu}_0^*$ △X/H~10
(A) 60° Oblique	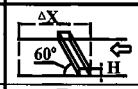	2.1 (4)	2.3 (5)	1.2 (3)	6.08 (6)	1.4 (7)
(B) 60° Broken V	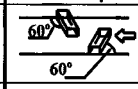	2.0 (7)	1.9 (9)	1.0 (4)	3.15 (8)	1.4 (7)
(C) 45° V U	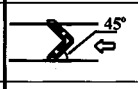	2.8 (1)	3.7 (1)	1.8 (1)	3.78 (7)	2.5 (1)
(D) 45° V D	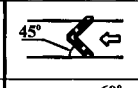	2.1 (4)	2.0 (7)	1.0 (4)	7.60 (5)	1.1 (9)
(E) 60°V U	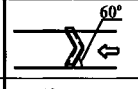	2.8 (1)	3.3 (2)	1.7 (2)	9.12 (4)	1.8 (4)
(F) 60°V D	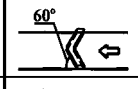	2.1 (4)	2.0 (7)	0.5 (9)	13.7 (1)	1.0 (10)
(G) Delta Wing I U	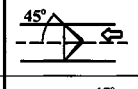	2.3 (3)	2.7 (3)	0.8 (8)	1.32 (11)	2.5 (1)
(H) Delta Wing I D	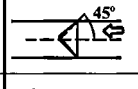	1.7 (12)	1.9 (9)	0.4 (11)	1.52 (10)	1.7 (5)
(I) Delta Wing II U	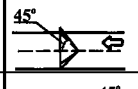	1.9 (9)	1.8 (11)	0.4 (11)	10.6 (3)	0.9 (11)
(J) Delta Wing II D	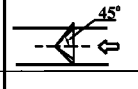	1.8 (10)	1.8 (11)	0.5 (9)	12.2 (2)	0.8 (12)
(K) Delta Winglet I Pair U	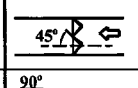	2.0 (7)	2.4 (4)	0.9 (7)	3.04 (9)	1.7 (5)
(L)Winglet Pair with gap	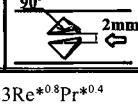	1.8 (10)	2.2 (6)	1.0 (4)	1.28 (12)	2.0 (3)

[1] $\mathrm{Nu}_0 = 0.023\mathrm{Re}^{*0.8}\mathrm{Pr}^{*0.4}$ [2] U: facing upstream D: facing downstream
[3] Number in ( ) represents the relative rank of magnitude in the same column
[4] $(\mathrm{Nu}/\mathrm{Nu}_0)_{\mathrm{Std}}$: standard deviation of $\mathrm{Nu}/\mathrm{Nu}_0$

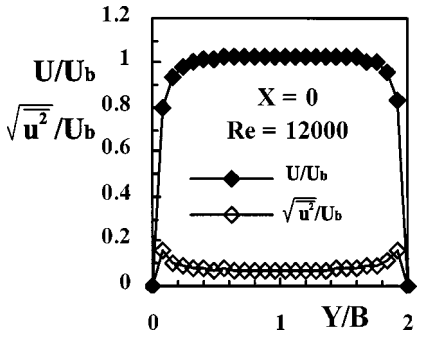

Fig. 3 Streamwise mean velocity and turbulence intensity profiles at inlet reference station $X=0$ (smooth wall)

walls are made of insulating material. Radiation is negligible because the entire walls of the channel are heated by the mainstream at fairly uniform temperature.

The secondary-flow velocity vector mappings were performed over a cross-sectional plane 1 mm behind the vortex generator's rear edge for the case of single vortex generator study, models (C), (G) and (H) in Table 1. Moreover, detailed velocity vector mappings for the region from 8 H upstream to 10 H downstream of $X_N=0$ in the $Z=0$ plane were made for the case of single vortex generator, models (C) and (G) in Table 1. Figure 3 depicts the flow conditions at the inlet reference plane $X=0$ in terms of streamwise mean velocity and turbulence intensity profiles. The corresponding boundary layer thickness, δ_{99} defined at 99 percent $U_{\max}$, is 5.9 mm, which is higher than the vortex generator height (3 mm). $\underline{U}/\underline{U}_b$ and $\sqrt{u^2}/\underline{U}_b$ are rather uniform in the region of $Y/B=1\pm0.6$ and have values of 1.03 and 0.08, respectively. In the present study, the mean velocity and turbulence data were calculated from the probability density distribution function of the measurements. Typically, 4096 realizations were ensemble averaged at each measuring location. The statistical errors in the ensemble averaged mean velocity and turbulence intensity were less than $0.018\,\underline{U}_b$ and $0.031\,\underline{U}_b$, respectively, for a 95 percent confidence level. Refer to our previous work (Liou and Chen, 1997) for a more detailed discussion of other error sources.

Results and Discussion

Single Vortex Generator (SVG).

Heat Transfer and Friction Loss. Detailed heat transfer distributions for all 12 configurations of single longitudinal vortex generator (VG) examined are presented in Fig. 4. Figure 4(A) presents Nu/Nu_0 distributions around the 60 deg oblique VG. Highest Nu/Nu_0 are obtained on top of the VG and near the outer wall $(Z/A=1)$. There is larger spanwise variation in the Nusselt number ratio distribution along the VG. Nu/Nu_0 decreases from 6 around $(X_N/H\sim-5,\ Z/A=1)$ to 2 around $(X_N/H=0,\ Z/A=-1)$. Heat transfer is very low immediately behind the VG due to the presence of flow separation zone. In fact, the shape of high heat transfer region downstream of the VG suggests that the induced longitudinal vortex diagonally moves away from the outer wall $(X_N/H=-2,\ Z/A=1)$ toward the divider wall $(X_N/H=15,\ Z/A=-1)$. The vortex structure is weakened or even broken after its retardation by the divider wall near $X_N/H=15$. As a result, Nu/Nu_0 decreases to 1 for $X_N/H>15$. In the previous study

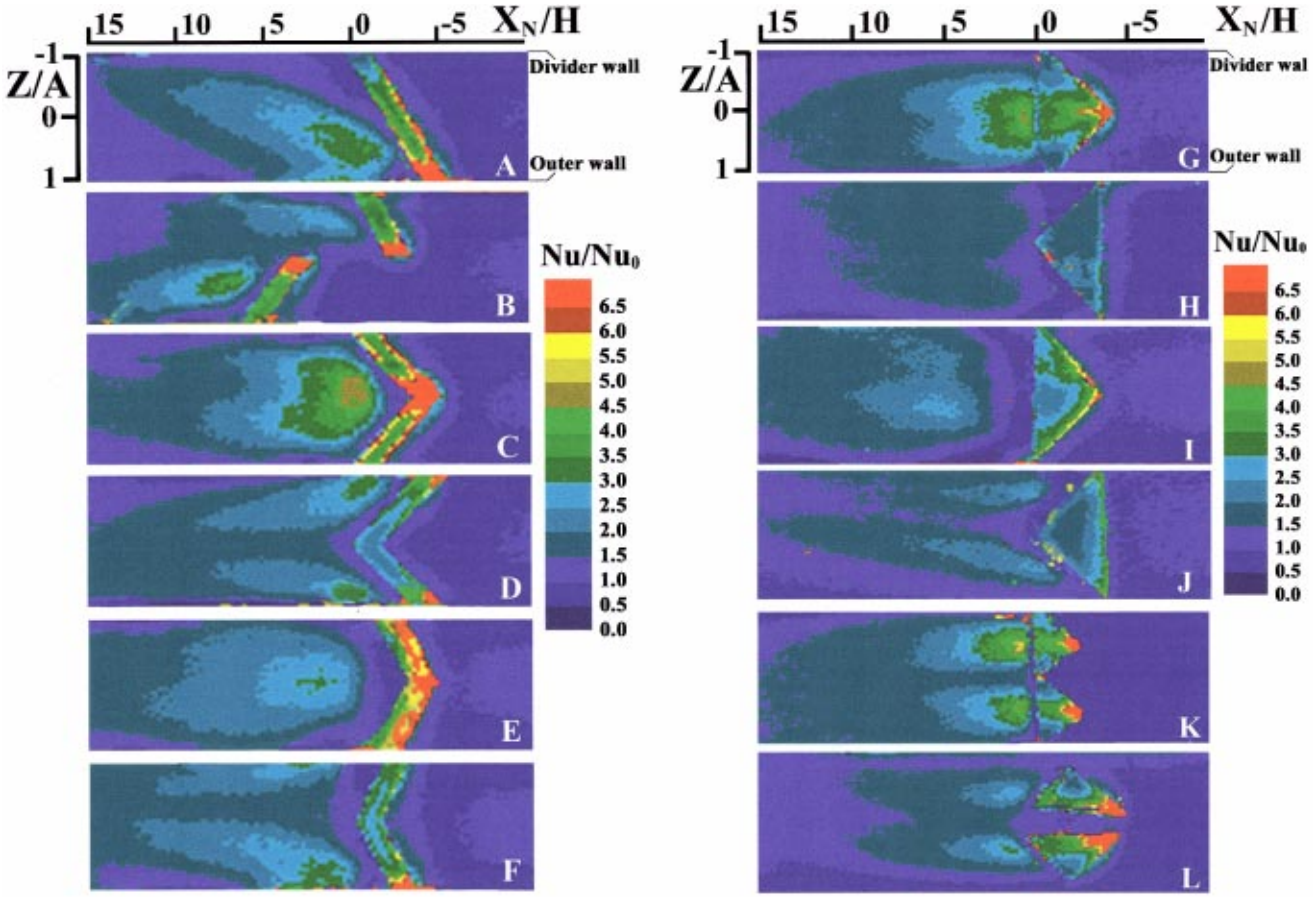

Fig. 4 Detailed local Nusselt number ratio distributions near 12 different configurations of SVG at $Re=1.2\times10^4$ (fluid flow from right to left)

([13]). $H/2A=0.125$, $Pi/H=10$, square rib, and $Re=1.2\times10^4$), the shape of high heat transfer region behind the 60 deg parallel VGs is approximately parallel to the VG itself. For comparison, it diagonally moves away from the outer wall towards the divider wall in the present single 60 deg oblique VG case. An additional retardation of the upstream VG-induced longitudinal vortex by the downstream VG in the case of multiple 60 deg oblique VGs, lacking in the case of single 60 deg oblique VG, is the main cause for the above difference in the orientation of high heat transfer region behind the VG. Heat transfer distribution around the 60 deg broken *V* VG is depicted in Fig. 4(*b*). It is approximately equivalent to two Fig. 4(A) arranged in a staggered form but half in VG length, longitudinal vortex size, and characteristic-zone size. The regional averaged Nusselt number Nu_{rg}/Nu_0 for the 60 deg broken *V* VG is, therefore, slightly lower than that for the 60 deg oblique VG; however, the 60 deg broken *V* VG provides a more uniform heat transfer distribution than the 60 deg oblique VG, as indicated in Table 1. Comparing with the case of multiple VGs ([13]) one finds that the presence of the consecutive VGs makes the heat transfer enhancement limited to the mid-channel region and exhibited a snaky shape, significantly different from that of present single VG case.

Figure 4(C) depicts the Nu/Nu_0 contours around the single 45 deg *V*-shaped VG with its tip pointing upstream (designated as U in Table 1). Nu/Nu_0 ratios are highest on the top of the VG, particularly around the tip top. The narrow low heat transfer region immediately behind the VG is again due to the flow separation inherent with the solid-type rib. A large area of high heat transfer enhancement region ranging from $X_N/H=-2$ to 10 and $Z/A=-0.9$ to 0.9 is obtained, e.g., $Nu/Nu_0=3$ to 4 in the region $X_N/H=-1$ to 4. The merge of downward washes of two counterrotating longitudinal vortices induced by each angled side of the *V* VG in the mid-channel region, as shown in Fig. 5, is responsible for the large area of high heat transfer augmentation shown in Fig. 4(C) (rank number one in Table 1). The heat transfer near the outer and divider walls ($Z/A=0.9$ to 1 and $Z/A=-0.9$ to -1) is low (Fig. 4(C)) where the secondary flow is directed away from the liquid crystal coated bottom wall ($Y/B=0$) (Fig. 5). Figure 4(D) depicts the Nu/Nu_0 contours around the single 45 deg *V*-shaped VG with its tip pointing downstream (designated as D in Table 1). Again, flow acceleration over the VG leads to the higher heat transfer on the VG top and flow separation behind the VG causes the low heat transfer region immediately after the VG. The high heat transfer areas, including the VG tip, in this case are located in the regions adjacent to the outer and divider walls where the velocity vectors of the longitudinal vortices (or secondary flow) are directed towards the bottom wall as depicted in Fig. 5. In the mid-channel area where the secondary flow is directed away from the bottom wall (Fig. 5), the heat transfer is lower there (Fig. 4(D), $Z/A=-0.4$ to 0.4). The completely opposite rotating directions of the longitudinal vortices induced by the 45 deg *V* U and D VGs (Fig. 5) result in the difference in the heat transfer enhancement distributions between the two cases (Figs. 4(C) and 4(D)). It is also worth mentioning here that the wall confinement reduces the regions where the secondary flows are directed away from the bottom wall and, hence, largely augments the heat transfer for the case of 45 deg *V* U VG (Fig. 5). In contrast, the wall confinement reduces the regions where the secondary flows are directed towards the bottom wall and, therefore, curtails the heat transfer augmentation for the case of 45 deg *V* D VG (Fig. 5).

Figure 4(E) depicts the Nu/Nu_0 contours around the 60 deg *V*-shaped U VG. The heat transfer enhancement distribution is basically similar to that of Fig. 4(C). However, the downward wash of the secondary flow induced by the 60 deg *V* U VG is slightly weaker than that by the 45 deg *V* U VG. Figure 4(E) thus presents a slightly larger low-heat-transfer region immediately downstream of the VG. Moreover, heat transfer uniformity has a slight improvement (rank second in Table 1). For the corresponding case of multiple VGs, the results of Ekkad and Han [13] also reveals a thick region of low heat transfer with Nu/Nu_0 as low as 0.5. A similar comparison is valid between the 60 deg *V* D VG and 45 deg *V* D VG.

The Nu/Nu_0 color contours around the delta wing I U VG are depicted in Fig. 4(G). The downward wash of the longitudinal vortices induced by the leading edge of the delta wing extends from $Z/A=-0.75$ to 0.75, as shown in Fig. 5, where the heat transfer enhancement prevails. Note that the longitudinal vortices sweep over the downstream inclined VG top making high heat transfer elevation prevail in the region of $X_N/H=-4$ to 4 and $Z/A=-0.5$ to 0.5 with $Nu/Nu_0=3$ to 4. It also makes the lowest heat transfer region (usually around $X_N/H=0$), typically associated with flow separation immediately behind the solid-type rib ([8]) vanish. The delta wing I U VG thus ranks third in Table 1 in terms of regional averaged heat transfer enhancement. Nevertheless, a more uniform heat transfer enhancement, twofold improvement in terms of $(Nu/Nu_0)_{std}$, defined as $\sqrt{\overline{(Nu-\overline{Nu})^2}}$, is obtained for the delta wing I U VG than for the 45 deg *V* U and D VGs since the former lacks a low heat transfer region immediately behind the VG. Figure 4(H) depicts the Nu/Nu_0 contours around the delta wing I D VG. The delta wing I D VG acts like a ramp which leads to a large flow separation zone immediately behind the VG and raises the longitudinal vortices further away from the bottom. As a result, it provides the poorest heat transfer enhancement, as indicated in Table 1.

Figure 4(I) presents the Nu/Nu_0 contours around the delta wing II U VG whose widest part is the highest and spans the whole channel width. As seen from Fig. 4(I), its heat transfer characteristics downstream of the VG resemble to those downstream of a 90 deg angled square rib. The Nu/Nu_0 contours presented in Fig. 4(J) for the case of the delta wing II D, whose angled sides are the highest, provide heat transfer characteristics downstream of the

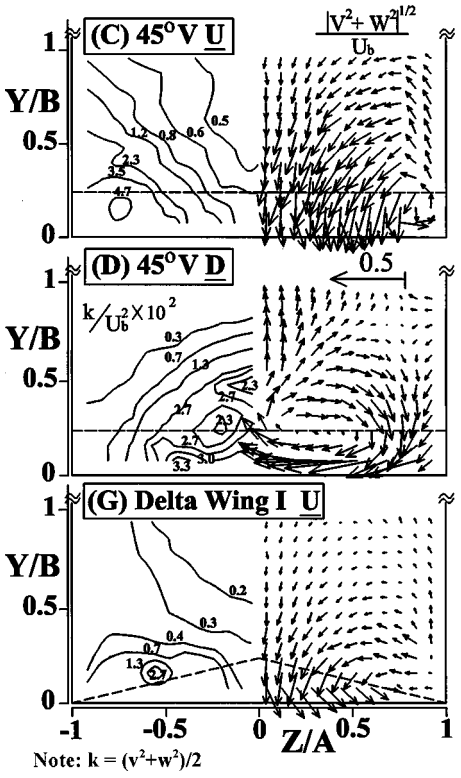

Fig. 5 Secondary flow patterns and turbulent kinetic energy contours at a selected cross section located 3 mm behind a SVG for $Re=1.2\times10^4$: (C) 45 deg *V* U VG; (D) 45 deg *V* D VG; and (G) delta wing I U VG. (Note that the secondary flow patterns are plotted facing the downstream direction.)

VG similar to those of the *V*-shaped VG cases (Figs. 4(D) and 4(F)). However, its heat transfer augmentation is lower due to the ramp effect on raising the longitudinal vortices further above the bottom wall.

Figure 4(K) depicts the Nu/Nu_0 contours around the delta winglet I U VG pair and basically consists of two smaller figures similar to Fig. 4(G). According to Fig. 5, the secondary flows in the border region between the two delta wing I U VGs are directed away from the bottom wall; hence, the heat transfer enhancement obtained from the delta winglet I U VG pair ($Nu_{rg}/Nu_0=2.00\sim2.39$, Table 1) is lower than from the single delta wing I U VG ($Nu_{rg}/Nu_0=2.28\sim2.66$, Table 1). It is interesting to compare with other researchers' results. Chyu et al. [21] studied the heat transfer enhancement around the delta winglet I U VG pair in an array. Their operating conditions (versus our operating conditions) are $H/2A=0.4(0.12)$, $Pi/H=5(10)$, $A/B=2(1)$, oval cross section (square cross section), and $Re=3\times10^4$ (1.2×10^4). They obtained $Nu_{rg}/Nu_0\approx1.6$ whereas the present study obtains a higher value $Nu_{rg}/Nu_0=2.00\sim2.35$. One of the reasons for the above difference in Nu_{rg}/Nu_0 between the two studies is attributed to the Reynolds number. Ekkad and Han [13] reported a decrease of Nu_{rg}/Nu_0 with an increase in Reynolds number for Re ranging from 6×10^3 to 6×10^4, thus explaining the present result.

Figure 4(L) presents the Nu/Nu_0 contours around the winglet pair with gap (Table 1), a configuration not investigated in the open literature. It is seen that the heat transfer is not elevated in the gap region of the winglet pair although one expects an increase of the convective velocity through the gap. The heat transfer enhancement mainly results from the longitudinal vortices generated by the delta winglets, as revealed from Fig. 4(L). The above observation may suggest that the downward washes of longitudinal vortices plays a more important role than the convective velocity in augmenting heat transfer using VGs.

As a summary, Table 1 shows that the V-shaped U VG provides the highest heat transfer (Nu/Nu_0) promotion under a constant flow rate condition but the lowest heat transfer uniformity (or largest $(Nu/Nu_0)_{std}$). On the other hand, the lowest Nu/Nu_0 augmentation, but the highest heat transfer uniformity, is obtained by using the delta wing I D VG, delta wing II U VG, and delta wing II D VG. The delta wing I U VG gives the third Nu/Nu_0 enhancement, the fifth low $(Nu/Nu_0)_{std}$, and the second low friction loss (f/f_0). Table 1 also shows that the highest frictional loss with $f/f_0>10$ is generated by the 60 deg *V*-shaped VG and delta wing II U and D VGs which behave more like a right-angled rib with large recirculation zone immediately behind the rib. The lowest frictional loss with $f/f_0<2$ can be obtained by using the delta wing I U or D VG and winglet pair with gap. The rationale is that the delta wing I U VG does not induce flow separation behind it and the winglet pair with gap has a gap to reduce the blockage effect. When two small delta wing I U VGs are used to form the delta winglet I pair U VG, the Nu/Nu_0 enhancement is reduced 20 percent but the f/f_0 is doubled. The delta winglet I pair U VG is therefore not recommended. The last column of Table 1 gives a comparison in terms of the heat transfer (Nu_{rg}/Nu_0^*) augmentation under a constant pumping power condition. Among the VG configurations examined, the top three VG configurations in terms of Nu_{rg}/Nu_0^* enhancement are in the following order: the delta wing I U VG (first), the 45 deg *V* U VG (first), and the winglet pair with gap VG (third). Note that the delta wing I U VG ranking second in terms of Nu_{rg}/Nu_0 enhancement (i.e., at a constant flow rate condition) moves to the first place in terms of Nu_{rg}/Nu_0^* enhancement due to its lower f/f_0 loss. The most interesting outcome is the winglet pair with gap VG which generates poorer Nu_{rg}/Nu_0 enhancement but provides the third highest Nu_{rg}/Nu_0^* enhancement due to its lowest frictional loss.

Mean Flow and Turbulent Kinetic Energy. The velocity vectors and turbulent kinetic energy contours of the secondary flow at station $X_N/H=1$ or 3 mm behind VG's rear edge are depicted in Fig. 5 for three representative VGs. The descriptions of the flow patterns and their effects on heat transfer enhancement have been given in the preceding sections. The most distinct differences in the secondary mean flow patterns behind the three VGs are: (1) counterclockwise rotation with vortical center ($Z/A=0.7\sim0.8$) near side wall ($Z/A=1$) for the 45 deg *V* U VG and the delta wing I U VG versus clockwise rotation with vortical center ($Z/A=0.2\sim0.3$) near channel centerline ($Z/A=0$) for the 45 deg *V* D VG; and (2) most of the bottom wall is impinged by the downward vertical velocities for the former versus swept by the spanwise velocities for the latter. All the vortex centers are situated above the bottom wall and approximately at VG's local height. The wall confinement of the square duct on the longitudinal vortical structures induced by the 45 deg *V* U VG and the delta wing I U VG significantly improves the heat transfer elevation by cutting out the part of vortical structure which is directed away from the bottom wall. In contrast, Eibeck and Eaton [4] and Pauley and Eaton [6] (channel aspect ratio of 4.8 and VG-to-channel width ratio of 0.03) found very complete concentric circles of longitudinal vortex structures due to lacking of wall confinement. They concluded that a designer wishing to obtain the high heat transfer augmentation should avoid common-flow-up vortices that are in close proximity. The wall confinement on the present 45 deg *V* U VG and delta wing I U VG effectively removes not only other common-flow-up vortices but the upwash side of the primary vortex.

As for the k/U_b^2 ($k=3(v^2+w^2)/4$) distributions, the mean velocity gradients of the secondary flow are the maximum near the vortex centers ($Z/A=0.2\sim0.3$) for the 45 deg *V* U VG ($k_{max}/U_b^2=$seven percent) and the delta wing I U VG ($k_{max}/U_b^2=$four percent) and decrease away from the vortex centers towards the channel centerline ($k\approx0.1k_{max}$ near centerline). Since the spanwise mean velocities sweep over the bottom wall for the case of the 45 deg *V* D VG, the mean velocity gradients of the secondary flow are maximum adjacent to the bottom wall and, in turn, $k_{max}/U_b^2=$five percent occurs there.

Figure 6 presents the streamwise mean velocity vector fields around the 45 deg *V* U VG and the delta wing I U VG. The approaching flow below the VG height is retarded and turned upward near VG's front edge to flow over the vortex generator. It is interesting to note that there is no corner vortex formed in front of the vortex generators, as often observed in the case of the right-angled rib ([8]). The reason is that for the two VGs examined in Fig. 6 part of the approaching flow can split from the V shape's tip into two streams along the two angled sides. It should be also noted that the LDV measurement plane does not cut through sections off the channel centerline where vortices roll up. A major difference exists between the two flow patterns depicted

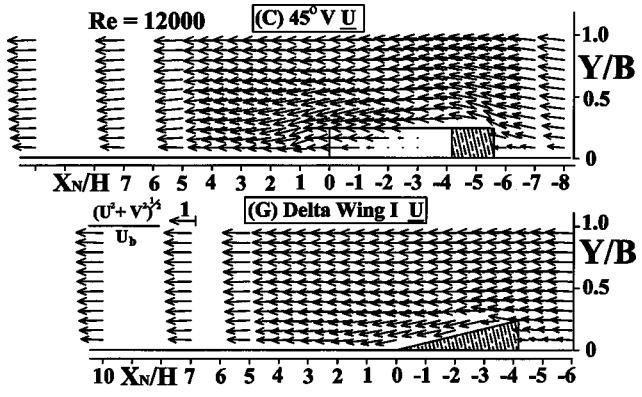

Fig. 6 Vector plot of the flow patterns near a SVG along *Z* = 0 plane for Re=1.2×10⁴: (C) 45 deg *V* U VG and (G) delta wing I U VG.

in Fig. 6. Flow separation bubble occurs immediately behind the 45 deg V U VG but not behind the delta wing I U VG. Its effects on the pressure loss (Table 1) and heat transfer enhancement immediately behind the VG is evidenced as one compares Fig. 4(C) and Fig. 4(G).

Main Fluid Dynamic Parameters Affecting Heat Transfer. One of the purposes of the present study is to find out the dominant fluid dynamic factors controlling the heat transfer augmentation. Figure 7 is an attempt to achieve this goal. Overall speaking, the shapes of $-V/U_b$ distribution are most consistent with those of $\mathrm{Nu/Nu_0}$ distribution for all three selected VGs. In particular, that the downwash regions of the secondary flow are associated with the highest $\mathrm{Nu/Nu_0}$ enhancement and the upwash regions with the low $\mathrm{Nu/Nu_0}$ enhancement is evidenced from Fig. 7. Consequently, the magnitude and direction of the cross-sectional secondary flow with respect to the heat transfer wall are the dominant fluid dynamic factors in affecting the $\mathrm{Nu/Nu_0}$ enhancement. When the effect of the convective mean velocity U/U_b is added to that of $-V/U_b$, the resulting influence is even more consistent with $\mathrm{Nu/Nu_0}$ distribution shown in Fig. 7. The local heat transfer augmentations can attain as high as $\mathrm{Nu/Nu_0}=4$ and 3.5 around the channel centerline $(Z/A=0)$ for the cases of the 45 deg V U VG and the delta wing I U VG, respectively.

At $X_N/H=1$, the cross section still cuts across the flow reversal region(s) behind the two angled sides of the 45 deg V U VG, $Z/A=-0.7$ to -1.0 and 0.7 to 1.0, and behind the tip of the 45 deg V D VG, $Z/A=-0.2$ to 0.2, as indicated by the negative values of U/U_b in Fig. 7. Also note that there is no flow reversal behind the delta wing I U VG. The two low velocity regions around $Z/A=\pm 0.7$ are the locations of two vortex centers. Comparing U/U_b profiles with k/U_b^2 $(k=(u^2+v^2+w^2)/2)$ profiles in Fig. 7, one sees that the high k/U_b^2 regions are associated with the low velocity or flow reversal regions, and vice versa. The deceleration is usually associated with high flow instability and, in turn, high fluctuation. Comparing $-V/U_b$ profiles with k/U_b^2 profiles in Fig. 7, one finds that the downwash regions are correlated with low k/U_b^2 and upwash regions with high k/U_b^2. In general, the distributions of k/U_b^2 are less correlated with those of $\mathrm{Nu/Nu_0}$.

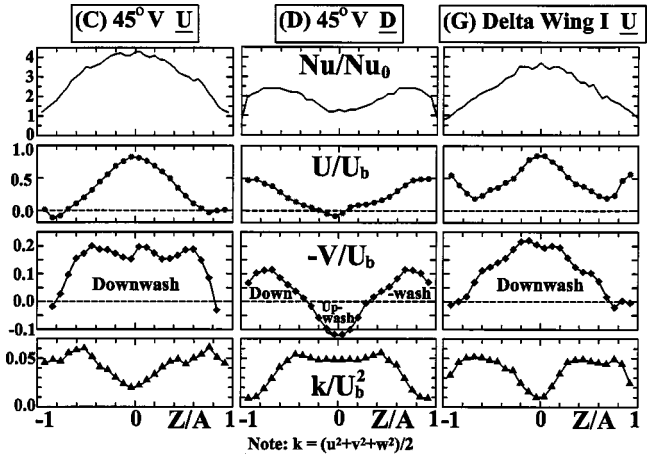

Fig. 7 The spanwise distributions of (1) $\mathrm{Nu/Nu_0}$, (2) U/U_b, (3) $-V/U_b$, and (4) k/U_b^2 at a stage 1H (3 mm) behind a SVG for $\mathrm{Re}=1.2\times10^4$: (C) 45 deg V U VG; (D) 45 deg V D VG; and (G) delta wing I U VG (LDV measurements performed at 1-mm distance away from the wall $Y/B=0$)

Vortex Generator Array (VGA)

In practical applications, multiple vortex generators are used and arranged in an array. Figure 8 depicts the $\mathrm{Nu/Nu_0}$ contours over two selected VGAs. The spatially periodic $\mathrm{Nu/Nu_0}$ distributions are realized as revealed from Fig. 8. Owing to the presence of the consecutive vortex generator and its V shape, the fluid flow and longitudinal vortices induced by the upstream vortex generator tend to be pushed apart spanwisely, as evidenced by comparing Fig. 8(C) with Fig. 4(C) and Fig. 8(G) with Fig. 4(G) in terms of $\mathrm{Nu/Nu_0}$ enhancement. As a result, the separation recirculation zone behind the vortex generator is pushed upstream and confined to the rear corner of the V-shaped tip, comparing Fig. 8(C) and Fig. 4(C). Note that the friction-loss decrease due to the reduction in the size of the flow separation zones happens to compensate the friction-loss increase due to the presence of the successive VGs for the 45 deg V U VGA case. The rationale for having the same $f/f_0=3.8$ as that of the corresponding SVG case (45 deg V U in Table 2) is thus provided. A similar behavior dose not occur for the delta wing I U VGA due to the lack of flow separation and an increase in f/f_0 from its corresponding SVG case is expected, as shown in Table 2. The above side push also facilitates most of the fluid layer in front of the VG and below the VG's height to flow along the two angled sides of the 45 deg V U VG and the delta wing I U VG. One thus expects that relatively less fluid below the VG's height will turn upward to flow over the VG's top. This speculation is supported by the flatter velocity vector fields exhibited in Fig. 9 than in Fig. 6. The higher-velocity core flow can thus move smoothly and closely sweep over the VG's top (Fig. 9), as compared with the SVG case shown in Fig. 6. Hence, the area of the highest heat transfer promotion, with $\mathrm{Nu/Nu_0}$ as high as 6 (red color), are larger in Fig. 8(C) and Fig. 8(G) than in Fig. 4(C) and Fig. 4(G), respectively.

Figure 10 compares the spanwise-averaged Nusselt number ratio $(\overline{\mathrm{Nu}}/\mathrm{Nu_0})$ distributions between two selected VGAs of the present study and the 60 deg V U VGA available from Ekkad and Han [13] at $\mathrm{Re}=1.2\times10^4$. All $\overline{\mathrm{Nu}}/\mathrm{Nu_0}$ distributions in Fig. 10 exhibit periodic spikes. $\overline{\mathrm{Nu}}/\mathrm{Nu_0}$ is the highest on the vortex generators $(\overline{\mathrm{Nu}}/\mathrm{Nu_0}=4.5\sim5)$, and the lowest $(\overline{\mathrm{Nu}}/\mathrm{Nu_0}=1.5\sim2)$ immediately upstream of the VGs. The small downward spikes appear in the delta wing I U VGA. Their presence is due to the lower heat transfer enhancement spanwisely along the interface of

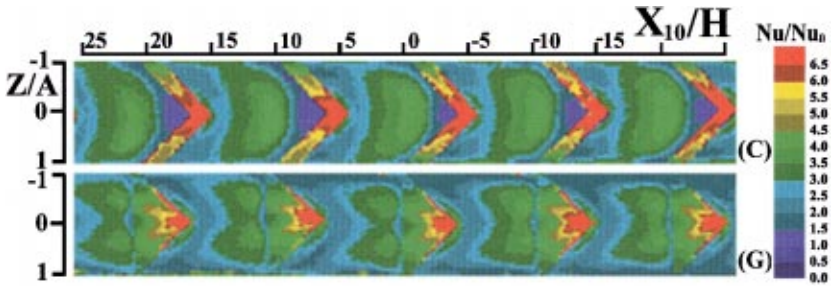

Fig. 8 Detailed local Nusselt number ratio distributions around VG in an array: (C) 45 deg V U VGA and (G) delta wing I U VGA.

Table 2 A list of regional averaged Nusselt number ratios, standard deviations of regional averaged Nusselt number ratios, and friction factors for two selected VGAs at Re=1.2 ×10⁴

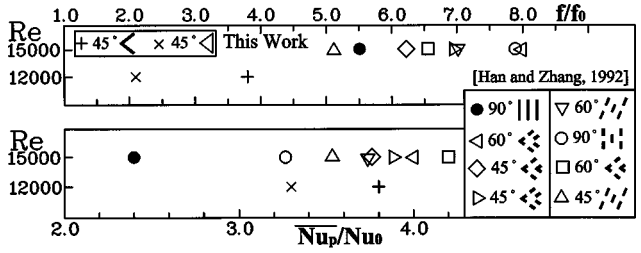

VG Type Pi/H=10		$\overline{Nu}_p/Nu_0$	$(Nu/Nu_0)_{Std}$	f/f_0	$\overline{Nu}_p/Nu_0^*$
(C) 45° V U	VGA	3.8	2.3	3.8	2.6
	SVG	3.7	1.8	3.8	2.5
(G) Delta Wing I U	VGA	3.3	1.6	2.1	2.6
	SVG	2.7	0.5	1.3	2.5

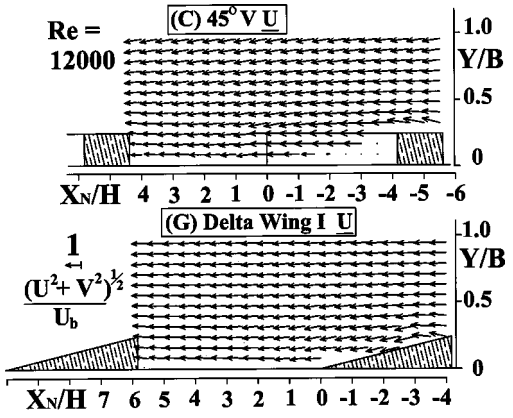

Fig. 9 Mean velocity vector plots of flow patterns in a pitch module along $Z=0$ plane for Re=1.2×10⁴: (C) 45 deg V U VGA and (G) delta wing I U VGA.

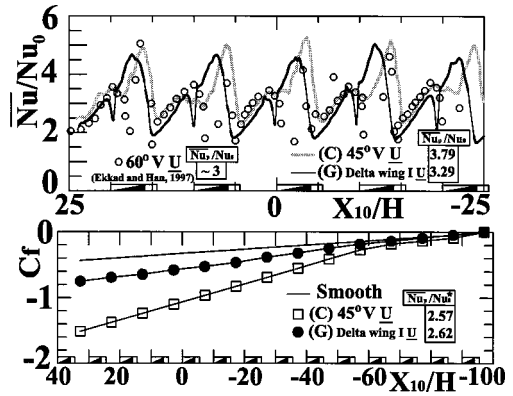

Fig. 10 Streamwise distributions of (1) spanwise averaged Nu/Nu_0 and (2) wall static pressure coefficient in VGAs along $Z=0$ plane for Re=1.2×10⁴: (C) 45 deg V U VGA and (G) delta wing I U VGA

the delta wing and channel wall in each pitch module, as indicated by the narrow-band light blue color between the two broad-band green colors in Fig. 8. The poor heat transfer augmentations behind the tips of 45 deg V U VGs have been spanwisely compensated by the high heat transfer augmentation on the two angle sides of the V-shaped generators in the process of spanwise averaging. Hence, there is no downward spike in the 45 deg V U VGA. When the spanwise-averaged Nusselt number ratios are further averaged over a pitch module, $\overline{Nu_p}/Nu_0$, the difference in heat transfer enhancements between the 45 deg V U VGA ($\overline{Nu_p}/Nu_0=3.8$) and the delta wing U VGA ($\overline{Nu_p}/Nu_0=3.3$) becomes smaller than between the corresponding SVG cases ($Nu_{rg}/Nu_0=3.7$ and 2.7). Similarly, accounting for the C_f distributions depicted in Fig. 10, the heat transfer augmentations under a constant pumping power for the 45 deg V U VGA and the delta wing U VGA are now comparable ($\overline{Nu_p}/Nu_0^*=2.6$). Table 2 summarizes the comparison of the thermal performance, heat transfer uniformity, and friction loss between the two selected SVGs and VGAs. In addition, the auxiliary figure in Table 2 compares present results with those of Han and Zhang [18]. Note that their test ducts have two opposite walls roughened whereas ours have only one roughened, which contributes to the difference in $\overline{Nu_p}/Nu_0$ and f/f_0 between two studies.

Concluding Remarks

The following main results are drawn from the data presented:

1 When the side-wall confinement is appropriately utilized, most of the upwash sides of the longitudinal vortex pairs induced by the vortex generators arranged in a proper pitch can be truncated resulting in a large area of the vortex-generator mounted wall exposed to the downwash sides of the longitudinal vortex pairs and, in turn, high heat transfer augmentation.

2 Among the various fluid dynamic factors affecting the heat transfer enhancement in a square channel generated by the 12 configurations of vortex generators examined, the direction and strength of the secondary flow with respect to the channel wall are found to be the dominant ones, followed by the convective mean velocity. The turbulent kinetic energy distribution seems to be less correlated with the Nusselt number ratio distribution.

3 Among the 12 vortex-generator configurations studied, the 45 deg V U vortex generator and the delta wing I U vortex generator provide the highest pitch-averaged Nusselt number ratio augmentation under a constant pumping power, $\overline{Nu_p}/Nu_0^*\approx2.5$. The former generates the highest pitch-averaged Nusselt number ratio promotion under a constant flow rate, $\overline{Nu_p}/Nu_0\approx3.7$, but the lowest heat transfer uniformity and high friction loss, $f/f_0=3.8$. In contrast, the latter gives very high $\overline{Nu_p}/Nu_0$ enhancement, $\overline{Nu_p}/Nu_0\approx2.7$, and favorable heat transfer uniformity and friction loss, $f/f_0=1.3$, due to lacking of flow reversal immediately behind the vortex generator.

4 For the case of the single vortex generator, the winglet pair with gap, not investigated in the past, leads to the least pressure loss, $f/f_0=1.28$, and ranks third in terms of heat transfer enhancement under a constant pumping power among all the vortex-generator configurations studied

5 When a single vortex generator mounted on one wall of a square channel is replaced with a vortex generator array for the 45 deg V U and the delta wing I U cases studied, the thermal performances both at a constant flow rate and at a constant pumping power are increased and the friction loss is increased for the case of delta wing I U model or remains the same for the case of 45 deg V U model.

Acknowledgment

Support for this work was partially provided by the National Science Council of the Republic of China under contract NSC-85-2212-E007-056.

Nomenclature

A = half-width of duct=12.5 mm, Fig. 1.
B = half-height of duct=12.5 mm, Fig. 1
C_f = wall static pressure coefficient, $(P\text{-}P_0)/0.5\rho U_b^2$
C_p = specific heat, kJ/(kg·K)
D_H = hydraulic diameter, $4AB/(A+B)=25$ mm
D = tip of the vortex generator facing downstream
f = Darcy friction factor, $(\Delta P/\Delta X)\cdot D_H/(\rho U_b^2/2)$
f_0 = friction factor of fully developed tube flow=$0.316\times \mathrm{Re}^{-0.25}$
H = vortex generator height=3 mm
h = heat transfer coefficient, W/(m^2·K)
k = turbulent kinetic energy, m^2/s^2
k_a = thermal conductivity of air, W/(m·K)
k_w = thermal conductivity of wall, W/(m·K)
Nu = local Nusselt number
Nu_0 = Nusselt number in fully developed tube flow
Nu_{rg} = regional averaged Nusselt number
$\overline{\mathrm{Nu}}$ = total averaged Nusselt number
P = pressure, N/m^2
Pi = vortex generator pitch=30 mm
Pr = Prandtl number of air, $\rho C_p \nu/k_a$
Re = Reynolds number, UD_H/ν
T_i = initial temperature of wall, K
T_r = bulk mean temperature of main stream, K
T_w = wall temperature=liquid crystal green-point temperature, K
U = streamwise mean velocity, m/s
U_b = duct bulk mean velocity, m/s
U = tip of the vortex generator facing upstream
u = streamwise velocity fluctuation, m/s
V = transverse mean velocity, m/s
VG = vortex generator
v = transverse velocity fluctuation, m/s
W = spanwise mean velocity, m/s
W_{VG} = vortex generator width, mm
w = spanwise velocity fluctuation, m/s
X = streamwise coordinate ($X=0$ at inlet reference station, Fig. 1)
X_N = streamwise coordinate, ($X_N=0$ at the tenth vortex generator's rear edge, where $X=355$ mm, Fig. 1)
Y = transverse coordinate, Fig. 1
Z = spanwise coordinate, Fig. 1

Greek Symbols

α = angle of attack, degree
α_w = thermal diffusivity of wall, m^2/s
ρ = air density, kg/m^3
ν = kinematic viscosity, m^2/s
δ_{99} = boundary layer thickness, mm

Subscripts

b = bulk
rg = regional averaged

References

[1] Bergles, A. E., 1997, ''Heat Transfer Enhancement—The Encouragement and Accommodation of High Heat Fluxes,'' ASME J. Heat Transfer, **119**, pp. 8–19.
[2] Biswas, G., Deb, P., and Biswas, S., 1994, ''Generation of Longitudinal Streamwise Vortices—A Device for Improving Heat Exchanger Design,'' ASME J. Heat Transfer, **116**, pp. 588–597.
[3] Tiggelbeck, St., Mitra, M. K., and Fiebig, M., 1994, ''Comparison of Wing-Type Vortex Generators for Heat Transfer Enhancement in Channel Flows,'' ASME J. Heat Transfer, **116**, pp. 880–885.
[4] Eibeck, P. A., and Eaton, J. K., 1987, ''Heat Transfer Effects of a Longitudinal Vortex Embedded in a Turbulent Boundary Layer,'' ASME J. Heat Transfer, **109**, pp. 16–24.
[5] Wroblewski, D. E., and Eibeck, P. A., 1991, ''Measurements of Turbulent Heat Transport in a Boundary Layer With an Embedded Streamwise Vortex,'' Int. J. Heat Mass Transf., **34**, No. 7, pp. 1617–1631.
[6] Pauley, W. R., and Eaton, J. K., 1994, ''The Effect of Embedded Longitudinal Vortex Arrays on Turbulent Boundary Layer Heat Transfer,'' ASME J. Heat Transfer, **116**, pp. 871–879.
[7] Jacobi, A. M., and Shah, R. K., 1995, ''Heat Transfer Surface Enhancement Through the Use of Longitudinal Vortices: A Review of Recent Progress,'' Exp. Therm. Fluid Sci., **11**, pp. 295–309.
[8] Liou, T. M., Wu, Y. Y., and Chang, Y., 1993, ''LDV Measurements of Periodic Fully Developed Main and Secondary Flow in a Channel With Rib-Disturbed Walls,'' ASME J. Fluids Eng., **115**, pp. 109–114.
[9] Han, J. C., Zhang, Y. M., and Lee, C. P., 1991, ''Augmented Heat Transfer in Square Channels With Parallel, Crossed, and V-Shaped Angled Ribs,'' ASME J. Heat Transfer, **113**, pp. 590–596.
[10] Chyou, Y. P., 1997, ''Investigation of Fluid Dynamic Characteristics of Longitudinal Vortices,'' Trans. Aeronaut. Astronaut. Soc. ROC, **29**, No. 4, pp. 375–387.
[11] Hibbs, R. G., Acharya, S., Chen, Y., Nikitopoulos, D. E., and Myrum, T. A., 1998, ''Heat Transfer in a Two-Pass Internally Ribbed Turbine Blade Coolant Channel With Cylindrical Vortex Generators,'' ASME J. Turbomach., **120**, pp. 589–600.
[12] Ekkad, S. V., and Han, J. C., 1995, ''Local Heat Transfer Distributions Near a Sharp 180-deg Turn of a Two-Pass Smooth Square Channel Using a Transient Liquid Crystal Image Technique,'' J. Flow Visualization Image Process., **2**, pp. 285–297.
[13] Ekkad, S. V., and Han, J. C., 1997, ''Detailed Heat Transfer Distributions in Two-Pass Square Channels With Rib Turbulators,'' Int. J. Heat Mass Transf., **40**, No. 11, pp. 2525–2537.
[14] Mochizuki, S., Murata, A., and Fukunaga, M., 1997, ''Effects of Rib Arrangements on Pressure Drop and Heat Transfer in a Rib-Roughened Channel With a Sharp 180 deg Turn,'' ASME J. Turbomach., **119**, pp. 610–616.
[15] Liou, T. M., Chen, C. C., and Tsai, T. W., 1998, ''Liquid Crystal Measurements of Heat Transfer in a 180-Deg Sharp Turning Duct With Different Divider Thicknesses,'' *The 8th International Symposium on Flow Visualisation*, Sorrento, Italy, G. M. Carlomagno, Università di Napoli Federico II, Napoli, Italy and I. Grant, Heriot Watt University, Edinburgh, UK.
[16] Liou, T. M., and Chen, C. C., 1999, ''LDV Study of Developing Flows Through a Smooth Duct With 180 Deg Straight-Corner Turn,'' ASME J. Turbomach., **121**, pp. 167–174.
[17] Han, J. C., Huang, J. J., and Lee, C. P., 1993, ''Augmented Heat Transfer in Square Channels With Wedged-Shaped and Delta-Shaped Turbulence Promoters,'' J. Enhanced Heat Transf., **1**, No. 1, pp. 37–52.
[18] Han, J. C., and Zhang, Y. M. , 1992, ''High Performance Heat Transfer Ducts With Parallel and V-Shaped Broken Ribs,'' Int. J. Heat Mass Transf., **35**, No. 2, pp. 513–523.
[19] Dutta, S., and Han, J. C., 1996, ''Effect of Model Orientation on Local Heat Transfer in a Rotating Two-Pass Square Duct With and Without Rib Turbulators,'' ASME J. Heat Transfer, **118**, No. 3, pp. 578–584.
[20] Edwards, F. J., and Alker, C. J. R., 1974, ''Improvement of Forced Convection Surface Heat Transfer Using Surface Protrusions in the Form of (A) Cubes and (B) Vortex Generators,'' *Tribune du CEBEDEAU (Center Belge d'Etude et de Documentation des Eaux)*, Japan Society of Mechanical Engineering, pp. 244–248.
[21] Chyu, M. K., Ding, H., Downs, J. P., Van Sutendael, A., and Soechting, F. O., 1997, ''Determination of Local Heat Transfer Coefficient Based on Bulk Mean Temperature Using a Transient Liquid Crystal Technique,'' *ASME Paper No. 97-GT-489*.
[22] Liou, T. M., Kao, C. W., and Chen, S. H., 1998, ''Flowfield Investigation of the Effect of Rib Open Area Ratio in a Rectangular Duct,'' ASME J. Fluids Eng., **120**, pp. 504–512.
[23] Liou, T. M., Yang, G. P., and Lee, H. L., 1997, ''LDV Measurements of Spatially Periodic Flow Over a Detached Solid-Rib Array,'' ASME J. Fluids Eng., **119**, pp. 383–389.
[24] Rohsenow, W. M., and Choi, H., 1961, *Heat, Mass and Momentum Transfer*, Prentice-Hall, Englewood Cliffs, NJ, pp. 192–193.
[25] Vedula, R. P., Metzger, D. E., and Bickford, W. B., 1988, ''Effects of Lateral and Anisotropic Conduction on the Determination of Local Convection Heat Transfer Characteristics With Transient Tests and Surfaces Coatings,'' *Collected Papers in Heat Transfer*, Vol. 104, ASME, New York, pp. 21–28.

Moving and Rotating Sphere in the Thermal Entrance Region of a Heated Pipe

N. Shahcheraghi
e-mail: nshahcheraghi@ucdavis.edu

H. A. Dwyer

Mechanical and Aeronautical
Engineering Department,
University of California,
Davis, CA 95616

Flow and unsteady heat transfer around a moving and rotating sphere is considered as it passes through the thermal entrance region of a heated pipe. The flow is incompressible and viscous with constant properties, and the heated pipe wall is kept at a constant temperature. Two Peclet numbers of 25 and 100 are considered along with two sphere-to-pipe-diameter ratios of 0.2 and 0.4. The flow is made three dimensional by an eccentric positioning of the sphere inside the pipe. The governing equations are solved by a validated numerical method which uses a finite volume formulation in a generalized body-fitted coordinate system. An overset (Chimera) grid scheme is used to resolve the two geometries of the pipe and sphere. The results are presented in terms of the steady pressure and viscous lift and drag forces on the sphere. In addition the unsteady heat transfer characteristics of the flow are presented in terms of the local and overall Nusselt number evolution around the sphere as it passes through the thermal entrance region of the pipe. Sphere heat-up is also given as the lumped mass sphere temperature as a function of distance from the thermal entrance. [S0022-1481(00)02402-6]

Keywords: Heat Transfer, Moving Boundaries, Numerical Methods, Spheres, Transient

Introduction

Flow and heat transfer of an incompressible, viscous fluid in the thermal entry region of a pipe has been studied for years. This type of flow has applications in design of heat exchangers, and in material, chemical, and food-processing equipment. For laminar flow in a pipe analytical solutions exist for the fully developed region, where, variations are only in the radial direction. In the entrance region of a pipe, assuming fully developed parabolic velocity profile and a constant heat flux at the pipe wall, an energy balance on an incremental pipe volume gives the temperature variations in the radial and axial directions. A similar procedure can be used to arrive at the solution for the case of constant pipe wall temperature ([1]). These solution are used to calculate important variables such as the thermal entry length, L_{th}, and the asymptotic pipe Nusselt number, Nu_{∞} ([2]).

Another flow of great interest is that of an incompressible fluid with heat transfer over a three-dimensional object such as sphere. This type of flow has applications in various branches of combustion including droplet dynamics and vaporization, and particle migration. A large collection of work in this type of flow is gathered in the text by Clift et al. [3]. This work includes recent analytical, numerical, and experimental studies of various external flows over rigid and fluid spheres.

Combination of the two cases presented above is of particular interest. This class of flow is a realistic model for heating and transport of particles through a pipe. More specifically, in combustion, it can represent the heating and movement of fuel droplets in the ducts leading to the combustion chamber. In food processing this type of flow models the heating of grains or vegetables in a cooking process. In biological flows the transfer of heat and mass to and from live blood cells moving through arteries can be modeled.

Traditionally, this type of flow is solved by simplifying assumptions, which lead to either a simple pipe flow or an external flow over a sphere. Important features of the flow are lost by such assumptions. For example, using external flow models for a sphere inside a pipe would ignore the important wall effects. Inversely, using simple pipe flow models would ignore the blockage effects of the sphere.

Recently, with the use of computational methods, these simplifying assumptions were eliminated in order to better understand the pipe wall and sphere interactions. Shahcheraghi and Dwyer [4] studied steady three-dimensional incompressible flow and heat transfer over a fixed sphere in a pipe. This study extends their work to the unsteady thermal condition of a moving and rotating sphere in the thermal entrance region of the pipe. The sphere is placed off-center to induce three-dimensional effects.

Method of solution consists of a finite volume formulation of the incompressible continuity equations, Navier-Stokes equations, and the thermal energy equation ([5]). An overset (Chimera) grid scheme is used in order to, effectively, resolve the geometry and flow features ([5,6]). This includes a major (background) cylindrical mesh for the pipe and a separate (minor) spherical mesh around the sphere.

In the following sections the problem statement is described, followed by method of solution. Next, some code validation results are stated, followed by the presentation of results. Finally, some concluding remarks are made.

Problem Statement

The basic problem consists of flow with fully developed velocity profile in a pipe of diameter, D_p. Inside the pipe there is a sphere of diameter, D_s, which is centered at an eccentric distance, E, from the pipe center line (Fig. 1). For $E=0$, the flow is axisymmetric, however, since $E\neq 0$ the flow becomes three dimensional with a plane of symmetry (see Section A-A Fig. 1) (plane passing through $\phi=0$ and $\phi=180$ deg). The sphere is moving along the pipe axial direction while rotating around its own center. As the sphere moves it enters a region where the pipe wall temperature is hotter than that of the fluid and the sphere (at $X=0$) and a thermal entrance region develops downstream of the sphere ($X>0$). The length of the pipe section under consideration is L, which is chosen based on two important criteria. First, the length must be chosen such that the sphere blockage effects are negligible at the pipe section entrance location. Second, the pipe length

Contributed by the Heat Transfer Division for publication in the JOURNAL OF HEAT TRANSFER and presented at the ASME Annual Fluids Engineering Conference, Aug. 1995. Manuscript received by the Heat Transfer Division Jan. 5, 1999; revision received Dec. 10, 1999. Associate Technical Editor: R. Douglass.

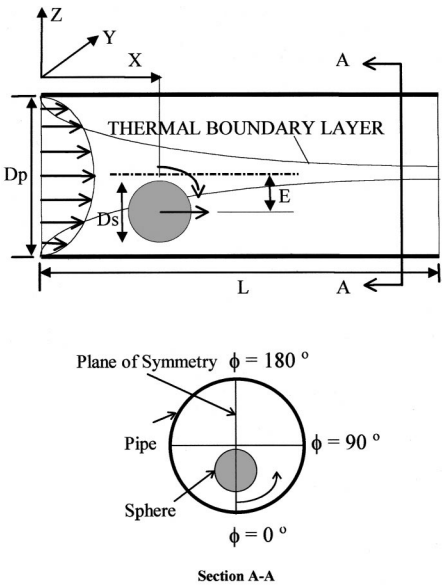

Fig. 1 Basic arrangement for the moving and rotating sphere inside the pipe

should be larger than the thermal entry length for the given pipe flow conditions (Pe=25 and 100) in order to see the flow and heat transfer features of the problem within the thermal entrance region. Results from a previous study by Shahcheraghi and Dwyer [4] suggests that pipe L/D of five satisfies the first criterion, specially, since the sphere is moving with the flow and, therefore, has less blockage effect. This length also satisfies the second criterion as it is nearly one and half times the thermal entrance length for the largest pipe Peclet number of 100. Therefore, for $L/D_p=5$, the flow is fully developed at the pipe entrance. For the sphere, the velocity is equal to the local fluid velocity and rotation rate is one-half of the local flow vorticity at the sphere-center position. These conditions were chosen in order to approximate a freely moving sphere in a pipe (shear) flow ([7]).

The fluid is viscous and incompressible with constant properties, and the flow regime is assumed to be laminar. The pipe Reynolds number is defined as

$$\mathrm{Re}_p=\frac{U_a D_p}{\nu}.$$

The diameter ratio (DR) is defined by

$$\mathrm{DR}=\frac{D_s}{D_p}$$

In this study, two Re_p values of 25 and 100 are considered in combination with two diameter ratios of 0.2 and 0.4.

In this problem the fluid mechanics is made steady by using a coordinate system that is moving with the sphere. For an observer attached to the sphere the fluid mechanics of the flow are steady. Such an observer sees the pipe wall passing by at the sphere translational velocity, while the sphere rotates around its center. Also, with respect to this observer, at the pipe section entrance location, fluid particles that are radially closer to the pipe centerline than the sphere are approaching the sphere while those that are radially further from the pipe centerline are moving away from the sphere. This means that the velocity profile at the pipe entrance has a shifted parabolic shape with positive velocity values for points with $r=(y^2+z^2)^{1/2}<E$, and negative velocity values for points with $r=(y^2+z^2)^{1/2}>E$.

The unsteady nature of the flow is in the passing of the sphere through the thermal entrance region. As the sphere is moving through this region it disturbs the thermal boundary layer and is heated by it. This means that, to an observer, attached to the moving coordinate system the heated pipe wall (and the thermal entrance region) approach and pass by at the sphere translational speed. At the same time the heated fluid from the boundary layer heats up the sphere, which is assumed to be at uniform temperature.

Initial and Boundary Conditions. The nondimensional fluid temperature is defined as

$$T=\frac{T_f-T_{s_i}}{T_w-T_{s_i}}$$

and the dimensionless sphere temperature is defined by

$$T_s^*=\frac{T_s-T_{s_i}}{T_w-T_{s_i}}.$$

Initially, the sphere, the entering fluid, and pipe wall temperatures are at zero. Then, as time progresses the pipe wall temperature is set to one beginning with the pipe exit location and advanced towards the pipe entrance with each time-step. The distance by which the hot pipe wall is advanced each time-step is a product of the time-step and the sphere translational speed. As the hot pipe wall is advanced towards the sphere and eventually passed it, the thermal boundary layer develops and heat diffuses into the fluid. By the time the hot pipe wall reaches the sphere location the temperature field downstream of the sphere is that of a developing thermal entrance region, with the distortions due to the presence of the moving and rotating sphere. The hot fluid starts to heat up the sphere, whose temperature is updated at each time-step using

$$T_s^{n+1}=T_s^n+\Delta T_s.$$

The temperature change, ΔT_s, is calculated from the heat transfer to the sphere using the overall sphere Nusselt number, Nu_s. By an energy balance on the sphere it can be shown that in nondimensional terms

$$\Delta T_s=\frac{6\Delta\overline{t}\mathrm{Nu}_s}{\overline{\rho C}_p\mathrm{Pe}}$$

where $\Delta\overline{t}=(\Delta t U_a/D_s)$ is the nondimensional convective time-step, and the product $\overline{\rho C}_p=(\rho_s C_{P_s})/(\rho_f C_{P_f})$ is the nondimensional sphere heat capacity as normalized by the fluid bulk heat capacity.

The velocity and pressure fields are at steady condition because the coordinate system is attached to the moving sphere. This means that the velocity at the pipe wall is set to the sphere translational velocity due to the no slip condition. At the sphere surface the fluid velocity is the same as the rotational velocity of the sphere. Mass-driven flow is assumed, therefore, at the pipe section inlet a shifted parabolic velocity profile is specified, given by

$$\overline{V}_i=2\left(1-\frac{r^2}{R_p^2}\right)-\overline{V}_{s_t}$$

where, $\overline{V}_{s_T}$ is the sphere translational velocity and is equal to $2(1-E^2/R_p^2)=1.68$ for $E=0.2$ and $R_p=0.5$ as chosen in this problem. Pressure is set to zero at the outlet of the pipe section, then, outlet velocity and inlet pressure are solved for, by constant gradient boundary conditions. At the solid surfaces the pressure gradient is set to zero.

Solution Method

The governing equations for this problem are the low Mach number version of the incompressible continuity equation, Navier-Stokes equations, and the thermal energy equation. In dimensionless integral form they are

$$\int\int_s \mathbf{V}\cdot\mathbf{n}dA = 0$$

$$\frac{\partial}{\partial t}\int\int\int_v \mathbf{V}\,dV + \int\int\int \mathbf{V}\cdot\nabla\mathbf{V}dV$$

$$= -\int\int_s p\mathbf{n}dA + \frac{1}{\mathrm{Re}}\int\int_s \mathbf{n}\cdot\bar{\bar{\tau}}dA$$

$$\frac{\partial}{\partial t}\int\int\int_v T\,dV + \int\int\int_v \mathbf{V}\cdot\nabla T dV = \frac{1}{\mathrm{Re\,Pr}}\int\int_s (\nabla T)\cdot\mathbf{n}dA.$$

Prandtl number, $\mathrm{Pr}=\nu/\alpha$, is set to unity in this study, therefore, the Peclet number is equal to the Reynolds number.

These equations are solved in three-dimensional generalized (body-fitted) coordinates, finite volume formulation. The solution algorithm is described in detail by Dwyer [5] and Shahcheraghi [8]. It will only be briefly outlined here. The three Cartesian components of velocity and temperature are marched in time using an implicit discretization of three momentum equations plus the thermal energy equation. The pressure change or ''correction'' is solved in a Poisson equation, which results from application of continuity, and definition of a ''velocity correction'' potential function. The discrete system of linear equations is solved using a predictor-corrector line-relaxation solver.

Chimera Grid Scheme. The overset (Chimera) grid scheme ([9]) is a method in which different regions of the flow field have a separate mesh, depending on their geometric features. Baysal et al. [10] have demonstrated the use of the overset grid scheme by solving a supersonic flow past a blunt-nose cylinder at high angle of attack and an interference flow past an ogive-nose-cylinder in the close proximity of a flat plate. Fouladi and Baysal [11] have used this method in a viscous compressible turbulent flow past an ogive-nose-cylinder near and inside a cavity. The overset grid scheme is, specially, useful in resolving flow fields that involve multiple bodies with at least one of the bodies moving with respect to the others. Yen and Baysal [12] have resolved the unsteady inviscid flow field past an oscillating cylinder near a vertical wall. In this study separate grids are used for the pipe and the sphere. The major mesh is that of the pipe and the sphere has the minor mesh (Fig. 2(*a*)).

Holes and Fringe Points. Some points of the major mesh may fall on the interior of the sphere, where the fluid does not flow. Similarly, some points of the minor mesh may fall outside the flow region (the pipe). These points are called ''holes.'' The holes are marked with hollow squares in Fig. 2(*a*). In order to prevent the governing equations from being solved at holes, the off-diagonal coefficients and the right-hand side of the linear discrete equations are set to zero at these points.

The two separate meshes communicate by means of ''fringe points.'' These are points in the flow region of each mesh that completely separate the holes from the regular mesh points. They are found after all the holes are determined, by converting holes with at least one regular point as a neighbors, to fringe points. Figure 2(*a*) shows a typical set of fringe points marked with solid squares.

Trilinear Interpolation Scheme. A Chimera scheme uses interpolation at the fringe points, in order to transfer data between the meshes. In this work a typical variable, g, is interpolated using a trilinear interpolation,

$$g(x',y',z') = a_1 + a_2x' + a_3y' + a_4z'$$

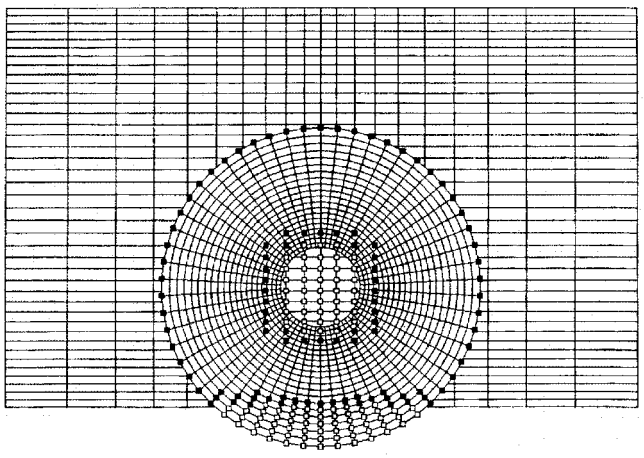

(*a*)

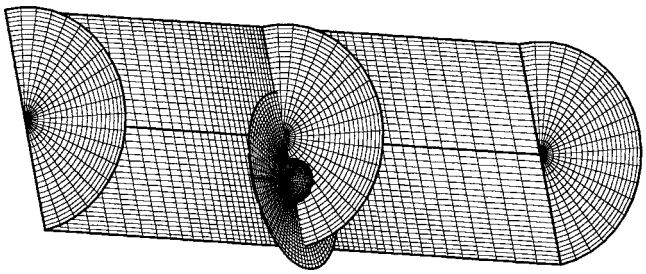

(*b*)

Fig. 2 (*a*) Typical Chimera grid with holes (hollow squares) and fringe points (solid squares) (*b*) Typical Chimera grid used in this study

for given fringe point coordinates, x',y',z'. The coefficients, a_i, are found using Cramers rule. This is done by four simultaneous equations based on known values of g, and coordinates (x,y,z), at the four corners of the tetrahedron containing the point.

Lift, Drag, Shear Stress, and Heat Transfer. Forces exerted on the sphere by the fluid are, generally, lift and drag. The dimensionless form of these forces are lift coefficient, C_L, and drag coefficient, C_D, defined by

$$C_L = \frac{F_L}{1/2\rho U_\infty{}^2 A_s}, \quad \text{and} \quad C_D = \frac{F_D}{1/2\rho U_\infty{}^2 A_s}$$

where A_S is the sphere frontal area.

F_L, and F_D are the dimensional lift and drag forces given by integration of local pressure and viscous forces over the sphere surface. Shear stress is given in terms of the local friction factor, f, defined by

$$f = \frac{8\tau_w}{\rho U_a^2}.$$

This factor, is known as the Darcy friction in an unblocked pipe and is equal to $64/\mathrm{Re}_p$ in a laminar flow ([13]). The dimensionless heat transfer coefficient is the Nusselt number and is defined as

$$Nu = \frac{hL_c}{k} = \frac{L_c}{A(\Delta T_{\mathrm{ref}})}\int\int_s (\nabla T)\cdot\mathbf{n}dA$$

The integral is over the sphere surface area, or the pipe wall area. The characteristic length, L_c, either D_s for the sphere, or D_p for the pipe. ΔT_{ref} is the reference temperature difference $(T_w - T_{f_b})$ for the pipe and $(T_w - T_{si})$ for the sphere.

Code Validation

Validation of the computer code used in this study was performed in a previous study, ([4]). There, the flow around a stationary sphere located in the center of a pipe was calculated. The blockage ratio in the test case was set to one percent and the results were compared to that of a sphere in external unbounded flow. The fluid dynamic forces represented by the sphere lift and drag coefficients, and the heat transfer rates in terms of Nusselt number were in agreement to the published results of Clift et al. [3] and Dandy and Dwyer [14].

In addition pipe thermal entrance length calculations were made in this study and the results were compared with those reported by Salazar and Campo [2]. They report the dimensionless thermal entrance length, $L_{th}^{*}=L_{th}/(R_p\mathrm{Pe})=0.06693$, and the asymptotic Nusselt number, $\mathrm{Nu}_{\infty}=3.6568$, in a circular pipe. All of the results calculated with the present code were in agreement with the published results within three percent.

Results

The results are presented for Re_p of 25 and 100 along with diameter ratios, DR, of 0.2 and 0.4. The sphere is located off-center at $E=0.2\,D_p$, in order to induce a three-dimensional effect. The computation is performed on half of the physical domain due to the symmetry of the flow (see Fig. 1). In these studies the grid densities are $21\times21\times41$ for both the sphere and the pipe meshes for the $\mathrm{Re}_p=25$ cases. For the cases with $\mathrm{Re}_p=100$ the pipe grid density is set to $21\times21\times61$ and the sphere grid density is $21\times21\times41$. A typical grid is shown in Fig. 2(*b*).

The results of this study can be subdivided into two basic categories. First, there are the steady fluid dynamic aspects of the flow, which describe the pressure and viscous forces on the sphere due to the imposed pipe flow. Next, the unsteady heat transfer aspects of the flow are presented in terms of the sphere Nusselt number and temperature variations as the sphere moves through the pipe thermal entrance region. In addition, the change in the temperature field in the vicinity of the sphere is examined.

For the purpose of presenting the three-dimensional results, two angles, θ and ϕ, are defined as follows (see Fig. 1). Angle θ is measured around the sphere starting at the upstream sphere geometric stagnation point. Angle ϕ (Section A-A, Fig. 1.) is measured around the pipe (or sphere) perimeter in a cross-sectional plane perpendicular to the flow direction. Angle ϕ starts from the location with the least distance between the sphere and the pipe wall, $\phi=0$ deg, and follows the pipe (or sphere) perimeter to the point with largest distance between the sphere and the pipe wall, $\phi=180$ deg. The plane of symmetry passes through the $\phi=0$ deg and $\phi=180$ deg locations.

Fluid Dynamics. The fluid dynamics of the flow is presented from the point of view of an observer riding on the sphere as it moves through the pipe. From this perspective, and assuming the fluid properties are independent of temperature, the flow field seems steady. Therefore, the pressure and velocity field around the sphere can be presented as steady-state results. First, the pressure field is described by introducing the dimensionless sphere surface pressure, defined by

$$P_{s^{\infty}}=\frac{P_s-P_{\infty}}{1/2\rho U_{\infty}{}^2}.$$

P_{∞}, is a reference pressure chosen on the outer grid surface in the sphere mesh, at 90 deg from the stagnation point, in the plane of symmetry, and $U_{\infty}=\overline{V}_{s_T}$ as previously defined. There is a typical sphere surface pressure pattern for all four cases. The case with $\mathrm{Re}_p=25$ and $\mathrm{DR}=0.4$ has the largest variations and is discussed in detail here. Figure 3 shows the normalized sphere surface pressure, $P_{S^{\infty}}$ versus angle θ (from front of the sphere) in three different planes (lower symmetry plane; $\phi=0$, upper symmetry plane; $\phi=180$, and the plane in between; $\phi=90$).

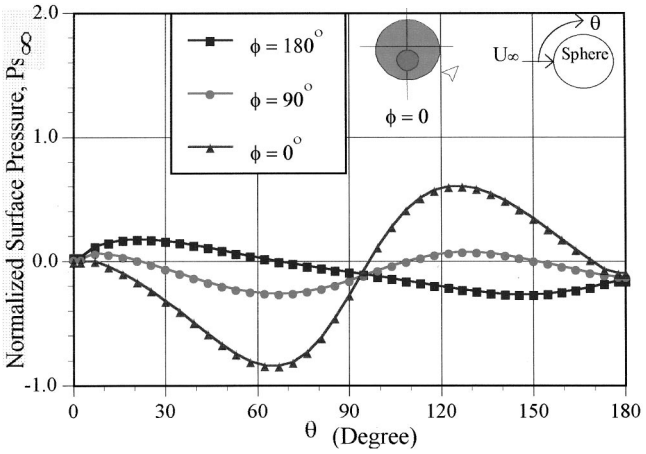

Fig. 3 Sphere surface pressure, $\mathrm{Re}_p=25$, $D_s/D_p=0.4$

In the front the stagnation point is shifted approximately 20 deg with maximum $P_{S^{\infty}}$ of nearly 0.2 in the $\phi=180$-deg plane. This shift is due to the fact that the sphere centerline is not aligned with the pipe centerline, therefore, the maximum pipe flow velocity is aligned with a point above the sphere centerline ($\theta=0$ deg). In the $\phi=0$-deg plane, which is closest to the pipe wall there is an interesting pattern. First, at approximately $\theta=68$ deg there is a minimum value of ~-0.85 then at $\theta=\sim123$ deg a second maximum pressure of ~0.65 is reached. The basic shape of this pattern is the result of the sphere moving faster than the fluid near the pipe wall and creating a low-pressure zone upstream of sphere ($\theta<90$ deg) and a high-pressure zone downstream of the sphere ($\theta>90$ deg). The asymmetry of the pressure curve in this plane ($\phi=0$ deg) is due to the sphere rotation. The pressure in the $\phi=90$ deg plane curve passes in between the other two extremes ($\phi=0$ deg, and $\phi=180$ deg) as expected from the three-dimensional nature of the flow. This pattern is the same for other (3) cases, however, magnitudes of the minimum and maximum pressure values are different.

The local shear stress around the sphere has a similar pattern in all cases as well. The common pattern is discussed by referring to the case with $\mathrm{Re}_p=25$ and $\mathrm{DR}=0.4$ (Fig. 4(*a*)) which has the largest maximum. Here, again there are three different planes (lower symmetry plane; $\phi=0$ deg, upper symmetry plane; $\phi=180$ deg, and the plane in between; $\phi=90$ deg) to the show the three-dimensional nature of the flow. The pattern shown in Fig. 4(*a*) consists of a maximum value (~8.4) at $\theta=\sim90$ deg in the $\phi=0$-deg plane. This is the point closest to the pipe wall with maximum flow acceleration due to blockage effects. For comparison, note that the pipe Darcy friction factor, f, at $\mathrm{Re}_p=25$ is 2.56. The minimum occurs in the $\phi=180$-deg plane between $\theta=40$ deg and $\theta=130$ deg, where the distance between the sphere surface and the pipe wall is maximum. Also, this represents the plane in which the relative velocity between the sphere and the surrounding fluid is at its minimum. The rotation of the sphere is an additional factor in reducing the velocity gradient in this particular plane ($\phi=180$ deg). In the $\phi=90$ deg variation of the local friction factor has the same pattern as the $\phi=0$-deg plane, however, the maxima and minima are attenuated since the pipe blockage is reduced as the distance between the sphere and pipe wall is increased. Figure 4(*b*) shows the three-dimensional friction factor contours on the sphere surface corresponding to the cases shown in Fig. 4(*a*).

A typical flow pattern is shown in Fig. 5, where the velocity vectors on the sphere and near the sphere surface are given in the plane of symmetry for the cases of $\mathrm{Re}_p=25$ and $\mathrm{DR}=0.4$. As shown, there is little change in the parabolic velocity profiles upstream of the sphere. The most significant change is in the vicinity

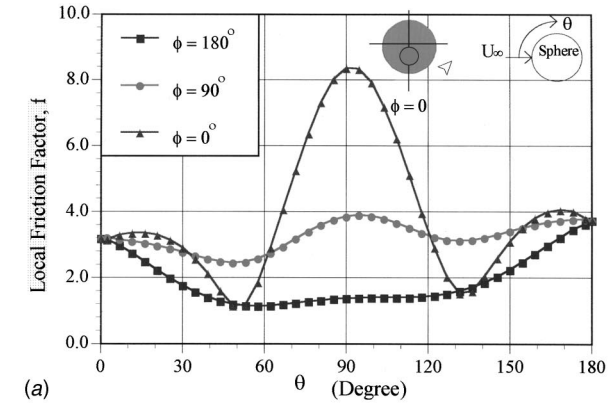

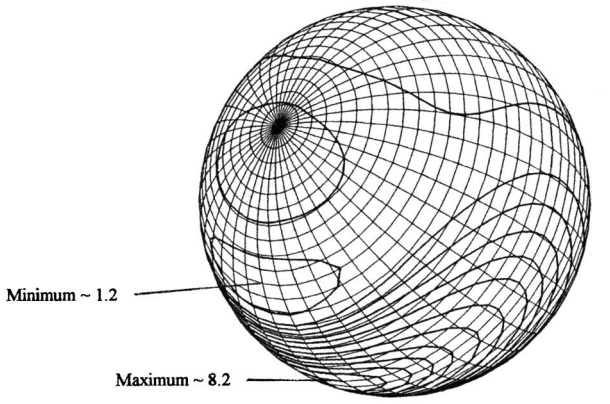

Fig. 4 (*a*) Local friction factor on sphere surface at various angles, $Re_p=25$, $D_s/D_p=0.4$ (*b*) Local friction factor contours on sphere surface, $Re_p=25$, DR=0.4

of the sphere, where there are recirculation zones just upstream and in the wake of the sphere. This recirculation helps transfer the hot fluid from near the pipe wall into the center of the pipe. In the area with least distance between the sphere and the pipe wall the velocity gradient near the sphere surface increases due to the flow acceleration through the constriction, as confirmed by the increase in the local shear stress levels in Fig. 4(*a*).

The fluid dynamic forces on the sphere are represented in terms of the lift and drag coefficients. These coefficients are given in terms of their pressure and friction components in Table 1. These values are typically smaller (in magnitude) than those for a stationary sphere in a pipe flow ([4]). This indicates that the chosen values for the sphere translational and rotational velocities are

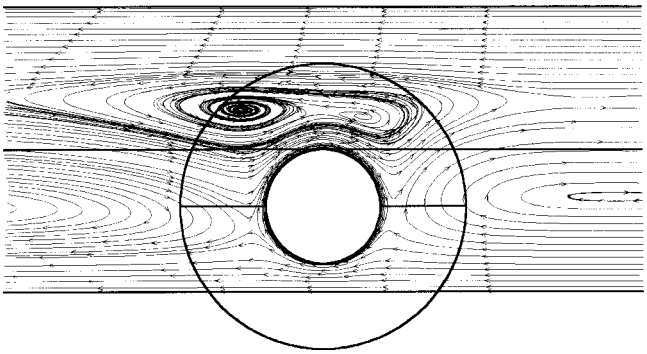

Fig. 5 Stream lines in the plane of symmetry, $Re_p=25$, $D_s/D_p=0.4$

Table 1 Sphere Lift and Drag Coefficients

Re_p, DR	C_{Lp}	C_{Lf}	C_L	C_{Dp}	C_{Df}	C_D
25, 0.2	−0.03	0.00	−0.03	0.06	−0.28	−0.22
25, 0.4	−0.09	0.02	−0.07	−0.21	−0.76	−0.97
100, 0.2	−0.05	−0.02	−0.07	−0.04	−0.15	−0.19
100, 0.4	−0.10	0.01	−0.09	−0.09	−0.21	−0.30

approaching those values for a freely moving sphere in a pipe flow. The negative drag coefficients indicate that a freely moving sphere would be slowed down and travel at a slower translational speed. In all cases the friction drag is negative and larger than the pressure drag in magnitude. Therefore, under specified conditions of these problems the friction drag is the main component that slows the sphere down. The lift coefficient is reduced to nearly zero, which indicates that the transverse location of the sphere is only slightly different from that of a freely moving sphere. The negative sign for the overall lift coefficient tells us that the sphere would move closer to the pipe wall before coming to an equilibrium position. In all cases it is the pressure component that dominates the lift force.

Heat Transfer. The unsteady nature of the problem can be seen in the thermal characteristics of the flow. Here, the variations in the sphere overall Nusselt number, Nu_s, and temperature, T_s^*, are given as a function of the dimensionless distance from the thermal entrance location, X^*. The distance from thermal entrance, X, is normalized by the pipe radius, R_p and Peclet number, Pe,

$$X^* = \frac{X}{R_p \mathrm{Pe}}.$$

Figure 6 shows the variation of Nu_s as a function of X^* for all four cases considered in this study. In all cases there is a maximum in the Nusselt number at a distance less than the thermal entrance length of $L_{th}^*=0.06693$ for an unblocked pipe (at this distance an asymptotic pipe wall Nusselt number of ~3.66 is reached in a simple pipe flow). The sphere-to-pipe-diameter ratio, DR, has a great influence on the overall Nusselt number. This is evident by noting that the maximum Nusselt number for the DR=0.4 cases (~1.35 for Pe=100 case and ~1.1 for Pe=25 case) are at least two times that of the DR=0.2 cases (~0.55 for Pe=100 case and ~0.45 for Pe=25 case). The second important factor is the flow Peclet number. If we group the curves into two sets, DR=0.4 and DR=0.2 with two curves in each set, we see that the case with the larger flow Peclet number has the larger maximum Nusselt number. Another effect of Pe is the point at which the sphere heat-up starts. In each set of curves the one with

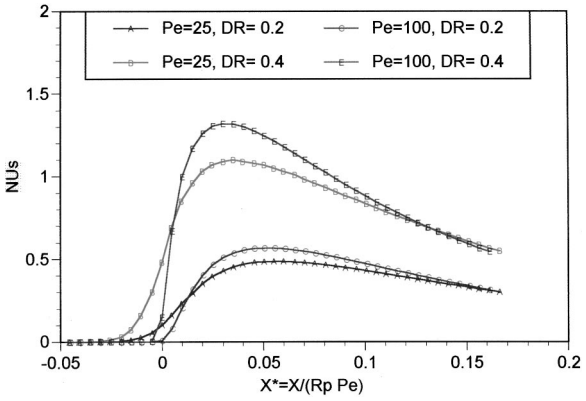

Fig. 6 Sphere Nusselt Number, Nu_s, versus distance, X^*, from pipe thermal entrance

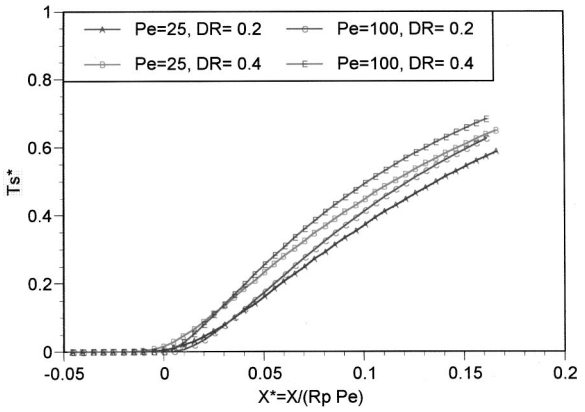

Fig. 7 Sphere temperature, T_S^*, versus distance, X^*, from pipe thermal entrance

smaller Pe has an earlier sphere heat up start point. The case of Pe=100 and DR=0.4 has the earliest starting point ($X^* \sim -0.025$). Low Pe means a thicker thermal boundary layer and more heat diffusion upstream of the thermal entrance point. The larger heat diffusion region upstream of the thermal entrance region means that the sphere reaches the hotter fluid sooner and starts to heat up earlier. Of course, the larger sphere has a larger radius and sees the heated fluid sooner than the one with smaller radius as it approaches the thermal entrance point. This difference is shown by the earlier start point for the larger DR value in the curves of Fig. 6.

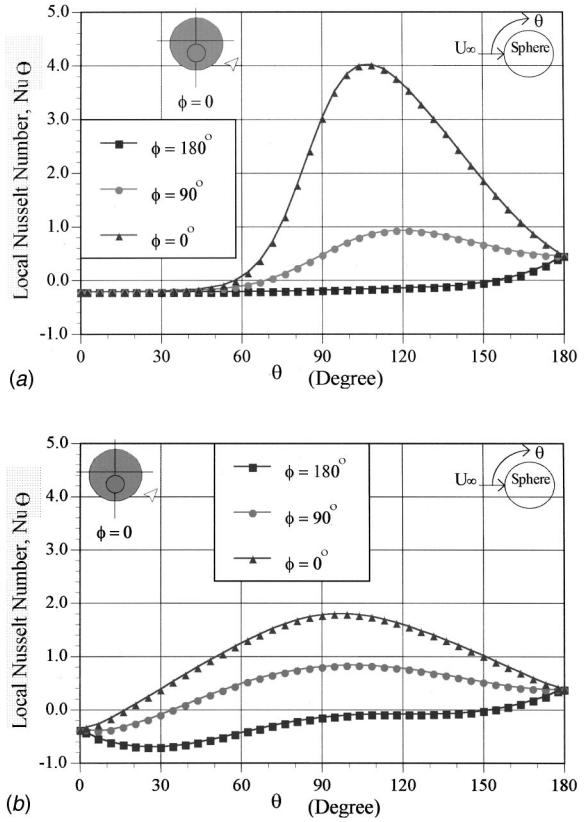

Fig. 8 (*a*) Local Nu around the sphere at various angles, Re_p =25, D_s/D_p=0.4, X^*=0.0 (*b*) Local Nu around the sphere at various angles, Re_p=25, D_s/D_p=0.4, X^*=0.168

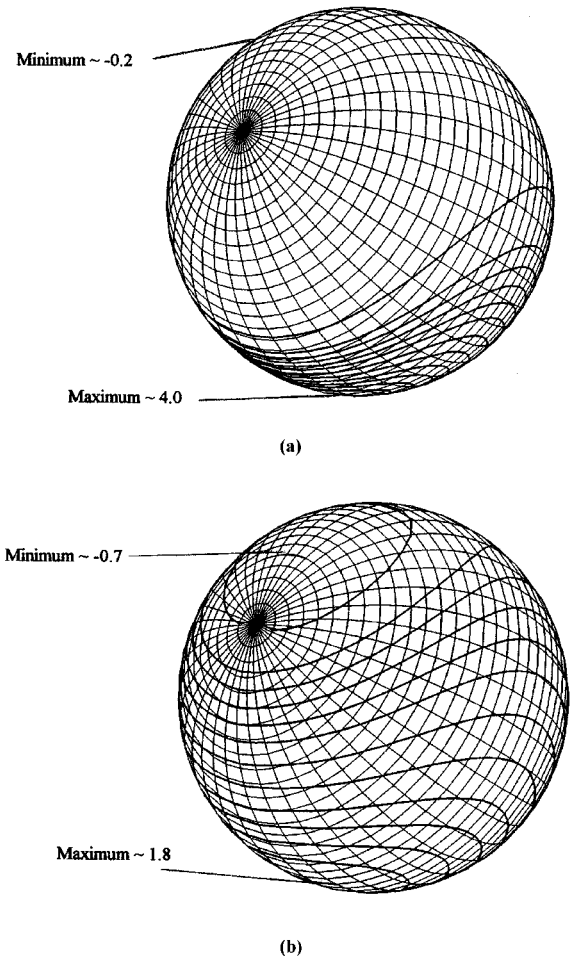

Fig. 9 Nusselt number contours on sphere surface, Re_p =25, D_s/D_p=0.4, X^*=0.0 (*a*) and X^*=0.168 (*b*)

The overall Nusselt number decreases after reaching a maximum. The decrease in Nu_s is due to the heating of the sphere as it moves through the thermal entrance region. The sphere heat-up reduces the average temperature gradient at the sphere surface and eventually as the sphere reaches the pipe wall temperature the overall sphere Nusselt number is expected to become zero at a distance beyond the X^* range of these calculations. The sphere temperature evolution is presented in Fig. 7, where T_s^* is plotted against X^*. The sphere temperature has nearly a linear dependence on X^*. The overall slope of this linear dependence is nearly the same in all cases. However, the cases with larger diameter ratio have a shorter heat up distance as they start the heat up process earlier. At a distance equal to the unblocked pipe thermal entrance length ($X^* \sim 0.067$) the sphere temperature is between 20 percent to 35 percent of the pipe wall temperature depending on the flow Peclet number and the sphere to pipe diameter ratio DR. At the end of the computation ($X^* \sim 0.165$) the sphere has reached anywhere between 60 percent to 70 percent of the pipe wall temperature. The sphere temperature is expected to asymptotically reach the wall temperature at some point beyond the end of the computational range.

The local Nusselt number around the sphere, Nu_θ versus θ is given at two locations ($X^*=0.0$, and $X^*=0.168$) for the case of Pe=25 and DR=0.4 in Figs. 8(*a*) and 8(*b*). These figures give typical Nusselt number distributions on the sphere surface as it moves through the pipe thermal entrance region. In these figures negative Nusselt number indicates heat loss from the sphere to the cooler fluid and positive Nusselt number indicates heat gain by the

sphere from a hotter fluid. At the entrance of the region Fig. 8(*a*) sphere temperature in a large portion of the sphere ($\theta < 60$ deg) is warmer than the approaching cold fluid and, therefore, there is a heat loss from the sphere. The maximum heat gain is in the plane closest to the wall ($\phi = 0$ deg) with a maximum Nusselt number of ~4.0 at $\theta \sim 100$ deg. Further along the thermal entrance region (Fig. 8(*b*)) the Nusselt number has a smaller maximum value of ~1.8 in the plane closest to the pipe wall ($\phi = 0$ deg), confirming previous results that indicate smaller temperature gradient at the sphere surface as the it heats up. This is partially due to the fact that the sphere temperature is assumed to be uniform during the heating process, meaning the heat gain from the fluid is instantaneously distributed throughout the sphere resulting in an average overall temperature increase. This assumption limits the use of these Nusselt number curves to spheres that can be treated as a lumped mass. Note that the largest positive values are always in the $\phi = 0$-deg plane (closest to the pipe wall) and the smallest (negative) values are always in the $\phi = 180$-deg plane (furthest from the pipe wall). Also, note that the plane furthest from the wall has mostly negative Nusselt number values with almost negligible heat gain towards the back of the sphere ($\theta > 160$ deg).

Figure 9 shows the three-dimensional local Nusselt number contours on the sphere surface corresponding to the $X^* = 0$ and $X^* = 0.168$ locations, for the Pe = 25 and DR = 0.4 case discussed above. The actual values of the contour lines can be deduced from Figs. 8(*a*) and 8(*b*), respectively. The Nusselt number contours confirm the maximum and minimum points of heat transfer on the sphere surface.

A typical run required approximately 1 hour and 25 minutes of single Central Processing Unit (CPU) time on a microcomputer (with Intel Pentium II 350 MHz dual processors running under NT 4.0 operating system) for the steady flow calculations. The unsteady heat transfer portion of the calculations required nearly the same amount of time.

Accuracy, Convergence, and Mass Conservation. The numerical method used in the present study is second-order accurate in space and first-order accurate in time. The fluid dynamics aspects of all cases considered in this study are in steady-state condition for a coordinate system attached to the sphere and moving with its translational velocity. Therefore, we can look at the convergence history of the flow as the steady-state solution is reached for the velocity and pressure fields. In this study the convergence criteria was chosen to be the maximum change in the velocity and pressure fields in each iteration step. Figures 10(*a*) and 10(*b*) show the convergence history of these flow variables as a function of iteration step. In Fig. 10 the global maximum absolute value (Sup norm) of the velocity change is plotted against iteration step for the four cases considered here. The pressure correction variable, ϕ, is closely related to the pressure change by the relation

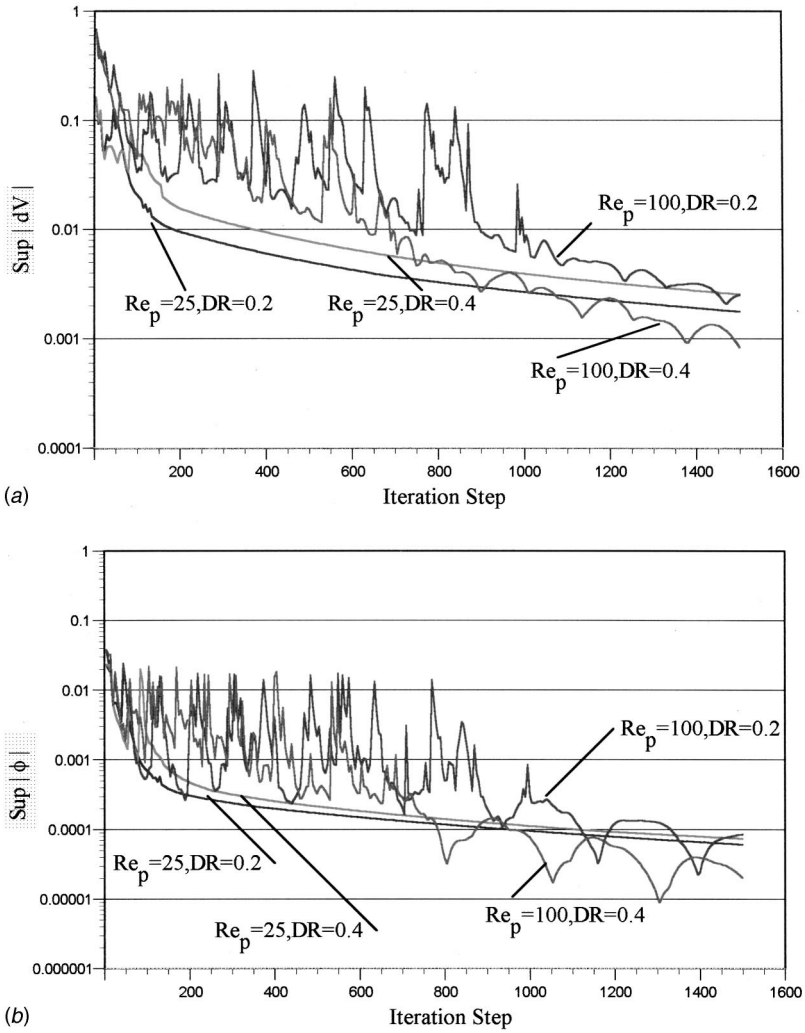

Fig. 10 (*a*) Convergence history for the velocity field (*b*) Convergence history for the pressure correction variable, ϕ

Table 2 Velocity Divergence

Re_p, DR	25, 0.2	25, 0.4	100, 0.2	100, 0.4
$\left\|\int\int_s \overline{V}\cdot d\overline{A}\right\|_{\text{pipe}}$	1.2E-3	2.0E-2	5.6E-2	1.3E-3
$\left\|\int\int_s \overline{V}\cdot dA\right\|_{\text{sphere}}$	4.6E-3	1.0E-2	1.3E-2	4.3E-3

$\Delta p = \phi/\Delta t$. Figure 10(*b*) shows the Sup norm of ϕ as function of iteration step. In both figures it is evident that the cases with larger pipe Reynolds number ($Re_p = 100$) have some oscillations before approaching a steady-state solution after 1000 iteration steps. On the other hand the cases with the smaller pipe Reynolds number ($Re_p = 25$) approach a steady-state solution smoothly after 100 iteration steps. This Reynolds number dependence is typical for flows considered here. In all cases the maximum change in the fluid dynamic variables (u,v,w,p) were less than 0.5 percent after 1500 iteration steps.

The unsteady heat transfer results are first-order accurate in time. The diffusion time-step, which is the ratio of physical time step (Δt) over the momentum diffusion time step $(\Delta t_{\text{diff}} = D_p{}^2/\nu)$, for the unsteady calculations is of order 1.E-4. The results at each time-step were iterated until the sup norm of the temperature field was reduced to 1.E-5.

In low Mach number flows an important consideration is a divergence-free velocity field. In the cases considered here, where the density is constant with a dimensionless value of one, the surface integral

$$\int_s \int \overline{V}\cdot\overline{dA}$$

was evaluated over the entire pipe surface area, including the inlet and outlet areas, at the end of the iteration process. This insures the satisfaction of mass continuity in the entire computational domain. Table 2 shows the value of the above integral for each of the four cases considered here. In nondimensional values the average velocity at the pipe inlet is set to one and the pipe diameter is also set to one. Therefore, total mass flux into the pipe is of order $\pi/4$. The results of Table 2 show that the velocity field is divergence free within a few percentage points of the total mass flux into the pipe for all cases considered. For comparison the divergence of the velocity field around the sphere is also given in Table 2. Mass conservation for the spherical mesh is satisfied within the same order of magnitude as the pipe mesh.

Concluding Remarks

Flow and heat transfer calculations were performed over a moving and rotating sphere in the thermal entrance region of a pipe, in the moderate Peclet number range. The solution method was a finite volume generalized coordinate formulation of the low Mach number continuity, Navier-Stokes, and thermal energy equations. In addition an overset (Chimera) grid scheme was successfully used to resolve the sphere and pipe geometries with two independently generated meshes. The coordinate system was chosen to be moving with the translational velocity of the sphere. In this coordinate system the fluid dynamics of the problem are at steady state for a constant property fluid. The steady fluid dynamic results show one distinct sphere surface pressure pattern, which has a shifted stagnation point and largest variations in the plane closest to the pipe wall. There is also one distinct sphere surface shear stress pattern with minimum values in the plane furthest from the pipe wall. In this plane velocity gradients are smallest due sphere translation and rotation, which cause a small relative velocity between the fluid and the sphere. The largest sphere shear stress values are in the plane closest to the pipe wall, where blockage effects and sphere rotation create the largest velocity gradient region. The parabolic velocity profile in the pipe is significantly disturbed in the close proximity of the sphere (approximately one sphere diameter), where there are two recirculation regions just upstream and in the wake of the sphere.

The flow has an unsteady temperature field, which changes as the sphere moves through the thermal entrance region of the pipe. The unsteady overall sphere Nusselt number reaches a maximum at approximately one half of the pipe thermal entrance length and then falls towards an asymptotic value of zero as the sphere is heated to the pipe wall temperature. The sphere Nusselt number primarily increases with an increase in the sphere to pipe diameter ratio and, secondly, increases with the flow Peclet number. Sphere local Nusselt number patterns show that the maximum heat transfer rate is in the region closest to the pipe wall, where heat is transferred from the heated fluid near the wall to the sphere. In addition, as the sphere heats up, these patterns indicate some areas of heat loss from the sphere to the cooler fluid, mainly, in the plane furthest from the pipe wall.

The solution convergence for the cases with the higher Reynolds number have large oscillations at the beginning of the iteration process and later accelerate to overtake the convergence rate of the lower Reynolds number cases (at $\sim$ 1200 iteration steps). The lower Reynolds number cases, on the other hand, have a smooth but slow convergence behavior. The mass conservation was confirmed through divergence of the velocity field for both the spherical (minor) mesh and the pipe (major) mesh.

Nomenclature

A_s = sphere frontal area
BR = blockage ratio
C_D = sphere drag coefficient
C_L = sphere lift coefficient
D_p = pipe diameter
D_s = sphere diameter
E = sphere eccentric distance
f = local friction factor
F_D = drag force on sphere
F_L = lift force on sphere
h = heat transfer coefficient
k = fluid thermal conductivity
L = pipe length
Nu_s = overall sphere Nusselt number
Nu_θ = local sphere Nusselt number
$\mathbf{n}$ = area unit normal
Pe = Peclet number
Pr = fluid Prandtl number
P_s = sphere surface pressure
$P_{s\infty}$ = sphere normalized surface pressure
P_∞ = far field reference pressure
Re = Reynolds number
Re_p = pipe Reynolds number
$Re_{s\infty}$ = sphere Reynolds number
T = dimensionless fluid temperature
T_f = dimensional fluid temperature
T_s = dimensional sphere surface temperature
T_s^* = dimensionless sphere surface temperature
T_w = dimensional pipe wall temperature
U_a = average pipe inlet flow velocity
U_∞ = pipe entrance velocity along sphere centerline
$\mathbf{V}$ = fluid velocity vector
X^* = dimensionless distance (X)
x,y,z = Cartesian coordinates
x',y',z' = fringe point coordinates
α = fluid thermal diffusivity
ν = fluid kinematic viscosity
ρ = fluid density
$\bar{\bar{\tau}}$ = viscous stress tensor
τ_w = local shear stress

Subscripts

b = bulk fluid (temperature)
f = friction component
i = initial
p = pressure component
th = thermal entrance

References

[1] Kreith, F., and Bohn, M. S., 1986, *Principles of Heat Transfer*, 4th Ed. Harper and Row, New York.
[2] Salazar, A. J., and Campo, A., 1990, ''Prediction of the Thermal Entry Length Without Solving the Complete Entrance Length Problem,'' Int. J. Heat Fluid Flow, **11**, No. 1, Mar., pp. 48–53.
[3] Clift, R., Grace, J. R., and Webber, M. E., 1978, *Bubbles, Drops, and Particles*, Academic Press, San Diego, CA.
[4] Shahcheraghi, N., and Dwyer, H. A., 1998, ''Fluid Flow and Heat Transfer Over 3-D Spherical Object in a Pipe,'' ASME J. Heat Transfer, **120**, p. 985.
[5] Dwyer, H. A., 1989, ''Calculation of Droplet Dynamics in High Temperature Environments,'' Prog. Energy Combust. Sci., **15**, pp. 131–158.
[6] Nirschl, H., Dwyer, H. A., and Denk, V., 1994, ''A Chimera Grid Scheme for Calculation of Particle Flows,'' J. Fluid Mech., accepted for publication.
[7] Nirschl, H., Dwyer, H. A., and Denk, V., 1995, ''Three-Dimensional Calculation of the Simple Shear Flow Around a Single Particle Between Two Moving Walls,'' J. Fluid Mech., **283**, pp. 273–285.
[8] Shahcheraghi, N., 1996, Ph.D. thesis, University of California, Davis, CA, June.
[9] Dougherty, F. C., 1985, ''Development of a Chimera Grid Scheme With Applications to Unsteady Problems,'' Ph.D. thesis, Stanford University, Stanford, CA.
[10] Baysal, O., Fouladi, K., and Lessard, R., 1991, ''Multigrid and Upwind Viscous Flow Solver on Three-Dimensional Overlapped and Embedded Grids,'' AIAA J., **29**, No. 6, p. 903.
[11] Fouladi, K., and Baysal, O., 1992, ''Viscous Simulation Method for Unsteady Flow Past Multicomponent Configurations,'' J. Fluids Eng., **114**, June, pp. 161–169.
[12] Yen, G. W., and Baysal, O., 1994, ''Computation of Unsteady Flow Past an Oscillating Cylinder Near a Vertical Wall,'' J. Spacecr. Rockets, **31**, No. 4, p. 630.
[13] White, F. M., 1994, *Fluid Mechanics*, 3rd Ed., McGraw-Hill, New York.
[14] Dandy, D. S., and Dwyer, H. A., 1990, ''A Sphere in Shear Flow at Finite Reynolds Number: Effect of Shear on Particle Lift, Drag and Heat Transfer,'' J. Fluid Mech., **216**, pp. 381–410.

Vaporization Kinetics During Pulsed Laser Heating of Liquid Hg

T. D. Bennett
Assistant Professor
e-mail: bennett@engineering.uscb.edu

M. Farrelly

Department of Mechanical and Environmental Engineering,
University of California,
Santa Barbara, CA 93106-5070

There is a growing body of experimental evidence showing that the kinetics of nascent vapor produced during pulsed laser heating of metals cannot always be ascribed to the surface thermal conditions. Some investigators have proposed that the discharge of energetic (nonthermal) atoms from metals can involve light coupling to surface plasmons. This requires surface roughness to facilitate wave vector matching of laser light with surface electromagnetic excitation modes. If true, superthermal vaporization kinetics should disappear from time-of-flight measurements when an optically smooth surface is used. Unfortunately, maintaining such an ideal surface is infeasible on a solid target because each laser pulse introduces nanometer sized roughness through the process of melting and resolidification. We have investigated the nature of vaporization from a liquid Hg surface using a nanosecond laser emitting 5 eV photons. Surface tension of the liquid provides an optically smooth surface for this experiment. Nevertheless, we observe superthermal vaporization kinetics from liquid Hg. Yet, the shape of the energy distribution is Boltzmann (the thermal expectation), and the energy distribution does not demonstrate any quanta characteristic of vaporization mediated by an electronic excitation.
[S0022-1481(00)01602-9]

Keywords: Heat Transfer, Laser, Liquid Metals, Thermophysical, Vaporization

Introduction

Over the past few years, there has been active research concerning short pulsed laser vaporization of metals ([1–6]). The recent interest stems from observations of superthermal vaporization kinetics. Because important applications frequently operate in a plasma regime, the nascent character of vaporization went unexplored for many years after pulsed laser processing of metals became technologically important. Since a plasma is heated directly by the laser, subsequent vapor kinetics no longer reflect surface processes in this regime. However, when sub-plasma conditions were eventually investigated, high translational energies were still observed. In the initial attention given to this departure from expectation, it was often argued that collisional effects in the plume could explain these experimental results. This line of reasoning was made popular by a number of theoretical papers ([7,8]) devoted to the effect of Knudsen layer formation on time-of-flight (TOF) measurements. The Knudsen layer is region adjacent to the surface in which the nascent velocity distribution acquires a stream velocity. In the simplest idealization, the velocity distribution past the Knudsen layer is fully Maxwell-Boltzmann, in a coordinate system moving with the stream velocity. In contrast, the nascent velocity distribution is half Maxwell-Boltzmann, with zero stream velocity. When the ''vapor pressure'' generated by the peak thermal conditions of the target is small, collisional effects are unimportant to the translational energy distribution of the vapor. However, given a sufficient number of vapor-phase collisions, the most probable flight time will shift to a higher value.

The formation of a Knudsen layer can be significant to the interpretation of raw TOF measurements. However, an important point, frequently overlooked, is that the shift in the most probable flight time does not reflect a change in the mean translational energy, since energy is conserved. Development of a nonzero flow velocity results from the transfer of internal energy to translational energy of the center-of-mass. This can result in smaller value of internal energy (''temperature'') than the total translation energy of the vapor. However, the temperature of the vapor is no longer related simply to the surface thermal conditions. An adiabatic expansion of an ideal monatomic gas offers at most an order k_BT increase in center-of-mass translational energy (or decrease in internal energy). Flow velocities exceeding this value cannot be explained by energy provided by the surface thermal conditions alone.

Interestingly, the observation of superthermal vaporization kinetics has also been encountered in the extreme low-vapor pressure limit, where the surface temperature does not rise above the melting point ([1–4]). Here, the influence of vapor-phase phenomena can be ruled out, and TOF measurements unambiguously probe the nascent energetics of the vaporization process. So, where does this extra energy come from? A proposed explanation involves energy coupling of surface plasmons to the vaporization process ([1–4,9]). A plasmon is the energy quanta of the collective wave motion of free electrons in a metal ([10]). Plasmon energies in many metals range from 3 to 16 eV. Consequently, if the plasmon energy is given to a desorption process, when a plasmon is annihilated through a collision with a phonon, then the desorbing atom could have energies far exceeding the thermal conditions of the surface ([9]). However, several issues arise with adopting this explanation. First, simultaneous energy and momentum conservation requires some qualification of conditions under which surface plasmons can be excited with laser light. In traditional optical-plasmon interaction studies, light is introduced to the backside of a metal film that plates the surface of a prism. Under these geometries of frustrated total internal reflection, the evanescent light wave at the interface can couple to surface plasmons in the film ([11]). This is not similar to typical conditions used in pulsed laser vaporization. However, conversion of photon energy to surface plasmon energy can also be facilitated by surface roughness, where the reciprocal space of the roughness augments the plasmon wave vector to permit momentum and energy matching with the incident photon. Therefore, it is argued that either intentionally placed or inherent surface roughness can facilitate light coupling to surface plasmons, and that the decay process of surface plasmons provides for superthermal desorption of atoms.

To test this hypothesis, one would like to be able to control the process by which surface plasmons are excited to demonstrate whether there exists a correlation with superthermal vaporization kinetics. However, development of surface roughness, having

Contributed by the Heat Transfer Division for publication in the JOURNAL OF HEAT TRANSFER. Manuscript received by the Heat Transfer Division, Mar. 28, 1999; revision received, Oct. 7, 1999. Associate Technical Editor: D. Poulikakos.

scales between nanometers to micrometers, is intrinsic to the process of nanosecond pulsed laser melting of metal surfaces. The development of high-frequency roughness is due to asynchronous resolidification of the surface ([5]). Low-frequency surface roughness is due to hydrodynamic instabilities in the molten surface ([12]). To avoid these effects, in the present study we have investigated a liquid Hg system. In the liquid state, surface tension provides and maintains an optically smooth surface throughout the experiment. Since light coupling to surface plasmons is prohibited when the smooth surface is irradiated from the vacuum side ([13]), the proposed liquid Hg system should be free from possible effects of surface plasmons. In this paper, we report measurements of the vaporization kinetics of liquid Hg using 16-ns pulsed ultraviolet laser light.

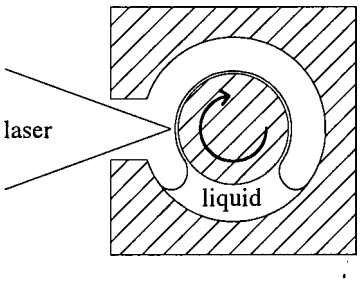

Fig. 2 Illustration of the liquid Hg crucible used in TOF measurements

Experiment and Results

The laser, vacuum chamber, and detector are shown schematically in Fig. 1. The detector, used to measure atomic material liberated from the target by the laser, is a fixed appendage to the chamber. The detector placement requires the sample to be held vertically in the vacuum chamber, which poses a significant problem for investigating liquid samples. We have resolved this problem with a specially designed crucible that raises a liquid film of metal to the vertical position. Figure 2 shows schematically this crucible. We chose to study liquid Hg to alleviate the need to heat the crucible. The crucible contains a center brass cylinder (0.75-cm diameter and 1.0-cm length) that is polished to a mirror finish and is free to rotate within the body of the crucible. The cylinder is coupled to a small Dc motor using stranded wire, and is rotated at approximately 5 rpm during measurements. The lower portion of the cylinder rotates through a pool of liquid Hg that wets the surface of the cylinder. The meniscus between the pool and cylinder remains stable during rotation, and no rippling of the Hg surface is observed during rotation. The front of the crucible is open, exposing the cylinder to the incident laser beam just above the meniscus and providing an unobstructed view of the liquid surface for the detector. The vapor recoil-pressure will introduce hydrodynamic motion of the Hg surface after the laser generates the peak vapor pressure. The damping time for capillary waves scales as $\rho_l \Lambda^2/\mu$ ([14]), where Λ is the wavelength of the disturbance, and ρ_l and μ are the density and viscosity of the liquid, respectively. All but the longest wavelengths of capillary waves are damped out in the period between pulses, and only the short wavelengths (on the order of the laser light) are involved in light coupling to surface plasmons. The damping time for a 0.25-μm capillary wave on the liquid Hg surface is about 0.5 μs.

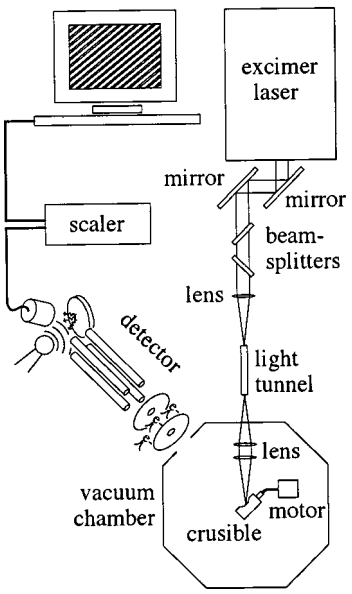

Fig. 1 Schematic of the major components in the TOF measurement system

The laser is a Luminonics Excimer operated with a KrF gas fill for 248 nm light. The output of the laser is shaped into a uniform top-hat profile using a light tunnel. The intensity of the top-hat is uniform to better than ten percent over the nominal spot area. At the target surface, the irradiated area is nominally 0.7 mm$\times$1 mm. To achieve the low fluences required in the following experiment beamsplitters were used to attenuate the beam. Pairs of beamsplitters having 10 percent and 30 percent or 10 percent and 50 percent nominal transmittance (at 45 deg angle of incidence) were used. Although the light leaving the cavity of the laser is unpolarized, the beamsplitters transmit preferentially *p*-polarized light. From the manufacture's specifications, it was calculated that the 10–30 percent and 10–50 percent beamsplitter combinations transmit 91 percent and 87 percent *p*-polarized light, respectively. Pulse energies are measured in situ with a joulemeter measuring a portion of the beam energy split from the main beam before entering the light tunnel. The joulemeter is cross-calibrated with a calorimeter measurement used to determine the fluence delivered to the target surface in the main vacuum chamber. The main chamber has o-ring seals and can be pumped down to 10^{-6} torr. For the Hg experiment, the base pressure was about 5×10^{-6} torr due to the steady-state evaporation of Hg.

The detector was built at the IBM Almaden Research Center, San Jose, CA, and is described in detail by Krajnovich ([15]). The detector TOF tube is differentially pumped to a base pressure of 10^{-10} torr. The first stage of the detector ionizes approximately one in ten thousand neutrals entering the TOF tube with an electron beam. Ions then pass through a quadrapole mass filter that is used to block the transmission of species not having the charge to mass ratio of Hg^+. Since Hg has a large atomic weight relative to the residual background gases in the chamber, the resolution of the quadrapole can be set relatively low to obtain a high Hg^+ transmission efficiency. In the final stage, transmitted ions are detected by accelerating them with a 25 kV field into a stainless steel surface that ejects numerous secondary electrons. The secondary electrons are accelerated into an organic scintillation pad that emits a photon burst that is detected with a photomultiplier tube. The scaler is used to count the number of photon bursts (ions) arriving in consecutive 6 μs time ''bins'' over a period of 6000 μs after the laser fires. From this information, TOF measurements are obtained. The measured temporal distribution is offset by the ''ion flight time'' between the first and final stage of the detector. The ion flight time is largely established by the electric fields in the detector, with a small correction accounting for the velocities of neutrals entering the detector. The accuracy of the TOF measurements has been tested with measurements performed on a chopped effusive flux of N_2 gas at a known temperature.

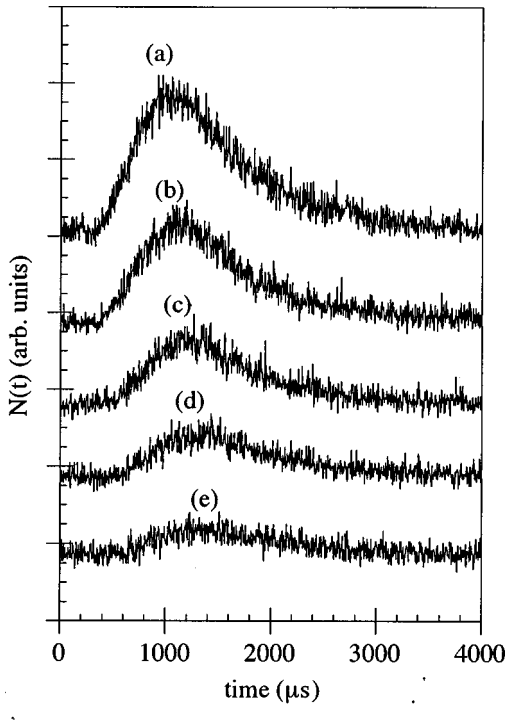

Fig. 3 Raw time-of-flights from liquid Hg. Distributions reflect 100-shot measurements. The five cases shown are for laser fluences of (a) 0.211, (b) 0.193, (c) 0.176, (d) 0.155, and (e) 0.135 J/cm^2.

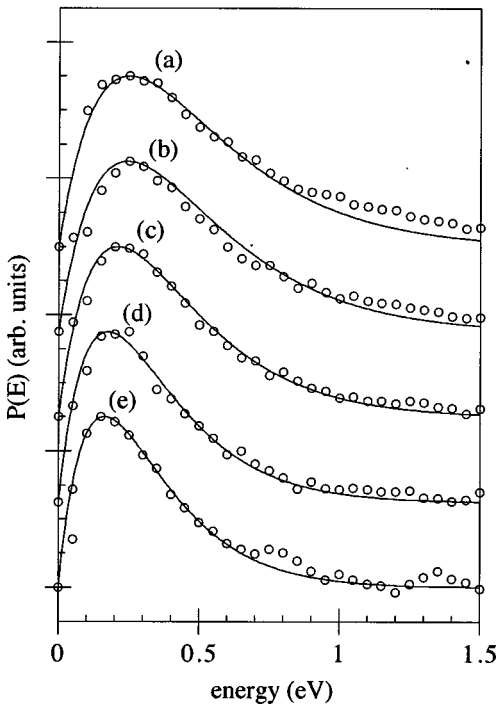

Fig. 4 Energy distributions of Hg corresponding to TOF measurements in Fig. 3. The distributions reflect the experimental measurements (○) as well as Boltzmann fits (—).

These measurements reveal the expected Boltzmann distribution with a measured mean translational energy within five percent of the gas temperature value.

At the background pressure of non-Hg gases (10^{-6} torr), less than monolayer coverage of oxide can occur on the surface of the liquid Hg for the rotation rate of the cylinder and the laser repetition rate used. To minimize the potential effect of surface oxides, an initial five-pulse sequence of ''clean-up'' laser pulses are used immediately before the TOF measurements. During the measurement, new surface area is continuously introduced into the irradiated area by the rotation of the cylinder. However, the fraction of new surface area to the total area irradiated is always small because of the low rotational speed used.

The laser is operated at 10 Hz during TOF measurements. The detector signal is averaged over 100 laser pulses to obtain good signal to noise. Typical raw TOF measurements are shown in Fig. 3. The temporal distribution is converted into an energy distribution using the following factors: At time t, the detector signal $N(t)$ can be related to the value of $P(E)$ at $E=(m/2)(L/t)^2$. The $N(t)$ signal is proportional to the transient number density of neutrals in Stage one of the detector. Consequently, the total flux of atoms passing through the detector in a time interval dt is proportional to $n(t)\sim N(t)/t$, and conservation of flux requires that $n(t)dt = P(E)dE$ be satisfied. Since $dE\sim dt\cdot t^{-3}$, the following relationship holds between the raw TOF signal and the energy distribution:

$$N(t)\sim P(E)/t^2. \tag{1}$$

Using Eq. (1), the raw TOF measurements, shown in Fig. 3, are converted to energy distributions, shown in Fig. 4. The mean translational energy can be determined directly from the measured energy distribution. A normalized Boltzmann distribution, $P(E) \sim E\cdot\exp(-2E/\overline{E})$, is plotted over the experimental data in Fig. 4 using only the measured mean translational energy to establish the distribution. No stream velocity is used to fit the experimental data. The oscillation in the energy distribution observed in the weakest TOF signal shown in Fig. 4 is temporal TOF noise that is stretched out in energy space. High energies correspond to short time intervals in the TOF data. Consequentially, there is smaller signal to noise in the high-energy tails of the $P(E)$ distributions.

As can be seen from Fig. 4, the experimental energy distribution is well described by a Boltzmann fit. The mean translational energies for the distributions range from 0.31 eV, corresponding to the low fluence, to 0.54 eV at the high fluence. If the energetics of vaporization can be ascribed to the thermal conditions of the surface, then, based on the classical thermal expectation that

$$\overline{E}=2k_BT \tag{2}$$

the peak surface temperatures of the target should fall between 1800 K to 3100 K for our experimental conditions. To assess how reasonable these temperatures are, we have numerically modeled the thermal conditions generated during a laser pulse. The code used for our calculations has been described in detail elsewhere ([16]) and the principles only are highlighted below.

Numerical Model

The peak temperature rise at the target surface is calculated considering the transient heating provided by the laser, competing with heat dissipation through diffusion. In the present work, the fact that melting is not present greatly simplifies the calculation. The problem is further simplified with the observation that heat transfer can be assumed one-dimensional, since the diffusion depth is three orders of magnitude smaller than the lateral extent of the heated area. Volumetric laser heating of the target is model using Beer's law weighted by the temporal profile of the laser pulse:

$$g(z,t)=\phi(I-\Re)\cdot I(t)\cdot\zeta e^{-\zeta z}, \tag{3}$$

where $\zeta=4\pi n_{im}/\lambda$. n_{im} is the imaginary part of the surface index of refraction, $\Re$ is the surface reflectance, and $I(t)$ is the normalized temporal profile of the laser pulse. $I(t)$ has been measured

Table 1 Thermophysical properties

Symbol	Value	Symbol	Value
λ (nm)	248	T_m (K)	234.4
τ_p (μs)	16 (FWHM)	T_b (K)	629.7
n_{re}	0.414	Δh_l^v (kJ/mol)	59.1
n_{im}	1.806	ρ_l (kg/m^3)	13593.9

Symbol	Value
K_l (W/m/K)	$1.026+0.030684\cdot T-2.2287\cdot 10^{-5}\cdot T^2+2.4915\cdot 10^{-9}\cdot T^3$
C_{pl} (J/kg/K)	$154.29-0.075121\cdot T+8.7772\cdot 10^5\cdot T^2-2.5294\cdot 10^{-8}\cdot T^3$
log[P_v (Pa)]	$-3305/T-0.795\log T+12.48$
χ_l (1/K)	$5.9487e-5+1.7379\cdot 10^{-9}\cdot (T-T_m)+2.8554\cdot 10^{-13}\cdot (T-T_m)^2$

experimentally, and is well described by a triangular shape, with a pulse length of 28 ns at the base and having a maximum intensity occurring at 7 ns. The surface reflectance depends on the polarization state of the light incident off-normal to the target surface. The general Fresnel formulas for light polarized normal ($\perp$) or parallel ($\parallel$) to the plane of incident are

$$\Re_{\parallel}=\left|\frac{\tan(\vartheta_i-\vartheta_t)}{\tan(\vartheta_i+\vartheta_t)}\right|^2 \quad \Re_{\perp}=\left|\frac{\sin(\vartheta_i-\vartheta_t)}{\sin(\vartheta_i+\vartheta_t)}\right|^2, \tag{4}$$

where ϑ_i is the (real) angle of incidence with respect to the surface normal and ϑ_t is the complex angle of refraction in the absorbing medium. The angles ϑ_i and ϑ_t are related by Snell's law:

$$\sin\vartheta_t=\frac{\sin\vartheta_i}{n_{re}-in_{im}}. \tag{5}$$

For partially *p*-polarized light, with degree of polarization $V_{\parallel}$, the surface reflectance is

$$\Re=(1-V_{\parallel})(\Re_{\perp}+\Re_{\parallel})/2+V_{\parallel}\Re_{\parallel}. \tag{6}$$

Experimental measurements are made with the laser beam incident at 45 deg to the target surface normal. Due to the beamsplitters, the light is approximately 90 percent *p*-polarized for our experimental conditions. Using the optical properties in Table 1, the surface reflectance at the wavelength of the laser is 62 percent. In contrast, if the light were unpolarized, or if the laser beam was incident perpendicular to the target, the surface reflectance of liquid Hg would be 69 percent.

The principal difficulty in accurately calculating the thermal conditions during the laser pulse are (1) obtaining the correct temperature dependent thermophysical properties; (2) obtaining accurate optical constants for the surface at the wavelength of the laser; and (3) correct numerical treatment of thermophysical conditions at the target. Temperature-dependent thermophysical properties for Hg are available from references [17–22] and have been summarized in Table 1. A Lagrangian mesh is used to account for thermal expansion. Expansion of the mesh is calculated from a linear elastic hydrostatic model of the liquid ([16]). Because the timescale for sound propagation in the liquid is much shorter than that of the propagation of heat, the thermal expansion is nearly quasi-static. The importance of thermal expansion is simply the effect on Fourier law calculations. If temperature calculations are performed with and without Lagrangian motion of the mesh, the difference in peak temperature that results is about five percent. The coupled problems of heat transfer and thermal expansion are solved using a finite element code. The heat diffusion equation is solved with a heat generation source near the surface of the Hg specified by Eq. (3). A domain 16 μm into the surface is modeled, the back surface is held at the ambient temperature. The linear elastic equations of motion of the hydrostatic fluid are solved with a free surface boundary condition applied to the surface. The lower boundary is constrained.

Figure 5 illustrates the thermal physical conditions near the liquid Hg surface at the peak of a thermal cycle generated with a 0.16 J/cm^2 pulse. The top panel shows the temperature distribution below the surface of the liquid Hg. The bottom panel shows the density as a function of depth. Local values of density are determined by contrasting the current element volume with the initial value, of known density. In the calculation, densities oscillate within a few percent of value dictated by the local temperature, because of sound wave propagating through the numerical domain. Figure 6 summaries the peak surface temperature as a function of pulse fluence.

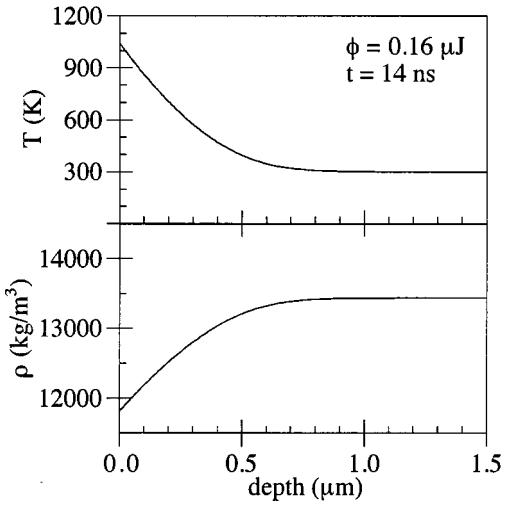

Fig. 5 Thermal physical conditions near the liquid Hg surface at the peak of the thermal cycle (14 ns). Top panel: the temperature distribution; bottom panel: the density as a function of depth.

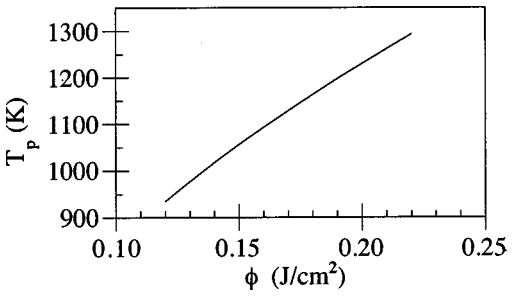

Fig. 6 Peak surface temperature as a function of pulse fluence

Discussion

Using the calculated surface temperatures, the mean translational energies of distributions shown in Fig. 7 are contrasted with the classical thermal expectation of $\bar{E}=2k_BT$ plotted as a line. There are two striking results. The first is that the measured translational energy of Hg significantly exceeds values for a thermal process. Measured translational energies are higher than classical expectation by about a factor of 2. The second observation is that the mean translational energies do not exhibit a $2k_B$ slope with respect to the peak surface temperature. Instead, the measured slope exceeds the classical expectation by about a factor of two. These results show clearly the inadequacy of describing vaporization kinetics using purely classical theory. The measured energies correspond to surface temperatures ranging from 1800 K to 3100 K, while the calculated temperatures are between 900 and 1300 K. The critical temperature of Hg is about 1500°C, lower than any of the experimentally measured ''translational-temperatures.'' The kinetics of vaporization might be reconciled with the thermal expectation if vapor-phase heating occurs through a plasma. However, a plasma requires extensive ionization of the vapor, such that inverse bremsstrahlung absorption of laser light can efficiently heat the plume. For the experimental conditions reported in this manuscript, there is less than 1 ion per 1 million neutrals in the plume sampled with the detector. Consequently, the lack of ions in the plume shows that there is no significant interaction between the laser and the vapor phase.

As mentioned in the Introduction, another possible source for misinterpreting the vaporization energetics is collisional effects, this can change the ''most-probable'' flight time. However, we have determined mean translational energies from the energy distribution, and not the most-probable flight time. Interatomic collisions cannot change the mean energy of the vapor plume (unless a substantial amount of vapor recondenses back to the surface of the target), and consequently cannot provide an explanation for the high observed mean translational energies. Therefore, these results provide some important facts with which to reevaluate the nature of pulsed laser vaporization of metals, and the potential role of surface plasmons. We have created experimental condition that prohibit surface plasmon excitations but still yield superthermal vaporization kinetics. The energy distribution does not demonstrate any signature quanta characteristic of the surface plasmon energy; the shape of the energy distribution is Boltzmann (the thermal expectation) despite the fact that the energetics of vaporization is inconsistent with the surface thermal conditions.

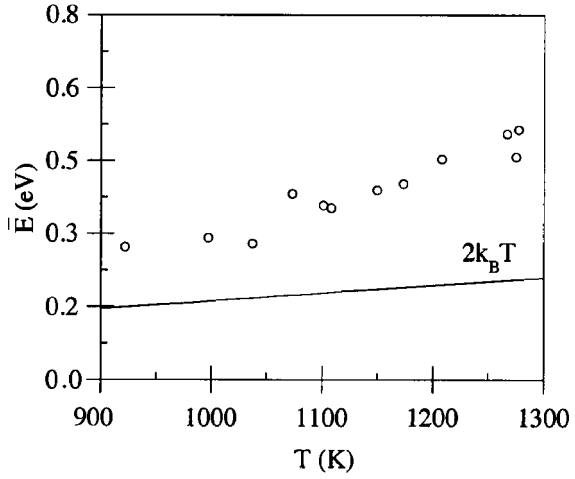

Fig. 7 Summary of measured mean translational energies versus calculated peak surface temperatures. The theoretical $2k_BT$ relation for mean translational energy is plotted as a reference.

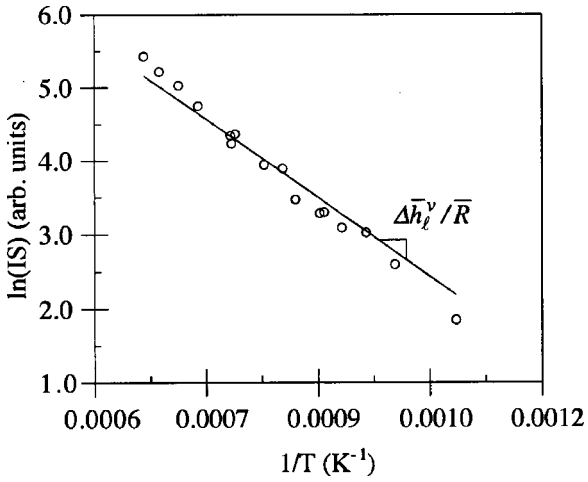

Fig. 8 Natural log of integrated TOF signal versus the reciprocal of calculated peak surface temperature. The solid lines correspond to the anticipated slope of $-\Delta\bar{h}_l^v/\bar{R}$ for a thermal mediated process, with $\Delta\bar{h}_l^v=59.1$ kJ/mol for Hg.

The TOF integrated signal (IS) is a measure of the vapor pressure generated by the laser pulse. This quantity provides another measure with which the vaporization process can be evaluated. Using the equilibrium vapor pressure, the integrated signal can be related to temperature by

$$\ln(IS)\sim-\Delta\bar{h}_l^v/\bar{R}\bar{T}+\text{constant}. \tag{7}$$

Equation 7 predicts that plotting $\ln(IS)$ against $1/T$ will result in a straight line having slope of $-\Delta\bar{h}_l^v/\bar{R}$ if the vaporization process is thermally mediated. Since the vapor pressure depends exponentially on temperature, the integrated signal is heavily weighted by peak temperature of the thermal cycle. Figure 8 plots the natural log of the integrated TOF signal against the reciprocal calculated peak surface temperature. The solid lines appearing in this figure correspond to the slope of $-\Delta\bar{h}_l^v/\bar{R}$ using the literature value of $\Delta\bar{h}_l^v$ for Hg. The best linear fit of the experimental data in Fig. 8 yields a value of 69.8 kJ/mol for the latent heat of vaporization of Hg, 18 percent higher than the literature value. Within experimental errors, the vaporization yield suggests that the vaporization process is thermally mediated. In other words, the energy ''bath'' driving the vaporization process is the thermal energy of the surface.

Conclusion

The nascent mean translational energy of vapor released in pulse laser heating fails to produce the classical $\bar{E}=2k_BT$ expectation on liquid Hg. The observed superthermal translational energy is strong evidence that pulsed laser vaporization relies on pooling energy from the electronic structure of a metal. However, the nascent Boltzmann energy distribution and the dependence of mean translational energy on fluence do not appear to be consistent with previous views of a surface plasmon assisted desorption process. Furthermore, light coupling to surface plasmons should be prohibited for the optically smooth surface of the liquid. The measured Hg translational energies are a factor of 2 higher than classical theory, with an apparent temperature dependence that is a factor of 2 steeper than the classical expectation. However, the dependence of yield on surface temperature appears indicative of a thermal process, despite the irreconcilably high mean translational energy of the vapor. This suggests that the measured superthermal translational energy is not available for overcoming the latent heat of vaporization, but is acquired at some point in the process of atoms leaving the surface.

Acknowledgments

This work was partially supported under the auspices of the U.S. Department of Energy by the Lawrence Livermore National Laboratory under contract No. W-7405-ENG-48. Additional support for this work comes from the IBM Corporation.

Nomenclature

C_{pl} = liquid heat capacity
$\underline{E}$ = translational energy
$\overline{E}$ = mean translational energy
$g(z,t)$ = volumetric heating function
Δh_l^v = latent heat of vaporization
$I(t)$ = normalized temporal profile
IS = integrated signal
k_B = Boltzmann constant
K_l = liquid thermal conductivity
L = atomic flight distance
m = atomic mass
$N(t)$ = TOF temporal distribution
$n(t)$ = flux of atoms in detector
n_{im} = imaginary part of refractive index
n_{re} = real part of refractive index
$P(E)$ = normalized energy probability distribution
$P_{\underline{v}}$ = vapor pressure
R = ideal gas constant
$\Re$ = surface reflectivity
$\Re_\perp$ = reflectivity for *s*-polarized light
$\Re_\parallel$ = reflectivity for *p*-polarized light
t = time
T = temperature
T_m = melting point temperature
T_b = boiling point temperature
$V_\parallel$ = degree of *p*-polarization
z = into target coordinate direction

Greek

χ = linear expansion coefficient
ϕ = laser fluence
λ = laser wavelength
Λ = capillary wavelength
μ = viscosity
ϑ_i = angle of incidence with respect to the surface normal
ϑ_t = complex angle of refraction in an absorbing medium
ρ_l = liquid density
τ_p = pulse width (FWHM)
ζ = 1/optical penetration depth

References

[1] Kim, H. S., and Helvajian, H., 1991, ''Threshold Level Laser Photoablation of Oxidized Aluminum (111)—Photoejected Ion Translational Energy Distributions,'' J. Phys. Chem., **95**, No. 17, pp. 6623–6627.
[2] Hoheisel, W., Vollmer, M., and Trager, F., 1993, ''Desorption of Metal Atoms With Laser Light—Mechanistic Studies,'' Phys. Rev. B, **48**, No. 23, pp. 17,463–17,476.
[3] Lee, I., Callcott, T. A., and Arakawa, E. T., 1993, ''Desorption Studies of Metal Atoms Using Laser-Induced Surface-Plasmon Excitation,'' Phys. Rev. B, **47**, No. 11, pp. 6661–6666.
[4] Shea, M. J., and Compton, R. N., 1993, ''Surface-Plasmon Ejection of Ag^+ Ions From Laser Irradiation of a Roughened Silver Surface,'' Phys. Rev. B, **47**, No. 15, pp. 9967–9970.
[5] Bennett, T. D., Krajnovich, D. J., and Grigoropoulos, C. P., 1996, ''Separating Thermal, Electronic, and Topographic Effects in Pulsed Laser Melting and Sputtering of Gold,'' Phys. Rev. Lett., **76**, No. 10, pp. 1659–1662.
[6] Elam, J. W., and Levy, D. H., 1997, ''Low Fluence Laser Sputtering of Gold at 532 nm,'' J. Appl. Phys., **81**, No. 1, pp. 539–541.
[7] Kelly, R., and Dreyfus, R. W., 1988, ''On the Effect of Knudsen-Layer Formation on Studies of Vaporization, Sputtering, and Desorption,'' Surf. Sci., **198**, No. 1–2, pp. 263–276.
[8] Kelly, R., and Dreyfus, R. W., 1988, ''Reconsidering the Mechanisms of Laser Sputtering With Knudsen-Layer Formation Taken Into Account,'' Nucl. Instrum. Methods Phys. Res. B, **32**, No. 1–4, pp. 341–348.
[9] Ritchie, R. H., Manson, J. R., and Echenique, P. M., 1994, ''Surface-Plasmon-Ion Interaction in Laser Ablation of Ions from a Surface,'' Phys. Rev. B, **49**, No 4, pp. 2963–2966.
[10] Pines, D., 1956, ''Collective Energy Losses in Solids,'' Rev. Mod. Phys., **28**, No. 3, pp. 184–198.
[11] Lemberg, H. L., Rice, S. A., and Guidotti, D., 1974, ''Surface Plasmons in Liquid Mercury: Propagation in a Nonuniform Transition Layer,'' Phys. Rev. B, **10**, No. 10, pp. 4079–4099.
[12] Bennett, T. D., Grigoropoulos, C. P., and Krajnovich, D. J., 1995, ''Near-Threshold Laser Sputtering of Gold,'' J. Appl. Phys., **77**, No. 2, pp. 849–864.
[13] Ritchie, R. H., 1973, ''Surface Plasmons in Solids,'' Surf. Sci., **34**, pp. 1–19.
[14] Levich, V. G., 1962, *Physicochemical Hydrodynamics*, Prentice-Hall, Englewood Cliffs, NJ.
[15] Krajnovich, D. J., 1995, ''Laser Sputtering of Highly Oriented Pyrolytic Graphite At 248 Nm,'' J. Chem. Phys., **102**, No. 2, pp. 726–743.
[16] Bennett, T. D., and Krajnovich, D. J., 1997, ''Dynamics of Surface Melting During Laser Processing of Materials,'' *ASME Proceedings of the 32nd National Heat Transfer Conference*; ASME, New York.
[17] Touloukian, Y. S., 1970, *Specific Heat: Metallic Elements and Alloys*, IFI/Plenum, New York.
[18] Touloukian, Y. S., 1970, *Thermal Conductivity: Metallic Elements and Alloys*, IFI/Plenum, New York.
[19] Touloukian, Y. S., 1970, *Thermal Expansion: Metallic Elements and Alloys*, IFI/Plenum, New York.
[20] Choyke, W. J., Vosko, S. H., and O'Keeffe, T. W., 1971, ''A Comparison of the Optical Properties of Single Crystal and Liquid Mercury in the Energy Range 0.5 to 8.25 eV,'' Solid State Commun., **9**, No. 6, pp. 361–367.
[21] Zinov'yev, V. E., and V. P. Itkin, 1990, *Metals at High Temperatures: Standard Handbook of Properties*, Hemisphere, New York.
[22] Iida, T., and Guthrie, R. I. L., 1993, *The Physical Properties of Liquid Metals*, Clarendon, Oxford.

Neck Down and Thermally Induced Defects in High-Speed Optical Fiber Drawing

Z. Yin

Y. Jaluria
e-mail: jaluria@jove.rutgers.edu
Fellow ASME

Mechanical Engineering Department,
Rutgers University,
New Brunswick, NJ 08903

The drawing speeds employed in the manufacturing of optical fibers have been rising in recent years due to growing worldwide demand. However, increasing speeds have placed stringent demands on the manufacturing process, mainly because of large temperature gradients that can generate thermally induced defects and undesirable variations in fiber characteristics. Heat transfer and glass flow that arise in drawing fibers of diameters 100–125 microns from cylindrical silica preforms of diameters 5–10 cm play a critical role in the success of the process and in the maintenance of fiber quality. This paper presents an analytical and numerical study of the optical fiber drawing process for relatively large diameter preforms and draw speeds as high as 20 m/s. The free surface, which defines the neck-down profile, is not assumed but is determined by using a balance of forces. An iterative numerical scheme is employed to obtain the profile under steady conditions. The transport in the glass is calculated to obtain the temperature, velocity and defect distributions. A zone radiation model, developed earlier, is used for calculating radiative transport within the glass. Because of the large reduction in the diameter of the preform/fiber, the velocity level increases dramatically and the geometry becomes complicated. A coordinate transformation is used to convert the computational domains to cylindrical ones. The numerical results are compared with experimental and numerical results in the literature for smaller draw speeds for validation. The effects of high draw speeds and of other physical variables on defects generated in the fiber, on the neck-down profile, and on the feasible domain for the process are determined.
[S0022-1481(00)02302-1]

Keywords: Computational, Heat Transfer, Manufacturing, Materials, Modeling

Introduction

One of the most widely used methods for drawing optical fibers is based on heating a specially fabricated silica glass preform in a cylindrical furnace above its softening point of around 1900K for silica glass and pulling it into a fiber. As the preform traverses through the heating zone of the furnace, its temperature is elevated, resulting in a decrease in its viscosity and surface tension. An axial draw tension is applied simultaneously at the end of the preform so that the preform is drawn into a fiber through a neck-down region, as shown in Fig. 1. The neck-down profile depends upon the drawing conditions as well as on the physical properties of silica glass. Due to the complexity of determining the neck-down profile, several investigators ([1–5]) assumed the neck-down profile in their studies of the transport process in the neck-down region. But, in reality, the neck-down profile is an unknown and should be obtained as a solution to the coupled transport equations in order to yield accurate results on the temperature and velocity profiles. In addition, the feasibility of the process is determined by the existence of a physically acceptable and stable neck-down profile.

Glicksman [6] generated the shape of a heated free jet of molten glass using a one-dimensional model. Paek and Runk [7] determined the neck-down profile on the basis of a simple surface radiation model, assumed heat transfer coefficient, and one-dimensional transport of momentum and energy. Yarin [8] developed an analytical expression for the neck-down shape, neglecting axial conduction and using radial lumping of the axial velocity. Sayles and Caswell [9] carried out a finite element analysis of the neck-down region, considering variable properties but very small draw-down (preform diameter/fiber diameter) ratios. Myers [10] used the Rosseland approximation for radiation in the glass, neglected convection to the surrounding gas, and assumed one-dimensional transport. Rosenberg et al. [11] carried out a two-dimensional analysis of the viscous flow in the draw process. More recently, Roy Choudhury and Jaluria [12–13] conducted a comprehensive study of the thermal transport in the optical fiber drawing furnace. They solved the full coupled problem involving both the glass preform/fiber and the purge gas. Even though a two-dimensional axisymmetric problem was solved, Roy Choudhury et al. [14] used radial lumping of the axial velocity to obtain a simplified equation for the numerical iteration of the radius in the necking profile. However, relatively low draw speeds of around 3 m/s and small preform diameters of around 2 cm were considered.

In most earlier studies, the radiative transport within the glass was considered using the optically thick and Rosseland approximations ([15]). The neck-down profiles and the velocity and temperature distributions obtained on the basis of these approximations were inaccurate because the assumptions are not applicable in the actual optical fiber drawing process, especially in the lower neck-down region. Kaminski [16] employed the P_1 method to calculate radiation in the glass, focusing largely on the upper neck-down region. Song et al. [17] analyzed radiation in glass jets using the discrete ordinates method, considering small variations in the diameter. The geometry is much more complicated in the optical fiber drawing process. In the current study, the zonal method, as developed by Yin and Jaluria [18], is employed to calculate the radiative heat transfer in the glass. This model determines the radiative transport within the glass preform/fiber more accurately than the earlier studies of fiber drawing.

Another important consideration in optical fiber manufacture relates to defects and fiber quality. When optical fibers are drawn from silica preforms, point defects are generated at high temperature and are frozen in the fibers during the cooling process

Contributed by the Heat Transfer Division for publication in the JOURNAL OF HEAT TRANSFER. Manuscript received by the Heat Transfer Division, Feb. 28, 1999; revision received, Dec. 9, 1999. Associate Technical Editor: M. Modest.

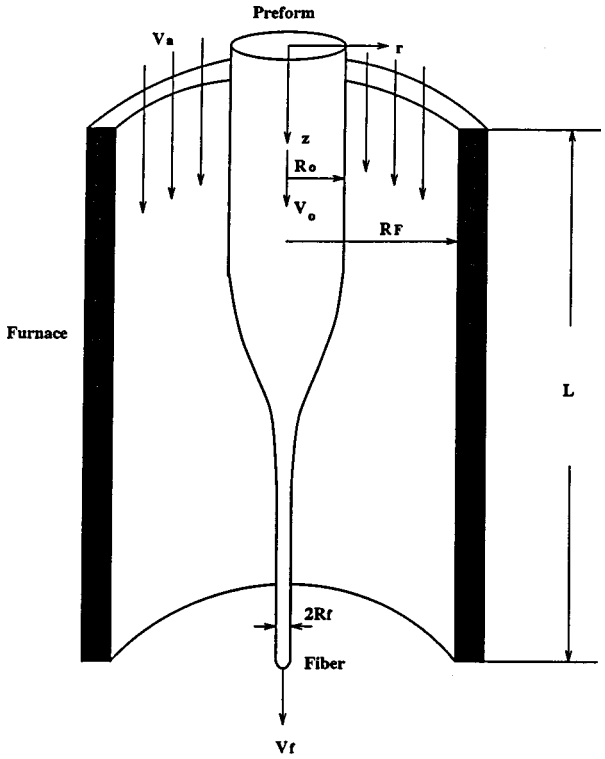

Fig. 1 Schematic diagram of the optical fiber drawing furnace with aiding purge gas, along with the coordinate system

([19,20]). Point defects lead to transmission loss in the fiber and lower the mechanical strength of the fiber. One important type of drawing-induced defect is the E' defect, the concentration of which is found to depend on the drawing temperature, drawing speed and fiber diameter ([19]). In silica glass, every oxygen site is a potential precursor and can lead to an E' defect. But only one Si–O bond per site is broken, generating the nonbridging-oxygen hole center (≡Si–O.) as well as the E' defect (≡Si.) ([19]). This process is described by the equation ≡Si–O–Si≡→≡Si–O. +.Si≡ ([21]). Hanafusa et al. [19] employed the theory of the thermodynamics of lattice vacancies in crystals to analyze the behavior of E' defects during the fiber drawing process. They assumed that the defects were in equilibrium state at the drawing temperature and the defect generation term was negligible during the cooling process. Based on this simplified model, an equation was derived for E' defect concentration in fibers. The equation formulated by Hanafusa et al. [19] is used here to compute the E' defect concentration. This analysis yields the defects resulting from the thermal process in the furnace. However, the number of defects frozen in the fiber will depend on the subsequent cooling process. Though the cooling process is not studied here, the quality of the fiber will largely depend on the defects generated during the drawing process.

Previous investigators considered relatively small preform diameters, of order 1–4 cm, and low drawing speeds. Draw-down ratios of less than 100 and drawing speeds of less than 10 m/s were commonly used in earlier fiber manufacturing processes. With the explosive growth in demand for optical fibers, the draw-down ratio and drawing speed have increased to much greater values. Currently, the draw-down ratio and the drawing speed are close to 400 and higher, and to 20 m/s, respectively. In the present study, the draw-down ratio and the drawing speed considered are 400 and greater than 10 m/s, respectively.

This study builds on the earlier work done by Yin and Jaluria [22] who considered the much simpler problem of transport in a preform/fiber with a specified neck-down profile. The results obtained by them indicated the importance of various design variables and operating conditions. However, the neck-down profile is itself a function of the drawing conditions and may vary substantially for typical conditions over which optical fibers are drawn. In order to simulate the actual physical problem and to obtain quantitative inputs for design and optimization of the process, it is necessary to solve the much more involved problem of determining the neck-down profile for each circumstance, as done in this study. In addition, this paper focuses on large preform diameters, high drawing speeds, draw-induced defects, and feasible drawing conditions, which are based on the calculations of the neck-down profile. All these aspects lead to very stringent demands on the numerical scheme and on the imposition of appropriate boundary conditions. Also, the results and the feasible domain are significant affected by the shift to large preforms and high speeds.

Analysis

Governing Equations. The governing equations and the boundary conditions used here have been presented in earlier papers ([4,12,13]). Assuming glass and inert gas flow to be laminar, axisymmetric, and incompressible, the governing equations are obtained for the coordinate system of Fig. 1 as

$$\frac{\partial v}{\partial z}+\frac{1}{r}\frac{\partial (ru)}{\partial r}=0 \tag{1}$$

$$\frac{\partial v}{\partial t}+u\frac{\partial v}{\partial r}+v\frac{\partial v}{\partial z}=-\frac{1}{\rho}\frac{\partial p}{\partial z}+\frac{1}{r}\frac{\partial}{\partial r}\left[r\nu\left(\frac{\partial v}{\partial r}+\frac{\partial u}{\partial z}\right)\right]+2\frac{\partial}{\partial z}\left(\nu\frac{\partial v}{dz}\right) \tag{2}$$

$$\frac{\partial u}{\partial t}+u\frac{\partial u}{\partial r}+v\frac{\partial u}{\partial z}=-\frac{1}{\rho}\frac{\partial p}{\partial r}+\frac{2}{r}\frac{\partial}{\partial r}\left(r\nu\frac{\partial u}{\partial r}\right)+\frac{\partial}{\partial z}\left[\nu\left(\frac{\partial v}{\partial r}+\frac{\partial u}{\partial z}\right)\right]-\frac{2\nu u}{r^2} \tag{3}$$

$$\rho C_p\left(\frac{\partial T}{\partial t}+u\frac{\partial T}{\partial r}+v\frac{\partial T}{\partial z}\right)=\frac{1}{r}\frac{\partial}{\partial r}\left(rK\frac{\partial T}{\partial r}\right)+\frac{\partial}{\partial z}\left(K\frac{\partial T}{\partial z}\right)+\Phi+S_r \tag{4}$$

where Φ is the viscous dissipation and is given by

$$\Phi=\mu\left\{2\left[\left(\frac{\partial u}{\partial r}\right)^2+\left(\frac{u}{r}\right)^2+\left(\frac{\partial v}{\partial z}\right)^2\right]+\left(\frac{\partial u}{\partial z}+\frac{\partial v}{\partial r}\right)^2\right\}. \tag{5}$$

Here, S_r is the radiation source term which represents the net gain of radiative energy per unit volume at any point due to the excess of absorbed radiation over that emitted. The purge gases are inert gases such as nitrogen, argon, and helium, which can be assumed to be nonparticipating, resulting in a zero radiative source term for the gases. The radiative source term for the glass preform/fiber is nonzero because glass emits and absorbs energy in certain wavelength bands. A two-band absorption coefficient distribution is used ([10]) and the zone model developed by Yin and Jaluria [18] is employed to calculate the radiation source term. Also, viscous dissipation effects cannot be neglected in glass flow due to the large viscosity of the material and are included.

The momentum and continuity equations are converted to streamfunction and vorticity equations by appropriate definitions of these quantities and elimination of the pressure terms in the momentum equations. The equations for both the glass and the purge gas regions are transformed using the transformations defined by Lee and Jaluria [4]. When the transformations are applied to the axisymmetric system shown in Fig. 1, the computational domains are converted to cylindrical ones. Variations in all the relevant properties of glass including viscosity, thermal conductivity, specific heat, and surface tension between the glass and the purge gas are considered here. The main effect is the temperature

dependence of the glass viscosity, the other properties being affected to a much smaller extent by temperature. The absorption coefficient of glass has been taken from Myers [10] and all other properties of glass have been taken from Fleming [23]. The properties of the purge gas are considered as constant since their variations are small over the temperature ranges encountered ([12]). They are evaluated at the average of the furnace and purge gas entrance temperatures.

The boundary conditions are the same as those used by Roy Choudhury and Jaluria [12] except for the thermal boundary condition at the interface between the preform/fiber and the purge gas. This condition has been modified to take into account the zone model analysis of Yin and Jaluria [18]. Symmetry conditions at the axis, force balance at the glass-gas interface, as outlined in the next section, and no-slip at the solid boundaries yield the remaining conditions. Far downstream, at the furnace exit or beyond, the axial diffusion terms are set equal to zero for both the glass and the gas.

Generation of Neck-Down Profile. Based on the axial force balance equation, Roy Choudhury et al. [14] have developed an equation for the iteration of preform/fiber radius by using radial lumping of axial velocity. This equation is

$$R(z)=\sqrt{\frac{R_0^2 v_0}{\bar{v}}} \tag{6}$$

where $\bar{v}$ is the average axial velocity in the glass and is given as ([14])

$$\begin{aligned}\bar{v}=C_1\int_0^z\frac{dz}{\mu R^2}-\int_0^z\frac{\rho g}{C_2\mu R^2}\left(\int_0^z R^2dz\right)dz\\ -\int_0^z\frac{1}{C_2\mu R^2}\left[\int_0^z\zeta\left(\frac{R}{\sqrt{1+R'^2}}+\frac{1}{R_1}\right)dz\right]dz\\ -2\rho R^4 v_0^2\int_0^z\frac{1}{C_2\mu R^2}\left(\int_0^z\frac{R'}{R^3}dz\right)dz\end{aligned} \tag{7}$$

where C_1, C_2, and R_1, the curvature, are defined as

$$\begin{aligned}C_1=v_f-v_0+\int_0^L\frac{\rho g}{C_2\mu R^2}\left(\int_0^z R^2dz\right)dz\\ +\int_0^L\frac{1}{C_2\mu R^2}\left[\int_0^z\zeta\left(\frac{R}{\sqrt{1+R'^2}}+\frac{1}{R_1}\right)dz\right]dz\\ +2\rho R^4 v_0^2\int_0^L\frac{1}{C_2\mu R^2}\left(\int_0^z\frac{R'}{R^3}dz\right)dz\end{aligned} \tag{8}$$

$$C_2=2+\frac{1-2R'^2+2R'-RR''}{1+R'^2} \tag{9}$$

$$R_1=\frac{R''}{[1+(R')^2]^{3/2}}. \tag{10}$$

Thus, Eq. (6) is employed for iteration in order to generate the neck-down profile. This analysis ensures that the radial and axial force balances are satisfied for the converged profile.

Concentration of E' Defects. The differential equation for the time dependence of the E' defect concentration was determined by Hanafusa et al. [19]. It was assumed that the E' defects are generated through breaking of the Si–O band, and, at the same time, part of the defects recombine to form Si–O again. The net concentration of the E' defects is the difference between the generation and the recombination. If the concentration and activation energy of the E' defects are represented by n_d and E_d, respectively, and those of the precursors by n_p and E_p, the differential equation is given by

$$\frac{dn_d}{dt}=n_p\nu^*\exp\left(-\frac{E_p}{kT}\right)-n_d\nu^*\exp\left(-\frac{E_d}{kT}\right) \tag{11}$$

where, ν^* is the frequency factor for this reaction and k the Boltzmann constant. The first term on the right-hand side of this equation expresses the generation of the defects while the second term expresses the recombination. When this equation is applied to a mass point which moves along the streamline with radial and axial velocity components u and v, it can be rewritten as

$$v\frac{dn_d}{dz}=n_p\nu^*\exp\left(-\frac{E_p}{kT}\right)-n_d\nu^*\exp\left(-\frac{E_d}{kT}\right). \tag{12}$$

For pure silica, the initial concentration of E' defect is assumed to be zero. When one Si–O band is broken, one precursor disappears and one E' defect is generated. Thus, we have the relation between the concentrations of the E' defects and the precursors as

$$n_d=n_p(0)-n_p \tag{13}$$

where n_p is the initial concentration of precursors. These equations yield

$$\begin{aligned}v\frac{dn_d}{dz}=n_p(0)\nu^*\exp\left(-\frac{E_p}{kT}\right)-n_d\nu^*\left[\exp\left(-\frac{E_p}{kT}\right)\right.\\ \left.+\exp\left(-\frac{E_d}{kT}\right)\right].\end{aligned} \tag{14}$$

The boundary condition for this equation is given by

$$n_d(0)=0. \tag{15}$$

The values of E_p, E_d, ν^*, and $n_p(0)$ are all taken from Hanafusa et al. [19] and are given as $E_p=6.4087\times10^{-19}$ J, $E_d=0.3204\times10^{-19}$ J, $\nu^*=8\times10^{-3}\,s^{-1}$, and $n_p(0)=7\times10^{22}\,g^{-1}$. If the preform is assumed to be in an equilibrium state at temperature T_{melt}, the relation

$$\frac{dn_d}{dt}=0 \tag{16}$$

holds. Therefore, from the preceding equations, the defect concentration in the equilibrium state at T_{melt} is

$$n_d(T_{melt})=\frac{n_p(0)\exp\left(-\frac{E_p}{kT}\right)}{\exp\left(-\frac{E_p}{kT}\right)+\exp\left(-\frac{E_d}{kT}\right)} \tag{17}$$

At $T_{melt}=1900$ K, the value of $n_d(T_{melt})$ is $1.832\times10^{12}\,g^{-1}$.

Draw Tension. The calculation of the externally applied draw tension F_T is based on the work of Vasilijev et al. [24], who considered an imaginary cut at an axial location z in the soft region of the neck-down and gave the force balance as

$$\begin{aligned}F_T=F_\mu+F_\zeta+F_I+F_e-F_g=3\pi\mu R^2\frac{\partial v}{\partial z}+\pi R^2\zeta H\\ +\pi\rho\int_z^{L_f}R^2v\frac{\partial v}{\partial z}dz+2\pi\int_z^{L_f}\tau_s R dz-\pi\rho g\int_z^{L_f}R^2dz\end{aligned} \tag{18}$$

where, the terms on the right-hand side, from left to right, represent the forces due to viscous stress, surface tension, inertia, external shear, and gravity, respectively. The integration is carried out to a location $z=L_f$, which is beyond the end of the neck-down region. Thus, this location is generally at the furnace exit or, in some cases, beyond it. It is ensured that the integrals reach constant values by $z=L_f$ and no significant change occurs if L_f is increased further. Therefore, the force components on the right-hand side of Eq. (18) are functions of the axial location z where

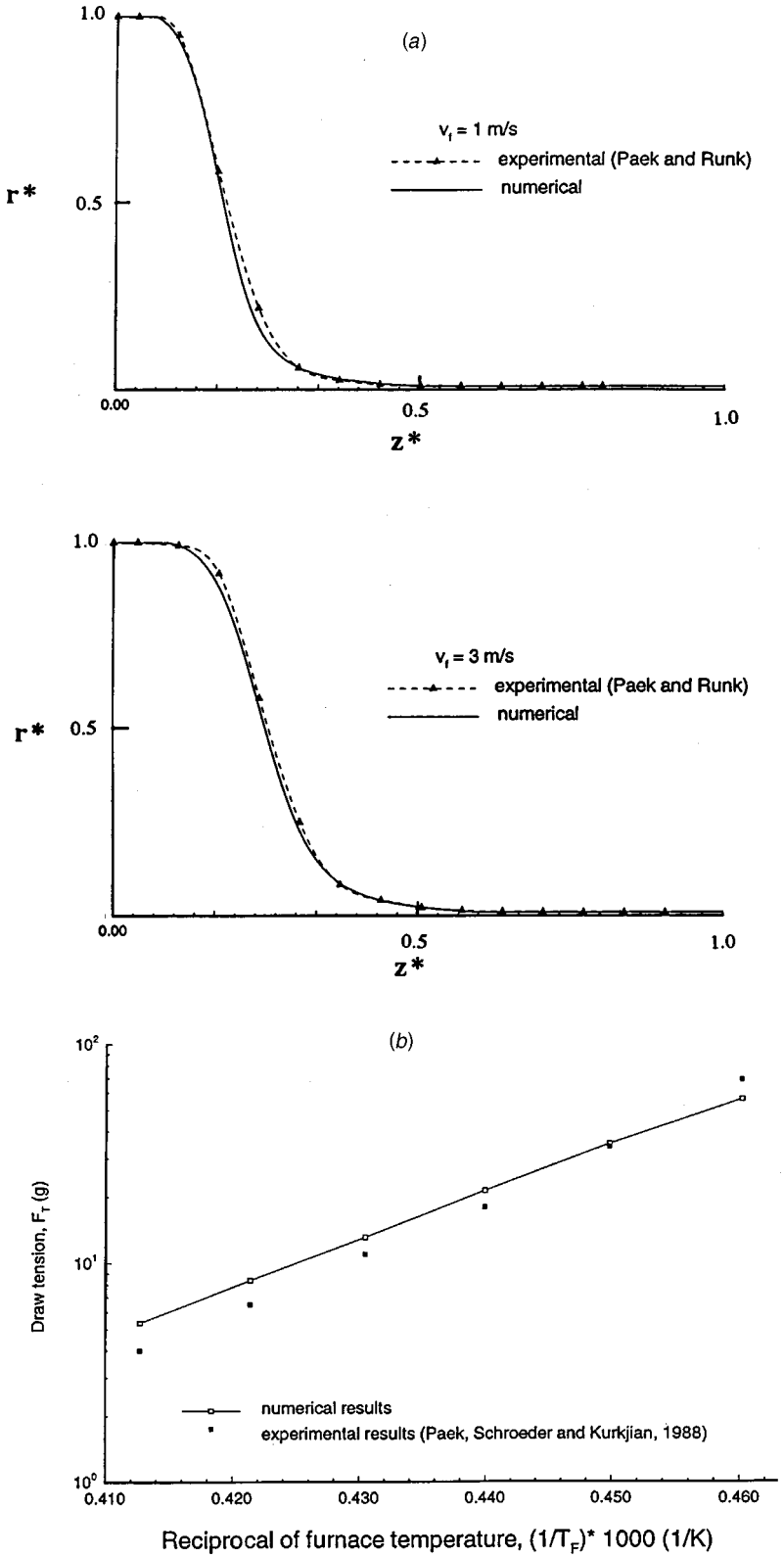

Fig. 2 (*a*) **Validation of the numerical predictions of the neck-down profile at v_f=1 m/s and v_f=3 m/s by comparing these with the experimental results of Paek and Runk [7]; (*b*) comparison of the computed draw tension applied to the fiber with the corresponding experimental results obtained by Paek et al. [27]**

the imaginary cut is considered. As pointed out by Roy Choudhury et al. [14], at relatively low temperatures, the viscous effects dominate and the first term on the right-hand side of Eq. (18) is the main contributor to the tension. However, at higher temperatures, the viscous effects are smaller and gravity effects become significant. In general, all forces acting in the neck-down region must be considered for an accurate calculation of the draw tension applied to the fiber in the draw process.

Method of Solution. The strategy used here to solve the transport equations is basically the same as that given by Roy Choudhury and Jaluria [12,13] and Yin and Jaluria [22]. The streamfunction, vorticity, and energy equations are solved using a nonuniform grid, with finer grids located in regions where large gradients are expected. The optimal grid was obtained by numerical experimentation as 369×41 (axial and radial, respectively) for the fiber/preform and 369×61 for the purge gases. A false transient approach with the alternating direction implicit method is used for the governing equations ([25,26]). Successive underrelaxation is used, with a relaxation factor of order 0.1, for the temperature and vorticity to obtain convergence for this strongly nonlinear problem. The accuracy/uncertainty of the results was checked by comparisons with earlier results in the literature and with benchmark solutions, as well as by grid refinement.

The generation of profile is realized by iteration using the equations given earlier. To obtain the neck-down profile, one can iterate the transport equations to steady state for an arbitrary neck-down profile, and then from the steady-state solution, obtain a corrected profile using the correction equation, Eq. (6). In this study, the neck-down profile is corrected before the steady state is reached, i.e., after about 2000 steps of iteration. Roy Choudhury et al. [14] have demonstrated that this strategy saves a lot of computational time. Yin and Jaluria [22] showed that the difference between the temperature distributions predicted using the optically thick approximation and the zonal method is not very large. Therefore, the optically thick approximation is first used to generate the neck-down profile, then this profile is used as the initial guess to generate the final neck-down profile with the zonal method. The computation shows that usually only two to three iterations are needed to obtain the final neck-down profile. The grid and other numerical variables, such as the convergence parameter, were varied to ensure that the results were independent of the values chosen.

Results and Discussion

Validation. The approach for the generation of neck-down profile is based on that proposed by Roy Choudhury et al. [14] for relatively low draw speeds. A comprehensive validation of this approach has been carried out by them. It was verified that this approach generates the neck-down profile uniquely and robustly. The force balance has also been verified. Comparisons were made with the experimental results obtained by Paek and Runk [7] and by Paek et al. [27]. Figure 2 shows these comparisons from the earlier study. The applied tension was measured in the fiber beyond the soft region of the fiber. The furnace is taken as 30 cm long and 7 cm in diameter. The wall is taken at a uniform temperature of 2500 K. The preform is taken as 5 cm in diameter, the fiber diameter as 125 μm, and the drawing speed is taken as 10 m/s. Argon enters the furnace as aiding flow at 0.1 m/s.

The starting neck-down profile is taken as a Gaussian distribution. Figure 3(*a*) shows that the profile generated using the zonal

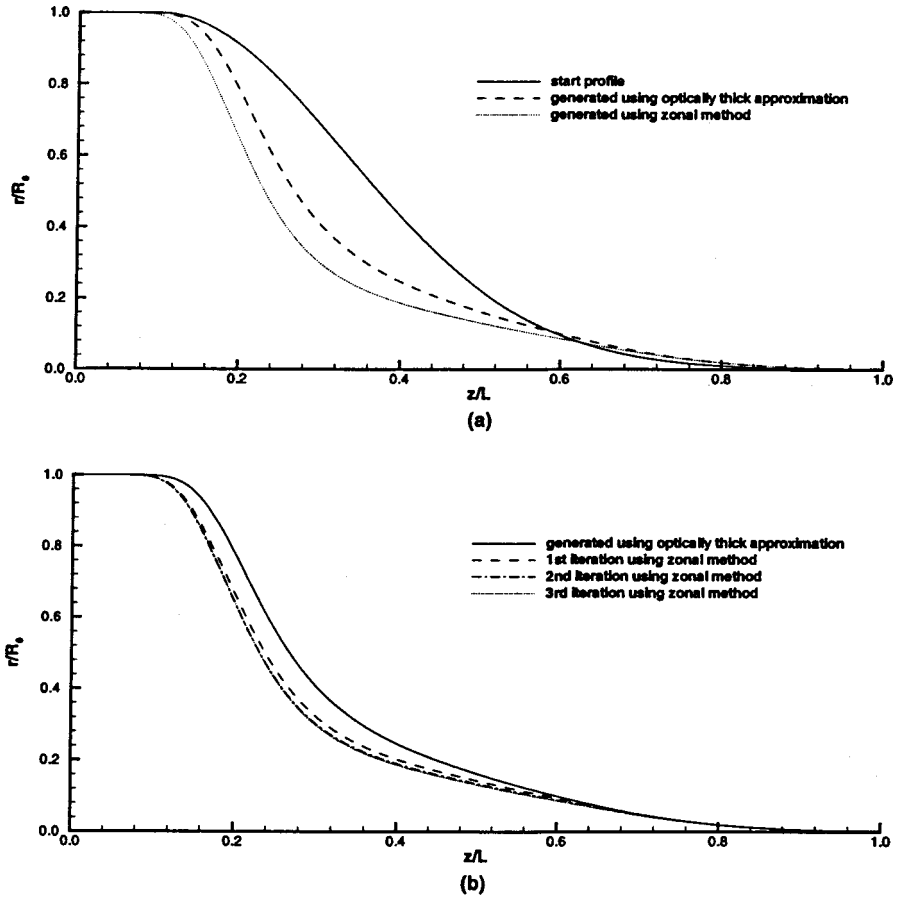

Fig. 3 Neck-down profiles generated using the optically thick approximation and the zonal method

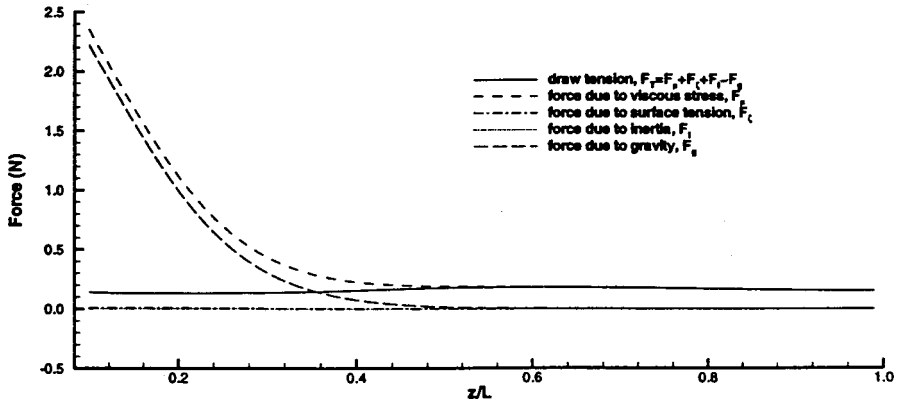

Fig. 4 Dependence of different forces contributing to draw tension on the axial location *z* at which an imaginary cut in the preform/fiber is taken to calculate the tension

method for radiation is close to that generated using the optically thick approximation, as pointed out previously. Figure 3(*b*) demonstrates the iteration process using the zonal method. The profile generated using the optically thick approximation is used as the initial guess. It is seen that only three iteration steps are enough to reach the final converged neck-down profile. The results with the optically thick assumption were identical to those obtained earlier by Roy Choudhury et al. [14] for the small preform diameters and low draw speeds considered by them. Figure 4 shows the force balance in the preform/fiber. It is seen that the calculated draw tension is essentially independent of the axial location *z* where the imaginary cut is taken, as expected for a steady-state fiber drawing process and as obtained by Roy Choudhury et al. [14]. Thus, the basic trends are similar to those obtained in earlier studies.

Process Simulation. The effect of the process parameters on the fiber drawing process has been investigated by changing their values. For all the results, unless otherwise mentioned, the base, or reference, values given earlier with a draw speed of 15 m/s have been used, the purge gas is Argon flowing in the same direction as the preform movement. The fiber diameter is taken as 125 μm. The furnace temperature distribution is taken as a parabolic function with maximum of 2500 K in the middle and minimum of 2000 K at both ends on the basis of results obtained by Issa et al. [28]. Both the preform and the purge gas enter the furnace at 300 K.

Fiber Drawing Speed. Figure 5 shows the generated neck-down profiles for fiber drawing speeds of 10, 15, and 20 m/s. It is found that the necking process starts further downstream as the drawing speed increases. This is caused by the fact that when the drawing speed increases, the preform takes a larger distance to get heated up to the softening temperature. The profile is very flat

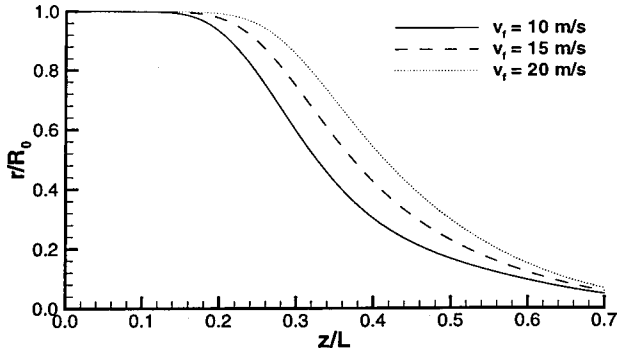

Fig. 5 Neck-down profiles generated using the zonal method for different drawing speeds

near the end and an accurate prediction of the exact location of the end of the neck-down region is difficult. However, the location L_f is varied in the numerical calculation of the draw tension to ensure that the results are essentially independent of the chosen value of L_f.

Figures 6 shows the thermal field in terms of the isotherms in the furnace. The flow patterns were found to be very similar for different drawing speeds. However, it is found that, as expected, the preform takes a larger distance to be heated up to a given temperature level when the drawing speed increases. The temperature lag, $(T_s\text{-}T_c)/T_c$, was also found to increase with an increase in the drawing velocity. It was found that the maximum temperature lag exists near the entrance where the temperature is low while in the neck-down region where the temperature is very high, the lag is relatively small, being less than 0.1.

The convective heat transfer coefficient, based on the temperature difference from the ambient, was also calculated from the temperature distributions by calculating the gradient at the surface. Figure 7 shows the Nusselt number at the interface of the preform and the purge gas. It is clearly seen that an increase in drawing speed has a minor effect on the convective heat transfer coefficient except near the exit. This is because, when the drawing speed increases, the difference between the fiber and the purge gas velocities increases significantly in the region near the exit, while in the upper neck-down region, the change in this difference is very small. The magnitude of the convective heat transfer coefficient is found to be around 10 W/m^2K for most of the region. Though not shown here, it was found that the viscous dissipation becomes important in the lower neck-down region because the diameter in this region becomes very small. This is an important effect since radiation is small near the end of the neck-down region because of the geometry. When the drawing speed increases, the viscous dissipation reaches a higher level due to the higher velocity gradients and the higher viscosity resulting from lower temperatures.

Figure 8 shows the generation of E' defects in the fiber. It is found that the concentration of E' defects at the surface is higher than that at the centerline, and the generation of E' defects mainly occurs in the upper neck-down region where the temperature undergoes a significant increase. It is seen that the concentration of the E' defects increases with a decrease in the drawing speed. This is due to the preform temperature being higher for lower drawing speeds. According to the defect generation equation, Eq. (12), the higher the temperature, the higher the defect generation term.

Furnace Wall Temperature. Two different furnace wall temperature distributions have been considered here. Both distributions are parabolic with the maximum at the mid-point. The maximum temperatures are 2500 and 3000 K, and the minimum

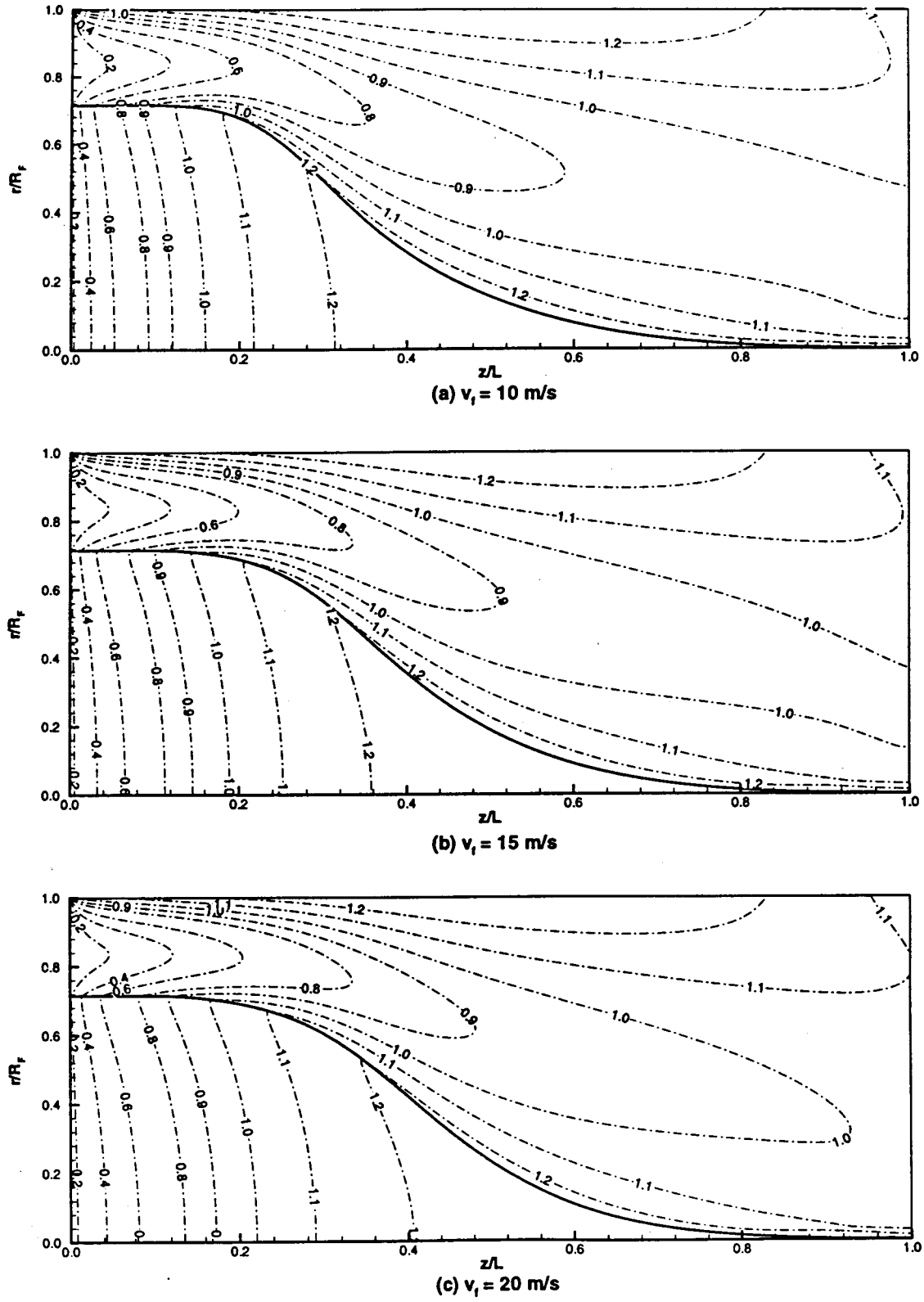

Fig. 6 Isotherms in the preform/fiber and the purge gas for different drawing speeds

temperatures 2000 and 2500 K, respectively. Figure 9(*a*) compares the neck-down profiles generated using the zonal method for different furnace temperatures. It is found that the neck-down process begins much earlier and a much steeper profile is generated when the furnace temperature is raised by 500 K. This means that the furnace temperature has a very important effect on the neck-down process, as also concluded by Lee and Jaluria [4]. Figure 9(*b*) compares the neck-down profiles generated using the zonal method and the optically thick approximation with maximum furnace temperature at 3000 K, showing that the difference in the profiles is small but significant.

A few other trends may be mentioned here ([29]). The corre-

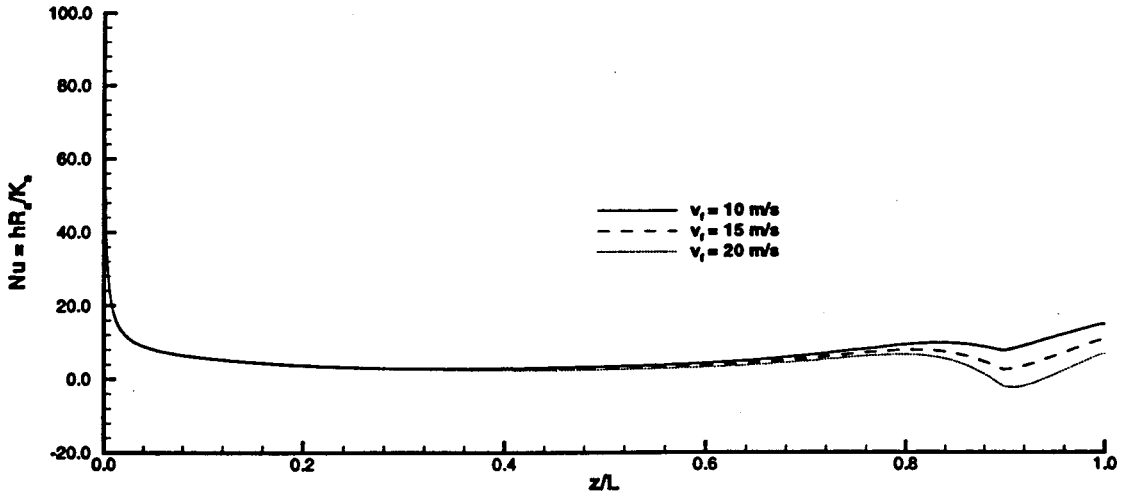

Fig. 7 Nusselt number at the outside surface of preform/fiber for different fiber drawing speeds

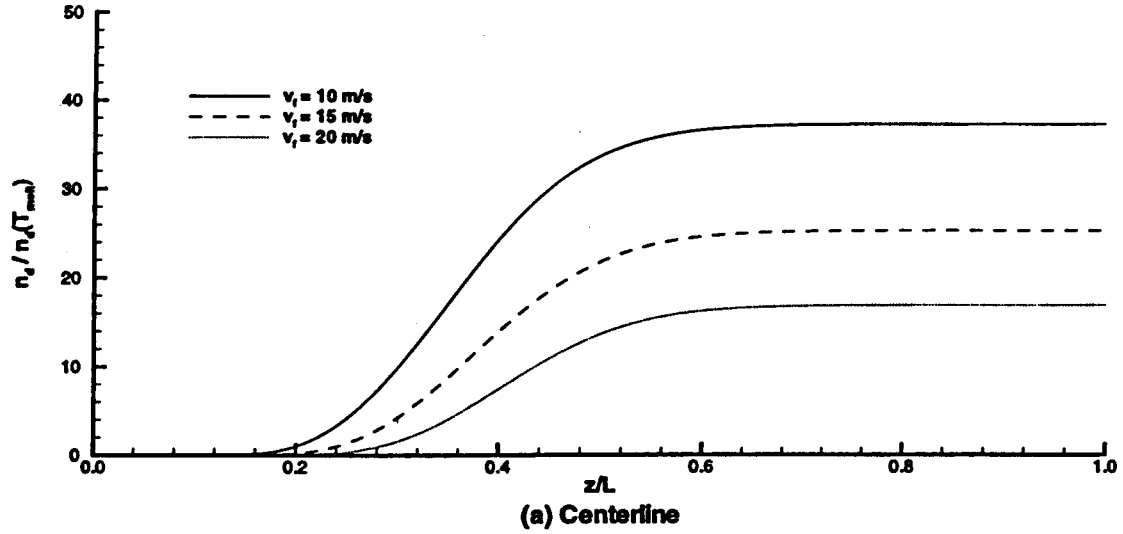

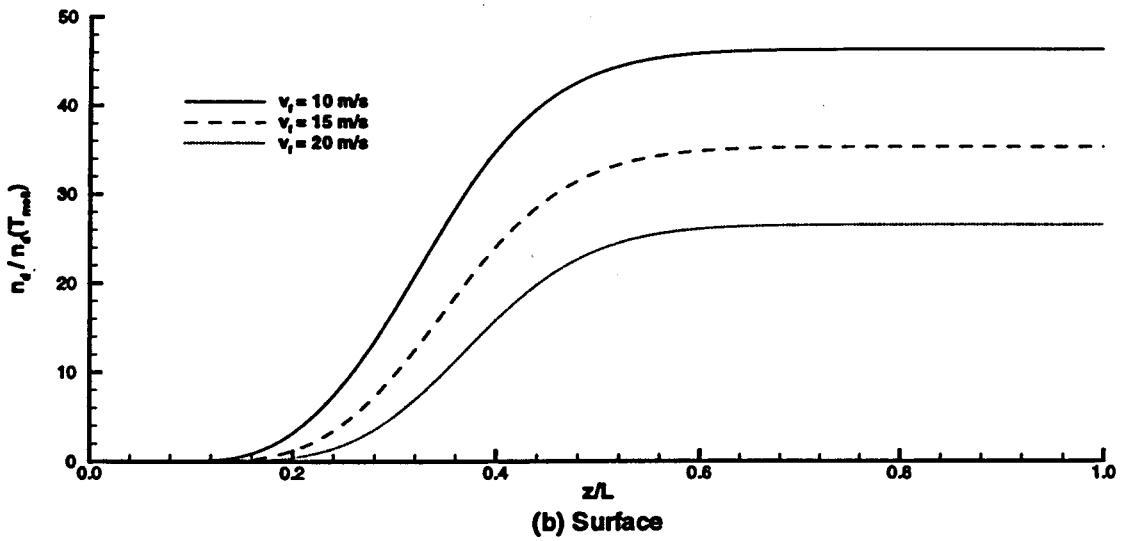

Fig. 8 Variation of the concentration of *E′* defects in the axial direction at the surface and at the centerline for different drawing speeds

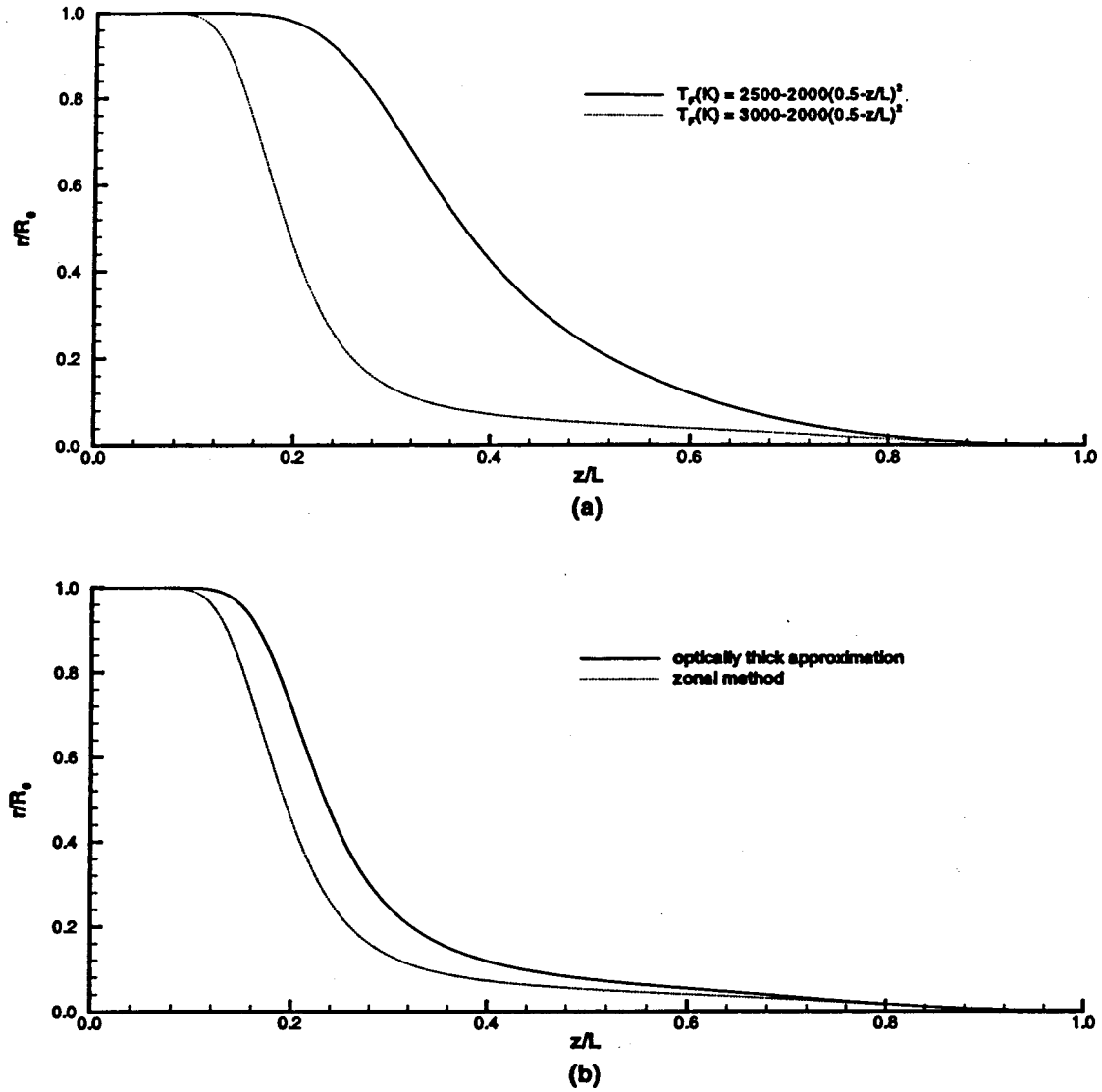

Fig. 9 Neck-down profiles: (*a*) generated using the zonal method for two different furnace temperatures; (*b*) generated using the zonal method and optically thick approximation for $T_F(\mathrm{K}) = 3000 - 2000(0.5 - z/L)^2$

sponding figures are not shown for conciseness. As expected, it was found that when the furnace temperature increases, the preform is heated up more quickly. Furthermore, the final fiber temperature is elevated to a higher level. The furnace temperature had a minor effect on the convective heat transfer coefficient except near the exit where the convective heat transfer coefficient increases noticeably. This increase is possibly caused by the difference in the neck-down profiles. The viscous dissipation in the preform for the higher furnace temperature was found to attain a much lower level. This mainly results from the fact that the viscosity decreases substantially due to the higher temperature level attained by the fiber. The concentrations of E' defects generated for different furnace temperatures were also compared. It was found that the magnitude of the concentration increases to almost ten times when the furnace temperature increases by 500 K. Therefore, in terms of the defects as well as energy efficiency, it is desirable to draw the fibers at a lower furnace temperature.

Purge Gas. Three different velocities, i.e., 0.1, 0.3, and 0.5 m/s, were considered. A comparison of the neck-down profiles generated for different purge gas velocities showed that the profiles were very close. This is because in the high-temperature furnace, radiation is the dominant mode of thermal transport while convection is less important. The temperature field in the preform/fiber did not show any noticeable difference. The concentration of E' defects was found to show very little change for different purge gas velocities because these depend on the temperature field in the preform/fiber.

Two different purge gases, Argon and Helium, were also considered. The main differences between Argon and Helium lie in the thermal diffusivity, α, and in the kinematic viscosity, ν. For Argon, $\alpha = 2.082 \times 10^{-5}\ \mathrm{m^2/s}$, $\nu = 1.41 \times 10^{-5}\ \mathrm{m^2/s}$ and for Helium, $\alpha = 1.764 \times 10^{-4}\ \mathrm{m^2/s}$, $\nu = 1.24 \times 10^{-4}\ \mathrm{m^2/s}$. It was found that a change in purge gas properties has little effect on the neck-down profile. This is due to the same reason pointed out in last section that in the high temperature furnace, radiation is the dominant mode of thermal transport while convection is of minor consequence. The flow patterns in the preform/fiber did not indicate any noticeable difference. This means that the purge gas has negligible effect on the flow field in the preform/fiber. Figure 10 shows the isotherms for the two purge gases. Because the thermal diffusivity of Helium is almost ten times higher than that of Argon, Helium is heated up much faster and finally reaches a much higher temperature level at the exit. But the isotherms in the preform/fiber are quite similar, which demonstrates that the

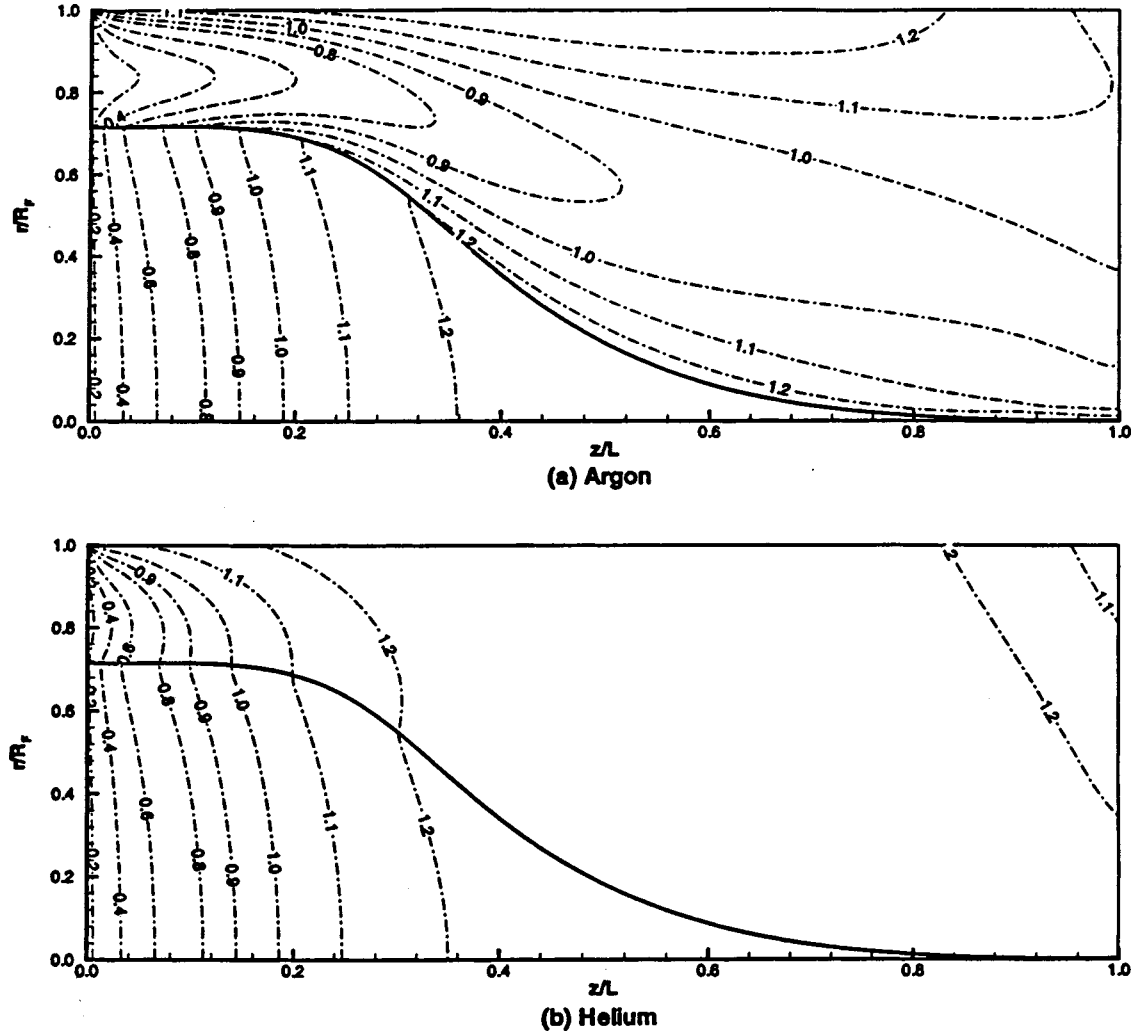

Fig. 10 Isotherms in the preform/fiber and the gas with Argon and Helium as the purge gases

change in the purge gas has little impact on the temperature field in the preform/fiber. This again demonstrates that the change in purge gas has little effect on the temperature field in the preform/fiber.

It was found that near the entrance, Helium has a higher heat transfer coefficient due to higher thermal diffusivity, but, as it is heated up faster than Argon, the heat transfer coefficient soon drops below that for Argon ([29]). Near the exit, Helium has a negative heat transfer coefficient, because its temperature has been elevated to such a high level that it begins to lose heat to the fiber.

Preform Diameter. Preform diameters of 2.5 cm and 5.0 cm were considered and the results are presented. Figure 11 shows the centerline temperature in the preform for two different preforms. It is seen that the smaller diameter preform is heated up to a lower temperature. This occurs because the 2.5-cm-diameter preform, due to its smaller diameter, receives less radiative energy from the furnace, moves at higher speed, and is cooled by a purge gas with higher flow rate. Besides, due to the lower temperature level, the 2.5-cm-diameter preform starts necking later. As expected, the 2.5-cm-diameter preform had smaller temperature lag. The maximum lag is only half of that for 5-cm-diameter preform.

The concentrations of E' defects in the fiber at the exit for two preforms were also compared. The concentration in the fiber generated from the 2.5-cm-diameter preform was found to be much lower than that in the fiber generated from the 5-cm-diameter diameter. This can be explained by the fact that the 2.5-cm-diameter preform undergoes a thermal process with lower temperature which generates fewer defects.

Feasible Drawing Conditions. A parametric study has been carried out to identify feasible drawing conditions. When the furnace dimensions, preform diameter, draw-down ratio and drawing speed are given, the fiber cannot be drawn at any arbitrary temperature. If the furnace temperature is not high enough, the iterative process shows a break in the fibers, a phenomenon that is known as viscous rupture ([30]). Similarly, when the furnace temperature is given, there is a limit on the drawing speed beyond which drawing is not possible. As the fiber speed increases, the preform/fiber temperature decreases and eventually drops below the softening point, making drawing impossible ([13]).

The furnace wall temperature distribution is assumed to be parabolic with a minimum temperature of 2000K at both ends. The maximum temperature which is referred as the furnace temperature is located at the midpoint of the furnace length and is changed to identify the feasible drawing conditions. Other parameters are the same as given previously. Figure 12 shows the relation between the maximum allowable drawing speed and furnace temperature for successful drawing. It indicates that with an increase in the furnace temperature the maximum allowable drawing speed also increases, as expected. The feasible drawing conditions are given by the region below the curve. In practical fiber

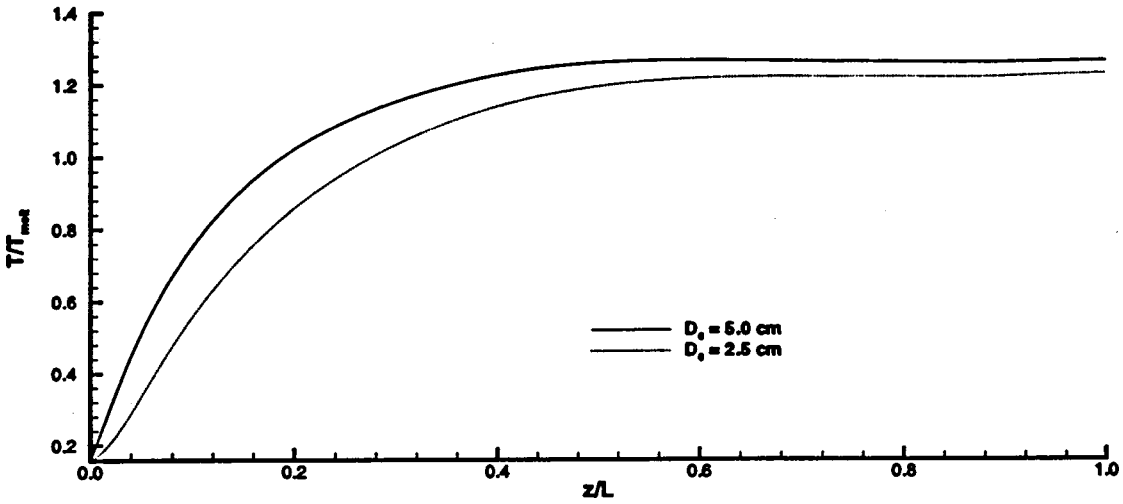

Fig. 11 Axial variation of the centerline temperature in the preform/fiber for two different diameter preforms

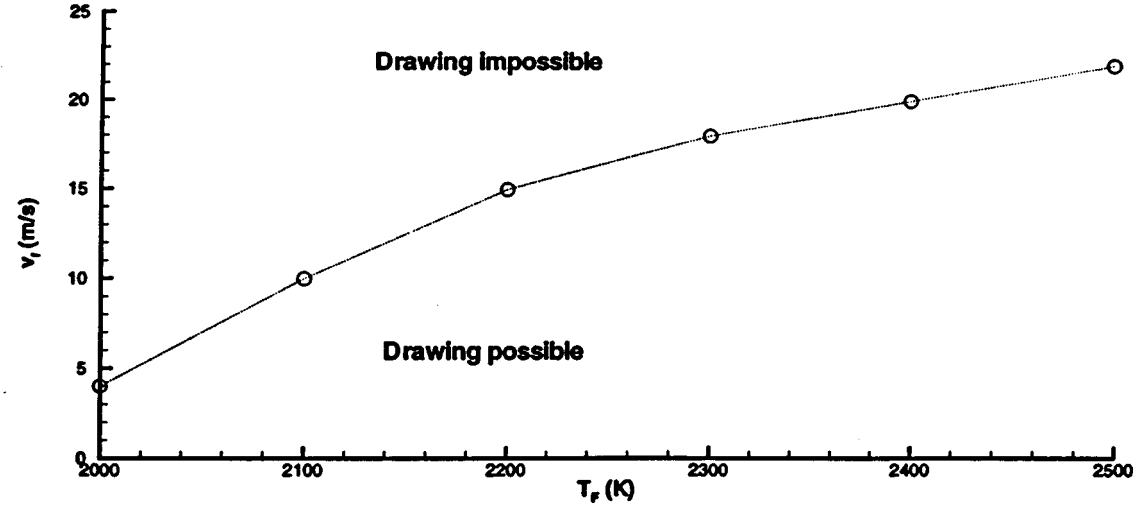

Fig. 12 Feasible drawing conditions in terms of the furnace wall temperature and fiber drawing speed

drawing, these results are very valuable, since appropriate drawing conditions can be chosen for a feasible process.

Conclusions

It is found that the fiber drawing speed and the furnace wall temperature have significant influence on the generated neck-down profiles, while the purge gas velocity and type have very minor effect. The increase in fiber drawing speed delays the start of neck-down process, while increase of the furnace temperature advances the start and causes steeper neck-down shape. The difference between the profiles generated using the zonal method and the optically thick approximation is not very large. Therefore, the latter can be used as a good approximation.

The preform takes a larger distance to get heated up to its softening point with an increase in the fiber drawing speed. When the furnace temperature increases, the preform is heated up to its softening point earlier and the fiber reaches a higher temperature at the exit. Smaller diameter preforms are heated up more slowly and reach a lower final temperature level. The viscous dissipation in the preform/fiber is found to become important in the lower neck-down region. It is affected strongly by the fiber drawing speed, furnace temperature, and preform diameter. The convective heat transfer coefficient at the surface of the preform/fiber is found to be of the order of 10 W/m^2K for most of the region. It is influenced strongly by the purge gas velocity and properties and by the preform diameter. An increase in purge gas velocity increases the heat transfer coefficient. An increase in the thermal diffusivity of purge gas increases the heat transfer coefficient near the entrance but decreases it downstream. For smaller diameter preforms, the heat transfer coefficient is higher near the exit.

The concentration of E' defects at the fiber surface is found to be higher than that at the centerline. In general, the generation of E' defects depends on the thermal history of the preform/fiber. A higher temperature level results in a higher defect concentration. Therefore, measures which lower the temperature level in the preform/fiber, such as higher drawing speed, lower furnace temperature, and smaller preform diameter, are desirable in terms of the low defect concentration.

The relation between the allowed fiber drawing speed and the furnace temperature has been studied. With the increase in the furnace temperature, the allowed fiber drawing speed also increases, as expected. A feasible drawing domain has been obtained for a given furnace. The importance of such a feasibility study to the real fiber drawing process is pointed out.

Acknowledgments

The authors acknowledge the financial support provided by the National Science Foundation, under Grant Nos. DDM-92-13458 and DMI-96-33194, and the computing facilities provided by the Pittsburgh Supercomputing Center, Under Grant No. CBT920017P, for this work. Helpful discussions with Prof. C.E. Polymeropoulos and G.H. Sigel and with Dr. S. Roy Choudhury are also acknowledged. The authors also acknowledge insightful and useful comments made by one of the reviewers on the calculation of the draw tension applied to the fiber.

Nomenclature

C_p = specific heat at constant pressure
g = magnitude of gravitational acceleration
h = local convective heat transfer coefficient
H = mean surface curvature of fiber profile
K = thermal conductivity
L = height of furnace
L_f = axial coordinate distance by which neck-down is complete
Nu = Nusselt number
p = pressure
R = radius of preform, fiber, furnace
r = radial coordinate distance
r^* = dimensionless radial distance, $r^*=r/R_0$
S_r = radiative source term
t = time
T = temperature
T_{melt} = glass softening point, typically around 1900 K for silica glass
u = radial velocity
U = nondimensional radial velocity, $U=u/v_0$
v = axial velocity
$\overline{v}$ = average axial velocity in the glass
V = nondimensional axial velocity, $V=v/v_0$
z = axial coordinate distance
z^* = dimensionless axial coordinate distance, $z^*=z/L$

Greek Symbols

β = nondimensional axial coordinate distance, $\beta=z/L$
η = nondimensional radial coordinate distance, $\eta=r/R(z)$
η_a = nondimensional radial coordinate distance in the purge gas, $\eta_a=r_a/[R_F-R(z)]$
μ = dynamic viscosity
ν = kinematic viscosity
ν^* = frequency factor in generation/recombination of E' defects
Φ = viscous dissipation
ρ = density
ψ = physical streamfunction, $u=-(1/r)(\partial\psi/\partial z)$, $v=(1/r)(\partial\psi/\partial r)$
Ψ = nondimensional streamfunction, $\Psi=\psi/(v_0R_0^2)$
θ = nondimensional temperature, $\theta=T/T_{\text{melt}}$
ω = physical vorticity
Ω = nondimensional vorticity, $\Omega=\omega R_0/v_0$
ζ = surface tension between glass and purge gas

Superscripts

$'$ = first derivative with respect to z
$''$ = second derivative with respect to z

Subscripts

0 = preform at furnace entrance
a = purge gas
c = fiber axis
f = fiber
F = furnace
s = fiber surface

References

[1] Krishnan, S., and Glicksman, L. R., 1971, ''A Two-Dimensional analysis of a Heated Free Jet at Low Reynolds Numbers,'' J. Basic Eng., **93**, pp. 355–364.
[2] Homsy, G. M., and Walker, K., 1979, ''Heat Transfer in Laser Drawing of Optical Fibers,'' Glass Technol., **20**, No. 1, pp. 20–26.
[3] Papamichael, H., and Miaoulis, I. N., 1991, ''Mixed Convection Effects During the Drawing of Optical Fibers,'' Submol. Glass Chem. Phys., SPIE, **1590**, pp. 122–130.
[4] Lee, S. H.-K., and Jaluria, Y., 1996, ''Effects of Variable Properties and Viscous Dissipation During Optical Fiber Drawing,'' ASME J. Heat Transfer, **118**, pp. 350–358.
[5] Papamichael, H., Pellon, C., and Miaoulis, I. N., 1997, ''Air Flow Patterns in the Optical Fiber Drawing Furnace,'' Glass Technol., **38**, pp. 22–29.
[6] Glicksman, L. R., 1968, ''The Dynamics of a Heated Free Jet of Variable Viscosity Liquid at Low Reynolds Numbers,'' J. Basic Eng., **90**, pp. 343–354.
[7] Paek, U. C., and Runk, R. B., 1978, ''Physical Behavior of the Neck-down Region During Furnace Drawing of Silica Fibers,'' J. Appl. Phys., **49**, pp. 4417–4422.
[8] Yarin, A. L., 1983, ''Stationary Configuration of Fibers Formed Under Nonisothermal Conditions,'' J. Appl. Mech. Tech. Phys., **24**, pp. 865–870.
[9] Sayles, R., and Caswell, B. A., 1984, ''A Finite Element Analysis of the Upper Jet Region of a Fiber Drawing Flow Field of a Temperature Sensitive Material,'' Int. J. Heat Mass Transf., **27**, No. 1, pp. 57–67.
[10] Myers, M. R., 1989, ''A Model for Unsteady Analysis of Preform Drawing,'' AIChE J., **35**, pp. 592–602.
[11] Rosenberg, S., Papamichael, H., and Miaoulis, I. N., 1994, ''A Two-Dimensional Analysis of the Viscous Problem of a Glass Preform During the Optical Fiber Drawing Process,'' Glass Technol., **35**, pp. 260–264.
[12] Roy Choudhury, S., and Jaluria, Y., 1998, ''Thermal Transport due to Material and Gas Flow in a Furnace for Drawing an Optical Fiber,'' J. Mater. Res., **13**, pp. 494–503.
[13] Roy Choudhury, S., and Jaluria, Y., 1998, ''Practical Aspects in the Drawing of an Optical Fiber,'' J. Mater. Res., **13**, pp. 483–493.
[14] Roy Choudhury, S., Jaluria, Y., and Lee, S. H.-K., 1999, ''Generation of Neck-Down Profile for Furnace Drawing of Optical Fiber,'' Numer. Heat Transf., **35**, pp. 1–24.
[15] Modest, M. F., 1993, *Radiative Heat Transfer*, McGraw-Hill, New York.
[16] Kaminski, D. A., 1995, ''Thermal Transport in Optical Fiber Manufacturing,'' *Proceedings of the First International Symposium on Radiative Heat Transfer*, M. P. Menguc, ed., Begell House, New York, pp. 667–681.
[17] Song, M., Ball, K. S., and Bergman, T. L., 1998, ''A Model for Radiative Cooling of a Semitransparent Molten Glass Jet,'' ASME J. Heat Transfer, **120**, pp. 931–938.
[18] Yin, Z., and Jaluria, Y., 1997, ''Zonal Method to Model Radiative Transport in an Optical Fiber Drawing Furnace,'' ASME J. Heat Transfer, **119**, pp. 597–603.
[19] Hanafusa, H., Hibino, Y., and Yamamoto, F., 1985, ''Formation Mechanism of Drawing-Induced E′ Centers in Silica Optical Fibers,'' J. Appl. Phys., **58**, No. 3, pp. 1356–1361.
[20] Hibino, Y., Hanafusa, H., and Sakaguchi, S., 1985, ''Formation of Drawing-Induced E′ Centers in Silica Optical Fibers,'' Jpn. J. Appl. Phys., **24**, No. 9, pp. 1117–1121.
[21] Griscom, D. L., 1991, ''Optical Properties and Structure of Defects in Silica Glass,'' J. Ceram. Soc. Jpn., **99**, pp. 923–942.
[22] Yin, Z., and Jaluria, Y., 1998, ''Thermal Transport and Material Flow in High Speed Optical Fiber Drawing,'' ASME J. Heat Transfer, **120**, pp. 916–930.
[23] Fleming, J. D., 1964, ''Fused Silica Manual,'' Final Report for the U.S. Atomic Energy Commission, Oak Ridge, Tennessee, Project No. B-153.
[24] Vasilijev, V. N., Dulnev, G. N., and Naumchic, V. D., 1989, ''The Flow of a Highly Viscous Liquid With a Free Surface,'' Glass Technol., **30**, pp. 83–90.
[25] Pantankar, S. B., 1980, *Numerical Heat Transfer and Fluid Flow*, Hemisphere, New York.
[26] Jaluria, Y., and Torrance, K. E., 1986, *Computational Heat Transfer*, Taylor and Francis, Washington, DC.
[27] Paek, U. C., Schroeder, C. M., and Kurkjian, C. R., 1988, ''Determination of the Viscosity of High Silica Glasses During Fiber Drawing,'' Glass Technol., **29**, pp. 263–266.
[28] Issa, J., Yin, Z., Polymeropoulos, C. E., and Jaluria, Y., 1996, ''Temperature Distribution in an Optical Fiber Draw Tower Furnace,'' J. Mater. Process. Manuf. Sci., **4**, pp. 221–232.
[29] Yin, Z., 1997, ''Numerical Investigation of Thermal Transport in Optical Fiber Drawing Process,'' Ph.D. thesis, Rutgers University, New Brunswick, NJ.
[30] Dianov, E. M., Kashin, V. V., Perminov, S. M., Perminova, V. N., Rusanov, S. Y., and Sysoev, V. K., 1988, ''The Effect of Different Conditions on the Drawing of Fibers from Preforms,'' Glass Technol., **29**, No. 6, pp. 258–262.

Journal of Heat Transfer

Technical Notes

This section contains shorter technical papers. These shorter papers will be subjected to the same review process as that for full papers.

Fourier Versus Non-Fourier Heat Conduction in Materials With a Nonhomogeneous Inner Structure

H. Herwig
e-mail: h.herwig@tu-harburg.de

K. Beckert
Technische Thermodynamik, TU Hamburg-Harburg, D-21073 Hamburg, Germany

Distinct non-Fourier behavior in terms of finite propagation velocity and a hyperbolic wave like character of heat conduction has been reported for certain materials in several studies published recently. However, there is some doubt concerning these findings. The objective of this note is to present experimental evidence for a perfectly Fourier-like behavior of heat conduction in those materials with nonhomogeneous inner structure that have been under investigation in the other studies. This controversy needs to be settled in order to understand the physics of heat conduction in these materials. [S0022-1481(00)00102-X]

Keywords: Conduction, Heat Transfer, Transient

1 Introduction

It is well known that the Fourier heat conduction equation is only an approximation as far as the speed of propagation of thermal waves is concerned: It assumes an infinite speed. Whenever heat transfer occurs at a certain location within a heat-conducting material according to Fourier's law this can be felt everywhere instantaneously, though, of course, with decreasing impact the further away from the source the effect is detected. The Fourier heat conduction equation nevertheless in most cases is an excellent description of heat conduction physics since real propagation speeds are very high and therefore a model that assumes infinite speed often is sufficient.

For example, Özisik and Tzou [1], in their review paper point out that thermal wave speeds in metals are of the order of 10^5 m/s, those for gases considerably lower but still of the order of 10^3 m/s. Due to these high speeds effects in conjunction with the fact that they are finite will be important only in highly unsteady situations like laser pulse heating (see, for example, [2]). Materials like metals and gases will be called ''engineering materials.'' They are characterized by a basically homogeneous inner structure.

However, there are materials with a nonhomogeneous inner structure like sand with an irregular grain structure or processed meat with a more or less preserved cell structure. These materials, called ''materials with a nonhomogeneous inner structure,'' are claimed to show strong deviation from Fourier heat conduction behavior. Mitra et al. [3] as well as Kaminski [4] found strong experimental evidence for wave propagation speeds that were several orders of magnitude smaller than those reported for engineering materials. Typical values found in these studies are 0.1 mm/s (!) for sand and for processed meat.

Since from our heat transfer experience we come to the conclusion that these results are either wrong or totally misinterpreted we decided to conduct our own experiments with the same thermal boundary and initial conditions but with a different experimental design. Prior to describing this experimental setup we present some characteristic results from Mitra et al. [3] which we tried to reproduce.

2 Typical Results Claiming Non-Fourier Behavior

In their study ''Experimental Evidence of Hyperbolic Heat Conduction in Processed Meat'' [3] the authors, from their point of view, clearly showed non-Fourier heat conduction behavior. The experiments were designed to show that heat waves take a finite time to reach a particular point inside the sample contrary to the instantaneous heat propagation as predicted by the Fourier model. In a typical experiment (their ''experiment I'') two identical meat samples at different initial temperatures T_c, T_w (c = cold; w = warm) were brought into contact with each other. One sample was refrigerated to $T_c = 8.2°C$ and the other was left at room temperature of $T_w = 23.1°C$.

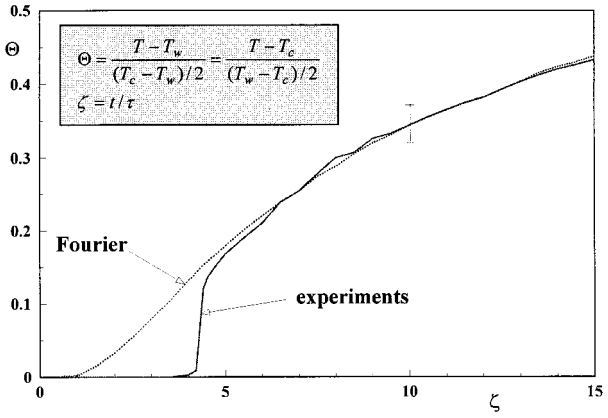

Fig. 1 Experimental result according to [3]. Temperature 6.3 mm deep in the warm side.

Contributed by the Heat Transfer Division for publication in the JOURNAL OF HEAT TRANSFER. Manuscript received by the Heat Transfer Division, June 6, 1999; revision received, November 17, 1999. Associate Technical Editor: S. S. Sadhal.

Thermocouples were embedded in the cold sample and in the room temperature sample at distances of 6.6 and 6.3 mm, respectively, from the plane of contact.

They interpreted their experimental results in terms of an extended heat conduction equation proposed by Cattaneo [5] and Vernotte [6]. It reads

$$\mathbf{q}+\tau\frac{\partial \mathbf{q}}{\partial t}=-k\nabla T. \tag{1}$$

The relaxation time constant τ is directly linked to the non-Fourier behavior. For $\tau=0$ Eq. (1) is the classical Fourier law of heat conduction. With nonzero values of τ a finite propagation speed of heat waves is introduced resulting in a hyperbolic equation for the temperature field

$$\frac{\partial T}{\partial t}+\tau\frac{\partial^2 T}{\partial t^2}=\alpha\nabla^2 T \qquad \alpha=\frac{k}{\rho c_p} \tag{2}$$

which emerges when Eq. (1) is combined with the thermal energy equation. Again, for $\tau=0$, the classical Fourier behavior is described by Eq. (2).

Based on τ, a propagation speed is defined as

$$C=\sqrt{\alpha/\tau}, \tag{3}$$

also called ''thermal wave speed.'' For $\tau=0$ it is infinitely high in accordance with the instantaneous heat propagation predicted by the Fourier model. Figure 1 shows a typical result of the experiments of Mitra et al. [3] briefly described above. It shows the thermocouple reading at the position 6.3 mm deep in the initially warm part (at room temperature $T_w=23.1°\mathrm{C}$).

After a certain delay time the temperature curve jumps to a level which corresponds to the classical Fourier behavior. The interpretation is obvious: at that moment the wave front passes through the thermocouple location causing the sharp increase in temperature. From the delay time Mitra et al. found a time constant of $\tau=(15.5\pm 2.1)$s as a mean value out of four similar experiments. With the thermal diffusity $\alpha=1.4\times10^{-7}\ \mathrm{m^2/s}$ for processed meat this corresponds to a wave speed of $C=0.095$ mm/s.

It should be noted that the temperature jump was nearly 1°C, i.e., easily detectable with thermocouples of $\pm0.2°\mathrm{C}$ uncertainty used in the reported experiments.

Results like in Fig. 1 are typical for those studies that claim non-Fourier behavior for materials with a nonhomogeneous inner structure (see, for example, [4]) for a study conducted with sand.

3 Our Own Experimental Setup

In order to get as much information as possible about the whole temperature field of the unsteady heat conduction process we choose the following experimental setup:

The crucial element is a box (size $(160\times120\times80)\ \mathrm{mm^3}$ inside; wall material 10 mm acryl; outside insulation) that can be filled with the material of interest. Heat conduction within the material is initiated by a temperature jump on the outer surface of a pipe (copper pipe; inner diameter 7 mm; wall thickness 0.5 mm) that lies within the material a small distance below the free upper surface as shown in Fig. 2. The temperature jump occurs shortly after a valve is opened (water flow speed ≈4 m/s) and water at a temperature different from that of the material (and the initial pipe filling) starts flowing through the pipe. With a pipe wall of high thermal conductivity the time constant of the pipe wall cooling (until its final temperature is reached) is very short compared to the relaxation time constant $\tau\approx15$ s that is under investigation here. Thus with the arrangement shown in Fig. 2 a temperature ''jump'' can be realized.

The temperature distribution on the free surface was detected with an infrared (IR) camera (temperature resolution 0.1°C) in fixed time-steps and stored for later data processing. In addition

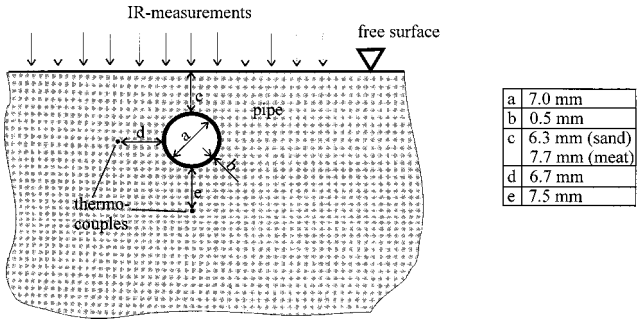

Fig. 2 Geometrical details of the experimental arrangement

we mounted two thermocouples in roughly the same distance from the heat transfer surface as in the study by Mitra et al. (temperature uncertainty $\pm0.2°\mathrm{C}$).

4 Experimental Results

With the experimental setup shown in Fig. 2 we studied the unsteady heat conduction behavior of processed meat and dry sand. Figure 3 shows a typical result for processed meat. The three temperature curves $\Theta(t)$, detected with the IR-camera show the increase of the nondimensional surface temperature with time at three different points right above the pipe. There is definitely no indication for non-Fourier behavior. Especially where, according

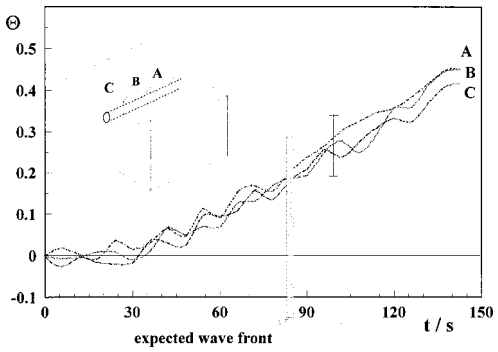

Fig. 3 Nondimensional temperature $\Theta=(T-T_w)/((T_c-T_w)/2)$ of processed meat at points A, B, and C at the free surface (see inserted sketch for these points); IR-thermography ($T_w=17.5°\mathrm{C}$ (initial temperature), $T_c=4.7°\mathrm{C}$ (water/pipe temperature after temperature jump))

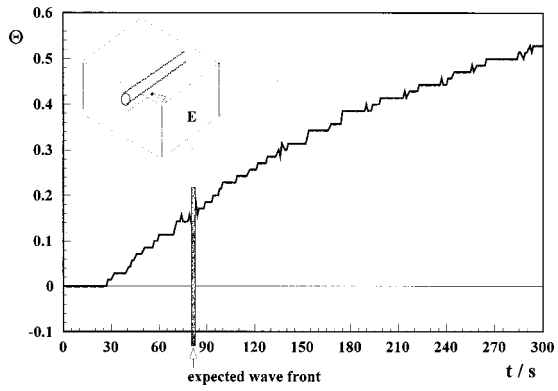

Fig. 4 Nondimensional temperature $\Theta=(T-T_w)/((T_c-T_w)/2)$ of dry sand at point E_i thermocouple reading ($T_w=21.0°\mathrm{C}$ (initial temperature), $T_c=7.0°\mathrm{C}$ (water/pipe temperature after temperature jump))

to [3], the wave front with a sharp temperature increase should be expected, we found a perfectly smooth Fourier-like behavior. Exactly the same holds for dry sand. For dry sand in Fig. 4 we show the reading of the thermocouple located $e=7.5$ mm below the pipe (see Fig. 2 for this location). Again, no non-Fourier behavior could be found.

In order to verify our assumption of a Fourier-like behavior we compared our experimental results to numerical solutions of the Fourier heat conduction equation. With initial and boundary conditions that simulate our experiments, the numerical solutions based on Fourier law compare very well with our experiments.

5 Conclusions

Our experimental results can be summarized by the statement: there is no evidence of non-negligible non-Fourier heat conduction effects for the materials and parameter ranges under consideration. Contrary results published recently by [3] and [4] from the authors point of view are doubtful. Several attempts by the authors to discuss the discrepancies remained unanswered. Maybe this study can help to settle this dispute in one way or the other.

A recent publication by Tzou and Chen [7] shows that non-Fourier behavior is still under investigation and of real interest. They found that time constants for these effects are of the order of micro to picoseconds which, however, are several orders of magnitude smaller than the time constants questioned in this study.

Nomenclature

C = thermal wave speed, m/s
c_p = specific heat capacity, m^2/s^2 K
k = thermal conductivity, W/mK
$\mathbf{q}$ = heat flux vector, W/m^2
T = temperature, °C
t = physical time, s
α = thermal diffusity, m^2/s
ρ = density, kg/m^3
Θ = nondimensional temperature
τ = relaxation time constant, s
ζ = nondimensional time

References

[1] Özisik, M. N., and Tzou, D. Y., 1994, ''On the Wave Theory in Heat Conduction,'' ASME J. Heat Transfer, **116**, pp. 526–535.
[2] Li, J. D., Gu, Y., and Guo, Z. Y., 1993, ''The Thermal Wave Phenomena and Analysis in the Pulse-Laser Processing for the Reduction of Core Loss in Silicon Steels,'' presented at 4th National Conference of Thermophysics, Hongzhou, P.R.C. (in Chinese).
[3] Mitra, K., Kumar, S., Vedavarz, A., and Moallemi, M. K., 1995, ''Experimental Evidence of Hyperbolic Heat Conduction in Processed Meat,'' ASME J. Heat Transfer, **117**, pp. 568–573.
[4] Kaminski, W., 1990, ''Hyperbolic Heat Conduction Equation for Materials With a Nonhomogeneous Inner Structure,'' ASME J. Heat Transfer, **112**, pp. 555–560.
[5] Cattaneo, C., 1958, ''A Form of Heat Conduction Equation Which Eliminates the Paradox of Instananeous Propagation,'' C. R. Acad. Sci. Paris, **247**, pp. 431–433.
[6] Vernotte, P., 1958, ''Les Paradoxes de la Theorie Continue de l'Equation de la Chaleur,'' C. R. Acad. Sci. Paris, **246**, pp. 3154–3155.
[7] Tzou, D. Y., and Chen, J. K., 1998, ''Thermal Lagging in Random Media,'' J. Thermophys. Heat Transfer, **12**, pp. 567–574.

Equivalent Thermal Resistance of a Corrugated Contact Boundary

C. Y. Wang
Mem. ASME, Departments of Mathematics and Mechanical Engineering, Michigan State University, East Lansing, MI 48824

The heat conduction across a corrugated contact boundary between two different materials is solved by perturbations.

[S0022-1481(00)00802-1]

Keywords: Conduction, Contact Resistance, Heat Transfer

1 Introduction

When different materials are bonded together there exists a contact resistance which often reduces thermal energy transfer. If the bonding surface is flat, then one-dimensional analysis is sufficient to determine the thermal resistance ([1], [2]). Consider a corrugated bonding surface, which may be due to surface roughness such as that from machining, or may be intentional in order to increase adhesion. Fletcher [3] noted bonding corrugations increase interface surface area and may enhance energy transfer. The present note is an analytic study of the effect of corrugation on the overall thermal resistance. The amplitude of the surface is assumed to be small compared to its wavelength, such that perturbation theory can be applied.

2 Formulation

Figure 1 shows a corrugated boundary $y'=cg(x'/l)$ separates two different materials designated I and II. The amplitude of the surface is c and the period is $2\pi l$. In order to determine the thermal resistance, impose a constant flux $-q$ at $y'\to\infty$. The boundary condition at infinity is

$$-q=-\kappa_{\mathrm{I}}\left.\frac{\partial T_{\mathrm{I}}'}{\partial y'}\right|_{\infty}=-\kappa_{\mathrm{II}}\left.\frac{\partial T_{\mathrm{II}}'}{\partial y'}\right|_{-\infty}. \tag{1}$$

Here T' is the temperature and κ is the thermal conductivity. On the corrugated boundary the conditions are

$$T_{\mathrm{I}}'-T_{\mathrm{II}}'=\frac{\kappa_{\mathrm{I}}}{h}\frac{\partial T_{\mathrm{I}}'}{\partial n'},\quad \kappa_{\mathrm{I}}\frac{\partial T_{\mathrm{I}}'}{\partial n'}=\kappa_{\mathrm{II}}\frac{\partial T_{\mathrm{II}}'}{\partial n'} \tag{2}$$

where h is the interface transfer coefficient specific to the bonding ([2]) and n' is the unit normal to the wavy surface. Normalize all lengths by l, the temperatures by ql/κ_{I} and drop primes. The governing equation is

$$\nabla^2 T_{\mathrm{I}}(x,y)=0,\quad \nabla^2 T_{\mathrm{II}}(x,y)=0. \tag{3}$$

The wavy boundary becomes $y=\varepsilon g(x)$ where $\varepsilon=c/l\ll 1$. The boundary conditions are

$$\left.\frac{\partial T_{\mathrm{I}}}{\partial y}\right|_{\infty}=1,\quad \left.\frac{\partial T_{\mathrm{II}}}{\partial y}\right|_{-\infty}=\frac{\kappa_{\mathrm{I}}}{\kappa_{\mathrm{II}}}\equiv\frac{1}{\alpha} \tag{4}$$

and on the corrugated surface

$$T_{\mathrm{I}}-T_{\mathrm{II}}=\beta\frac{\partial T_{\mathrm{I}}}{\partial n},\quad \frac{\partial T_{\mathrm{I}}}{\partial n}=\alpha\frac{\partial T_{\mathrm{II}}}{\partial n}. \tag{5}$$

Contributed by the Heat Transfer Division for publication in the JOURNAL OF HEAT TRANSFER. Manuscript received by the Heat Transfer Division April 29, 1999; revision received November 15, 1999. Associate Technical Editor: M. Hunt.

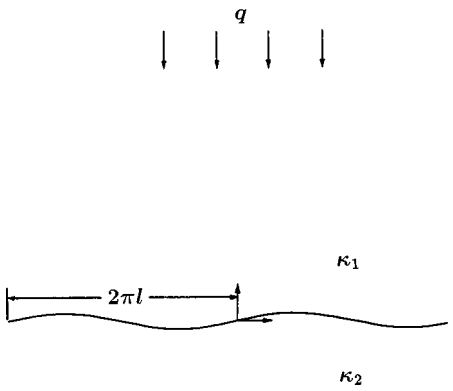

Fig. 1 The wavy bonding surface. Constant heat flux from above.

Here $\beta \equiv \kappa_1/(lh)$ is the normalized contact resistance. For perfect bonding $\beta = 0$. Due to the Neumann conditions at infinity, we can also stipulate $T_{\mathrm{I}}(0,0) = 0$. Eqs. (3)–(5) are to be solved.

3 Perturbation Solution

When the bonding surface is flat, $\varepsilon = 0$. The solution is $T_{\mathrm{I}} = y$, $T_{\mathrm{II}} = y/\alpha - \beta$. We perturb from this state

$$T_{\mathrm{I}} = y + \varepsilon t_1(x,y) + \varepsilon^2 t_2(x,y) + \cdots \tag{6}$$

$$T_{\mathrm{II}} = \frac{y}{\alpha} - \beta + \varepsilon s_1(x,y) + \varepsilon^2 s_2(x,y) + \cdots . \tag{7}$$

Then t_i, s_i satisfy Laplaces' equation. A Taylor series expansion about $y = 0$ gives

$$T_{\mathrm{I}}|_{\varepsilon g(x)} = T_{\mathrm{I}}|_0 + \varepsilon g(x) \left.\frac{\partial T_{\mathrm{I}}}{\partial y}\right|_0 + \varepsilon^2 \frac{g^2(x)}{2} \left.\frac{\partial^2 T_{\mathrm{I}}}{\partial y^2}\right|_0 + \cdots$$

$$= \varepsilon(t_1|_0 + g(x)) + \varepsilon^2(t_2|_0 + g(x) t_{1y}|_0) + \cdots . \tag{8}$$

The normal derivative needs some work. Note that

$$\frac{\partial}{\partial n} = \hat{n} \cdot \nabla = \frac{\nabla(y - \varepsilon g(x))}{|\nabla(y - \varepsilon g(x))|} \cdot \nabla = \frac{-\varepsilon g'(x) \dfrac{\partial}{\partial x} + \dfrac{\partial}{\partial y}}{\sqrt{1 + \varepsilon^2 (g'(x))^2}} . \tag{9}$$

Thus

$$\left.\frac{\partial T_{\mathrm{I}}}{\partial n}\right|_{\varepsilon g(x)} = 1 + \varepsilon t_{1y}|_0 + \varepsilon^2 \left[t_{2y}|_0 - g'(x) t_{1x}|_0 - \frac{1}{2}(g'(x))^2 + g(x) t_{1yy}|_0 \right] + \cdots \tag{10}$$

$$T_{\mathrm{II}}|_{\varepsilon g(x)} = -\beta + \varepsilon \left[s_1|_0 + \frac{1}{\alpha} g(x) \right] + \varepsilon^2 [s_2|_0 + g(x) s_{1y}|_0] + \cdots \tag{11}$$

$$\left.\frac{\partial T_{\mathrm{II}}}{\partial n}\right|_{\varepsilon g(x)} = \frac{1}{\alpha} + \varepsilon s_{1y}|_0 + \varepsilon^2 \left[s_{2y}|_0 - g'(x) s_{1x}|_0 - \frac{1}{2\alpha}(g'(x))^2 + g(x) s_{1yy}|_0 \right] + \cdots . \tag{12}$$

Comparing like powers of ε in Eq. (5) we find

$$t_1|_0 + g - s_1|_0 - \frac{g}{\alpha} = \beta t_{1y}|_0, \quad t_{1y}|_0 = \alpha s_{1y}|_0 \tag{13}$$

$$t_2|_0 + g t_{1y}|_0 - s_2|_0 - g s_{1y}|_0 = \beta \left(t_{2y}|_0 - g' t_{1x}|_0 - \frac{1}{2}(g')^2 + g t_{1yy}|_0 \right) \tag{14}$$

$$t_{2y}|_0 - g' t_{1x}|_0 + g t_{1yy}|_0 = \alpha(s_{2y}|_0 - g' s_{1x}|_0 + g s_{1yy}|_0). \tag{15}$$

Usually $g(x)$ has some symmetry such that it can be expanded in a Fourier series

$$g(x) = \sum_1^\infty c_n \sin(nx). \tag{16}$$

Since t_1 and s_1 satisfy the Laplace equation and are bounded at infinity they can be expressed as

$$t_1 = \sum_1^\infty a_n \sin(nx) e^{-ny} \quad s_1 = \sum_1^\infty b_n \sin(nx) e^{ny}. \tag{17}$$

The boundary conditions Eq. (13) then give, for each harmonic,

$$a_n = \frac{c_n(1-\alpha)}{\alpha + 1 + n\alpha\beta}, \quad b_n = \frac{c_n(1 - 1/\alpha)}{\alpha + 1 + n\alpha\beta}. \tag{18}$$

Because t_1 and s_1 has no mean, the changes in effective resistance of the bonding enters in the next order. Let an overbar denote the mean over a period. The governing equation is

$$\overline{t_{2yy}} = 0, \quad \overline{s_{2yy}} = 0. \tag{19}$$

Equations (14) and (15) become

$$\overline{t_2}|_0 - \frac{1}{2} \Sigma n c_n (a_n + b_n) - \overline{s_2}|_0 = \beta \left(\overline{t_{2y}}|_0 - \frac{1}{4} \Sigma n^2 c_n^2 \right) \tag{20}$$

$$\overline{t_{2y}}|_0 = \alpha \overline{s_{2y}}|. \tag{21}$$

Since $\overline{t_2}$ and $\overline{s_2}$ are bounded at infinity, Eq. (19) shows they can only be constants. Thus to an observer at infinity,

$$T_{\mathrm{I}} \sim y + \varepsilon^2 \overline{t_2}, \quad T_{\mathrm{II}} \sim \frac{y}{\alpha} - \beta + \varepsilon^2 \overline{s_2}. \tag{22}$$

The additional temperature drop is $\varepsilon^2(\overline{t_2} - \overline{s_2}) \equiv \varepsilon^2 D$ where

$$D = \frac{1}{2} \Sigma n c_n (a_n + b_n) - \frac{\beta}{4} \Sigma n^2 c_n^2$$

$$= \Sigma \frac{n c_n^2}{2} \left[\frac{2 - \alpha - 1/\alpha}{\alpha + 1 + n\alpha\beta} - \frac{n\beta}{2} \right] \leqslant 0. \tag{23}$$

Since the total (dimensional) temperature drop due to the bonding surface is $(\beta + \varepsilon^2 D) g l/\kappa_{\mathrm{I}} = g/h + \varepsilon^2 D g l/\kappa_{\mathrm{I}}$, negative D means a smaller equivalent contact resistance $\overline{\beta}$,

$$\overline{\beta} = \beta + \varepsilon^2 D. \tag{24}$$

Thus the thermal conductivity is equivalent to a flat bonding surface with an higher interface transfer coefficient $\overline{h} = \kappa_{\mathrm{I}}/(l\overline{\beta})$.

4 Examples and Finite Thickness Effects

The basic wavy bonding surface is sinusoidal, $g(x) = \sin x$, where $c_1 = 1$ and all other Fourier coefficients are zero. Equation (23) gives

$$D = \frac{1}{2} \left[\frac{2 - \alpha - 1/\alpha}{\alpha + 1 + \alpha\beta} - \frac{\beta}{2} \right], \tag{25}$$

the value of $-D$ is plotted in Fig. 2 where we see that D has an extremum when the materials are same ($\alpha = 1$). Equivalent contact resistance is decreased for increased β and increased $|\alpha - 1|$.

For a saw-tooth bonding surface

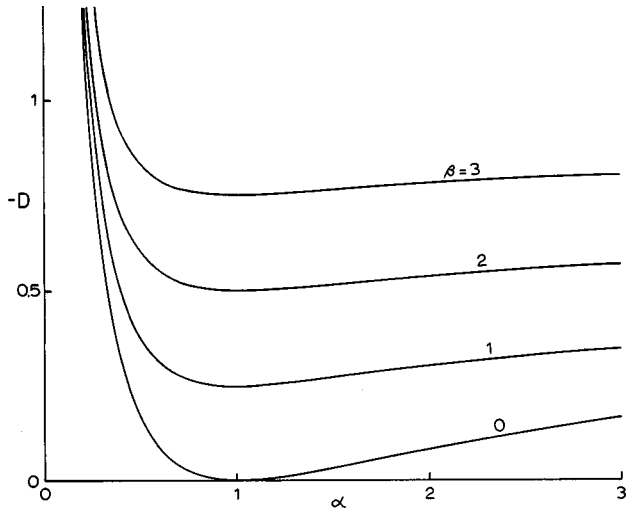

Fig. 2 Normalized additional temperature drop D versus conductivity ratio $\alpha=\kappa_{II}/\kappa_I$ for various constant normalized contact resistance $\beta=\kappa_I/(lh)$ (sinusoidal surface, Eq. (25))

$$g(x)=\Sigma c_n \sin(nx)=\begin{cases}\dfrac{2x}{\pi} & -\dfrac{\pi}{2}<x<\dfrac{\pi}{2}\\[2ex] 2-\dfrac{2x}{\pi} & \dfrac{\pi}{2}<x<\dfrac{3\pi}{2}.\end{cases} \tag{26}$$

Equation (23) gives

$$D=\sum_{n=1,3,5}^{\infty}\frac{32}{\pi^4 n^3}\left[\frac{2-\alpha-1/\alpha}{\alpha+1+n\alpha\beta}-\frac{n\beta}{2}\right]. \tag{27}$$

The dominant term is $n=1$, thus the behavior is essentially similar to that of the sinusoidal bonding surface shown in Fig. 2.

We considered the bonding of the two semi-infinite domains. A question is whether the results can be applied to finite thickness layers. To illustrate, let the upper layer (Region I) be finite with the boundary at $y=\lambda$. Equation (17) is replaced by

$$t_1=\sum_{1}^{\infty} a_n \sin(nx)\frac{\cosh[n(y-\lambda)]}{\cosh(n\lambda)}. \tag{28}$$

Without going through the details, we find

$$D=\Sigma\frac{nc_n^2}{2}\left[\frac{(2-\alpha-1/\alpha)\tanh(n\lambda)}{\alpha+\tanh(n\lambda)(1+n\alpha\beta)}-\frac{n\beta}{2}\right]. \tag{29}$$

Equation (29) reduces to Eq. (23) if $\tanh(n\lambda)\approx 1$. Thus if $\lambda>2.1$ one can consider the finite layer as infinite, with error less than three percent.

5 Conclusion

Our analysis shows the effect of corrugations of the bonding surface is equivalent to a flat bonding surface with a decreased contact resistance. Equation (24) shows this decrease is proportional to amplitude ratio squared and a function $D\leqslant 0$ which depends nonlinearly on the ratio of conductivities α and the original normalized contact resistance β. This decrease can be partially attributed to an increase in the conducting surface area.

The present analysis assumes small amplitude corrugations. Our results for equivalent thermal resistance have an error of $0(\varepsilon^4)$. For more convoluted contact surfaces, such as those occurring in biology, the thermal resistance would be lowered as well. Wang [4] studied the related problem of heat transfer across a homogeneous saw-tooth wavy plate. Although there are no contact boundaries, the increase in surface area does enhance heat transfer.

The present work can also be applied to mass transfer across corrugated membranes.

References

[1] Schneider, P. J., 1985, ''Conduction'' *Handbook of Heat Transfer—Fundamentals*, 2nd Ed., W. M. Rohsenow, J. P. Hartnett, and E. N. Ganic, eds., McGraw-Hill, New York, Chapter 4.
[2] Gebhart, B., 1993, *Heat Conduction and Mass Diffusion*, McGraw-Hill, New York, Chapter 2.
[3] Fletcher, L. S., 1988, ''Recent Developments in Contact Conductance Heat Transfer,'' ASME J. Heat Transfer, **110**, pp. 1059–1070.
[4] Wang, C. Y., 1995, ''Diffusion Across a Corrugated Saw-Tooth Plate,'' Mech. Res. Commun., **22**, pp. 589–597.

Evaluation of a Two-Dimensional Conductivity Function Based on Boundary Measurements

M. Tadi
Department of Mathematics, University of North Carolina at Charlotte, Charlotte, NC 28223

This paper is concerned with an inverse problem for the conduction of heat in a two-dimensional domain. It seeks to recover the subsurface conductivity profile based on the measurements obtained at the boundary. The method considers a temporal interval for which time-dependent measurements are provided. It formulates an optimal estimation problem which seeks to minimize the error difference between the given data and the response from the system. It uses a combination of the zeroth-order and the first-order Tikhonov regularization to stabilize the inversion. The method leads to an iterative algorithm which, at every iteration, requires the solution to a two-point boundary value problem. A number of numerical results are presented which indicate that a close estimate of the thermal conductivity function can be obtained based on the boundary measurements only.
[S0022-1481(00)00902-6]

Keywords: Computational, Conduction, Heat Transfer, Inverse, Modeling, Transient

1 Introduction

In this note we consider the problem of recovering the thermal conductivity profile based on the temperature measurements obtained at the boundary. We consider a two-dimensional material whose thermal conductivity is a function of space. Such problems are known as inverse problems, where the interest is to recover an unknown system parameter based on the output measurements from the system. Inverse problems appear in various fields of study and numerous methods have been developed for specific applications ([1–3]). For applications involving nondestructive evaluation, NDE, also known as thermal imaging, one makes use of laser sources to illuminate an external surface of the material in order to induce thermal waves. The interactions of the thermal wave field with the material inhomogeneities give rise to the scattered fields which propagate and are ultimately measured at the

Contributed by the Heat Transfer Division for publication in the JOURNAL OF HEAT TRANSFER. Manuscript received by the Heat Transfer Division, May 15, 1999; revision received, December 9, 1999. Associate Technical Editor: T. Avedisian.

surface of the material. The inverse problem of interest in this paper is to recover subsurface material properties based on the given temperature measurements and the specified applied heat flux.

Motivated by numerous physical applications, inverse problems for parabolic systems have received considerable attention. Recent results include a linearization method which has been developed and applied to an inverse problem in optical tomography ([4]), a spectral method for solving the sideway heat equations ([5]), and a discrete diffusive model for the recovery of the absorption coefficient from diffused reflected light ([6]). Additional methods for various applications include nonlinear optimization using genetic algorithms ([7]) and Marquardt' procedure ([8]). Thermal wave slice tomography has also been developed for applications in thermal imaging ([9,10]). Approximate methods such as Born iterations ([11]) have also been developed for applications in recovering permittivity distribution. Additional results have also been reported which deal with the existence and uniqueness of the solution to the inverse problems involving such systems ([12–14]).

The purpose of this note is to consider an inverse heat conduction problem for a two-dimensional domain. The inverse problems for higher dimensions are more complicated. However, in two-dimensional domains it is also physically possible to collect measurements at more than one location on the boundary. The present formulation considers a temporal interval during which time-dependent measurements are provided, and introduces regularization terms at the boundary of this temporal interval. In Section 2 we present the formulation and obtain the associated two-point boundary value problem. We also present the algorithm in detail. In Section 3 we discuss the numerical scheme that is used to integrate the working equations and present a number of numerical examples, and Section 4 is devoted to the closing remarks.

2 Formulations of the Optimal Estimation Problem

Consider the conduction of heat in the two-dimensional domain shown in Fig. 1. Let the material thermal conductivity, i.e., $k(x,y)$, be a function of space. The conduction of heat is governed by the Fourier's law given by

$$T_t=(kT_x)_x+(kT_y)_y, \quad t\in[0:\tau], \quad x\in[0:l], \quad y\in[0:h], \tag{1}$$

where $T(t,x,y)$ is the material temperature. For simplicity, we are assuming that the material density and specific heat are constants and are equal to one. The heat flux is specified at the surrounding boundaries except at the bottom surface for which the temperature is specified. The material is heated at the boundaries and at the same time the value of the temperature is also collected at the boundaries. For example, if the material is heated at one location x_1 on the top surface, then the appropriate boundary and initial conditions are given by

$$T(0,x,y)=T(t,x,0)=T_x(t,0,y)=T_x(t,l,y)=0,$$
$$kT_y(t,x,h)=g(t,x), \tag{2}$$

where $g(t,x)$ is an applied heat flux which is specified. The temperature is also recorded at the boundary, i.e., at $x=x_1$ on the top surface. The inverse problem is then to recover the subsurface thermal conductivity profile, $k(x,y)$, based on the given data and the known applied heat. For more measurement points or more applied heat fluxes additional terms can be added to the formulation. The data are then given in the form

$$y(t)=\int_0^l T(t,x,h)\hat{\delta}_1 dx, \tag{3}$$

where $\hat{\delta}_1=\delta(x-x_1)$ is the Dirac delta function centered at $x=x_1$.

The approach is based on considering a temporal interval, $[0:\tau]$, during which the system output measurements are provided. We then formulate an optimal estimation problem which seeks to minimize the error diference between the given data and the output response from the system. In other words we seek to minimize a cost functional given by

$$J=\frac{1}{2}\int_0^\tau\left[y(t)-\int_0^l T(t,x,h)\hat{\delta}_1 dx\right]^2 dt. \tag{4}$$

The direct solution to the above minimization problem requires the assumed conductivity profile to suddenly change to the actual value, which almost always, becomes numerically unstable. We can regularize this process by introducing a bound on the changes that can occur to the conductivity after each iteration. The appropriate term to add to the cost functional is given by $\int_0^l\int_0^h(\delta k)^2 dxdy$, which is the zeroth-order Tikhonov regularization ([2]). By putting a bound on the change in the unknown function, δk, we are essentially eliminating large deviations form the initial guess for the unknown. Initial investigations have shown that the zeroth-order regularization alone results in highly oscillatory conductivity functions and higher-order regularization is needed to further stabilize the inversion. Therefore, the appropriate cost functional is given by

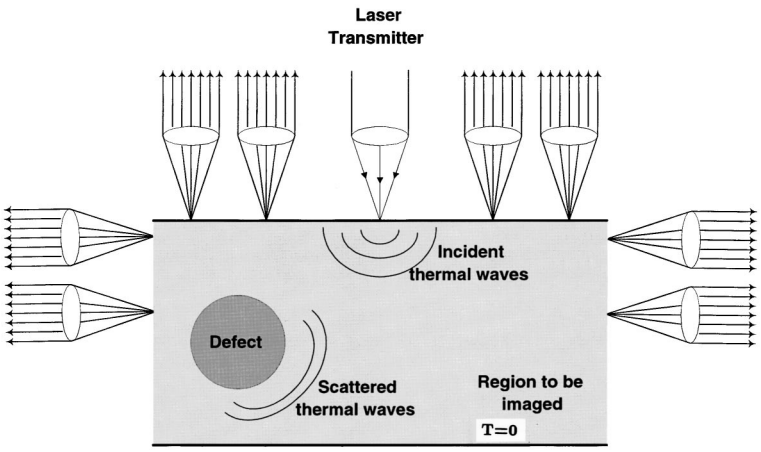

Fig. 1 A two-dimensional domain

$$J=\frac{1}{2}\int_0^{\tau}\left[y(t)-\int_0^{l}T(t,x,h)\hat{\delta}_1 dx\right]^2 dt+\frac{\alpha}{2}\int_0^{l}\int_0^{h}(\delta k)^2 dxdy + \frac{\beta}{2}\int_0^{l}\int_0^{h}[(k_x)^2+(k_y)^2]dxdy. \quad (5)$$

The parameter β is a positive constant chosen by the designer. It limits the slope of the sought after function in space. Often the unknown function has sharp discontinuity in space and the algorithm should be allowed to converge to a function with nonzero slopes in space. Therefore, choosing a large value for β will limit the ability of the algorithm to converge to the true function. By reducing the value of the parameter β we can essentially allow the algorithm to converge to an approximation to the solution, which is often a function with nonzero slopes in space, and at the same time eliminate unwanted oscillations in the solution by requiring some degree of smoothness. We can obtain a good guess for this parameter after a few iterations. The parameter α is also chosen in a similar manner. This parameter controls how fast the conductivity can change after each iteration. For large values of α the algorithm limits the change in the conductivity δk and, therefore, the convergence is slow. For small values of α the convergence is faster. In the limiting case when $\alpha\rightarrow 0$, the algorithm is ill-posed and numerical instability sets in. A suitable value can be chosen after a few initial trials. Once an initial value for the α is chosen, then reducing its value as the iteration proceeds increases the speed of the convergence. The above cost functional is minimized subject to the heat conduction equation, Eq. (1). We can form an unconstrained minimization problem using the Lagrange multipliers. The modified objective functional is given by

$$J=\frac{1}{2}\int_0^{\tau}\left[y(t)-\int_0^{l}T(t,x,h)\hat{\delta}_1 dx\right]^2 dt+\frac{\alpha}{2}\int_0^{l}\int_0^{h}(\delta k)^2 dxdy + \frac{\beta}{2}\int_0^{l}\int_0^{h}(k_x)^2+(k_y)^2 dxdy + \int_0^{\tau}\int_0^{l}\int_0^{h}\lambda(T_t-(kT_x)_x-(kT_y)_y)dxdydt, + \int_0^{\tau}\int_0^{l}\int_0^{h}\sigma k_t dxdydt, \quad (6)$$

where $\lambda(t,x,y),\sigma(t,x,y)$ are the Lagrange multipliers. Note that we are also enforcing the condition $k_t(t,x,y)=0$ through the use of the Lagrange multiplier σ. This is similar to the Kalman filtering approach for the estimation problems involving ordinary differential equations ([15]). Similar approach is also used in adjoint methods for continuous systems ([3]). Necessary minimization conditions are obtained by setting the first variation of J equal to zero. It follows that

$$\delta J=\int_0^{\tau}\left[-\hat{y}\int_0^{l}\delta T(t,x,h)\hat{\delta}_1 dx\right]dt + \int_0^{\tau}\int_0^{l}\int_0^{h}\delta\lambda(T_t-(kT_x)_x-(kT_y)_y)dxdydt + \int_0^{\tau}\int_0^{l}\int_0^{h}\lambda(\delta T_t-\delta(kT_x)_x-\delta(kT_y)_y)dxdydt + \alpha\int_0^{l}\int_0^{h}\delta(\delta k)\delta k dxdy+\frac{\beta}{2}\int_0^{l}\int_0^{h}(\delta(k_x)^2+\delta(k_y)^2)dxdy + \int_0^{\tau}\int_0^{l}\int_0^{h}(\delta\sigma k_t+\sigma\delta k_t)dxdydt, \quad (7)$$

where $\hat{y}$ is the error and is given by

$$\hat{y}(t)=y(t)-\int_0^{l}T(t,x,h)\hat{\delta}_1 dx, \quad (8)$$

and the term $\delta(\delta k)=\Delta k$ is the second variation of the thermal conductivity at time $t=0$. After integrating various terms by parts and using the fact that the state variables can have arbitrary variations, we can arrive at the equations for the adjoint system given by

$$\lambda_t-(k\lambda_x)_x-(k\lambda_y)_y=0 \quad (9)$$

$$\sigma_t-\lambda_x T_x-\lambda_y T_y=0. \quad (10)$$

The boundary conditions are given by

$$\lambda_x(t,0,y)=\lambda_x(t,l,y)=\lambda(t,x,0)=\lambda(\tau,x,y)=\sigma(\tau,x,y)=0, \quad \lambda_y k(t,x,h)=\hat{y}(t)\hat{\delta}_1. \quad (11)$$

The error $\hat{y}(t)$ appears as a flux boundary condition for the adjoint variable. Note that we are neglecting the boundary terms that appear from performing the integration by parts on the regularization terms k_x, k_y. We now have a complete two-point boundary value problem involving T, λ, σ, and k. The forward problem is given by the heat conduction equation, Eq. (1), and $k_t=0$ with the appropriate boundary conditions given by Eqs. (2). The adjoint equations are given by Eqs. (9)–(10), for which the appropriate boundary conditions are given by Eqs. (11). The solution to this TPBVP provides the change that needs to occur at thermal conductivity, i.e.,

$$k=k_0+\Delta k, \quad \Delta k=\frac{1}{\alpha}[\sigma(t,x,y)|_{t=0}-\beta(k_{xx}+k_{yy})]. \quad (12)$$

The error between the given measurements and the response from the system $\hat{y}(t)$ which is given in Eq. (9) enters as a boundary condition for the adjoint equation, i.e., Eqs. (10)–(11). The adjoint equations are solved backward from $t=\tau$ to $t=0$, starting from the final conditions

$$\lambda(\tau,x,y)=0, \quad \sigma(\tau,x,y)=0. \quad (13)$$

Therefore, the only nonzero component is introduced into λ and, in turn into σ, through the error $\hat{y}(t)$. For vanishing error, the adjoint variables are equal to zero everywhere for all times and, as a result, $\Delta k=\sigma(0,x,y)=0$, after which convergence is obtained. We can now formulate an iterative algorithm.

2.1 Algorithm

1 Assume a distribution for the conductivity k_0 and using the appropriate boundary conditions, solve the heat equation forward from $t=0$ to $t=\tau$, thereby obtaining the error given by Eq. (8). Store the value of, $T_x(t,x,y)$ and $T_y(t,x,y)$ for $t\in[0:\tau]$.

2 Use the boundary conditions for λ and solve the adjoint equation backward from $t=\tau$ to $t=0$. Simultaneously, use the stored values for T_x and T_y and solve the equation for the adjoint variable σ, i.e., Eq. (10).

3 Update the value of the conductivity according to Eq. (12) and repeat the processes 1–3, until the errors are arbitrarily small.

We next use a number of numerical examples to show the applicability of the algorithm and explain the method in detail.

3 Numerical Approximations and Examples

The forward equations and the adjoint equations are similar except for their boundary conditions at the top surface. A finite volume formulation ([16]) can be used for the spacial dimension and the implicit Crank-Nicolson method can be used for the time integration. At every time-step, this approach requires the solution to a large sparse linear system of equations which is solved using a conjugate gradient method with incomplete factorization ([17]). We consider the geometry given in Fig. 2 and let $l=1.0$ and h

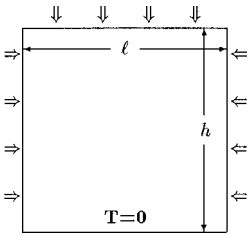

Fig. 2 A two-dimensional domain

$=1.0$. The spatial step size in the x and y-directions is equal and is given by $\Delta x=\Delta y=1.0/50$. Also the time-step size is equal to $\Delta t=0.002$. (See Fig. 2.)

3.1 Example 1. Consider the problem of recovering a two-dimensional profile given in Fig. 3. The temperature at the bottom surface is set equal to zero and no measurement is collected there. The heat is applied at four points on each of the remaining three surfaces. The points are equally spaced, i.e., $x_1=.2$, $x_2=.4$, $x_3=.6$, and $x_4=.8$. A smooth Gaussian function in both time and space is used to model the heat flux at a point. For the top surface we have

$$g(t,x)=\exp\left[-\frac{(t-0.1)^2}{0.001}\right]\exp\left[-\frac{(x-x_i)^2}{0.0005}\right], \quad i=1,4, \quad (14)$$

and for the sides, we have

$$g(t,y)=\exp\left[-\frac{(t-0.1)^2}{0.001}\right]\exp\left[-\frac{(y-y_i)^2}{0.0005}\right], \quad i=1,4 \quad (15)$$

for both $x=0$ and $x=l$. The temperature is measured at all 12 points and are provided for the inverse problem. We are using only three sides of the object for measurements. This situation is often encountered in the application where parts of the boundary cannot be accessed for measurements. We first solve the forward problem and obtain the temperatures, i.e., $T_i(t)$, $i=1,12$. The temperatures are then provided as observations for the inverse problem. The time τ should be chosen large enough so that there is enough time for the heat to diffuse into the material. For our purpose, we provide the data for up to $\tau=1.0$. We then use the above algorithm to recover the conductivity function.

The parameter β is chosen as $\beta=0.3\times10^{-7}$ and the parameter α is chosen as $\alpha=0.015$. These values were chosen after a few initial trials. Figure 4 shows the conductivity profile after 1800 iterations. Comparing Fig. 4 to the actual conductivity function given in Fig. 3 shows that a good estimate of the unknown profile can be recovered. The parameter α is reduced gradually to improve the convergence.

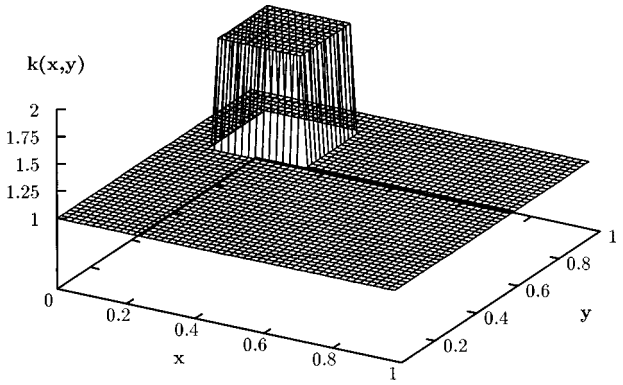

Fig. 3 The unknown conductivity profile to be recovered in example 1

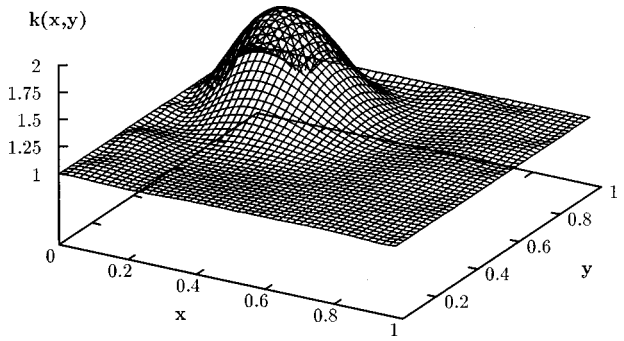

Fig. 4 The conductivity profile after 1800 iterations for example 1

3.2 Example 2. In this example we apply the method to recover the conductivity profile given in Fig. 5. Figure 6 shows the computed value of the unknown function after 1800 iterations. Figures 7 and 8 compare the actual function to the computed functions at two values of y, i.e., $y=0.375$ and $y=0.82$. Results at these two intersections indicate that for sharply discontinuous functions the method can recover a function which is a close approximation to the function. This is somewhat expected due to the smoothing character of the heat conduction equation. Figure 9 shows the monotonic reduction in the error as a function of the number of iterations, and Fig. 10 shows a contour plot of the error after 1800 iterations for this example. As is expected there exists some error close to the location of the sharp discontinuities in the sought-after unknown function.

All of the iterations are started from the nominal value of $k=1$. In all the examples we are collecting data at 12 locations on

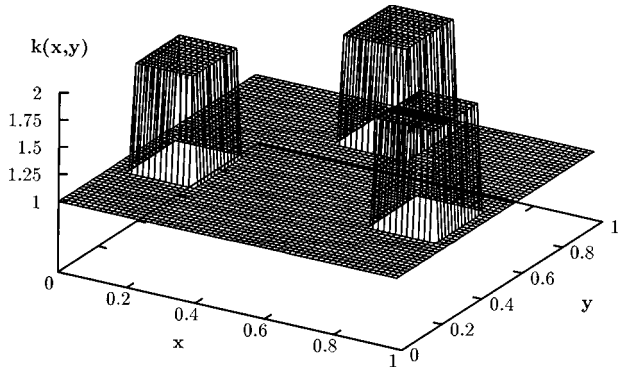

Fig. 5 The unknown conductivity profile to be recovered in example 2

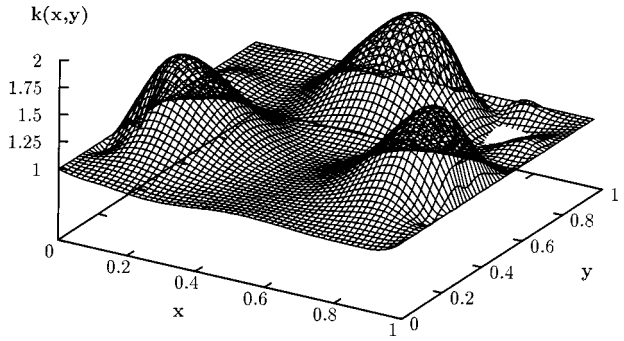

Fig. 6 The conductivity profile after 1800 iterations for example 2

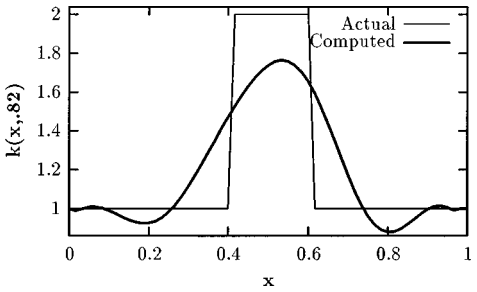

Fig. 7 The actual and computed conductivity profile at $y = 0.82$ for example 2

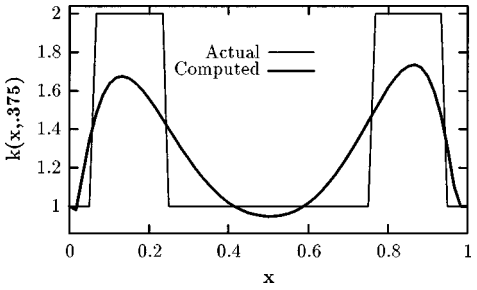

Fig. 8 The actual and computed conductivity profile at $y = 0.375$ for example 2

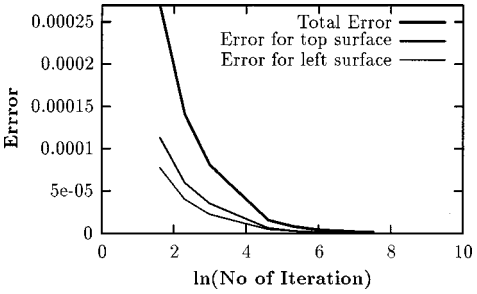

Fig. 9 The monotonic reduction in error for example 2 as a function of the number of iterations

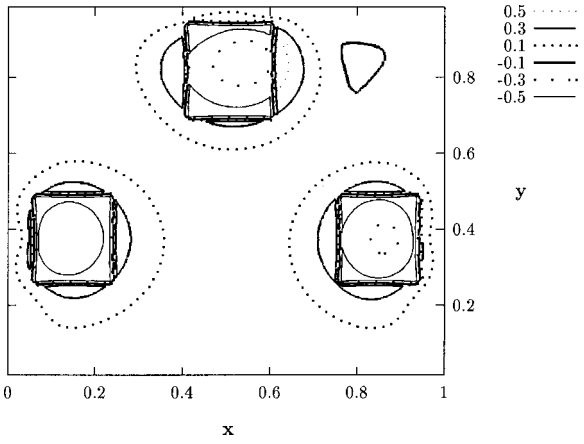

Fig. 10 A contour plot of the error after 1800 iterations for example 2

the boundary. In a diffusive system, the perturbation applied at one point in the domain affects the entire domain instantly and, in principle, it is not necessary to provide numerous observations. However, providing additional observations enhances the convergence of the scheme. It is also physically possible to collect temperature measurements at the boundaries. We have considered a one-dimensional version of this problem in ([18]) where the inversion was based on the data collected at one point. In that problem a zeroth-order regularization term was able to stabalize the inversion. For the two-dimensional problem studied here, first-order regularization was also needed for the inversion problem. In all the cases the iterations can be continued and the results can be further improved. Increasing the number of mesh points in both x and y directions can also improve the convergence at the expense to the computational time due to the implicit nature of the time integration.

4 Conclusions

In this paper we studied the problem of thermal imaging for a two-dimensional domain. The proposed method is based on a variational formulation which seeks to minimize a given cost functional. The inversion is stabilized by making use of the zeroth-order and the first-order Tikhonov regularizations. We used a standard finite volume scheme to solve the associated initial/boundary value problems which is general and can be applied to any geometry under various conditions.

References

[1] Beck, J. V., Blackwell, B., and St. Clair, C. R., 1985, *Inverse Heat Conduction: Ill-Posed Problems*, Wiley-Interscience, New York.

[2] Tikhonov, A. N., and Arsenin, V., 1977, *Solutions of Ill-Posed Problems*, John Wiley and Sons, New York.

[3] Alifanov, O. M., Mayinger, E., Bergles, A. E., and Grigull, U., 1994, *Inverse Heat Transfer Problems*, Springer-Verlag, New York.

[4] Klibanov, M. V., and Lucas, T. R., 1999, ''Numerical Solutions of a Parabolic Inverse Problem in Optical Tomography Using Experimental Data,'' SIAM (Soc. Ind. Appl. Math.) J. Appl. Math., **59**, pp. 1763–1789.

[5] Berntsson, F., 1999, ''A Spectral Method for Solving the Sideways Heat Equation,'' Inverse Probl., **15**, pp. 891–906.

[6] Martiz, M. F., Herman, G. T., and Yee, C., 1998, ''Recovery of the Absorption Coefficient From Diffused Reflected Light Using a Discrete Diffusive Model,'' SIAM (Soc. Ind. Appl. Math.) J. Appl. Math., **59**, pp. 58–71.

[7] Stoffa, P. L., and Sen, M. K., 1991, ''Nonlinear Multiparameter Optimization Using Genetic Algorithms: Inversion of Plane-Wave Seismograms,'' Geophysics, **56**, pp. 1794–1810.

[8] Keys, R., 1986, ''An Application of Marquardt's Procedure to the Seismic Inversion Problem,'' IEEE Proc., **74**, p. 476.

[9] Pade, O., and Mandelis, A., 1993, ''Computational Thermal-Wave Slice Tomography With Back-Propagation and Transmission Reconstructions,'' Rev. Sci. Instrum., **64**, pp. 3548–3562.

[10] Pade, O., and Mandelis, A., 1994, ''Thermal-Wave Slice Tomography Using Wave-Field Reconstruction,'' Inverse Probl., **10**, pp. 185–197.

[11] Chew, W., and Wang, Y., 1990, ''Reconstruction of Two-Dimensional Permittivity Distribution Using the Distorted Born Iterative Method,'' IEEE Trans. Med. Imaging, **9**, No. 2, pp. 218–225.

[12] Knowles, I., 1999, ''Uniqueness for an Elliptic Inverse Problem,'' SIAM (Soc. Ind. Appl. Math.) J. Appl. Math., **59**, pp. 1356–1370.

[13] Isakov, V., 1999, ''Some Inverse Problems for the Diffusion Equation,'' Inverse Probl., **15**, pp. 3–10.

[14] Gatti, S., 1998, ''An Existance Result for an Inverse Problem for a Quisilinear Parabolic Equation,'' Inverse Probl., **14**, pp. 53–65.

[15] Anderson, B. D. O., and Moore, J. B., 1990, *Optimal Control, Linear Quadratic Methods*, Prentice-Hall, Englewood Cliffs, NJ.

[16] Patankar, S. P., 1980, *Numerical Heat Transfer and Fluid Flow*, Taylor & Francis, New York.

[17] Axelsson, O., 1996, *Iterative Solution Methods*, Cambridge University Press, New York.

[18] Tadi, M., 1997, ''Inverse Heat Conduction Based on Boundary Measurements,'' Inverse Probl., **13**, pp. 1585–1605.

Fractional-Diffusion Solutions for Transient Local Temperature and Heat Flux

V. V. Kulish
Assoc. Mem. ASME, Assistant Professor, School of Mechanical and Production Engineering,
Nanyang Technological University, Singapore 639798

J. L. Lage
Mem. ASME, Associate Professor, Mechanical Engineering Department, Southern Methodist University, Dallas, TX 75275-0337
e-mail: jll@seas.smu.edu

Applying properties of the Laplace transform, the transient heat diffusion equation can be transformed into a fractional (extraordinary) differential equation. This equation can then be modified, using the Fourier Law, into a unique expression relating the local value of the time-varying temperature (or heat flux) and the corresponding transient heat flux (or temperature). We demonstrate that the transformation into a fractional equation requires the assumption of unidirectional heat transport through a semi-infinite domain. Even considering this limitation, the transformed equation leads to a very simple relation between local time-varying temperature and heat flux. When applied along the boundary of the domain, the analytical expression determines the local time-variation of surface temperature (or heat flux) without having to solve the diffusion equation within the entire domain. The simplicity of the solution procedure, together with some introductory concepts of fractional derivatives, is highlighted considering some transient heat transfer problems with known analytical solutions. [S0022-1481(00)01002-1]

Keywords: Conduction, Heating, Heat Transfer, Transient, Unsteady

Introduction

Transient, particularly periodic, diffusion problems are very common in practicing engineering. Some examples are the cyclic heating of the cylinder surface of internal combustion engines, the diurnal heating and nocturnal cooling of building structures, lakes and water reservoirs by radiation, the periodic (pulse) laser heating of solid surfaces in materials processing, the cyclic heating of laminated steel during pickling, the periodic heating and cooling of vials contained DNA for polimerase-chain-reaction activation, and the heating of electronics, which is also cyclic in most cases.

Frequently, these heat transfer processes are diffusion-dominated or at least influenced by the initial diffusion-dominated evolution. Obtaining analytic solutions of transient diffusion problems, when possible, can be very complicated (as demonstrated in detail by Carslaw and Jaeger [1], Arpaci [2], Özisik [3], Kakaç and Yener [4], and Poulikakos [5]) because of the mathematical intricacies involved in solving the differential equations governing the phenomenon.

The method of choice for solving problems involving time-periodic temperature boundary conditions analytically, for instance, is the method of complex temperature ([5]). This method, however, applies only when the boundary condition is expressed as a sine or cosine function of time. Moreover, the solution does not cover the initial transient regime, but only the steady-periodic regime.

Analytic solution of the one-dimensional diffusion problem with a continuous, transient, temperature boundary condition $f(t)$, including the initial transient regime, can be obtained using the Duhamel's theorem ([5])

$$T(x,t)=\int_{\tau=0}^{\tau=t}\frac{df(\tau)}{d\tau}T_s(x,t-\tau)d\tau \tag{1}$$

with $T_s(x,0)=0$, where $T_s(x,t)$ is the solution for the unit step boundary condition applied at $t=0$. Although very powerful, Duhamel's theorem can lead to mathematically complex problems because of the integral in Eq. (1), making it very difficult to find an analytic solution except for very simple cases.

A more general analytic approach for solving diffusion problems with transient boundary condition exists leading to solutions involving the Green functions and kernels. Even for relatively simple boundary conditions the mathematical analysis can be daunting, again because of the integrals involved, as shown by Özisik [3].

When only localized thermal responses are of interest, the thermal engineer has no choice but to first find the solution to the diffusion equation (using one of the usual analytic methods) throughout the entire domain, and then particularize the solution to a specific location. The possibility of determining analytically the temperature (or heat flux) at a particular location within the domain knowing only the local heat flux (or temperature), i.e., without having to solve the diffusion problem within the entire domain, is very advantageous in these circumstances.

The fractional-diffusion technique, originally presented by Oldham and Spanier [6], can be used for determining in a simple and elegant way the local temperature or heat flux of a medium with uniform properties undergoing heat diffusion. Our primary objective is to review this technique, and by doing so to demonstrate why the technique is limited to a semi-infinite and unidimensional configuration, complementing the work by Oldham and Spanier [6].

The general analytic solutions (one for local temperature and one for local heat flux) resulting from the fractional-diffusion technique are then validated for several heat diffusion problems with known analytic solutions obtained by different methods considering, in particular, the determination of boundary temperature or heat flux. These validations are important also for demonstrating how easy it is to find analytical solutions using the fractional-diffusion technique as compared to the mathematical difficulties of other methods.

Fractional Diffusion Equation

Consider initially a three-dimensional time-dependent diffusion equation, assuming constant and uniform properties

$$\frac{\partial T(x_1,x_2,x_3,t)}{\partial t}-\alpha\nabla^2 T(x_1,x_2,x_3,t)=0, \tag{2}$$

where T is temperature, t is time, (x_1,x_2,x_3) are three coordinates of an orthogonal system, and α is the thermal diffusivity of the medium. The system is initially at equilibrium, so $T(x_1,x_2,x_3,t)=T_0$ for $t<0$, with T_0 being a constant and uniform value. Implementing the change of variables $(\xi_1,\xi_2,\xi_3)=\alpha^{-1/2}(x_1,x_2,x_3,t)$ and $\theta(x_1,x_2,x_3,t)=T(x_1,x_2,x_3,t)-T_0$, Eq. (2) becomes

$$\frac{\partial\theta(\xi_1,\xi_2,\xi_3,t)}{\partial t}-\nabla^2\theta(\xi_1,\xi_2,\xi_3,t)=0 \tag{3}$$

with the initial condition now written as $\theta(\xi_1,\xi_2,\xi_3,0)=0$. Taking the Laplace transform of Eq. (3), and using the initial condition $\theta(\xi_1,\xi_2,\xi_3,0)=0$,

Contributed by the Heat Transfer Division for publication in the JOURNAL OF HEAT TRANSFER. Manuscript received by the Heat Transfer Division, August 27, 1999; revision received, December 9, 1999. Associate Technical Editor: T. Avedisian.

$$s\theta^*(\xi_1,\xi_2,\xi_3,s)-\nabla^2\theta^*(\xi_1,\xi_2,\xi_3,s)=0 \tag{4}$$

where $\theta^*(\xi_1,\xi_2,\xi_3,s)$ represents the Laplace transform of $\theta(\xi_1,\xi_2,\xi_3,t)$.

Using the separation of variables $\theta^*(\xi_1,\xi_2,\xi_3,s)=X_1(\xi_1)X_2(\xi_2)X_3(\xi_3)$, Eq. (4) is replaced by the system of equations

$$\frac{1}{X_j}\left[\frac{1}{\prod_j h_j}\frac{\partial}{\partial\xi_j}\left(\frac{h_p h_q}{h_j}\frac{\partial X_j}{\partial\xi_j}\right)\right]=\lambda_j^2 s,\quad p\neq q\neq j=1,2,3 \tag{5}$$

with the additional condition: $\lambda_1^2+\lambda_2^2+\lambda_3^2=1$. In Eq. (5), h_j are multipliers (or scaling functions) of the orthogonal system (e.g., in spherical coordinates: $h_1=1$, $h_2=r$, $h_3=r\sin\theta$) (see [7], p. 34). Considering Cartesian coordinates for simplicity ($h_1=h_2=h_3=1$), the solution of Eq. (5) is

$$X_j(\xi_j,s)=\sum_{m_j=-\infty}^{\infty}\left[A_{jm_j}(s)e^{s^{1/2}\lambda_{jm_j}\xi_j}+B_{jm_j}(s)e^{-s^{1/2}\lambda_{jm_j}\xi_j}\right] \tag{6}$$

where A_{jm_j} and B_{jm_j} are arbitrary functions of s. The solution θ^* becomes

$$\theta^*=\sum_{m_1=-\infty}^{\infty}\sum_{m_3=0}^{m_1}\sum_{m_2=0}^{m_1}\left[\prod_{j=1,2,3}\left(A_{jm_j}e^{s^{1/2}\lambda_{jm_j}\xi_j}+B_{jm_j}e^{-s^{1/2}\lambda_{jm_j}\xi_j}\right)\right]. \tag{7}$$

Now, observe from Eq. (7) that the equality

$$\frac{\partial\theta^*(\xi,s)}{\partial\xi}=-s^{1/2}\theta^*(\xi,s) \tag{8}$$

holds only when $A_{jm_j}=0$ or $B_{jm_j}=0$ (depending on λ_{jm_j} being positive or negative, respectively) and when λ_{jm_j} is unity. The requirements on A_{jm_j} and B_{jm_j} are automatically satisfied when seeking a finite solution valid for a semi-infinite domain along ξ_j. The requirements on λ_{jm_j} implies in $\lambda_{1m_1}=1$, therefore $\lambda_{2m_2}=\lambda_{3m_3}=0$, and the problem degenerates to the unidirectional case. Therefore, Eq. (8) is valid only when the problem is unidirectional and the domain is semi-infinite. It will become clear later on that Eq. (8) is a fundamental necessary step along the derivation of the fractional-diffusion equations. As a consequence, the equations are limited to the semi-infinite and unidirectional case. Aside this limitation, the technique is extremely powerful, as will be demonstrated in the following sections.

The development of the fractional-diffusion technique continues by inverting Eq. (8), recognizing first that the inverse Laplace transform commutes with the $\partial/\partial\xi$ operator, i.e., $L^{-1}[\partial\theta^*(\xi,s)/\partial\xi]=\partial\{L^{-1}[\theta^*(\xi,s)]\}/\partial\xi=\partial[\theta(\xi,t)]/\partial\xi$. It is also necessary to use the property $L[\partial^f\theta(\xi,t)/\partial t^f]=s^fL[\theta(\xi,t)]=s^f\theta^*(\xi,s)$, valid for a function $\theta(\xi,t)$ that satisfies $\theta(\xi,0)=0$, where $\partial^f/\partial t^f$ is the fractional derivative operator of order f. Thus, Eq. (8), on restoring the original variables, becomes

$$\alpha^{1/2}\frac{\partial T(x,t)}{\partial x}=-\frac{\partial^{1/2}[T(x,t)-T_0]}{\partial t^{1/2}}. \tag{9}$$

Using the properties (*A*2) and (*A*10) listed in the Appendix, Eq. (9) is rewritten as

$$\alpha^{1/2}\frac{\partial T(x,t)}{\partial x}=-\frac{\partial^{1/2}T(x,t)}{\partial t^{1/2}}+\frac{1}{(\pi t)^{1/2}}T_0. \tag{10}$$

Now, recalling the Fourier Law for the heat flux $q''(x,t)=-k\partial T(x,t)/\partial x$, valid at any point within the domain, and using Eq. (10) to substitute the $\partial T(x,t)/\partial x$ term, we obtain

$$q''(x,t)=\frac{k}{\alpha^{1/2}}\left[\frac{\partial^{1/2}T(x,t)}{\partial t^{1/2}}-\frac{T_0}{(\pi t)^{1/2}}\right]. \tag{11}$$

Therefore, the heat flux at any location within the domain (including along the boundary) can be obtained from Eq. (11) by simple semidifferentiating the temperature T in time at that location. Note that for a given $q''(x,t)$, the corresponding $T(x,t)$ value can be obtained by inverting Eq. (11), i.e., by taking $\partial^{-1/2}$ [Eq. (11)]$/\partial t^{-1/2}$. Using properties (*A*3), (*A*5), and (*A*8), the result is

$$T(x,t)=\frac{\alpha^{1/2}}{k}\frac{\partial^{-1/2}[q''(x,t)]}{\partial t^{-1/2}}+T_0. \tag{12}$$

It is important to emphasise that the transformation of the diffusion Eq. (2) into the extraordinary PDE Eq. (10) is restricted only by the assumption of the domain being semi-infinite and the process unidirectional. One can use this transformation in heat and mass transfer for analysing the early regime within a finite domain during which the diffusion process takes place as if the domain were semi-infinite. In the next section Eqs. (11) and (12) are validated by considering problems with known analytic solutions.

Validation for Heat Transfer Problems

Consider, for instance, the problem of a semi-infinite planar medium with a time-varying temperature condition along the boundary (the temperature is considered uniform along the boundary, where $x=0$). The one-dimensional heat conduction equation in this case is

$$\frac{\partial T(x,t)}{\partial t}-\alpha\frac{\partial^2 T(x,t)}{\partial x^2}=0. \tag{13}$$

The initial and boundary conditions are $T(x,0)=T_0$, $T(0,t)=T_b(t)$ and $T(\infty,t)=0$. Using Eq. (11), the heat flux $q_b''(t)$ crossing the boundary of the medium is

$$q''(0,t)=q_b''(t)=\frac{k}{\alpha^{1/2}}\left[\frac{d^{1/2}T_b(t)}{dt^{1/2}}-\frac{1}{(\pi t)^{1/2}}T_0\right] \tag{14}$$

for any time-varying temperature boundary condition $T_b(t)$.

To gain confidence on the validity of Eq. (14), consider some simple heat transfer cases with known analytic solution. For instance, the constant boundary temperature problem, i.e., $T(0,t)=T_b$. From Eqs. (14) and (*A*10)

$$q_b''=\frac{k}{\alpha^{1/2}}\left(\frac{1}{\pi t}\right)^{1/2}(T_b-T_0), \tag{15}$$

which is exactly the same as the result obtained by solving the diffusion equation analytically for the temperature within the entire domain, using the similarity method and separation of variables, and then obtaining an expression for the boundary heat flux via the Fourier Law (see Eq. (4.43), p. 150, of Bejan [8]). Observe that with the fractional approach the same result is obtained in one simple operation, i.e., finding the semiderivative of the constant T_b.

Now, to verify the inverse relation, Eq. (12), consider first the problem of a continuous plane source q'' within an infinite domain. The boundary temperature, according to Eq. (12), is

$$T(0,t)=T_b(t)=\frac{\alpha^{1/2}}{k}\frac{d^{-1/2}q''}{dt^{-1/2}}+T_0. \tag{16}$$

When q'' is a constant, expression (*A*13) can be used to evaluate the fractional derivative of Eq. (16), and the result is

$$T_b(t)=\frac{\alpha^{1/2}}{k}2q''\left(\frac{t}{\pi}\right)^{1/2}+T_0 \tag{17}$$

which is exactly the result found via the similarity method, reported by Poulikakos ([5], p. 191) for this particular problem. The simplicity and clarity (it does not require *finding* a similarity variable) of the fractional method is again noteworthy.

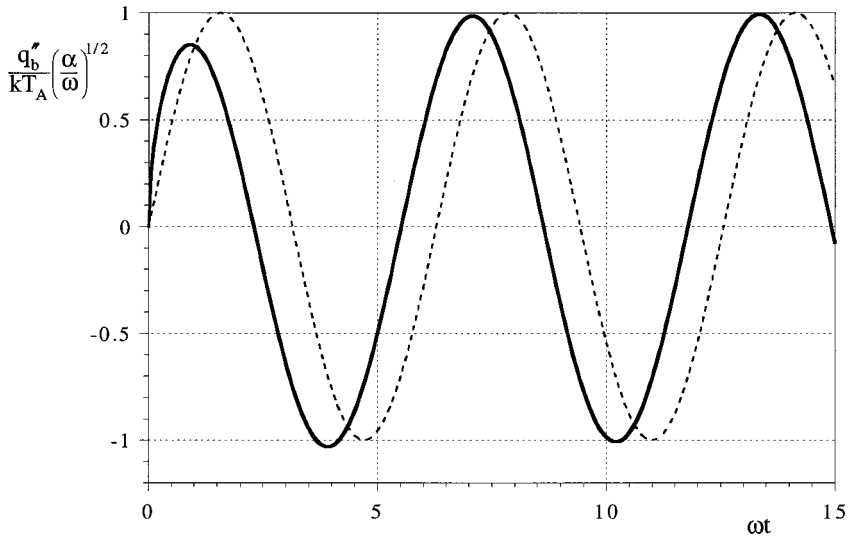

Fig. 1 Time evolution of surface heat flux, Eq. (20), and the imposed boundary condition (dashed line): $[T_b(t)-T_0]/T_A=\sin(\omega t)$

Consider now a more complicated class of problems in which the boundary condition is time-dependent. For instance, when the surface temperature is time-dependent and varies as $T_b(t)=T_0+T_A\sin(\omega t)$, the boundary heat flux is obtained from Eq. (11) as

$$q''_b(t)=\frac{k}{\alpha^{1/2}}\left\{\frac{d^{1/2}[T_0+T_A\sin(\omega t)]}{dt^{1/2}}-\frac{1}{(\pi t)^{1/2}}T_0\right\}. \quad (18)$$

Using, in order, properties (*A*2) and (*A*10), listed in the Appendix, and simplifying the result,

$$q''_b(t)=\frac{k}{\alpha^{1/2}}\frac{d^{1/2}[T_A\sin(\omega t)]}{dt^{1/2}} \quad (19)$$

Now, using (*A*3), (*A*6), and (*A*11) into Eq. (19), yields

$$q''_b(t)=\frac{k}{\alpha^{1/2}}T_A\omega^{1/2}\left\{\sin\left(\omega t+\frac{\pi}{4}\right)-2^{1/2}\Lambda\left[\left(\frac{2\omega t}{\pi}\right)^{1/2}\right]\right\} \quad (20)$$

where Λ is the auxiliary Fresnel function (see Appendix). Observe that the term proportional to the auxiliary Fresnel function Λ in Eq. (20) governs the initial unsteady regime. When time is long enough the contribution of the auxiliary Fresnel function becomes negligible because $\Lambda(\tau)$ approaches zero as τ increases (for instance, at $t\sim 10\pi/\omega$, $|\max\{\Lambda[(2\omega t/\pi)^{1/2}]\}|<0.001$), and the heat flux variation reaches a steady-periodic regime, as shown in Fig. 1.

The surface heat flux at the steady-periodic regime, for this particular case of boundary condition, can be obtained also by first modifying the diffusion equation to a complex temperature model, solving the differential equation for the complex temperature, extracting the temperature solution from the complex temperature and then using the Fourier's law to obtain the corresponding heat flux (see [5], p. 167). The final result is

$$q''_b(t)=\frac{k}{\alpha^{1/2}}T_A\left(\frac{\omega}{2}\right)^{1/2}[\sin(\omega t)+\cos(\omega t)] \quad (21)$$

which is the asymptotic result of Eq. (20) for very large time.

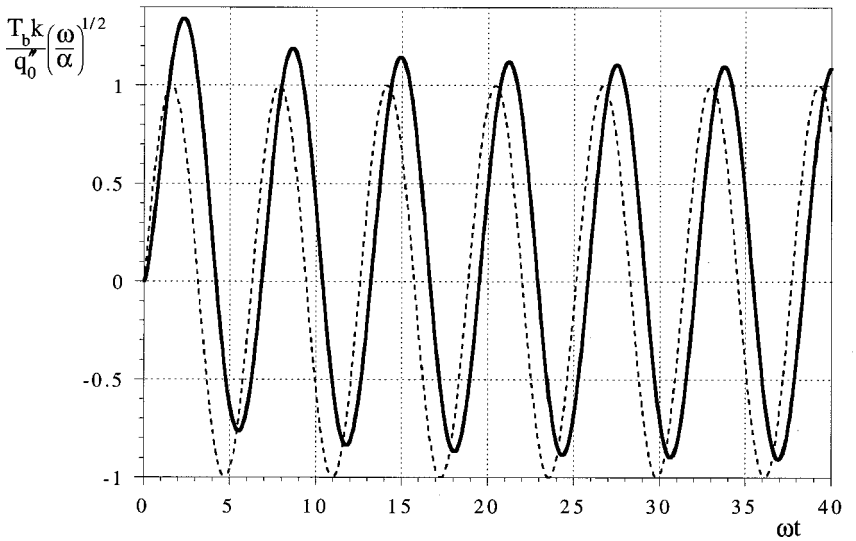

Fig. 2 Time evolution of surface temperature, Eq. (23), and the imposed boundary condition (dashed line): $q''(t)/q''_0=\sin(\omega t)$

Consider now the boundary condition $q''_b(t)=q''_0\sin(\omega t)$ imposed at the boundary ($x=0$) of a semi-infinite medium. Using the fractional Eq. (12) the boundary temperature is directly related to the boundary heat flux via

$$T_b(t)=\frac{\alpha^{1/2}}{k}\frac{d^{-1/2}q''_b}{dt^{-1/2}}=\frac{\alpha^{1/2}}{k}\frac{d^{-1/2}[q''_b\sin(\omega t)]}{dt^{-1/2}}. \tag{22}$$

The final solution is obtained by applying (*A*3), (*A*6), and (*A*14) to Eq. (22):

$$T_b(t)=\frac{\alpha^{1/2}}{k}q''_0\omega^{1/2}\left[\sin\left(\omega t-\frac{\pi}{4}\right)+2^{1/2}\Omega\left(\frac{2\omega t}{\pi}\right)^{1/2}\right]. \tag{23}$$

Observe, again, that the term proportional to the auxiliary Fresnel function Ω in Eq. (23) governs the initial unsteady regime (Fig. 2). When time permits the contribution of the auxiliary Fresnel function becomes negligible (for instance, at $t\sim 40\pi/\omega, |\max\{\Omega[(2\omega t/\pi)^{1/2}]\}|<0.04$), and the temperature variation reaches a steady-periodic regime.

The steady-periodic general solution to this problem is (see [3], p. 114, to verify the mathematical complexity behind this solution)

$$T(x,t)=(\omega\alpha)^{1/2}\frac{q''_0}{k}\exp\left[-\left(\frac{\omega}{2\alpha}\right)^{1/2}x\right]\sin\left[\omega t-\left(\frac{\omega}{2\alpha}\right)^{1/2}x-\frac{\pi}{4}\right]. \tag{24}$$

At the boundary, $x=0$, the solution simplifies to

$$T_b(t)=(\alpha\omega)^{1/2}\frac{q''_0}{k}\sin\left(\omega t-\frac{\pi}{4}\right) \tag{25}$$

which is exactly the same as the asymptotic result of Eq. (23), when the auxiliary Fresnel function contribution becomes negligible.

Other more complex functions can be considered as boundary conditions and used in Eqs. (20) and (23), following the same steps demonstrated previously. A very general set of fractional derivatives and rules of derivation can be found in Odham and Spanier [9].

Summary and Conclusions

By attempting to extend to vectorial form the development presented by Oldham and Spanier [6], it is demonstrated why the fractional-diffusion technique is restricted to unidirectional problems within a semi-infinite domain.

The two resulting equations, one for local temperature and one for local heat flux, depend on local quantities only (heat flux and temperature, respectively). Therefore, when the temperature (or heat flux) time evolution is known at any point within the domain, the time evolution of the corresponding heat flux (or temperature) at the same point can be found without having to solve the diffusion equation for the entire domain.

The resulting fractional-diffusion equations are applied to the boundary and validated considering several problems with known analytic solution. The simplicity involved in obtaining the local system response (temperature or heat flux) to a transient excitation within a semi-infinite diffusion system using the fractional approach is highlighted.

Observe that the extension to mass diffusion problems is straightforward by considering the parallel between heat and mass transfer. The same can be said about mass and heat diffusion within a porous medium following the macroscopic diffusion equation for a system in (thermal) equilibrium. In this case care should be taken when replacing the diffusion coefficient α and the thermal conductivity k with the appropriate effective coefficients of the porous medium.

Appendix

In this section some useful definitions and properties of fractional derivatives are presented. From the several equivalent definitions of fractional derivatives, the most elegant is the Riemann-Liouville definition ([10]), namely

$$\frac{d^f[g(t)]}{dt^f}=\frac{1}{\Gamma(-f)}\int_0^t\frac{g(\tau)}{(t-\tau)^{1+f}}d\tau \tag{A1}$$

where f is any negative number and Γ is the Gamma function. Some of the useful properties derived from Eq. (*A*1) are

$$\frac{d^f[u(t)+v(t)]}{dt^f}=\frac{d^f[u(t)]}{dt^f}+\frac{d^f[v(t)]}{dt^f} \tag{A2}$$

$$\frac{d^f[Cg(t)]}{dt^f}=C\frac{d^fg(t)}{dt^f} \tag{A3}$$

$$\frac{d^f[tg(t)]}{dt^f}=t\frac{d^fg(t)}{dt^f}+f\frac{d^{f-1}g(t)}{dt^{f-1}} \tag{A4}$$

$$\frac{d^h}{dt^h}\left(\frac{d^fg(t)}{dt^f}\right)=\frac{d^{h+f}g(t)}{dt^{h+f}} \tag{A5}$$

$$\frac{d^f[g(Ct)]}{dt^f}=C^f\frac{d^fg(Ct)}{d(Ct)^f} \tag{A6}$$

$$\frac{d^f\delta(t-\tau)}{dt^f}=\frac{1}{\Gamma(-f)}(t-\tau)^{-f-1},\quad f<0 \tag{A7}$$

$$\frac{d^f[t^n]}{dt^f}=\frac{\Gamma(n+1)}{\Gamma(n+1-f)}t^{n-f} \tag{A8}$$

$$\frac{d^f[C]}{dt^f}=\frac{Ct^{-f}}{\Gamma(1-f)} \tag{A9}$$

where $\delta(t-\tau)$ is the Dirac delta function, defined as $\delta(t-\tau)=\infty$, if $t=\tau$, otherwise, $\delta(t-\tau)=0$. In the previous formulas, C is a nonzero constant. Observe that expression (*A*5) holds for any positive h and f, and for $d^{-f}[d^fg(t)/dt^f]/dt^{-f}=g(t)$ if f and/or h are negative (see Oldham and Spanier, [9], p. 117).

The semiderivatives (case of f being $\pm 1/2$) of some common functions are

$$\frac{\partial^{1/2}[C]}{\partial t^{1/2}}=C(\pi t)^{-1/2} \tag{A10}$$

$$\frac{d^{1/2}[\sin(t)]}{dt^{1/2}}=\sin\left(t+\frac{\pi}{4}\right)-2^{1/2}\Lambda\left[\left(\frac{2t}{\pi}\right)^{1/2}\right] \tag{A11}$$

$$\frac{d^{1/2}[\cos(t)]}{dt^{1/2}}=\frac{1}{(\pi t)^{1/2}}+\cos\left(t+\frac{\pi}{4}\right)-2^{1/2}\Omega\left[\left(\frac{2t}{\pi}\right)^{1/2}\right] \tag{A12}$$

$$\frac{d^{-1/2}[C]}{dt^{-1/2}}=2C\left(\frac{t}{\pi}\right)^{1/2} \tag{A13}$$

$$\frac{d^{-1/2}[\sin(t)]}{dt^{-1/2}}=\sin\left(t-\frac{\pi}{4}\right)+2^{1/2}\Omega\left[\left(\frac{2t}{\pi}\right)^{1/2}\right] \tag{A14}$$

$$\frac{d^{-1/2}[\cos(t)]}{dt^{-1/2}}=\cos\left(t-\frac{\pi}{4}\right)-2^{1/2}\Lambda\left[\left(\frac{2t}{\pi}\right)^{1/2}\right] \tag{A15}$$

In Eqs. (*A*11), (*A*12), (*A*14), (*A*15), Ω and Λ are the auxiliary Fresnel integrals (functions f and g, respectively, in Abramowitz and Stegun [11] p. 300).

References

[1] Carslaw, H. S., and Jaeger, J. C., 1959, *Conduction of Heat in Solids*, 2nd Ed., Oxford University Press, Oxford, UK.

[2] Arpaci, V. S., 1966, *Conduction Heat Transfer*, Addison-Wesley, Reading, PA.
[3] Özisik, M. N., 1980, *Heat Conduction*, John Wiley and Sons, New York.
[4] Kakaç, S., and Yener, Y., 1985, *Heat Conduction*, Hemisphere, Washington, DC.
[5] Poulikakos, D., 1994, *Conduction Heat Transfer*, Prentice-Hall, Englewood Cliffs, NJ.
[6] Oldham, K. B., and Spanier, J., 1972, ''A General Solution of the Diffusion Equation for Semiinfinite Geometries,'' J. Math. Anal. Appl., **39**, pp. 655–669.
[7] Cohen, H., 1992, *Mathematics for Scientists and Engineers*, Prentice-Hall, Englewood Cliffs, NJ.
[8] Bejan, A., 1993, *Heat Transfer*, John Wiley and Sons, New York.
[9] Oldham, K. B., and Spanier, J., 1974, *The Fractional Calculus*, Academic Press, New York.
[10] Riesz, M., 1949, ''L'intégral de Riemann-Liuoville et le Problème de Cauchy,'' Acta Math., **81**, p. 1.
[11] Abramowitz, M., and Stegun, I. A., 1964, *Handbook of Mathematical Functions*, Dover, New York.

Numerical Study of Vortex/Flame Interaction in Actively Forced Confined Non-Premixed Jets

K. R. Anderson
Lecturer, Mechanical Engineering Department, California State Polytechnic University, Pomona, 3801 West Temple Avenue, Pomona, CA 91768-4062

S. Mahalingam[1]
Mem. ASME, Associate Professor, Center for Combustion and Environmental Research, Department of Mechanical Engineering, University of Colorado at Boulder, Campus Box 427, Boulder, CO 80309-0427
e-mail: Shankar.Mahalingam@Colorado.edu

Numerical simulations of coplanar reacting jets subjected to near wall confinement have been performed. The primary conclusion is that for a fixed level of heat release, the mechanism of baroclinic vorticity production increases with more severe wall confinement. [S0022-1481(00)00602-2]

Keywords: Combustion, Computational, Heat Transfer, Jets, Vortex

Introduction

Active forcing of reacting flows has recently gained much attention as a means for controlling and stabilizing combustion processes in a variety of engineering applications. Tailoring the combustion process by means of pulsing, or otherwise altering the mass flow rate using injectors placed strategically, has recently been adopted as a novel approach to increasing reactor combustion efficiencies. A comprehensive summary regarding the use of active forcing to tailor combustion processes is provided by Coats [1].

The literature regarding premixed flame/wall interactions currently dwarfs the amount of information regarding nonpremixed flame/wall interactions. In the study of Poinsot et al. [2] Direct Numerical Simulation (DNS) of a premixed flame/wall interaction, with provisions for heat release and variable density and viscosity, is considered. They found that turbulent flamelets behave differently as they approach walls. The effects of thermal boundary conditions on premixed flame shape and quenching in duct flows are examined by Hackert et al. [3]. Roberts et al. [4] investigate premixed flame quenching induced by flame/vortex interactions in an effort to quantify various regimes of turbulent combustion.

Nonpremixed flame/wall interaction studies are surprisingly limited. Peters [5] considered the effects of flame stretch on local quenching in nonpremixed flames using perturbation methods. Wichman [6] employed large activation energy asymptotics to derive an expression for the quenching distance in a nonpremixed flame undergoing a one-step exothermic reaction near a cold wall. The study of Katta et al. [7], which considers quenching in methane-air diffusion flames, is one of the few DNS works that have focused on the dynamics of nonpremixed flame quenching.

The effect of extremely close proximity walls on the vorticity distribution in reacting jets is the focus of this work. The implications of such near wall confinement on combustion-driven instabilities can be found in engineering applications such as lean-premixed gas turbine engines and compact hazardous waste incinerators ([8]). In this paper, time-dependent numerical simulation is used to study the combined effects of increased heat release and semi-confinement on the vorticity dynamics in the near-field region of nonpremixed, actively forced, momentum dominated, coflowing jets. The jets are modeled as unsteady, compressible, reacting flows with temperature-dependent viscosity. Because the primary focus of this study is on the effects heat release and confinement on vorticity production, a simple one-step global reaction model governed by temperature-dependent finite-rate Arrhenius kinetics is used to represent the chemistry. The jets are subjected to large-amplitude low-frequency perturbations in order to induce vortex formation.

Problem Formulation

A schematic representation of the two-dimensional planar computational domain used is shown in Fig. 1. The stoichiometric mixture fraction is used to examine flame surface dynamics. For

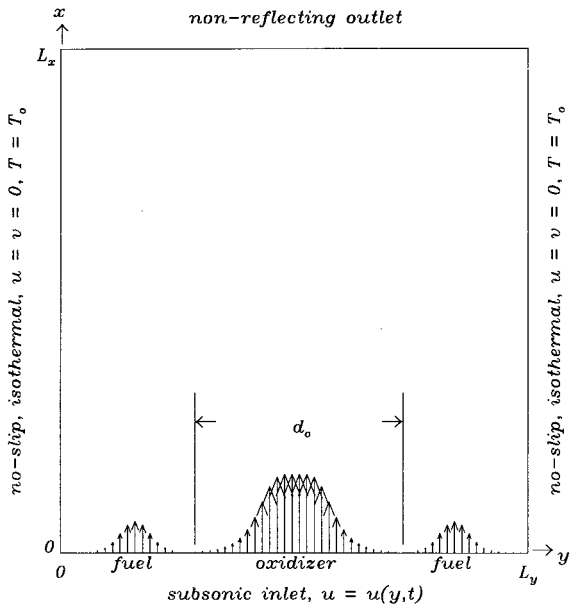

Fig. 1 Computational domain showing fuel and oxidizer jets, and boundary conditions

[1]To whom correspondence should be addressed.

Contributed by the Heat Transfer Division for publication in the JOURNAL OF HEAT TRANSFER. Manuscript received by the Heat Transfer Division, January 15, 1999; revision received November 9, 1999. Associate Technical Editor: T. Avedisian.

the global one-step chemistry used $F+rO\rightarrow(1+r)P$, the mixture fraction is defined as $Z=(SY_F-Y_O+1)/(1+S)$, where Z ranges from $0<Z<1$. The flame is located where fuel and oxidizer meet in stoichiometric proportion at $Z_c=1/(1+S)$, where the effective air/fuel stoichiometric ratio, $S=rY_{F,o}/Y_{O,o}$. The formulation used herein allows for fuel and/or oxidizer dilution ($Y_{F,o}$ and/or $Y_{O,o}$ not equal to unity). Here, for simplicity only $Z_c=0.5$ is discussed. A detailed investigation of the effects of varied stoichiometry on vorticity and flame structure can be found in Anderson et al. [9].

Numerical Solution

A compressible direct simulation code ([10]) was adapted and utilized for the current investigation. A compact sixth-order finite difference scheme ([11]) is used to approximate spatial derivatives in the governing equations. The order of accuracy is fourth and third, respectively, at points adjacent to and on the boundary of the computational domain. The scheme used for time advancement is an explicit third-order Runge-Kutta method ([12]).

Boundary conditions are prescribed by the Navier-Stokes Characteristic Boundary Condition (NSCBC) technique ([13]). They are shown in Fig. 1. At the outflow boundary, a nonreflecting boundary condition is imposed. Subsonic conditions are used at the inlet of the domain where the streamwise velocity profiles are perturbed according to

$$u(y,t)=\overline{u}(y)[1+\varepsilon\sin(2\pi ft+\psi)], \tag{1}$$

where $\overline{u}(y)$ is the mean streamwise velocity, ε controls the amplitude of the perturbations, ψ is a phase angle, and f is the frequency of perturbations ([14]). In this paper, fuel frequency is twice that for an oxidizer, with $\psi=0$ ([15]). Data collected from eight phases over a cycle, in angular increments of $\pi/4$, were used to construct the results presented in this paper.

In the present investigation, $\epsilon=0.5$ was used to mimic the study of Gutmark et al. [15], where large-amplitude fluctuations were used to study the merits of active forcing in compact waste incinerators. The overall size of a compact waste incinerator is smaller than conventional hazardous waste incineration chambers causing closer proximity of inlet jets. The jets used to inject fuel/oxidizer in compact waste incinerators are typically separated by less than 2 or 3 jet diameters ([8]). Also there are typically several jets situated near a wall. The current study has idealized the confinement effects by examining only one pair of jets. It was found that for $\epsilon<0.4$, the flame did not respond well to active forcing. Hence, the value of $\epsilon=0.5$ was selected. Clearly, a point of diminishing returns is reached when perturbation energy exceeds the energy of the unperturbed flow.

The large-amplitude low-frequency perturbation used in the current investigation is somewhat larger than that used in other studies. Hosangadi et al. [16] imposed a five percent sinusoidal variation of the fuel jet velocity at a Strouhal number based on the radius equal to 3.5. They concluded that reacting jets are much less responsive to active forcing than their isothermal counterparts, lending support to the suspected stabilizing nature of heat release. The reacting circular jet configuration investigated by Miller et al. [17] employed 15 percent inlet velocity perturbations with a Strouhal number based on the jet diameter of 0.40. For axisymmetric jets, the preferred-mode Strouhal number based on the diameter of the jet falls within the range 0.20 to 0.50 ([18]). For the planar jet simulations presented herein, the Strouhal number based on the oxidizer jet width d_o is $St_{d_o}=0.41$. Gutmark and Ho [19] suggest that extremely low level, spatially coherent disturbances in individual experimental facilities change the initial/inlet conditions of a laminar shear layer. Thus, an across the board comparison of the present results with those presented in the literature for other simulations and experimental studies of coplanar jets should be made with care.

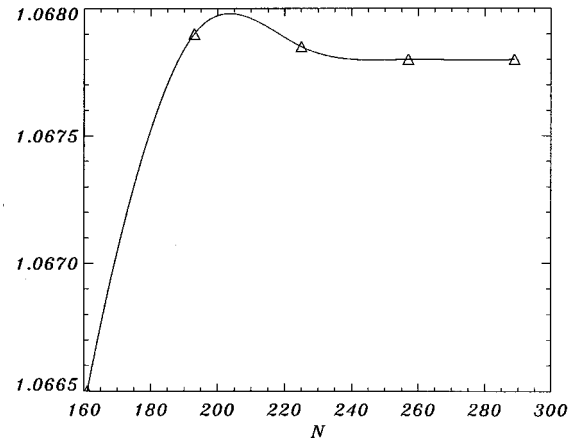

Fig. 2 Grid independence study representative output. Instantaneous density variation at $x=0.02335$, $y=0.07004$. Δ: data points, (——): spline fit.

Numerical Code Validation. The DNS code used in the present study was validated by the originators in Guichard et al. [10]. Since exact reacting flow solutions do not exist for the present configuration, a nonreacting stagnation point flow and a Poiseuille channel flow with isothermal walls were modeled. The numerical results agreed with theoretical predictions to within five percent.

Accuracy of the unsteady numerical simulations carried out in this study depends on both spatial and temporal resolutions. The time-step is selected according to

$$\Delta t=\min(\Delta t_f,\Delta t_r) \tag{2}$$

where Δt_f and Δt_r are the convection and reaction time steps calculated as

$$\Delta t_f=\max\left(\frac{\sigma_f\Delta x_i}{(u_i+c)}\right)\quad \text{for } i=1,2 \tag{3}$$

where $c=\sqrt{\gamma p/\rho}$ denotes the local speed of sound, and

$$\Delta t_r=\max\left(\frac{\sigma_r\rho}{\dot{\omega}_T}\right) \tag{4}$$

where σ_f and σ_r, respectively, denote the convection and reaction Courant-Friedrichs-Lewy (CFL) numbers and $\dot{\omega}_T$ is the reaction rate term of the energy conservation equation. In this study, $\sigma_f=0.5$ and $\sigma_r=0.07$.

A grid independence study was performed to ensure adequate spatial resolution. To isolate the spatial dependence of flow variables on the grid used, a very small time-step on the order of $\Delta t_f\sim O(10^{-6})$ was used by adjusting the value of σ_f. This study involved monitoring all flow variables at various locations within, and outside the shear layer, as the resolution of the grid was increased. For example, Fig. 2 shows the computed fluid density at a fixed location as a function of the mesh size N. The variation in density (and other variables) asymptotes out at a value of $N=257$, indicating that the resolution is sufficient for results to be grid independent. All results presented herein are for a grid resolution of $N=257$.

Results and Discussion

A Database Parameters. The reader is referred to the Nomenclature section of the paper for definitions of the following parameters. Reference values used were $\gamma=1.4$, $c_o=340$ m/s, $\nu_o=1\times10^{-5}$ m^2/s, $\rho_o=1$ kg/m^3, $T_o=300$ K, $Y_{O,o}=1$ and $B=2\times10^{14}$ m^3/kg−s. The domain size used was $L_x=1$, $L_y=1$. Dimensionless numbers used include $\mathrm{Ma}_{in}=0.5$, $\mathrm{Pr}=0.7$, $\mathrm{Sc}=1.0$, Re_{ac}

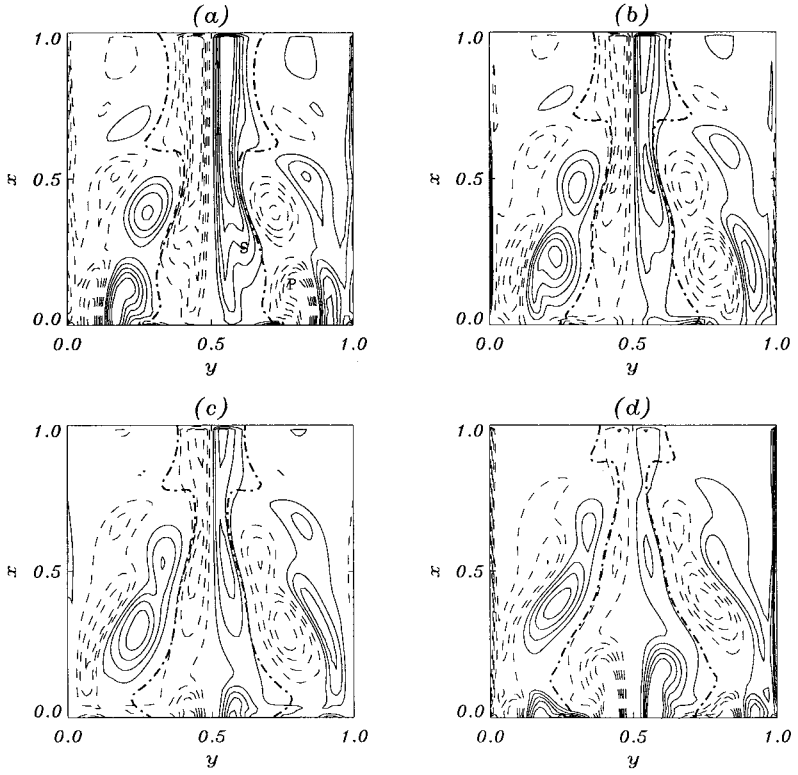

Fig. 3 Case 2 signed vorticity and stoichiometric mixture fraction. $\omega_z=-5$ to 5, $\Delta=1$. $Z_c=0.5$: (-···-). (*a*) to (*d*): $t=29.32$ to 31.68, in time increments of $\Delta t=\pi/4$.

$=12500$, Re$=2030$, and $Pe=2030$. The period of forcing was $\tau_O=2\pi/\hat{\beta}_r$, $\tau_F=\pi/\hat{\beta}_r$ with $\hat{\beta}_r=1$. In the context of the current literature, heat release effects are considered low when the ratio of maximum to minimum temperature in the system, $T_f/T_o\sim 2$ ([20]) while high levels of heat release occur when $T_f/T_o\sim 4$ ([21]). Cases 1, 2, and 3 will henceforth refer to results with $T_f/T_o=1.7$, 2.5, and 2.7 respectively. Thus, the simulations given in this paper range from low to moderate heat release scenarios.

B Vorticity Transport Equation. The most important processes in reacting flows with heat release are the production of vorticity due to baroclinicity and the destruction of vorticity due to gas expansion processes. Thus, in order to ascertain the dynamic effects of heat release, one must analyze the volumetric expansion and also the establishment of pressure and density gradients. This is readily achieved by examining the transport equation for vorticity $\omega\equiv\nabla\times\mathbf{u}$,

$$\frac{D\omega}{Dt}=(\omega\cdot\nabla)\mathbf{u}-\omega(\nabla\cdot\mathbf{u})+\frac{(\nabla\rho\times\nabla p)}{\rho^2}+\frac{1}{\mathrm{Re}_{ac}}\nabla\times\nabla\cdot\left(\frac{\mathbf{T}}{\rho}\right), \tag{5}$$

where $\mathbf{T}$ denotes the shear stress tensor. The right-hand side of Eq. (5) is comprised of the stretching, dilatational, baroclinic torque and viscous diffusion terms, respectively. For the present two-dimensional flow, the contribution due to stretching is zero. Heat release produces significant contributions to the dilatational and baroclinic torque terms. The mechanism of vorticity production through dilatation depends upon the sign of the velocity divergence. Baroclinic torques are produced when iso-surfaces of density and pressure are misaligned in a flow field. In the current study, the more general form of the viscous diffusion term given in Eq. (5) is used, since the viscosity is temperature-dependent.

C Signed Vorticity. Vortex formation histories are shown in Fig. 3 for Case 2. Similar results for the other two cases were analyzed, but are not presented in this paper for brevity. The frames of Fig. 3 show the *z*-component of vorticity,

$$\omega_z=\left(\frac{\partial v}{\partial x}-\frac{\partial u}{\partial y}\right). \tag{6}$$

Regions of positive (negative) vorticity are indicated by solid (dashed) lines in each frame. Also shown is the location of the stoichiometric surface $Z_c=0.5$, indicated by the heavy dashed dotted line.

Primary and secondary vortices are evident in Fig. 3. In frame (*a*), primary vortices are formed in the fuel region of the jet near $x=0$, $y\simeq 0.5,0.75$. The formation of a secondary braid region is evident. A braid is defined as the vortex anchor which is connected to the inlet plane ([22]). In Fig. 3, braids of counterrotating direction are located near $x=0$, $y\simeq 0.45,0.55$. These braids occur in the oxidizer region of the flow. The convection speeds of the primary (fuel region) and secondary (oxidizer) vortices were calculated as $u_{c,i}\equiv\Delta x/\Delta t$, where Δx is the distance traversed by the center of the structure over a time Δt. This yielded $u_{c,p}=0.16$ and $u_{c,s}\approx 2u_{c,p}$, where *p* and *s* denote primary and secondary, respectively. The presence of vorticity along the lateral walls of the domain is also apparent in Fig. 3. Recirculation zones along the lateral boundaries are evident from the signed vorticity structures generated along the walls.

The degree of vortex/wall interaction does not seem to change significantly when comparing simulations with different levels of heat release. This is because the proximity of the flame to the walls is the same in each case through the parameter $L_y=1$. Effects of vortex/wall interaction are not expected to become pronounced unless the value of the lateral wall distance parameter L_y

is changed ([14]). However, the degree of elongation of the structures is slightly different for each heat release case. The underlying mechanisms responsible for the local distribution of the signed vorticity are the variable density mechanisms of Eq. (5). These mechanisms are also responsible for the severity of undulation experienced by the flame surface. The average structure of the gas expansion and baroclinic torque terms are presented in the following subsection.

D Average Vorticity Distribution. The effect of increased heat release on the global distribution of vorticity is quantified in the following manner. Using data for the three heat release cases, the magnitude of each term on the right-hand side of Eq. (5) was computed using a spatial-time averaging technique. The terms which comprise the right-hand side of Eq. (5) are denoted here as Ω_i, where $i=D$ for dilatation, B for baroclinic torque and V for viscous diffusion. Traversing the streamwise extent of the domain, the Ω_i terms were integrated in the transverse y-direction, over a period of oxidizer forcing $t=\tau_O$ leading to

$$\langle \Omega_i \rangle \equiv \int \int \Omega_i^2 dy dt. \tag{7}$$

Another metric used in our post-processing of the numerical databases was the averaged value of the vorticity transport budget defined as

$$\langle D\omega/Dt \rangle \equiv \sum_i \langle \Omega_i \rangle. \tag{8}$$

The average values of the pressure gradient term $\langle \Omega_B \rangle_m$, gas expansion term $\langle \Omega_D \rangle_m$ and global vorticity budget $\langle D\omega/Dt \rangle_m$ are shown in Table 1. Also shown in Table 1 is the ratio of the mean global baroclinic term to the mean global dilatational term defined as

$$V_g \equiv \frac{\langle \Omega_B \rangle_m}{\langle \Omega_D \rangle_m}. \tag{9}$$

This vorticity generation ratio differs from that defined by Chen et al. [23] in their analysis of low-speed buoyant jet diffusion flames. They employed a generic flame structure of jet diffusion flames in the context of a single conserved scalar to obtain their dimensionless vorticity generation parameter. This works out to be the ratio of the Reynolds number to the Froude number multiplied by the square root of the Schmidt number. In contrast, the ratio V_g used herein is simply based on values of the $\langle \Omega_i \rangle_m$ terms. From Table 1, it can be seen that as the heat release parameter increases, global baroclinic torque production diminishes, while global gas expansion effects become larger. From the values of the ratio V_g in Table 1 it is evident that baroclinic torque mechanisms dominate for each case.

The reason why baroclinic production dominates the overall distribution of the vorticity budget is believed to be related to the presence of the walls. Other studies have demonstrated that one of the primary side effects of confinement is an increase in the local pressure in coflowing reacting jets ([24]). Thus, in comparison to unconfined flows, confined flows are subject to larger freestream pressure magnitudes, causing increased pressure gradients and thus larger baroclinic torques. The magnitude of the pressure field is lowered as the proximity of the walls is increased. This was verified by performing a series of numerical experiments varying the lateral wall distance parameter L_y and monitoring the overall baroclinic torque production within the domain. The results of this exercise are shown in Table 2.

Table 1 Effect of heat release on vorticity generation ratio

Case	$\langle \Omega_B \rangle_m$	$\langle \Omega_D \rangle_m$	$\langle D\omega/Dt \rangle_m$	V_g
1	1700	500	1300	3.4
2	1600	550	1200	2.9
3	1500	575	1000	2.6

Table 2 Effect of wall confinement and heat release on baroclinic torque production

L_y	T_f/T_o	$\langle \Omega_B \rangle_m$
1.00	1.7	1700
1.25	1.7	1500
1.50	1.7	1300
1.00	2.5	1600
1.25	2.5	1450
1.50	2.5	1250
1.00	2.7	1500
1.25	2.7	1300
1.50	2.7	1100

From Table 2, we see that as the walls are moved further away from the coflowing jets, for a given level of heat release, the average baroclinic torque term drops in magnitude. Thus, the resulting pressure gradient term contribution to the vorticity budget is reduced with increased lateral wall proximity. Another reason that the baroclinic torques dominate these reacting flow fields may have to do with the relatively high speeds of the flows considered (the mean flow Mach number is on the order of Ma$\sim$0.50). As the local velocity increases the density decreases and the temperature increases leading to larger values of local baroclinic torque in comparison to low speed simulations.

Summary and Conclusions

Simulations of coplanar jets subjected to close proximity confinement and increased levels of heat release have been performed. This study has quantified the effect of wall confinement on the contribution of baroclinic torque on the vorticity dynamics of flame-vortex-wall interactions. The primary conclusion is that for a fixed level of heat release, the mechanism of baroclinic torque vorticity production decreases with less severe wall confinement.

Acknowledgments

The authors would like to thank Luc Vervisch for providing us with the numerical simulation code used in our investigation. This research was supported in part by ONR Grant N00014-93-1-1305 under the direction of Klaus Schadow. The authors gratefully acknowledge computing support on the Cray C-90 provided by the San Diego Supercomputing Center.

Nomenclature

$\overline{B}$ = reduced pre-exponential factor
c = speed of sound
c_o = reference speed of sound
d_o = width of oxidizer jet
f = frequency of forcing
L_x = size of domain in streamwise direction
L_y = size of domain in lateral direction
Ma_{in} = Mach number based on inlet velocity
N = number of grid points
p = pressure
Pe = Peclet number
Pr = Prandtl number
r = mass of oxidizer required to burn a unit mass of fuel
Re_{ac} = Reynolds number based on reference speed of sound
Re = Reynolds number based on oxidizer jet width
S = effective fuel/air mass stoichiometric ratio
Sc = Schmidt number
St_{d_o} = Strouhal number based on oxidizer jet width d_o
t = time

t_f = convection time
t_r = reaction time
$\mathbf{T}$ = shear stress tensor
T_f = maximum flame temperature
T_o = minimum flame temperature
$\mathbf{u}$ = velocity vector
u = streamwise velocity
$\overline{u}$ = mean streamwise velocity
$u_{c,p}$ = convection speed of primary vortex pair
$u_{c,s}$ = convection speed of secondary vortex pair
V_g = vorticity generation ratio
Y_δ = mass fraction of δth species
$Y_{\delta,o}$ = reference value of δth species mass fraction
Z = mixture fraction
Z_c = stoichiometric value of mixture fraction

Greek

$\hat{\beta}_r$ = most amplified frequency
γ = specific heat ratio
ε = perturbation amplitude
ν_o = reference value of kinematic viscosity
ρ = density
ρ_o = reference value of density
σ_f = Courant-Friedrichs-Lewy number for convection
σ_r = Courant-Friedrichs-Lewy number for reaction
τ_δ = forcing period of species δ
ψ = phase angle of inlet forcing
ω = vorticity vector
ω_z = signed vorticity
$\dot{\omega}_T$ = reaction rate
Ω_i = ith vorticity transport term
$\langle\Omega_i\rangle$ = ith averaged vorticity transport term
$\langle\Omega_i\rangle_m$ = mean ith averaged vorticity transport term

References

[1] Coats, C. M., 1996, ''Coherent Structures in Combustion,'' Prog. Energy Combust. Sci., **22**, pp. 427–509.
[2] Poinsot, T., Haworth, D., and Bruneaux, G., 1993, ''Direct Simulation and Modeling of Flame-Wall Interaction for Premixed Turbulent Combustion,'' Combust. Flame, **95**, pp. 118–133.
[3] Hackert, C. L., Ellzey, J. L., and Ezekoye, O. A., 1998, ''Effects of Thermal Boundary Conditions on Flame Shape and Quenching in Ducts,'' Combust. Flame, **112**, pp. 73–84.
[4] Roberts, W. L., Driscoll, J. F., Drake, M. C., and Goss, L. P., 1993, ''Images of the Quenching of a Flame by a Vortex to Quantify Regimes of Turbulent Combustion,'' Combust. Flame, **94**, pp. 58–69.
[5] Peters, N., 1983, ''Local Quenching due to Flame Stretch and Non-premixed Turbulent Combustion,'' Combust. Sci. Technol., **30**, pp. 1–17.
[6] Wichman, I. S., 1989, ''On the Quenching of a Diffusion Flame Near a Cold Wall,'' Combust. Sci. Technol., **64**, pp. 295–313.
[7] Katta, V. R., Hsu, K. Y., and Roquemore, W. M., 1996, ''Simulation of Local Quenching in a Methane-Air Jet Diffusion Flame,'' Chemical and Physical Processes in Combustion Fall Technical Meeting, Hilton Head, SC, pp. 381–384.
[8] Schadow, K., 1995, private communications.
[9] Anderson, K. R., Mahalingam, S., and Hertzberg, J. R., 1999, ''A Two-Dimensional Planar Computational Investigation of Flame Broadening in Confined Non-Premixed Jets,'' Combust. Flame, **118**, pp. 233–247.
[10] Guichard, L., Vervisch, L., and Domingo, P., 1995, ''Numerical Study of the Interaction Between a Mixing Zone and a Pressure Discontinuity,'' AIAA Paper 95-0877.
[11] Lele, S. V., 1992, ''Compact Finite Difference Schemes With Spectral-Like Resolution,'' J. Comput. Phys., **103**, pp. 16–42.
[12] Spalart, P. R., Moser, R. D., and Rogers, M. M., 1991, ''Spectral Methods for the Navier-Stokes Equations With One Infinite and Two Periodic Directions,'' J. Comput. Phys., **96**, pp. 297–324.
[13] Poinsot, T., and Lele, S., 1992, ''Boundary Conditions for Direct Simulations of Compressible Viscous Flows,'' J. Comput. Phys., **101**, pp. 104–129.
[14] Anderson, K. R., Hertzberg, J. R., and Mahalingam, S., 1996, ''Classification of Absolute and Convective Instabilities in Premixed Bluff Body Stabilized Flames,'' Combust. Sci. Technol., **112**, pp. 257–269.
[15] Gutmark, E., Parr, T. P., Hanson-Parr, D. M., and Schadow, K. C., 1993, ''Control of Sooty High Energy Fuel Combustion,'' *Proceedings from the Sixth O.N.R. Propulsion Meeting*, University of Colorado, Boulder, CO, pp. 54–59.
[16] Hosangadi, A., Merkle, C. L., and Turns, S. R., 1990, ''Analysis of Forced Combusting Jets,'' AIAA J., **28**, pp. 1473–1480.
[17] Miller, R. S., Madnia, C. K., and Givi, P., 1995, ''Numerical Simulation of Non-Circular Jets,'' Comput. Fluids, **24**, pp. 1–25.
[18] Petersen, R. A., 1978, ''Influence of Wave Dispersion on Vortex Pairing in a Jet,'' J. Fluid Mech., **89**, pp. 469–495.
[19] Gutmark, E., and Ho, C. M., 1983, ''Preferred Modes and the Spreading Rates of Jets,'' Phys. Fluids, **26**, pp. 2932–2938.
[20] Mahalingam, S., Cantwell, B. J., and Ferziger, J. H., 1990, ''Full Numerical Simulation of Coflowing, Axisymmetric Jet Diffusion Flames,'' Phys. Fluids, **2**, pp. 720–728.
[21] Clemens, N. T., and Paul, P. H., 1995, ''Effects of Heat Release on the Near-Field Flow Structure of Hydrogen Jet Diffusion Flames,'' Combust. Flame, **102**, pp. 271–284.
[22] Gutmark, E., Parr, T. P., Hanson-Parr, D. M., and Schadow, K. C., 1989, ''Azimuthal Structure of an Annular Diffusion Flame,'' Combust. Flame, **75**, pp. 229–240.
[23] Chen, L.-D., Roquemore, W. M., Goss, L. P., and Vilimpoc, V., 1991, ''Vorticity Generation in Jet Diffusion Flames,'' Combust. Sci. Technol., **77**, pp. 41–57.
[24] Strawa, A. W., and Cantwell, B. J., 1985, ''Visualization of the Structure of a Pulsed Methane-Air Diffusion Flame,'' Phys. Fluids, **28**, pp. 2317–2320.

Nonequilibrium Natural Convection in a Differentially Heated Cavity Filled With a Saturated Porous Matrix

A. A. Mohamad
Department of Mechanical Engineering, University of Calgary, Calgary AB T2N 1N4, Canada

Steady-state natural convection in an enclosure filled with a saturated porous medium is investigated numerically. Brinkman-Forchheimer's extension of Darcy flow with a nonequilibrium model is used in the analysis. The paper intends to address the validity of the equilibrium model for natural convection. The predicted results indicated that the equilibrium model is difficult to justify for non-Darcy regime and when the solid thermal conductivity is higher than the fluid thermal conductivity. The maximum differences in the temperatures between the two phases take place at the bottom-left corner and due to skew-symmetry of the problem at the upper-right corner. [S0022-1481(00)00402-3]

Keywords: Cavities, Heat Transfer, Natural Convection, Nonequilibrium, Porous Media

Introduction

Natural convection in an enclosure filled with a saturated porous matrix is a fundamental problem, with many applications considered by various authors ([1]). Frequently, authors considered that the porous matrix is in thermal equilibrium with the fluid, i.e., the temperature of the solid and the fluid are assumed to be the same within a representative control volume. Thermal equilibrium is not valid when heat is released in the solid or in the fluid, such as in combustion in porous media ([2]) or in catalyst converters. Furthermore, when the length scale of the representative control volume is of the order of the length of the system, then the thermal equilibrium model can become inaccurate ([3]). In the nonequilibrium modeling, one needs to know the volumetric heat transfer coefficient between the solid and fluid phases (particle Nusselt parameter). In the literature there are some attempts to measure the volumetric heat transfer coefficient indirectly under forced convection conditions ([4–5]). No experimen-

Contributed by the Heat Transfer Division for publication in the JOURNAL OF HEAT TRANSFER. Manuscript received by the Heat Transfer Division March 14, 1999; revision received January 11, 2000. Associate Technical Editor: C. Beckermann.

tal or theoretical analyses identified in the literature regarding the volumetric heat transfer coefficient for natural convection conditions. Nonequilibrium models have been considered by several authors ([6–8],[3]) and applied to forced convection problems. To the author's best knowledge, nonequilibrium models have not been applied to the natural flow, which is the subject of this work.

The analysis showed that the equilibrium model could not be justified for a certain range of the controlling parameters. Especially when the thermal conductivity of solid phase is higher than the thermal conductivity of fluid phase and for non-Darcy regime, $\mathrm{Ra}_m(\mathrm{RaDa})>100$. The deviation from the equilibrium condition is profound in the region of the boundary layer development.

Model Equations

Steady, laminar, natural convection is considered in a square cavity filled with a saturated porous matrix. The thermophysical properties are assumed to be constant, except the density variation with temperature in the buoyancy term. The standard Forchheimer, Brinkman extension Darcy momentum equation ([3]) is adopted in the analysis with the following energy equations:
(a) fluid phase:

$$U\frac{\partial\theta_f}{\partial X}+V\frac{\partial\theta_f}{\partial Y}=\nabla^2\theta_f+\frac{\mathrm{Nu}_p}{\Phi}(\theta_s-\theta_f) \tag{1a}$$

(b) solid phase:

$$0=\nabla^2\theta_s+\frac{\mathrm{Nu}_p}{(1-\Phi)K_r}(\phi_f-\theta_s). \tag{1b}$$

Height (H), α/H and ΔT are used for scaling length, velocity, and temperature, respectively. The parameters K_r, Φ, Nu_p, α stands for the thermal conductivity ratio (solid/fluid), porosity, particle Nusselt number, and thermal diffusivity, respectively.

At the vertical boundaries, the local Nusselt parameters for solid and fluid phases are defined as

$$\mathrm{Nu}_s=\frac{\partial\theta_s}{\partial\xi}\quad\text{and}\quad\mathrm{Nu}_f=\frac{\partial\theta_f}{\partial\xi}. \tag{2}$$

Note that Nu_s and Nu_f are based on the thermal conductivity of the solid matrix and of the saturated fluid, respectively. By considering the energy balance at the boundary $(q''_t=q''_s(1-\Phi)+q''_f\Phi)$, the total Nusselt parameter can be written as

$$\mathrm{Nu}_t=(1-\Phi)K_r\mathrm{Nu}_s/\Phi+\Phi\mathrm{Nu}_f/[(1-\Phi)K_r]. \tag{3}$$

It should be mentioned that the definition of the total Nusselt parameter is based on the effective thermal conductivity of the medium (parallel model). Average Nu parameter is obtained by integrating the local Nu along the heated boundary. Average temperature difference between the two phases is calculated as

$$\Delta\theta_{av}=\int_0^1\int_0^1\Delta\theta_{sf}\,d\xi\,d\eta. \tag{4}$$

The above definition may be helpful in justifying a nonequilibrium model globally. For local evaluation, the maximum temperature difference between the two phases is presented.

Free convection heat transfer from an isolated sphere can be calculated from the correlation suggested by Churchill [9]; $\mathrm{Nu}_d=2+0.589\ \mathrm{Ra}_d^{1/4}/[1+(0.496/\mathrm{Pr})^{9/16}]^{4/9}$, where the Nusselt and the Rayleigh parameters are based on the sphere diameter. This correlation can be used to estimate natural convection heat transfer from particles in a bed. For small bead diameters, d, (order of cm) and since the temperature difference between the beads and saturated fluid is order of unity, then the $\mathrm{Nu}_d(h\,d/K_f)$ can be estimated in the range of 2 to 10. The volumetric heat transfer h_v, which is defined as h multiplied by the surface area of the solid matrix per unit volume, can be expressed as $h_v=6(1-\Phi)h/d$. Then, the Nu_p can be formulated as

Table 1 Comparison of average Nusselt parameter predictions with [13] and [14] results

Ra	Da	Present	[13]	[14]
10^5	10^{-1}	4.30	4.36	
10^5	10^{-4}	1.07		1.067 ($\Phi=0.4$); 1.071 ($\Phi=0.6$)
10^6	10^{-4}	2.70		2.55 ($\Phi=0.4$); 2.72 ($\Phi=0.6$)
10^8	10^{-4}	18.27	18.4	
10^{12}	10^{-8}	47.25	44.30	

$$\mathrm{Nu}_p=h_vH^2/K_f=6(1-\Phi)\mathrm{Nu}_d(H/d)^2. \tag{5}$$

The geometric parameter H/d is the number of beads in a linear dimension of the container (height). In practical applications this number can be of order 1000.

Remarks on the Boundary Conditions

The velocity components are set to zero at the boundaries. The solid and fluid temperature derivatives normal to the horizontal boundaries are set to zero, i.e., adiabatic condition. For vertical boundaries, it is assumed that the fluid and solid phases have the same temperature at the hot and cold vertical boundaries, i.e., equilibrium condition. In fact, the latter boundary condition is not valid, due to the channeling effect. The channeling has significant effect on the rate of heat transfer which is considered by different authors ([10–11]). In this work, the issue of a nonequilibrium boundary condition and variable porosity model is not used.

Method of Solution

A control volume approach is used to solve the model equations with the SIMPLER algorithm. Central difference is used to approximate advection-diffusion terms (second-order accurate scheme). To alleviate the convergence problem due to using the central difference scheme, the deferred correction method of Khosla and Rubin [12] is adopted. Different numbers of grids were tested to insure that the results are grid size independent. The denser grids were clustered near the boundaries. The difference between predictions of 41×41 and 81×81 grid sizes in predicting the temperature field was not that significant. The maximum difference in the prediction of the average Nusselt number was about 1.0 percent between two grid sizes for $\mathrm{Ra}=10^8$, $\mathrm{Da}=10^{-5}$, $\mathrm{Pr}=1$, $K_r=1.0$, $\mathrm{Nu}_p=1000$. Nonuniform 81×81 grids were used to generate the results.

Furthermore, the predicted results were compared with available results in the literature for an equilibrium model. If the Nu_p is

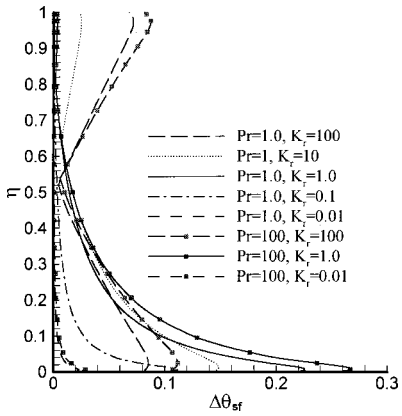

Fig. 1 Effect of K_r on the maximum temperature difference between the solid and the fluid as function of height and in the left half of the cavity, for $\mathrm{Ra}=1\times10^8$, $\mathrm{Da}=1\times10^{-5}$, and $\mathrm{Nu}_p=1000$

set to zero in Eq. (1), then Eq. (1*a*) simulates the thermal equilibrium condition, and Eq. (1*b*) simulates heat conduction in stagnant media. Since the vertical boundary conditions are adiabatic, the solid temperature must linearly vary from hot to cold walls. For the Nu_p equal to zero, the solid temperature distribution was linear and the average Nusselt parameter for saturated porous medium is tabulated in Table 1 and well compared with results of Lauriat and Prasad [13] and Nithiarasu et al. [14]. It should be mentioned that for $Ra=10^{12}$, convergent results are obtained by adopting 121 $\times$121 nonuniform grids.

Results and Discussions

The results are presented for a fixed value of porosity, $\Phi=0.4$. The maximum temperature difference between the solid and fluid phases is monitored along the height and in the left half of the enclosure and plotted in Fig. 1 for $Pr=1.0$ and $Pr=100$ and for $Ra_m=1000$ ($Ra=10^8$, $Da=10^{-5}$) and for $Nu_p=1000$. Since the problem is centro-symmetry, there is no need to consider the other half of the enclosure. Figure 1 shows that the highest value of the maximum difference takes place at the bottom left and by skew-symmetry of the problem at the upper right corners of the enclosure, where the boundary layer starts to develop. The $\Delta\theta_{sf,\max}$ decreases along the height of the enclosure for K_r less than or equal to one. For $K_r=100$, the highest value of $\Delta\theta_{sf,\max}$ takes place at the corners of the enclosure; this is due to the horizontal heat conduction effect at these regions. The $\Delta\theta_{sf,\max}$ enhances as the Pr parameter increases to 100. It is found that the results for $Pr=10$ is similar to the results for $Pr=100$, and the difference is significant, i.e., the effect of the Pr parameter on the results decreases for $Pr>10$.

Typical $\Delta\theta_{sf}$ profiles are shown in Fig. 2(*a*) and 2(*b*) at the first quarter and at the midheight of the cavity as a function of ξ, respectively. The results are for the modified Ra_m of 1000 ($Ra=10^8$, $Da=1\times10^{-5}$), $Nu_p=1000$ and for $Pr=1.0$. It is evident

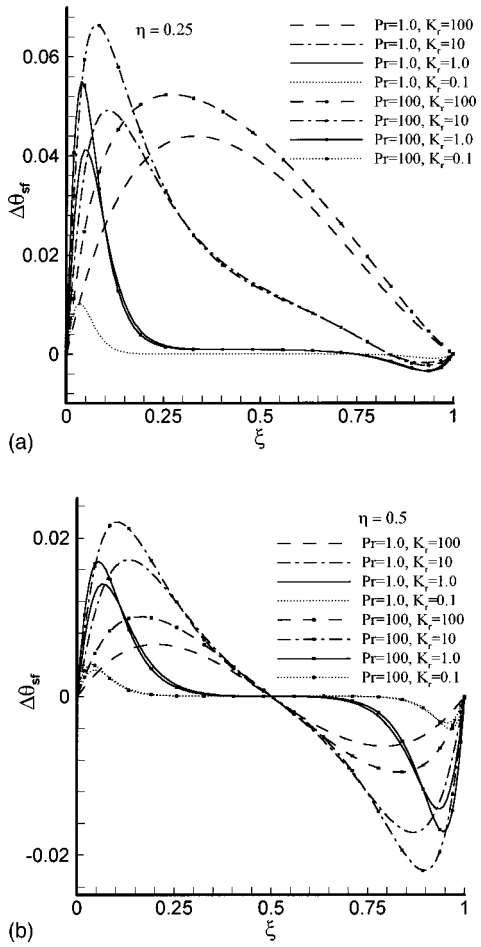

Fig. 2 (*a*) Effect of K_r on the temperature difference between solid and fluid phases at the first quarter of the enclosure for the same parameters as for Fig. 1. (*b*) Effect of K_r on the temperature difference between solid and fluid phases at the midheight of the enclosure for the same parameters as for Fig. 1.

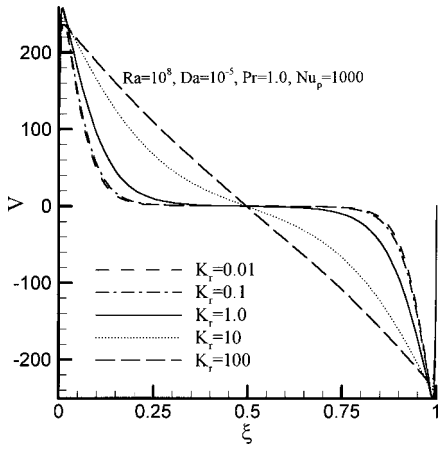

Fig. 3 Effect of K_r on the *V*-velocity profiles at the midheight of the enclosure

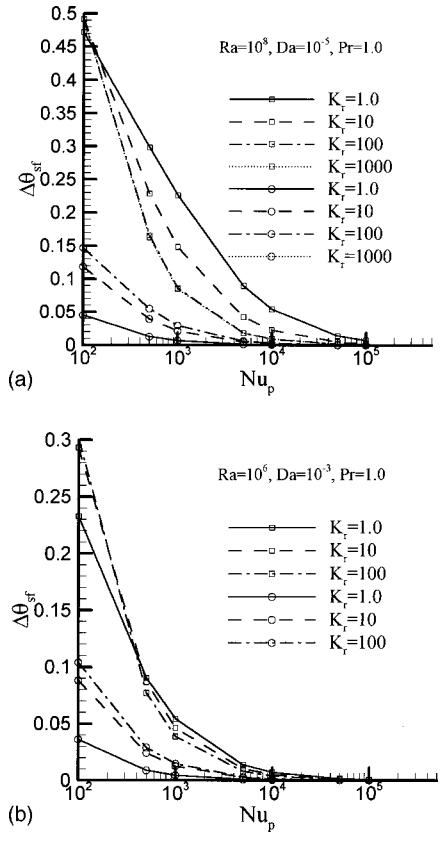

Fig. 4 (*a*) Effect of K_r on the maximum (square symbol) and average (circle symbol) temperature difference between solid and fluid for $Ra=1\times10^8$, $Pr=1.0$, $Da=1\times10^{-5}$ as a function of Nu_p. (*b*) Effect of K_r maximum (square symbol) and average (circle symbol) temperature difference between solid and fluid for $Ra=1\times10^6$, $Pr=1.0$, $Da=1\times10^{-3}$ as a function of Nu_p.

Table 2 (*a*) **Effect of K_r on the rate of heat transfer for the parameters: $Ra=1\times10^8$, $Da=1\times10^{-5}$, $Nu_p=1000$.** (*b*) **Effect of K_r on the rate of heat transfer for the parameters of $Ra=1\times10^8$, $Pr=1.0$, $Nu_p=100$.**

(*a*)

	Pr=1.0			Pr=10			Pr=100		
K_{sf}	Nu_f	Nu_s	Nu_t	Nu_f	Nu_s	Nu_t	Nu_f	Nu_s	Nu_t
0.01	10.47	10.34	10.47	11.92	11.73	11.92	12.16	11.96	12.14
0.10	9.86	9.05	9.74	11.26	10.08	11.11	11.49	10.25	11.33
1.00	7.13	5.29	6.02	8.38	5.82	6.85	8.60	5.90	6.98
10.0	2.81	1.85	1.91	3.53	2.02	2.12	3.67	2.05	2.15
100.	1.26	1.04	1.04	1.48	1.07	1.07	1.50	1.06	1.07

(*b*)

	$Da=1\times10^{-5}$			$Da=1\times10^{-6}$		
K_{sf}	Nu_f	Nu_s	Nu_t	Nu_f	Nu_s	Nu_t
0.01	10.49	9.53	10.47	3.03	2.99	3.03
0.10	10.07	6.90	9.65	2.81	2.60	2.78
1.00	8.50	3.43	5.46	1.95	1.59	1.73
10.0	6.08	1.45	1.74	1.26	1.07	1.08
100.	5.10	1.05	1.07	1.16	1.03	1.03

that, as the thermal conductivity ratio decreases, the difference between the solid and fluid temperatures decreases. For $K_r \leq 1.0$, the difference in the temperature is profound at the boundaries. The solid temperature becomes higher than the fluid temperature in the region of ascending flow and the reverse is true in the region of descending flow. Also, it can be seen from Fig. 3 that, as the thermal conductivity of the solid increases compared with fluid conductivity, more heat conducts into the horizontal direction and enhances the buoyancy force in the *x*-direction. For $K_r = 100$, heat transfer is mainly conductive and the velocity profile at midheight of the cavity is almost linear. The results indicate that using the Prandtl parameter based on fluid properties is not appropriate. The Prandtl parameter should be based on effective medium properties.

The *V*-velocity (Fig. 3) is sensitive to the thermal conductivity ratios greater than one ($K_r > 1.0$), while it is not the case for $K_r < 1.0$. This is due to the fact that heat conduction in the horizontal direction enhances the buoyancy force at the core of the cavity. While for $K_r < 1$, the vertically advected heat is higher than the horizontal conduction; accordingly, buoyancy force almost diminishes at the core. Also, it can be noticed that the peak value of the velocity decreases as K_r increases. For Pr=10, similar velocity profiles are obtained as for Pr=1.0, except that the peak value of the velocity is higher for Pr=10.

The effect of the particle Nusselt parameter (Nu_p) is addressed by changing Nu_p from 10^2 to 10^5 (Figs. 4(*a*) and 4(*b*)). These figures show maximum values of $\Delta\theta_{sf}$ (square symbols) and average values of $\Delta\theta_{sf}$ (circle symbols) for the same $Ra_m(1000)$ but for $Ra=10^6$ and 10^8, respectively. It is evident that the average maximum value of $\Delta\theta_{sf}$ increases as Nu_p decreases and the equilibrium model prediction can be quite erroneous for $Nu_p < 1000$. This argument is valid for Ra_m greater than or equal to 1000. Also, it is found that the difference in the temperature of solid and fluid becomes insignificant for low Ra_m (less than 500) values. From the previous discussion, it is expected that decreasing the modified Rayleigh parameter and/or Darcy parameter will decrease the influence of the thermal conductivity ratio on the temperature difference between the two phases.

Based on the above results, the equilibrium model is difficult to justify for high Ra and/or Da (Ra_m order of 1000 and above). Also, if the Nu_p parameter is low, then the nonequilibrium model should be adopted.

Table 2(*a*),(*b*) summarizes the influence of K_r on the rate of heat transfer for $Ra=1\times10^8$. It can be noted that for $Pr \geq 10$, the rate of heat transfer is not a strong function of the Prandtl parameter. Also, the Nu_s and Nu_f parameters decrease as K_r increases. The total Nusselt parameter, Nu_t, approaches the conduction limit (becomes unity) as K_r increases. For Pr=1.0, Nu_f decreases and Nu_s increases by decreasing Nu_p from 1000 to 100, but the total effect on the total Nu_t is not that strong. Furthermore, as Da decreases Nu values decrease significantly, this is due to the decrease in the permeability of the medium.

Conclusions

As a conclusion, the results indicate that one of the important parameters is the particle Nusselt parameter. If this parameter is of order 1000 or less, then the equilibrium model is difficult to justify for $Ra \geq 1\times10^6$ and for $Ra_m \geq 1000$. Also, for $Ra=1\times10^8$ and $Ra_m \geq 10^4$, the equilibrium model is difficult to justify even for high Nu_p (order of 1000). The above discussion is valid for K_r equal to or greater than unity. The difference between solid and fluid phase temperatures is profound at the bottom left corner and upper right corner of the cavity for K_r equal or less than unity. For $K_r > 1.0$, the horizontal heat conduction enhances the buoyancy force at the core of the cavity.

The results are presented for an equilibrium boundary condition due to lack of information. Further analysis is needed to address the effect of a nonequilibrium boundary condition and justify the analyses experimentally.

References

[1] Nield, D. A., and Bejan, A, 1992, *Convection in Porous Media*, Springer-Verlag, New York.

[2] Mohamad, A. A., Ramadhyani, S., and Viskanta, R., 1994, ''Modelling of Combustion and Heat Transfer in a Packed Bed With Embedded Coolant Tubes,'' Int. J. Heat Mass Transf., **37**, pp. 1181–1197.

[3] Kaviany, S., 1995, *Principles of Heat Transfer in Porous Media*, 2nd Ed., Springer-Verlag, New York.

[4] Younis, L. B., and Viskanta, R., 1993, ''Experimental Determination of the Volumetric Heat Transfer Coefficient Between Stream of Air and Ceramic Foam,'' Int. J. Heat Mass Transf., **36**, No. 6, pp. 1425–1434.

[5] Galitseisky, B. M., and Loshkin, A. L., 1997, ''Unsteady Method of Experimental Investigation of Heat Transfer in Porous Material,'' *Int. Symp. On Transient Convective Heat Transfer*, J. Padet, and F. Arinc, eds., Begell House, New York, pp. 201–214.

[6] Vortmeyer, D., and Schaefer, B. J., 1974, ''Equivalence of One- and Two-Phase Models for Heat Transfer Processes in Packed Beds, One Dimensional Theory,'' Chem. Eng. Sci., **29**, pp. 485–491.

[7] Zanotti, F., and Carbonell, R. G., 1984, ''Development of Transport Equations for Multiphase System—I, General Development for Two-Phase Systems,'' Chem. Eng. Sci., **39**, pp. 263–278.

[8] Quintard, M., and Whitaker, S., 1993, ''One and Two-Equation Models for Transient Diffusion Processes in Two-Phase Systems,'' Adv. Heat Transfer, **23**, pp. 369–464.

[9] Churchill, S. W., 1983, ''Free Convection Around Immersed Bodies,'' *Heat Exchanger Design Handbook*, E. U. Schlunder, ed., Hemisphere, New York.

[10] Hong, J. T., Yamada, Y., and Tien, C. L., 1987, ''Effect of Non-Darcian and

Nonuniform Porosity on a Vertical Plate Natural Convection in Porous Media,'' J. Heat Transfer, **109**, pp. 356–362.
[11] David, E., Lauriat, G., and Cheng, P., 1991, ''A Numerical Solution of Variable Porosity Effects on Natural Convection in a Packed-Sphere Cavity,'' J. Heat Transfer, **113**, pp. 391–399.
[12] Khosla, P. K., and Rubin, S. G., 1974, ''A Diagonally Dominant Second-Order Accurate Implicit Scheme,'' Comput. Fluids, **2**, pp. 207–209.
[13] Lauriat, G., and Prasad, V., 1989, ''Non-Darcian Effects on Natural Convection in a Vertical Porous Enclosure,'' Int. J. Heat Mass Transf., **32**, No. 11, pp. 2135–2148.
[14] Nithiarasu, P., Seetharamu, K. N., and Sundararajan, T., 1997, ''Natural Convective Heat Transfer in a Fluid Saturated Variable Porosity Medium,'' Int. J. Heat Mass Transf., **40**, No. 16, pp. 3955–3967.

Enhanced Natural Convection in a Vertical Rectangular Cavity on Account of the Mixing of Two Pure Gases

A. Campo
College of Engineering, Idaho State University, Pocatello, ID 83209

B. Zamora
Dpto. de Ingeniería Mecánica y Energética, Universidad Politécnica de Cartagena, 30203 Cartagena, Murcia, Spain

[S0022-1481(00)00901-4]

Keywords: Binary, Cooling, Enhancement, Heat Transfer

Introduction

An important class of natural convection phenomena in industry refers to the confined flows inside stationary cavities when a temperature differential is impressed at two opposing walls ([1]). In such cavities, the fluid circulation occurs by gravitational effects and consists of two major streams: (a) a vertical fluid stream that rises along the hot wall and (b) a cold fluid stream that descends along the cold wall.

In general, the enhancement of heat transfer in gas-filled cavities is a very difficult task because of the low fluid velocities involved. In view of this characteristic, it is of fundamental and practical interest to explore alternative instruments for the heat transfer augmentation that are power-independent, and on the other hand exclude modifications of the wall surfaces. Correspondingly, the central objective of this technical note is to explore the capabilities of different gaseous media to be utilized in natural convection cavities. And from here, to determine whether a mixture of two pure gases yields levels of heat transfer increments that are unattainable: (a) by each pure gas separately or (b) by air.

Transport Properties of a Mixture of Two Pure Gases

The composition of a mixture of two gases, x, is defined as $x=m_2/(m_1+m_2)$, where m_1 and m_2 designate the respective masses of gas 1 and gas 2. Dimensional analysis stipulates that the four transport properties that affect natural convection flows are: density, isobaric heat capacity, dynamic viscosity, and thermal conductivity.

1 Density. The density of a mixture of two pure gases, ρ_m, may be expressed by the linear combination of specific volumes:

$$\frac{1}{\rho_m}=\frac{(1-x)}{\rho_1}+\frac{x}{\rho_2}. \tag{1}$$

2 Isobaric Heat Capacity. At moderate temperatures and low pressures, the isobaric specific heat capacity of a mixture of two pure ideal gases, $c_{p,m}$, may be written by the linear form

$$c_{p,m}=(1-x)c_{p,1}+xc_{p,2}. \tag{2}$$

3 Dynamic Viscosity. The dynamic viscosity of a mixture of two pure gases, μ_m, at moderate temperatures and low pressures does not vary linearly with the composition, x. Wilke [2] proposed the nonlinear model

$$\mu_m=\frac{\mu_1}{\left[1+\phi_{1,2}\left(\frac{x}{1-x}\right)\left(\frac{M_1}{M_2}\right)\right]}+\frac{\mu_2}{\left[1+\phi_{2,1}\left(\frac{1-x}{x}\right)\left(\frac{M_2}{M_1}\right)\right]} \tag{3}$$

in which $\phi_{1,2}$ and $\phi_{1,2}$ signify the viscosity parameters of the gas mixture

$$\phi_{1,2}=\frac{\left[1+\left(\frac{\mu_1}{\mu_2}\right)^{1/2}\left(\frac{M_2}{M_1}\right)^{1/4}\right]^2}{\sqrt{8}\left[1+\left(\frac{M_1}{M_2}\right)\right]^{1/2}},\quad \phi_{2,1}=\left(\frac{\mu_2}{\mu_1}\right)\left(\frac{M_1}{M_2}\right)\phi_{1,2}. \tag{4}$$

4 Thermal Conductivity. The thermal conductivity of a mixture of two pure gases k_m is not a linear function of the composition x either. The method that is suitable for the estimation of k_m at moderate temperatures and low pressures is the one recommended by Wassiljeva [3],

$$k_m=\frac{k_1}{\left[1+A_{1,2}\left(\frac{x}{1-x}\right)\left(\frac{M_1}{M_2}\right)\right]}+\frac{k_2}{\left[1+A_{2,1}\left(\frac{1-x}{x}\right)\left(\frac{M_2}{M_1}\right)\right]}, \tag{5}$$

where the interaction parameters $A_{1,2}$ and $A_{2,1}$ are obtained from the linear relations ([4,5])

$$A_{1,2}=1.065\phi_{1,2},\quad A_{2,1}=1.065\phi_{2,1}. \tag{6}$$

Here, the symbols $\phi_{1,2}$ and $\phi_{1,2}$ stand for the viscosity parameters of a gas mixture which have already been defined in Eq. (4) ([2]).

Heat Transmission in a Vertical Rectangular Cavity

The vertical rectangular cavity depicted in Fig. 1 is defined as an enclosed space bounded by two vertical walls held at uniform temperatures, T_h and T_c, and two insulated horizontal walls. The gravity vector is aligned with the vertical walls.

The rate of heat transmission Q across the vertical rectangular cavity in question is calculated from ''Newton's equation of cooling:''

$$Q=\bar{h}A(T_h-T_c) \tag{7}$$

where $\bar{h}$ is the mean heat transfer coefficient associated with the impressed temperature differential T_h-T_c at the active walls, and A is the surface area of one active wall. Fundamentally, h is a function of the geometry of the cavity, the orientation of the cavity, the fluid transport properties, and the applied temperature difference.

Empirical correlation equations for natural convection in cavities induced by opposing hot and cold walls abound in the heat

Contributed by the Heat Transfer Division for publication in the JOURNAL OF HEAT TRANSFER. Manuscript received by the Heat Transfer Division Jan. 6, 1999; revision received Sept. 29, 1999. Associate Technical Editor: F. Cheung.

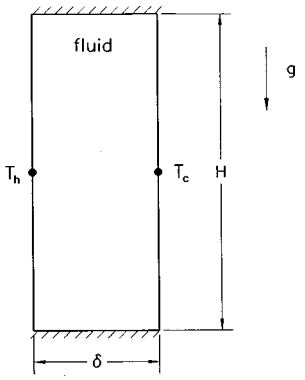

Fig. 1 Vertical rectangular cavity

transfer literature. Jakob [6] and Graff and Van der Held [7] developed a simple correlation equation of power form that accounts for the aspect ratio (H/δ)

$$\overline{\mathrm{Nu}}_\delta = \frac{\bar{h}\delta}{k} = C\,\mathrm{Ra}_\delta^n \left(\frac{H}{\delta}\right)^m \tag{8}$$

and covers the Prandtl number interval $0.5 \leqslant \mathrm{Pr} \leqslant 2$. In the experimental-based equation, the cavity width δ was selected as the characteristic length in the mean Nusselt number $\overline{\mathrm{Nu}}_\delta$ and in the Rayleigh number Ra_δ. All transport properties are evaluated at an average temperature $\bar{T} = (T_h - T_c)/2$.

Mean Heat Transfer Coefficients of a Mixture of Two Pure Gases

Natural convection heat transfer in stationary cavities is conformed by two mechanisms ([1]). The first mechanism is of molecular nature. It is prototypical of conduction of heat in a layer of quiescent fluid and persists up to the incipience of convective motion, namely the attainment of a critical Rayleigh number $\mathrm{Ra}_{\delta,cr} = 2\times 10^3$. For $\mathrm{Ra}_\delta > \mathrm{Ra}_{\delta,cr}$, buoyancy forces induced by the temperature differential at the active walls outweighs the viscous forces. As a result of this imbalance the circulation motion becomes stronger, giving rise to a second mechanism by natural convection of heat. Knowing that the mechanism by conduction of heat is susceptible to only one transport property, i.e., the thermal conductivity, one feasible way for passively enhancing heat transfer in gas-filled cavities is to stimulate the other mechanism by natural convection of heat.

We designate $\bar{h}_m$ as the mean heat transfer coefficient of a mixture of two pure gases whose composition is x. Alternatively, Eq. (8) may be recast in terms of the four transport properties as follows:

$$\bar{h}_m = B k_m^{1-n} \mu_m^{-n} \rho_m^{2n} c_{p,m}^n . \tag{9}$$

Here, B is an overall coefficient that absorbs the coefficient C, along with a group of geometric and thermal quantities in Eq. (8). Owing that the exponent n assumes values of 1/4 and 1/3 for the undivided interval $2\times 10^3 \leqslant \mathrm{Ra}_\delta \leqslant 10^7$ in Table 1, Eq. (9) elucidates direct proportionalities between $\bar{h}_m$ and three transport properties k_m, ρ_m, and $c_{p,m}$, and only one inverse proportionality between h_m and μ_m. In turn, each of these transport properties is affected by the composition of the gas mixture x through the functional relaxations $k_m = g_1(x)$, $\mu_m = g_2(x)$, $\rho_m = g_3(x)$, and $c_{p,m} = g_4(x)$ which are described explicitly in Eqs. (1)–(6).

The objective of this subsection is to explore the optimal value of the gas composition x[1] (in other words the extrema of x) for a specific mixture of two pure gases at a preselected pressure and temperature. Information regarding the maximization or minimization of the mean heat transfer coefficient $\bar{h}_m$ can also be drawn from the analysis.

Table 1 Numerical values of the coefficient *C*, the exponents *n* and *m* in Eq. (8)

Ra_δ	H/δ	C	n	m
$<2\times 10^3$	⋯	1	0	0
$(2\times 10^3, 2\times 10^5)$	(11,42)	0.197	1/4	−1/9
$(2\times 10^5, 10^7)$	(11,42)	0.073	1/3	−1/9

Discussion of Results

Since air is the most commonly used coolant in industry, it was deemed appropriate to contrast the heat transfer features of the vertical rectangular cavity containing (a) air, (b) helium,* (c) nitrogen, and (d) a mixture of helium and nitrogen with a composition ranging from $x=0$ to 1. The relative merits of helium, nitrogen, and a mixture of helium and nitrogen are examined against air which surely constitutes the baseline case in the present comparative study. Typical numerical values of the four transport properties for these three gases are taken from Mills [8] and are summarized in the adjoining Table 2 for two extreme temperatures, namely, a low average temperature of 200 K and a high average temperature of 1000 K. Additionally, numerical values of the same transport properties for the mixture of helium and nitrogen are obtained from evaluating the set of Eqs. (1)–(6).

A brief discussion of the traits inherent to helium and nitrogen using air as a reference datum seems to be in order. Irrespective of the average temperature of operation, it may be seen that all transport properties of air and nitrogen have comparable values. Correspondingly, attention has been directed to helium and nitrogen only. First, the thermal conductivity of helium is between five and six times greater than nitrogen. Second, helium is ten times lighter than nitrogen. Third, the isobaric specific heat capacity of helium is five times larger than nitrogen. Fourth, the dynamic viscosities of helium and nitrogen are more or less alike. The size of these computed ratios prevail for all average temperatures that are contained in the interval between 200 K and 1000 K.

For a vertical rectangular cavity filled with all proportions of a $\mathrm{He/N_2}$ gas mixture, two figures have been prepared showing the variation of the relative mean heat transfer coefficient, $\bar{h}_m/B$, with respect to the composition x at two average temperatures: a low value of 200 K and at a high value of 1000 K. The format of the abscissa implies that the left extreme, $x=0$, corresponds to pure helium, whereas the right extreme, $x=1$, corresponds to pure nitrogen. In order to have an adequate point of reference that facilitates the comparison, the figures also display in the ordinate the

[1]Hydrogen is superior than helium, but the explosive potential of this gas requires special safety precautions.

Table 2 Transport properties of air, helium, and nitrogen: (*a*) *T*=200 K and *p*=1 atm

	k (W/m K)	ρ (kg/m^3)	c_p (J/kg K)	$\mu\times 10^6$ (kg/m s)
air	0.020	1.767	1009	13.59
helium	0.116	0.224	5200	15.60
nitrogen	0.020	1.707	1045	13.10

(*b*) *T*=1000 K and *p*=1 atm

	k (W/m K)	ρ (kg/m^3)	c_p (J/kg K)	$\mu\times 10^6$ (kg/m s)
air	0.067	0.354	1130	41.52
helium	0.313	0.049	5200	43.30
nitrogen	0.066	0.341	1167	39.40

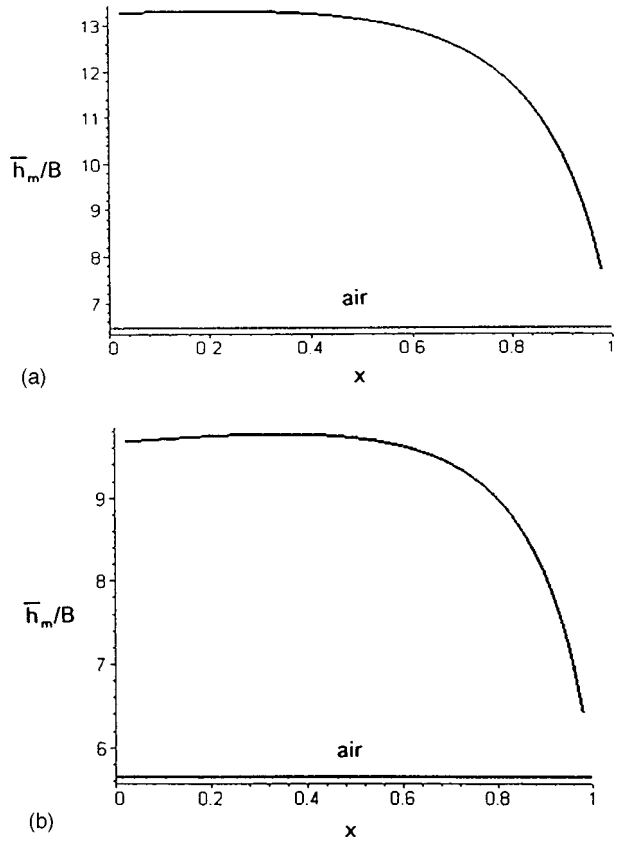

Fig. 2 Variation of the relative mean heat transfer coefficient, $\overline{h}_m/B$, with the composition, x, of a He/N_2 gas mixture for $n=1/4$: (*a*) 200 K, (*b*) 1000 K

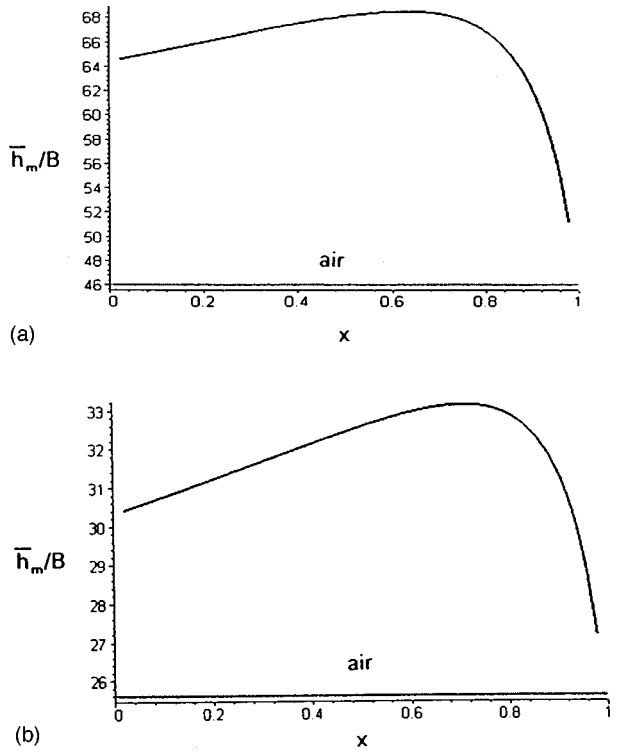

Fig. 3 Variation of the relative mean heat transfer coefficient, $\overline{h}_m/B$, with the composition, x, of a He/N_2 gas mixture for $n=1/3$: (*a*) 200 K, (*b*) 1000 K

appropriate value of $\overline{h}_m/B$ for a similar cavity, but filled with air. Figure 2 is associated with an exponent $n=1/4$, i.e., for a subinterval of application $2\times10^3<\mathrm{Ra}_\delta<2\times10^5$ in Table 1. Here, it may be observed that the two $\overline{h}_m/B$ curves descend gradually with increments of x and clearly no maxima is reached. This behavior is insensitive to the average temperature, and signifies that the largest heat transfer takes place when the cavity is filled with helium, in contrast the smallest heat transfer occurs when the cavity is filled with either nitrogen or air. An exponent $n=1/3$ is connected to Fig. 3, i.e., for a subinterval of application $2\times10^5<\mathrm{Ra}_\delta<10^7$ in Table 1. In this case, the two $\overline{h}_m/B$ curves follow a skewed bell shape. The maximum heat transfer $(\overline{h}_m/B)_{\max}$ happens at the optimal compositions of the gas mixture, $x^*=0.60$ for 200 K and 0.70 for 1000 K, respectively.

Further, it may be useful to assess the quantitative outcome of the heat transfer maximization from a different angle, that is constructing four ratios with each of the relative mean heat transfer coefficients $\overline{h}_m/B$ involving air, helium, nitrogen, and the optimal He/N_2 gas mixture. These ratios are called *heat transfer enhancement ratios* and are presented in Table 3.

In Table 3, the numbers listed in the second column reveal the discernible superiority of helium with respect to air; the *heat transfer enhancement ratio* is susceptible to the average temperature, raising from 18.9 to 40 percent as the average temperature diminishes from 1000 K to 200 K. On the contrary, the numbers listed in the third column substantiate the fact that, regardless of the average temperature, nitrogen is slightly inferior than air. As compared to air, the *heat transfer enhancement ratios* for the optimal He/N_2 mixture show marked ascending patterns; the ratios move up to ten percent (from 18.9 percent for He as compared to air to 28.9 percent for the optimal He/N_2 mixture as compared to He) at 1000 K and almost nine percent (from 40 percent for He as compared to air to 48.7 percent for the optimal He/N_2 mixture as compared to He) at 200 K. In view of the foregoing discovery, Eq. (9) may be particularized to the specific value of $n=1/3$ and recast explicitly by way of the four transport properties as follows:

$$\overline{h}_m = B\sqrt[3]{\frac{k_m^2\rho_m^2 c_{p,m}}{\mu_m}}. \tag{10}$$

Essentially, the nature of this equation uncovers the major contributions of k_m and ρ_m and the minor contributions of $c_{p,m}$ and μ_m towards the magnitude of $\overline{h}_m/B$.

For completeness, it should be mentioned that at very low Rayleigh numbers below $\mathrm{Ra}_{\delta,cr}=2\times10^3$, the transfer of heat in the vertical rectangular cavity is induced by the conduction mechanism across the gaseous layer. Under this limiting circumstance, the thermal conductivity is the only transport property that influences Newton's equation of cooling, Eq. (8). Among the three gases chosen in this comparative study, air, He, and N_2, unquestionably He is preferred over air and N_2 because He has the highest value of the thermal conductivity (see Table 2).

Table 3 Heat transfer enhancement ratios

average temperature	$\overline{h}$ (air)	$\overline{h}$(He)	$\overline{h}$(N_2)	$\overline{h}_{m,\max}$(He/N_2)
200 K	46	64.4 (40%)	44.91 (−2.37%) [−30.26%]	68.4 (48.7%) [6.2%]
1000 K	25.6	30.44 (18.9%)	24.71 (−3.48%) [−18.82%]	33 (28.9%) [8.4%]

Note: The numbers in parentheses are referred to as $\overline{h}$(air), whereas the numbers in brackets are referred to as $\overline{h}$(He).

The theoretical results presented in this technical note may be useful to thermal design engineers that are involved with the packaging of gas-filled vertical rectangular cavities. Interestingly, the vast improvement in heat transfer performances provided by the optimal mixture of helium and nitrogen (oscillating between 60 percent He+40 percent N_2 and 70 percent He+30 percent N_2) over air is remarkable. This design option may lead to substantial reductions in the dimensions and in the weight of vertical rectangular cavities in industrial environments.

Nomenclature

A = surface area of active wall
$A_{1,2}, A_{2,1}$ = conductivity parameters, Eq. (6)
c_p = isobaric specific heat capacity
g = acceleration of gravity
h = mean heat transfer coefficient
H = height of cavity
k = thermal conductivity
m = mass of gas
M = molecular weight of a gas
$\overline{\mathrm{Nu}}_\delta$ = mean Nusselt number, $h\delta/k$
Pr = Prandtl number, $\mu c_p/k$
Q = rate of heat transmission
Ra_δ = Rayleigh number, $(g\beta/\nu\alpha)(T_h - T_c)\delta^3$
T = temperature
$\overline{T}$ = average temperature, $(T_h + T_c)/2$
x = composition of a gas mixture, $m_2/(m_1+m_2)$
x^* = optimal composition of a gas mixture
α = thermal diffusivity
β = coefficient of thermal expansion
δ = width of cavity
μ = dynamic viscosity
ν = kinematic viscosity
ρ = density
$\phi_{1,2}, \phi_{2,1}$ = viscosity parameters, Eq. (4)

Subscripts

c = cold
h = hot
m = mixture of two gases
1,2 = gas 1, gas 2

References

[1] Gebhart, B., Jaluria, Y., Mahajan, R. L., and Sammakia, B., 1988, *Buoyancy-Induced Flows and Transport*, Hemisphere, New York.
[2] Wilke, C. R., 1950, ''A Viscosity Equation for Gas Mixtures,'' J. Chem. Phys. **18**, pp. 517–523.
[3] Wassiljeva, A., 1904, ''Heat Conduction in Gaseous Mixtures,'' Phys. Z. **5**, pp. 737–750.
[4] Mason, E. A. and Saxena, S. C., 1958, Phys. Fluids **1**, pp. 361–370.
[5] Mason, E. A. and Saxena, S. C., 1959, J. Chem. Phys. **31**, pp. 511–518.
[6] Jakob, M., 1946, ''Free Convection Through Enclosed Plane Gas Layers,'' Trans. ASME **68**, pp. 189–195.
[7] Graff, J. G., and Van der Held, E. F., 1952, ''The Relation Between the Heat Transfer and Convection Phenomena in Enclosed Plain Air Layers,'' Appl. Sci. Res. Ser. A, **3**, pp. 393–405.
[8] Mills, A. F., 1995, *Heat Transfer*, Richard Irwin, Boston, MA.

Evaporation Heat Transfer and Pressure Drop in Horizontal Tubes With Strip-Type Inserts Using Refrigerant 600a

S.-S. Hsieh
Sun Yat-Sen Professor of Mechanical Engineering, Dean of Engineering, Fellow ASME

K.-J. Jang
Graduate Student,
Department of Mechanical Engineering

Y.-C. Tsai
Graduate Student,
Department of Mechanical Engineering,

National Sun Yat-Sen University,
Kaohsiung, Taiwan 80424, R.O. China

Results of a study on saturated boiling heat transfer of refrigerant R-600a in horizontal tubes (ID=10.6 mm) with strip-type inserts (longitudinal strip LS with/without perforated holes and cross-strip CS inserts) are reported. Local heat transfer coefficients are measured for a range of heat flux (9.1~31.2 kW/m^2), mass velocity (8.23~603.3 kg/m^{2}s), and equilibrium mass quality (≤0.8) and the influences were studied. The data were compared with the performance of the corresponding smooth tubes. Enhancement factors are presented and discussed. Pressure drop measurement was also conducted and it is found that both single-phase and two-phase pressure drops increase with increasing heat flux levels and mass velocities. [S0022-1481(00)00302-9]

Keywords: Boiling, Enhancement, Heat Transfer, Refrigeration

1 Introduction

A lot of work has been carried out to obtain an understanding of boiling heat transfer from a smooth surface. These fundamental studies clearly brought out the complexities of the flow boiling mechanisms (see [1] for a comprehensive survey). At present, many aspects of boiling heat transfer on a smooth surface are well explored and reasonably good correlations have been developed for the design of efficient heat exchange equipment. However, with enhanced surfaces, boiling heat transfer is more complicated. Several comprehensive studies have been performed on microfinned tubes (see, for example, [2]). Singh et al. [3] conducted flow boiling observation of R-134a in a microfin tube and showed that at the mass velocity of 100 kg/m^2 s, a transition from a stratified to annular flow occurred. Recently, Liu [4] experimentally measured the evaporation heat transfer coefficients of R-134a and compared the corresponding values of R-22. Due in part to this complexity, heat transfer in horizontal tubes with strip-type inserts has received less attention than that in smooth tube annuli. Moreover, in-tube evaporations with strip-type inserts using R-600a as a refrigerant have not been conducted, especially for the strips with perforated holes.

Contributed by the Heat Transfer Division for publication in the JOURNAL OF HEAT TRANSFER. Manuscript received by the Heat Transfer Division, July 8, 1999; revision received, Dec. 20, 1999. Associate Technical Editor: F. Cheung.

This work is a continuation of our previous study regarding evaporative heat transfer and enhancement performance of a serpentine tube with strip-type inserts using R-134a ([5]). Attention was given to the heat transfer enhancement as well as the pressure drop measurement and to the influences of nucleate flow boiling on test tubes. Different cases in terms of varied insert-type horizontal tubes were tested. To accomplish these tasks, experiments were performed in a horizontal test tube (see Fig. 1 for details) with longitudinal strip (LS) with/without perforated holes and cross-strip (CS) type inserts, 10.6-mm inside diameter with refrigerant-600a (R-600a) as the boiling fluid.

2 Experimental Apparatus and Instrumentation

The heat transfer test apparatus is similar to Hsieh et al. [5] with slight modifications for test tubes. The test section consists of a horizontal tube flow channel. It is a copper tube (k = 386 W/mK) with a total heated length of 2000 mm, and outside and inside diameters of 12.7 mm and 10.6 mm, respectively. Inlet and outlet pressures were measured with a piezoresistive-type transducer, respectively, and differential pressure at a 500-mm interval each across the channel is measured with a strain-gage-type transducer. The pressure transducers were calibrated against a known method ([6]). The estimated uncertainty in the pressure measurements were ±8.5 percent. Heating was provided by conducting direct current through electric wire packed into the tube. A two-walled structure (MgO+quartz) was sandwiched between the copper tube and the electric wire as an electrical shield. Quartz was used as an electrical insulation. MgO can distribute heat energy uniformly.

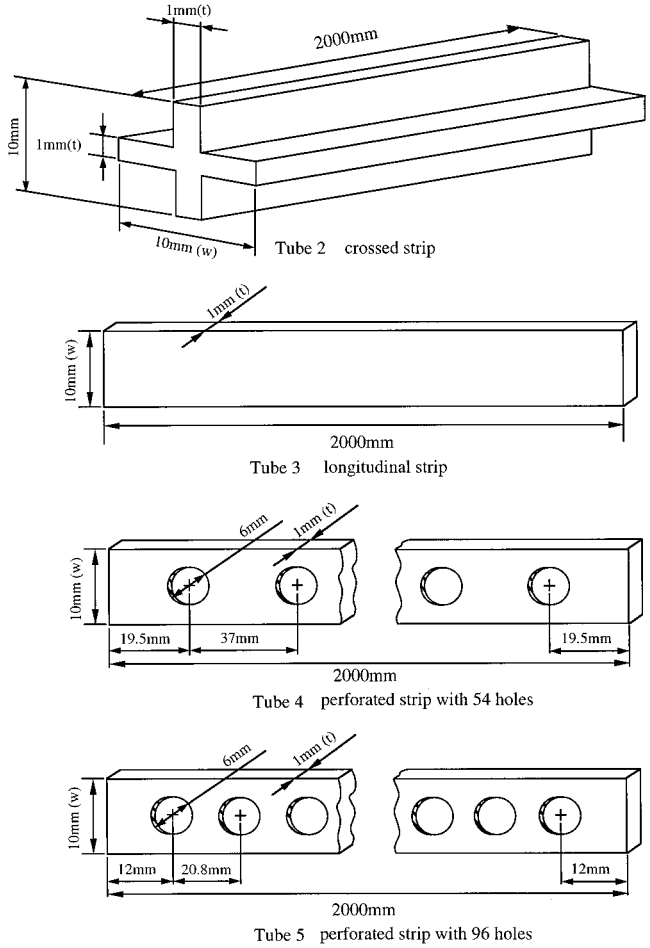

Fig. 1 The geometry of the inserts in present study

As R-600a (at T_{sat} = 6°C and P_{sat} = 192.7 kPa) flowed through the test section, it was uniformed heated by DC power, provided by a 100v, 550-amp capacity DC rectifier. The wall temperature was measured by four thermocouples circumferentially ([5]) spaced (90 deg apart) at nine axial downstream locations and an average value was used to calculate the local heat transfer coefficient. The soldering point of the thermocouples to the tube wall was less than 1 mm in diameter. It is estimated that the temperatures were accurate to within ±0.1°C. The inserts are in partial thermal contact with the heated wall and some heat flow through the inserts that would be expected. Such amount of heat was estimated less than 15 percent of the total heat input at the extreme case.

Prior to formal two-phase flow boiling tests, single-phase heat transfer and pressure drop tests were made. Single-phase tests were performed at mass flux ranging from 119 to 509 kg/m^2 s, which included a Reynolds number up to 30,000 which belongs to turbulent flow. The local heat transfer coefficient, at position z along the length of the tube, is defined as $h = \dot{q}/(T_{wz} - T_z)$ where T_{wz} and T_z stand for local wall and bulk fluid temperature at position z. The input heat flux $\dot{q}$ was obtained from the enthalpy increase of the fluid over the heated length with a nominal cross-sectional area A_c as

$$\dot{q} = \frac{(GA_cC_p)(T_o - T_i)}{\pi D_i L_H}. \tag{1}$$

For a given mass velocity, as mentioned before, outside-wall temperatures were obtained at nine axial positions along the length of the test channel. Because the temperature difference across the wall of the copper tube was large, the measured outside wall temperatures were corrected to give the inside tube wall temperatures following Wen and Hsieh [7] with a heat loss factor η ([8]) where η is defined as the heat loss factor ($= \dot{q}/q$ and $q = EI/\pi D_o L_H$; where E denotes electric voltage and I is the electric circuit). For the present study, the η ranged from 0.89 to 0.93. The single-phase adiabatic friction factor is calculated from the measured total pressure drop and mass flux. The measured single-phase heat transfer as well as the pressure drop approach the well-known Gnielinski [9] and Petukhov-Popov [10] correlations and the Blasius equation ($f = 0.316\,\mathrm{Re}^{-0.25}$) well within ±9.5 percent and ±9.7 percent for Nu and f, respectively. To evaluate the two-phase friction factor associated with the present study, the friction pressure drop ΔP_f was obtained by deducting the acceleration pressure drop ΔP_a which can be estimated by the homogeneous model for simplicity with possible errors at higher quality for two-phase gas-liquid flow. Namely,

$$\frac{dP_a}{dz} = G^2 v_{lg} dx/dz. \tag{2}$$

An uncertainty analysis was made to consider the error caused by the interpolation procedure of the measuring instruments. The estimated uncertainties in G, $\dot{q}$, x, ΔP, T_w, h, and f are ±1.3, ±5.2, ±6.4, ±8.5, ±0.2, ±12.3, and ±8.9 percent, respectively.

3 Results and Discussion

The flow boiling tests were performed at selected values of mass velocity of 83, 166, 239, 356, 475, and 602 kg/m^2 s. The fluid entered the test section as saturated liquid in all tests. The experimental heat flux range from 9.1 to 3.1 kW/m^2. Application of the flow pattern maps to predict quality at the transition to annular flow indicated that annular flow generally did not start until qualities of 0.6 to 0.8. Figure 2 shows the flow pattern map following Taitel and Dukler [11] for the present flow boiling in smooth tubes and the tubes with inserts. It clearly shows that all the tests under study seem in annular, intermittent, stratified-

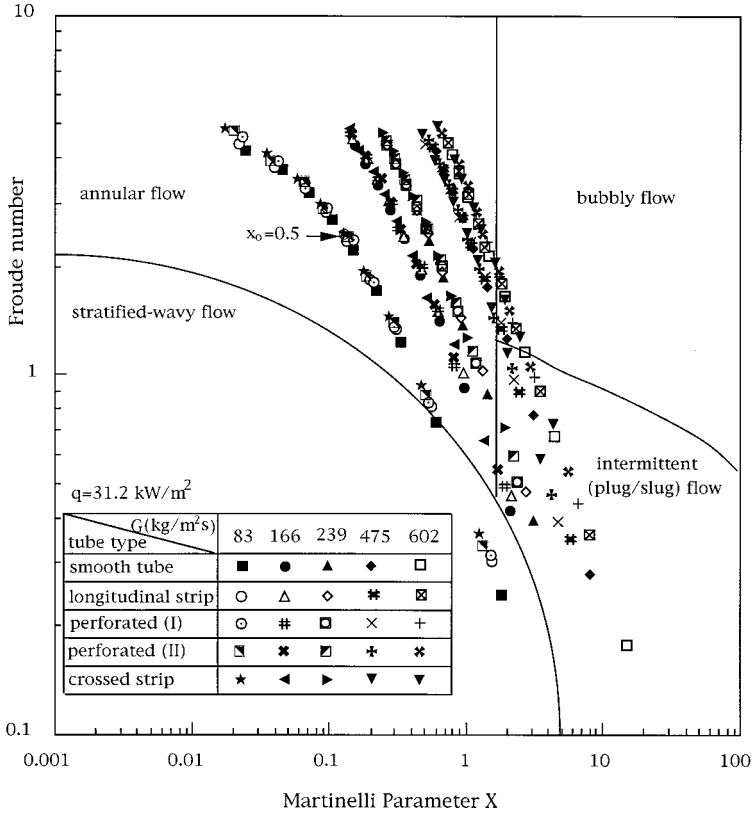

Fig. 2 Flow pattern map for test tubes

wavy, and bubbly flow regime. The majority of the boiling data from both the smooth tubes and tubes with inserts used in the present study falls into the annular region, with only a few measurements also falling into stratified-wavy (at low mass flux)/or bubbly (at high mass flux) and intermittent flow (slug+plug) pattern regions. It is recognized that in the stratified-wavy flow regime ($x<0.5$), the trend in heat transfer coefficient versus vapor quality is an extension to that for annular flow, where it is termed ''partial nucleate boiling,'' and both forced convection and nucleate boiling are significant. The gradual suppression due possibly to flow stratification of the latter leads to a temporary reduction of the local heat transfer coefficients. Later, they will increase until finally merging into a single line with increasing vapor quality, in annular flow regime where is also termed forced convection vaporization region. The map also indicates the influence of stratification at low flow rates (i.e., $G \leqslant 166\ \mathrm{Kg/m^2\,s}$) in the present smooth tubes. The visual observation (not shown here) of the flow through the sight glass indicated that for mass velocities less than 166 Kg/m^2 s, the flow was predominantly stratified, but as the mass velocity increased the flow became annular. The 166 Kg/m^2 s mass velocity represents the transition value from stratified-wavy flow to annular for the smooth tube, such situation also happens for tubes with inserts except for the vapor quality and mass flux at the demarcation point (e.g., $x_0=0.5$ for the smooth tube; $x_0<0.5$ for inserted tubes). A smaller G for transition is expected for tubes with inserts. Like Hsieh et al. [5] for R-134a, the effect of tubes with inserts on heat transfer coefficients shows that an increase in mass velocity increases the heat transfer coefficients for all the qualities with R-600a. Moreover, for tubes with inserts and perforated holes, an increase in the quality increases the heat transfer coefficients for all the mass velocities under study. This is because the flow in the tubes with inserts was in forced convective boiling with reduced flow area and decreased hydraulic diameter in which the heat transfer coefficients would increase as the mass velocity increases.

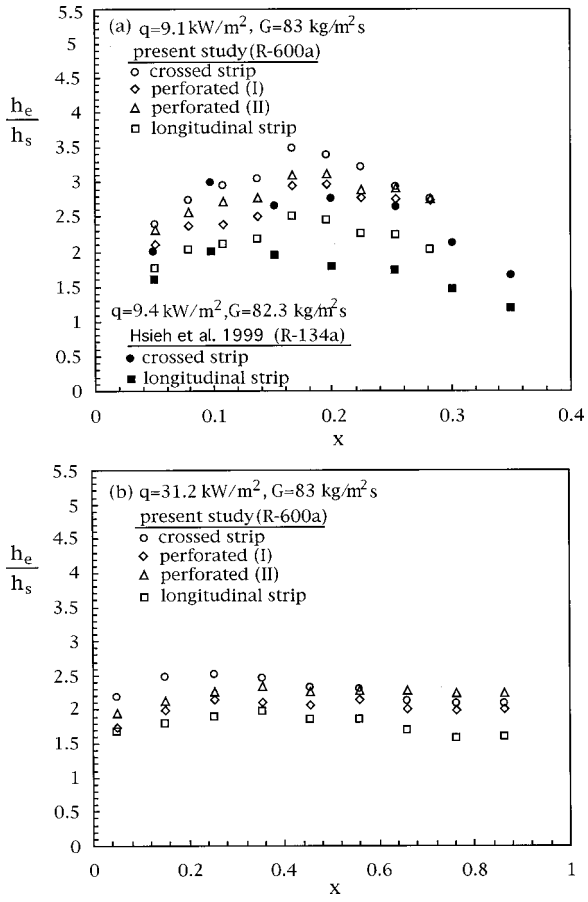

Fig. 3 Local heat transfer enhancement factor for tubes with inserts at $q=9.1\ \mathrm{kW/m^2}$ and $q=31.2\ \mathrm{kW/m^2}$

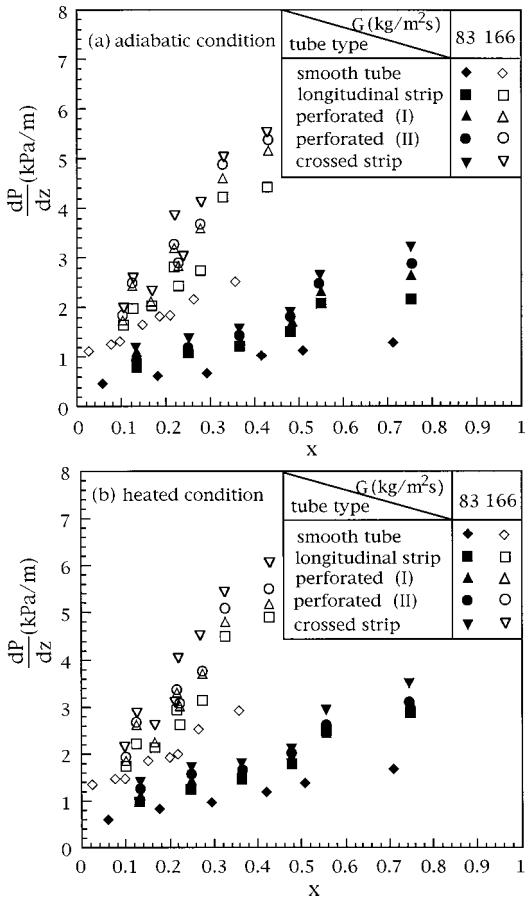

Fig. 4 ***dP/dz*** **versus** ***x*** **for different test tubes in present study under (*a*) adiabatic condition (*b*) heated condition**

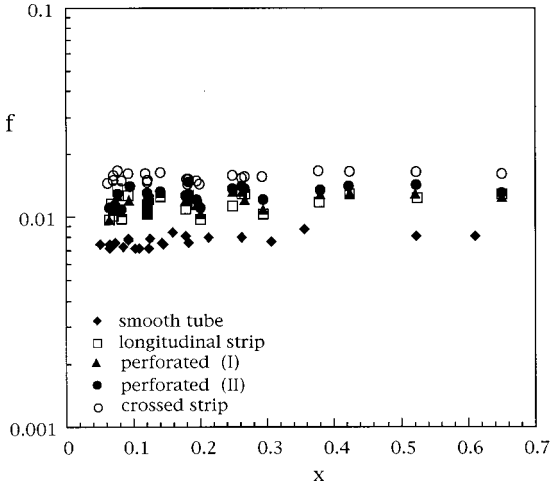

Fig. 5 ***f*** **(two-phase friction factor) versus** ***x*** **for different test tubes**

Of special interest for studies of heat transfer augmentation is the question of how much the heat transfer coefficient in tubes with inserts is increased relative to an equivalent smooth tube at the same condition for the present study. Local enhancement factors (h_e/h_s; the subscript e and s stand for the enhanced and smooth surface, respectively) were calculated by forming a ratio of experimentally measured heat transfer coefficients for the tubes with inserts and a smooth tube of the same heat transfer area. As shown in Fig. 3(*a*), the distribution enhancement of factors at $q=9.1\,\mathrm{kW/m^2}$ and $G=83\,\mathrm{Kg/m^2\,s}$ for four inserted tubes (four curves) show a common trend. For instance, it shows a steady increase starting from $x\cong 0.04$ and after reaching a peak at $x\cong 0.16$, then gradually decreases to a local minimum value about 2.1 at $x=0.28$ for the tubes with longitudinal insert. Furthermore, among four tubes with inserts the crossed strip inserts have the highest values compared to those corresponding values of the remaining three tubes with inserts followed by longitudinal strip inserts with and without perforated holes. Moreover, the more perforated holes it has, the higher the heat transfer rates would be—due possibly to the forced convection mechanisms involved, even though the heat transfer surface was reduced for a perforated LS insert. In spite of the different values for different inserted tubes, the common feature of these curves shown in Fig. 3(*a*) is that the local peak occurs at $x\cong 0.16$ for all the tubes tested. Also included in Fig. 3(*a*) for comparison are the results of R-134a for the similar study reported by Hsieh et al. [5] and Reid et al. [12] for a twisted tape. It is seen that both the values of Hsieh et al. [5] and Reid et al. [12] seem lower than those of the present study. However, the tendency and trend of the curves are similar. In contrast, as shown in Fig. 3(*b*) the distribution of the local enhancement factor exhibits a different trend. The discrepancy due to different tubes in (h_e/h_s) values does not seem large. The average value is about 2. Due to the inlet temperature below ambient in this study, the end losses may affect the local h at the ends of the tubes which result in the small minimum in the axial distribution of Figs. 3(*a*) and (*b*). In every case, higher measured heat transfer was found when compared with R-134a. This most likely occurs because of the larger wettability on surface and latent heat of R-600a.

Figure 4 shows pressure drop per unit length along a downstream distance versus vapor quality for adiabatic and heated conditions for two mass velocities and five different tubes with/without inserts. Figure 4(*a*) shows the results for the adiabatic condition. The pressure drop significantly increases with both the vapor quality and mass velocity as expected. For instance, the rate of increase by a factor of 2.5 and 1.5, respectively, for pressure drop in the tubes with cross-strip inserts at low ($=83\,\mathrm{Kg/m^2\,s}$) and high ($=166\,\mathrm{Kg/m^2\,s}$) mass velocities seems different due to the different slopes of the curves shown in Fig. 4(*a*). It is also seen that the pressure drop of the tubes with inserts is somewhat higher than that of the smooth tube for both mass velocities. In fact, such difference strongly depends on the local vapor quality and mass velocities. For instance, the pressure drop in tubes with longitudinal strip inserts may be up to 100 percent higher than that of smooth tube at $x=0.4$ for $G=166\,\mathrm{Kg/m^2\,s}$. However, the corresponding increase may be only 12.5 percent for $G=83\,\mathrm{Kg/m^2\,s}$. It is known that the total pressure gradient for a heated condition consists of two terms. One is ΔP_f; and one is ΔP_a which result in the total pressure drop for a heated condition a little bit higher than that corresponding value of the adiabatic condition due to an additional term of ΔP_a. Figure 4(*b*) actually exhibits such results. Except for the magnitude of dP/dz, the remaining behavior shown looks similar to that for the adiabatic condition. Figure 5 indicates the present f calculated for five tubes under study. It is found that the f seems independent of the quality. Among the tubes tested, the cross-strip insert has the largest f ($\cong 0.018$) followed by the perforated strip and longitudinal strip insert; while the smooth tube is the smallest ($f\cong 0.0078$).

References

[1] Collier, J. G., 1981, *Convective Boiling and Condensation*, 2nd ed., McGraw-Hill, New York.

[2] Schlager, L. M., Pate, M. B., and Bergles, A. E., 1990, ''Evaporation and Condensation Heat Transfer and Pressure Drop in Horizontal, 12.7 mm Microfin Tubes with Refrigerant 22,'' ASME J. Heat Transfer,, **112**, pp. 1041–1045.

[3] Singh, A., Ohadi, M. M., and Dessiatoun, E., 1991, ''Flow Boiling Heat Transfer Coefficients of R-134a in a Microfin Tube,'' ASME J. Heat Transfer, **118**, pp. 497–499.

[4] Liu, X., 1997, ''Condensing and Evaporating Heat Transfer and Pressure Drop

Characteristics of HFC-134a and HCFC-22,'' ASME J. Heat Transfer, **119**, pp. 158–163.
[5] Hsieh, S.-S., Jang, K.-J., and Huang, M.-T., 1999, ''Evaporative Heat Transfer and Enhancement Performance of Serpentine Tube With Strip-Type Inserts Using Refrigerant-134a,'' ASME J. Heat Transfer, **121**, pp. 752–757.
[6] Kline, S. J., and McClintock, F. A., 1953, ''Describing Uncertainties in Single-Sample Experiments,'' Mech. Eng., **75**, Jan., pp. 3–8.
[7] Wen, M.-Y., and Hsieh, S.-S., 1994, ''Evaporative Heat Transfer and Enhancement Performance of Rib-Roughened Tube Annuli With Refrigerant 114,'' Int. J. Heat Mass Transf., **37**, pp. 425–436.
[8] Wambsganss, M. W., France, D. M., Jendrzejczyk, J. A., and Tran, T. N., 1993, ''Boiling Heat Transfer in a Horizontal Small-Diameter Tube,'' ASME J. Heat Transfer, **115**, pp. 963–972.
[9] Gnielinski, V., 1976, ''New Equations for Heat and Mass Transfer in Turbulent Pipe and Channel Flow,'' Int. Chem. Eng., **16**, pp. 359–368.
[10] Petukhov, B. S., 1970, ''Heat Transfer and Friction in Turbulent Pipe Flow With Variable Properties,'' *Advances in Heat Transfer*, Vol. 6, J. P. Hartnett and T. F. Irvine, Jr., eds., Academic Press, New York, pp. 503–564.
[11] Taitel, Y., and Dukler, A. E., 1976, ''A Model for Predicting Flow Regime Transitions in Horizontal and Near Horizontal Gas-Liquid Flow,'' AIChE J., **22**, pp. 47–55.
[12] Reid, R. S., Pate, M. B., and Bergles, A. E., 1991, ''A Comparison of Augmentation Techniques During in-Tube Evaporation of R-114,'' ASME J. Heat Transfer, **113**, pp. 451–458.

Augmentation of Thin Falling-Film Evaporation on Horizontal Tubes Using an Applied Electric Field

J. Darabi

M. M. Ohadi

S. V. Dessiatoun

Enhanced Heat Transfer Laboratory, Department of Mechanical Engineering, University of Maryland, College Park, MD 20742

Heat transfer enhancement of falling-film evaporation on commercially available horizontal tubes using an applied electric field was studied experimentally. The tube surfaces tested included: smooth, 19 fins per inch (19 fpi) low-fin type, and Turbo BIII which is a state-of-the-art commercially available boiling tube. The nominal outside diameters of all the tubes were 19 mm. Experiments were performed with R-134a at a saturation pressure of 550 kPa. Effects of heat flux, film flow rate, applied electric field potential, and heat transfer surface on the heat transfer coefficient were investigated. In addition, the effect of Poloyl-ester oil on the heat transfer coefficients was also investigated. Experiments were conducted for oil concentrations ranging from 0.5 percent to 5 percent on a mass basis. Small concentrations of a poloyl-ester lubricant were found to improve the heat transfer performance, while large concentrations reduced the heat transfer coefficient. [S0022-1481(00)00702-7]

Keywords: Augmentation, Electric Fields, Enhancement, Evaporation, Film, Heat Transfer, Thin Films

Introduction

Horizontal tube evaporators in which a falling film flows over the tubes are used in the chemical processing, refrigeration/HVAC systems, the food industry, and Ocean Thermal Energy Conversion systems (OTEC). From the heat transfer point of view, higher heat transfer rates and a smaller temperature driving force are the main advantages of this process. In addition, much smaller liquid inventory charge and elimination of hydrostatic head are among the other industrial benefits. In spite of these advantages, relatively little information is available in the literature on the heat transfer characteristics and predictive models for falling film evaporation processes. Most previous work on falling-film heat transfer has been conducted with water and ammonia, due to their greater potential for practical applications in chemical processing and absorption systems. In the past few years, however, new alternate refrigerants such as R-123 and R-134a have attracted more attention from the research community. Even though this work emphasizes the effect of electric field, the results of previous studies are important in understanding fundamental phenomena.

An extensive literature review on falling film evaporation is given in Group and Schlunder [1], Chyu and Bergles [2], Palen et al. [3], and Parken et al. [4]. Nakayama et al. [5] performed experiments with falling film evaporation of R-11 on vertical plates. Smooth, vertically grooved, horizontally grooved, and porous surfaces were investigated in this study. They found that the porous plate resulted in higher heat transfer coefficients compared to other surfaces tested. For the porous plate, the heat transfer coefficient was found to be independent of flow rate and weakly dependent on heat flux. Heat transfer coefficient with the vertically grooved plate, however, was dependent on both flow rate and heat flux.

Moeykens and Pate [6] conducted single tube tests with R-134a on a smooth tube. It was reported that the falling film coefficients were 10 percent to 20 percent higher than those of pool boiling. Moeykens and Pate [7] and Moeykens et al. [8] also investigated the heat transfer performance of R-134a on a tube bundle. It was noted in this study that a low-finned tube bundle yielded film heat transfer coefficients up to 20 percent higher than those obtained with pool boiling.

The only previous work to address the effect of oil on falling film evaporation is that of Moeykens et al. [9]. They conducted single-tube experiments with R-134a on seven commercially available tubes. The oil concentration was varied from zero to five percent. Various tubes responded differently to the oil concentration, but it was shown that in most cases heat transfer performance continued to increase through three percent. Further increase in oil concentration degraded heat transfer performance.

The electrohydrodynamic enhancement of heat transfer refers to the coupling of an electric field with the fluid field in a dielectric fluid medium. The net effect is production of electrically induced secondary motions that destabilize the thermal boundary layer near the heat transfer surface, leading to heat transfer coefficients that are often an order of magnitude higher than those achievable by the conventional enhancement techniques. When a dielectric fluid of electric permittivity ε, mass density ρ, and temperature T is subjected to applied electric field E, the electric body force can be expressed as ([10])

$$\mathbf{f}=\rho_c\mathbf{E}-\frac{1}{2}E^2\nabla\varepsilon+\frac{1}{2}\nabla\left[E^2\rho\left(\frac{\partial\varepsilon}{\partial\rho}\right)_T\right] \tag{1}$$

where ρ_c is the electric field charge density. The first term on the right side of the above equation is the *electrophoretic* force that results from the net free charges within the fluid. This term is usually responsible for the generation of electrically induced secondary motions and the resulting enhancement mechanism in single-phase flows. The second term, called the *dielectrophoretic* force, is associated with the spatial change in the electrical permittivity within the dielectric. The last term, called the *electrostriction* force, represents the force produced by inhomogeneity of the electric field. This force refers to the tendency of the dielectric to increase its linear dimensions in the direction of the electric field.

Contributed by the Heat Transfer Division for publication in the JOURNAL OF HEAT TRANSFER. Manuscript received by the Heat Transfer Division February 28, 1999; revision received December 2, 1999. Associate Technical Editor: J. Han.

The effect of electrohydrodynamics on heat transfer has been under investigation for the past three decades. Previous work has involved studies for single-phase processes as well as phase-change processes involving boiling, condensation, melting, and freezing. However, due to their greater potential for practical applications, boiling and condensation have attracted more attention from industrial and academic researchers.

Although a significant amount of work has gone into investigating the heat transfer performance of conventional falling film evaporators, very little information is available on the electrohydrodynamic-assisted falling film evaporation. Yamashita and Yabe [11] conducted experiments with falling film evaporation of R-123 on vertical smooth tubes. The experiments were carried out on two vertical smooth stainless steel tubes 25.4 mm O.D. and 2 m long, and five different electrodes were tested. Their results showed up to six times enhancement with a punched electrode geometry.

Darabi et al. [12] investigated the heat transfer enhancement of R-123 and R-134a on vertical tubes utilizing electric fields. It was shown that the heat transfer performance for smooth, low-finned and mechanically re-entrant enhanced tubes increased substantially under the influence of electric fields.

Electrohydrodynamic-enhanced falling film and spray evaporation results of R-134a on a vertical plate were reported by Darabi et al. [13]. The effects of various parameters such as heat flux, refrigerant mass flow rate, electrode gap, and applied voltage were investigated. It was found that in the presence of an applied electric field, the maximum enhancement in the heat transfer coefficient for both falling film and spray evaporation modes was more or less the same. A maximum enhancement of fourfold in the heat transfer coefficient was obtained.

This paper focuses on characterizing the phenomena and identifying the feasibility of the electrohydrodynamic technique for horizontal falling film evaporators. The effects of heat flux, flow rate, applied voltage, and Poloyl-ester oil are investigated.

Experimental Apparatus

The experimental facility is shown schematically in Fig. 1. The setup includes a test chamber, a feed refrigerant loop, a water loop, a data acquisition system, and an environmental temperature control system.

As shown in Fig. 2, the test chamber was made of a tempered glass cylinder with aluminum flanges covering both ends. The entire structure was reinforced by four stainless steel rods. The chamber was designed to sustain up to 690 kPa pressure. The condenser was mounted horizontally on the upper flange and removed the heat generated in the test chamber. A pressure transducer, safety valve, and access valve for refrigerant charging were also mounted on the upper flange. The lower flange was the base support for the copper coils and the test section. Access fittings for thermocouples, electrical wiring, and a refrigerant discharge valve were also installed on the lower flange.

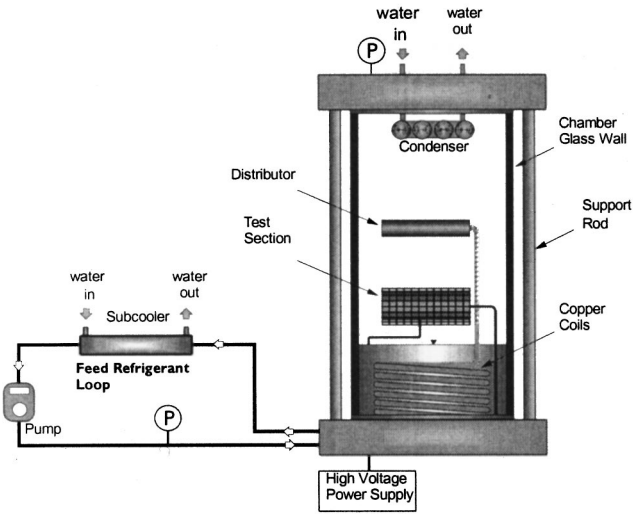

Fig. 2 Schematic diagram of the test chamber

The refrigerant feed loop consisted of a magnetic gear pump, a subcooler, a copper coil, and a liquid distributor. The refrigerant was passed through a subcooler to prevent vapor from entering the pump. The subcooler was a tube-in-tube heat exchanger where liquid refrigerant flowed in the tube side and chilled water in the shell side. When the refrigerant leaves the pump, its temperature could be slightly lower than the saturation temperature. To eliminate the subcooling problem, the refrigerant was passed through a copper coil, which was submerged in a pool of liquid refrigerant. The liquid refrigerant was then passed through the liquid distributor and flowed downward on the tube surface.

The water loop included a chiller, a pump, a stepper motor, and a flowmeter. This loop provided chilled water to the condenser and removed the heat generated by the test section. The water exited the chiller at the desired temperature and was pumped through the flowmeter and into the condenser. The water then exited the condenser and flowed back to the chiller unit. The

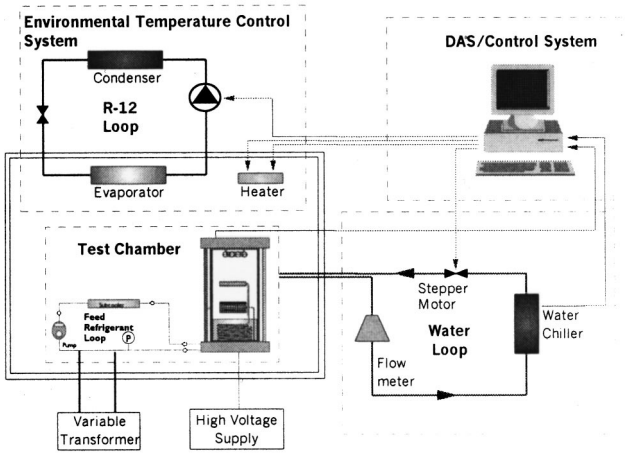

Fig. 1 Schematic of the experimental setup

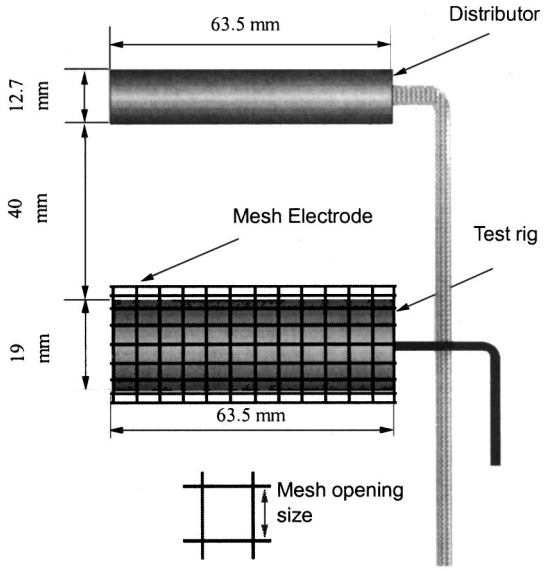

Fig. 3 Schematic diagram of the test section

Table 1 Specifications of the heat transfer surface/electrode configurations

Heat Transfer Surface	Electrode
Smooth tube Diameter=19 mm length=63.5 mm	Mesh electrode Gap=1 mm Opening size=0.9 mm Wire diameter=0.4 mm
Smooth tube Diameter=19 mm length=63.5 mm	Mesh electrode Gap=3 mm Opening size=1.5 mm Wire diameter=0.58 mm
Turbo BIII tube Diameter=19 mm length=63.5 mm	Mesh electrode Gap=3 mm Opening size=1.5 mm Wire diameter=0.58 mm
Turbo BIII tube Diameter=19 mm length=63.5 mm	Mesh electrode Gap=3.4 mm Opening size=5.2 mm Wire diameter=0.9 mm
19 fpi tube Diameter=19 mm length=63.5 mm	IWF electrode Wire diameter=0.24 mm Nylon strand diameter=0.4 mm

pressure of the test chamber was controlled by adjusting the temperature and flow rate of the water passing through the condenser.

To minimize heat losses to the surroundings, both the test chamber and the feed refrigerant loop were placed inside a temperature controlled chamber. The temperature of the chamber was controlled by a computer and was kept close to the saturation temperature at which the experiments were run. The control units were integrated with a computer for precise monitoring and control.

Three test sections were fabricated: a smooth tube, a Turbo BIII tube, and a 19-fpi tube. Each test section had an outside diameter of 19 mm (3/4 in.) and a length of 63.5 mm (2.5 in.). An electrical cartridge heater with an outside diameter of 6.35 mm (1/4 in.) and a heating length of 50.8 mm (2 in.) was used to provide heating energy to the test section. The cartridge heater was put inside a copper sleeve. The clearance between the tube and sleeve was filled with solder to provide a more uniform conduction heat transfer interface. In order to achieve wall temperature measurements, four thermocouple grooves of 1-mm width, 0.6-mm depth, and 90 deg apart from each other, were made on the outer surface of the sleeve. The thermocouple wires were mounted on the inside wall of the test section, and placed circumferentially 90 deg apart. The schematic diagram of the test section is shown in Fig. 3. Feed refrigerant was distributed by a 11-fpi copper tube with nine small holes 6 mm apart from each other. To ensure a well-distributed refrigerant flow rate over the tube, the distributor was carefully aligned with the tube. The distributor was fixed in place with a stainless steel strip support. To prevent additional liquid supply from the condenser to the test section, a shroud was placed on the top of the distributor. The shroud was made of a half-inch Teflon tube and was sliced longitudinally. Detailed specifications of the heat transfer surface/electrodes are listed in Table 1.

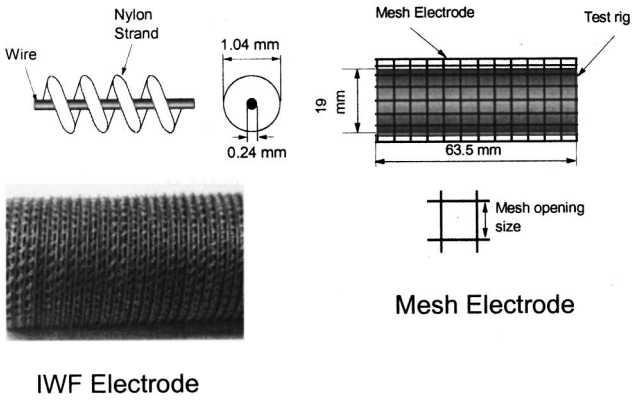

Fig. 4 Schematic diagram of the electrodes

Figure 4 shows the schematic diagram of electrodes. The IWF electrode was made of nickel-chromium wire with a diameter of 0.24 mm, and wrapped with an insulation material made from nylon strand with a diameter of 0.4 mm to elevate the electrode wire off of the tube surface. The pitch of the insulator was such that a significant portion of the electrode was exposed. The 19-fpi test-section tube with the nominal outside diameter of 19 mm and length of 63.5 mm was then wrapped with the IWF electrode. The electrode was wound into the root region of the tube fins. This design requires much lower applied voltage for a given electric field strength. The mesh electrodes were made of thin brass wire in the form of wire mesh. The actual openings between the parallel wires (mesh opening sizes) were 0.9, 1.5, and 5.2 mm, respectively. The gaps between the enhanced tube and the electrodes were 1, 3, and 3.4 mm. The only differences between the three configurations were mesh opening size and wire diameter. Positive polarity was applied to all the electrodes. Performance, cost, and ease of manufacturing and implementation were the main criteria in selecting these electrode configurations. The IWF electrode requires a lower applied voltage for a given electric field strength, leads to a more compact tube/electrode geometry, and is much easier to implement. However, the performance may not be as good as that of a mesh electrode. The mesh electrode, on the other hand, has a better performance than the IWF electrode, but it is bulky and may increase the size of tube-electrode configurations.

Experimental Procedure

A typical experimental run began by switching on the chiller pump. After several minutes, the pressure of the test chamber was brought within a predetermined margin, and the feed refrigerant pump was switched on. Next, power to the cartridge heater was controlled with a variac and was fixed at a predetermined value. The DC high-voltage power supply was then turned on and adjusted to the predetermined voltage level. The pressure of the test chamber was controlled by adjusting the flow rate and temperature of the chilled water. Preliminary adjustments were made until the pressure of the chamber stabilized within 2 kPa of the predetermined value. From then on, the computer-assisted pressure control system took over control of the chamber pressure by adjusting the water flow rate. Usually it took about three to four hours for the system to reach steady-state condition, where the fluctuation of saturation pressure, temperature, and electrohydrodynamic current were less than one percent of the reading. Once steady-state conditions were achieved, the wall temperatures at four different locations, the saturation vapor and liquid temperatures at three different locations, and the electrohydrodynamic current were recorded. The applied electrohydrodynamic voltage was then set to the next level to be tested and the above procedure was repeated. In general, eight to ten data points were taken in a given experimental run.

Data Reduction

The equations involved in reducing the experimental data to the parameters of interest such as flow rate, heat flux, average heat transfer coefficient, enhancement factor, and electrohydrodynamic power consumption are discussed in the following.

The input power to the heater was calculated from the measured voltage V and current I:

$$Q = VI. \tag{2}$$

The average heat flux was calculated using the heat transfer surface and the input power to the cartridge heater

$$q'' = \frac{Q}{A} = \frac{Q}{\pi D_o L} \tag{3}$$

where A, L, and D_o are the surface area, length, and the nominal outside diameter of the tube, respectively.

The average heat transfer coefficient h was found from

$$h = \frac{q''}{T_w - T_{\text{sat}}} \tag{4}$$

where T_w and T_{sat} are the mean wall and saturation temperatures, respectively. The wall temperature was taken as the average of the four thermocouple readings on the wall. The outer wall surface temperatures were then obtained from the inner wall temperature measurements assuming one-dimensional conduction through the tube wall,

$$T_{wo} = T_{wi} - \frac{Q \ln(r_o/r_i)}{2\pi L k}. \tag{5}$$

The saturation temperature was calculated as the mean of three thermocouple readings for saturation temperature. The average refrigerant flow rate per unit length was calculated as

$$\Gamma = \frac{\dot{m}}{L} \tag{6}$$

where Γ, $\dot{m}$, and L are refrigerant flow rate per unit length, refrigerant flow rate, and length of the test section, respectively.

A heat transfer enhancement factor η was defined to quantify the effectiveness of the electrohydrodynamic-assisted falling film evaporation process as compared to the conventional falling film evaporation,

$$\eta = \frac{h}{h_0}. \tag{7}$$

In this equation h is the average heat transfer coefficient for electrohydrodynamic assisted falling film evaporation, and h_0 represents the average heat transfer coefficient in the absence of the electrohydrodynamic effect.

The electrohydrodynamic power consumption for the heat transfer process was determined from the applied voltage ϕ_{EHD} and the associated electrical current I_{EHD}:

$$Q_{\text{EHD}} = \phi I_{\text{EHD}}. \tag{8}$$

Finally, the electrohydrodynamic power consumption ratio α was defined as

$$\alpha = \frac{Q_{\text{EHD}}}{Q} \times 100 \tag{9}$$

which quantifies the ratio of electrical power consumption by the electrodes over the total power input to the test section tube.

Uncertainty Analysis

The directly measured quantities included pressure, temperature, mass flow rate, applied voltage, and current. The heater voltmeter and ammeter had accuracies of 0.7 percent and 0.1 percent of the reading, respectively. All thermocouples were calibrated with an accuracy of ± 0.1°C. The accuracy of the pressure transducer was ± 0.11 percent of the reading. The applied electrohydrodynamic voltage and current had an accuracy of ± 0.1 percent of the reading. The uncertainties were calculated using the propagation of error suggested by Kline and McClintock [14] and Moffat [15]. The uncertainty in the heat transfer coefficient results from the uncertainties in total power to the heater and wall superheat. The uncertainty in the total power to the heater arises from the uncertainty in measured voltage and current across the heater, which was estimated to be 1.22 percent. The uncertainty in temperature, however, was the main cause of uncertainties in heat transfer coefficients. For example, at low heat fluxes where the wall superheat was as low as 0.5°C, the uncertainty in heat transfer coefficients due to temperature alone can be as high as 20 percent. The maximum uncertainty was at the lowest heat flux where the temperature difference was small, and the minimum uncertainty was at the highest heat flux. The uncertainties of heat flux and heat transfer coefficients are listed in Table 2.

Table 2 Results of the uncertainty analysis

Tube	Uncertainty in q''	Uncertainty in h at $q'' = 10$ kW/m^2	Uncertainty in h at $q'' = 30$ kW/m^2
Smooth tube	±1.22 percent	±14.98 percent	±2.50 percent
Turbo BIII	±1.22 percent	±28.89 percent	±6.29 percent
19 fpi tube	±1.22 percent	±10.55 percent	±4.57 percent

Results and Discussion

Experiments were performed with R-134a at a saturation pressure of 550 kPa. The measured T_{sat} and P_{sat} were compared with REFPROP 6, and found to be fairly consistent. The difference between the measured temperature and the saturated temperature corresponding to the measured pressure was found to be less than 0.15°C, which lies within the uncertainty in temperature measurements. The heat flux was calculated based on the nominal outside diameter of the tubes. The results of the experiments are discussed in the following.

Visual inspection revealed three common flow patterns as the liquid dripped between the distributor and the test section. At low flow rates, the liquid initially dripped as columns and broke into droplets as it fell down. This flow pattern was not uniform in the axial direction of the tube and the size of droplets was different from time to time. As flow rate increased, the droplets joined together and formed a continuous vertical column that bridged between the distributor and the test section. Similar to the droplet pattern, the dripping positions moved constantly right and left along the axial direction, leading to a nonuniform film distribution at any given instance. However, on a time-average basis, it is reasonable to assume a uniform film forms on the tube surface. At high flow rates the vertical columns also joined together in the axial direction and formed a sheet flow pattern. The dripping positions remained more or less the same for the sheet pattern.

In electrohydrodynamic-assisted falling film evaporation, an electric field can be utilized to extract liquid from the heat transfer surface, forming a thin and well-distributed liquid film layer on the surface. When the electric field is applied to a liquid, the liquid experiences electrical stress. This stress depends on the dielectric constant, spatial variations in the electric field, and the distribution of the free charges in the liquid. The effect of dielectric constant is more pronounced in the liquid-vapor interface, due to a significant difference between the liquid and vapor dielectric constants. In the case of falling-film evaporation, the electric field may be used to decrease the thermal resistance by thinning the film. Normal stresses at the interface extract the falling film from the surface, leading to a concentrated film over a small region of the heat transfer surface, reducing the film thickness over the remaining surface. As a result, heat is removed more effectively by the evaporation process from the thin film ([12–13]). For falling film evaporation process, the objective is to keep a very thin film of liquid close to the heat transfer surface. The enhancement mechanism is mainly governed by the Maxwell instability at the liquid-vapor interface, which creates the liquid extraction phenomenon and the electroconvection in the liquid. The liquid extraction phenomenon depends on the Maxwell stress and leads to a thin film at the heat transfer surface. Both uniform and nonuniform electric fields can be utilized to enhance falling film evaporation heat

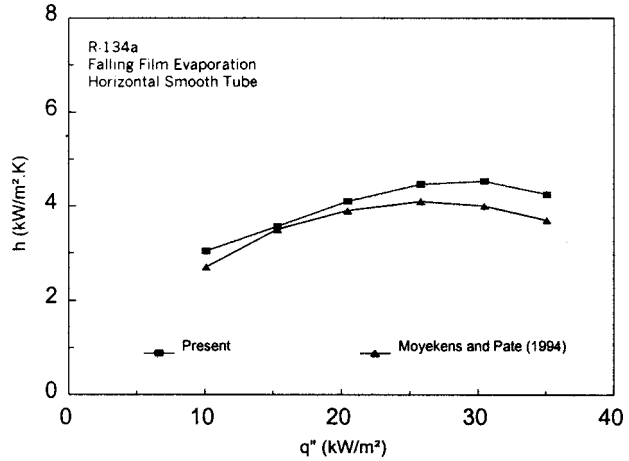

Fig. 5 Comparison of the nonelectrohydrodynamic results with the open literature

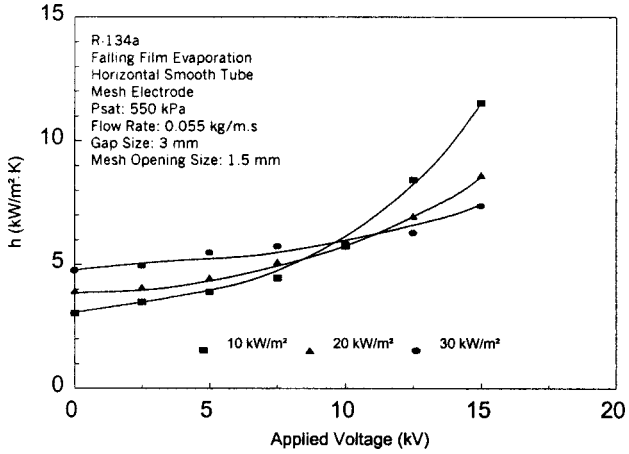

Fig. 6 *h* versus applied voltage on a smooth tube and mesh electrode I

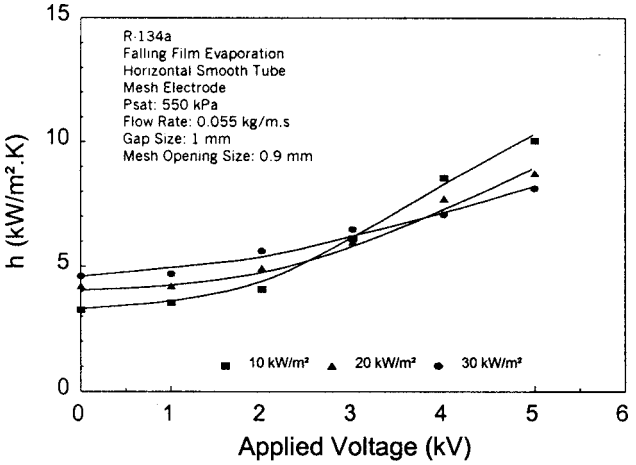

Fig. 7 *h* versus applied voltage on a smooth tube and mesh electrode II

transfer. Spraying of small liquid droplets by electrostatic atomization and surface perturbation and waviness are other effects of electric fields on enhancement of falling film evaporation.

Experimental results with R-134a on a smooth tube in the absence of electrohydrodynamic were compared with the open literature data. Our results agree well with those of the open literature. The comparison verified our setup and test methodologies. Figure 5 shows a satisfactory comparison of the data in the absence of electrohydrodynamics.

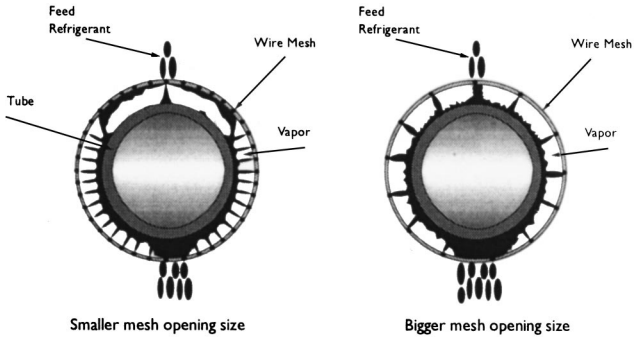

Fig. 8 Effect of mesh opening size on film distribution

Selected results showing the effect of heat flux on heat transfer coefficients are given in Figs. 6 and 7. These data were taken with R-134a on smooth tube and mesh electrodes. Results indicate that in the absence of the electric field or when the field is not strong (<3 MV/m), the heat transfer coefficient increases with an increase in heat flux. However, beyond a certain applied voltage, it tends to decrease as the heat flux increases. This can be attributed to the fact that in the absence of an electric field, or when the field is not strong, the thickness of the film covering the surface decreases with an increase in heat flux due to higher evaporation rate, leading to a higher heat transfer coefficient. However, further increase in applied potential will extract too much liquid from the heat transfer surface, causing dryout to occur at some parts of the surface at high heat fluxes. Visual observation during the experiments verified this postulate. It is clear that both the electric field intensity and the degree of liquid extraction are dominated by applied potential. A higher potential allows a higher degree of liquid extraction, leading to a thinner liquid film on the heat transfer surface, and higher heat transfer coefficients. On the other hand when the film is too thin, dryout may occur at some parts of the surface at high heat fluxes, leading to lower heat transfer coefficients. Maximum enhancement in the heat transfer coefficient was 280 percent at a heat flux of 10 kW/m^2 and a flow rate of 0.055 kg/m.s. As shown in Figs. 6 and 7, experiments with the smaller mesh opening size electrode showed lower heat transfer performance. One possible cause for a lower heat transfer coefficient with smaller mesh opening sizes could be that the film ini-

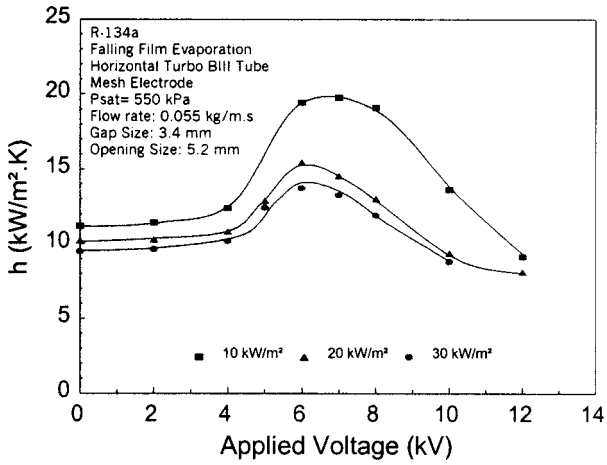

Fig. 9 *h* versus applied voltage at various heat fluxes with Turbo BIII tube

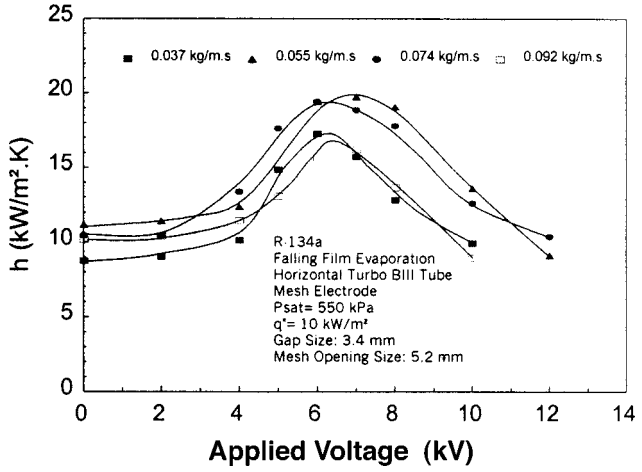

Fig. 10 ***h*** **versus applied voltage at various flow rates with Turbo BIII tube**

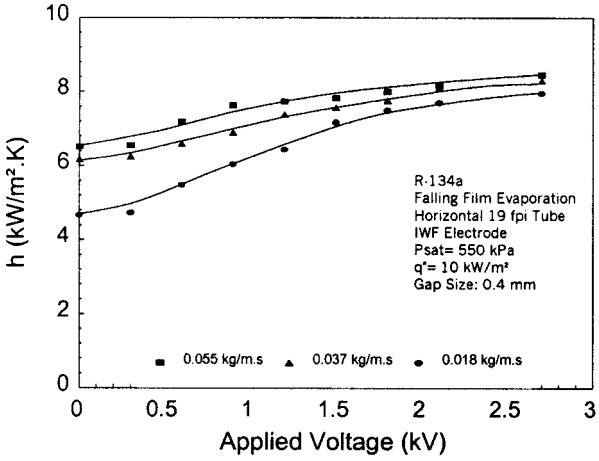

Fig. 12 ***h*** **versus applied voltage at various flow rates with 19 fpi tube**

tially falls down on the electrode surface. As a result, the upper half of the tube may not be completely covered with liquid. As shown in Fig. 8, the smaller mesh electrode creates a strong electric field (E) at the electrode intake, where it lifts more liquid from the surface and attracts it to the electrode grid. Less flow rate of refrigerant reaches the heat transfer surface, and consequently the heat transfer coefficient is lower.

Figure 9 depicts variations of heat transfer coefficients for the turbo BIII tube at various heat fluxes. When compared to the results obtained with the smooth tube, where the heat transfer coefficients increase with applied voltage, here the heat transfer coefficient initially increases with applied voltage, reaches a maximum, and then decreases with further increase in applied voltage. It is believed that this behavior is due to the enhanced surface structure of the Turbo BIII tube. Turbo BIII is a mechanically formed re-entrant cavity boiling tube. The cavity structure of this tube is such that it keeps the bubbles sufficiently long in the cavity before their release. The application of the electric field tends to help to this mechanism up to a certain applied voltage. However, as the applied voltage exceeds an optimum, the bubbles are trapped in the cavities due to the electrohydrodynamic force. As a result, the additional force from the electrohydrodynamic effect pushes the bubbles towards the boiling surface, leading to a reduced evaporation rate and a sharp drop in heat transfer coefficients. Results also indicate that for a given applied potential, the heat transfer coefficient decreases as the heat flux increases due to the formation of dry out zones at high heat fluxes. The effect of flow rate on heat transfer coefficient at a heat flux of 10 kW/m^2 is shown in Fig. 10. The heat transfer coefficient initially increases up to a certain flow rate and then decreases. This indicates that for a given heat flux, there is an optimum film flow rate at which the heat transfer coefficient is maximum. A maximum enhancement of 90 percent in the heat transfer coefficient was obtained with this tube and took place at a heat flux of 10 kW/m^2 and a flow rate of 0.055 kg/m.s. The maximum electrohydrodynamic power consumption was less than 0.15 percent.

Figure 11 demonstrates the heat transfer results on a 19-fpi tube and an IWF electrode. The magnitude of enhancement is about equal at all three heat flux levels (25–30 percent). The rather low-enhancement magnitudes can be attributed to the nonuniform liquid distribution. Visual inspection showed that the presence of fins prevented a flow of fresh liquid to the heat transfer surface between two adjacent falling jets. However, as shown in Fig. 4, the electric field between the fin and the electrode can provide some suction of the liquid from the lower half of the tube to the neighboring fins, resulting in a partial film distribution. The effect of flow rate on the heat transfer coefficient is shown in Fig. 12. For the range of parameters tested, the heat transfer coefficient increases with increasing flow rate. For the current experiments maximum enhancement of 30 percent to 60 percent was found

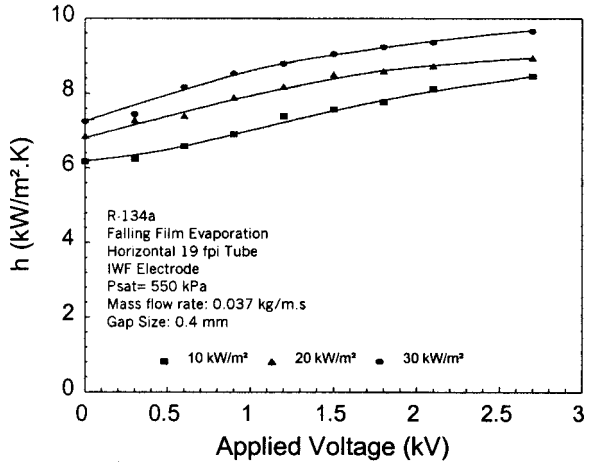

Fig. 11 ***h*** **versus applied voltage at various heat fluxes with 19 fpi tube**

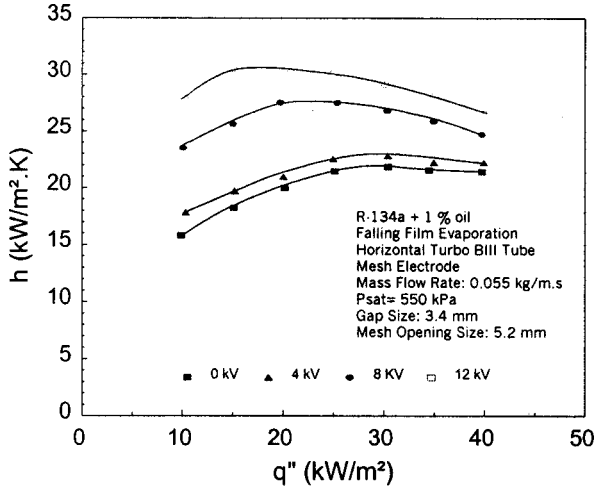

Fig. 13 ***h*** **versus heat flux at oil concentration of one percent**

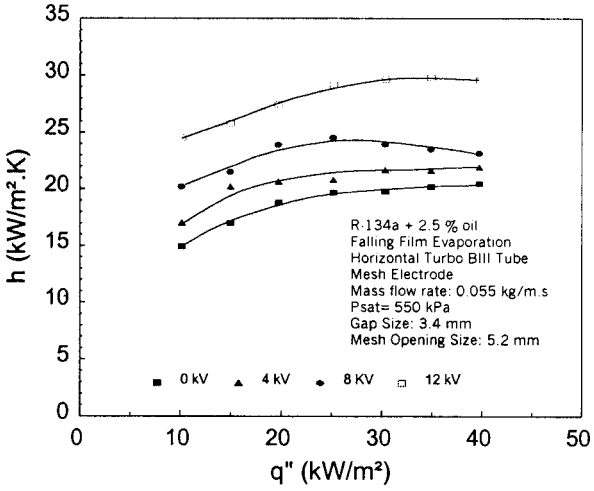

Fig. 14 *h* versus flux at oil concentration 2.5 percent

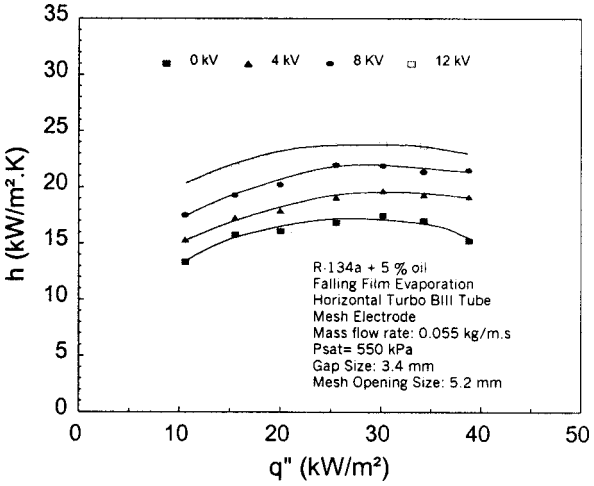

Fig. 15 *h* versus heat flux at oil concentration five percent

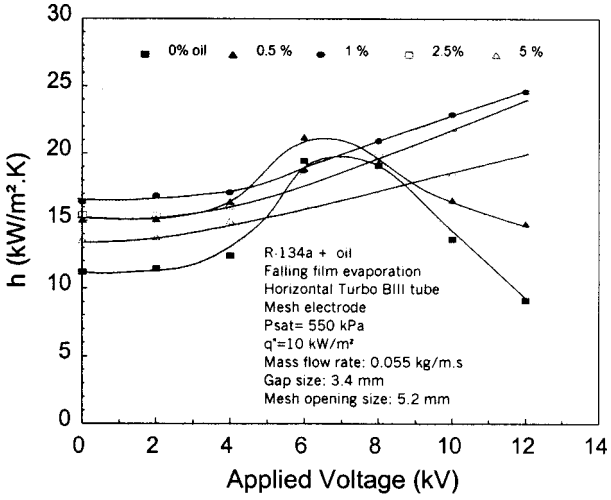

Fig. 16 *h* versus applied voltage at various oil concentration

with this tube/electrode geometry, depending on heat flux and flow rate. The electrohydrodynamic power consumption ratio (α) for the worst case was less than 0.25 percent.

Experiments were also performed to study the effect of polyolester oil on the heat transfer coefficient in the presence of the

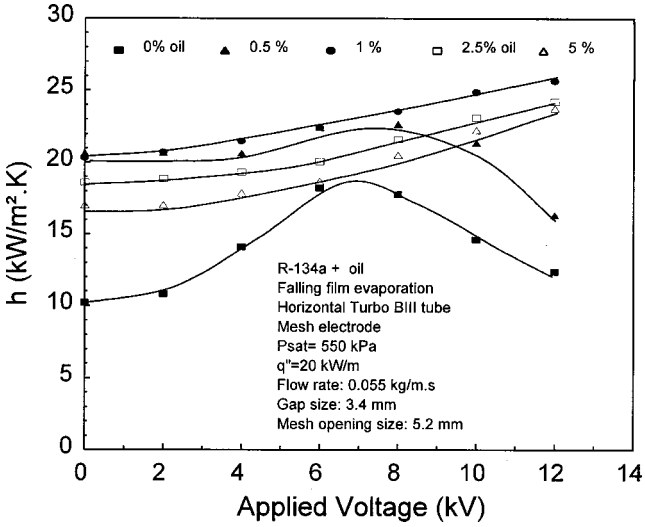

Fig. 17 *h* versus applied voltage at various oil concentration

electric fields. Four different concentrations of 0.5 percent, 1 percent, 2.5 percent, and 5 percent by mass fraction of the total mixture were investigated. Selected results depicting the effects of oil concentration as a function of heat flux are shown in Figs. 13–15. For all heat fluxes tested, as oil concentration increased from one to five percent, the heat transfer coefficient decreased. However, the heat transfer coefficient in the presence of oil was notably higher than that of pure R-134a for the range of oil concentrations studied. This applied to both the base case (0 kV) and when the field is applied. Up to 60 percent enhancement in the heat transfer coefficient was obtained at a heat flux of 10 kW/m^2 and an oil concentration of one percent. As seen in Figs. 16 and 17, unlike the pure refrigerant, where an increase in the applied voltage yielded an optimum point, the heat transfer coefficient in the presence of oil continued to rise with an increase in the applied potential.

It is likely that an improvement in the heat transfer coefficient is due to an increase in viscosity, surface tension, as well as electrical conductivity of the fluid, which serves to prevent the breakdown of the thin film over the heat transfer surface. A similar effect was observed during experiments with R-123 ([12]), which

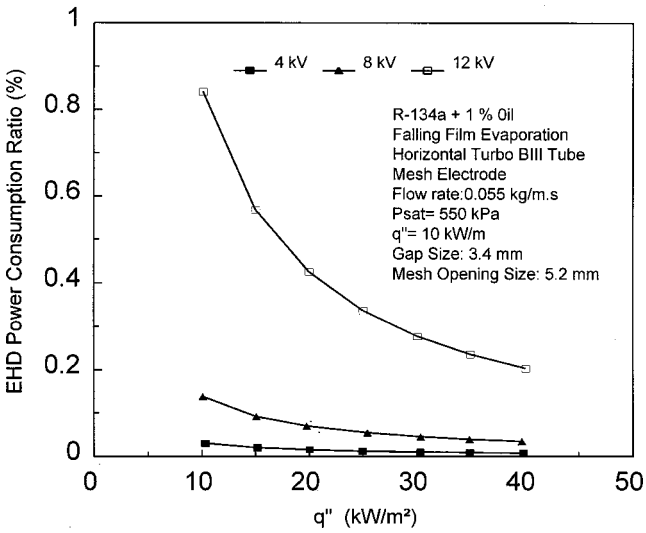

Fig. 18 Electrohydrodynamic power consumption at oil concentration of one percent

has a higher viscosity and surface tension than R-134. The effect of viscosity on the film breakdown was investigated by Bohn and Davis [16]. It was found that for a given heat flux, higher viscosities decrease the film breakdown. Increased viscosity yields better surface wettability and thus a lesser potential for film breakdown and surface dryout. After an optimum oil concentration (one percent in this case) is reached, a further increase in oil concentration tends to degrade the heat transfer performance. This may be due to deactivation of some of the internal cavities. For high oil concentrations, it is believed that residual oil accumulates in the cavities as the more volatile component of the oil/refrigerant mixture (the refrigerant in this case) evaporates. Thus, some of the cavities may become filled with oil. This would result in the blockage of fresh liquid to the cavities and the eventual degradation of the heat transfer coefficient.

Selected electrohydrodynamic power consumption data are depicted in Fig. 18, where the presence of oil caused considerably higher power consumption compared to the pure refrigerant case. The presence of the oil contributed to a higher electrical conductivity for the refrigerant/oil mixture. This leads to increased power consumption compared to the pure refrigerant (i.e., 0.15 percent at a heat flux of 10 kW/m^2).

Conclusions

Electrohydrodynamic-assisted falling film evaporation of R-134a on three horizontal tubes was examined experimentally. The results show that heat transfer performance can be significantly improved when compared to conventional technology. Enhancements up to 280 percent with the smooth tube, 90 percent with the Turbo Blll tube, and 60 percent with the 19-fpi tube were obtained. The corresponding electrohydrodynamic power consumption ratio in all cases was less than 0.2 percent. Experiments using smooth tubes and mesh electrodes indicated that a smaller mesh opening size and electrode gap at a given eclectic field strength resulted in lower heat transfer enhancement.

The enhancement factor decreased with increasing heat flux due to the presence of dryout zones on some parts of the heat transfer surface at high heat fluxes. It was found that for a given set of operating conditions, there is an optimum flow rate at which the electrohydrodynamic is most effective. It is believed that the enhancement mechanism is mainly due to the Maxwell instability at the liquid-vapor interface, electroconvection in the liquid, thinning of the liquid film, and atomization of the falling liquid into small droplets.

Small concentrations of a poloyl-ester lubricant were found to improve the heat transfer performance for the range of parameters tested. This applied to both the base case and when the electric field was applied. At an oil concentration of 1 percent up to a 60 percent enhancement in the heat transfer coefficient was obtained. However, the presence of oil resulted in higher electrohydrodynamic power consumption in all cases.

Nomenclature

A = heat transfer surface area (m^2)
D = diameter of the tube (m)
E = electric field (V/m)
fpi = fins per inch
f_e = electric body force (N/m^3)
h = average heat transfer coefficient (W/m^2.K)
I = current (A)
k = thermal conductivity (W/m.K)
L = test section length (m)
$\dot{m}$ = refrigerant flow rate (kg/s)
p = pressure (kPa)
q'' = heat flux (W/m^2)
Q = the test section heat transfer rate (W)
r = radius of the tube (m)
T = temperature (°C)
V = applied voltage (V)

Subscript

EHD = electrohydrodynamic
l = liquid
i = inside
o = outside
sat = saturation
v = vapor
w = wall

Greek

α = electrohydrodynamic power consumption ratio (percent)
δ = film thickness (m)
Γ = film flow rate per unit perimeter (kg/m.s)
ε = dielectric permittivity (N/V^2)
η = enhancement ratio (h/h_o)
ρ = mass density (kg/m^3)
ρ_c = electric charge density (Coul/m^3)
ϕ = electric field potential (V)

References

[1] Gropp, U., and Schlunder, E. U., 1986, ''The Effect of Liquid Side Mass Transfer on Heat Transfer and Selectivity During Surface and Nucleate Boiling of Mixtures in a Falling Film,'' Chem. Eng. Process., **20**, p. 103.

[2] Chyu, M. C., and Bergles, A. E., 1987, ''An Analytical and Experimental Study of Falling Film on a Horizontal Tube,'' J. Heat Transfer, **109**, pp. 983–990.

[3] Palen, J. W., Gropp, U., and Schlunder, E. U., 1986, ''The Effect of Liquid-Side Mass Transfer on Heat Transfer and Selectivity During Surface and Nucleate Boiling of Mixtures in a Falling Film,'' Chem. Eng. Process., **20**, pp. 103–114.

[4] Parken, W. H., Fletcher, L. S., Sernas, V., and Han, J. C., 1990, ''Heat Transfer Through Falling Film Evaporation and Boiling on Horizontal Tubes,'' J. Heat Transfer, **112**, pp. 744–750.

[5] Nakayama W., Daikoku, T., and Nakajima, T., 1982, ''Enhancement of Boiling and Evaporation on Structured Surfaces With Gravity Driven Film Flow of R-11,'' *Proceedings of the 7th International Heat Transfer Conference*, Vol. 4, Washington, DC, pp. 409–414.

[6] Moeykens, S. A., and Pate, M. B., 1994, ''Spray Evaporation Heat Transfer of R-134a on Plain Tubes,'' ASHRAE Trans., **100**, Part 2, pp. 173–184.

[7] Moeykens, S. A., and Pate, M. B., 1995, ''The Effects of Nozzle Height and Orifice Size on Spray Evaporation Heat Transfer Performance for a Low-Finned Triangular-Pitch Tube Bundle With R-134a,'' ASHRAE Trans., **101**, Part 2, pp. 408–419.

[8] Moeykens, S. A., Huebsch, W. W., and Pate, M. B., 1995, ''Effects of Surface Enhancement, Film-Feed Supply, and Bundle Geometry Upon Spray Evaporation Heat Transfer Performance,'' ASHRAE Trans., **101**, Part 2, pp. 420–433.

[9] Moeykens, S. A., Huebsch, W. W., and Pate, M. B., 1995, ''Heat Transfer of R-134a in Single-tube Spray Evaporation Including Lubricant Effects and Enhanced Surface Results,'' ASHRAE Trans., **101**, Part 1, pp. 111–123.

[10] Panofsky, W. K. H., and Phillips, M., 1962, *Classical Electricity and Magnetism*, Addison-Wesley, Reading, MA.

[11] Yamashita, K., and Yabe, A., 1997, ''Electrohydrodynamics Enhancement of Falling Film Evaporation Heat Transfer and its Long Term Effect on Heat Exchanger,'' J. Heat Transfer, ASME Transaction **119**, pp. 339–347.

[12] Darabi, J., Ohadi, M. M., and Dessiatoun, S. V., 1998, ''Heat Transfer Enhancement With Falling Film Evaporation on Vertical Tubes Using Electric Fields,'' *Proceedings of the ASME-Heat Transfer Division*, Vol. 1, ASME, New York, pp. 331–338.

[13] Darabi, J., Ohadi, M. M., and Dessiatoun, S. V., 1999, ''Falling Film and Spray Evaporation Enhancement Using Electric Fields,'' *Proceedings of the 5th ASME/JSME Joint Thermal Engineering Conference*, Mar. 15–19, San Diego, CA, to be published.

[14] Kline, S. J., and McClinock, F. A., 1953, ''Describing Uncertainties in Single Sample Experiments,'' Mech. Eng., **75**, Jan., pp. 3–8.

[15] Moffat, R. J., 1988, ''Describing the Uncertainties in Experimental Results,'' ASME J. Fluids Eng., **107**, pp. 250–260.

[16] Bohn, M. S., and Davis, S. H., 1993, ''Thermodynamic Breakdown of Falling Film at High Reynolds Numbers,'' Int. J. Heat Mass Transf., **36**, pp. 1875–1881.

Control-Volume Finite Element Analysis of Phase Change During Direct Chill Casting

X. Pu
Graduate Student, Department of Ocean Engineering, Florida Atlantic University, Boca Raton, FL 33431
e-mail: xiaoyanp@oe.fau.edu

A fully implicit control-volume finite element method is used to analyze the phase change during DC casting of aluminum alloy. The mathematical model is based on the integral form of the enthalpy equation. A Eulerian-Lagrangian transformation, together with a deforming grid technique, is introduced to efficiently track the evolution of the physical domain. The temperature distribution predicted by the numerical model is in good agreement with that measured in previous experiments. [S0022-1481(00)00502-8]

Keywords: Finite Element, Heat Transfer, Moving Boundaries, Numerical Methods, Phase Change, Solidification

Introduction

The control-volume finite element method has the features of both the traditional control-volume approach and the finite element technique in that the numerical approximation is obtained by the application of conservation principles on arbitrary control volume. The method has been widely used to solve problems of fluid flow and heat transfer. Voller and Peng [1] used a control-volume finite element method based deforming mesh technique and an enthalpy formulation to analyze a phase-change problem. Pu [2] and Minaie and Peng [3] applied it to study the solidification of aluminum alloy ingots during Direct Chill casting. The objective of this note is to provide some insights into the overall performance of the control-volume finite element method in solutions of alloy solidification.

In the present study, the numerical computation was performed to simulate the direct chill casting that was experimentally investigated by Drezet and Rappaz [4]. This casting process is schematically illustrated in Fig. 1. Initially, a rectangular empty mold is filled with molten aluminum from a top inlet. Solidification starts from the bottom block and side walls of the mold and continues toward the inside and top of the mold. When the mold is almost filled, the bottom block starts to move downward at a specific speed. As the ingot comes out of the mold, a water spray from the ends of the side walls of the mold impinges on the ingot. The casting process reaches a quasi-steady state when the ingot reaches 1.5~2 m in length with a 0.4~0.5-m-deep liquid pool occupying the top portion. At the quasi-steady state, with the ingot moving down, the depth of the liquid pool reaches a constant value while the temperature of the solid part decreases. The accurate prediction of the temperature distribution is important because all thermally induced failures such as butt curl or cold cracking are affected by temperature gradient ([5]).

Drezet and Rappaz [4] have also conducted the numerical analysis using the commercial finite element package ABAQUS. Since the energy equation used in their study was derived for a fixed physical domain, successive layers of elements had to be added to the computational domain at each time-step to account for the continuous growth of the ingot. The present model differs from the model of Drezet and Rappaz in that a deforming grid technique is adopted and the control-volume finite element method is used instead of the finite element method.

Contributed by the Heat Transfer Division for publication in the JOURNAL OF HEAT TRANSFER and presented at the 1998 AIAA/ASME Joint Thermodynamics Conference. Manuscript received by the Heat Transfer Division November 22, 1998; revision received December 1, 1999. Associate Technical Editor: C. Beckermann.

Mathematical model

The equation for energy balance in any arbitrary moving or deforming domain, without any internal energy generation, can be expressed in the integral form as follows ([1]):

$$\frac{d}{dt}\int_{V(t)}\rho H dV-\int_{S(t)}\left(\rho H v_j+k\frac{\partial T}{\partial x_j}\right)dS_j=0 \qquad (1)$$

where, for brevity, Einstein summation convention is used. In Eq. (1), $V(t)$ denotes the volume of the domain, $S(t)$ its boundary surface, and dS_j the jth component of vector differential area with the direction corresponding to normal outward vector of surface $S(t)$. V_j represents the relative velocity between the material and the control volume surface, ρ the specific mass, k the thermal conductivity, T the temperature, and H the enthalpy. The enthalpy H is the sensible heat for a solid body and the sum of sensible and latent heat for material in the liquid phase. Thus, H can be written as ([1])

$$H=(1-g)\int_{T_{\text{ref}}}^{T}C_{ps}(\zeta)d\zeta+g\int_{T_{\text{ref}}}^{T}C_{pl}(\zeta)d\zeta+gL \qquad (2)$$

where T_{ref} denotes the reference temperature, C_p the specific heat at constant pressure, g the liquid fraction, and L the latent heat. Subscripts s and l refer to solid phase and liquid phase, respectively. Equations (1) and (2) together with an appropriate formula for the determination of the liquid fraction, as given in a later section, give a heat conduction model for the numerical analysis of solidification problems.

Control-Volume Finite Element Formulation

Consider the computational domain as a union of four-node bilinear quadrilateral finite elements with nodes distributed at the element vertices. A control volume I surrounding each node is constructed by connecting midpoints of the element edges to the central point of the element, as illustrated in Fig. 2. Temperatures, liquid fractions, and thermophysical properties are specified at the node.

The energy equation for control volume I is obtained by replacing $V(t)$ and $S(t)$ in Eq. (1) with $V_I(t)$ and $S_I(t)$. Assuming thermophysical properties to be constant in the single-phase zones

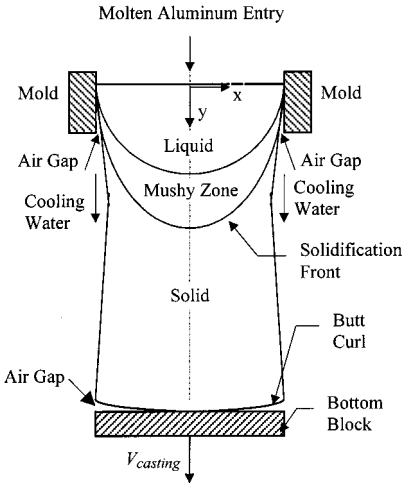

Fig. 1 Start-up stage of direct chill casting of an aluminum ingot

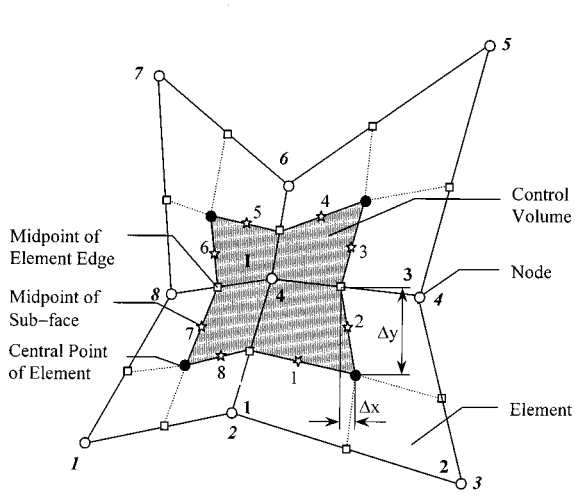

Fig. 2 The control volume *I* and its surrounding finite elements used in the control-volume finite element method

and to be linearly varying with respect to liquid fraction in the mushy zone, we obtain the governing equation for control volume I as

$$\frac{d}{dt}\int_{V_I(t)}(\lambda_g\theta+\rho_l gL)dV-\int_{S_I(t)}\left[(\lambda_g\theta+\rho_l gL)v_j+k_g\frac{\partial\theta}{\partial x_j}\right]dS_j=0 \tag{3}$$

where

$$\theta=T-T_{\text{ref}}\quad \lambda_g=(1-g)\rho_s C_{ps}+g\rho_l C_{pl}\quad k_g=(1-g)k_s+gk_l\,. \tag{4}$$

Here, $V_I(t)$ indicates the shaded area as shown in Fig. 2 and $S_I(t)$ the perimeter of the shaded area. The subscript g denotes linear interpolation of the quantity between liquid and solid phases.

Equation (3) is discretized using a fully implicit scheme. Applying a forward difference scheme to discretize the time derivative term associated with the volume integral, we obtain

$$\frac{d}{dt}\int_{V_I(t)}(\lambda_g\theta+\rho_l gL)dV = \frac{(\lambda_g\theta+\rho_l gL)_I^n V_I^n-(\lambda_g\theta+\rho_l gL)_I^{n-1}V_I^{n-1}}{\Delta t}. \tag{5}$$

Note the enthalpy is assumed to be uniform over the entire control volume I. Superscripts n and $n-1$ represent current time-step and previous time-step, respectively, and Δt the time-step size. $(*)_I$ denotes that the quantity in parentheses is evaluated at the node I. The integration around $S_I(t)$ is the sum of integration over eight subfaces numbered from 1 to 8. The area vector Δs^m over any subface m $(m=1,2,3,\ldots,8)$ is given by ([6])

$$\Delta s^m=\int_{S_I^m(t)}dS_j=\Delta y^m\mathbf{e}_x-\Delta x^m\mathbf{e}_y\,. \tag{6}$$

Δy^m and Δx^m denote the difference between y and x-coordinates, respectively, of the two end points of subface m. Both are measured in a counterclockwise sense around $S_I(t)$. The one-point Gauss integration rule is used for the integration over each subface m. Thus the surface integral term in Eq. (3) becomes

$$\int_{S_I(t)}\left[(\lambda_g\theta+\rho_l gL)v_j+k_g\frac{\partial\theta}{\partial x_j}\right]dS_j = \sum_{m=1}^{8}\left[\left(\lambda_g v_x\theta+k_g\frac{\partial\theta}{\partial x}\right)^m\Delta y^m-\left(\lambda_g v_y\theta+k_g\frac{\partial\theta}{\partial y}\right)^m\Delta x^m\right]^n + \sum_{m=1}^{8}\left[(\rho_l gLv_x)^m\Delta y^m-(\rho_l gLv_y)^m\Delta x^m\right]^n. \tag{7}$$

In Eq. (7), $(*)^m$ indicates that the quantity in parentheses is evaluated at the midpoint of subface m by interpolation. The interpolation is carried out using the nodal values and bilinear shape functions, as typically done in the finite element formulation ([7]).

For control volumes involving the external boundary, the relations are the same as in Eqs. (5) and (7), except that $m=1,2,3,4$ and an externally applied heat flux is incorporated in the energy equation to account for the energy balance over the external boundary. The same is true for control volumes at corners, but with $m=1,2$.

The governing equations are discretized on a control-volume by control-volume basis. The discretization process leads to a system of algebraic equations which are iteratively solved by following these steps:

1 The liquid fraction field at the current iteration is set to values from the previous iteration.

2 The system of algebraic equations is solved using the Gaussian elimination method for nodal temperatures.

3 Nodal liquid fractions of the current iteration are updated based on the temperature field obtained in Step 2.

4 As the next iteration, Steps 1 to 3 are repeated until the relative difference between the sum of all nodal temperatures at the current iteration and that at the previous iteration is less than a prescribed small value.

5 The temperatures and liquid fractions of previous time-step are updated with current values.

6 The computational mesh is deformed so as to conform to the updated shape of the physical domain.

7 As the next time-step, Steps 1 to 6 are repeated. Thus, the solution is advanced in time.

Solution Procedure Verification

To validate the numerical model, a one-phase Stefan problem was analyzed ([8]). A solid slab, which is initially at the phase-change temperature of $T_m=0$, is imposed a unit temperature at its left boundary at time $t=0$. The parameters are set as $\rho=C_p=k=1$ and $L=0.2$. The liquid region is chosen as the computational

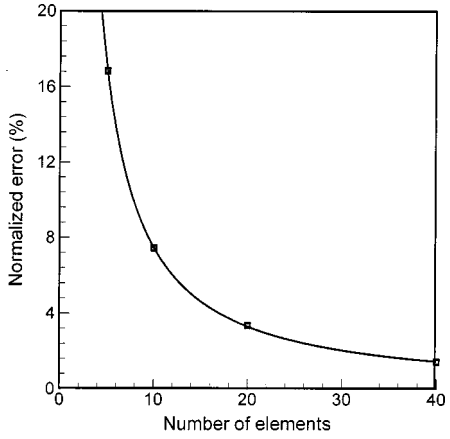

Fig. 3 Variation of the normalized errors in interface locations of the one-dimensional Stefan problem as a function of the number of elements

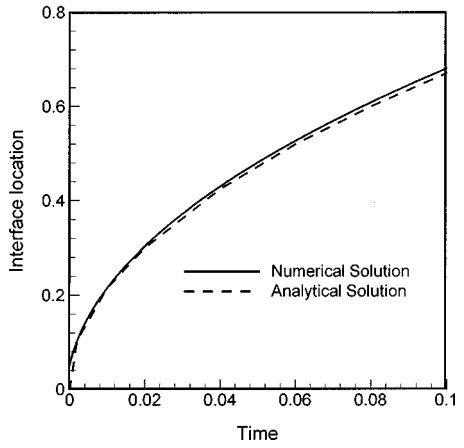

Fig. 4 Time evolution of the interface location corresponding to the one-dimensional Stefan problem

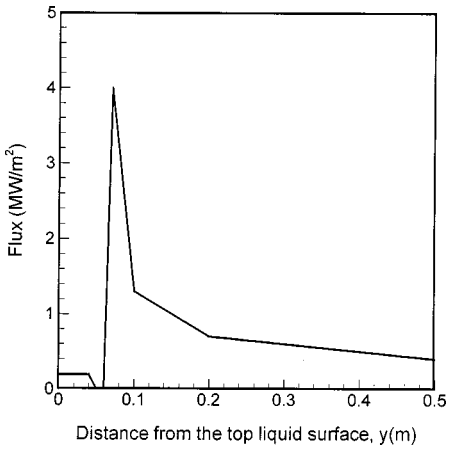

Fig. 5 Distribution of heat flux on the lateral surface of the ingot ([4], Fig. 4)

domain with its right moving boundary aligning with the interface location where $T=0$ and $g=0.5$. Calculations were carried out using 5, 10, 20, and 40 uniformly deforming elements and a time-step of $\Delta t=0.001$. Figure 3 shows the normalized error in interface locations up to $t=0.1$ as a function of the number of elements. It is obvious that the numerical error is largely reduced when the number of elements increases. Figure 4 compares the predicted interface locations with the exact solutions. Excellent agreements can be observed.

Numerical Results and Discussion

The prediction of the temperature distribution during direct chill casting of an AA1201 aluminum alloy ingot is explained in this section. A two-dimensional heat conduction model is assumed in the present study. As shown in Fig. 1, the symmetry of the ingot allows consideration of only the right half of the (xy)-plane. The computational domain, initially 0.255×0.06 m in size, evolves to 0.255×2 m by the end of the casting process, at a specific casting speed of 0.06 m/min.

The boundary conditions are as follows. Along the symmetry axis y, the zero flux condition, $\partial T/\partial x=0$, is applied. At the top liquid surface, temperature is specified as $T_{in}=943$ K, the melt temperature. The distribution of heat flux, $\dot{q}''(y)$, for $y\leqslant 0.5m$ on the lateral surface is as given in Fig. 5. In the region where $y>0.5m$, heat flux is assumed to be constant with a value equal to that at $y=0.5m$. At the convective boundary between the ingot and the bottom block, the heat transfer coefficient $h=2000\ \mathrm{W/m^2\cdot K}$. The temperature on the surface of the bottom block, T_f, is set to 373 K.

The thermophysical properties used in the numerical computation are as follows: $T_l=931$ K, $T_s=903$ K, $L=3.58\times 10^5$ J/kg,

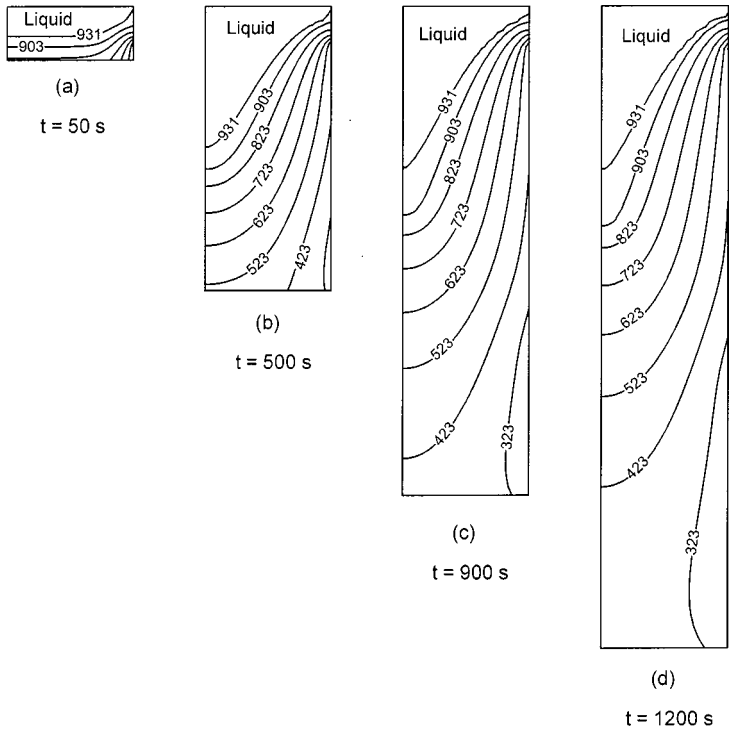

Fig. 6 Evolution of temperature (K) contours during the downward movement of the growing ingot

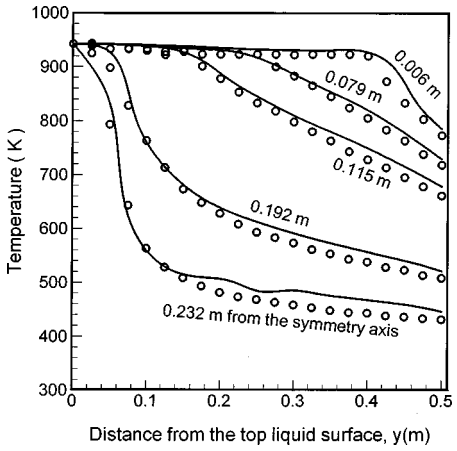

Fig. 7 Computed results (solid lines) and measurements (circles; [4], Fig. 3) of temperature distributions along the casting direction at five particular positions measured from the symmetry axis of the ingot under quasi-steady state

$\rho_l = \rho_s = 2650$ kg/m^3, $C_{pl} = 1086$ J/kg·K, $C_{ps} = 905$ J/kg·K, $k_l = 150$ W/m·K (enhanced by two-thirds of k_l to account for the effect of flow in the melt), and $k_s = 227$ W/m·K. The solidus temperature is used as the reference temperature. The liquid fraction is given as $g = \max(0,\min(1,(T - T_s)/(T_l - T_s)))$. Initial conditions correspond to $T_0 = 943$ K and $g = 1$ at all nodes.

To find an appropriate time-step and mesh size, a sensitivity analysis was first performed using 20×40, 20×100, 40×60, and 40×80 uniform elements with $\Delta t = 5$ s, 10 s, 15 s, and 30 s, respectively. The simulation was terminated at $t = 2000$ s. The temperature distribution along the symmetry axis was used for comparison. The calculated results show that refining the mesh in the *x*-direction improves the accuracy more efficiently than by refining in the *y*-direction. Thus, 40×60 elements with a time-step of five seconds were used. The element size in the *x*-direction is kept constant, while that in the *y*-direction is updated at each time-step by dividing the total cast length by the number of elements.

From the instantaneous isothermal contours in the ingot shown in Figs. 6(*a*) to 6(*d*), one can observe the development of the solidification pattern from initial stage to the final quasi-steady state. Figure 6(*a*) shows that at the beginning of the casting process, the liquid pool occupies more volume than the solidifying shell. This is because only a small portion of the lateral surface of the ingot is exposed to the cooling water, and the amount of heat extracted by the water flow is not enough to balance the heat transported by the incoming liquid metal. Figures 6(*b*) and 6(*c*) illustrate that as the ingot continuously moves, the region exposed to the cooling water increases and thereby solidifies more liquid. From Figs. 6(*c*) and 6(*d*), it is apparent that the depth of the liquid pool no longer changes with time after $t \approx 900$ s, implying that the casting process has reached its quasi-steady state. Under quasi-steady state, the variation of temperatures on a great portion of the ingot is stationary with respect to the top liquid surface although the temperature is slowly varying with time in the region near the bottom block. At this stage, heat input from the top inlet is equal to the heat removed from the system, and the volume of the liquid pool is constant. The growth of the ingot thus corresponds to the growth of the solidifying shell.

The calculated temperature distributions under quasi-steady state at positions of 0.006 m, 0.079 m, 0.115 m, 0.192 m, and 0.232 m from the symmetry axis of the ingot are plotted as functions of the distance from the top liquid surface of the ingot in Fig. 7. The experimental measurements given by Drezet and Rappaz [4] are also plotted for comparison. We find that the numerical results obtained using control-volume finite element method agree quite well with measurements. The small difference could be due to the assumptions in the model, as previously mentioned, such as piecewise constant thermophysical properties and the omission of the air gap between the ingot and the bottom block.

Conclusion

The control-volume finite element method has been applied to the solidification during direct chill casting. Good agreement found between numerical results and experimental data demonstrates that the control-volume finite element method together with the enthalpy formulation and a Eulerian-Lagrangian transformation, is a robust and efficient tool for analyzing phase change during direct chill casting.

Acknowledgments

The author would like to thank Prof. P. Ananthakrishnan of the Department of Ocean Engineering at Florida Atlantic University for his help in revising this note.

References

[1] Voller, V. R., and Peng, S., 1994, ''An Enthalpy Formulation Based on an Arbitrarily Deforming Mesh for Solution of the Stefan Problem,'' Comput. Mech., **14**, No. 5, pp. 492–502.
[2] Pu, X., 1998, ''Application of Control Volume Finite Element Method to Phase Change Problems During DC Casting,'' *Proceedings of the 1998 7th AIAA/ASME Joint Thermophysics and Heat Transfer Conference*, Part 3, ASME, New York, pp. 3–14.
[3] Minaie, B., and Peng, S., 1998, ''Implicit Analysis of Filling and Solidification During the Start-up Stage of DC Casting Process,'' *Modeling of Casting, Welding, and Advanced Solidification Processes VIII*, B. G. Thomas and C. Beckermann, eds., The Minerals, Metals & Materials Society, Warrendale, PA, pp. 647–654.
[4] Drezet, J.-M., and Rappaz, M., 1996, ''Modeling of Ingot Distortions During Direct Chill Casting of Aluminum Alloys,'' Metall. Mater. Trans. A, **27A**, pp. 3214–3225.
[5] Hannart, B., Cialti, F., and Van Schalkuijk, R., 1994, ''Thermal Stresses in DC Casting of Aluminum Slabs: Application of a Finite Element Model,'' *Light Metals*, U. Mannweiler, ed., The Minerals, Metals & Materials Society, Warrendale, PA, pp. 879–887.
[6] Schneider, G. E., 1988, ''Elliptic Systems: Finite-Element Method I,'' *Handbook of Numerical Heat Transfer*, Wiley, New York, pp. 379–420.
[7] Reddy, J. N., and Gartling, D. K., 1994, *The Finite Element Method in Heat Transfer and Fluid Dynamics*, CRC Press, Boca Raton, FL.
[8] Alexiades, A., and Solomon, A. D., 1993, *Mathematical Modeling of Melting and Freezing Processes*, Hemisphere, New York, pp. 218–220.

Journal of Heat Transfer

Discussion

Discussion: ''Thermal Contact Resistance of Silicone Rubber to AISI 304 Contacts'' [ASME J. Heat Transfer, 121, pp. 700–702 (1999)][1]

C. V. Madhusudana
School of Mechanical and Manufacturing Engineering, The University of New South Wales, Sydney 2052, Australia

The authors are to be complimented on this interesting and informative paper. I have, however, the following comments.

1 Elastomers are time sensitive and continue to deform under load (room temperature creep). Because of this, the contact resistance may be expected to vary with time. Were any attempts made to investigate the time-dependence of the resistance?

2 The Results and Discussion section of the paper appears to indicate that the conductivity, k_r, of the silicone rubber is accurately known. The bulk resistance, R_b, then equals (t/k_r), where t is the thickness of the rubber. How does this compare with the measured value of R_b?

3 In Tables 1 and 2, the mean asperity slopes are expressed in terms of [μm/m]. This means that the slopes for the metal surfaces range from 0.143×10^{-6} to 0.427×10^{-6}. These values seem to be extremely small. Our experience with similar metallic surfaces indicates that the slopes are of the order of 0.2. I believe, therefore, that the slopes should have been expressed in terms of [μm/μm] and not [μm/m].

4 In the second to last paragraph of the paper it is said that: ''At the lower interface the heat flow is from metal to elastomer . . . ''. This is incorrect. The heat flow is from elastomer to metal at the lower interface. (At the *upper* interface, the heat flow is from metal to elastomer, as correctly stated in the paper.)

I would appreciate the authors' response to the above remarks.

[1]Parihar, S. K., and Wright, N. T., 1999, ''Thermal Contact Resistance of Silicone Rubber to AISI 304 Contacts,'' ASME JOURNAL OF HEAT TRANSFER, Vol. 121, pp. 700–702.

Closure to ''Discussion of 'Thermal Contact Resistance of Silicone Rubber to AISI 304 Contacts' '' [ASME J. Heat Transfer, 122, p. 403 (2000)]

S. K. Parihar

N. T. Wright
e-mail: wright@umbc.edu

Department of Mechanical Engineering, University of Maryland, Baltimore, MD 21250

We appreciate Professor Madhusudana's careful reading of our paper and value his comments. Our response to his concerns follows.

1 Time Dependence of Resistance. During tests of more than 40 hours at constant mechanical load (0.1214 MPa) and heater power (3.2 kW/m^2), the resistances varied by less than $\pm$2.5 percent after reaching steady state. There was no trend, either increasing or decreasing, in the values of the resistances. Surface profiles of the contacting surfaces were measured before and after the test and, as shown in Table 2 of [1], no significant difference was found in the surface profiles of the specimen. This indicates that, within the range of temperatures and mechanical loads tested, no significant changes in the surface characteristics occur during the duration of the test.

2 Bulk Resistance. The thermal conductivity of the elastomer under investigation was measured before conducting the thermal contact resistance tests. Assuming a linear temperature distribution between adjacent thermocouples in an elastomer specimen, the thermal conductivity for the range of temperatures and mechanical loads to be tested was calculated using Fourier's equation. The thermal conductivity of the elastomer is temperature-dependent, so care must be taken in calculating the bulk resistance from the thickness and thermal conductivity. Nevertheless, the bulk resistances calculated from the thickness and the measured thermal conductivity values agree well ($\pm$5 percent) with the bulk resistance obtained by subtracting the sum of the measured interface resistances from the total resistance of the joint. The details may be found in Parihar [2].

3 Asperity Slope. You are right, the units in Table 1 and 2 should read μm/μm.

4 Heat Flow Direction. Yes, at the lower interface the heat flow is from elastomer to metal.

Reference

[1] Parihar, S. K., and Wright, N. T., 1999, ''Thermal Contact Resistance of Silicone Rubber to AISI 304 Contacts,'' ASME J. Heat Transfer, **121**, pp. 700–702.
[2] Parihar, S. K., 1997, ''Thermal Contact Resistance of Elastomer to Metal Contacts,'' Ph.D. dissertation, University of Maryland, Baltimore, MD.

Journal of Heat Transfer

Letter to the Editor

Standard Nomenclature List

Dear Editor,

It was with great interest that I learned of the efforts by a group of journal editors (including yourself) to produce a ''standard'' nomenclature list for heat transfer which will be used for all the journals represented. The adoption of such a list is obviously a considerable step forward for the journals and I was pleased to learn that the list developed through the discussions at the International Heat Transfer Conferences (led by Dr. Yon Mayhew) had served as basis. Indeed, the vast majority of symbols are identical to this earlier list and some of the best features of the IHTC list have been retained (for example, the use of consistent nomenclature for quantity, flow, and flux—e.g., M, $\dot{M}$, $\dot{m}$). The new list differs from the IHTC list only in essentials!

Having spent many tedious hours discussing these questions (both at the IHTC's and in many other meetings) I had thought that the question of nomenclature had been finally settled and I certainly do not wish to go through the unproductive and time-consuming process all over again. However, it does seem to me that symbols from the IHTC list had been developed as a result of input from a wide variety of sources and should not be abandoned without some thought being given to the matter! One of the most contentious issues (on which those of us involved in the original discussions spent many hours) was the symbol of heat transfer coefficient, arguably the most important symbol in the list. The use of the symbol α was common European practice whereas the U.S. and U.K. practice was to use h. Clearly, the use of h was not very sensible since the same symbol is used for enthalpy and there are a significant number of cases when both symbols might be used in the same equation. However, such was the tradition of using h that it was allowed as an *alternative* symbol in the IHTC list. In the original discussions, a compromise was reached in which α was adopted for film coefficient and U for overall coefficient. To simply choose h in the new list is to ignore all the earnest deliberations which had gone on before (not that there is anything new in this approach in this area!). I had been very reluctant to make the change to α but gradually, I got used to it! Now, if we used the Editors list, we will have to go through the reverse process—ugh!

An area which is also a cause for considerable concern is that of the symbols used for physical properties. Here, I think it is essential to use symbols which are consistent with those adopted by the ISO. People like myself have been brought up using μ for viscosity and it has been a real struggle to change to the ISO standard η. Now, the Editors have overruled the ISO, I suppose that the struggle has been in vain!

As a practical way out of the problem, the Editors might like to consider using the IHTC symbols as alternatives. It is very tempting to fix on a given symbol, but if the choice is debatable or even irrational, then an error is propagated into the future!

I realize that I have little hope of changing the newly adopted list and I certainly do not wish to enter into further protracted discussions about this area. This letter is mainly to assuage the guilt I would have felt had I not reacted in some way!

G. F. Hewitt
Department of Chemical Engineering
and Chemical Technology,
Imperial College of Science, Technology and Medicine
London SW7 2BY, England
e-mail: g.hewitt@ic.ac.uk

Journal of Heat Transfer

Errata

Erratum: "Mixture Fraction Statistics of Plane Self-Preserving Buoyant Turbulent Adiabatic Wall Plumes" [ASME J. Heat Transfer, 121, pp. 837–843 (1999)]

R. Sangras, Z. Dai, and G. M. Faeth

Table 3, which follows, was inadvertently omitted from the originally published paper.

Table 3 Summary of self-preserving properties of plane buoyant turbulent plumes[a]

Source	Plume Type	Z/b	$(x-x_o)/b$	$(Z/l_f)_{\min}$	$(x-x_o)/l_M$	$l_f/(x-x_o)$	$F_{\max}$	$\overline{f'}_{\max}/\overline{f}_{\max}$
Present	Adiabatic Wall	93	92–155	7.9	12–21	0.076	5.71	0.37
Lai et al. (1986)[b]	Adiabatic Wall	38	10–38	10.8	1–5	0.093	6.80	0.34
Grella and Faeth (1973)[b,c]	Adiabatic Wall	—	—	13.0	—	0.077	7.50	—
Liburdy and Faeth (1978) and Liburdy et al. (1979)[b,c]	Isothermal Wall	—	—	5.9	—	0.112	5.20	0.25
Sangras et al. (1998)	Free Line	93	76–155	2.6[d]	9–21	0.120	2.10	0.47

[a]Plane buoyant turbulent plumes in still and unstratified environments. Wall plumes are along vertical smooth surfaces. Range of streamwise distances are for conditions where measurements were made over the cross section of the plumes. Adiabatic wall plume entries are ordered chronologically.

[b]These flows were evolving over the range of the measurements so that the values of $l_f/(x-x_o)$, $F_{\max}$, and $\overline{f'}_{\max}/\overline{f}_{\max}$ pertain to results obtained farthest from the source.

[c]Source was a linear array of round jets so that slot properties cannot be defined.

[d]This value is $(Z/(2l_f))_{\min}$, which is the full characteristic width of the flow, similar to the other entries in this column.

